SUPER SUBSTORM RELATED SIGNATURES AT MIDDLE AND LOW LATITUDE IONOSPHERE

A THESIS SUBMITTED TO THE

CENTRAL DEPARTMENT OF PHYSICS

INSTITUTE OF SCIENCE AND TECHNOLOGY

TRIBHUVAN UNIVERSITY
NEPAL

FOR THE AWARD OF

DOCTOR OF PHILOSOPHY
IN PHYSICS

BY
DRABINDRA PANDIT

APRIL 2022

SUPER SUBSTORM RELATED SIGNATURES AT MIDDLE AND LOW LATITUDE IONOSPHERE

A THESIS SUBMITTED TO THE

CENTRAL DEPARTMENT OF PHYSICS

INSTITUTE OF SCIENCE AND TECHNOLOGY

TRIBHUVAN UNIVERSITY
NEPAL

FOR THE AWARD OF

DOCTOR OF PHILOSOPHY
IN PHYSICS

BY
DRABINDRA PANDIT

APRIL 2022

DECLARATION

Thesis entitled **"Super Substorm Related Signatures at Middle and Low Latitude Ionosphere"** which is being submitted to the Central Department of Physics, Institute of Science and Technology (IoST), Tribhuvan University, Nepal for the award of the degree of Doctor of Philosophy (Ph.D.), is a research work carried out by me under the supervision of Prof. Dr. Narayan Prasad Chapagain, Department of Physics, Amrit Campus, Tribhuvan University, Thamel, Kathmandu, Nepal and co-supervision of Dr. Binod Adhikari, Department of Physics, Patan Multiple Campus, Tribhuvan University, Patandhoka, Lalitpur, Nepal.

This research is original and has not been submitted earlier in part or full in this or any other form to any university or institute, here or elsewhere, for the award of any degree.

Drabindra Pandit

RECOMMENDATION

This is recommended that **Mr. Drabindra Pandit** has carried out research entitled **"Super Substorm Related Signatures at Middle and Low Latitude Ionosphere"** for the award of Doctor of Philosophy (Ph.D.) in **Physics** under our supervision. To our knowledge, this work has not been submitted for any other degree.

He has fulfilled all the requirements laid down by the Institute of Science and Technology (IoST), Tribhuvan University, Kirtipur for the submission of the thesis for the award of Ph.D. degree.

. . . .

Dr. Narayan Prasad Chapagain
Supervisor
(Professor)
Department of Physics
Amrit Campus
Tribhuvan University
Thamel, Kathmandu
Nepal

. . . .

Dr. Binod Adhikari
Co-supervisor
(Assistant Professor)
Department of Physics
Patan Multiple Campus
Tribhuvan University
Patandhoka, Lalipur
Nepal

APRIL 2022

LETTER OF APPROVAL

[Date: 04/10/2022]

On the recommendation of Prof. Dr. **Narayan Prasad Chapagain** and Dr. **Binod Adhikari**, this Ph.D. thesis submitted by **Drabindra Pandit**, entitled **"Super Substorm Related Signatures at Middle and Low Latitude Ionosphere"** is forwarded by Central Department Research Committee (CDRC) to the Dean, Institute of Science and Technology (IoST), Tribhuvan University.

. . . .

Dr. Om Prakash Niraula

Professor

Head

Central Department of Physics

Tribhuvan University

Kirtipur, Kathmandu

Nepal

ACKNOWLEDGEMENTS

Drabindra Pandit
APRIL, 2022

ABSTRACT

The knowledge and understanding of space weather events are necessary for many practical applications such as for alleviating the impact of space weather on communication technologies, navigation systems, electric appliances-power grids, space explorations, and other scientific experiments, research and applications. One of the most important factors that directly impacts on space weather is the ionospheric variability. The ionospheric refraction can induce errors of several meters in the satellite receiver ranges and frequent occurrence of plasma irregularity that may lead to signal degradation while passing through them.

In this thesis work, we have studied the characteristics of the solar wind plasma parameters and geomagnetic indices during super intense geomagnetic storms and Super Substorms (SSSs) using the data available from Omni web site. In order to study the spectral characteristics of SSSs events, Continuous Wavelet Transform (CWT) and Global Wavelet Spectrum (GWS) techniques are used. The CWT is used to identify the short-lived high frequency signals present as singularities and transient structures which are associated to the respective frequencies of the geomagnetic disturbances. The GWS identifies the most energetic periods present during the SSSs. Moreover, the cross-correlation analysis has been applied to analyze the degree of correlation and time lag between two variables. For such study, the cross correlation between Interplanetary Magnetic Field (IMF) B_z and AE index, and between variation in horizontal component of geomagnetic field at equatorial, mid, and high latitude with Field Aligned Current (FAC), Polar Cap Voltage (PCV), Ring Current (RC), Aurora Precipitation (AP), Joule's Heating (JH), and Total Energy (TE) deposited inside the magnetosphere are deployed to identify the degree of association and their leading or lagging. In addition, the characteristics of the regular variation of ionosphere has been studied using long-term ground based Global Positioning System (GPS) Total Electron Content (TEC) data from 2008 to 2018 from UNAVCO website over Nepal at low-mid latitude region. Similarly, the disturbed ionospheric variability has been examined in the course of four super intense geomagnetic storms in March 2015, June 2015, May 2017, and September 2017 of solar cycle 24. The GPS TEC obtained from Receiver Independent Exchange Format (RINEX) observations file is also compared to global ionospheric models: CODG and IGSG. The change in thermospheric O/N_2 ratio during super intense storm has been analyzed using Global Ultraviolet Imager (GUVI) Thermosphere, Ionosphere, Mesosphere Energetics and Dynamics (TIMED) satellite observations. The effect on horizontal (H) component of geomagnetic field during SSSs are examined using magnetic data from

high latitude (ABK, FCC, MGD, and UPS), mid-latitude (ABG, BOU, DUR, and PHU), and equatorial stations (API, GUA KOU and MBO). Furthermore, ionosonde data for the critical frequency of F_2 layer of the ionosphere (foF_2), virtual height of F layer of the ionosphere ($h'F$), and height of the peak electron density of F_2 layer of the ionosphere (hmF_2) from Boulder, Colorado, USA (40° N, 105° W) are used to investigate the ionospheric variability during SSSs events.

The results of regular inospheric variability show diurnal variation of Vertical Total Electron Content (VTEC) peak amplitude and the shape depend on solar cycle phases. The flat diurnal peak is observed during minimum and descending year of solar cycle, but Gaussian with varying peak amplitude is noticed during ascending and maximum phases. The maximum TEC is found at around 11:00LT to 14:00LT and minimum is noticed in the pre-dawn periods. The wavy nature of diurnal profile is identified in year 2008, 2009, and 2010, whereas the parabolic nature is detected in year from 2011 to 2017. During the minimum years of solar cycle, ionosphere is characterized by lower value of TEC and during the maximum year of solar cycle, it has higher TEC, which resembles with variation in the Sunspot Number (SSN) and solar flux of respective years. The correlation between VTEC and SSN and between VTEC and solar flux are found to be ~0.97. Moreover, the GPS VTEC obtained during super intense storm shows similarity between observed VTEC and the global ionospheric models CODG and IGSG. But during the geomagnetically quiet period, there is discrepancy between GPS VTEC and modeled (CODG and IGSG) based VTEC over Nepalese stations and it is significant beyond 5 TECU in absolute values. Decrease in O/N_2 ratio is identified during geomagnetic storms of March 2015 and June 2015, whereas increase in O/N_2 is noticed during storm of May 2015 and September 2017.

Moreover, the cross-correlation analysis between the IMF B_z and AE index during SSSs shows the average correlation coefficient ~ -0.88 between the AE and IMF B_z and approximately, with zero lag. Similarly, negative correlation about ~ -0.7 to -1.0 were obtained between delta H with FAC, PCV, RC, JH, AP, and TE. The zero-time lag is identified for FAC, PCV, JH, AP, and TE, although approximately 30 min time lag was obtained for ring current. This supports the coupling mechanism between IMF B_z and north component of geomagnetic field in the course of SSSs at the surface of magnetosphere during which many charge particles and energy are injected into Earth's magnetosphere and ionosphere. Similarly, decrease in foF_2 is noticed during SSSs of 24 August 2005 and 8 September 2017, and increase in foF_2 is identified during SSS of 7 September 2017. This study not only provides insight into SSSs, but also its effects on H-component of geomagnetic field and ionospheric parameters. Additionally, TEC variability over Nepal aims at providing a possible way to improve the space weather forecasting capability from the ground and space-based measurements.

LIST OF ACRONYMS AND ABBREVIATIONS

ACE	Advanced Composition Explorer
AE	Auroral Electrojet
AL	Auroral Low
AO	Artic Oscillation
AP	Aurora Precipitation
APL	Applied Physics Laboratory
AU	Astronomical Unit
AU	Auroral Up
C/A-code	Course/Acquisition-Code
CAS	Chinese Academy of Sciences
CCD	Charge-Coupled Device
CEJ	Counter Electrojet
CHAMP	Challenging Minisatellite Payload
CIR	Corotating Interaction Region
CME	Coronal Mass Ejection
CODE	Center for Orbit Determination in Europe
COSMIC	Constellation Observing System for Meteorology, Ionosphere, and Climate
CWT	Continuous Wavelet Transform
DDEF	Disturbance Dynamo Electric Field
Dst	Disturbed Storm Time
EEJ	Equatorial Electrojet
EIA	Equatorial Ionization Anomaly
EPB	Equatorial Plasma Bubble
ESA	European Space Agency
EUV	Extreme Ultraviolet
FAC	Field Aligned Current
FT	Fourier Transform
GIC	Geomagnetic Induced Current
GIM	Global Ionospheric Map
GIRO	Global Ionospheric Radio Observatory
GMD	Geomagnetic Disturbance
GNSS	Global Navigation Satellite Systems

GOES	Geostationary Operational Environmental Satellite
GPS	Global Positioning System
GSE	Geocentric Solar-Elliptic
GSM	Geocentric Solar-Magnetospheric
GUVI	Global Ultraviolet Imager
GWS	Global Wavelet Spectrum
HILDCAA	High Intensity Long Duration Continuous Auroral Activity
HSS	High Speed Streamer
ICME	Interplanetary Coronal Mass Ejection
IGS	International GNSS Service
IMF	Interplanetary Magnetic Field
IONEX	IONosphere Map Exchange
IRI	International Reference Ionosphere
JH	Joule's Heating
JHU	Johns Hopkins University
JPL	Jet Propulsion Laboratory
LEO	Low Earth Orbit
LT	Local Time
MC	Magnetic Cloud
NASA	National Aeronautics and Space Administration
NNSS	Navy Navigation Satellite System
P-code	Precise-Code
PC	Polar Cap
PCN	Polar Cap North
PCS	Polar Cap South
PCV	Polar Cap Voltage
PNT	Positioning, Navigation and Timing
PPEF	Prompt Penetration of Electric Field
PRE	Pre-reversal Enhancement
PRN	Pseudorandom Noise
RC	Ring Current
RINEX	Receiver Independent Exchange Format
RM	Russell McPherron
ROCSAT-1	Republic of China Satellite 1
RTI	Rayleigh-Taylor Instability
SCW	Substorm Current Wedge
SEM	Space Environment Monitor

SEP	Solar Energetic Proton
SFI	Solar Flux Index
SFU	Solar Flux Unit
SML	Super Magnetic Low
SMS	São Martinho da Serra
SOHO	Solar and Heliospheric Observatory
SSC	Sudden Storm Commencement
SSN	Sunspot Number
SSS	Super Substorm
STEC	Slated Total Electron Content
TAD	Travelling Atmospheric Disturbances
TE	Total Energy
TEC	Total Electron Content
TID	Travelling Ionospheric Disturbances
TIE-GCM	Thermosphere Ionosphere Electrodynamics General Circulation Model
TIMED	Thermosphere, Ionosphere, Mesosphere Energetics and Dynamics
UPC	Universitat Politècnica de Catalunya
USA	United State of America
UV	Ultra Violet
VTEC	Vertical Total Electron Content
WFT	Window Fourier Transform
WHU	Wuhan University

LIST OF SYMBOLS

B	Magnetic field
B_z	Southward component of interplanetary magnetic field
E	Electric field
E_y	Eastwards component of electric field
T_{sw}	Solar wind temperature
P_{sw}	Solar wind pressure
N_{sw}	Solar wind density
V_{sw}	Solar wind velocity
ϵ_0	Permittivity of free space
H	Horizontal
Z	Vertical component
D	Angle of declination
L	Lagrangian point
$foF2$	Critical frequency of F2 layer of the ionosphere
$h'F$	Virtual height of F2 layer of the ionosphere
hmF_2	Height of the peak electron density of F2 layer of the ionosphere
r	Correlation coefficient
N	North
S	South
E	East
W	West
$\%$	Percentage
ν	Frequency
λ	Wavelength
σ	Conductivity
J	Current density
L_1	First carrier waves
L_2	Second carrier waves
R_E	Radius of the Earth

LIST OF TABLES

LIST OF FIGURES

TABLE OF CONTENTS

CHAPTER 1

1. INTRODUCTION

1.1 Sun and Earth Connection

The geomagnetic and particle conditions in the short term in the near-earth environment are described by space weather occurrences. Space weather linked the solar variability and in the solar wind, magnetosphere, ionosphere and thermosphere. It is a major source of concern in people's daily lives because it affects a wide range of technological systems in orbit and on the ground, including satellites, ground-based power systems, oil pipelines, wireless communication systems, navigation systems, and human space exploration and development. There are several components associated with solar activities to influence space weather phenomena near-earth space environment. The main components are solar flares, coronal mass ejections, high-speed solar wind producing plasma, and solar energetic particles which emit the solar electromagnetic radiations (Jing et al., 2004).

1.1.1 Sun

The Sun is a huge star consisting of hot plasma that is constricted under its own gravitational attraction and is found at one of the foci of the Milky Way galaxy. It lies at distance is 1.496×10^8 km from the Earth, called as one Astronomical Unit (AU)). It occupies approximately 99.86 mass of that of the solar system and a radius of 109 times that of the Earth. The Sun generates a tremendous quantity of energy and a part of it imparts the Earth heat and light to the life on the Earth, so researches and exploration has a great concern. The Sun consists of Hydrogen (81.76 %), Helium (18.17 %) and other traces of gases such as C, N, O, Ne and various other metals. In 17th century, Galileo Galilei observed sunspot using telescope and also confirmed the rotation of the Sun. As the Sun spins along its axis, the rotational speed is faster at the equator is ~25.6 days and slower at poles which is ~35.5 days (Phillips, 1995). It deposits 1368 W m^{-2} energy near to the Earth.

1.1.1.1 Solar Interior

The solar interior is divided into three sections: the core, radiative zone, and convective Zone. The core is the innermost region of the Sun, with highest temperature about 1.5×10^7 K and density 120 g cm^{-3}. Inside the core tremendous energy is formed by means of the nuclear fusion reaction between Hydrogen atoms by converting into

Helium atom. The energy released at the core moves to the surface through two zones: radiative and convective zones. As we move away from the core and toward the surface, the temperature and density decrease gradually. The temperature of convective region falls through 7×10^6 K to 2×10^6 K and density from 20 g cm^{-3} to 2 g cm^{-3}. Energy transported through radiative zone is photons which collide with one other on a particle-by-particle basis. The convective layer is the solar interior's outer layer its temperature fall from 2×10^6 K to 5.7×10^3 K and density to excessively small 2×10^{-7} g cm^{-3}. The radiation transfer process is stopped as a result of decrease in the temperature and density and by means of convection process, the warmer materials moves outwards and continue to rise further carrying heat to the surface (Howe, 2009). The Figure 1 depicts the various zones, layers and several characteristics of the Sun.

1.1.1.2 Solar Atmosphere

Based upon the temperature and density after the solar interior, the solar atmosphere is divided in three layers: photosphere, chromospheres and corona. Each of these layer has its own characteristics and activities. Photosphere which lies above the core is the visible region has 400 km thick and it may extend up to the visible disk. In this region the density of Hydrogen falls rapidly and temperature decreases from 6000 K to 2000 K.

Sunspots: The bowl shaped darker region in photosphere with high magnetic and reduced surface temperature than the surrounding called sunspots. Sunspots come in all sizes and shapes. The size of sunspots varies from 16 km to 160000 km. Within an average period of 11 year called 'solar cycle' the numbers of sunspots rises from 2 to 200 and decreases to low number. Sunspots all the time occur in group and it can either be unipolar or bipolar. The activity of the Sun is expressed in reference to sunspot numbers, the higher value of sunspot refers to active periods whereas the quiet period is specified by fewer sunspots.

The chromosphere is a thin and irregular layer over the photosphere where temperature ascents from 6000 K to 20000 K. Due to its high temperature, the H-alpha emission occur in this region. The solar corona is a low-density zone surrounding chromospheres, with temperatures on the order of 10^6 K. The corona is highly transparent and is seen during a solar eclipse. The transition region is the layer that distinguishes the chromospheres from the corona. The rapid rise in temperature from chromospheres to corona can be the thermal origin which is possible due to coronal heating. Coronal holes are zones in solar corona at which plasma density is low and have open magnetic field lines in interplanetary space. During solar maxima, it lays near to the poles of the Sun but during the solar minimum, the coronal holes exits at lower latitudes (Mullan, 2000). The research on coronal holes is important because it is considered primary site of acceleration of high speed solar wind.
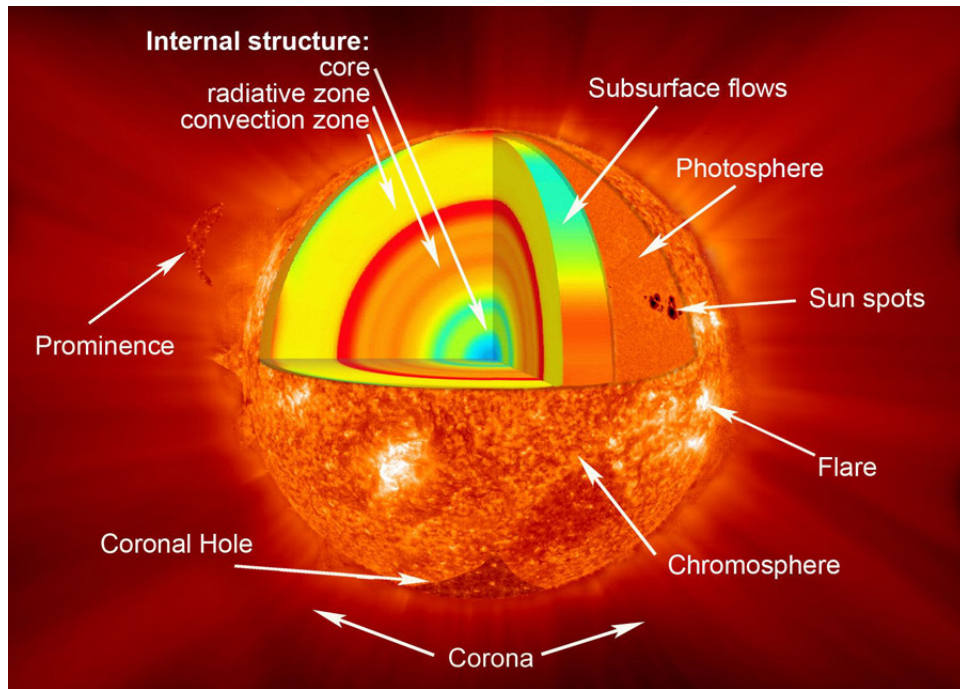
Figure 1: The Sun with different layers and features (`https://scied.ucar.edu/sun-regions`).

1.1.2 Solar Activity

The fundamental cause of the space weather is the Sun, which even 1.50×10^8 km away, has great influence the Earth and its surrounding. The geomagnetic and particle conditions in space near earth's surface are referred to as space weather. In general, space weather has a limited area on interest in people's daily lives, but it has a prominent impact on space born system or terrestrial technological systems such as satellites, power systems, oil pipelines, wireless communication and navigation systems. The continuous emitting stream of particles called solar wind and its interwoven magnetic field called Interplanetary Magnetic Field (IMF) occupied entire solar system. The effect of space weather phenomena is linked with solar activities either on surface of the Sun or its corona such as Coronal Mass Ejection (CME), solar flares, Solar Energetic Proton (SEP), and High Speed Streamer (HSS) that create change in the plasma, magnetic field, radiation, and particle flow in space and its interaction in with magnetosphere (Webb et al., 2000). A solar flare can release a total energy up to 6×10^{25} J. A CME is originated as a result of a large-scale reorganization of solar magnetic structure which results in a substantial volume of ionized particle and energy being expelled from the solar corona (Wang, 2005). A wide range of phenomena could be affected into interplanetary space as a result of these actions, influencing particle velocity, temperature, density, energy, and composition. As a result geomagnetic storms, substorms, super substorm (SSS), and High Intensity Long Duration Continuous Auroral Activity (HILDCAA) produced in the magnetosphere, depositing tremendous amounts of energy.

1.1.3   Sunspot Cycle and Regular Solar Electromagnetic Emissions

The darker and cooler area on the surface of the photosphere of the Sun is called sunspots. The Sun rotates faster at the equator than the poles ($\sim$ 27 day against $\sim$ 31 day). The differential rotation twists the lines of the poloïdal magnetic field and generates magnetic loops called sunspots (D'silva & Choudhuri, 1993). Sunspots are signs of magnetic field disruptions that can result in solar flares and CMEs. The sunspots are observed on the sun's surface which varies from year to year. The observation shows sunspot count varies in a periodic way on average of 11 year of cycle. The period of a sunspot cycle can be as short as 9 year or as lengthy as 14 year. It serves as a esteemed, relatively long-term indicator of solar activity. The sunspot cycle lasts 11 year, which is half of the solar activity's cycle of 22 years. Figure 2 represents yearly average of sunspot number from year 1610 to 2000. The sunspot cycles from 24 and 25 is represented in Figure 3. Aside from the typical cycles, the sun has occasionally displayed unusual sunspot counts. During year 1645 to 1715 there were very few sunspots even in some years no sunspot was observed. This time period is known as the Maunder minimum, and it corresponds to a period of extreme cold in Europe known as the Little Ice Age. The magnetic field of the Sun connected with sunspots reversed in polarity and the direction of the magnetic field in the sun's northern and southern flips in each cycle, and the sunspot count rise and fall (Miesch & Teweldebirhan, 2016). Figure 4 represents flipping of magnetic polarity for solar activity cycle 21, 22, and 23, respectively. During sunspot cycle along with the sunspot counts, its location shift far and near the equator in the sunspot cycle. Concerning to solar minimum, the sunspot tends to form around 30° to 45° latitudes on either side of equator of the Sun and as the cycle progresses through its maximum phases, the sunspot appears near to the equator around 15°. At the end of the cycle, again is the solar minimum during which the sunspot comes more closely around 7° on either side of the magnetic equator. Very often overlap in latitudinal migration around solar minimum occurs when sunspot of outgoing cycle is formed at low latitude and upcoming is formed at high latitude. In 1904, Edward Walter Maunder formed a "butterfly diagram" plotting migration of sunspot trend equatorward in each cycle (Maunder, 1904). Figure 5 represents butterfly diagram of migration of sunspot to the equator. The Sun emits electromagnetic radiation of shorter to longer wavelength which covers whole electromagnetic spectrum from high energetic gamma rays to low energy possessing long radio waves and the Figure 6 shows regular solar electromagnetic radiation emitted from the Sun. This figure represents solar radiation contains all the possible wavelength of radiation emitted from shorter wavelength to the longer wavelength.
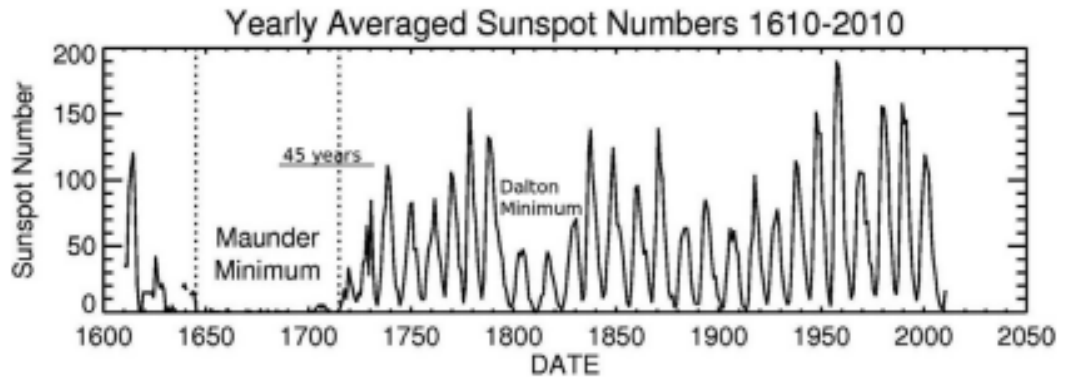
Figure 2: Yearly average of sunspot number from year 1610 to 2000 (Judge & Thompson, 2011).
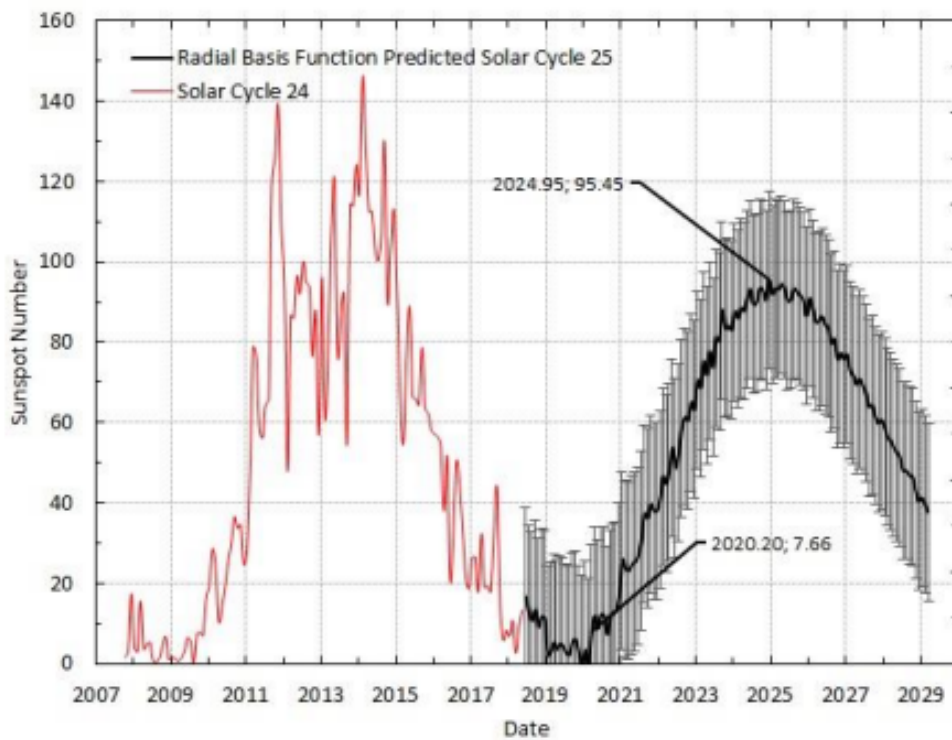
Figure 3: Sunspot cycles 24 and 25 (Dani & Sulistiani, 2019).

1.1.4 Solar Wind

The solar wind is a hot, tenuous, ionized, magnetic stream of plasma that constantly originating from the Sun and travels through interplanetary space. It mainly consists of electrons, protons, alpha particles, and traces of heavier ions. As it propagates into the interplanetary space, variation takes place in temperature, pressure, density, the velocity with time. This phenomenon was invented by Biermann in 1951 during examining comet tails (Biermann, 2013). He found the tails of the comet deflected near the vicinity of the Sun. Later, in 1958 Parker found that the solar corona is not in steadying as the atmosphere of Earth (Parker, 1958). The existence of solar corona is confirmed by satellites Russian Luniks, 2 and 3 and American spacecraft Explorer-10 (American
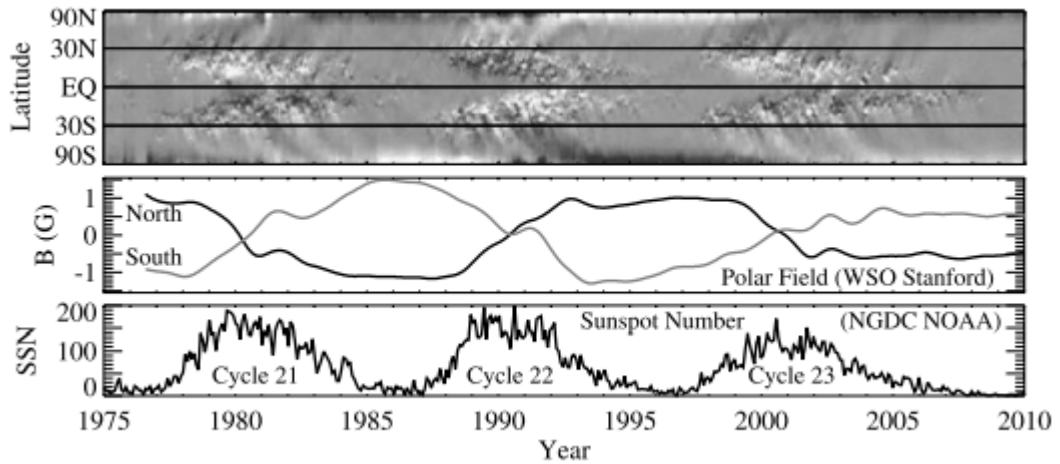
Figure 4: Flipping of magnetic polarity for solar activity cycle 21, 22 and 23, respectively (Li et al., 2011).
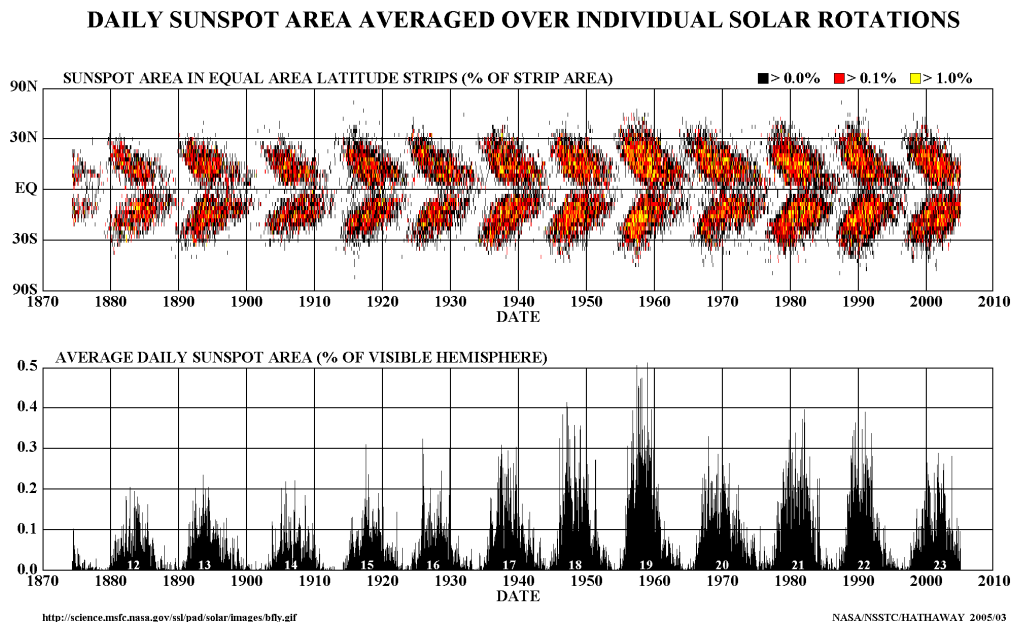
Figure 5: Butterfly diagram of migration of sunspots to the equator (`https://solarscience.msfc.nasa.gov/`).

Association for the Advancement of Science, 1962). They measured the speed of the solar wind as ~300 km s^{-1} (Dimmock et al., 2015) and suggested that solar wind reaches the Earth nearly in four days. The foot point of IMF is connected to the Sun and propagates with plasma form a spiral structure. The frozen magnetic field line (Alfvén, 1942) propagates with plasma has a magnitude of the order few nanotesla near the Earth surface (Koskinen, 2011). Based upon the average features of the plasma, the solar wind is classified into the fast solar wind and slow solar wind (Koskinen, 2011). Table 1 summarizes the basic difference of two categories of solar wind.
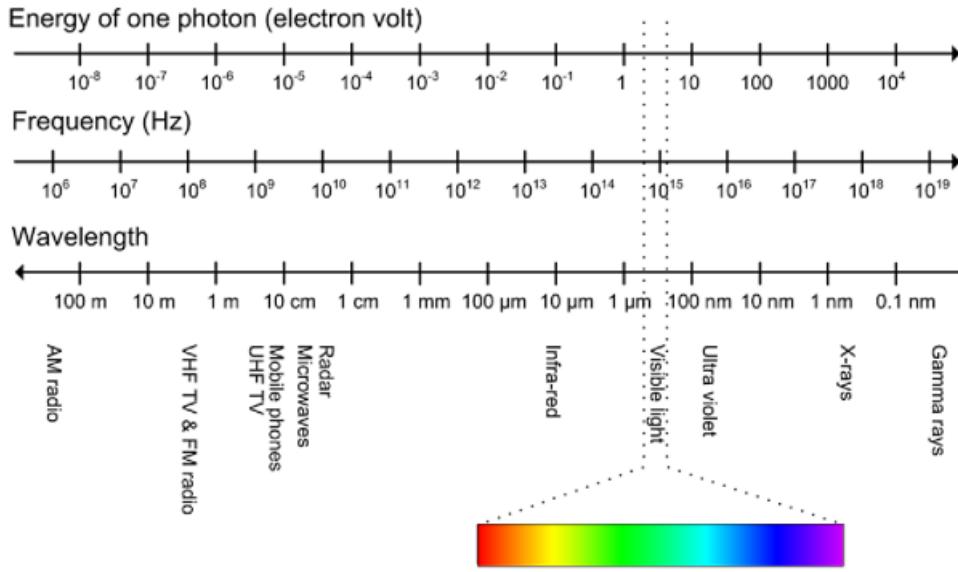
Figure 6: Regular solar electromagnetic emissions from the Sun (Macana et al., 2018).

Table 1: The characteristics of the fast and slow solar wind (Koskinen, 2011).

Solar wind parameters	Slow wind	Fast wind
Velocity (km s^{-1})	350	750
Electron number density (m^{-3})	1×10^7	3×10^6
Electron temperature (K)	1.3×10^3	1×10^5
Proton temperature (K)	3×10^4	2×10^5
Magnetic field (nT)	3	6
Alfvén speed (km s^{-1})	20	70

1.1.5 Coronal Mass Ejection and Interplanetary Coronal Mass Ejection

Coronal mass ejection (CME) is significant outburst of plasma and magnetic field originating at the Sun. CMEs have masses about 5×10^{12} kg to 5×10^{13} kg, speeds at intervals 200 km s^{-1} to 3000 km s^{-1} when it outflows from the Sun and have kinetic energies of the same order of magnitude as solar flares, 10^{24} J to 10^{25} J (Koskinen, 2011). CME continue to propagate and expand into the heliosphere along with the solar wind and these assembles are identified in the interplanetary space, called as Interplanetary Coronal Mass Ejections (ICMEs) and which may reach the Earth. ICME are characterized by region of low solar wind proton density than usual, high magnetic field strength, low plasma beta and smooth field rotation, referred as Magnetic Clouds (MCs) (Gosling, 1997). The ICME associated with shock wave and southwards interplanetary magnetic field can produce large geomagnetic disturbance. When a ICME hits Earth, it disrupts the magnetosphere, which has a variety of impacts ranging from the magnetic field to the ionosphere and lower atmosphere. During solar maximum, filaments and associated CMEs are erupted from the sun as primary interplanetary structures Burlaga et al. (1981). A forward shock is formed if the speed > 500 km s^{-1} of ICMEs coming from the sun into interplanetary space is greater in comparison with the magneto sonic

speed 50 km s^{-1} to 70 km s^{-1} (Hada & Kennel, 1985). Between the shocks and ICMEs is the sheath area, which is another powerful shocked field component (Tsurutani et al., 1988). The magnetic cloud is a configuration of gradually fluctuating and strong magnetic fields 10 nT to 25 nT that can be observed if the ICME has a well-organized magnetic field pattern (Burlaga et al., 1981). In comparison with ordinary solar wind the density magnetic cloud is moderately high. The magnetosphere get compressed as a result of interaction between these interplanetary structures with the front part of the magnetosphere. The interconnection causes the magnetopause current to intensify, resulting in a positive abrupt stimulus in the Dst index (Nishida & Akasofu, 1979), which referred as Sudden Storm Commencement (SSC) produced by the sudden rise in the solar wind ram pressure at interplanetary shock (Araki, 1977). The SSC may come after the initial phase of geomagnetic storm which can last anywhere from zero to > 25 hours. According to the common belief, not all geomagnetic storms begin with an initial phase or sudden commencement, variation in the geomagnetic field begins after geomagnetic storms (Tsurutani et al., 2001). The horizontal component of the geomagnetic field depressed during the interaction between IMF B_z and northward directed Earth's magnetic field (Tsurutani et al., 1988; Dungey, 1961) . During this interaction at the dayside of the magnetosphere, ram pressure increased and compress the magnetosphere which acts as an open field line so energy and plasma enter inside the magnetosphere (Gonzalez et al., 1994). These interactions cause an intensified in the movement of plasma into the magnetosphere. The plasma is then driven by magnified electric fields inside the magnetosphere and enhances electric currents both the magnetosphere and ionosphere (Gonzalez et al., 1994). The increase in energy in the magnetosphere increases the movement of plasma inside the magnetosphere which produces an enhance in several currents in the magnetosphere and ionosphere (Gonzalez et al., 1994). An intense geomagnetic storm is produced for a longer duration of the southward-directed IMF B_z. These injected particles enhance the ring current inside the magnetosphere resulting in a decrease in the Dst index (Daglis et al., 1999). The Dst value recovers its ambient value when the particle dissipated through wave-particle interactions, Coulomb scattering, and Joule heating during its recovery phase (Daglis et al., 1999). Figure 7 represents the prominent interplanetary features accountable for geomagnetic disturbances during maximum of a solar cycle.

1.1.6 Solar Flare

Solar flares are the intense, short-lived eruptions of electromagnetic radiation of the sun which is known to occur between minutes to hours. The Solar flare is formed due to the tearing and interconnection of strong magnetic fields in the solar corona. It is has been noted that the energy liberated during a flare lies in the range 10^{21} J to 10^{25} J (Koskinen, 2011). Solar flares produce radiation of radio wave, infrared, visible light,
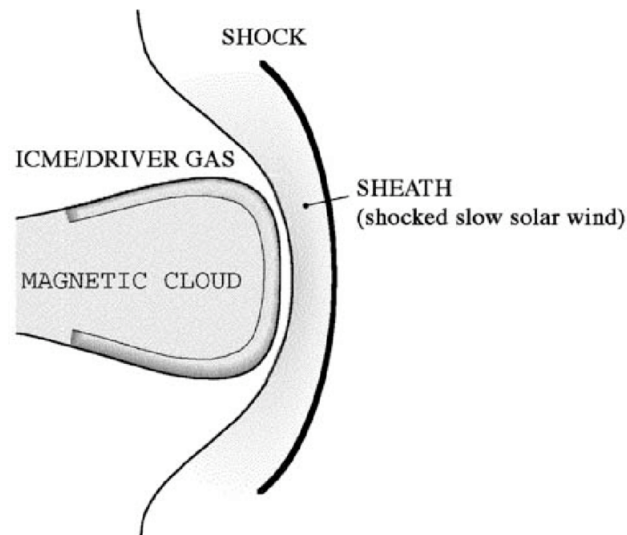
Figure 7: Schematic sketch of a CME (Gonzalez et al., 1999).

Ultra Violet (UV), Extreme Ultraviolet (EUV), X-rays, and gamma rays. Kinetic bulk energy, radiative energy, thermal, and nonthermal energy are the various form of energy released from solar flare (Shibata & Magara, 2011). This energy released during solar flare can heats and hike the plasma temperature upto 50×10^6 K and it has the ability to efficiently accelerate electrons to energies of up to 100 MeV and ions to energies of up to 1 GeV (Mari & Popescu, 2004). R.C. Carrington and R. Hodgson separately observed the solar flare on September 1, 1859, utilizing a white spectrum of light (Cliver, 2006). Solar flares are classified into four categories. The archetypal flare, which is impulsive and compact in space, is the initial type of flare. This type of flare is known to occur in the loop's active region, so it is also known as a confined flare. Large flares occur at greater altitudes, and are the second type of flare. The extinction of a prominence occurs before these flares occur. The third category of solar flare noted higher altitude in comparison with the second class called high coronal flares. The fourth class of solar flare has low energy and it occurs in quiet regions of the Sun and can reach thousands of kilometers in altitude. The incidence of flare increases with the prevalence of sunspots and it can affect the Earth's upper atmosphere. Recent research in coronal bright points have discovered microflares as a network of silent Sun granulation and the inside of super granular cells. Microflares are a million times weaker in compared to the flare invented by Carrington and Hodgson (Benz, 2008). The most strong microflares originate at the edge of super granular cells, while the largest gradual flares originate above the photosphere neutral lines. The current sheet linking the opposite polarity coronal magnetic fields is the next prospective location for flare generation. Microflares have been proposed as a possible explanation for the problem of coronal heating in recent years.

1.1.7   Coronal Hole

Coronal holes are large, dark areas when examined through X-ray wavelengths. Its size is sometimes as large as one fourth the Sun's surface. Coronal holes are open field line design that grant an uninterrupted outwards flow of the high-speed solar wind; their field lines stretched far out into the solar system. Coronal holes have a long-term cycle that does not correspond to the solar cycle but numerous coronal holes. In general, coronal holes appear at the solar north and south poles at some stages of the solar cycle.

Coronal holes are described by a regions of open field lines in which the particles flow at high speed is called a fast beam or HSS (Krieger et al., 1973; Tsurutani et al., 2006). These holes are diagnosed by the sector of open magnetic field lines in the solar corona that has less temperatures in compared to its neighboring region. In satellite images coronal regions seems as dark region. The magnetic field and speed of the solar wind emanating from open field are fluctuating which are known as Alfven waves which are long-lived and more common coronal holes and it plays an important role in the geomagnetic perturbations (Garrett et al., 1974). The velocities of high-speed streams are of the order 750 km s^{-1} to 800 km s^{-1} which are substantially faster than the average solar wind velocities. As result of difference in velocity between the slow and fast streams, an overlapped region is built and it is bound by fast forward and fast reverse shocks at far heliocentric distances (Pizzo, 1985; Balogh et al., 1999). It may remain greater than one solar rotation resulting to a special recurring high-slow speed solar wind conditions, known as Corotating Interaction Regions (CIRs) (Schwenn, 2006). Figure 8 illustrates an X-ray image for huge coronal hole emanated at pole in the course solar minimum.

Figure 8: The X-ray image of the Sun, photographed on Feb 21, 2000, by the Japanese Yohkoh X-ray Observatory (`https://www.ngdc.noaa.gov/stp/solar/yohkoh.html`).

1.1.8 High Speed Streamer

The fast solar wind 500 km s^{-1} to 800 km s^{-1} originates primarily through the coronal holes. Furthermore, the slower solar wind moves over and about equatorial with the velocities between 300 km s^{-1} to 400 km s^{-1} near the Earth orbit. The velocity of solar wind velocity varies relative to the region from which it originates, the faster solar wind emanating can overcome the slower wind originated ahead of it generating a compression sector. Thus formed big scale-structures are revolving along with the Sun called a CIRs. As a result, the IMF is interweaved with the solar wind plasma, the magnetic fields of the slow-moving solar wind are comparatively more twisted than that of the fast solar wind. In general, the existence of HSSs and CIRs have a periodicity of 27 day because the coronal holes can survive for many solar rotations. The following features are used to identify the CIR are: 1) solar wind flow transit from low to high, 2) proton density increases to high values near the leading edge of the stream, 3) the IMF strength is proportional to bulk speed with constant polarity throughout the high-speed stream part and 4) the proton temperature flips similar to the flow speed (Mavromichalaki & Vassilaki, 1998). Moreover, only HSS events are used to identify by using many other definitions. For an example the HSS has been designated by means of an increase of solar wind speed greater than 150 km s^{-1} for five days interval (Bame et al., 1976) or a duration of in which one day mean solar wind speed rise above 500 km s^{-1} (Broussard et al., 1978). The other definitions can be known from the introduction by Xystouris et al. (2014) in they calculated the monthly recurrence of the HSS by calculating the ratio between the times when the solar wind surpassed 600 km s^{-1} and the total period of the measurements in the course of the month. Figure 9 represents the co-rotating interaction region formed by overlapping due to faster and slower solar wind.
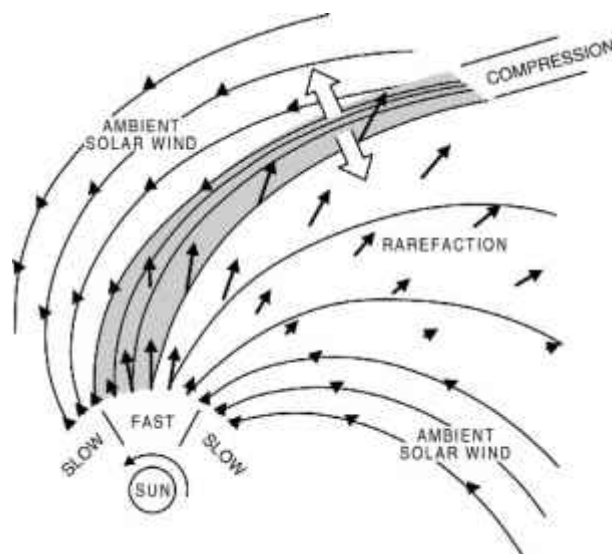
Figure 9: Schematic sketch of a co-rotating interaction region. Solid lines represents the magnetic field lines and the length of the arrows shows the flowing speed of solar wind (Forsyth & Gosling, 2001).

1.1.9   Interplanetary Magnetic Field

Interplanetary magnetic field (IMF)is originated from the Sun that pervades the space between the planets and other bodies of solar system. The IMF is carried by solar wind into interplanetary space; it is called "frozen in" with the solar wind plasma (Roberts, 2007). The IMF originated on the sun's surface which are open field lines i.e. field lines emerge from a region and continue nearly forever into space, not returning to their conjugate region. The direction of IMF in the northern and southern hemispheres is diametrically in opposite and get reverse with each solar cycle. The interplanetary mediums are thinly scattered matter of week magnetized plasma originated with supersonic solar wind that pervades the space between the planets and other bodies of solar system. When it interacts with the planetary magnetosphere and it produces geomagnetic storm. The interplanetary medium regulates the cosmic rays flux within the heliosphere and gets modulated by slow and fats solar wind streams, co-rotating shocks and particle acceleration. These days, the recently launched space missions such as Parker solar probe, solar orbiter provides the new insights into their physical processes related to the Sun and the interplanetary medium using more accurate high-resolution in situ instruments for monitoring the evolution of solar wind parameters. Study of interplanetary variability helps to characterize large scale structures and coupling between the solar wind plasma and different interplanetary environments. These observations are used to verify the pre-existing theoretical model and helps for advancing numerical simulations to reveal many facets of both known and unknown physical phenomena, progressing from previous achievements to future problems

1.1.10   The Earth's Magnetic Field

A thin outer crust, a silicate mantle, an outer core, and an inner core are the components of the Earth's structure. The temperature and pressure increase as we proceed deeper into the Earth. Predicted temperature at the surface of core mantle boarder is 4800 K. As a result of high temperature, the outer core remains in liquid state and due to the high pressure, the inner core remains in solid. The inner core mainly consists of iron with few traces of lighter elements. Rotation and convection keep the outer core remain in moving. The convection is driven by lighter elements move upwards and the heavier elements freezes into inner core. The geomagnetic field is produced by series of aspects (Olsen et al., 2010). The method through which the magnetic field of the Earth is created is tremendously intricate and the complete set of parameters required to report the Earth's magnetic field is not clearly known. According to some research, a conducting fluid with enough energy to induce the fluid to travel at a sufficient velocity in a suitable flow pattern, a seed magnetic field to produce a magnetic field on the Earth. All these requirements are met in the Earth's outer core, where convective motion is linked with

the rotation of the Earth and provides sufficient flow pattern. Electric currents are generated by the movement of liquid iron, which then form magnetic fields. Charged metals travelling across these fields generate their own electric currents, continuing the cycle. The geodynamo is the name for this self-sustaining process. The external source of magnetic field that contribute to the geomagnetic field are the several type of electric currents in the ionosphere and magnetosphere. During geomagnetic calm conditions, their contribution is relatively minor, accounting for only a certain percent of the overall field on the Earth's surface. Geomagnetic disturbances are caused by these external currents (Chapman & Bartels, 1940). All the fluctuations in electrical currents in the Sun-Earth system are measured by the magnetic field at the Earth's surface. Figure 10 illustrates a model of origin of magnetic field as a consequences of dynamo action in the Earth. The total magnetic field B at the Earth's surface is given by

$$B = B_p + B_a + B_e + B_i \tag{1.1}$$

where

B_p = main field has magnetic strength 30000 nT to 60000 nT which shows secular variations;

B_a = magnetization of the rocks which are found in the Lithosphere and it has magnetic field $\sim$ 10 nT to 20 nT which has constant values;

B_e = external field related to ionosphere and magnetosphere has magnetic strength 10 nT to 2000 nT;

B_i = this is the induced field generated by the external field B_e, (Kamide & Brekke, 1975)
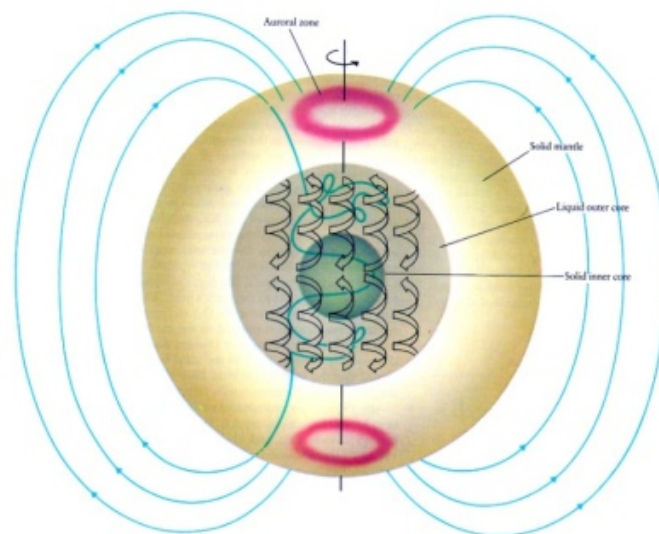
Figure 10: Dynamo action in the Earth for generation of geomagnetic field (Friedman, 1986).

13

1.1.11 Interaction of Solar Wind and the Magnetosphere

Ionospheric activities are understood by the interconnection of the solar wind and magnetosphere which greatly influences the ionosphere at high latitude. In the Sun-Earth system, there are magnetic storms or solar flares that cause ionospheric characteristics to fluctuate. The continual energy output of the Sun in the form of solar wind and interwoven 'frozen-in' IMF changes the magnetosphere's boundaries. Because of its high conductivity and collisionless nature, the solar plasma is coupled to the IMF (Kamide & Chian, 2007) which is explained by 'frozen-in' theorem using combining of Maxwell's equations and magnetodynamics theory (Alfvén, 1942). From the Sun masses and energy are emitted continuously by means of huge reaction releasing protons and electrons when Sun rotates in elliptic plane. The average rate of particle emitted is 5 cm^{-3} but it varies with the compression and rarefaction following CMEs. The IMFs are as open field lines radiated outward spirally when the Sun rotates similar to the ejection of water droplets from a rotating garden sprinkler. The radial velocity of solar wind near the Earth's distance is 300 km s^{-1} to 400 km s^{-1} but it increases over 700 km s^{-1} due to the fast streams led by CME shock fronts (Feldman et al., 2005). The orientation and magnitude of the IMF in space is determined by its three dimensions component. The component of IMF which lies in the solar ecliptic plane has an oscillating north-south component represented by B_z. IMF's component Bz affects whether the solar wind is diverted aside or reconnected to the magnetosphere via magnetic reconnection (Sandholt et al., 2006). The two opposing field lines split and converge at the magnetosphere, allowing plasma of various origins to connect and interchange mass, momentum, and energy. Kinetic energy is produced by converting magnetic energy into kinetic energy. A chapter of a book by Kamide & Chian (2007) clearly explains the magnetic connection within Earth-space system. On the day side of the magnetosphere, geomagnetic field lines get connected to the negative polarity of IMF B_z (Coker et al., 1995). When shock waves present in the solar wind containing intense plasma clash with the magnetosphere, a large amount of solar particle energy may be supplied to the cusp areas of the ionosphere at high latitudes. After dayside reconnection, the solar wind moves, and magnetospheric convection transport completely open field lines around the poles to the night side, and far away to the stretched plasma tail (Dungey, 1961). A conglomeration of magnetic flux leads to an intensification of field lines toward the plasma tail current sheet at a location around 100 R_E to 200 R_E beyond the Earth. A substorm is produced when magnetic reconnection is massive at this location, stored potential in the stretched solar field lines is transmitted to freshly formed closed geomagnetic field lines that flow back to the Earth. During substorm, the energetic particles coming out of the plasma sheet are transferred to the ionosphere, causing tremendous auroral activity even at night. In 1964, Akasofu identified as a recurrent characteristic of the

magnetospheric convection system observing ground-based images of subsequent auroral emissions (Akasofu, 1964). The magnetic reconnection during dayside and night side summarizes the key characteristics of magnetospheric convection system. Even during quiet periods, the magnetosphere linked with solar wind is a waving and creating interaction as a result of which the particles can enter the atmosphere in several places (Figure 11). Scientist has noted chances of geomagnetic reconnection when IMF B_z is northward, but for this instances the east/west components B_y component regulates the magnetospheric circulation design and connection regions. The conditions of interplanetary medium and magnetospheric linkage mostly studied using in situ satellites data. In recent two decade, the Advanced Composition Explorer (ACE) spacecraft which lies at Lagrangian orbit has been making continuously monitoring of solar wind composition, density, speed, temperature, and inclination of IMF. It can also provide advance messages of shock arriving or IMF fluctuations at the magnetosphere, which is crucial for astronauts and satellite operations and also to the research related to the ionosphere. The research carried by Hunsucker & Hargreaves (2007) gives the complete description of solar wind interaction to the magnetosphere. Figure 11 is a three-dimensional sketch of magnetosphere showing cross section, major current system and boundary layers from where particles enter in the magnetosphere from solar wind. The following plasma regions have been marked: (0) exterior cusp, (1) low-latitude boundary layer in the sun polar region, (2) high-latitude boundary layer (plasma mantle), (3) dayside elongation of the central plasma sheet, and (5) the low-latitude boundary layer along the post noon flank. In the sketch magnetospheric current sheets, Birkeland currents and the ring current have been marked by red, green, and blue arrows, respectively.
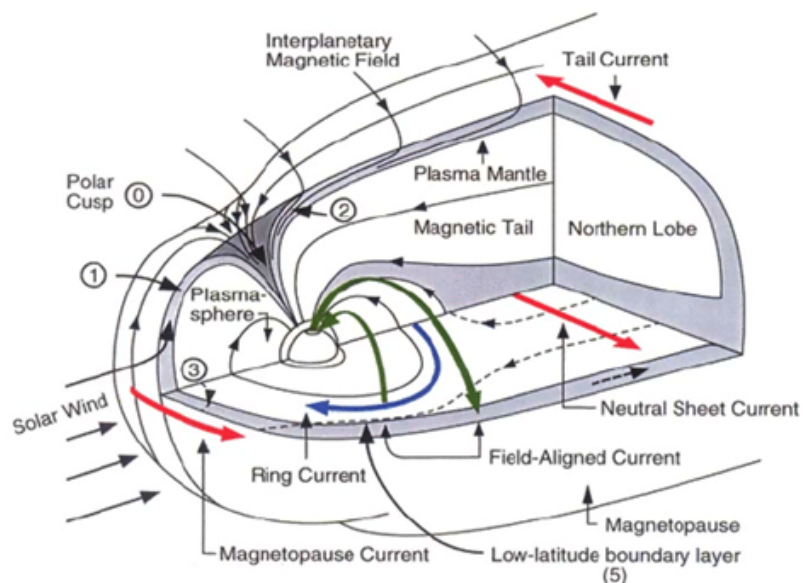
Figure 11: Schematic illustration of magnetosphere topology with boundary layers towards the solar wind (Sandholt et al., 2006).

1.1.12 Geomagnetic Disturbances

A Geomagnetic Disturbance (GMD) is a significant event that occurs in the magneto-sphere of the Earth. A geomagnetic storm is another name for GMD, is created by a highly effective flow of energy and plasma from the solar wind into the magnetosphere of the earth via a magnetic reconnection mechanism between the interplanetary magnetic field's southerly component and the northward directed geomagnetic field at its magne-topause (Chapman & Ferraro, 1930). The major causative factors of GMD are the solar flare and CME. The geomagnetic disturbances are storm, substorm, and super substorm characterized by the amount of energy deposited and duration of energy deposited into the magnetosphere. The massive outbursts from the Sun are responsible for the quiet time geomagnetic field disruption. The quiet time ionospheric disturbance is called S_q current and At high magnetic latitudes, disrupted ionospheric currents indicated as S_d, are linked to auroral activity. Enormous energy (approximately 10^{19} ergs), is dumped into auroral ionosphere during the auroral activity enhancing the conductivity of that region. Such a condition produces system of currents in eastward and westward direc-tions, termed as electrojet currents. Solar emitted electromagnetic radiations and highly energetic charged particle are highest source for causing disturbance in the systematic variations. The abundance of sunspots guides solar activity, which has a periodicity of 11 year, which means the solar activities increases and lowers once every duration of 11 year. During high solar activity, numerous and intense emissions of CMEs and solar flares deliver enormous amount of electromagnetic radiation and corpuscular as energy into space. When the energetic particle collides with the Earth's magnetosphere, the embedded solar magnetic field causes the magnetosphere's electromagnetic state to be disrupted, resulting in the generation of distinct current systems in various portions of the magnetosphere. In response to this phenomenon, the geomagnetic field displays a wide range of perturbations. Geomagnetic storm phenomenon, or GMD, is the most conspicuous perturbation in magnetic records. Depending upon some specific char-acteristics, the duration and its impact the geomagnetic disturbances are classified as magnetic storm, sub storm, and SSS.

1.1.12.1 Storm

The sudden variation in the geomagnetic fields in the earth is called a geomagnetic storm or simply a magnetic storm. The geomagnetic storm can last for several hours to days. There are two causes for magnetic storms, the first is when CME passes near the Earth-space environment, it intensifies the solar wind and produces a complex oscillation there, which in turn generates associated electric current. This additionally generated field causes the magnetic field variation in the magnetosphere. The second reason for the production of magnetic storms is the direct reconnection of the solar

magnetic field to the geomagnetic field at its magnetosphere (Dungey, 1961). During this reconnection process, energy and plasma enter into the magnetosphere resulting in variation in several magnetospheric currents for the magnetic storm. This process is uncommon. A large magnetic storm occurs when the solar magnetic field gets connected with the geomagnetic field during CME. The super-intense magnetic storm can produce damages to assets in the terrestrial and system fitted in space e.g. the most typical problems are power outages and satellite damages, as well as communication and navigational concerns.

1.1.12.2 Substorm

A magnetic substorm is a transient disturbance in the magnetosphere that occurs when the Earth's magnetic field is disrupted by southward directed interplanetary magnetic field and dayside reconnection begin (McPherron, 1991; Lakhina et al., 2006). A substorm is sometimes known a magnetospheric substorm or an auroral substorm, which involves the sudden, a massive discharge of energy in the magnetosphere of the Earth from the magnetosphere's "tail" and pumped into the ionosphere at high latitudes. The substorm sequence is described by three phases: growth, expansion, and recovery phase (Lewis et al., 1997). Energy is stored at the magnetotail during the growth phase, while the energy is released during the expansion phase, and during the recovery phase, intense ionospheric and auroral activities die out. The substorm takes place for a few hours and occurred primarily near the polar region. Energy dissipation during substorms is caused by two main processes- directly driven and loading-unloading (Rostoker, 1972). The energy was dissipated globally and consistently through the driven process, however, the transfer of energy for loading-unloading processes is dependent on the substorm phase. During the growth phase, energy is stored in the Earth's magnetotail, the auroral oval spreads equatorward, and the DP_2 auroral electrojet strengthens (Nishida, 1968; Kelley et al., 2003). During the expansion phase, the energy accumulated in the tail is liberated into the magnetosphere and ionosphere, causing major consequences in the surface magnetic field strength and currents in the high latitude and polar ionosphere (Baker et al., 1997). The observable magnetic disturbances viewed from Earth are the sudden intensification and spread of polar auroras. During the process of recovery, activity in the midnight sector may decrease as the magnetosphere returns to its normal form.

1.1.12.3 Super Substorm

Super substorms are extremely intense substorms. It is defined using the Super Magnetic Low (SML) index. The substorm with SML value < -2500 nT is called SSS (Tsurutani et al., 2015). The SML index is a modification of the common Auroral low (AL) index

but it has greater longitudinal and latitudinal coverage. The AL index contains the data of 12 standard auroral stations. The SSSs are significant not only for describing the physical mechanisms of the event, but also they can cause power failures (Tsurutani et al., 2015). For the very first time, in 2016, Harjra et al. investigated the interplanetary causal aspects, the seasonal and solar cycle dependences of SSSs from 1981 to 2012 (Hajra et al., 2016). SSS were shown to occur in all periods of the solar cycle, however, the declining phase it occurred with (3.8 year^{-1}) the highest rate of occurrence and the lowest at the minimum phase (0.9 year^{-1}). The SSSs were associated with southward IMF and it was also found that 54 % of SSSs were related to sheath field and 46 % with the magnetic clouds. About 77 % of SSSs were produced when very high-density solar wind plasma parcels impinge upon the magnetosphere. The majority of SSS events, 86.5 % occurred in the main phase of geomagnetic storms and 9.5 % occurred in the recovery phase.

1.1.13 Atmosphere

The atmosphere is a thick blanket of air around the Earth and it is a stable mixture composed of different origins. The earth's atmosphere stretches from its surface up to $10,000$ km. Earth's gravitational attraction has kept the atmosphere in space. Due to the gravitational force, the concentration of the atmosphere reduces as it moves outward. The atmosphere of the Earth contain roughly 99 % of nitrogen and oxygen, with the remaining 1 % made up of CO_2, inert gases, and traces of many other gaseous chemicals. Depending upon temperature profile and its constituents, the atmosphere has classified into four layers: troposphere, stratosphere, mesosphere, and thermosphere. The ionosphere is a layer that stretches from the mesosphere to the thermosphere, and it is the focus of this study. The temperature and ionosphere density curve are depicted in Figure 12.

Troposphere: It is the bottom layer of the earth's atmosphere which consists of about 75 % to 80 % mass of the atmosphere. Most of the weather phenomena are taking place in the troposphere. The height of the troposphere varies with altitude and season. Near the poles, its height is 8 km, and near the equator, it goes up to 16 km. The troposphere consists of 90 % of water vapor. The vapor present in this layer control tropospheric temperature by absorbing solar radiation and heat emitted by the earth. The stratosphere is second layer of the Earth's atmosphere. The lower boundary of the stratosphere the topmost part of the troposphere which demarcates between the troposphere and stratosphere called tropopause (Rishbeth & Garriott, 1969).

Stratosphere: It varies from the altitude of 8 km to 16 km from the poles to the equator and extends up to 50 km. The stratospheric temperature increases with an increase in its altitude (Mohanakumar, 2008). The ozone present in this layer absorbs harmful
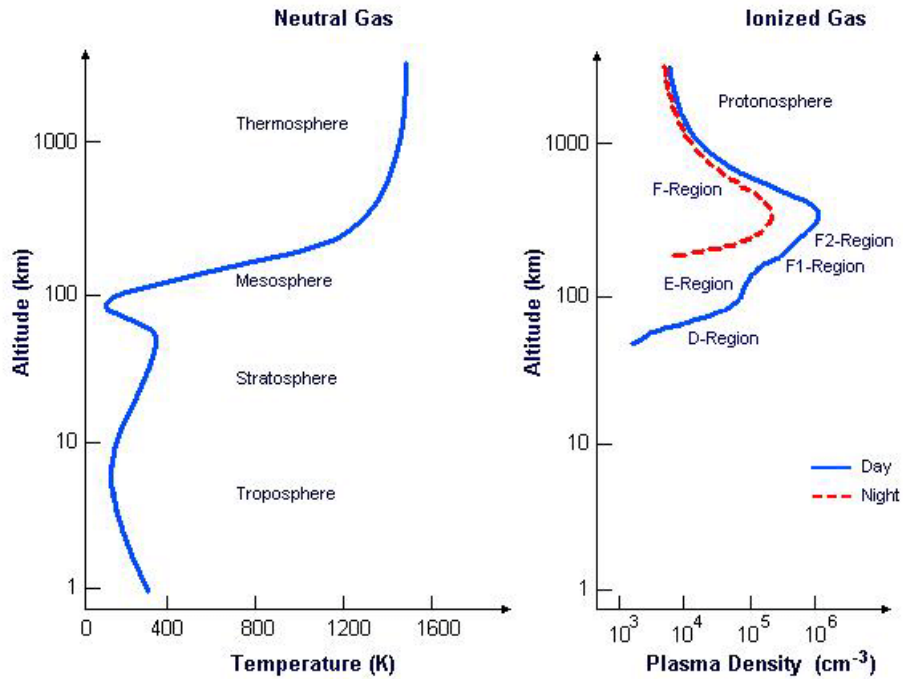
Figure 12: Schematic profile of neutral atmospheric temperature with the various designated layers, and ionospheric plasma density during both the day and night time (Kelley, 1989).

UV rays, keeping it off from reaching the Earth's surface. The outermost layer of the stratosphere is called stratopause which separates it from the mesosphere.

Mesosphere: It's a layer that stretches from 50 km to 80 km and is marked by a drop in temperature as altitude rises. This region is the coldest in the Earth's atmosphere, with the lowest temperature of $\sim$ 180 K at an altitude of 80 km. Chemical compositions are quite consistent, and pressures are extremely low. At the top, this is bounded by mesopause.

Thermosphere: It's a thin layer with a high temperature and low density. The thermosphere encompasses the ionosphere, it stretches for hundreds of kilometers. The absorption of intense solar radiation by the small amount of molecular oxygen available causes this layer's temperature to rise. The thermopause is the stratum where temperature no longer rises with height and is influenced by solar activity.

1.1.14 Chapman Layer Theory

Sydney Chapman in 1931, proposed a theoretical model for distribution of ionization as a function of height produced by absorption of solar radiation by atmospheric constituents. The basic assumptions of Chapman theory are: radiation is monochromatic, the atmosphere consists of single absorbing species, which decreases exponentially with altitude with constant scale H, and the atmosphere is plane and stratified.

When a photon flux with intensity I, incident of a neutral species has density n(z) to the

height z at solar zenith angle χ. The flux is attenuated by absorption. If σ represents the absorption cross-section then the decrease in its intensity after traversing a distance is given by

$$\frac{dI}{dz} \cos \chi = n(z) I \sigma \tag{1.2}$$

The flux intensity of a particular height can be expressed as

$$I(z, \chi) = I_\infty \exp\left(\frac{-Hn(z)\sigma}{\cos \chi}\right) \tag{1.3}$$

Where the I_∞ represents intensity of the attenuated flux at its topside of atmosphere. If η denotes ion-pair produced by means of absorption of photon, then the Chapman production function, P_c is obtained as

$$P_c(z, \chi) = I(z, \chi)\eta n(z) = I_\infty \exp\left(\frac{-Hn(z)\sigma}{\cos \chi}\right)\eta n(z) \tag{1.4}$$

This equation indicates that the rate of production of ion-pair depends upon the intensity of solar ionizing radiation and which increases with elevation and neutral density which decreases with altitude.

The maximum production of ion-pair can be obtained by using maximum condition as

$$\frac{dP_c}{dz} = 0 \tag{1.5}$$

The altitude of maximum ion-pair production is obtained by equation

$$z_{\max} = z_0 + H\left[\log(n(z_0))H\sigma \sec \chi\right] \tag{1.6}$$

1.1.15 Morphology of Ionosphere

Surrounding the earth, the ionosphere is a partially ionized layer of the Earth's atmosphere, between 60 km to 1000 km. The atoms and molecules of the ionosphere are ionized by solar radiation's EUV and X-ray. Besides solar radiation, the collision by the energetic particle deposited with neutral atoms or molecules at a higher latitude is another source of ionization (Kelley, 1989). The ionosphere is an electrically neutral medium because it consists of an equal number of ions and electrons (Hargreaves, 1992; Hunsucker & Hargreaves, 2007). The charged particles produced by either mechanism react with neutral atoms and diffuse within them by means of gravitational force and pressure gradient. The plasma may move under the influence of a geomagnetic field through neutral wind or an electric field. Depending upon the ionospheric composition

and its production rate, the ionosphere is divided into three layers: D, E, and F layers as shown in Figure 13. These layers are influenced by various physical phenomena and have varying ion compositions. Within D and E regions of ionosphere, the main molecular species present are O_2^+, N_2^+, NO^+ as shown in the Figure 13 and photochemistry is dominant. The recombination rate at these regions with electrons are dominant as a result, both layers vanish when the sun sets. On the other hand, atomic ions (O^+ and H^+) make up the majority of the F region. This layer has the highest concentration of electrons and ions as in Figure 13. Figure 14 represents a typical pattern of electron, ions, and neutral species in the middle latitude.

The rate of recombination with electrons in the F layer is much lesser as a result, this layer is maintained throughout the night, and the electron density is at its highest. Normally, the F layer is separated into three sub-layers. F_1 is the lowest layer, where photochemistry is dominant. Photoionization produces ionization in this region, which then fades away due to electron recombination. The F_2 layer is the next sub-layer, where the transition from chemical to diffusion takes place and where the greatest electron density normally occurs. The topside of the ionosphere is the uppermost region of the ionosphere, above the F_2 layer, where diffusion prevails and the chemical composition is H^+ and He^+ (Schunk & Nagy, 1925).

The ionosphere shows considerable fluctuations with time of day, latitude, longitude, season, solar activity, and geomagnetic activity, in addition to plasma density variation with altitude. A specific latitudinal feature in the ionosphere is formed due to the geometry of the Earth's dipolar magnetic field lines. As a result, the ionosphere is divided into three latitude regions: low, medium, and high, each controlled by a separate physical mechanism. Figure 15 depicts the consequence of the ionization and ion loss processes, as well as the dynamics of the ionospheric region, which determine the electron density profile with different roles in their vertical arrangement depending on ionizing radiation, seasons, latitude, and differences between day and night.

D Layer: It is the ionosphere's lower layer, which extends from 60 km above the earth to $\sim$ 90 km in height. This region has a low density and a high frequency of collision with electron between ions and neutral particles. This region disappears during the nighttime by recombining ions and electrons forming neutral atoms or molecules. In this region, the major sources of ionization are X-rays, Lyman-alpha radiation, and cosmic rays that ionizes NO. The density of electron in this region is low which ranges from 10^7 electrons m^{-3} to 10^{10} electrons m^{-3}, hence this region doesn't reflect high-frequency radio signals. This region absorbs high frequency alternating electric field of the wave. The energy loss in D-layer is greater due to the collision between free electrons and neutral atoms is obtained by $N\nu$ (The electron density is N, and the frequency of collisions between electrons and neutral molecules is ν). Loss during absorption is
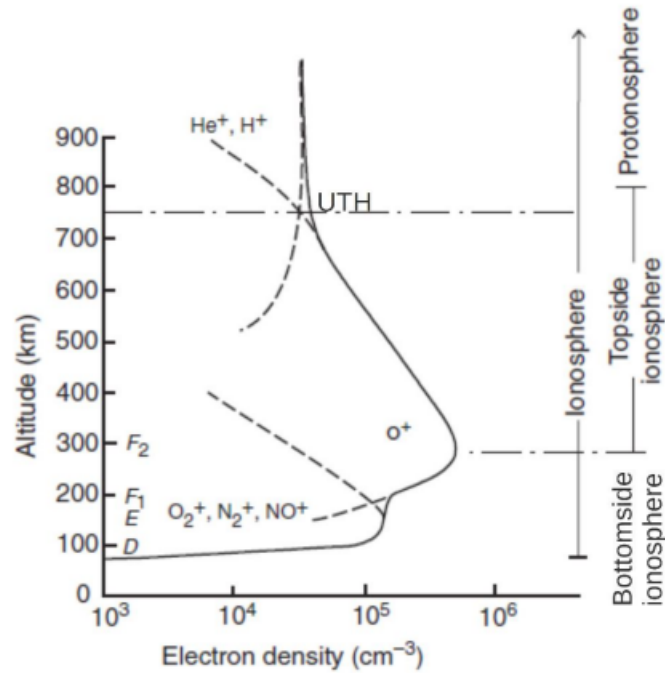
Figure 13: Ionospheric ion density profile for the daytime mid-latitude ionosphere along with its different layer. The Upper Transition Height (UTH) is the height at which the oxygen ion and hydrogen ion dominated plasma regions (Banks et al., 1976).
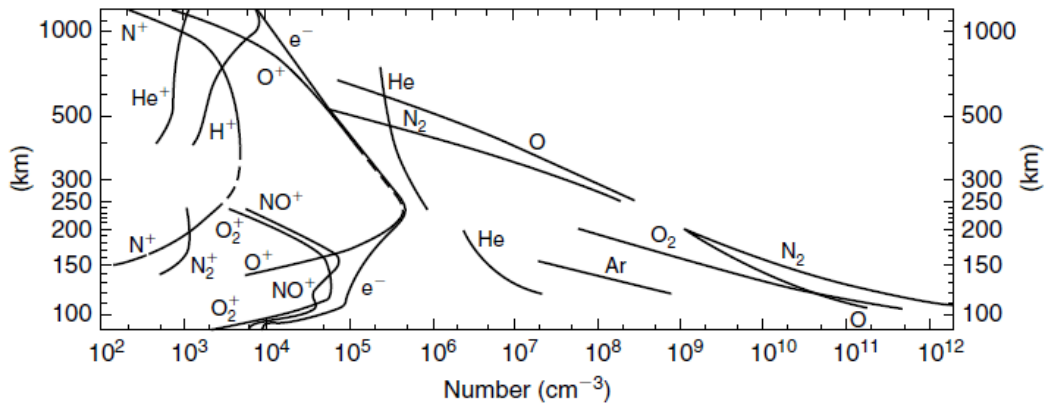
Figure 14: A typical profile of ions, electron and neutral species in the middle latitude (Rishbeth & Garriott, 1969).

proportional to $N\nu$ and may acquire its maximum value. The chemical process taking place in D-region is highly complex and it involves O, O_2, O_3, NO, NO_2, CO_2, H_2O, and alkali metals.

E Layer: This layer is around 90 km and 140 km high, with an enhanced electron density about 90 km and 110 km. Because of the presence of ionospheric electrical currents and their coupling with the Earth's magnetic field, this region of high electrical conductivity is extremely essential. Weak X-rays ($\lambda > 10$ Å) radiation, solar Lyman-beta (1025.7 Å), and EUV (1000Å) ionize the O_2 molecules and EUV (900 Å) ionize the N_2 molecules are the major causes of ionization. Highly variable concentrated and thin layers whose
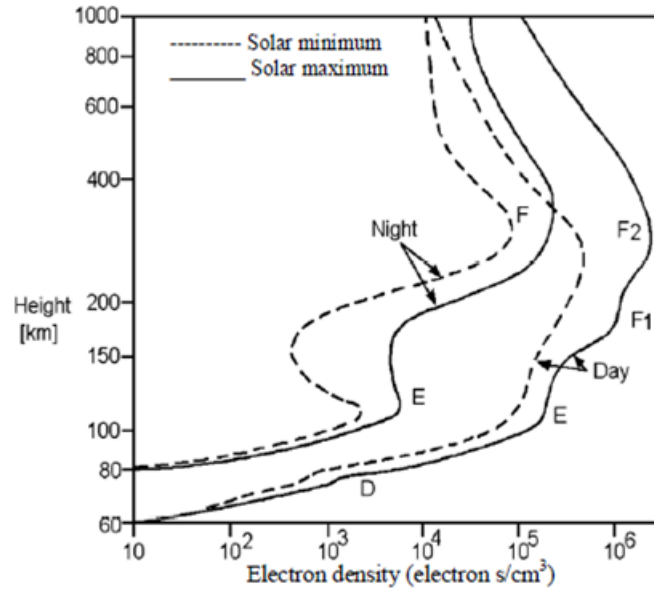
Figure 15: Vertical profile electron density during day and night side ionosphere (Hargreaves, 1992).

thickness ranges from 0.2 km to 2 km, known as E sporadic (E_s) layers, may arise within this region. At mid- and low-latitudes, the probability of these E_s layers forming is highest in summer daytime hours, but at high-latitudes, the probability is highest in nighttime hours.

F Layer: It is lies at a height of around 150 km to 1000 km. The EUV lines and the Lyman continuum of hydrogen are the principal causes of ionization. O^+ is the dominating ion in this region. F_1 and F_2, two more layers in the F region, can be distinguished. A third layer, termed F_3, may form in the equatorial area. An inflection or a peak in the curve electron density of approximately 180 km defines the layer F_1. The transition between linear and quadratic loss mechanisms takes place in this region. The F_2 layer lies near the peak electron density of $\sim$ 300 km to 400 km, and it is the ionosphere's layer with the highest ionization density. Its creation is mostly influenced by the winds, and its composition varies according to solar activity. During the day, especially around local noon, the maximum concentration of free electrons can be detected. Due to limited recombination of ion with neutral and wind transport effects, this concentration drops during the night, but the layer persists. The equatorial meridional wind is crucial in maintaining the density of the F layer at nighttime.

1.2 Physics of Ionosphere

1.2.1 Equation of Continuity in Ionosphere

The ionosphere is formed through the absorption of EUV and X-rays from the Sun, as well as auroral precipitation (in auroral zone), $P(N_r)$ is the term of production of

ionization. The ion pairs may loss by attachment and recombination $L(N_r)$. The transport with plasma drift $\vec{V}_r$ also affects the ionization. The equation of continuity is (Rishbeth & Garriott, 1969);

$$\frac{\partial N_r}{\partial x} = P(N_r) - L(N_r) - \vec{\nabla}.(N_r\vec{V}_r) \tag{1.7}$$

In the lower ionosphere, a part of electron is lost due to "attachment" by which the free electrons attach themselves to the neutral atoms to form negative ions. In the upper ionosphere, the recombination is the main cause of electron loss. Figure 16 describes the photoionization and photo-dissociation of ionospheric species with penetration of photons of different wavelengths.

The atmosphere of the Earth is comprised of a diverse number of chemical compounds, the most important of which are N_2, O_2, and Ar. Other constituents in the atmosphere are formed by photochemical process either by means of natural or artificial process. This process plays key role in the middle, low latitude, and ionosphere. Figures 16 illustrates the ionization and recombination process in ionosphere. The main photochemical absorption process and ion species recombination process of solar radiation are as follows (Rishbeth & Garriott, 1969);

Photochemical absorption

$AB + h\nu \rightarrow A + B$ (Photodissociation require photon of wavelength > 130 nm)

$AB + h\nu \rightarrow AB^*$ (Photoexcitation require photon of wavelength < 130 nm)

$A + h\nu \rightarrow A + e^-$ (Photoionization require photon of wavelength < 100 nm)

Ion species recombination

$X^+ + e^- \rightarrow X + h\nu$ (Radiative recombination with rate constant α_R)

$XY^+ + e^- \rightarrow X + Y$ (Dissociative recombination with rate constant α_D)

$XY^+ + Z^- \rightarrow XYZ$ (Ion-Ion recombination with rate constant α_I)
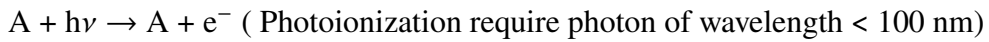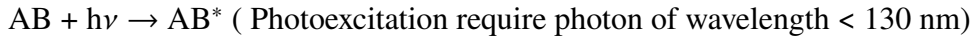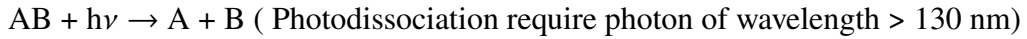
1.2.2 Equations of Motion of Ions and Electrons in Ionosphere

The ionosphere comprises the neutral atoms, ions, and the free electrons. The ions and electrons are affected by the force created by electric force, magnetic force, pressure gradient, gravitational force, force due to ion-neutral collision, and ion-electron collision. In general, the net force $\vec{F}$ acting on ions and electrons be expressed as

$$\vec{F} = \vec{F}_e + \vec{F}_m + \vec{F}_p + \vec{F}_g + \vec{F}_{cin} + \vec{F}_{cei} \tag{1.8}$$
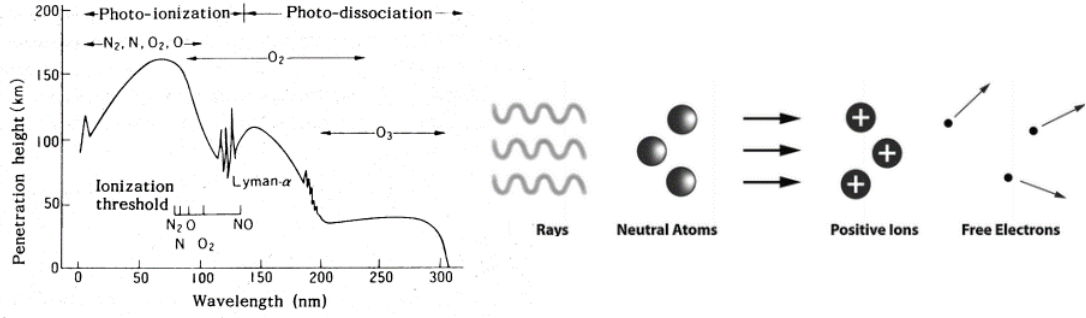
Figure 16: Altitude profile of photochemical process (`http://indico.ictp.it/event/9621/other-view?view=ictptimetable`).
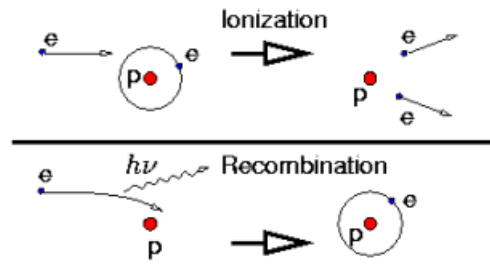
Figure 17: Illustration of photoionization and recombination process (`http://indico.ictp.it/event/9621/other-view?view=ictptimetable`).

where

$$\vec{F}_e = \text{electric force;}$$

$$\vec{F}_m = \text{magnetic force;}$$

$$\vec{F}_p = \text{pressure gradient;}$$

$$\vec{F}_g = \text{gravitational force;}$$

$$\vec{F}_{cin} = \text{force due to collision with ion-neutral;}$$

$$\vec{F}_{cei} = \text{force due to collision with electron-neutral}$$

Specifically, the equation of motion for ions and electrons be written as

Equation for ions:

$$m_i \frac{d\vec{V}_i}{dt} = 0 = m_i \vec{g} - \frac{1}{N_i}\vec{\nabla}(N_i kT) + e(\vec{E} + \vec{V}_i \times \vec{B}) - m_i \nu_{in}(\vec{V}_i - \vec{U}) - m_i \nu_{ie}(\vec{V}_i - \vec{V}_e) \quad (1.9)$$

Equation for electrons:

$$m_e \frac{d\vec{V}_e}{dt} = 0 = m_e \vec{g} - \frac{1}{N_e}\vec{\nabla}(N_e kT) + e(\vec{E} + \vec{V}_e \times \vec{B}) - m_e \nu_{en}(\vec{V}_e - \vec{U}) - m_e \nu_{ei}(\vec{V}_i - \vec{V}_e) \quad (1.10)$$

In the right-hand side of the equation the first term denotes gravitational force in which m stands for mass and $\vec{g}$ for acceleration due to gravity. The second term represents force obtained from pressure gradient in which N represents for the concentration of charge particle, T the temperature, and k for the Boltzmann's constant. The Lorentz force is represented by the third term in the equation, where e is the elementary charge, the '+' sign for positive ions and the '−' sign for electrons, and $\vec{B}$ and $\vec{E}$ are the electric and magnetic field intensities, respectively. The collision force is represented by the fourth and fifth terms in this equation, where m is the mass, $\vec{V}$ is the charge particle's velocity, $\vec{U}$ is the velocity of neutral species, and ν is the frequency of neutral atom collisions. There are two types of collisions: elastic and inelastic collisions. During elastic collision, the total amount of energy and impulses of the two particles does not change, there is transfer of energy from one particle to another. In this collision, the total kinetic energy is conserved. In the inelastic collision, a part of the kinetic energy of the particle is totally or partially converted into internal energy of one of the particle. Thus, in this collision, total kinetic energy is not conserved.

The motion of particle is right angle to the Earth's magnetic field, the equation of motion for ions reduces to

$$e(\vec{E}_\perp + \vec{V}_i \times \vec{B}) - m_i \nu_{in}(\vec{V}_i - \vec{U})_\perp = 0 \tag{1.11}$$

The force of gravity, collisions between particles and pressure gradients are neglected. Similar equation is written for an electron except the collision with ions is not negligible. Dividing equation (1.6) by m_i, it reduces to

$$\frac{e}{m_i}(\vec{E}_\perp + \vec{V}_i \times \vec{B}) - \nu_{in}(\vec{V}_i - \vec{U})_\perp = 0 \tag{1.12}$$

The gyrofrequency is defined as

$$\Omega_i = \frac{eB}{m_i} \tag{1.13}$$

Then above equation becomes

$$\frac{1}{B}(\vec{E}_\perp + \vec{V}_i \times \vec{B}) - \frac{\nu_{in}}{\Omega_i}(\vec{V}_i - \vec{U})_\perp = 0 \tag{1.14}$$

The ratio ν_{in}/Ω_i is very useful term to determine the existence of electric current in dynamo layer i.e. E-region.

Figure 18 represents the plot of the collision frequencies and the gyrofrequencies as a function of altitude. It is observed that above 160 km the gyrofrequencies of both ions and electrons are greater than the collision frequencies but below 100 km in the direction

26

right angle to the direction of the magnetic field, the electron gyrofrequency reach the same order of magnitude as the collision frequency between electrons and neutral atom. Such condition is good for electric current, but due to weak electron density there is no electric current in this region. The altitude below 80 km for both the ions and electrons the collision frequencies are smaller than the gyrofrequencies, so these particles are moving with the neutral atmosphere.

Since the gyrofrequencies of ions and electrons above 160 km is greater than its respective collision frequencies, hence, the velocity of ions and electron is given by

$$\vec{V}_{e\perp} = \vec{V_{i\perp}} = \frac{\vec{E} \times \vec{B}}{B^2} \tag{1.15}$$

Between the altitude of 100 km to 160 km, gyrofrequency and collision frequency are of the same order of magnitude, motion of ions $\vec{V}_{i\perp}$ are affected by the drag of neutral atmosphere and by the electric field. In this case the ion drift is

$$\vec{V}_{i\perp} = \frac{\vec{E} \times \vec{B}}{B^2} \frac{1}{1 + r_i^2} + \frac{\vec{E}_\perp}{B} \frac{r_i}{1 + r_i^2} + (\vec{V}_n \times \vec{B}) \frac{r_i}{1 + r_i^2} + \vec{V}_{n\perp} \frac{r_i^2}{1 + r_i^2} \tag{1.16}$$

where $r_i = \nu_{in}/\Omega_i$. Above E-layer when r_i becomes small, the first term is dominant then the velocity of ion becomes

$$\vec{V}_{i\perp} = \frac{\vec{E} \times \vec{B}}{B^2}$$

And at the bottom of E layer, where r_i is large, the last term dominant, so $\vec{V}_{i\perp} = \vec{V}_{e\perp}$, the ions and neutral atmosphere are equal. In the direction aligned to the Earth's magnetic field the equation for net force is expressed as:

For ions

$$0 = m_i \vec{g} - \frac{1}{N_i} \vec{\nabla}(N_i kT) - m_i \nu_{in}(\vec{V}_{i\parallel} - \vec{V}_{n\parallel}) \tag{1.17}$$

This implies $\vec{V}_{i\parallel} = \vec{V}_{n\parallel} + \vec{V}_{d\parallel}$; $\vec{V}_{d\parallel}$ is ambipolar diffusion drift due to gravity and pressure gradients.

For electrons

$$0 = m_e \vec{g} - \frac{1}{N_e} \vec{\nabla}(N_e kT) - e\vec{E}_\parallel + m_e \nu_{en}(\vec{V}_\parallel - \vec{V}_{n\parallel}) \tag{1.18}$$

This implies $\vec{V}_{e\parallel} = \vec{V}_{n\parallel} + \vec{V}_{d\parallel} - \frac{\vec{J}_\parallel}{N_e . e}$; $\vec{J}_\parallel$ is FAC.

If the contribution due to ambipolar diffusion drift below 180 km is neglected. Then
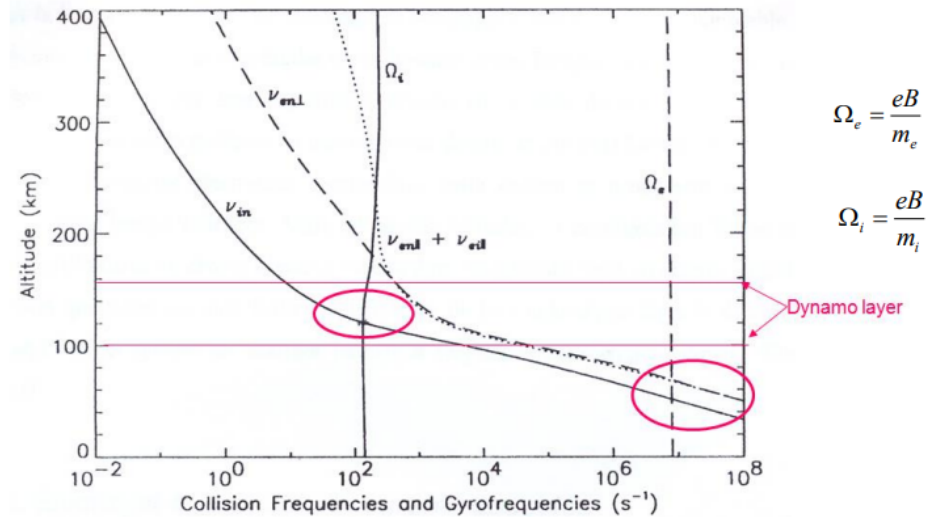
Figure 18: Variation in gyrofrequencies and collision frequencies with the altitude 0 km to 400 km (Richmond, 1995).

$$\vec{V}_{i\parallel} \cong \vec{V}_{n\parallel}$$

1.2.3 Equation of Electric Current in the Ionosphere

The ionosphere is a plasma. The force which induces the motion of ions and electrons decide the strength of electric current and the formation of ionospheric conductivities. The electric current density in a plasma is

$$\vec{J} = \sum N_q e_q \vec{V}_q \qquad (1.19)$$

where

N_q = particle density in N m^{-3};

e_q = charge of the particle in C;

$\vec{V}_q$ = velocity of the particle in m s^{-1}

In the ionosphere this equation reduces to

$$\vec{J} = N_e e(\vec{V}_i - \vec{V}_e) \qquad (1.20)$$

where

$\vec{J}$ = electric current density in A m^2;

N_e = density of electron in m^{-3}

e = electronic charge in C;

$\vec{V}_i$ = drift velocity of ions in m s^{-1}

$\vec{V}_e$ = drift velocity of electrons in m s^{-1}

Total current density is obtained as

$$\vec{J} = \sigma_p(\vec{E}_\perp + \vec{V}_n \times \vec{B}) + \sigma_H(\vec{E}_\perp + \vec{V}_n \times \vec{B}) + \sigma_\parallel \vec{E}_\parallel \tag{1.21}$$

$$\sigma_p = \frac{N_e e}{B}\left(\frac{\nu_{in}\Omega_i}{\nu_{in}^2 + \Omega_i^2} + \frac{\nu_{en\perp}\Omega_e}{\nu_{en\perp}^2 + \Omega_e^2} \right) \tag{1.22}$$

$$\sigma_H = \frac{N_e e}{B}\left(\frac{\Omega_e^2}{\nu_{en\perp}^2 + \Omega_e^2} - \frac{\Omega_i^2}{\nu_{in}^2 + \Omega_i^2} \right) \tag{1.23}$$

where, σ_p is called Pedersen conductivity in the oriented to electric field, σ_H is called Hall conductivity and its direction is right angle to the both electric and magnetic field and $\vec{V}_n \times \vec{B}$ is called dynamo electric field. Figure 19 represents the variation in noontime parallel conductivity $\sigma_\parallel$ along with the Pedersen and Hall conductivity with altitude. This shows Hall conductivity decreases faster rate than Pedersen conductivity, whereas the noontime parallel conductivity increases with altitude.
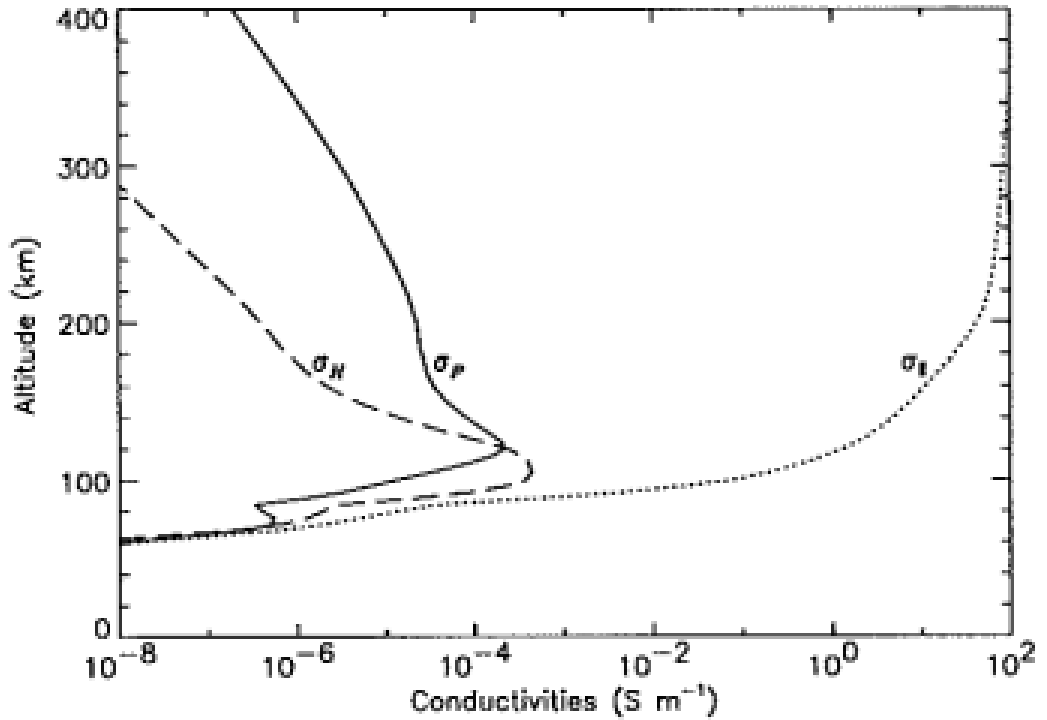
Figure 19: Altitude profile of noontime parallel conductivity, Pedersen conductivity, and Hall conductivity at 44.6° N, 2.2° E for solar minimum on 21 March 1990 (Richmond, 1995).

1.2.4 Low Latitudes Ionosphere during Magnetic Quiet Periods

In this section, we discuss about the phenomena related to the ionosphere at low latitude. The circulation of neutral wind produces the prominent effect to the density of ionospheric and its dynamics, which allow the plasma to move along the geomagnetic field line to produce an equatorward meridional flow and which pushes it equatorward and upward. The height of the fountain effect (Coley et al., 1990) is determined by the height of the ionized layers. Plasma dynamic also produces the phenomena such as polarization electric fields, day-night asymmetry of the zonal drift because of diurnal E-region conductivities (Rishbeth, 1971), and the ion drag effect, which permits the zonal wind to attain higher velocities earlier in the evening due to its upward plasma motion before sunset (Anderson & Roble, 1974).

1.2.4.1 Equatorial Ionization Anomaly

It is a double-humped structure in the ionosphere's latitudinal arrangement in low latitudes, created around 20° of the magnetic equator. During equatorial fountain, a trough within the ionization of F_2 layer occur near the magnetic equator and two crests of enhanced plasma on the either side around 17° in magnetic latitude (Appleton, 1946). This effect is produced when the geomagnetic field ($\vec{B}$) and zonal electric field ($\vec{E}$) above the magnetic equator are orthogonal and produces the vertical $\vec{E} \times \vec{B}$ drift which is driving the plasma higher and subsequent propagation along the geomagnetic field lines because of gravitational and pressure gradient forces develop the Equatorial Ionization Anomaly (EIA) (Martyn, 1955). Plasma is moved up and along magnetic field lines by solar heating and tidal movements in the lower ionosphere. The global scale neutral wind dynamo in E-region set up an electric field (Richmond et al., 1976), which provides the triggering force of equatorial fountain. High-conductivity geomagnetic field lines transmit this force to the F-layer. The hemispheric asymmetry in intensity and location of EIA crest is determined by the circulation of transequatorial neutral wind (Hanson & Moffett, 1966). The position and the intensity of the EIA crest was noticed varying with day, month, season, solar activity, and longitudes (Balan & Bailey, 1995). Figure 20 represents asymmetry in EIA crest in two hemispheres.

1.2.4.2 Equatorial Electrojet

The Equatorial Electrojet (EEJ) is a narrow ribbon-like structure of enhanced current moving east-west in the ionosphere near the magnetic equator around ± 5° (Chapman, 1951). At the dip equator, the Earth's magnetic field's horizontal configuration, combined with the global-scale daytime dynamo electric field, causes positive and negative charges to accumulate at the dawn and dusk terminators, respectively, giving rise to an eastward electrostatic field along the magnetic equator. This results to downward Hall
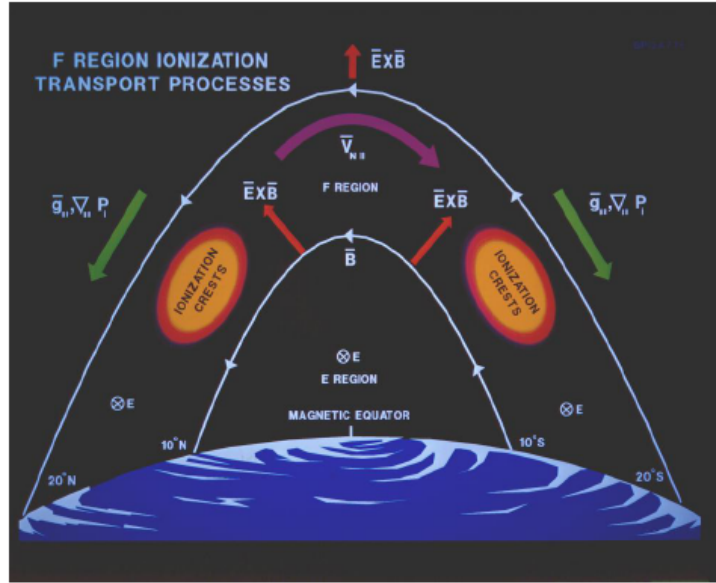
Figure 20: Schematic of formation of equatorial anomaly with two equatorial crests in two hemispheres. $\vec{E} \times \vec{B}$ upward plasma drift and its diffusion along the geomagnetic field lines shown by arrows, resulting Fountain effect. (Basu et al., 2002).

current and eastward-directed Pederson current. By the presence of non-conducting boundary layers, Hall current is restricted, which causes the effective (Cowling) conductivity aligned to the boundaries is tremendously strengthen far away the usual Pederson conductivity (Cowling, 1948). In E-region at the height 100 km to 130 km, the existence of low conducting sheets above and under is sufficient to drive this Cowling conductivity in the east-west direction. This process occurs mainly due to electrodynamics of horizontally stratified ionosphere with anisotropic conductivities. EEJ taken as a "proxy index" of equatorial fountain (Stolle et al., 2008). The sudden variation in the H-component of the geomagnetic field closer the magnetic observatory located at equator give the measurement of EEJ. The EEJ varies with season and with the solar activity level (Alken & Maus, 2007). After meeting at the equator, EEJ is produced by solar quiet (S_q) current result of global hemispheric dynamo activity of neutral wind, which expresses as an east-west electric field above the magnetic dip equator. The equatorial fountain effect is caused by $\vec{E} \times \vec{B}$ vertical plasma drift concerning the magnetic equator. Equatorial fountain and EEJ both effect the Total Electron Content (TEC) variation at low latitude (Anderson et al., 2002). The strength of EIA and the EEJ of the day have a high degree of association. (Rama Rao et al., 2006) during quiet days. Figure 21 demonstrates a model for the formation Pedersen and Hall current density along eastwards and upward/downward direction.

The equatorial electric current is stronger than the current at middle latitude because the geomagnetic field is horizontal there at the equator. In E-region ionosphere, near dip-equator the horizontal the Earth magnetic field $\vec{B}$ is northward and zonal electric field $\vec{E}_y$ produces eastward Pederson current $\vec{J}_{p1}$ and downwards Hall current $\vec{J}_{H1}$ associated

31

with $\vec{E} \times \vec{B}$ drift (Grodji et al., 2017).

$$\vec{J}_{\text{p1}} = \sigma_{\text{p}}\vec{E}_{\text{y}} \tag{1.24}$$

$$\vec{J}_{\text{H1}} = -\sigma_{\text{H}}\left(\frac{\vec{E}_{\text{y}} \times \vec{B}}{\vec{B}}\right) \tag{1.25}$$

When an ion drifted in E-region obstructed due to collision with neutral particle while the electrons are free to move, produces charge separation which creates the vertically upward polarized field $\vec{E}_{\text{p}}$. This $\vec{E}_{\text{p}}$ gives upward Pederson current $\vec{J}_{\text{p2}}$ which is given by

$$\vec{J}_{\text{p2}} = \sigma_p\vec{E}_{\text{p}} \tag{1.26}$$

The westward $\vec{E}_{\text{p}} \times \vec{B}$ drift gives an electron to eastwards, intense Hall current which is obtained by (Grodji et al., 2017)

$$\vec{J}_{\text{H2}} = -\sigma_{\text{H}}\left(\frac{\vec{E}_{\text{p}} \times \vec{B}}{\vec{B}}\right) \tag{1.27}$$

At equilibrium, the net upward flow of current is zero because of counter-balanced $\vec{J}_{\text{H1}}$
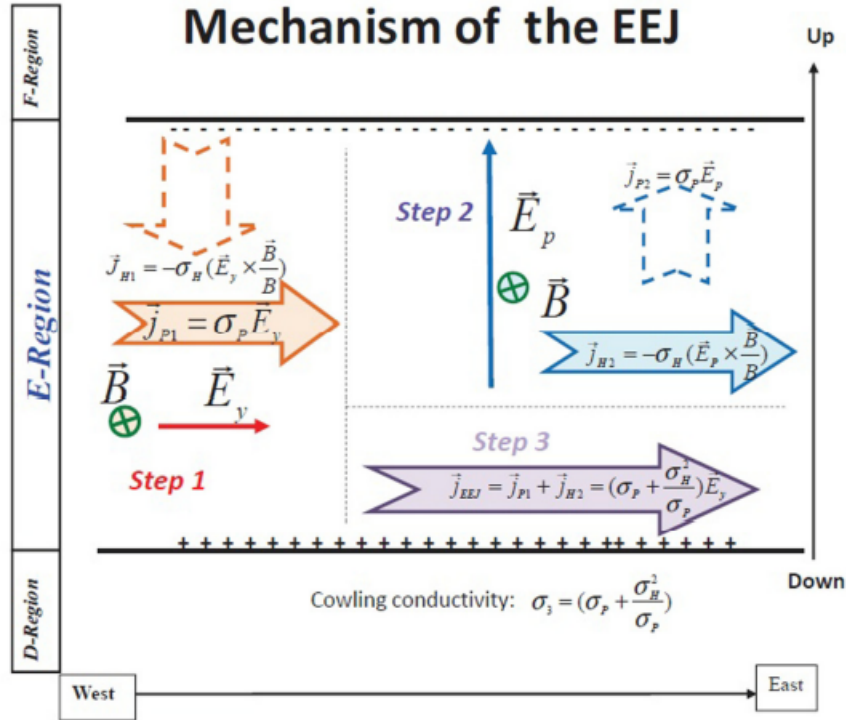
Figure 21: Mechanism of equatorial electrojet current in E-region (Grodji et al., 2017).

by $\vec{J}_{p2}$ ie

$$\vec{J}_z = \vec{J}_{p2} + \vec{J}_{H1} = 0 \tag{1.28}$$

Thus the net eastward current is given by the sum of the eastward Pederson current and eastward Hall current.

$$\vec{J}_{EEJ} = \vec{J}_{p1} + \vec{J}_{H2} = \sigma_p \vec{E}_y - \sigma_H \left(\frac{\vec{E}_p \times \vec{B}}{\vec{B}} \right) = (\sigma_p + \frac{\sigma_H{}^2}{\sigma_p}) \vec{E}_y = \sigma_C \vec{E}_y \tag{1.29}$$

where

$$\sigma_C = (\sigma_p + \frac{\sigma_H{}^2}{\sigma_p}) \tag{1.30}$$

is called Cowling conductivity, which gives an expression for enhance conductivity at the equator.

1.2.4.3   Pre-Reversal Enhancement

Ionospheric plasma drag caused by the east-west neutral wind generates an upward electric field which plays an essential role in plasma distribution in the low-latitude F-region of the ionosphere in night, resulting in post-sunset anomalies (Fejer et al., 2013). Under the effect of the eastward zonal component of the electric field, the polarized electric field causes plasma around the magnetic equator will raise throughout the day and fall at night (Eccles et al., 2015). In a study by Fejer et al. (1979) noted that a considerable and relatively quick increase in the eastward daytime electric field inside this E and F regions immediately before it reverses in the night in a westward direction. Figure 22 shows the result of latitudinal variation in equatorial plasma drift taken from satellite ROCSAT-1 during moderate solar flux. The Pre-reversal Enhancement (PRE) is a short and dramatic uplifting of the electric field near sunset that causes an increase in height within the equatorial ionosphere. In 2001, Abdu et al. found that PRE initiate for formation of Rayleigh-Taylor Instability (RTI), is one of the main factor contribute into the emergence of Equatorial Plasma Bubbles (EPBs) (Abdu, 2001). The intensity of PRE depends upon the factors such as magnetic activity, season, and phases of solar cycle (Farley et al., 1986).

1.2.4.4   Plasma Bubble

Plasma bubbles are a distinct occurrence of lower plasma density in the equatorial F-region of the ionosphere, which initially emerges on the bottom side of the F-layer (~ 200 km) and then travel upward to the topside of ionosphere. The plasma bubbles
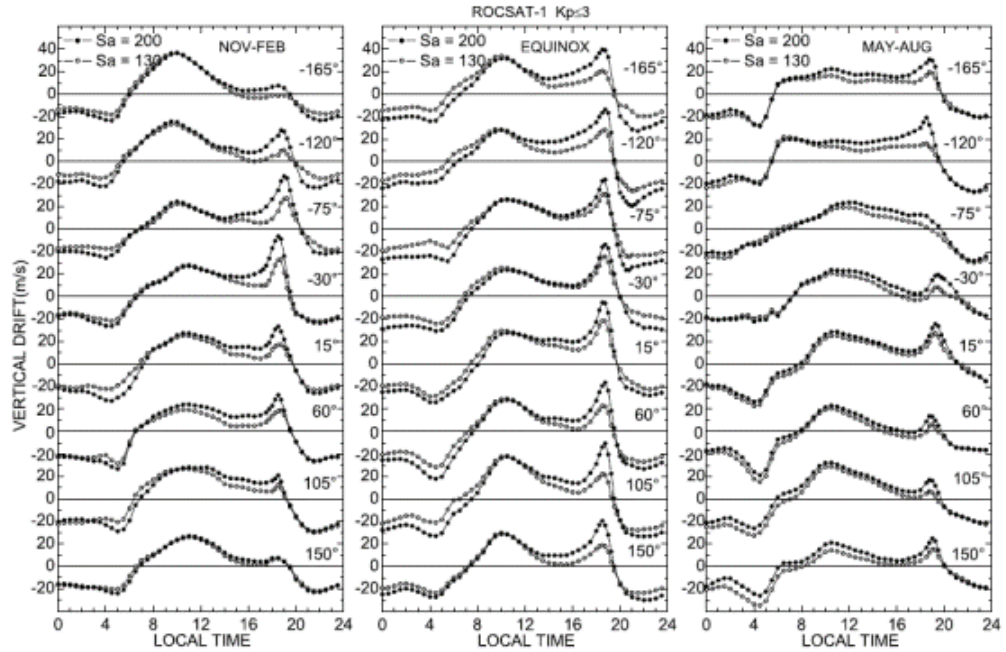
Figure 22: Longitudinal variability of equatorial plasma drift taken from ROCSAT-1 satellite for moderate solar flux (Fejer et al., 2008).

are also known as equatorial plasma bubbles (EPBs) or plasma depletion (Ondoh & Marubashi, 2001). Figure 23 represents a typical picture EPB taken from CCD camera from Christmas Island on September 28, 1995 (Chapagain, 2011). Plasma bubbles have large-scale structure which degrades the GPS signal by introducing phase delay when passes through it (Haase et al., 2011). Formation of plasma bubble starts when production of ion pair stops after sunset and recombination's of ion lower density of the ionized layer. The generation and evolution of EPBs can be explained through RTI (Chapagain et al., 2009; Chapagain, 2011). Several techniques such as airglow detection, incoherent backscatter radar, rocket soundings, ionogram analysis, in situ measurements, and GPS phase shift were employed to study the plasma bubble, but each method has limitations in their measurements (Portillo et al., 2008; Chapagain, 2011; Chapagain, Taylor, et al., 2012). Coherent scatter radar detect highly localized irregularity, the measurement of air glow is affected by clouds and moonlight whereas GPS system of measurement require continuous monitoring (Portillo et al., 2008).

1.2.5 Coupling between High and Low Latitudes

Increased geomagnetic activity can cause substantial perturbations in the global ionospheric electric field across a wide variety of temporal and geographical scales (Fejer et al., 2017). These disruptions are primarily caused by the dynamos of solar-wind/magnetospheric and ionospheric perturbation (Fejer et al., 2017). Following large variations in the high latitude current system, magnetospheric electric fields may reach

34
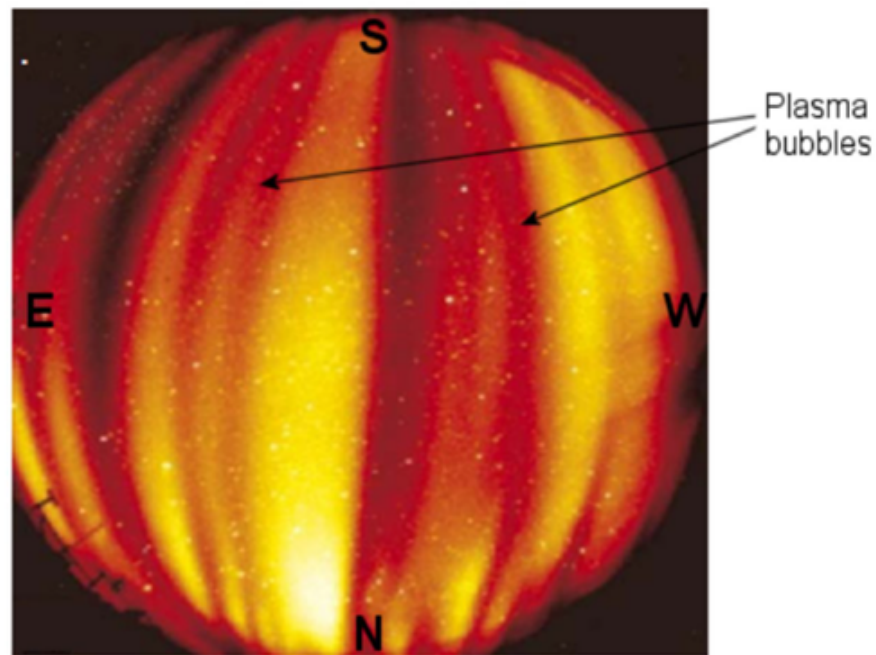
Figure 23: Plasma bubble produced by USU all-sky CCD camera from Christmas Island from September 28, 1995. White dots in the picture represents the stars and dark band for shows the plasma bubbles (Chapagain, 2011).

into the low latitude ionosphere (Fejer & Scherliess, 1997). The Prompt Penetration of Electric Fields (PPEFs) disturbances, which occur on a shorter time scale less a few hours, occur almost immediately from auroral to equatorial latitudes and the disruption in the ionospheric field over the equatorial ionosphere (Tsurutani et al., 2004; Mannucci et al., 2005; Tsurutani et al., 2008). The ionospheric disturbance dynamo is a wind-driven electric field with short-term and long term effects. The entanglement of dynamos disturbance can reach equatorial latitudes in 1 hour to 3 hour and can stay for up to 48 hour (Scherliess & Fejer, 1997).

1.2.5.1 Prompt Penetration of Electric Field

Prompt penetration of electric field is the penetration of a magnetospheric electric field within the low latitude ionosphere as a result of a sudden change in the convection electric field at high latitude, which can be noticed as a sudden rise or fall in the AE index (Fejer & Scherliess, 1995). Because of the solar wind-magnetosphere dynamo, huge changes take place in the high latitude field-aligned currents system (Sazykin, 2000). PPEF is eastward during daytime and westward at the night and southward from mid-night to noon and northward from noon to mid-night (Tsurutani et al., 2004; Mannucci et al., 2005; Tsurutani et al., 2008). After a drop in the polar cap potential and a sharp drop in the AE index, the observed polarity reverses (Kelley et al., 1979; Fejer

et al., 2008) . In general, PPEFs are the phenomena of short lived but during the storm of November 2003, this event was identified for longest duration (Fejer et al., 2008). Several model have already been developed to investigate PPEF, which are based on AE index (Fejer & Scherliess, 1997) and solar wind plasma parameters (Manoj et al., 2008). Other models based on disturbances such as solar flux irradiation, seasonal, and rotational changes identified in polar cap potential are accessible in the text of (Sazykin, 2000). PPEF and Disturbance Dynamo Electric Field (DDEF) have ability to affect low latitude ionosphere and their effect can have similar or opposite polarity. The effects of PPEF and DDEF can be identified by tracking and filtering out observations following a dramatic spike or fall in the convective electric field at high latitudes using the AE index (Fejer & Scherliess, 1997).

1.2.5.2 Thermal Expansion of Atmosphere

The major sources of energy deposited in the upper atmosphere and ionosphere of the Earth are extreme ultraviolet radiation from Sun, auroral particle precipitation, joule heating from electric current during geomagnetic storm, and gravity wave propagated from the lower atmospheric phenomena. The effect due to lower atmospheric phenomena is important during geomagnetically quiet periods, while during the disturbed periods of geomagnetic storms, auroral particle precipitation and Joule heating are dominant (Robinson & Zanetti, 2021). The Earth's magnetosphere is squeezed in the course of geomagnetic storms, resulting in the mapping of powerful electric fields across geomagnetic field lines to the high-latitude ionosphere (Yizengaw, 2004) and it penetrates to the low latitudes (Aarons & Rodger, 1991). In 2003, Blagoveshchensky identified this electric field at high latitude produces a rapid plasma convection of neutral wind by mean of collision (Blagoveshchensky et al., 2003). Similarly, the energetic particle dissipated lower the thermosphere and it's below, expand the auroral region producing intense ionization at higher latitudes. The coupling of the electric field to the magnetosphere at high latitudes increases the input energy, resulting in the heating of ionized and neutral gases. Due to this unequal means of expansion, a pressure gradient develops in the thermosphere, causing strong neutral winds (Buonsanto, 1999). This disruption in thermospheric circulation affects the neutral composition and causes the plasma to travel up or down along field lines, affecting the rate of ionized species generation and recombination. Polarization in electric field takes place in disturbed neutral wind due to dynamo effect (Aarons & Rodger, 1991) when collision occurs with plasma in presence of geomagnetic field (Blagoveshchensky et al., 2003). This electric field affects the ions and neutral species to couple in upper atmosphere (Chapagain, Taylor, et al., 2012; Chapagain, Makela, et al., 2012). The composition of ionosphere changes during disturbed electric field. The study shows molecular concentration increased and atomic concentration reduced during magnetic storm resulting reduction in the atomic to molecular

ratio by a factor of 20. Ionized species are then transported from the upper to the lower latitudes by the equatorward storm-induced wind. (Danilov & Lastovicka, 2001).

1.2.5.3 Disturbance Dynamo Electric Field

Equatorial wind surges are erupted during the geomagnetic storms, changing the meridional circulation and causing significant changes in the global conductivity and the ionospheric electric field. Blanc and Richmond first proposed a theoretical description for the ionospheric disturbance dynamo in 1980, demonstrating that storm-time heating at high latitudes can cause significant interruptions in the thermospheric wind as well as the worldwide conductivity distribution, resulting in ionospheric electric fields and currents. (Blanc & Richmond, 1980). Figure 24 represents a simplified diagram of the ionospheric disturbance dynamo (Mazaudier & Venkateswaran, 1990). To conserve angular momentum, the equatorial thermospheric wind circulation (V_s) causes the winds to blow westward (V_w). These wind patterns cause westward drifts, resulting in an equatorial ionospheric Pederson current (Jp) that is strongest about 150 km, where Pedersen conductivity is high. Such currents build up positive charges near the geomagnetic equator, resulting in a poleward current that enables eastward Hall currents and westward plasma drifts, which are most prevalent at mid-latitudes. Because of the enormous conductivity gradients, these currents are unable to pass across the dusk and dawn terminators. The dusk-to-dawn electric field is formed by the accumulation of electric charges, which is then diverted to high and low latitudes, resulting in the polar and equatorial vortex. At equatorial latitudes, the equatorial vortex develops in the opposite direction of the quiet-time current system, causing the ionospheric disturbance dynamo to have a counter-effect. The equatorial vertical disturbance dynamo drifts were discovered to be opposite to the normal quiet patterns by Fejer et al. (1983), which agrees well with the Blanc-Richmond model. Their research also identified for the most storm, there is a difficulty to isolate the competing the effects from the DDEF and PPEF (Fejer & Scherliess, 1997; Kivelson et al., 1995). This difficulty is short out using binning technique in which AE index is used as a proxy index (Fejer & Scherliess, 1995). The time lag between geomagnetic activity enhancements and the equatorial response were determined using drive disturbance dynamo disturbance. Fejer & Scherliess (1997) at first empirical model of equatorial disturbance dynamo vertical drift using extensive Jicamarca observations and AE indices and recognized that the disturbance dynamo vertical drifts are downward with lower magnitudes in the course of the day and upwards in the night with greatest magnitudes near the sunrise. The research found that the response times of the high latitude current and the related equatorial disturbance dynamo are approximately 1 hour to 12 hour and 12 hour to 28 hour, respectively.
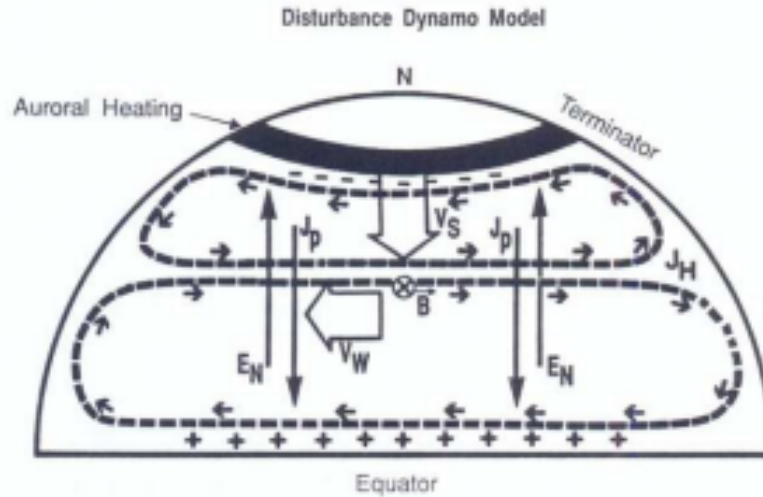
Figure 24: Illustration of ionospheric disturbance dynamo model. It shows equator ward wind circulation at high latitude ultimately produces an electric field opposite to the quiet-time electric field at equatorial latitude (Mazaudier & Venkateswaran, 1990).

1.3   Space Weather

The Earth and its magnetosphere are highly coupled with the solar activity. The continuous emission of stream of highly energetic particle from the solar origin is constantly modulating the Earth's magnetosphere and its atmospheric dynamics. The Earth's atmosphere and its magnetosphere acts as the protective layer by absorbing and deflecting the harmful radiation and particle from the Sun reaching to the Earth. The violent eruptive phenomena such as CME, solar flare are the major solar activities, which drive the space weather phenomena. The space weather is the study of new insight into the complicated influences and effect of the Sun and any other extra emission such as cosmic ray on interplanetary space, the ionosphere, thermosphere and magnetosphere of the Earth, the terrestrial and space based assets, including the endangering affects to the health and life (Bothmer & Daglis, 2007). Figure 25 is illustrating linking of the space weather phenomena with social infrastructure. The space weather is comparatively latest arena of research in the field of space science research although the first event of space weather was noticed in 1859 known as Carrington event by the eruption of intense white-light solar flare reaching to the Earth with intense and broad range responses (Cerveny, 2006). The visualization of aurora at low latitude, induced current in the telegraph wires in United State of America (USA) and in Europe and the some earlier noticed phenomena related to the space weather (Tsurutani & Zhou, 2003). In recent technological advance era of satellites, airplanes, electric power supply, and communication are more vulnerable to the solar activities. Hence, precise understanding and forecasting of the solar eruptive event and its impact to the space weather a great concern to the modern human society.
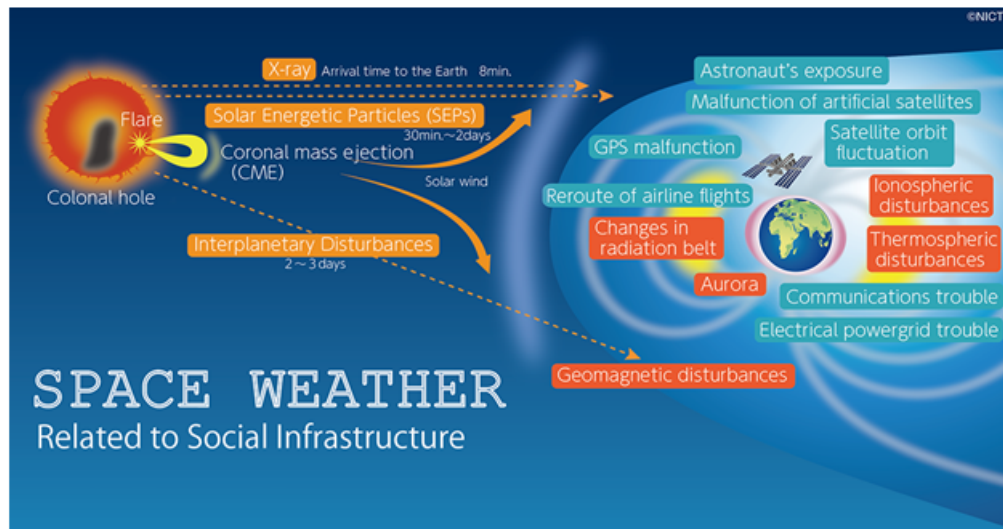
Figure 25: Illustrating solar eruptive phenomena and their space weather effect great concern for human society (`https://swc.nict.go.jp/en/knowledge/relation.html`).

1.4 Motivation

The geospace environment plays crucial role in several modern technologies such as communication, navigation and power grid that impact daily human activities. The physical process taking place near-Earth space environment is affected by solar activities. Among the various layer of the atmosphere, ionospheres is the one which is having a thin layer of plasma and has unique electrodynamics and affect the communication signal passes through it. Perturbation in density of ionospheric plasma creates challenging threats, which may produce extreme disruption in radio wave and failure in communication and navigation system. The scientific communities are trying to investigate the electrodynamics and seedling condition of occurrence of plasma irregularities till today. Climatological study on ionosphere figure out the normal, long-term and persistent feature of Earth's ionosphere, whereas the study on ionospheric weather point out the short-term variation from minutes to week. The study of climatic ionosphere provides the clue to scientists in estimating fast changing ionospheric weather phenomena, which produces adverse effect to the communications and navigation signals. The equatorial and polar region ionosphere highly affected by large scale electrodynamics than at mid-latitude region and it is suitable location for the construction of laboratory. Given the importance of ionospheric research in modern life, it seems appropriate to work on analysis of ionospheric variability and precision. With this purpose in mind, this thesis, a general analysis of the mid-low-latitudes ionospheric investigation has been conducted.

1.5 Rationale of the Study

This thesis intends to study characteristic features of SSSs and climatology of ionosphere over Nepal, which lies in mid low latitude region through observational analysis of ground based data, model and satellite data. This study attempted to answer a number of scientific problems, that are necessary and important to the space weather research community. What distinguishes SSSs from other similar events? Is it possible to pinpoint the physical mechanism responsible for these characteristics and variations?

1.6 Objectives

The general objective of the proposed work is to study SSSs related signatures at middle and low latitude ionosphere.

The following specific objectives have been setup to fulfill the general objective.

1. Study the solar wind parameters, IMF Bz and geomagnetic indices during SSSs.

2. Study the variation in horizontal component of geomagnetic field at middle and low latitude regions during SSSs events.

3. Study the effect on ionospheric parameters during SSSs.

4. Study the climatology of ionosphere over Nepal using GPS total electron content (TEC) data from 2008 to 2018.

5. Study the TEC profile at middle latitude during intense geomagnetic storms of solar cycle 24.

1.7 Outlines of Thesis

This thesis work is organized as follows:

Chapter-1: Introduction, this chapter discusses about Sun and solar activities, background of SSSs, ionospheric dynamics, the motivation of this research work, rationale of the study and research objectives.

Chapter-2: In this section, the literature review of TEC, SSSs, horizontal component of the Earth's magnetic fields and ionospheric parameters have been presented. Its aim is to identify the research problem and verify the fundamental basis of the work.

Chapter-3: Materials and methods, this chapter provides the insight of fundamental concept of theory, methods and datasets used. It includes the necessary mathematical relation used to calculate the parameters studied in the research work.

Chapter-4: In this chapter, the outcomes of the research are documented and their interpretations and analysis have been discussed.

Chapter-5: This chapter includes conclusions of the present work and its possible extension in the future research have been recommended.

Chapter-6: In this chapter, the concise description of the overall work has been presented.

Finally, the references used in this research work are included. The major published articles, information of participation and presentation in scientific conferences are incorporated at the end of the thesis.

CHAPTER 2

2. LITERATURE REVIEW

The ionospheric electrodynamics is highly variable during geomagnetic storms. Its variability has drawn the awareness to the space scientists to explore some facts since last few decades. There are many ionospheric parameters used to study its electrodynamics and some of them with their research status have been underline below.

2.1   Total Electron Content

The amount of free electrons in the atmosphere is large enough to interfere with electromagnetic wave propagation (Budden, 1985). Due to intense X-ray and UV ray, ionized region of the atmosphere are formed. This is referred as ionosphere (Budden, 1985). As we move to the lower altitude, rate of absorption of radiation by atmospheric particles increases, but some of it get absorbed in upper layer. The degree of ionization also increases, which again increases the recombination rate at lower atmosphere. A height is reached, where lower radiation, greater ionization, higher degree of recombination rate, balance out and ionization starts to decreases at lower height (Budden, 1985; Kelley, 2009). This causes formation of different layers or ionization peaks in the ionosphere. Klobuchar (1991) has described the various TEC measurement techniques used during the middle of the 20th century viz. Faraday rotation, differential carrier phase, and group delay techniques. Ciraolo & Spalla (1997) compared the TEC from the Navy Navigation Satellite System (NNSS) and the GPS. The TEC values were calculated from the satellite using Doppler method. The Doppler method relies on measuring the differential phase between two coherent carriers transmitted by satellite and scaled to the same nominal frequency. The comparison between these two sets of TECs contributes to a better knowledge of the electron composition of the upper ionosphere. Arikan et al. (2004) has described a brief idea for the calculation of TEC. They used GPS data for the regularized estimation of vertical total electron content (VTEC). Examining the TEC can reveal both short- and long-term changes in ionospheric structure, as well as anomalies and disturbances. Studies about the prompt penetrations on ionosphere are described for the intense geomagnetic storms, in a research paper of Mannucci et al. (2008). They discussed about the variation of TEC in different time interval during geomagnetic storms. The TEC data were acquired from the ground based GPS receivers using Challenging Minisatellite Payload (CHAMP) satellite. Shim (2009), calculated the variation of TEC in the low- and middle-latitude Ionosphere. She also studied the modeled TEC variation

during low and medium solar activities at low and middle latitude in the afternoon and post-sunset at three different longitude sectors. Based upon the analysis of 1000 GPS ground-based receivers data across the globe, she projected the spatial correlations of day-to-day ionospheric TEC variations on a global scale. Furthermore, a paper by Heelis et al. (2009) describes about the variation of the ionospheric plasma concentration and the causes of such variation. They discovered that sustained exposure to low-level EUV radiation caused ionosphere dynamics and plasma density variation. Chapagain (2011) has studied the climatology of post sunset equatorial spread F including formation and height of initial spread F along with the radar plumes using long term radar data. They have also analyzed the relationships between spread F onset velocities and pre-reversal drift peak velocities, the dynamics of equatorial spread F using ground-based optical and radar measurements. In addition, using the airglow image measurements, they analyzed the formation, development, and dynamics of EPBs (Chapagain, 2011; Chapagain, Taylor, et al., 2012; Sharma et al., 2012), elucidated the response of the geomagnetic storm of 24 August 2005 at low-latitude ionosphere. They used TEC data obtained from the GPS receivers. In their research, they also discussed the ionospheric influence of the different geomagnetic disturbances and solar wind parameters using TEC measurements. Similarly, Yue et al. (2011) studied the quantitative evaluation of slant TEC using the Low Earth Orbit (LEO) satellite based observation. On this research, the measuring technique was the LEO based on Slated Total Electron Content (STEC) in the Constellation Observing System for Meteorology, Ionosphere, and Climate (COSMIC) . With this research, one can have a better concept about the TEC evaluation, the different factors affecting this evaluation along with the source and the possible remedies of the errors arising in the whole process.

According to worldwide research on TEC shows that the influence on TEC was greater during the day than at night, and at low latitudes than at high latitudes. Effect on TEC is noticed more on either side of the dip equator than at the dip equator (L. Liu et al., 2009). In 2015, Dashora and Suresh examined the properties of TEC data at low latitude from solar cycles 23 and 24 over the Indian sector in 2015 using global ionospheric data (Dashora & Suresh, 2015). In the study of ionospheric response utilizing GPS TEC, International Reference Ionosphere (IRI), and Thermosphere Ionosphere Electrodynamics General Circulation Model (TIE-GCM) TEC of solar cycle 24 Rao, Chakraborty, et al. (2019) identified a two-fold hump pattern in solar flux as well as TEC at low latitude station Varanasi, India. Mahesh et al. (2019) has studied latitudinal variability of ionospheric TEC in the northern hemispheric and found that the low latitude has a higher diurnal TEC peak value than mid and high latitude, and spring and fall have the greatest seasonal variability than summer and winter.

Various studies on TEC have been conducted throughout Asia, however, no results for

the climatology of TEC over Nepal for a long period of time of roughly one solar cycle have been reported. This thesis discusses for the first time the ionospheric features of Nepal such as diurnal, yearly, seasonal, and solar cycle dependency of TEC on local ionospheric conditions using GPS TEC data from four Nepalese GPS stations of solar cycle 24 from year 2008 to 2018.

2.2   Characteristics of Super Substorms

A magnetospheric substorm is a common and basic phenomenon that happens when energy is released in the Earth's magnetosphere and ionosphere (Akasofu, 1964). The substorm was accompanied by a brief increase in earthward convection in the magnetotail, which was followed by a global alteration in the tail's magnetic morphology, indicating a transfer of stored magnetic energy due to an imbalance in day-side and night-side reconnection rates (McPherron et al., 1973). Energy is transmitted into the magnetosphere/magnetotail by magnetic reconnection in the southbound directed IMF and the northward pointed geomagnetic field at the dayside magnetopause (Tsurutani & Meng, 1972; Echer et al., 2008). Substorms were once thought to be an important feature of magnetic storms (Gonzalez et al., 1994), but they were later shown to occur independently of the storm (Tsurutani & Meng, 1972) and outside the main phase of the magnetic storm (Gonzalez et al., 1994; Hajra et al., 2013). The SSSs are extremely powerful substorms with SML or AL indices of < -2500 nT or more (Tsurutani et al., 2015). The SML index is an extension of the AL index that is produced by all SuperMAG network stations located not only at auroral latitude (60° to 70° geomagnetic latitudes), but also at higher and lower latitudes (Rostoker, 1972; Gjerloev, 2012). The SSSs as a singular event were invented by Tsurutani et al. (2015). The SSSs are generated by a small zone of highly concentrated solar wind pressure pulse impinging on the magnetosphere with a duration spanning from 17 minute to 50 minute, according to the researchers. The long-term southern tendency of IMF B_z records the SSSs events. SSSs has been studied in 2016 by Hajra et al. and found that SSSs occurred during all parts of the solar cycle, although the maximum occurrence rate of 3.81 year^{-1} was discovered in the descending phase, while the lowest frequency was recorded during the solar cycle's minimum phase (Hajra et al., 2016). In addition, roughly 77 % of SSSs were linked to a narrow zone of very high-pressure pulses impinging on the magnetosphere, according to their research. Despirak et al. (2018) found that 42 % of SSSs events occurred during the magnetic cloud (MC), 45.2 % in the sheath, and 8.3 % in the ejecta. In 2019, Despirak et al. analyzed two supersubstorms that occurred on 7 - 8 September 2017 during the powerful magnetic storm and discovered that ionospheric currents created during SSSs were documented on a global scale across the Earth (Despirak et al., 2019). Tsurutani et al. (2020) suggested that the SSS could generate Geomagnetic Induced

Current (GIC)/power outages, which are common in magnetic storms. The effect of SSSs evolved on a global scale in longitude, from before midnight, through the night and morning, and also into the day sector, according to a recent paper titled "Longitude geomagnetic effect of the SSSs during magnetic storm of March 9, 2012" by Despirak et al. (2021). However, no previous research have published simultaneous data for fluctuation in horizontal component of the Earth's magnetic field and energy deposition during SSSs in Field Aligned Current (FAC), Polar Cap Voltage (PCV), Ring Current (RC), Joule's Heating (JH), Auroral Precipitation (AP), and Total Energy (TE).

2.3 Ionospheric Parameters

The ionosphere is a delicate environment that is influenced by a variety of factors:

- ionizing radiation emitted by the Sun changes with solar rotation, solar cycle variation, and the formation and decay of active regions.

- neutral atmosphere including acoustic and gravity waves, planetary waves, Earth's surface phenomena such as earthquakes and volcanic eruption.

- electrodynamics for examples dynamo effects of low latitude phenomena, penetration of magnetospheric electric field, electric fields from lightning and sprites.

- geomagnetic effects of solar wind such as magnetic storms, substorms, IMF/solar wind sector structure, energetic particle precipitation, and Joule heating.

The current study focuses on inospheric variation during a SSS (SML$\leq$ -2500 nT), which is a particularly intense substorm. According to Tsurutani et al. (2015), understanding the physical interaction mechanisms in the solar wind-magnetosphere-ionosphere Earth's system in the course of this event is critical for researchers. Thermospheric and ionospheric storms will emerge from the massive amount of energy injected in combination with the super substorm. During this super substorm, the ionosphere will alter in a variety of ways, including changes in critical frequency foF_2, maximum electron density height hmF_2, and virtual height $h'F$. Many previous studies have found that the ionosphere alters in complex ways during storms. Its fundamental physical processes are still poorly understood due to its complexity. In 1997, Lakshmi et al. used ionosonde data to study the response of the huge storm of 13 March 1989 on the top of the equatorial and F-regions of India (Lakshmi et al., 1997). In 2002, Pincheira et al. used an interhemispheric plasma model to investigate the effects of a magnetic storm on the ionosphere and thermosphere over the South American region, employing foF_2, hmF_2, and neutral winds extracted from recorded hmF_2 (Pincheira et al., 2002). In 2014, De Abreu et al. discovered that the occurrence of Equatorial Spread-F (ESF) is closely associated to daily fluctuations of the $h'F$ near the equator in the Brazilian

sector (De Abreu, Fagundes, Bolzan, de Jesus, et al., 2014; De Abreu, Fagundes, Bolzan, Gende, et al., 2014) . Rungraengwajiake et al. (2013); Smith et al. (2015); G. Liu & Shen (2017) investigated the link connecting spread-Fs and other ionospheric parameters, foF_2 and $h'F$ fluctuations with the spreads-Fs. Manju et al. (2007); Narayanan et al. (2014, 2017) explored the seasonal, solar, and magnetic activity variations on the $h'F$ threshold. Many studies on storms, substorms, and ionospheric parameters have been undertaken at various latitudes, but no results on variability of SSSs on ionospheric parameters have been reported to yet. There are many researchers who have carried research on SSSs (Tsurutani et al., 2015; Hajra et al., 2016; Adhikari et al., 2017; Adhikari, Baruwal, & Chapagain, 2017; Adhikari, Dahal, & Chapagain, 2017; Despirak et al., 2018, 2019; Tsurutani et al., 2020). In this thesis, the ionosonde data from Boulder, Colorado, USA (40.0° N, 105.0° W) were used to report for the first time to study the ionospheric responses during the SSSs events on 24 August 2005, 7 September 2017, and 8 September 2017.

CHAPTER 3

3. MATERIALS AND METHODS

3.1 Ground Based Observations

In-depth understanding of several complex mechanisms taking place in the Sun and near to the Earth and far in space be obtained by continuous observations and measurements taken at suitable location. The field variations in internal and external origin are recorded at the magnetic observatories. In earlier method of recording geomagnetic elements: horizontal component (H), vertical component (Z), and angle of declination (D) were recoded using optical based photographic plate. However, these days, the modern equipment fluxgate magnetometer is used to measure the magnetic variation, which uses variation in permeability with strength of magnetization to the ferromagnetic alloy. Due to high permeability, the ferromagnetic core gets saturated by means of electromotive force present to the external field aligned to the axis of core. The voltage generated appears as asymmetric pulses, which are proportional to the external field applied. The magnetic observatories located at equatorial region influenced by east-west equatorial electrojet current system. Low-latitude observatories are located outside of the effects of the electrojet current system and other high-latitude current systems. The ring current intensity is derived using magnetic data of low latitude observatories. The magnetic observatories situated at high latitudes are affected by auroral electrojet and auroral precipitation near auroral region. In this thesis, digital magnetic data of one-minute time resolution from equatorial, mid and high-latitude magnetic observatories are used.

3.2 Near and Far Earth-Space Coverage

In comparison to terrestrial measurements, satellite observations give worldwide coverage. Several satellites have been lunched in space to monitor the solar wind plasma parameters and IMF of the Sun. The satellite can observe the fluctuation in magnetic field and particle flow in space if it is motionless in space but it is not practicable from the Earth. Satellites are locked at Lagrangian point or Liberation point, L1, where the Earth pulls the satellite in the opposite direction and cancels some of the gravitational force of the Sun, in order to stay up and hold out against gravity. The spacecraft at L1 is reporting continuously to the weather monitoring station if there is any change before it reaches to the Earth. But some spacecraft operates from different altitude. Seeking the need of parameters, the scientific community has been introduced several types of orbit called as the polar, equatorial and geostationary satellites. Each sort of orbiting satellite

provides differently on the way of its monitoring. Each satellite is operating in fixed inclination, which is the angle connecting equatorial plane and satellite orbital plane.

3.2.1 Equatorial Plane Orbiting Satellite

These satellites move in an inclination of $\sim 0°$ with equatorial plane. Their orbital altitude varies from ~ 600 km to 2000 km with the orbital period ~ 1.5 hour to 3.5 hour. These satellites observed at a place in varying time.

3.2.2 Geostationary Satellite

These satellites move in geosynchronous orbit in inclination of $\sim 0°$ with having a period 24 hour. These satellites orbits at 6.6 R_E in the same position concerning a location on the Earth. The geosynchronous satellites have been used for communication and meteorological purposes.

The satellite data provide evidences for several processes taking in space in its analytical study with the help of different particle species. In-situ measurements of different parameters have been made possible by several satellites lunched in geospace connecting the Sun and the Earth. The dynamics of Sun-Earth system has been noticed by satellites at L1 points, which are never shadowed by the Earth or Moon. The Advanced Composition Explorer (ACE) stationed at L1 in August 1997 to monitor solar, interplanetary, interstellar and galactic origin solar wind ions and cosmic nuclei having energy range from keV to 600 MeV. The ACE was designed and developed by Johns Hopkins University (JHU)/Applied Physics Laboratory (APL) under National Aeronautics and Space Administration (NASA) Office of Space. Solar and Solar and Heliospheric Observatory (SOHO) stationed at L1 on December 1995 by NASA and European Space Agency (ESA) provides information about CME using coronographs. Geostationary Operational Environmental Satellite (GOES) measures X-rays, energetic particles and magnetic field using onboard Space Environment Monitor (SEM) subsystem. GEOTAIL monitors the global energy flow and its change in the magnetotail, which aids in understanding the fundamentals of magnetospheric processes.

3.3 Remote Radio Wave Technique

3.3.1 Global Positioning System

Global positioning system (GPS) was first developed by United State Department of Defense for military use but later comes under joint venture with Department of Transportation Control; and was open to both the civilian and public. It is made up of 32 or even more artificial satellites system that orbit the Earth in six symmetrically dispersed planes at a height of 20200 km. Each satellite provides information of Positioning,

Navigation and Timing (PNT) to military and civilian orbiting in precise twice a day in its orbit with speed 14000 km h^{-1}. GPS satellites are not geosynchronous satellites; at least four (and no more than twelve) satellites can be seen from any place on the Earth's surface. Figure 26 shows the six different orbital planes of GPS system orbiting the Earth. Each satellite consists of a clock with accuracy of one nano second and they are seen in triangulated pattern. Signal from navigation is passing through a thin layer of ionosphere on its way to the receiver. In each passes, there added a delay of Pseudorandom Noise (PRN)-code signal and phase advance in carrier's signal due to free electrons. To achieve high accuracy in its applications, the perturbation in its signal are taken into its account (Langley, 2000).

GPS uses dual frequencies L$_1$-carrier wave (1575.42 MHz) and L$_2$ (1227.60 MHz). These dual frequencies help to eliminate the ionospheric scintillation. Pseudo ranges are calculated using two PRN codes and are generated from signal transit time to the receiver. Carrier frequencies were used to modulate these codes. The first code available to civilian is Course/Acquisition-Code (C/A-code), which has wave length of 300 m and is modulated only upon L$_1$. The second is Precise-Code (P-code) which is available to the military and specific user has a wavelength of 300 m and is regulated on both L$_1$ and L$_2$. The pseudo-random sequences formulated carefully are being transmitted from the satellite. The transmitted and received signals are analyzed and times of transit for the both signals are determined by means of correlation coefficient. The navigation massages

Figure 26: Six different orbital planes of GPS system (`https://seos-project.eu/GPS/GPS-c01-p03.html`).

include broadcast ephemeris, satellite almanac, satellites time correction, ionospheric information, health status of satellite, which are based on L_1 channel and are actually communicated at slow rate of 50 bps (Spilker Jr et al., 1996). The performance of GPS signal depends upon composition its system and external environmental factors. GPS system consists of space, signal and user segment. The system errors involve thermal noise, hardware channel biases, satellite geometry effect and errors in its clock and ephemeris information. The environmental factors includes ionospheric effect, radio interference with external sources, multipath, obscuration, tropospheric delay basically related to the propagation phenomena (Klobuchar, 1996). Figure 27 shows a measurement of ionospheric events utilizing space and ground-based instruments.

3.3.2 Ionosondes

Ionosondes are instruments that are used to study the vertical profile in the part of ionosphere. The physical structure of atmosphere varies with solar and cosmic activities. The study shows the atmospheric temperature, pressure, chemical composition varies with altitude as a result of it several horizontal layers has been identified in atmosphere. The electron density and hence its refractive index varies in each layer. Time taken by each frequency of broadcasted wave reflected from several layers is used to determine the density of electron and its respective altitude. Ionosonde measures not only the concentration of plasma as the function of height but also it identifies the location of peak layer density. The limitation associated with the Ionosonde is, it cannot provide the information of plasma above the peak layer. The free electrons of the atmosphere affect the path of the electromagnetic radiation traversed. The concentration of electron,
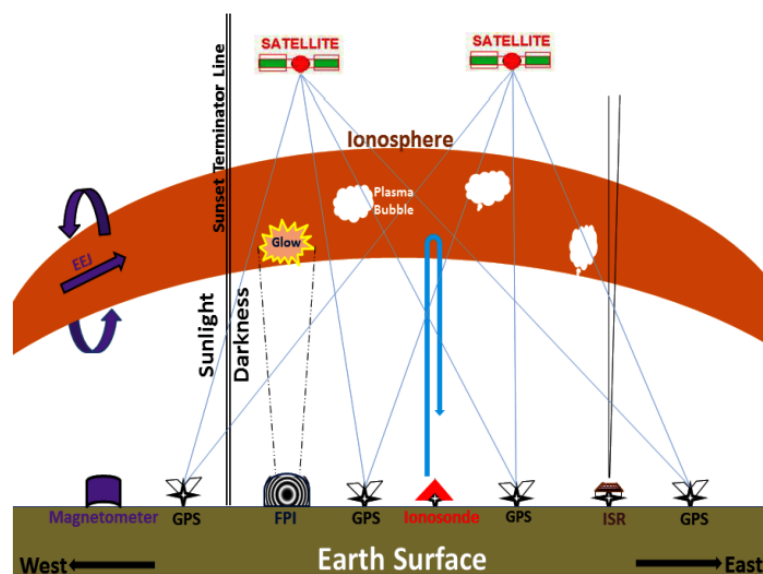
Figure 27: Measurement of ionospheric events applying space and ground-based instruments (Khadka, 2018).

50

magnetic field, frequency, and polarization of the communicated wave determine the refractive index of the medium. Mathematically, the refractive index of the medium of atmosphere varies inversely with the frequency of the transmitted wave. Depending upon polarization of the transmitted wave, the geomagnetic field splits into ordinary and extraordinary wave (Mochalov & Mochalova, 2019).

Ionosonde uses frequencies from 0.1 MHz to 30 MHz and with increase in frequency, the radio signal reflected from the higher layer and at the point of reflection its group velocity ceases, which increases time of flight of the signal. The ordinary wave escapes from a layer when it's transmitted frequency is more than its plasma frequency. In case of extra ordinary wave, the reflection occurs at higher frequency than ordinary wave due to additional effect cause by the magnetic field (Khadka, 2018). In 1991, Hunsucker explain basic principle of ionosonde as follows: at first an oscilloscope sweep starts after a while a short pulse of radio frequency in upward in the ionosphere. The reflection of transmitted short pulse from atmosphere is detected and displayed on the same oscilloscope weep. The time delayed between transmitted and received pulse is used to calculate the "virtual height". A plot if virtual height is obtained by varying slowly the frequency of the transmitter and receiver over a wide range of 1 MHz to 20 MHz (Hunsucker, 1991). The center for atmospheric research at the University of Massachusetts Lowell recently developed a small-power version of its Digisonde sounders that incorporates intrapulse phase coding, digital pulse compression, and Doppler integration. When compared to older transmitters, this device consumes extremely little power (300 W vs. 10000 W for previous systems). Figure 28 depicts a typical ionogram plot taken around midday. The different layers are represented by flattened region the parabola. In terms of electron concentration and radio wave frequency, the refractive index of a medium is given as

$$n = \sqrt{1 - \frac{Ne^2}{4\pi^2 \epsilon_0 m_e f^2}} \qquad (3.1)$$

where

n = represents the refractive index of the medium;

e = electronic charge;

m_e = mass of electron;

ϵ_0 = the permittivity of free space;

N = electron density;

f = the frequency of the radio wave;

When the refractive index of the medium approaches to zero, then the substantial reflec-
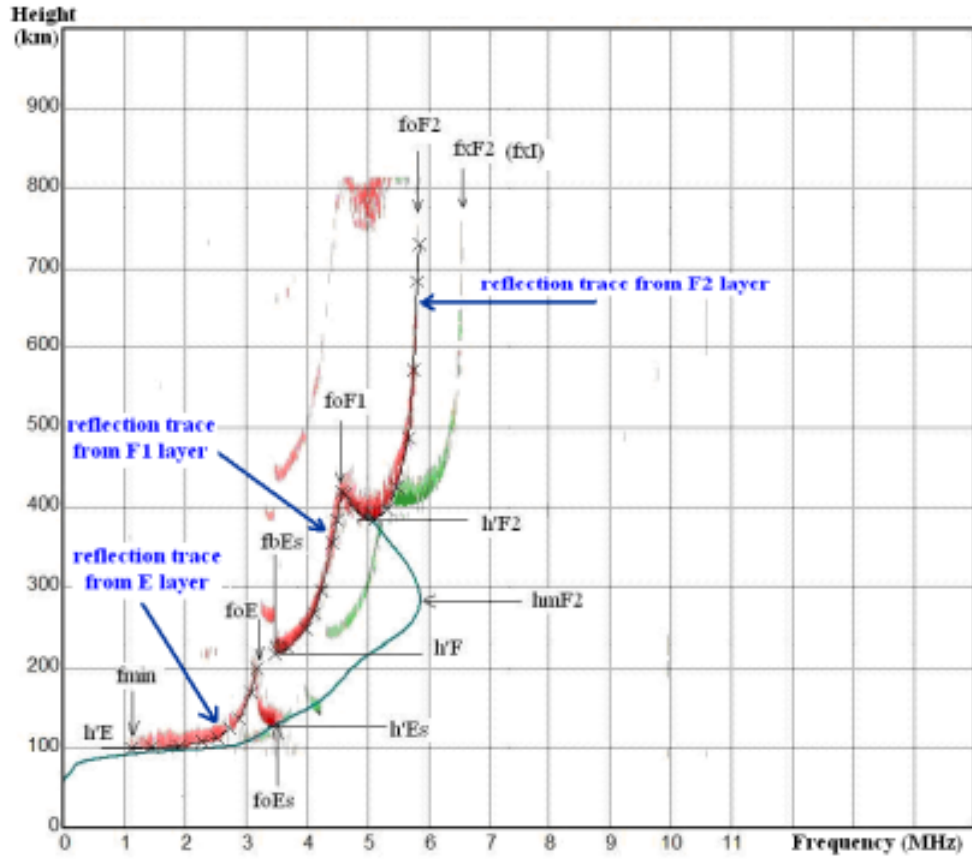
Figure 28: A typical plot of vertical ionogram with main measurable parameters made near noon of the day. The different layers are represented by flattened region the parabola (Mochalov & Mochalova, 2019).

tion of the signal takes place and the electron density required for frequency f_c reflected is given by

$$N = 4\pi^2 \epsilon_0 m_e f_c^2 / e^2 \tag{3.2}$$

The refractive index of the medium in terms of critical frequency is given by

$$n^2 = 1 - \left(\frac{f_c}{f}\right)^2 \tag{3.3}$$

The critical frequency of a signal for a particular layer is the frequency that can penetrate the respective layer of ionosphere. The critical frequency for the ordinary and the extraordinary wave is given by

$f_c = 9.99\sqrt{N}$; for ordinary mode

$f_c = 9.99\sqrt{N} + 0.5\frac{Be}{m_e}$; for extraordinary mode

where

$B =$ the magnetic field;

As the signal transmitted through an ionized layer, their group velocity slowed down by ionization and it is added to it time of flight. When a signal transmitted through a layer meet next layer for which plasma frequency is greater in comparison to frequency of the transmitted signal, then reflected back from that layer and it get further delayed by the ionization of the underlying layer. The time delay results in a virtual height measurement, that is higher in comparison to the genuine height. The measuring ionization through which the signal has passed is determined by the difference between real and apparent heights. The ionogram represents transmitted frequency and ionospheric reflection height with frequency from bottom side E-layer to the top of F_2 layer (under the except of spread in F-layer). In each plot, a smooth curve separated by a cusp represents critical frequency foE, foF_1 and foF_2 and these frequencies of signal can pass through the respective layer. A characteristics signatures of echo from different ionospheric layer is observed in Figure 29 indicating ionogram (left) during non-turbulence and (right) turbulence condition with height. The lowest point in each curve gives the measurement of virtual height and the critical frequency is measured from the asymptote in plot (Mochalov & Mochalova, 2019). In this thesis, the data for the critical frequency (foF_2), height of peak electron density (hmF_2), and virtual height ($h'F$) is taken from ionosonde station from Boulder, Colorado, USA.
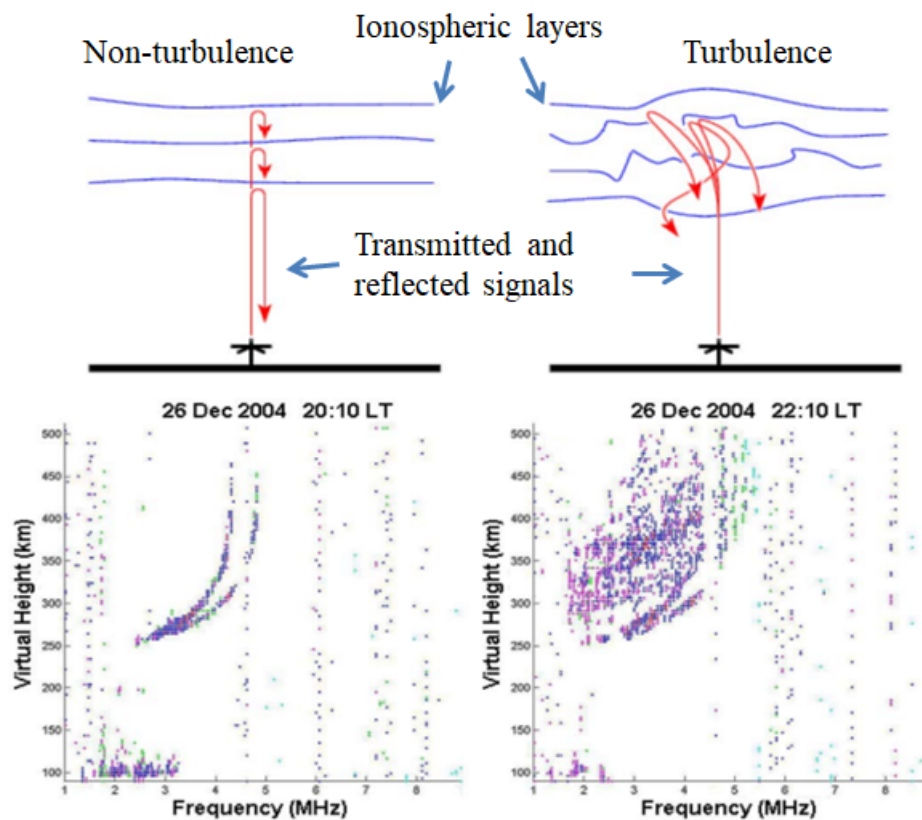
Figure 29: Characteristics signatures of echo from different ionospheric layers observed in ionogram during (left) non-turbulence and (right) turbulence condition with height (Khadka, 2018).

3.4 Parameters Analyzed in Our Study

3.4.1 Ground Based Data

3.4.1.1 Horizontal Component of the Earth's Magnetic Field

This study focuses on analysis of geomagnetic disturbances in response to change in solar wind plasma parameters and IMF. The horizontal (H) component of geomagnetic field is suppressed during magnetic storm and recovered into normal value (Akasofu & Chapman, 1972). To illustrate the impact of SSSs on 7 and 8 September 2017 on geomagnetic field at high, mid, and equatorial latitude, the magnetic data set for 1 minute resolution of horizontal component is downloaded from website `www.intermagnet .org`. The data for quiet day is calculated by the average data of horizontal component of 10 quietest days of that month. The data for delta H is obtained by subtracting quiet days from storm days. Table 2 shows the geophysical positions of the observatories included in this investigation. Figure 30 shows distribution of magnetic observatory in a world map used in this research work. Several indices have been used to examine

Table 2: Geographic and geomagnetic coordinates of magnetometers stations.

Station ID	Geographic	Geomagnetic	Local time
KOU, Kourou	5.21° N, 307.27° E	14.22° N, 20.44° E	UT−3:00
GUA, Guam	13.59° N, 144.87° E	5.91° N, 216.48° E	UT+10:00
MBO, Mbour	14.39° N, 343.04° E	19.64° N, 58.11° E	UT+00:00
API, Apia	−13.85° N, 171.78° E	−17.82° N, 246.87° E	UT+13:00
ABG, Alibag	18.62° N, 72.87° E	10.68° N, 146.87° E	UT+5:30
PHU, Phuthuy	21.02° N, 105.96° E	11.42° N, 178.63° E	UT+7:00
BOU, Boulder	40.14° N, 105.24° E	30.55° N, 178.08° E	UT−4:00
DUR, Duronia	41.65° N, 14.46° E	41.43° N, 95.59° E	UT+1:00
FCC, Fort Churchil	58.75° N, 265.91° E	67.43° N, 330.31° E	UT−6:30
UPS, Uppsala	59.90° N, 17.35° E	58.55° N, 106.00° E	UT+1:00
MGD, Magadan	60.05° N, 150.72° E	52.54° N, 214.27° E	UT+11:00
ABK, Abisko	68.35° N, 18.82° E	66.19° N, 113.98° E	UT+1:00

the geomagnetic activity induced by plasma injection into the magnetosphere at various latitudes. In this dissertation AE, Dst, and SYM-H indices are used.

3.4.1.2 AE Index

Auroral electrojet (AE) index measures geomagnetic field disturbances caused by increased ionospheric currents at higher latitudes, particularly in the global auroral zone. The AE index is a common way to characterize how a geomagnetic substorm evolves. It was developed by Davis & Sugiura (1966). It is derived by taking 1 minute datasets of fluctuations of geomagnetic field from 12 magnetometer stations near auroral zone in northern hemisphere (Rostoker, 1972). A base value is produced for each station by
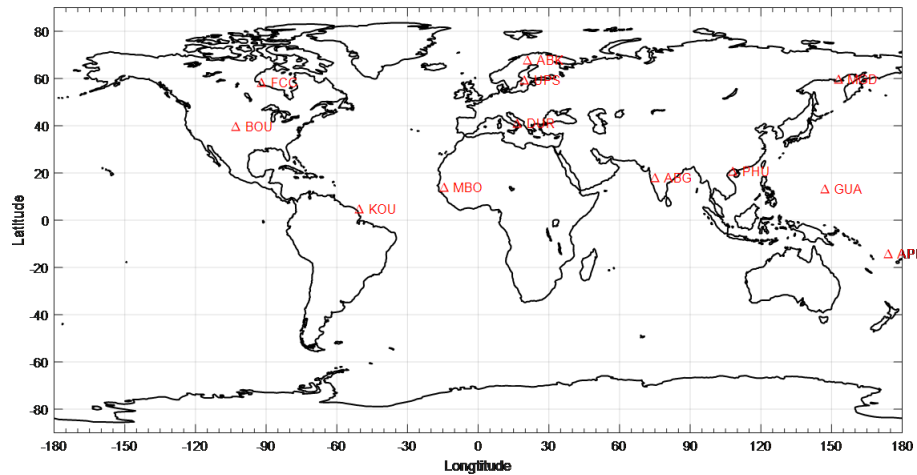
Figure 30: A world map showing location of magnetometer network stations used in our study.

taking the mean of all of the data from that station on the five quietest days. The base value is subtracted from each 1 minute dataset from that station for that month to get disturbances by the events. Thus, the constructed value for all the station is plotted along with universal time to show the induced perturbations. The largest and smallest value from superposed plot corresponds to the AU and AL indices. The AE index is defined as AE= AU – AL and AO index is the average of AU and AL, where The largest magnetic disturbance induced by the eastward electrojet in the afternoon sector is denoted by AU, while the maximal disturbance caused by the westward electrojet in the morning and midnight sectors is denoted by AL. Because they can vary separately from one another, the AU and AL indexes are used separately to determine the strength of eastward and westward electrojet (Rostoker, 1972). The two-component structure of the AE index can be assumed. The first is linked to changes in the ionosphere's directly driven two-cell convection pattern, and the second to the creation of Substorm Current Wedge (SCW) (Kamide & Kokubun, 1996). Figure 31a and 31b shows longitudinal and polar view of distribution of magnetic observatory for computing AU, AL, AO, and AE, respectively. The AE index begins to rise quite quickly when solar wind conditions favor dayside connection, and the other criterion for index intensifying occurs after tail-side reconnection begins.

3.4.1.3 Dst and SYM-H Indices

The worldwide strength of geomagnetic storm is monitored by Dst index (Sugiura & Menvielle, 1991). It defines fluctuations in the *H*-component of the earth's magnetic field as measured by observatories near the dipole equator on the surface of the Earth. It is derived from four magnetic observatories. The negative value of Dst index represents the effect of geomagnetic disturbance. Actually, it measures the intensity of east-west flow
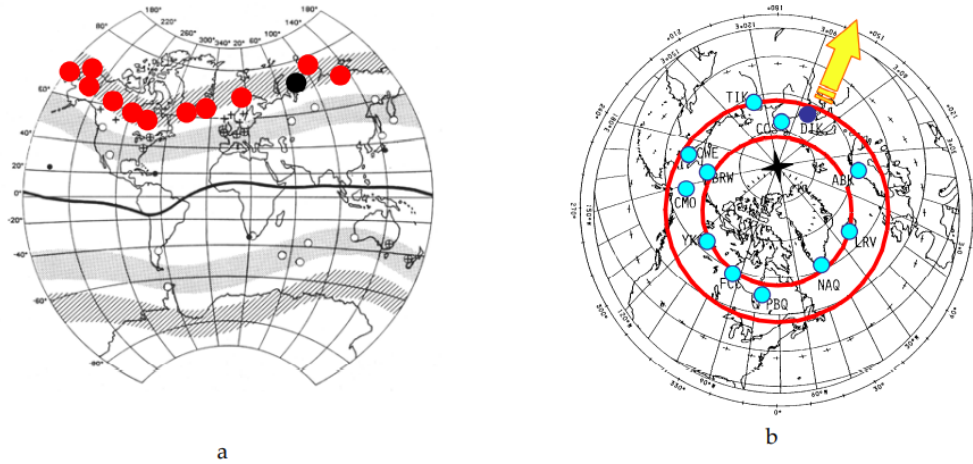
Figure 31: Distribution of observatory for computing AU, AL AO, and AE indices. a) The longitudinal distribution and b) Observed from pole (Menvielle & Marchaudon, 2007).

of ring current within the equatorial plane. When IMF B_z reconnect with geomagnetic field, the ring current is significant (Daglis et al., 1999). The geomagnetic field on its surface is reduced by the magnetic field variance caused by ring current. Understanding ring current aids in forecasting the magnetosphere's magnetic field. The range of Dst depends upon the solar activity. Approximately, value of Dst ranges from +100 nT to −600 nT (Gonzalez et al., 1994). Compression of the magnetosphere results the positive value of Dst (Verbanac et al., 2011). The Dst index is calculated with an one-hour time resolution, which limits its utility in studies with a greater time precision. Figure 32 shows the distributions of magnetic observatory to compute Dst index. SYM-H is another index has 1 minute time resolution (Iyemori, 1990). It measures the symmetric variation of ring current. Before SYM-H reacts to variation in solar wind driving conditions, it takes a long time. SYM-H is derived from six magnetic observatories.
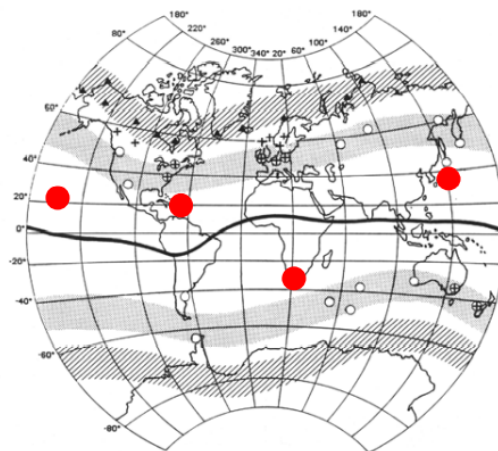
Figure 32: Distribution of observatories to compute Dst index (Menvielle & Marchaudon, 2007).

3.4.2 Satellite Based Data

The data from far space satellite ACE, SOHO, WIND and GOES program give the sufficient information about solar wind plasma parameters and IMF. The solar wind plasma parameters and IMF used in this study are as follows:

1. Solar wind velocity (V_{sw})

2. Solar wind proton temperature (T_{sw})

3. Solar wind plasma density (N_{sw})

4. Solar wind plasma pressure (P_{sw})

5. IMF B_z

6. Total magnetic field (B)

Analyzing data from far space satellite to the solar wind plasma parameters and IMF near-Earth environment provide detailed information of the complex mechanism occurring during solar-terrestrial interaction. It is a useful tool for studying causal connections in the context of space weather.

To analyze long-term solar activity, solar indices data of SSN and SFI (F10.7) were obtained from the Royal Observatory of Belgium, Brussels, via the websites `sidc .oma.be/silso/home` and OMNI data obtained from `http://omniweb.gsfc.nasa .gov/`. SSN is the most constant solar index, which accurately reports solar activity and is a useful method for predicting space weather occurrences. The SFI indicates the net amount of radiation emitted from the Sun wavelength of F10.7 cm at the Earth's surface. It is also a very good indicator of solar activities, which correlates nicely with SSN, UV and EUV and visible solar irradiance. It is measured in Solar Flux Unit (SFU) and its value varies below 50 SFU to above 300 SFU over a solar cycle. The measurement of F10.7 is provided from the National Research Council of Canada in partnership with Natural resources Canada. Figure 33 shows the variation in SSN and SFIs of year 2008 to 2018 of solar cycle 24. Furthermore, the data of F10.7 and other related information can be accessed at the website `https://www.swpc.noaa.gov/ phenomena/f107-cm-radio-emissions`.

Thermospheric O/N$_2$ Ratio:- The TIMED spacecraft, which is the first operation of the NASA solar connection program, is equipped with a global ultraviolet imager. It is constructed by Johns Hopkins University Applied Physics Laboratory in collaboration with Aerospace cooperation. The image of thermospheric O/N$_2$ ratio obtained GUVI is used to examine the energetic and dynamical features of the mesosphere and lower thermosphere in global behavior in far UV radiation. In this work, the thermospheric O/N$_2$ concentration ratio is obtained from the website `http://guvitimed.jhuapl`
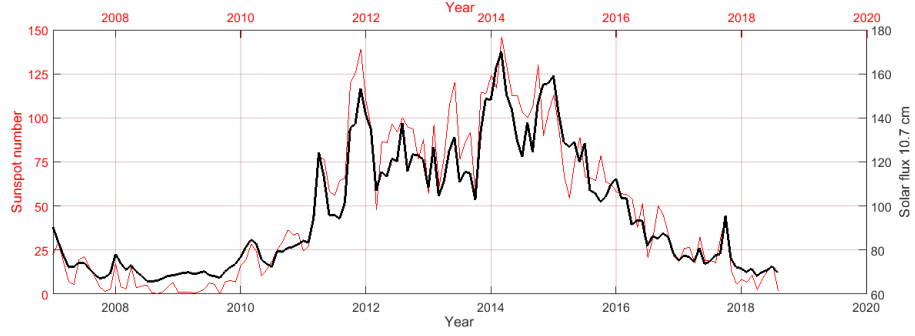
Figure 33: Variation of SSN and SFI for the year 2008 to 2018 (Pandit et al., 2021).

`.edu/` to compare with ground observation of GPS data.

3.5 Method of Analysis

3.5.1 Cross Correlation

The term correlation is used to determine the degree of association in two variables. Several types of correlation has been using as per requirement of the set of variable. The cross correlation is used for two different set of variables to obtain lagging between them. The value of cross correlation coefficient lying in the range from -1 to $+1$. When the it's value approaches 1, it designates a strong directly relationship between the set of variables and the higher value of negative correlation coefficient means variables are highly inversely associated. The set of variables are not correlated if the cross correlation becomes zero (Katz, 1988). In this method, the cross correlation coefficient is determined using Pearson product moment method by correlating lagged data set in the company of another unlagged data set. The value of cross correlation coefficient is determined using following formula.

$$P_{xy}(L) = \frac{\sum\limits_{k=1}^{N-|L|} (x_{k+|L|} - \bar{x})(y_k - \bar{y})}{\sqrt{\sum\limits_{k=1}^{N} (x_k - \bar{x})^2 \cdot \sum\limits_{k=1}^{N} (y_k - \bar{y})^2}} \tag{3.4}$$

In this study, the cross correlation is extensively used to estimate the degree association between several solar wind and interplanetary parameters with ground based measurements.

3.5.2 Continuous Wavelet Transform and Global Wavelet Spectrum

This section discusses the continuous wavelet transform (CWT) and global wavelet transform (GWT), their properties and method used to know multiscale structure in the

time of SSSs events noted at equatorial, middle and high latitude magnetometers. These techniques are used to understand, energy, potential and current system such as FAC, PCV, RC, JH, AP, and TE inside the magnetosphere. Fourier Transform (FT) is unable to provide information about the signal, such as when a specific frequency appears (Daubechies, 1992). To overcome this difficulty, Window Fourier Transform (WFT) technique is used, which apply two arguments time and frequency. WFT has fixed time frequency resolution that and can be changed by manipulating the size of the window. A sliding window is used in this conversion to determine ideas about time and frequency, which are depicted using a spectrogram. Because of the fixed length of its window, this approach is likewise unable to reveal exact information regarding time and frequency. In order to remove the limitation of a scale presentation, the wavelet transformation has been evolved (Hubbard, 1996). More precisely, in wavelet transform, the data are transformed into its multilevel components using its mathematical tool. In early 1980, Geophysicist Jean Morlet and Physicist Alex Grassman gave necessary condition for a wavelet function (Grossmann et al., 1985):

a) Integral of wave function is zero and it satisfy admissibility condition

$$\int \psi(t)dt = 0 \tag{3.5}$$

b) The wave function is normalized and it must have unitary energy

$$\int |\psi(t)|^2 \, dt = 1 \tag{3.6}$$

In this study to identify the redundant and continuous complete description of the signal in time (t) and scale (a), CWT and GWS techniques are utilized. The wavelet decomposes data into different frequency and scale components (Daubechies, 1992). The high frequency band is of shorter duration, whereas the low frequencies are broad. This technique zooms into the short pulse of signal to identify respective frequencies of geomagnetic disturbances. The coefficients of continuous wavelet transform is define as

$$W(a, b) = \int f(t)\psi^* \left(\frac{t - b}{a} \right) dt \tag{3.7}$$

where $\psi*$ is the complex conjugate of ψ and $W(a, b)$ is the wavelets coefficients. Variation of the scale parameter produces dilation of the mother wavelet function for $a > 0$ and contraction of the mother wavelet function for $a < 0$. As a result, it's simple to detect the signal's high- and low frequencies, as well as its longer and shorter duration.

The GWS has been used to find the most energetic periods in a cross-wavelet analysis

and it is obtained by (Torrence & Compo, 1998)

$$GWT = \int \mid TW(a, b) \mid^2 db \qquad (3.8)$$

3.5.3 Energy, Potential and Current Inside the Magnetosphere

Field Aligned Current:- Geomagnetic field produced because of motion of electrically charged particles inside the Earth (Kivelson et al., 1995) and extends in outer up a region called magnetosphere (Chun & Russell, 1997), in which it reacts with the solar wind's magnetic field and facilitate to transfer of energy into the magnetosphere (Dungey, 1961). This reconnection leads to movement of plasma inside the magnetosphere and ionosphere, causes increase in some major current system such as magnetopause current, Ring Current (RC), partial RC, tail current, Field Aligned Current (FAC) and auroral electrojet (shown in figure 11). Among which the FAC is also called Birkeland current (Birkeland, 1913) provides strong connection between ionosphere and magnetosphere. The FAC is a series of currents that flow parallel to the geomagnetic field and provides coupling between the magnetosphere and the ionosphere, this connection is regulated by the solar wind and the interplanetary magnetic field. The study of FAC broadens the concept to understand magnetic reconnection, FAC acceleration, plasma convection and auroral activities. Due to low magnitude of current density of FAC ($\leq 1\mu$A m^{-2}), it is difficult to measure directly. The intensity and distribution of FAC is measured using ground based, rocket and satellite (Iijima & Potemra, 1976). In 1960, FAC over high latitude was measured using satellite. Iijima & Potemra (1976) identified two types of FAC using magnetometer data from TRIAD satellite. Two regions of large scale FAC called region 1 and region 2 encircling polar cap has been identified. The Region 1 current flows outward into the ionosphere from pre-midnight to the morning sector and away from the ionosphere from the afternoon to pre-midnight sector near the poleward border of 70° to 75° latitude. The current flow in area 2 is detected near the equatorward and flowing toward the ionosphere in the afternoon to the pre-midnight sector, and away from the ionosphere in the pre-midnight to the early-noon sector. Iijima & Potemra (1982) proposed a formula for FAC intensity as

$$FAC = 0.328 \left[n_{\mathrm{p}}^{1/2} V_{\mathrm{sw}} B_{\mathrm{T}} \sin \theta/2 \right]^{1/2} + 1.4 \qquad [\mu \, \mathrm{A} \, \mathrm{m}^{-2}] \qquad (3.9)$$

where,

n_{p} = solar wind density ncm^{-3};

V_{sw} = solar wind speed km s^{-1};

B_{T} = the transverse interplanetary magnetic field in nT

$$B_{\mathrm{T}} = \sqrt{B_y{}^2 + B_z{}^2} \tag{3.10}$$

B_y and B_z are y and z components of magnetic field. And θ is angle measured joining the positive z-axis and the IMF vector in the y-z plane and defined as

If $B_z > 0 \rightarrow \theta = \arctan \mid \frac{B_y}{B_z} \mid$

If $B_z < 0 \rightarrow \theta = 180 - \arctan \mid \frac{B_y}{B_z} \mid$

Polar Cap Voltage:- Polar cap voltage (PCV) is a magnetospheric convection indicator that may also be used to figure out how solar wind interacts with the magnetosphere and ionosphere (Weimer et al., 1990). Cross electric field is produced when IMF embedded with solar wind approaches towards the magnetosphere. During magnetic reconnection with IMF B_z and geomagnetic field, some of the electric field is transferred to the polar ionosphere to produce potential at polar region called cross PCV, which is measured by low orbiting satellite (Papitashvili et al., 1999), radar (Ruohoniemi & Greenwald, 1995) and ground magnetometer (Kamide et al., 1981). The study shows that increase in IMF B_z increases cross-magnetosphric electric field, which ultimately enhances cross PCV. The difference between the maximum and minimum potential in one hemisphere yields the magnetospheric-ionospheric convection condition. Depending upon the configuration of the magnetic reconnection, Kan & Lee (1979) gave a formula for calculation of polar cap potential, which is expressed as

$$PCV = V_{\mathrm{sw}} \, B_{\mathrm{T}} \, \sin^2 \frac{\theta}{2} \times 7 R_{\mathrm{E}} \qquad [kV] \tag{3.11}$$

where,

$R_{\mathrm{E}} = $ radius of the Earth (6.38×10^6 m);

$\qquad B_{\mathrm{T}} = \sqrt{B_y{}^2 + B_z{}^2}$

$\theta = \arccos(B_z/B)$; B is total magnetic field (in nT)

Total Energy:- During a geomagnetic storm, magnetic reconnection creates an electrodynamics link between the solar wind plasma and the magnetosphere, which boosts numerous current systems within the magnetosphere. Enhancement in ionospheric current at mid and low latitude and increase in ring current at low latitude are the some examples of increased in current system. Depression in the magnetometer at low latitude confirms ring current intensification. Magnetospheric particles energized by increased interplanetary magnetic field $E_y = V_{\mathrm{sw}} B_z$ during magnetic reconnection in presence of high value of IMF B_z and solar wind for longer duration. The energy injected into magnetosphere during magnetic reconnection by IMF B_z and geomagnetic field dissipated in different magnetospheric and ionospheric region (Akasofu, 1981; De Lucas et al.,

2007). The energy are dissipated as at high latitude and a part of energy is deposited as JH, AP in auroral region, RC energization near equator and heating of plasma sheet near the magnetotail. The TE is the sum of energies deposited due to all these contributions into magnetosphere during magnetic reconnection is calculated by

$$W_\epsilon = \int_{t_0}^{t_m} \epsilon \, dt \qquad [J] \tag{3.12}$$

$$\epsilon = 10^7 \, V_{\text{sw}} \, B^2 \, l_0^2 \, \sin^4 \frac{\theta}{2} \qquad [W] \tag{3.13}$$

where B is the IMF strength, θ is the angle of IMF clock angle and defined by $\theta = \arctan(B_y/B_z)$ and the empirical determined value of $l_0 = 7 \, R_E$ (De Lucas et al., 2007). The TE, W_ϵ is acquired by integrating ϵ over the main phase of the storm from t_0 to t_m.

Joule's Heating:- It is produced by ionospheric current which heat the atmosphere through Pederson current associated with FAC in resistive ionosphere (Koskinen & Tanskanen, 2002) very similar to the electric current flow through resistive medium. In physical sense, it can be considered as frictional heating from relative motion between plasma and neutral species near auroral region. There are several methods and techniques for estimation of Joule's Heating JH, but here in this study the formula used for JH (Tenfjord & Østgaard, 2013) is

$$JH = (0.54 \, AE + 1.8) \times 10^9 \qquad [W] \tag{3.14}$$

where AE is the auroral electrojet index and it is measured in nT.

Aurora Precipitation:- Particles of solar wind deposit their energy near the auroral oval region through ionization, is called Aurora Precipitation (AP). Here AP is calculated using formula given by Østgaard et al. (2002).

$$AP = (4.4 \times (| \, AL \, |)^{1/2} - 7.6) \times 10^9 \qquad [W] \tag{3.15}$$

where AL is auroral low index in nT.

Ring Current:- The particle trapped by geomagnetic field moves toroidally around the equatorial region called Ring Current (RC). Charge particle pressure difference and drift motion combine to generate RC (Zhao et al., 2015). The direction of magnetic field produced by RC is opposite to the geomagnetic field. It is generated due to the depression in magnetometer data near the equatorial region the RC energy (Tenfjord & Østgaard, 2013) is calculated by

$$RC = 4 \times 10^4 \left[\, | \frac{\Delta SYMH}{60} | + | \frac{SYMH}{4 \times 60 \times 60} | \, \right] \times 10^9 \qquad [W] \tag{3.16}$$

where, $\Delta SYMH = SYMH(i+1) - SYMH(i)$ and SYMH is in nT.

3.5.4 Total Electron Content

Total electron content (TEC) is columnar density of electron along the path between receiver to the satellites. TEC is calculated as

$$TEC = \int_R^S N_e(h)dh \tag{3.17}$$

where, N_e is electron density, R is receiver altitude and S satellite altitude. Vertical TEC (VTEC) is calculated using the conventional approach for processing GPS pseudo-range measurements (Hofmann-Wellenhof et al., 1992; Schaer, 1999). At 420 km, we apply the single layer mapping function to convert slant TEC (STEC) to VTEC (Schaer, 1999; Azzouzi et al., 2015). The STEC is traditionally calculated by combining two dual-frequency pseudo-range measurements from the daily RINEX 30 s files. The TEC is calculated from dual frequencies f_1 and f_2 and two pseudo-range P_1 and P_2 (Hofmann-Wellenhof et al., 1992) as

$$STEC = \frac{1}{40.3}(\frac{f_1^2 \, f_2^2}{f_2^2 - f_1^2})(P_1 - P_2) \tag{3.18}$$

The STEC acquired by such method is a measurement of the TEC of the ionosphere along the ray path from the satellite to the receiver, and it must be converted to VTEC using equation. (Titheridge, 1972).

$$VTEC = (STEC - B_s - B_u)\sqrt{1 - (\frac{R_E \times \cos\epsilon}{(R_E + h)^2})} \tag{3.19}$$

where B_s and B_u are the biases of satellite instruments and receivers, respectively, ϵ is the satellite's elevation angle, and $R_E = 6371$ km is the Earth's mean radius.

Figure 34 shows measurement of STEC and VTEC using GPS receiver.

The TEC data for this study consists of the four GPS stations in Nepal: DLPA, JMSM, KKN4, and GRHI. The descriptions of geophysical location of the station are shown in Table 3. Figure 35 is a map of Nepal showing the locations of the GPS stations utilized in this work. The GPS data were obtained from `www.unavco.org`. This data available from this source is in RINEX v2.1 format with the temporal resolution of 15 minute. This data is processed using Fleury software (19 July 2018, on the website `www.girgea.org`). The data of TEC obtained is calibrated at 15 minute for all measurements. When calculating VTEC for 30 second intervals, the altitude might change, resulting in VTEC deviations based on the GPS constellation, not just the content over. In this calculation,

we have selected for regression over 15 minute to obtain VTEC in the middle of this period. Hence, four points are possible in 1 hour, so VTEC calculated is 4 times better accuracy in compared to Global Ionospheric Map (GIM), which uses the steps of 1 hour or 2 hour based upon the organization. As a result, RINEX data has a stronger ability to configure precise local structure over GIMs data. The diurnal, seasonal, annual variations, and during super intense storm of VTEC are analyzed during all four phases of solar cycles 24. The Table 4 shows the classification of years in different phases are presented below. The local season of Nepal are classified as winter (November, December, January and February), spring (March and April), summer (May, June, July and August), and autumn (September and October).

Table 3: Geographic and geomagnetic coordinates of GPS stations.

Station ID	Geographic	Geomagnetic	Dip latitude	LT(hours)
KKN4, Kakani	27.80° N, 85.27° E	18.62° N, 159.41° E	43.86°	UT+5:45
GRHI, Ghorahi	27.95° N, 82.49° E	18.94° N, 156.82° E	44.25°	UT+5:45
JMSM, Jomsom	28.80° N, 83.74° E	19.71° N, 158.06° E	45.31°	UT+5:45
DLPA, Dolpa	28.98° N, 82.81° E	19.94° N, 157.21° E	46.03°	UT+5:45

Table 4: Classification of selected years based on the phases of solar cycle 24.

Interval	Years	Solar cycle phases
I	2008, 2009	The minimum phase
II	2010, 2011	The increasing phase
III	2012, 2013, 2014	The maximum phase
IV	2015, 2016, 2017, 2018	The decreasing phase

3.5.5 Model Data

CODG:- In 1998, the scientific community of International GNSS Service (IGS) and others organizations Center for Orbit Determination in Europe (CODE), European Space Agency (ESA), Jet Propulsion Laboratory (JPL) and Universitat Politècnica de Catalunya (UPC) have developed an Ionospheric Working Group (IONO-WG) to generate global and daily VTEC maps using ground based data. A grid of 2.5° latitude 5° longitude was adopted to provide the data in IONosphere Map Exchange (IONEX) format. The temporal resolution was set 2 hour, then to 1 hour, and later to 15 minute by UQRG (Spain). The main concern arises in the determination of differential biases of satellite due to non-uniformity in ground station manufacture and environmental changes. The STEC obtained is converted in VTEC using Spherical Harmonics by ESA, Wuhan University (WHU), Chinese Academy of Sciences (CAS), CODG; three-shell mode by JPL and tomographic method using Splines function by UPC. The quality of each model was examined on ancillary measure of altimeter and radio occultation (Hernández-Pajares et al., 2009; Chen et al., 2020). The performance and quality of GIM has
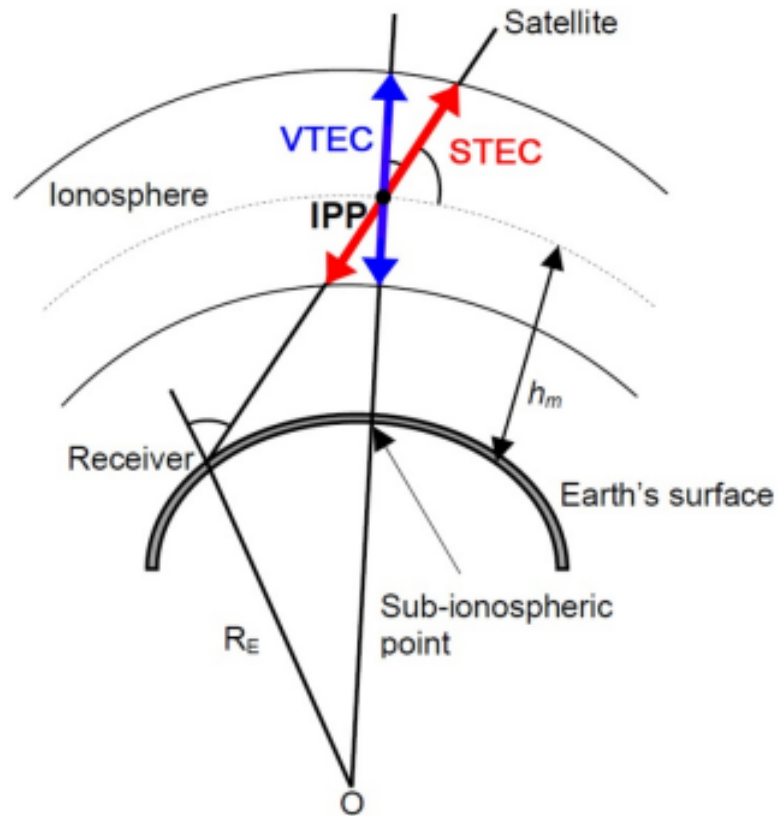
Figure 34: Sketch showing measurement of Slanted Total Electron Content (STEC) and Vertical Total electron Content (VTEC) strategy using GPS receiver (Ya'acob et al., 2008).
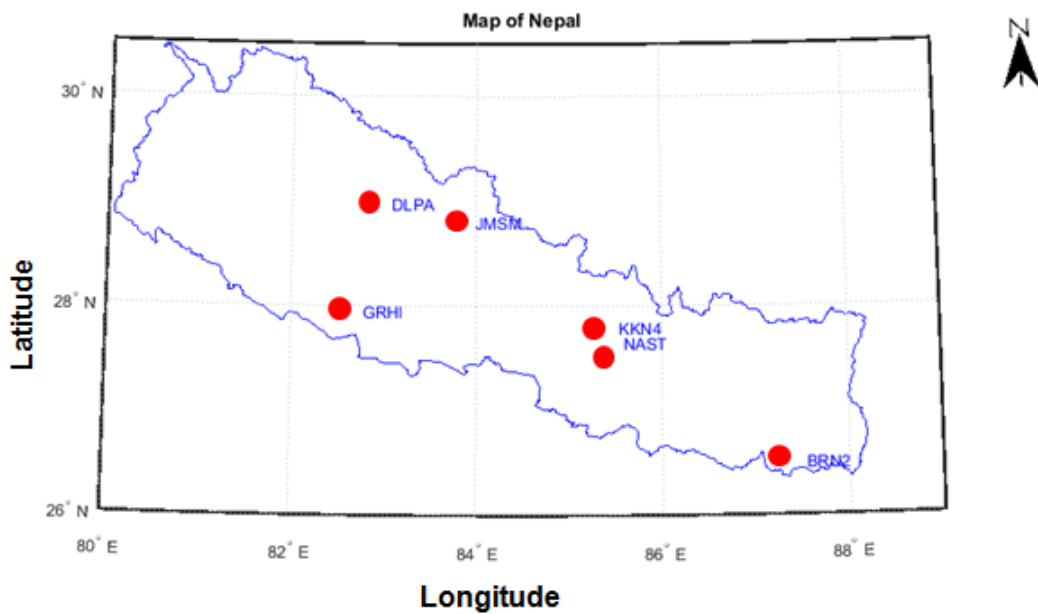
Figure 35: Locations of GPS stations in Nepal used in our study.

increased a lot due to increase in number of ground stations and also with the addition of new navigation systems e.g. Glonass, Galileo, Beidou etc. The degree of accuracy has been observed between GIM and observation is 2 TECU during sunspot minimum

and 10 TECU during sunspot maximum. In our study, the GIM provided by CODG downloaded from website `http://aiuws.unibe.ch/ionosphere` is compared with GPS TEC from RINEX observation file in three stations (BRN2, NAST and JMSM) of Nepal. Table 5 shows the the geophysical location of three GPS stations of Nepal used for comparing VTEC from RINEX GPS data and VTEC taken from CODG and IGSG ionospheric map.

Table 5: Geographic and geomagnetic coordinates of GPS stations.

Station ID	Geographic	Geomagnetic	dip latitude	LT(hours)
BRN2, Biratnagar	26.51° N, 87.27° E	17.22° N, 161.19° E	41.56°	UT+5:45
NAST, Kathmandu	27.65° N, 85.32° E	17.47° N, 169.37° E	43.61°	UT+5:45
JMSM, Jomsom	28.80° N, 83.74° E	19.71° N, 158.06° E	45.31°	UT+5:45

IGSG:- There are many Scientific Ionospheric Organizations to produce GIMs from the IGS stations network. The results obtained by each group are not exactly same because of different mathematical approach used. The IGS (IONO-WG) under supervision of A. Krankowski has proposed an algorithm scheme to incorporate all the particular solutions in a single solution and has been given a name called IGSG. In our study the GIM map produced by IGSG group available at `ftp://cddis.gsfc.nasa.gov/pub/gps/products/ionex/` has been used to compare with the RINEX observation data of VTEC obtained from three GPS stations of Nepal.

3.6 Ionospheric Parameters

This thesis investigates the impact of three SSSs appeared on 24 August 2005, 7 September 2017, and 8 September 2017 at mid latitude F-region parameters: critical frequency (foF_2), virtual height (h′F) and height of peak electron density (hmF_2) using ionosonde data originating at station Boulder, Colorado, USA (40.0° N, 105.0° W). The table 6 shows the geophysical location of ionosonde station used for our study. The data were compared to selected parameters on quiet days corresponding to the storm timings. Table 7 lists the days for three SSSs, including a reference the quietest day for each SSS. For this investigation, the ionosonde data for such parameters critical frequency (foF_2), virtual height (h′F) and height of peak electron density (hmF_2) were taken from the Global Ionospheric Radio Observatory (GIRO) website `https://ulcar.uml.edu/DIDBase/`.

Table 6: Geographic and geomagnetic coordinates of ionosonde station.

Location	Geographic	Geomagnetic
Boulder,USA	40.14° N, 105.24° W	47.66° N, 37.77° W

Table 7: The list of SSS events with a reference the quietest days for each SSS.

Event	SSS	Reference the quietest day
1	24 August 2005	20 August 2005
2	7 September 2017	28 September 2017
3	8 September 2017	28 September 2017

3.7   Geocentric Solar-Magnetospheric and Geocentric Solar-Elliptic

The interplanetary datasets are classified into magnetic and plasma data since their measurements are taken through different set of devices. The magnetic data possesses greater temporal resolution and consists of components of magnetic vector. The measurements such as plasma velocity (has vector component), ion density, pressure, and temperature have low temporal resolution because of limitation of devices. Generally, two coordinate systems, the Geocentric Solar-Magnetosphere (GSM) and Geocentric Solar-Elliptic (GSE) are used to measure the interplanetary datasets. The Earth is at the center of the GSM system, with the vector X referring to the Earth-Sun line, the vector Z oriented in the plan including the earth dipole, and the vector Y rounding out the coordinate system (Russell, 1971). The Sun is also at the center of the GSE coordinate system, with the X-axis referring to the Sun-Earth line, the Y-axis connecting to the ecliptic plane, and the Z-axis completing the coordinate system. (Russell, 1971; Kivelson et al., 1995). Figure 36 depicts the relationship between GSE and GSM, the ecliptic and magnetosphere reference systems. (Mendes, 1992). The XGSE axis is oriented from the Earth to the Sun, whereas the ZGSE axis is orthogonal to the Ecliptic, which is the plane defined by the earth's translation movement.
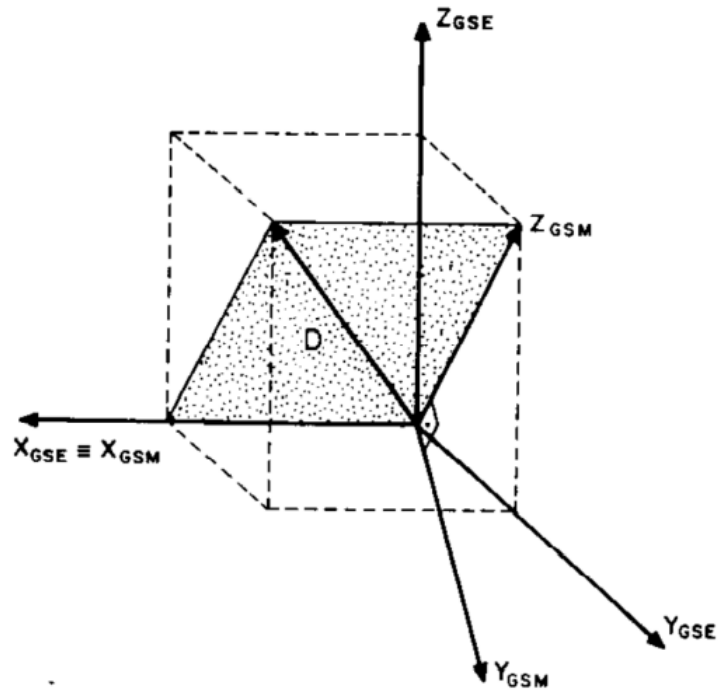
Figure 36: Relation between GSM and GSE coordinate systems (Mendes, 1992).

CHAPTER 4

4. RESULTS AND DISCUSSION

This chapter contains detailed presentation and discussion of the results of the thesis work. This work is basically related to regular and disturbed time variability of ionosphere at mid-latitude (Nepal). In addition, SSSs related signatures on horizontal components of geomagnetic fields and ionospheric parameters (foF_2, $h'F$ and hmF_2) have been presented. The findings are presented under the following major headings:

- Section 4.1 demonstrates the long-term variability of ionosphere over Nepal using GPS data. It provides the brief discussion on daily, monthly, seasonal, yearly, and solar cycle variations of VTEC.

- Section 4.2 depicts the disturbed ionosphere due to super substorms and storms. This section has further divided into three sub-sections. The subsection 4.2.1 presents the solar wind plasma parameters and magnetic indices during SSSs. The subsection 4.2.2 briefly discusses the effects of SSSs on magnetic data and energy deposited in various form inside the magnetosphere. The subsection 4.2.3 briefly discusses the effects of SSSs on ionospheric parameters (foF_2, $h'F$ and hmF_2). And the subsection 4.2.4 discusses the signatures of super intense storms on VTEC and thermospheric O/N$_2$ ratio over Nepal.

4.1 Regular Ionosphere above Nepal

The regular daily variation in total electron content during the geomagnetic quiet condition is created by solar heating and it produces tidal winds in the E region of the ionosphere, where conductivity dominates over the loss of ion-pair due to recombination. On solar quiet days, such variation is responsible for the ionospheric current system. During quiet magnetic condition, the daily change in position of focal latitude influences the pattern of solar quiet current system (Hasegawa, 1960). Neutral dynamo system is present in equatorial and low-latitude ionosphere during quiet condition. This dynamo system transports plasma through $\vec{E} \times \vec{B}$ drift, where $\vec{E}$ is electric field along east direction and $\vec{B}$ is the geomagnetic field near the magnetic equator. This drift is upward during day time and causes plasma to drift at higher altitude which ultimately diffuse along geomagnetic field lines to the region of higher latitudes. This up lifting of plasma at higher altitude called fountain effect, which produces plasma crests on either side of geomagnetic equator called EIA (Anderson & Roble, 1974). Solar EUV, UV

and X-rays are the major sources of ionization at low and mid-latitudes on the dayside of the earth. Earth's rotation introduces a diurnal variation in ionization. The ionizing rays (EUV, UV and X-ray) are emitted on the sun depend upon the sunspots. The sunspots have a cycle of about 11 years. Ionization of the ionosphere follows this 11-years cycle. Morphological characteristics of the ionosphere based on the NmF_2 are known since several decades:

- annual and semi-annual variations, with stronger electron densities at the equinoxes (Rishbeth et al., 2000)

- winter anomaly in F_2 region electron densities with greater daytime electron densities at the F_2 peak NmF_2 in winter than in summer (Rishbeth & Garriott, 1969)

- ionospheric equinoctial asymmetry defined as different ionospheric behaviour in the two equinoxes

- night time maximum of ionization and ionospheric variabilty related to the post sunset $\vec{E} \times \vec{B}$ drift (Sastri, 1998).

4.1.1 Diurnal Variation

Figure 37a shows the diurnal variability of VTEC in LT time at KKN4 station in Nepal during the lowest, inclining, maximum, and decreasing stages of solar cycle 24 on February 2, 2009 (black), 2012 (blue), 2014 (light green), 2016 (red), and 2017 (pink). VTEC becomes minimum before sunrise at 5:00 LT, gradually increases as time progresses, and then reaches a peak around 11:00 LT to 14:00 LT, and then it drops off in the sunset and at night. Between 11:00 LT and 14:00 LT, the diurnal peak occurs, with peak values varying from one month to the another month. The plots of VTEC show a rise from sunrise to a peak of roughly 5 TECU to 98 TECU following light of the day, then a drop to a minimum with a time change of 1 hour to 2 hour just before sunset. During the minimum and descending phases, a smooth curve with modest peaks be visible, however in the course the maximum phase, a dome shape is visible, and several peaks and troughs at various location is visible. Overall, the VTEC exhibits a typical diurnal pattern, of minimal at sunrise and twilight and maximal values at midday. The largest VTEC in the diurnal curve was observed during the solar cycle's maximum phases in 2014, then ascending stages in 2012, and minimum phases in 2016, 2017, and 2009, respectively. The diurnal fluctuation of VTEC was investigated by producing comparable curves with all four locations between 2008 to 2018. The diurnal VTEC behavior, in general, is solar cycle dependent. Due to a lack of space, the entire day's diurnal variations of VTEC is not shown. Figure 37b shows for the years from 2008 to 2010, the average diurnal curves of VTEC to the KKN4 station have a wavy-pattern,

however, the average diurnal curves for the years from 2011 to 2017 have a parabolic pattern. All of the stations studied had a diurnal profile that was similar. The diurnal graphs (Figure 37) indicate superior synchronization with variation of SSN and solar flux plot as shown in Figure 33. The diurnal plots of VTEC pattern suggests the fingerprints of many solar activities. In the diurnal pattern, it seems non-symmetric maxima around mid-day, parabolic profile during noon, a wavy pattern with small peaks in the morning, evening, and night, along with some complicated structures. The quiet day behavior at minimum phase, fluctuating operation during the increasing phase, shock occurrence during the maximum phase, and recurrent event during declining phase were observed in research of ionospheric characteristics at Ouagadougou ionosonde station data in West Africa by Ouattara et al. (2009).

An upward $\vec{E} \times \vec{B}$ drift velocity is critical in providing the nighttime after sunset boost. Jain (1987) discovered $(2.2 \pm 0.9) \times 10^{12}$ m^{-2}s^{-1} as the average plasma flux is needed for equatorial latitude intensification in India. In 2015, Tariku investigated the pattern of GPS-VTEC over the African region from 2008 to 2009 and 2012 to 2013 in 2015 and discovered minor rises in VTEC in the evening during 21:00 LT and 23:00 LT, mainly in equinoctial months, and a decline thereafter 23:00 LT. Pre-reversal boost was most noticeable during equinoctial months when solar activity was high, and it was much smaller at the solstice as solar activity was low (Tariku, 2015). Figure 37 shows a diurnal ionospheric profile over Nepal, which shows alike pre-reversal enhancement under high solar activity in 2012 and 2014, and not in the course of weak solar activity in 2009 and 2017. Probably, mountains generate relief waves that travel to the stratosphere and lower thermosphere as reported by previous study by Leutbecher & Volkert (2000) and similar findings of such wave generation from the lower atmosphere of Nepal have been reported from previous study by Regmi et al. (2017). Other studies in the Andes (De La Torre et al., 2014) and Tibet have shown that relief waves have an influence on the ionosphere (Khan & Jin, 2018). Figure 37a depicts oscillations that may not be directly perceived as wave signatures. In our study, we interpreted GPS data using pseudo-range signals, that could be impacted by reflected nearby reliefs as well as waves.
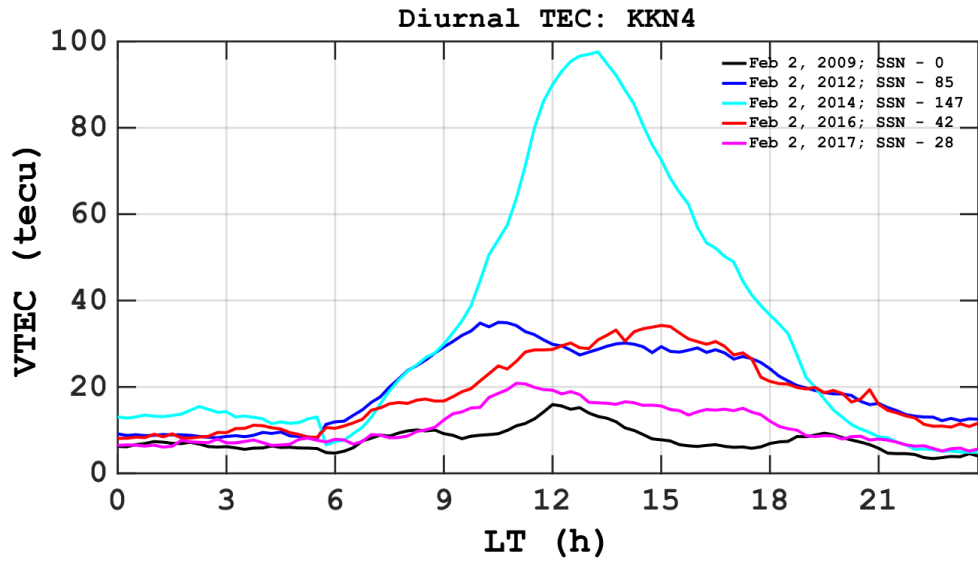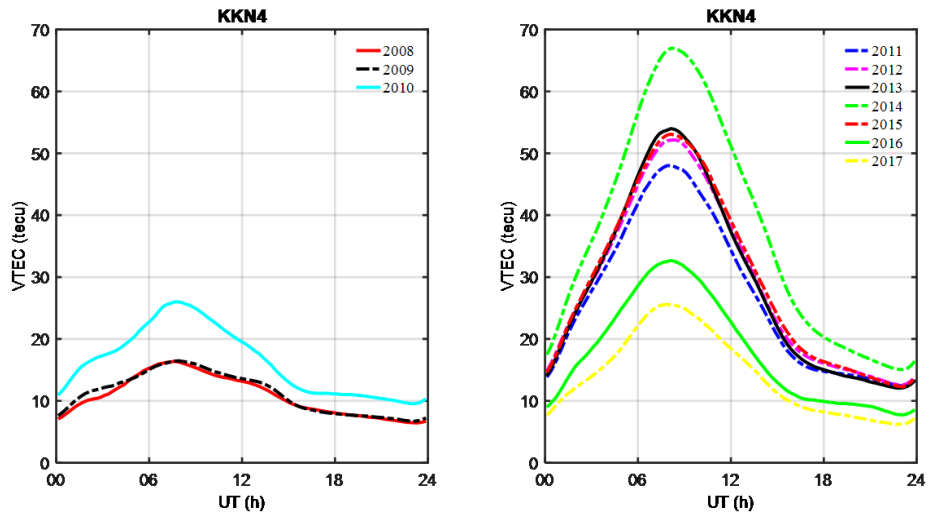
Figure 37: (a) Diurnal variability of VTEC in LT at the KKN4 GPS station of February 2 for year 2009, 2012, 2014, 2016, and 2017. (b) The first panel represents wavy pattern in the diurnal curves of year from 2008 to 2010 and the second panel the curves represent parabolic profile in the year from 2011 to 2017 (Pandit et al., 2021).

4.1.2 Monthly Variation

Figure 38 depicts the monthly fluctuation of VTEC in year 2014 at the KKN4 station in the course of the solar maxima stages of the solar cycle 24. The graph was created by averaging daily data. The figure illustrates that the highest VTEC occurs during the equinoctial months ie in the month of March and April and the lowest VTEC observes during the solstices ie in the month of January and June. Each curve's rise or decrease in TEC follows a diurnal pattern, with a pronounced peak in the middle of the day with variable maximal peak values. The weakest VTEC peak occurred in January, while the greatest occurred in March. Delayed afternoon peaks were observed in March, June, and September, with the remaining of the months' peaks focused around 2:00 LT. In December, there is a substantial flat peak, whereas in March, April, and October, there is a high rise in VTEC. The monthly fluctuation in VTEC was investigated by arranging comparable curves with all four stations for each month from 2008 to 2018. The graph demonstrates distinct wave like profile in the mean diurnal plots in years from 2008 to 2010, and a steep surge in VTEC from 2011 to 2017 (the plots of all the stations are not comprehend with this thesis). Typically in Nepal, the sunrise times in the summer and winter season are 5:15 LT and 6:45 LT, respectively, which is a 1.5 hour difference. The highest and minimum TECs observed during summer 2014 were 21 TECU and 12 TECU, and in winter its values were 25 TECU and 15 TECU respectively (Figure 38). In the summer, the VTEC appears to be smooth, while in the winter season, it appears to be stiff.
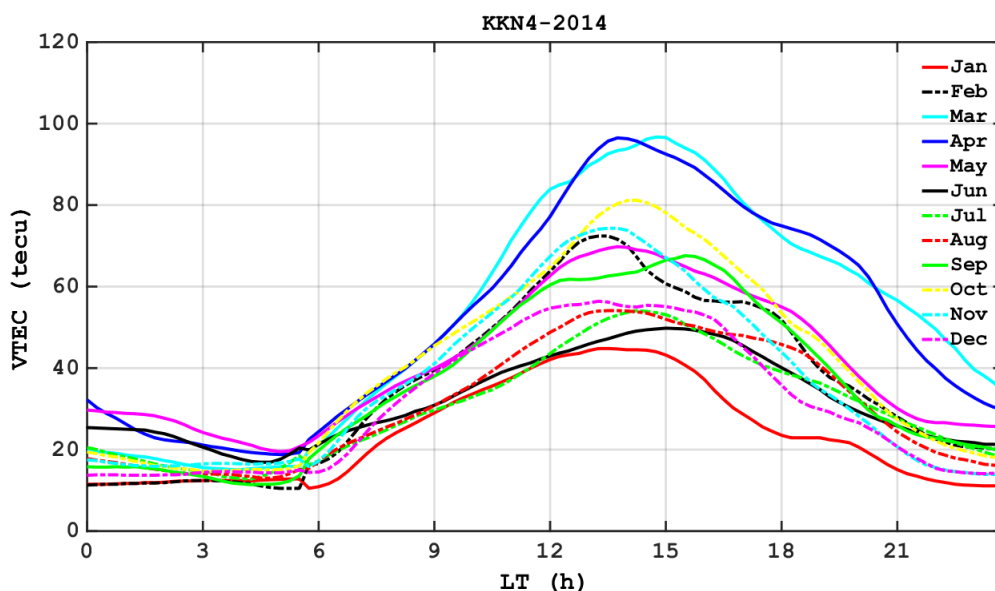
Figure 38: Monthly variability of VTEC in LT of year 2014 at the KKN4 station (Pandit et al., 2021).

4.1.3 Seasonal Variation

Figure 39(a-d) illustrates diurnal variability of hourly VTEC during four phases of solar cycle 24 in two-dimensional pattern. The graphics include one plot for each phases 2009-minimum-I, 2011-ascending-II, 2014-maximum-III and 2015-descending-IV phases at the JMSM station. Figure 39(a-d) show the features of equinoctial asymmetry in the ionosphere over Nepal in two dimensional plots for the years 2009, 2011, 2014, and 2015. Figures 39a, 39b, 39c, and 39d indicate the absence of equinoctial asymmetry in 2009, in 2011 autumn is much stronger in comparison with spring, and in 2014 and 2015 in spring is higher relative to autumn. In the time of quiet solar duration in 2009, equinoctial asymmetry is not visible. Autumn, on the other hand, is more severe over spring in 2011, and that is a typical characteristic of the EIA crest latitude region, and the equinoctial asymmetry difference is smaller in 2014 (spring > fall), which is a typical feature of the EIA trough stations. This asymmetry was particularly strong in 2015 (spring > fall), which is a common feature of TEC at all latitudes. Each panel in Figures 40a, 40b, 40c, 40d, and 40e illustrates the VTEC variability in the time of four seasons fall, spring, summer, and winter at the stations KKN4, GRHI, JMSM, and DLPA for the years 2008, 2009, 2011, 2014, and 2015. In Figures 40d and 40e, the plot for DLPA station is not available due to lack of data. The plots show that in spring 2014 the largest VTEC value was 95 TECU, in the time of the solar cycle's maximum year, while the lowest value was 10 TECU during winter 2009, in the course of the sunspot cycle's minimum year. The VTEC gradually increases and falls in the time of increasing and reducing stages of the solar cycle, based on the quantity based on UV reaching to the Earth. The graphs show that VTEC is highest in the spring, followed by fall, summer, and winter, with a few exceptions. In a similar study by Ghimire et al. (2020), a prior research of GPS TEC over Nepal in 2014 found that the maximum value of VTEC occurred in March and the lowest occurred in December, with noticeable seasonal patterns, with greater value in the spring and smaller values in the winter. The semi-annual variation is not noticed in the VTEC during the solar minimum years of 2008, 2009, and 2010, and it appears that the summer VTEC is similar to the autumn VTEC. The semi-annual variations can be seen from 2011 to 2016. Summer VTEC was just as robust as autumn VTEC in 2017, following the same pattern as 2008, 2009, and 2010. At the KKN4 station in autumn 2015 VTEC has lower value and it is less in comparison with the summer VTEC. At KKN4, the winter VTEC is higher in comparison with the summer VTEC in 2011, however at the GRHI and JMSM, the winter VTEC is lower when compared with the summer VTEC in 2011 and 2014. The winter VTEC at DLPA is not higher relative to the summer VTEC. Spring VTEC detected more in contrast to autumn to the station GRHI, JMSM, and DLPA in 2008, however fewer in comparison with autumn for KKN4. Only at JMSM in 2009 was spring noticed to be greater relative to fall. In 2011, the autumn
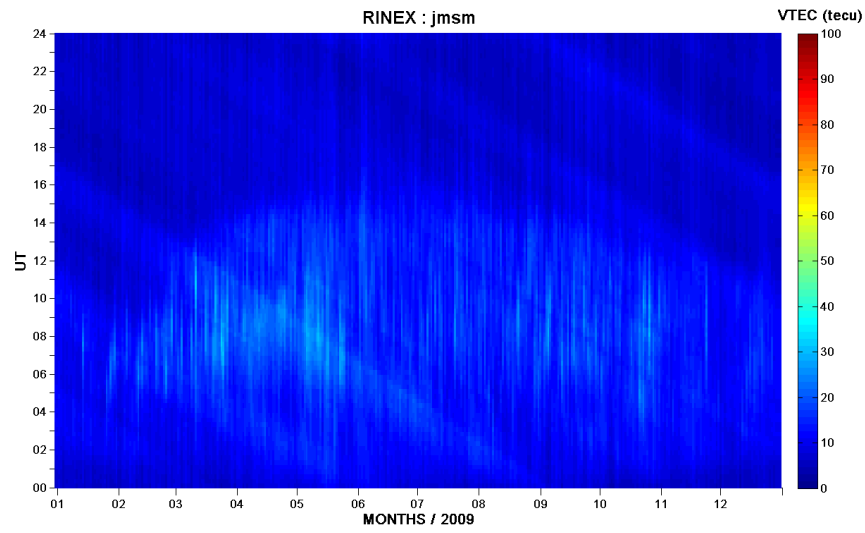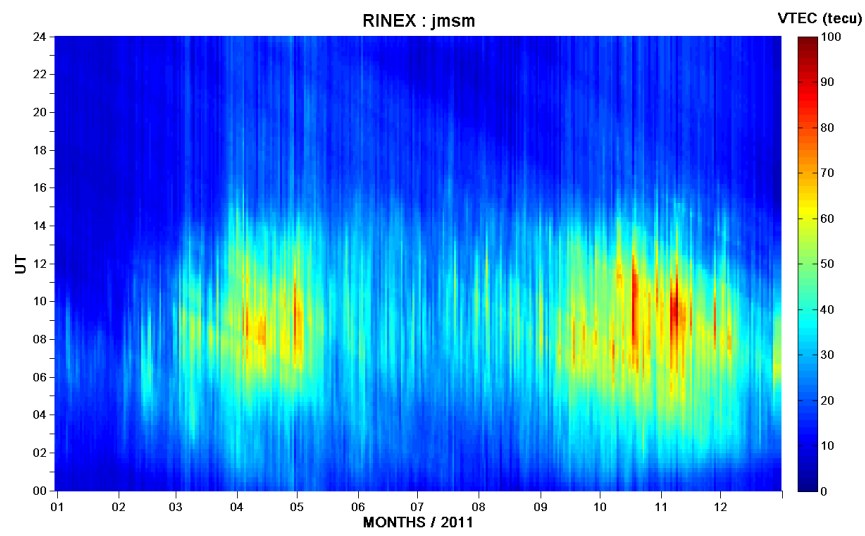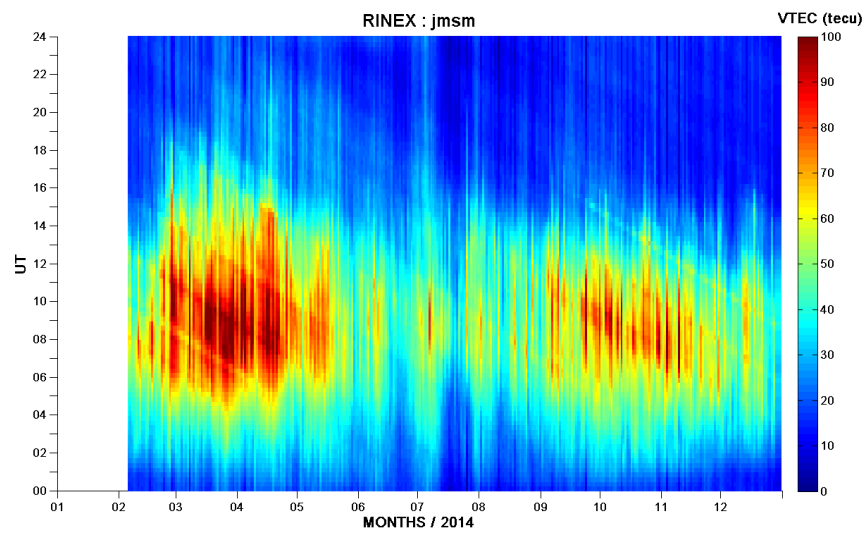
Figure 39: Two dimensional VTEC variability at the JMSM stations during (a) 2009-minimum, (b) 2011-ascending, (c) 2014-maximum, and (d) 2015-declining phases of solar cycle 24 (Pandit et al., 2021).
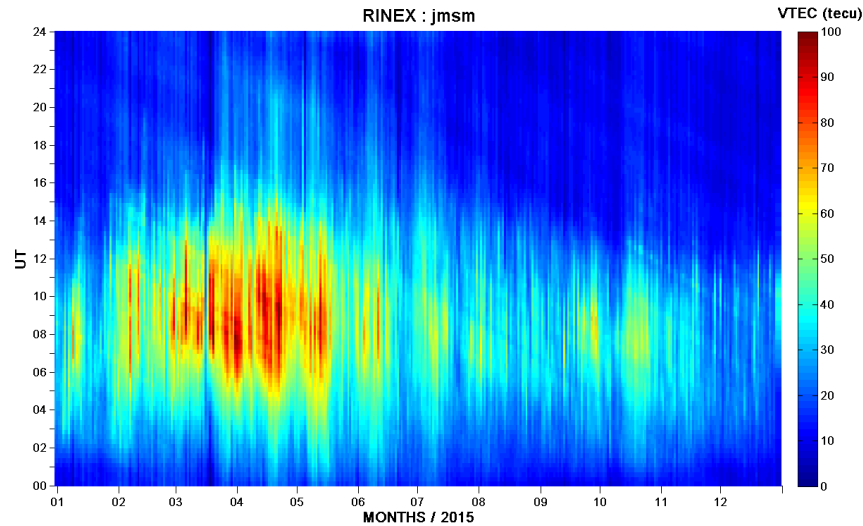
(d)

Figure 39: (Contd.) Two dimensional VTEC variability at the JMSM stations during (a) 2009-minimum (b) 2011-ascending, (c) 2014-maximum, and (d) 2015-declining phases of solar cycle 24 (Pandit et al., 2021).

VTEC is bigger than the spring VTEC at every station considered however at the JMSM, it is equivalent to the spring. The summer peak in 2015 is larger in comparison the autumn peak. At present study found VTEC greater in the winter when compared to the summer in 2011 and 2014. In the year 2014, the VTEC at KKN4 station was greater in the winter compared to the summer; in the years 2014 and 2016, the VTEC at GRHI was higher; and in the years 2014 and 2016, the VTEC at JMSM was higher. At DLPA, the VTEC is bigger in the winter in compared with the summer (Figure 40c and 40d). Rao, Sharma, & Pandey (2019) investigated the winter anomaly in GPS TEC in relation to solar flux. Winter anomaly occurs when the intensity of solar flux in the winter month is higher in comparison with the summer month, regardless of the solar cycle's high or low phases. The winter anomaly in GPS VTEC, according to their findings, may not be a geophysical relevant feature. The winter or seasonal anomaly caused by temperature changes (Appleton & Ingram, 1935), interhemispheric ion transport (Rothwell, 1963), notable change in distance from the Sun-Earth (Yonezawa, 1959), seasonal variability in concentration of O/N_2 (Rishbeth & Setty, 1961; Wright, 1963; Rishbeth et al., 2000; Zhang et al., 2005), and movement of energy density in upward (Maeda et al., 1986). Solar activity is linked to the winter anomaly. Tyagi & Das Gupta (1990); Bagiya et al. (2009) have documented the absence of a winter anomaly in weak solar activities at lesser latitudes.

Rishbeth & Setty (1961) developed the term "winter anomaly" to describe the change in constituent composition that has been recognized as the source of the winter anomaly. Asymmetric heating, which causes neutral components to be moved to the winter

hemisphere from the summer, could explain the lowest VTEC at June solstice (in Northern hemisphere) in high- and low solar activity phases. The recombination rate is lower in the winter than in the summer, resulting in a greater VTEC. The TEC above Delhi was examined by Gupta & Singh (2000), who discovered the winter anomaly occurs just when solar activity is higher. The Earth's the closest distance from the Sun plus the change in wind direction from summer to winter generates this winter anomaly (Shimeis et al., 2014). Krankowsky et al. (1968); Cox & Evans (1970) noted that the ratio of O/N_2 becomes twice as high in winter as it is in summer. This is owing to a quicker electron rate of loss in summer than that in winter.

Figure 41 shows the variation of VTEC at KKN4 over spring, autumn, summer, and winter from 2008 to 2017. In the spring, the difference in VTEC across low and high solar activity is 65 TECU, in the fall, 53 TECU, in the summer, 45 TECU, and in the winter, 40 TECU. In year 2014 and 2015, the plot for DLPA station is missing due to unavailability of data. Similarly, the plot 42 shows VTEC variability at the GRHI GPS station throughout the minimum and increasing phases of solar cycle 24 in the upper two panels, while the bottom two panel shows the maximum and decreasing phases. The graph demonstrates absence of equinoctial asymmetry during the minimal of solar cycle ie in 2008 and 2009, these are plainly visible throughout other stages of solar cycle.

The variability in concentration of atomic/molecular ratio, i.e. O/N_2 ratio, is an important characteristic for semiannual variation in ionospheric ionization. In the middle and low latitudes, at the solstice, a meridional wind flows with a speed about 25 m s^{-1} blows from the summer to the winter hemisphere (Rishbeth et al., 2000) B_y upwelling in higher latitudes, which transport nitrogen-containing air created in the summer hemisphere to lower latitudes, lowering the O/N_2 ratio. At the equinox, there is no predominant meridian circulation. The horizontal circulation has a strong influence on the O/N_2 ratio, which fluctuates seasonally when the global thermospheric circulation around the solstices, the pattern swings from summer to winter, and at the equinoxes, it becomes symmetrical. Rishbeth (1998) discusses six probable causes for seasonal and semiannual fluctuations in the F_2 layer: a) compositional changes in the thermosphere due to large-scale dynamical factors b) geomagnetic activity variations c) solar wind energy d) lower-atmospheric influences such as waves and tides; e) changes in atmospheric turbulence; and f) intensity of solar and EUV emission is anisotropy in solar latitude (Burkard, 1951). In year 2019, Ansari et al. discovered using data of three stations CHML, JMSM and GRHI that VTEC is lowest in January, grows to a peak in April, then drops in June-July, accompanied by a significant increase to a second peak in September-October, and lastly decreases till December (Ansari et al., 2019). According to Figure 42, the lowest value of VTEC is found in January, which increases to a maximum in March-April, then decreases in June-July, there was a rise in height of the second peak in
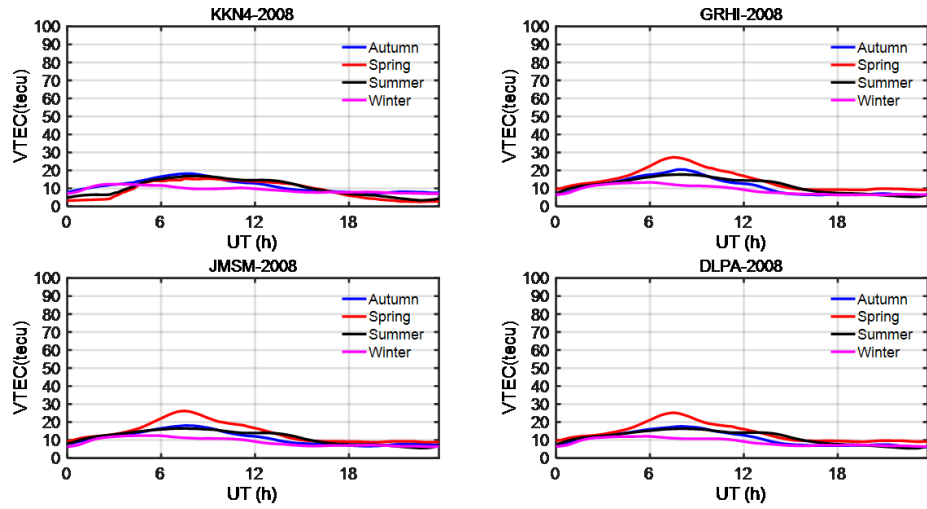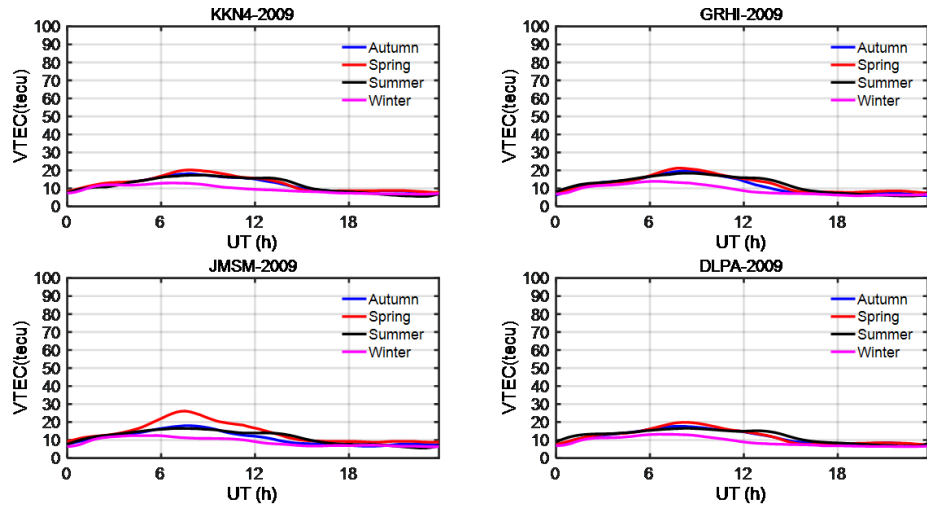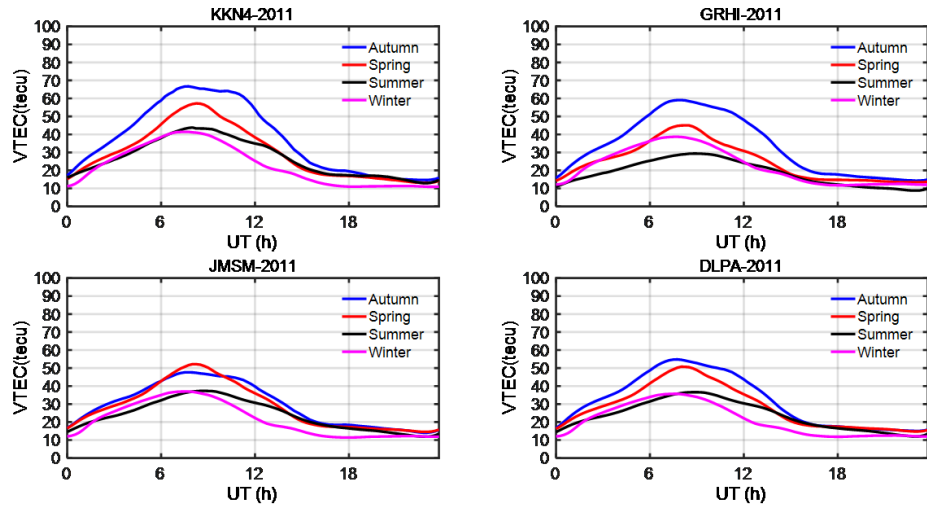
Figure 40: Seasonal variability of VTEC during year (a) 2008, (b) 2009, (c) 2011, (d) 2014, and (e) 2015 for KKN4, GRHI, JMSM, and DLPA stations (Pandit et al., 2021).
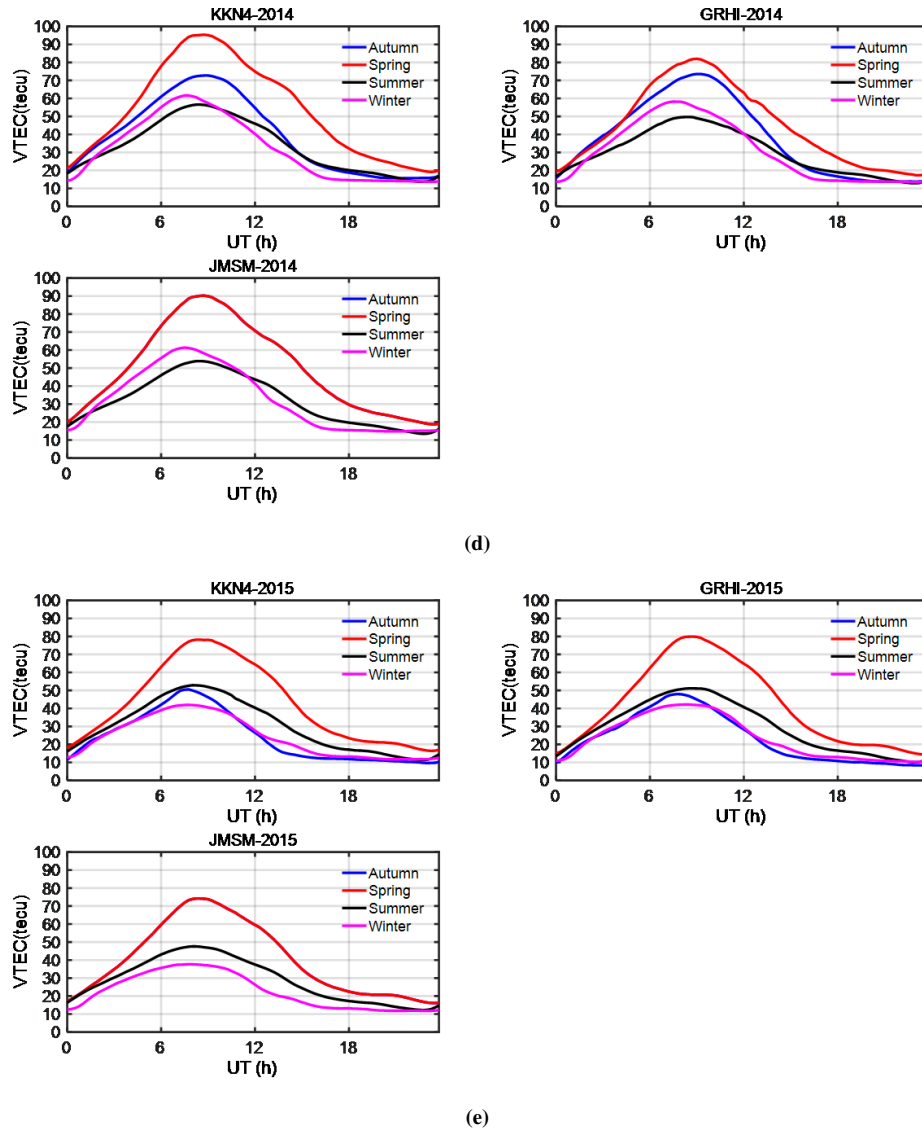
Figure 40: (Contd.) Seasonal variability of VTEC during year 2008, 2009, 2011, 2014 and, 2015 for KKN4, GRHI, JMSM, and DLPA stations. (Pandit et al., 2021).

October-November, followed by a fall until December at the GRHI of the year from 2008 to 2018. Geophysical characteristics associated to geomagnetic activity noted in the magnetic indices (Triskova, 1989) and the IMF B_z is responsible for the imbalance between the two equinoxes (Russell & McPherron, 1973). Three theories that explains the equinoctial imbalance observed in VTEC are the Russell McPherron (RM) effect, the axial hypothesis, and the equinoctial hypothesis proposed by Lal (1996); Shimeis et al. (2014).

Using data of three sunspot cycles Ouattara & Amory-Mazaudier (2012) developed a statistics based model near equatorial region over of the F_2 layer. Later this model is used to determine the impact of various categories of geomagnetic activities as specified by Legrand & Simon (1989) and also the asymmetry during equinoxes are caused by different magnetic activities. The imbalance seen between two equinoctial peaks also is
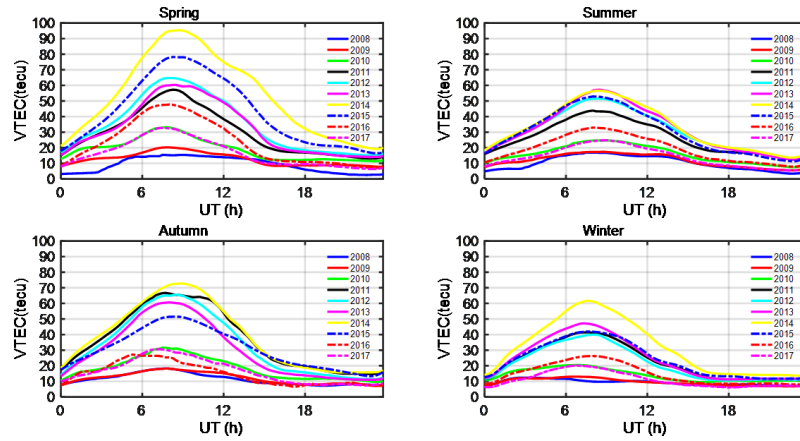
Figure 41: Mean yearly seasonal variations of VTEC during year from 2008 to 2017 at KKN4 (Pandit et al., 2021).
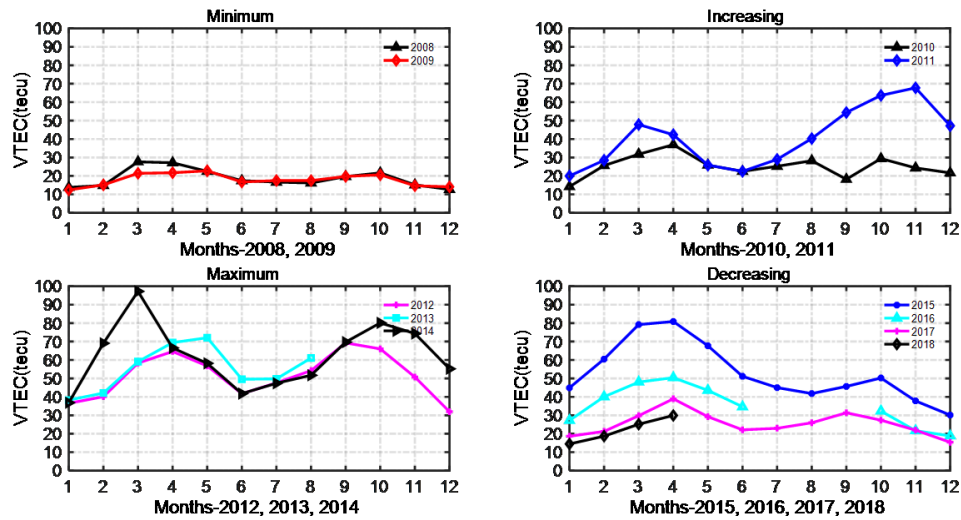
Figure 42: Maximum VTEC variability during four phases (minimum, increasing, maximum, and decreasing) of solar cycle 24 at GRHI station (Pandit et al., 2021).

due to the asymmetry of thermospheric properties that influence the ionosphere, such as neutral wind and composition change. (Balan et al., 1998).

4.1.4 Mean Yearly Variation

Figure 43(a-d) represents the mean yearly variation from year 2008 to 2018 for station KKN4, GRHI, JMSM and DLPA, respectively. The VTEC variation in each plot synchronize with the four phases of the solar cycle 24 i.e. 2008, 2009 minimum phase, 2010, 2011 the increasing phase, 2012 to 2014 the maximum phase, and 2015 to 2018 the declining phase. Among the four stations, the VTEC is highest at KKN4, then at JMSM, then at GRHI and least value is observed at DLPA.
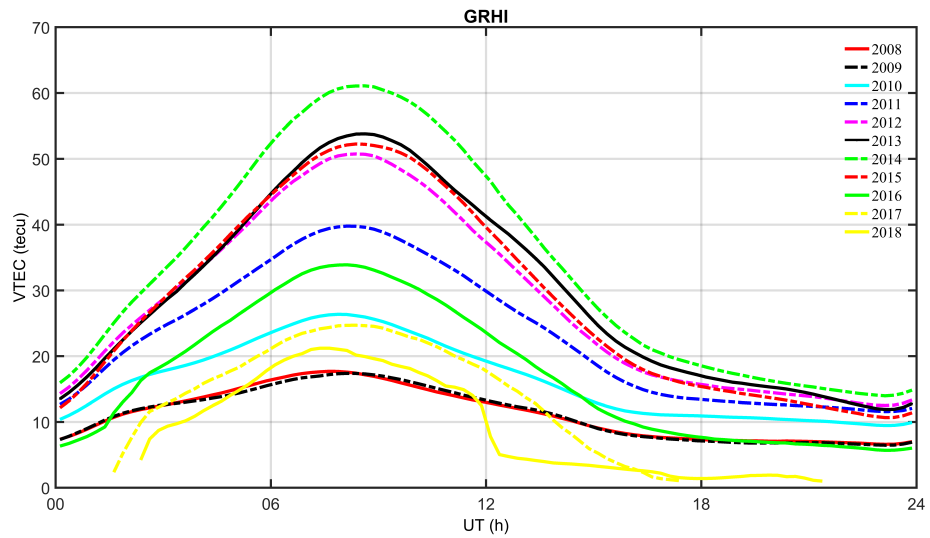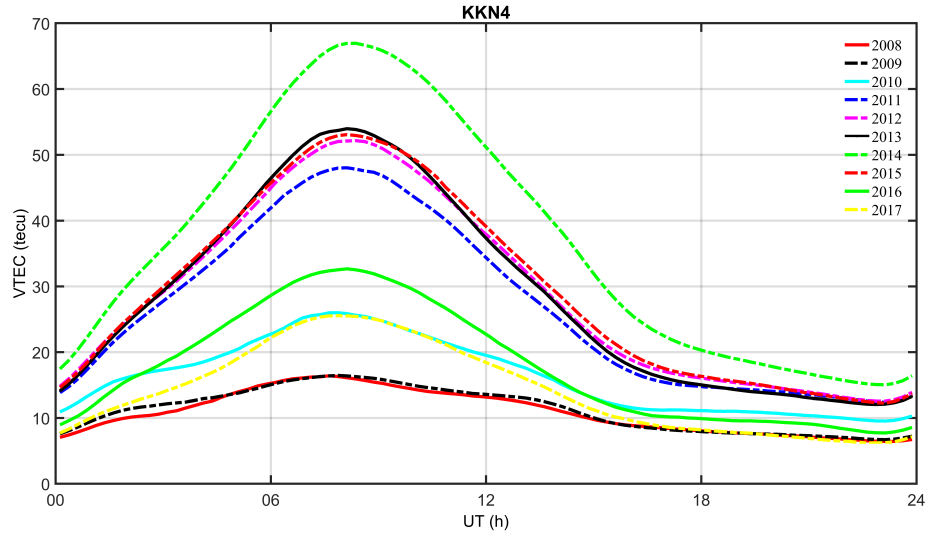
Figure 43: Mean yearly variation of VTEC at KKN4, GRHI, JMSM, and DLPA from year 2008 to 2018.
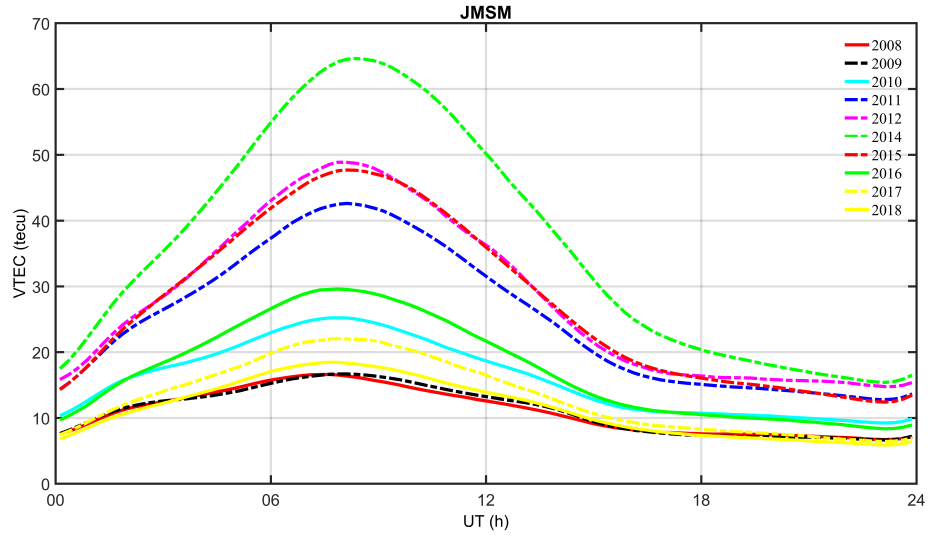
(c)
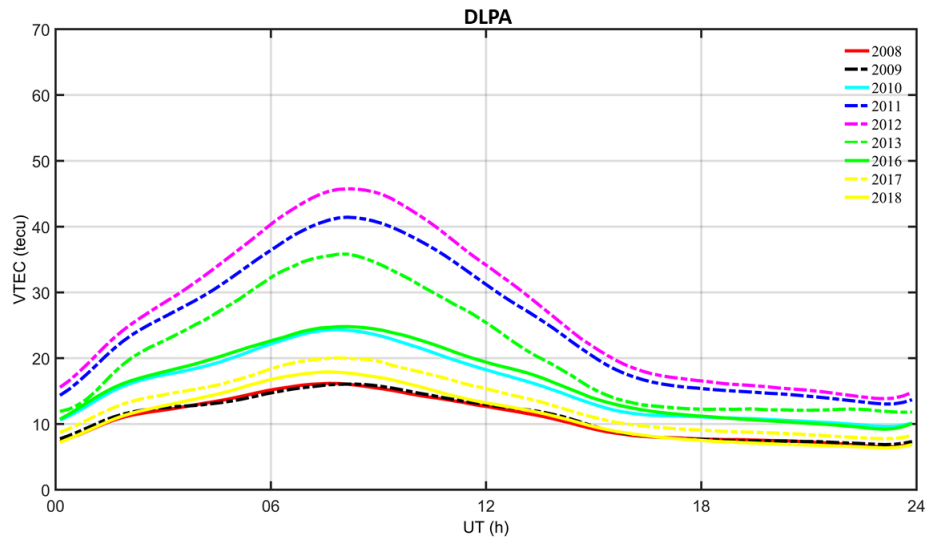
(d)

Figure 43: (Contd.) Mean yearly variation of VTEC at KKN4, GRHI, JMSM, and DLPA from year 2008 to 2018.

4.1.5 Solar Cycle Variation

Figure 44 depicts the yearly average values of VTEC, SSN, and SFI from year 2008 to 2018 of the solar cycle 24. VTEC variabilty of the four stations KKN4, GRHI, JMSM, and DLPA is indicated by the black, blue, green, and red color lines, respectively, while SSN and SFI variation is presented by the pink and light green color curves. The graph illustrates that VTEC gradually increases from 2009 to 2014, peaking in 2014 and it starts to decline till 2018, that corresponds to the variation in sunspot number and solar flux as shown Figure 44. In the highest phase of the solar cycle, the ionization peak was noted around 37 TECU in 2014, and the minimum value was around 11 TECU in 2008. The quantity of UV reaching the Earth is expressed in the observed VTEC fluctuation.

Similarly, from 2011 forward, the solar flux increases; the measured VTEC likewise reaches its maximum magnitude in 2014. All of the sites considered in this analysis have seen a decrease in maximum VTEC value from 2015 to 2018. The graph demonstrates that yealy mean VTEC is more synchronized with SSN and SFI. Phases of the solar cycle has a significant impact on solar variation, including solar flux emission and SSN which effect the ionosphere. After 1957, the solar cycle 24 is the shortest, the maximum of this solar cycle lies in 2014 in which some intense solar flares has found originating at the Sun in February and October of that year. (Kane, 2002). As a result, the maximum VTEC is observed in the month of February and October of that year, as illustrated in Figure 44. Figure 44 illustrates that in February 2011, a greater value of sunspot and solar radiation was observed, resulting in an X-class solar flare in which the station studied saw a higher VTEC. Sharma et al. (2012) investigated VTEC variability in Delhi, that is situated near the equatorial crest region, in the course of the low solar activity years from 2007 to 2009. They discovered that TEC has a short-lived daytime minimal around 5:00 and 6:00 LT, then steadily rises to attain the highest value between 12:00 and 14:00 LT. During the majority of the nighttime hours, the minimal of day was determined to be flat 22:00 LT to 06:00 LT. Their findings demonstrate that the amplitude of daily maximum TEC has decreased due to a drop in solar radiation from 2007 to 2009. They also discovered that TEC seasonal behavior is influenced by the solar cycle, with the highest daily TEC measured at Delhi during the equinoctial month. Ghimire et al. (2020) studied daily TEC at JMJG (Lamjung, Nepal) station for year 2015 and observed a lowest in the pre-dawn, a gradual ascent in the early morning hours, peak in the afternoon , and then a steady decrease towards sunset, which really is consistent with our findings. Tariku (2015) reported low VTEC values from 2008 to 2009 and high VTEC values from 2012 to 2013 in the African sector during high and low solar activity phases. Their study shows, diurnal VTEC was peaked between 13:00 LTand 16:00 LT, with the lowest values occurring usually around 06:00 LT. During the low solar active phases of solar cycle 24, the same profile of VTEC is observed with all GPS stations of
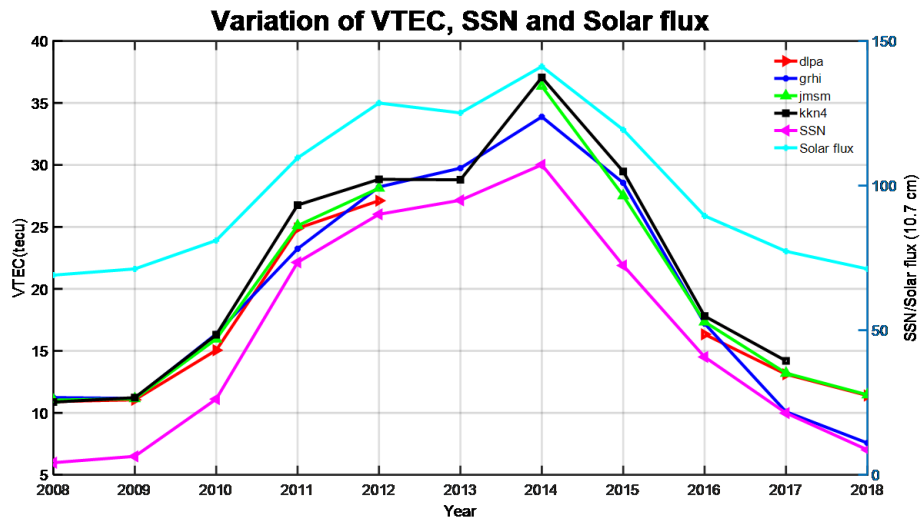
Figure 44: Annual mean variation of VTEC with SSN and solar flux index during years 2008 to 2018 at four stations KKN4, GRHI, JMSM, and DLPA (Pandit et al., 2021).

Nepal. Solar active cycle causes highest diurnal variation in VTEC in 2014, as indicated by the highest SSN and SFI (shown in Figure 33), the next VTEC greater in 2012 as a result of second maximal peak values in SSN and SFI, and lowest value VTEC in 2009 and 2017 assisted by minimal SSN and SFI, as evidenced by VTEC synchronization with SSN and solar flux as illustrated in Figure 44. In the ionosphere above Nepal, the highest value of diurnal SFI lies within 12:00 LT and 14:00 LT. The diurnal lowest value was noted flat over the almost every nighttime; similar to Delhi station in Nepal between 22:00 LT to 06:00 LT. Other than in 2011, the diurnal maximum in VTEC is highest at the spring equinoxes, when it is greatest during the autumn equinoxes. The daily maximum VTEC readings indicate a downward trend from 2008 to 2009 as the solar flux declines.

4.1.6 Correlation between SSN Number and SFIs

Figure 45 shows correlation between SSN (x-axis) and annual mean VTEC (y-axis) for station KKN4, GRHI, JMSM, and DLPA from 2008 to 2018, respectively. Similarly, Figure 46 represents the correlation between mean solar flux (x-axis) and VTEC (y-axis) for station KKN4, GRHI, JMSM, and DLPA from 2008 to 2018, respectively. The correlation coefficient between SSN and VTEC found to be 0.98, 0.97, 0.99, and 0.93 and between SFI and VTEC the correlation coefficient is found to be 0.98, 0.97, 0.99, and 0.93 at KKN4, GRHI, JMSM, and DLPA, respectively. The correlation computed between these two series of data in the annual mean of SSN, solar flux and VTEC taken from 2008 to 2018. Our result of correlation obtained between SSN and VTEC is in accordance with the result obtained by Ouattara et al. (2009) in Africa whose value lies between 0.95 to 0.98 for the solar cycles 20, 21, and 22. In Asia, Pham Thi Thu et al.

(2011) obtained the correlation between 0.836 and 0.848 for the same solar cycle. In 2012, Sharma et al. studied the correlation between solar flux and TEC at Delhi (very near to Nepalese GPS stations) during extreme minimum solar cycle from year 2007 to 2009 for equinox, winter and summer and found highly with correlation coefficient 0.99, 0.99, and 0.95 (Sharma et al., 2012).
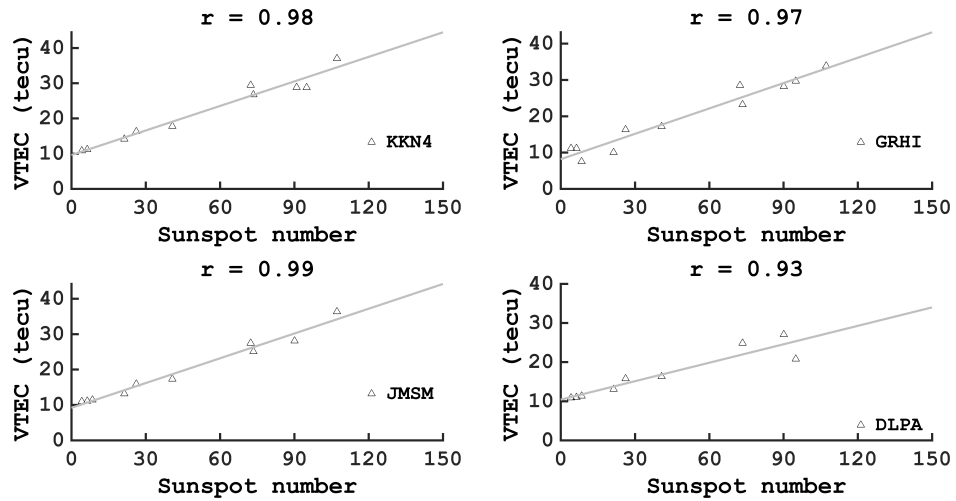
Figure 45: Correlation between VTEC and SSN at stations KKN4, GRHI, JMSM, and DLPA from years 2008 to 2018.
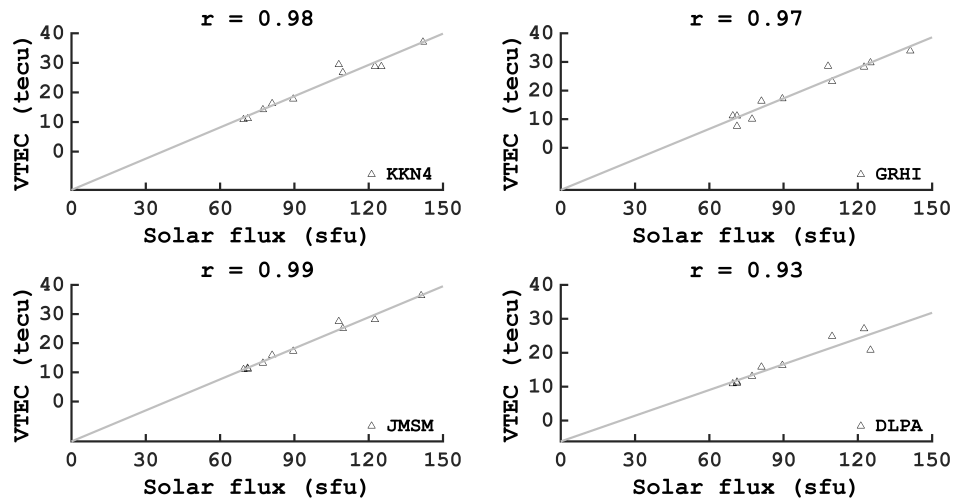
Figure 46: Correlation between VTEC and SFI at stations KKN4, GRHI, JMSM, and DLPA from years 2008 to 2018.

85

4.2 Disturbed Ionosphere Due to Storm and Super Substorm

The regular and irregular solar activities affect the physical and chemical characteristics of the ionosphere that modulates the structure and evaluation of ionosphere and thermosphere (L. Liu et al., 2011). In the course of geomagnetic storms, the coupling of solar wind and magnetosphere causes worldwide changes in the Earth's magnetic field including its ionospheric TEC. Magnetic storm produced by sudden increase in speed of solar wind (Schunk & Sojka, 1996) intensified by southward orientation of the B_z component of IMF. Intense particles precipitated during growth phase enhance JH, auroral intensification and electrojet current. By means of Joule heating, the Auroral electric currents transfer energy to the neutral gases. JH and the momentum transfer force drives pressure fields, thermospheric winds, generated gravity waves and thermospheric wind at F region heights and forced them to extend from auroral region to middle and lower latitudes causing changes the composition, density, and movement of the ionosphere-thermosphere system including TEC on global scale (Nava et al., 2016). Ionospheric irregularities during intense ionospheric storm embark GPS scintillation (Sridharan et al., 2014). There is increase in TEC during positive ionospheric storm, caused by a) an enhance in density of oxygen, b) changes in meridional winds propel the ionosphere to higher altitudes, where the rate of recombination is lower c) lifting of ionosphere to the region of lower recombination rate by an eastward electric field d) downward protonospheric fluxes e) Travelling Ionospheric Disturbances (TID) and f) redistribution of plasma due to disturbed electric fields. TEC decrease during negative ionospheric storm produced by change in neutral composition created by atmospheric disturbances decreases in O/N_2 density ratio (Goncharenko et al., 2007; De Abreu, Fagundes, Gende, et al., 2014). During the Sun's solar cycle, changes in solar and geomagnetic activity cause changes in all ionospheric parameters. (Bremer, 2005). On the basis of Dst values, geomagnetic storms are classified as severe (Dst $\leq$-200 nT), intense (-100 nT $\leq$ Dst $\leq$-200 nT), moderate (-50 nT $\leq$ Dst $\leq$-100 nT) and week (-30 nT $\leq$ Dst $\leq$-50 nT) storms (Gonzalez et al., 1994). In this section, we focus only variation VTEC during four super intense geomagnetic storms of solar cycle 24. We leave the study of effect on VTEC due to other storm for the future work.

4.2.1 Characteristics of Solar Wind Plasma Parameters and Magnetic Indices during SSSs

4.2.1.1 General Background and Global Context of the Events

A magnetospheric substorm occurs when a massive amount of magnetic energy trapped in the nightside magnetotail is released. Akasofu & Chapman (1961) were the first to propose the concept of a geomagnetic substorm during magnetic storms to describe

magnetic disturbances in the polar area. Earlier researcher believed that storm is formed by the summation of many substorms, but later it was proved to occur independently. Reversing of the polarity of the IMF B_z or the interplanetary electric field (E_y), increases in solar wind ram pressure, and other factors might cause a magnetic storm. But a substorm can occur without any obvious triggering mechanism, and these are known as "spontaneously triggered substorms"(Henderson et al., 1996). Till today, the exact triggering mechanism for the substorm is not known to the scientific community (Johnson & Wing, 2014). Substorm occurs randomly however, some periodicity has also been identified. During substorm, highly structured and intense aurora appears and it has been noticed for 2 hour to 3 hour. A substorm, like a storm, has three distinct phases: growth, expansion, and recovery. Energy is stored in the magnetotail during growth phase is released explosively during expansion. Dipolarization occurs during recovery where magnetosphere comes back to pre-storm condition.

During substorm onset, the magnetic reconnection near magnetotail produces diversion of cross-tail current through auroral ionosphere generate heating of plasma sheet, particle precipitation near auroral region and also diversion of these hot gases to the geosynchronous orbit. These electrons again get deposited to the auroral region through field lines enhancing auroral electrojet AE, a current in auroral E-region. AE, AU, AL, and AO are the proxy's indices for the substorm occurrence. Several space and terrestrial based measurements and numerical simulation has tried to understand the basic facts on substrom mechanism. The rapid varying magnetic field during depolarization of substorm induces larger electric field than the electric field established by solar wind on the magnetospheric surface. The field produced are highly localized and make their characterization difficult (Pulkkinen et al., 2007). In 2002, Sarries et al. identified the localized electric field enhances $\vec{E} \times \vec{B}$ drift to produce effective transport of plasma in eastward (Sarris et al., 2002). This field may penetrate to high latitude ionosphere and strengthen the auroral electrojet. This electric disturbance is called DP$_1$ effect and occurred during expansion phase of the substorm (Obayashi & Nishida, 1968). The field at tail of magnetosphere collapses and form "SCW "through which it is connected with polar ionosphere (Kepko et al., 2015). In 2017, Hui et al. reported that low latitude ionosphere is also affected by the induced field (Hui et al., 2017). But, none of the approach could have fully explain the entire characteristics' of substorms. In this study, we discuss the "super substorm"an extremely intense sunstorm defined by SML index a generalized form of AL index. For a substorm to be SSS, its SML or AL index is $< -2500 \, \text{nT}$ (Tsurutani et al., 2015). In this section, the characteristics of four SSSs have been discussed on the basis of IMF B_z and Auroral indices.

The SSS of 11 April 2001:- Figure 47a shows global context the solar wind plasma parameters and magnetic indices on 11 April 2001. Top to bottom in the plot show, the

variation of solar wind velocity (V_{sw}), temperature (T_{sw}) pressure/ density (P_{sw}/N_{sw}), total magnetic field /IMF (B/B_z), interplanetary electric field (E_y), auroral electrojet (AE), SYM-H and auoral up and low (AU/AL), respectively. Discontinuity in each plot appears due to unavailability of the data for that instant. At 16:09 UT and 20:23 UT, two abrupt decrease in AL suggest the presence of two SSSs. At the first peak, the value of AL is −2903 nT and at the second peak its value is −2339 nT. SYM-H has a value of +15nT at the start of the first SSS and acquires −68nT at the peak of the AL. In the due course of second SSS, the value of SYM-H goes to −160 nT. The interplanetary sheath is the causative of these two SSS events (Tsurutani et al., 1988). Multiple magnetic fluctuation is the signature of sheath region which has started after second shock at ~ 15:50 UT, it carries until the starts of magnetic cloud around 22:00 UT. The IMF B_z has moved southward in the due course of the SSS onset phase. The values of V_{sw}, T_{sw}, N_{sw}, E_y, and AE were 650 km s^{-1}, ~10^6 K, ~11 cm^{-3}, ~30 mV m^{-1}, and ~3500 nT (first onset); ~744 km s^{-1}, ~ 8×10^5 K, ~23 cm^{-3}, ~10 mV m^{-1}, and ~2500 nT (second onset). The two occurrences are distinct and huge (Tsurutani et al., 2015), with the first event lasting ~40 minute and the second event lasting ~35 minute, respectively. The interval between two SSSs peaks from the magnetic storm maximal found was ~7.8 hr and ~3.6 hr, respectively. Two fast forward shocks ~13:41 UT and ~15:50 UT were detected, during second shock, the velocity increased from ~610 km s^{-1} to 750 km s^{-1}, N_{sw} from ~9.5 cm^{-3} to 23 cm^{-3}, B from ~14.3 nT to 42.2 nT, and P_{sw} from ~7.1 nPa to 21.6 nPa, respectively.

The SSS of 24 November 2001:- Figure 47b shows global context the solar wind plasma parameters and magnetic indices on 24 November 2001. Top to bottom in the plot show variation of solar wind velocity (V_{sw}), temperature (T_{sw}) pressure/ density (P_{sw}/N_{sw}), total magnetic field/IMF (B/B_z), interplanetary electric field (E_y), auroral electrojet (AE), SYM-H, and auoral up and low (AU/AL), respectively. Two sharp decreases in AL at 6 UT and 13 UT indicate the position of two SSSs. During the first SSS maximal, the value of AL is −2800 nT and at the instant of second SSS, its maximal value is −3200 nT. SYM-H is positive +95 nT at first SSS and goes to -130 nT at the peak value of AL. The positive value increase in SYM-H indicates the rise in plasma parcel pressure on the magnetosphere due to solar wind, forcing magnetopause current comes nearer to the Earth. SYM-H acquired maximum value at second SSS with value −240 nT. The CME hits the magnetosphere ~6 UT and transfers energy to the magnetosphere during magnetic reconnection occurs during dayside of magnetosphere (Echer et al., 2008). The IMF B_z has turned southward since the commencement of SSS. The value of the southward component of IMF B_z during the SSS event was ~-30 nT and ~-20 nT, respectively. There is sudden increase in plasma temperature and during both SSS events. The value of V_{sw}, T_{sw}, N_{sw}, E_y, and AE in the course of the first and second

SSS were noted ~1000 km s^{-1}, ~35×10^5 K, ~30 cm^{-3}, ~35 mV m^{-1}, and ~3600 nT; ~ 900 km s^{-1}, ~25×10^5, ~30 cm^{-3}, ~30 mV m^{-1}, and ~3200 nT, respectively. The two events are independent and huge, with the first event lasting ~50 minute and the second event lasting ~30 minute, respectively (Tsurutani et al., 2015). The time interval between two SSSs was ~8 hr.

The SSS of 24 August 2005:- Figure 47c shows global context the solar wind plasma parameters and magnetic indices on 24 August 2005. Top to bottom in the plot show variation of solar wind velocity (V_{sw}), temperature (T_{sw}) pressure/ density (P_{sw}/N_{sw}), total magnetic field/IMF (B/B_z), interplanetary electric field (E_y), auroral electrojet (AE), SYM-H, and auoral up and low (AU/AL), respectively. The rapid drop in AL at 10:20 UT reflects the position of SSS, with the value of AL peaking at −3954 nT. SYM-H has a value of +95 nT at the commencement of SSS and −170 nT at its maximal value of AL. In the course of SSS, the IMF B_z has shifted southward. The value of solar wind and magnetic indices V_{sw}, T_{sw}, N_{sw}, E_y, and AE during the occurrence of event were ~700 km s^{-1}, ~15×10^5 K, ~58 cm^{-3}, ~35 mV m^{-1}, and ~3800 nT, respectively. The large fluctuation of IMF due to rare occurring extremely intense storm depend on (Cid et al., 2013) magnetic vector and the solar wind speed. The major cause of such event is interplanetary magnetic cloud or sheet field as a triggering structure is described in paper by Gonzalez et al. (2007); Echer et al. (2008).

The SSS of 7 and 8 September 2017 :- Figure 47d shows global context the solar wind plasma parameters and magnetic indices on 7 and 8 September 2017. Top to bottom in the plot show variation of solar wind velocity (V_{sw}), temperature (T_{sw}) pressure/ density (P_{sw}/N_{sw}), total magnetic field/IMF (B/B_z), interplanetary electric field (E_y), auroral electrojet (AE), SYM-H, and auoral up and low (AU/AL), respectively. The two dramatic drops in AL (with AL <−2500 nT), seen on 7 September at 23:45 UT and 8 September at 13:00 UT suggest the presence of two SSS. The first peaks the value of AL is −3000 nT on September 7 at 23:45 UT and at the second peak its value is −2700 nT on September 8 at 13:00 UT. During the maximal value of AL, the value of SYM-H at the commencement of the first and second SSS is −145 nT and −100 nT, respectively. The AE indices in the plot's sixth panel depict comparable types of high peaks during two SSSs events. During the two SSSs episodes of , rapid, high but positive fluctuations were seen in P_{sw}, N_{sw}, P_{sw}, T_{sw}, and V_{sw}. The origins of these two SSSs were distinct. The SSS events of September 7 is caused by the interplanetary sheath and for the SSS on September 8 is caused by a magnetic cloud (Despirak et al., 2019). The sheath region is characterized by many magnetic variations. There was an extreme IMF B_z turning southward at the start of SSS on September 7 compared to SSS on September 8. During the onset of first (7th September) and second (8th September) SSSs, the values of V_{sw}, T_{sw}, N_{sw}, E_y, and AE were 575 km s^{-1}, 10^6 K, 6 cm^{-3}, 25 mV m^{-1}, and 2500 nT;

750 km s^{-1}, 5×10^5 K, 7 cm^{-3}, 10 mV m^{-1}, and 2700 nT, respectively. These two SSSs events occur separately and substantial (Tsurutani et al., 2015), continuing for 15 minute and 25 minute, respectively.
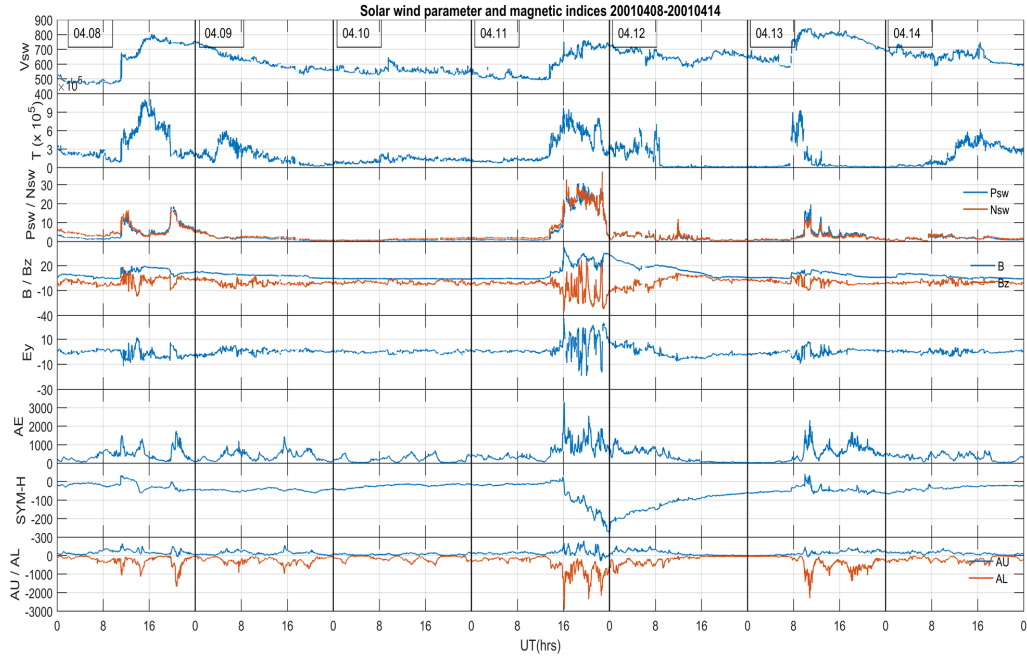
(a)
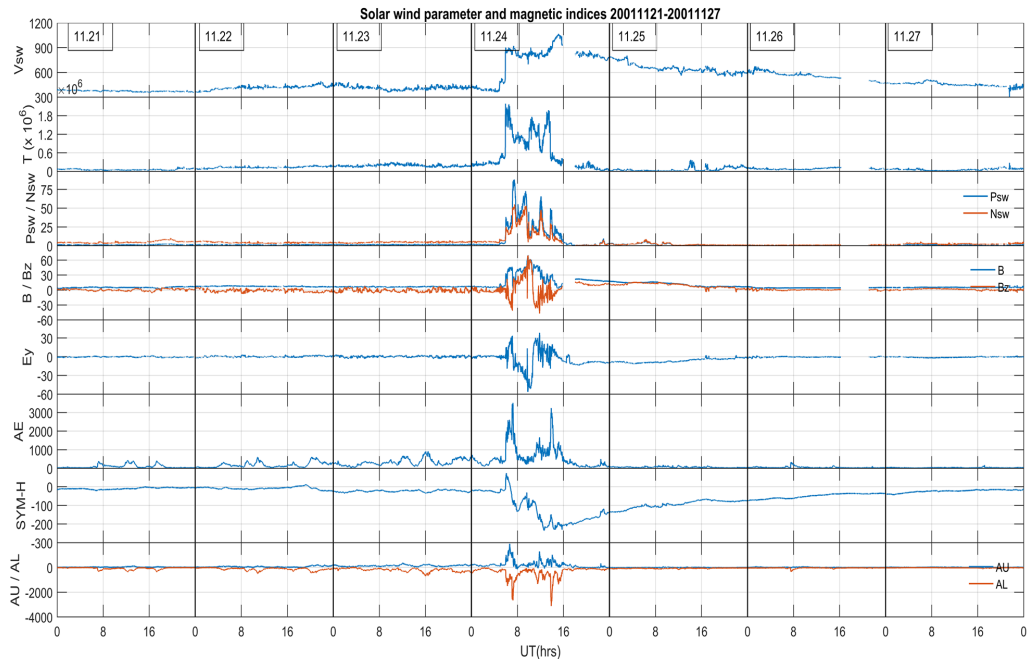
(b)

Figure 47: In each panel from top to bottom represents the variations of solar wind speed (V_{sw}) in km s^{-1}, temperature (T_{sw}) in K, pressure (P_{sw}) in nPa, plasma density (N_{sw}) in cm^{-3}, total magnetic field (B) in nT, IMF B_z in nT, interplanetary electric field (E_y) in mV m^{-1}, AE in nT, SYM-H in nT, AU in nT and AL in nT characterizing SSS of 11 April 2001, 24 November 2001, 24 August 2005, and 7 and 8 September 2017, respectively.
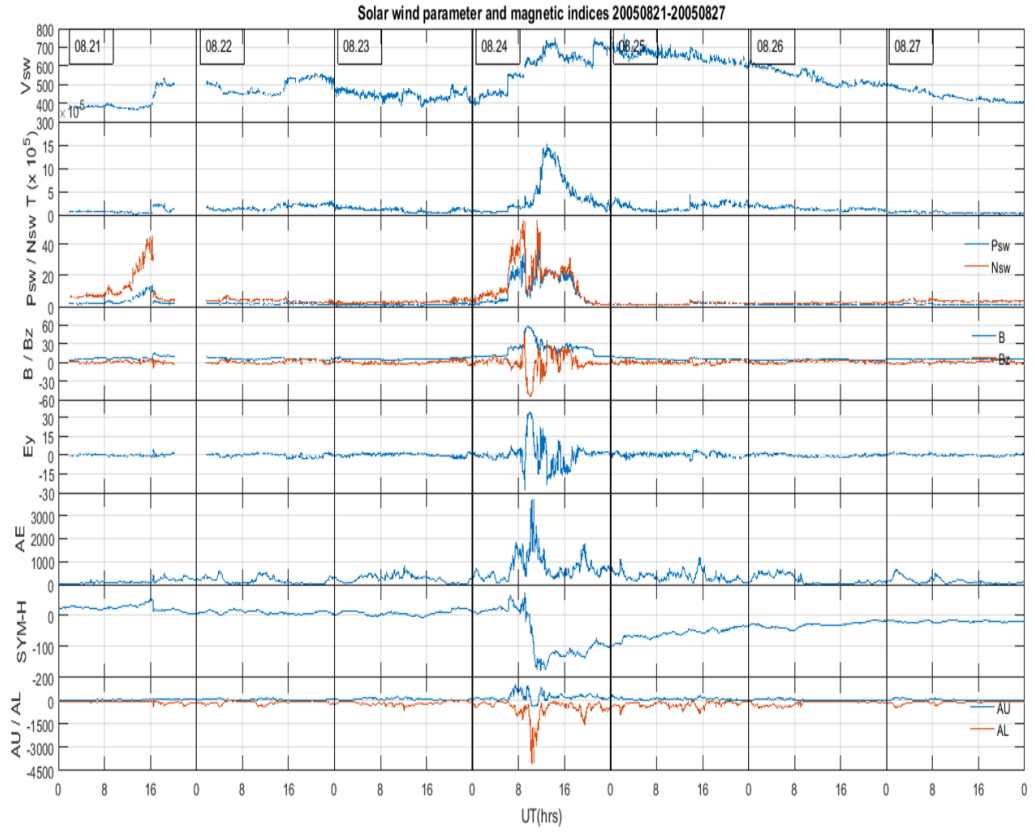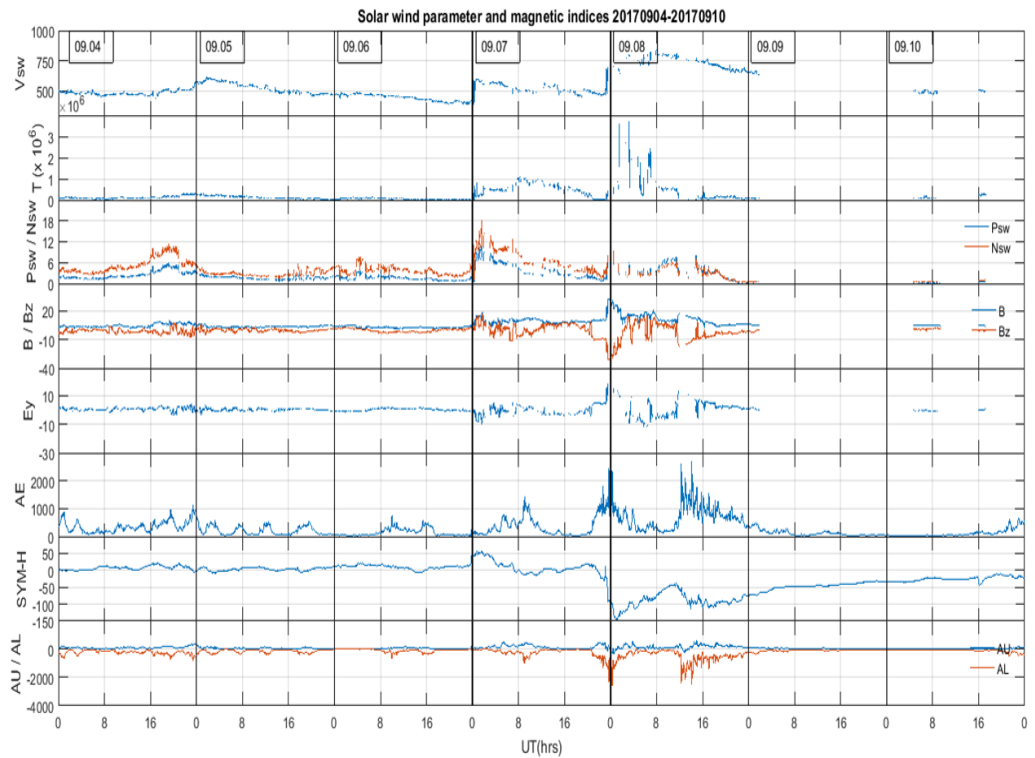
Figure 47: (Contd.) In each panel from top to bottom represents the variations of solar wind speed (V_{sw}) in km s^{-1}, temperature (T_{sw}) in K, pressure (P_{sw}) in nPa, plasma density (N_{sw}) in cm^{-3}, total magnetic field (B) in nT, IMF B_z in nT, interplanetary electric field (E_y) in mV m^{-1}, AE in nT, SYM-H in nT, AU in nT and AL in nT characterizing SSS of , 11 April 2001, 24 November 2001, 24 August 2005, and 7 and 8 September 2017, respectively (Pandit et al., 2020).

In this subsection, we discuss the relationship between IMF B_z and auroral indices using CWT, GWS and cross correlation analysis between IMF B_z and AE.

4.2.1.2   Analysis of IMF B_z and Auroral Indices: CWT

Figures 48 to 52 in each sub-panel, the sub-sub-panel depicts a) time series variations, b) power spectrum, and c) GWS of the southward component of the IMF B_z, AE, AU, and AL during SSS on April 11, 2001, November 24, 2001, August 24, 2005, September 7 and 8, 2017, respectively. In each Figure, the power spectrum graphic provides, the square modulus of the wavelet coefficient and the distribution of energy on the time scale. A slight disturbance in signal energy is seen using a log2 function in wavelet space, as shown in the scalogram. It helps to understand energy dynamics at a specific scale (Domingues et al., 2005). A scalogram is a graph that shows a sudden change in properties like magnetic field. Even short and intermediate spans have their large amplitudes, these perturbations emerge on scalograms through scattering frequencies. The most significant benefit of scalogram analysis is that it allows observing the distribution of amplitudes on bigger sizes. In this scalogram, the horizontal axis represents an hour of time, while the vertical axis indicates the periodicity in minute. The color indicator bar on the right-hand side of the plot presents the square of the actual amplitude of the coefficients of wavelet displayed with units in $(nT)^2$. They reflect a square estimation of the parameters' real values. The region of higher wavelet power is displayed in black on the scalogram (horizontal color indicator chart), whereas the region with lower wavelet power is visualized in blue. The scalogram's highest and minimum wavelet power correlate to high and low peak intensity, respectively. It exhibits extremely varied signals in time with no constant periodicity in each plot. In Figure 48 the sub panel shows that the background intensity of 1 $(nT)^2$ has increased to 11 $(nT)^2$ for IMF B_z, 1 $(nT)^2$ to 8 $(nT)^2$ for AE, 2 $(nT)^2$ to 12 $(nT)^2$ for AU, and 1 $(nT)^2$ to 9 $(nT)^2$ for AL for times 16:00 UT and 20:00 UT, respectively, the power area of higher intensity is seen time scale between approximately for IMF B_z between 2 $(nT)^2$ to 1 $(nT)^2$ and 5 $(nT)^2$ to 4 $(nT)^2$; AE between 16 $(nT)^2$ to 4 $(nT)^2$ and 4 $(nT)^2$ to 2 $(nT)^2$; AU between 16 $(nT)^2$ to 8 $(nT)^2$ and 4 $(nT)^2$ to 2 $(nT)^2$; and AL between 8 $(nT)^2$ to 4 $(nT)^2$ and 4 $(nT)^2$ to 2 $(nT)^2$ for SSSs event of 11 April 2001, respectively. The scalogram revealed that the abrupt change in the magnetic field is verified by some properties of solar wind and interplanetary parameters. The effect produced by the SSS occurrences is indicated by the high intensity with maximum periodicity observed in all panels. During SSSs, the short-term trend has a substantial impact on the indices AE, AL, AU, and IMF B_z. It indicates that thermal energy and energetic particles are pumped into the magnetosphere/magnetotail during the short pulse, potentially causing a power blackout on Earth.   Figures 49-52 are identical to Figure 48, with the exception that it refers to the SSSs of November 24, 2001, August 24, 2005, and September 7 and 8,

Figure 48: In each sub-panel, the sub-sub-panel a) Time series b) Cross-wavelet spectrum periodogram and c) The GWS for B_z, AE, AU, and AL for SSS of 11 April 2001 (Pandit et al., 2021).

Figure 48: (Contd.) In each sub-panel, the sub-sub-panel a) Time series b) Cross-wavelet spectrum periodogram and c) The GWS for B_z, AE, AU, and AL for SSS of 11 April 2001 (Pandit et al., 2021).

2017, respectively. In Figure 49 the two SSSs were identified, one at 7:00 UT and the other at 13:45 UT. In this Figure in sub-panels, it shows that the background intensity 2 $(nT)^2$ has increased to 14 $(nT)^2$ for the IMF B_z, AE, and AL indices, and from 1 $(nT)^2$ to 12 $(nT)^2$ for the AU indices. This plot also shows the locations corresponding to strong power for the IMF B_z between 16 $(nT)^2$ and 4 $(nT)^2$ and 4 $(nT)^2$ to 2 $(nT)^2$; AE between 10 $(nT)^2$ to 6 $(nT)^2$ and 4 $(nT)^2$ to 2 $(nT)^2$; Au between 8 $(nT)^2$ to 4 $(nT)^2$ and 4 $(nT)^2$ to $(nT)^2$2 and AL between 10 $(nT)^2$ to 6 $(nT)^2$ and 2 $(nT)^2$ to 1 $(nT)^2$ during the time at 7:00 UT and 13:00 UT of SSSs event on November 24, 2001. In Figure 50 for SSS of 24 August 2005 only one SSS is identified at 10:20 UT. In this Figure in sub-panels, it shows that the background intensity has increased from 2 $(nT)^2$ to 14 $(nT)^2$ for the IMF B_z, AU, and AL indices, and from 2 $(nT)^2$ to 16 $(nT)^2$ for the AE indices. This plot also shows the locations corresponding to strong power for the IMF B_z between 4 $(nT)^2$ and 2 $(nT)^2$; AE between 8 $(nT)^2$ to 2 $(nT)^2$ and 4 $(nT)^2$ to 2 $(nT)^2$; AU between 8 $(nT)^2$ to 2 $(nT)^2$ and AL between 8 $(nT)^2$ to 2 $(nT)^2$ during the time at 10:20 UT of SSS event on August 24, 2005. Similarly, in Figure 51 and Figure 52, the SSSs are identified at 23:25 UT and 13:00 UT on September 7 and 8, 2017, respectively. The background intensity in Figure 51 has found to increase from 2 $(nT)^2$ to 12 $(nT)^2$ for the IMF B_z, AU, and AL indices, and from 2 $(nT)^2$ to 14 $(nT)^2$ for the AE indices. This plot also shows the locations corresponding to strong power for the IMF B_z, AE, AU and AL found between 8 $(nT)^2$ to 4 $(nT)^2$ during the time of SSS event. And the background intensity in Figure 52 has found to increase from 2 $(nT)^2$ to 14 $(nT)^2$ for the IMF B_z, for AE and AL indices it has increased from 2 $(nT)^2$ to 12 $(nT)^2$ for AU indices it has increased from 2 $(nT)^2$ to 10 $(nT)^2$. This plot also shows the locations corresponding to strong power for the IMF B_z between 8 $(nT)^2$ to 4 $(nT)^2$; AE between 8 $(nT)^2$ to 4 $(nT)^2$; AU between

Figure 49: In each sub-panel, the sub-sub-panel a) Time series b) Cross-wavelet spectrum periodogram and c) The GWS for B_z, AE, AU, and AL for SSS of 24 November 2001 (Pandit et al., 2021).

95

Figure 49: (Contd.) In each sub-panel, the sub-sub-panel a) Time series b) Cross-wavelet spectrum periodogram and c) The GWS for B_z, AE, AU, and AL for SSS of 24 November 2001 (Pandit et al., 2021).

8 (nT)^2 to 2 (nT)^2 and AL between 8 (nT)^2 to 4 (nT)^2 during the time at 13:00 UT of SSS event on September 8, 2017. The log2 function in wavelet space, illustrated in the scalogram, is used to visualize the tiny disruption in signal energy in this plot, and the findings are interpreted in the same way as the prior event. Some of the strong power locations in each Figure is outside the cone of effect. The spectral characteristics of the IMF B_z, AE, AU, and AL indices are nearly identical. As a result, the IMF B_z and the AE, AU, and AL indices have a one-to-one correlation. During SSS events, this wavelet analysis strongly supports the existing link between solar-wind and magnetosphere and also during the SSSs, several characteristic effects on auroral electrojet indices can be noticed, according to this investigation. These indices were strongly affected during SSSs, with the largest relative amplitudes visible on the scalogram. The identification of quiescent and non-quiescent phases in magnetic signals is possible because to their relative amplitudes. The intrinsic processes of energy transmission are thus surveyed utilizing this method. This fact supports the theory that charged particle penetration and energy injection are more common during SSSs during the reconnection mechanism between the IMF B_z and the magnetic field of the Earth at the magnetosphere (Morioka et al., 2003; Mendes Jr et al., 2005).

4.2.1.3 Analysis of IMF B_z and Auroral Indices: Using GWS

The GWS of the IMF B_z, AE, AU, and AL indices during SSS of 11 April 2001 and 24 November 2001, 24 August 2005, and 7 and 8 September 2017, respectively, are shown in sub-sub-plot (c) of Figures (48-52). It examines the distribution of the two variables' associated main periods. Figure 48 shows two periods of increased correlation with energy values of 2500 (nT)^2 and 2200 (nT)^2 for IMF B_z; 10×10^6 and
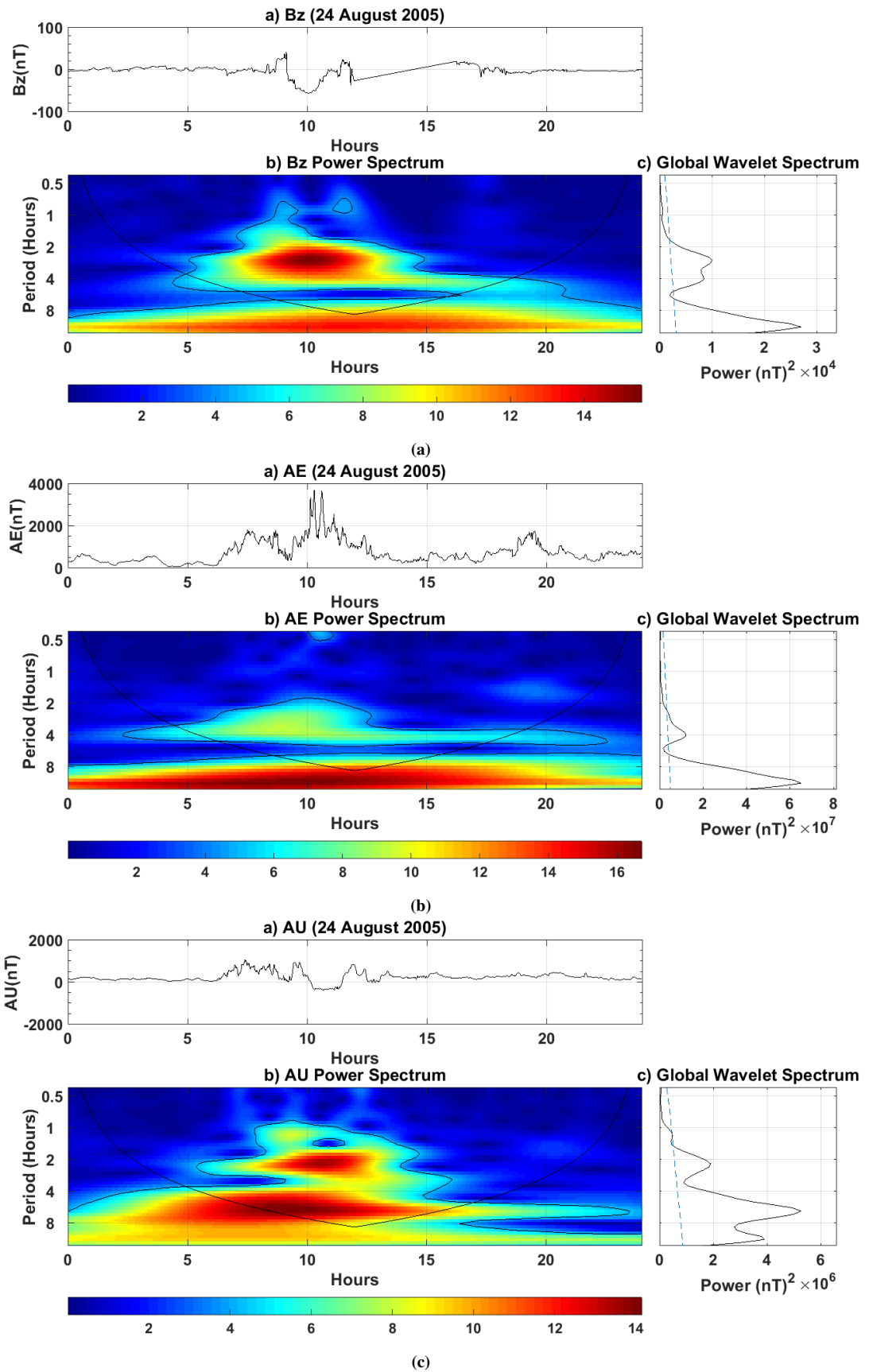
Figure 50: In each sub-panel, the sub-sub-panel a) Time series b) Cross-wavelet spectrum periodogram and c) The GWS for B_z, AE, AU, and AL for SSS of 24 August 2005.
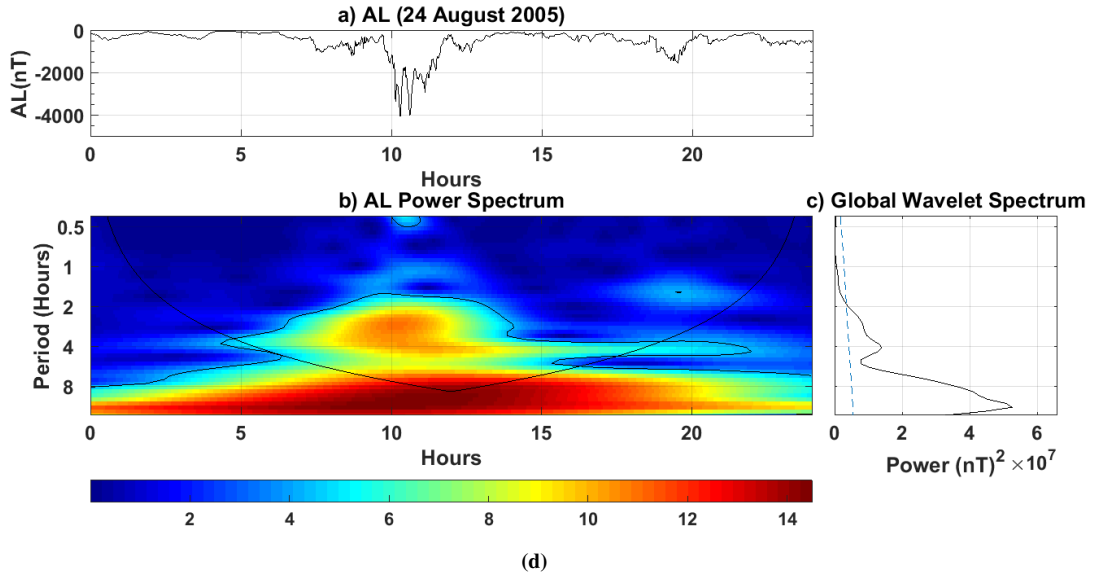
Figure 50: (Contd.) In each sub-panel, the sub-sub-panel a) Time series b) Cross-wavelet spectrum periodogram and c) The GWS for B_z, AE, AU, and AL for SSS of 24 August 2005.

5×10^6 $(\text{nT})^2$ for AE; 2.4×10^6 and 1×10^6 $(\text{nT})^2$ for AU; and 6×10^6 and 5×10^6 $(\text{nT})^2$ for AL, which coincides to the duration of the two SSSs on April 11, 2001. During two SSSs occurrence on November 24, 2001 (in Figure 49), the two periods of higher correlation were detected at 7:00 UT and 13:00 UT with energy values of 3×10^4 $(\text{nT})^2$ and 2×10^4 $(\text{nT})^2$ for IMF B_z; 4.2×10^7 $(\text{nT})^2$ and 1.5×10^7 $(\text{nT})^2$ for AE; 4.2×10^6 $(\text{nT})^2$ and 3×10^6 $(\text{nT})^2$ for AU; 2×10^7 $(\text{nT})^2$ and 0.5×10^7 $(\text{nT})^2$ for AL. Figure 50 shows the periods of increased correlation with energy values of 2.5×10^4 $(\text{nT})^2$ for IMF B_z; 6.5×10^7 $(\text{nT})^2$ for AE; 5.5×10^6 $(\text{nT})^2$ for AU; 5.2×10^7 $(\text{nT})^2$ for AL, which coincide to the duration 10:20 UT of the SSS on August 24, 2005. In Figure 51 during SSS occurrences on September 7, 2017, the periods of higher correlation were detected at 23:45 UT with energy values of 6500 $(\text{nT})^2$ for IMF B_z; 2.0×10^7 $(\text{nT})^2$ for AE; 2.2×10^6 $(\text{nT})^2$ for AU; 1×10^7 $(\text{nT})^2$ for AL. Similarly, in Figure 52 during SSS occurrences on September 8, 2017, the periods of higher correlation were detected at 13:00 UT with energy values of 6500 $(\text{nT})^2$ for IMF B_z; 2.0×10^7 $(\text{nT})^2$ for AE; 2.2×10^6 $(\text{nT})^2$ for AU; 1×10^7 $(\text{nT})^2$ for AL. According to Adhikari et al. (2018), the ICME related storm on November 20-21, 2003 was identified during the period of 64 minute to 16 minute with an energy value of 2.5×10^{10} V^2, the HSS related storm on July 17, 2004, was identified during the period of 64 minute with an energy value of 9×10^{10} V^2, and the ICME related substorm on October 24, 2002 was identified during the period of 24 minute with an energy value of 7.2×10^9 V^2. Adhikari et al. (2018) discovered the correlation coefficient during a 30 minute examination of SSS on January 21, 2005, with an energy value of 9×10^{11} V^2 in PCV. The IMF B_z, AE, AU, and AL indices have nearly identical spectral features, resulting in a one-to-one correlation on both SSSs between the IMF B_z and the AE, AU, and AL indices. The current association between the IMF B_z and the AE, AU,
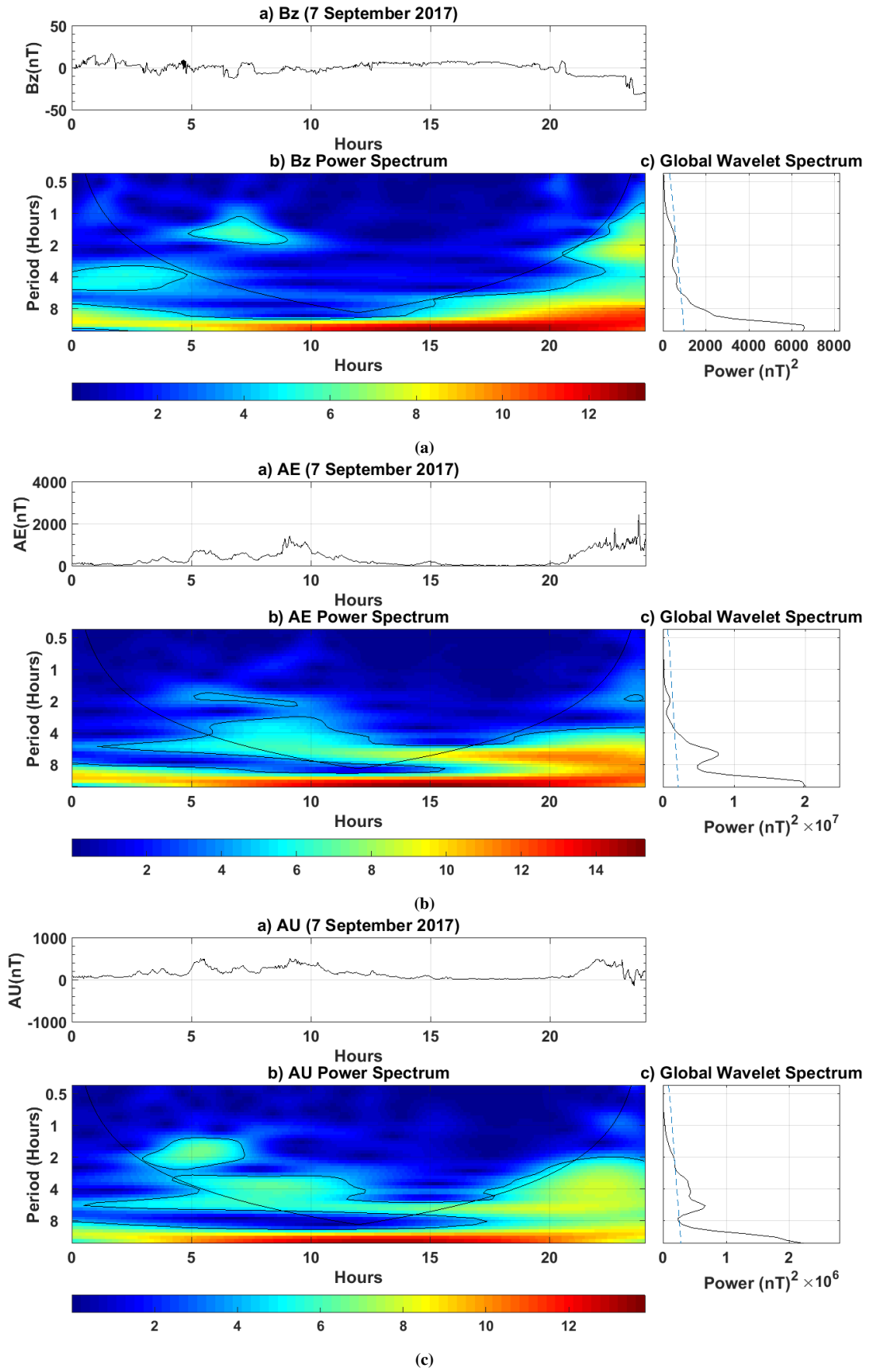
Figure 51: In each sub-panel, the sub-sub-panel a) Time series b) Cross-wavelet spectrum periodogram and c) The GWS for B_z, AE, AU, and AL for SSS of 7 September 2017.
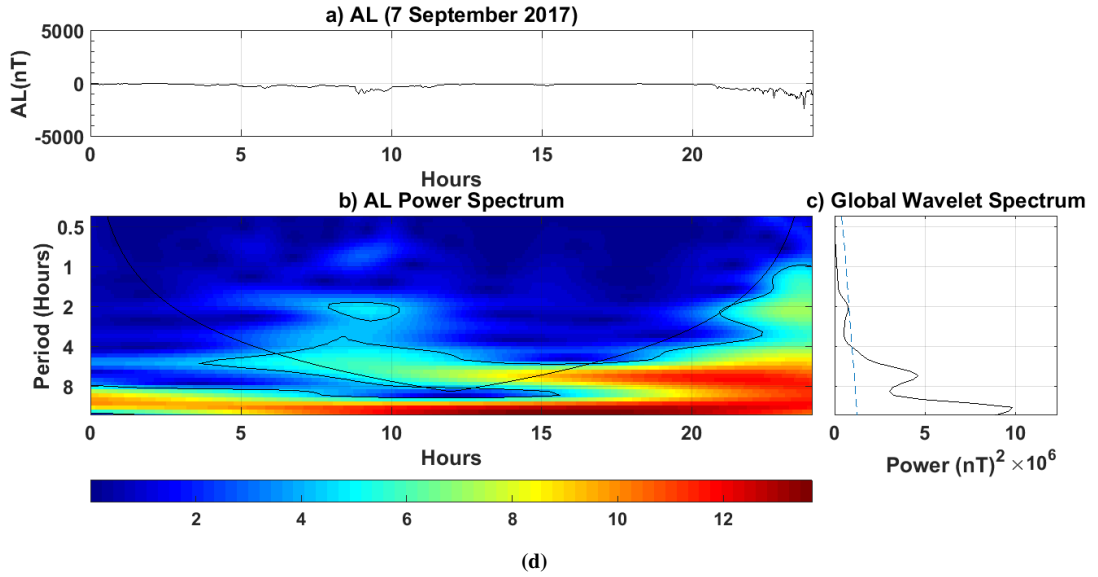
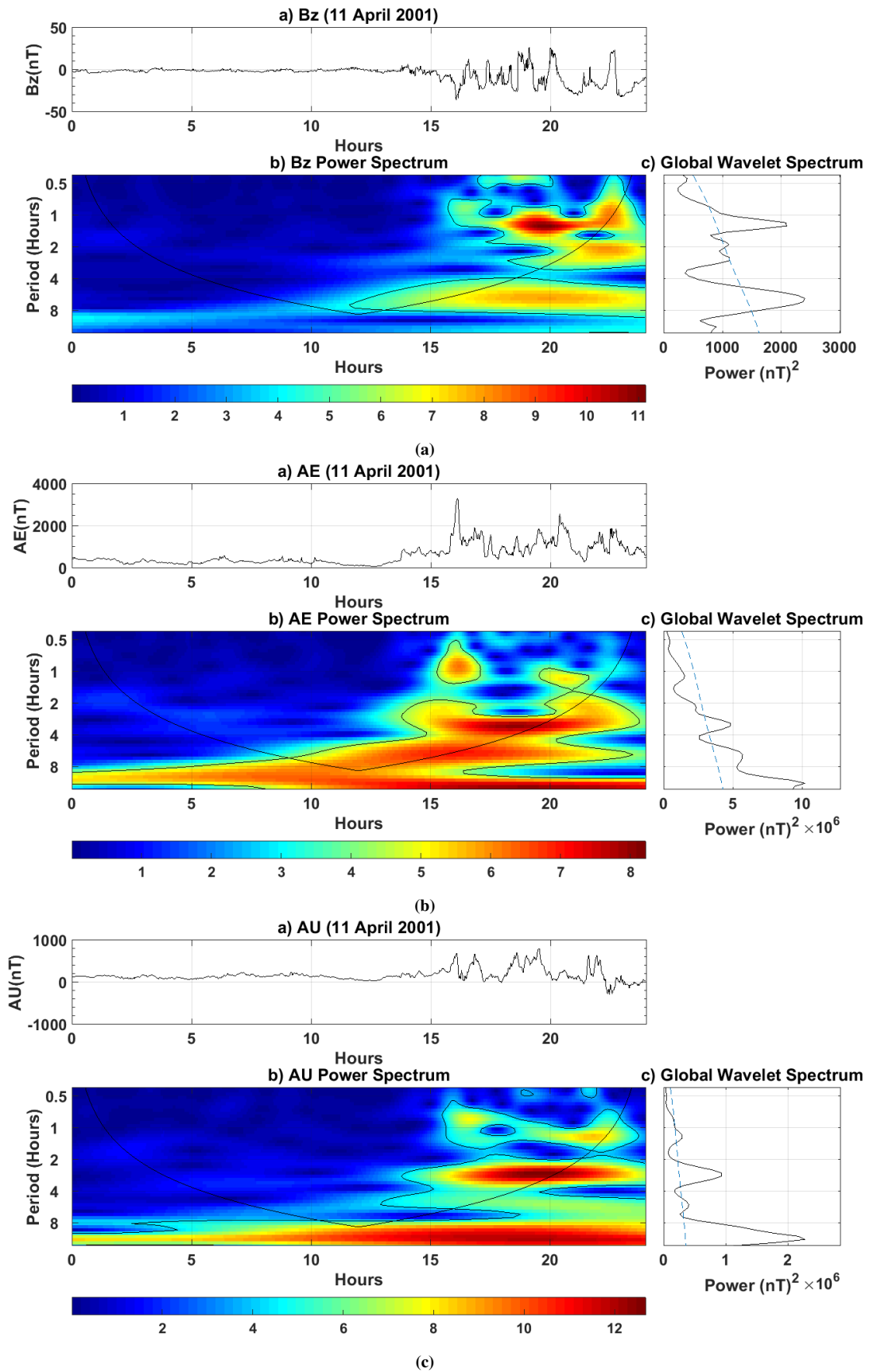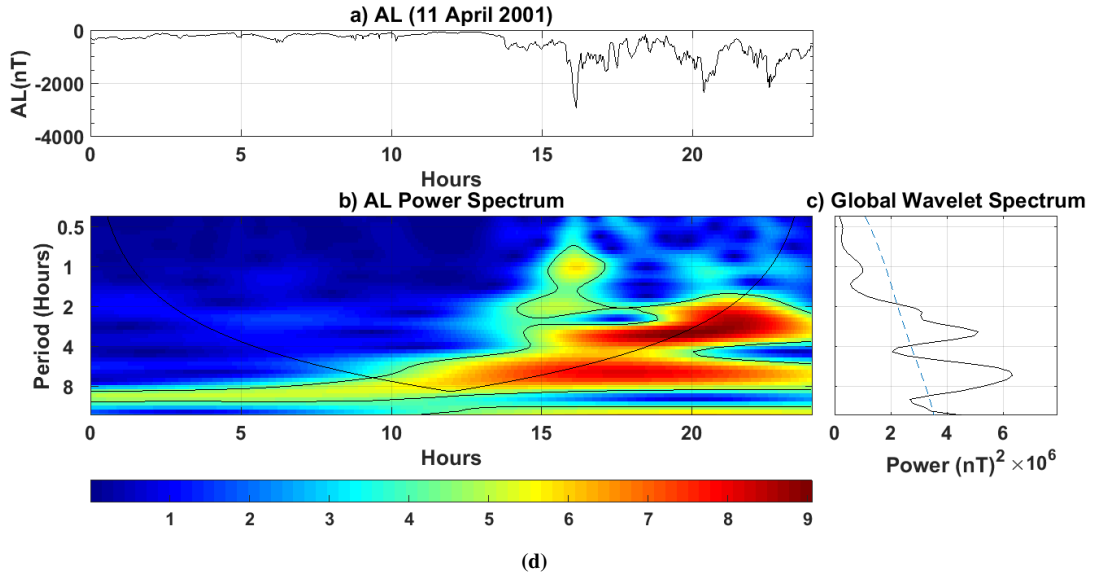**Figure 51:** (Contd.) In each sub-panel, the sub-sub-panel a) Time series b) Cross-wavelet spectrum periodogram and c) The GWS for B_z, AE, AU, and AL for SSS of 7 September 2017.

and AL indices is supported by these findings. During the study of HILDCAA with maximum energy 1.2×10^6 (nT)^2, Marques de Souza et al. (2018) identified three periods of higher correlation due to efficient solar wind coupling between IMF B_z associates with Alfvan wave fluctuation and geomagnetic field, which was identified as the main cause of geomagnetic activity related to HILDCAA (Tsurutani & Gonzalez, 1987). During SSS, the short pulse coupling mechanism between IMF B_z and the geomagnetic field may unleash a substantial amount of energy that might be used to destroy space and terrestrial assets (Tsurutani et al., 2015).

4.2.1.4 Cross Correlation Analysis between Auroral Indices AE and IMF B_z

Figures 53 (a - g) show the cross-correlation between the IMF B_z and the AE index during two SSSs on April 11, 2001, November 24, 2001, August 24, 2005 and September 7 and 8, 2017, respectively. Two SSSs have occurred on April 11, 2001 at 15:53 UT and 20:16 UT and on November 21, 2001 at 7:00 UT and 13:45 UT. A SSS has occurred on August 24, 2005 at 10:20 UT; on September 7, 2017 at 23:45 UT, and on September 8, 2017 at 13:00 UT, respectively. The time lag between two time series and their degree of correlation are determined by cross-correlation. The time delays between two time series are represented on the horizontal axis, while the correlation coefficient is represented on the vertical axis. Before and after they are correlated, the time scale in minute reveals which index is leading or lagging. Figures 53a and 53b show that the IMF B_z and the AE index are associated with a correlation coefficient of ~ -0.95 and 0.90 for first and second occurrence of SSSs with zero-time lag on April 11, 2001. In Figures 53c and 53d, the correlation between IMF B_z and AE was noticed 0.60 for first SSS and 0.90 during second SSS of November 24, 2001 with approximately zero time
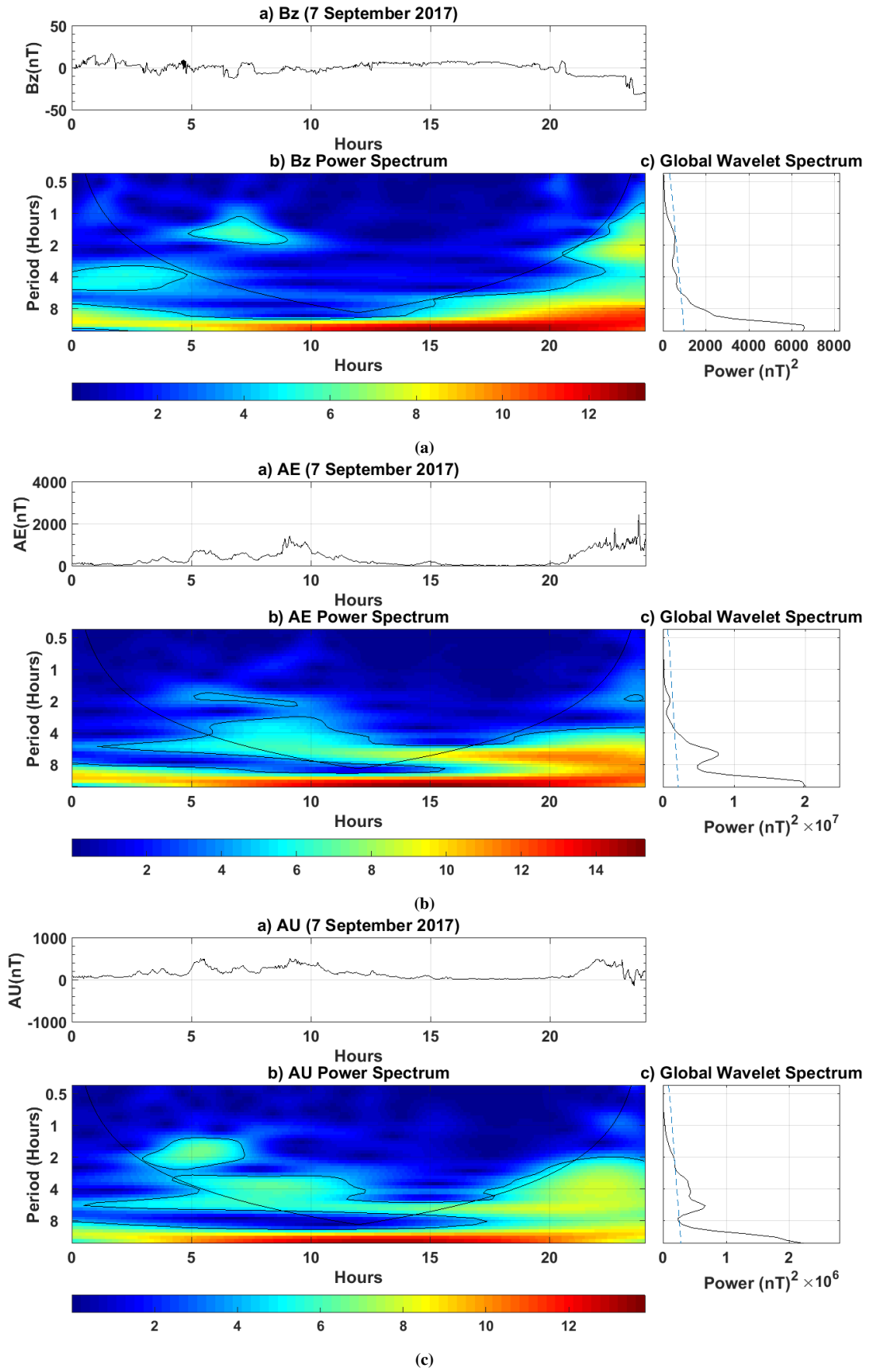
Figure 52: In each sub-panel, the sub-sub-panel a) Time series b) Cross-wavelet spectrum periodogram and c) The GWS for B_z, AE, AU, and AL for SSS of 8 September 2017.

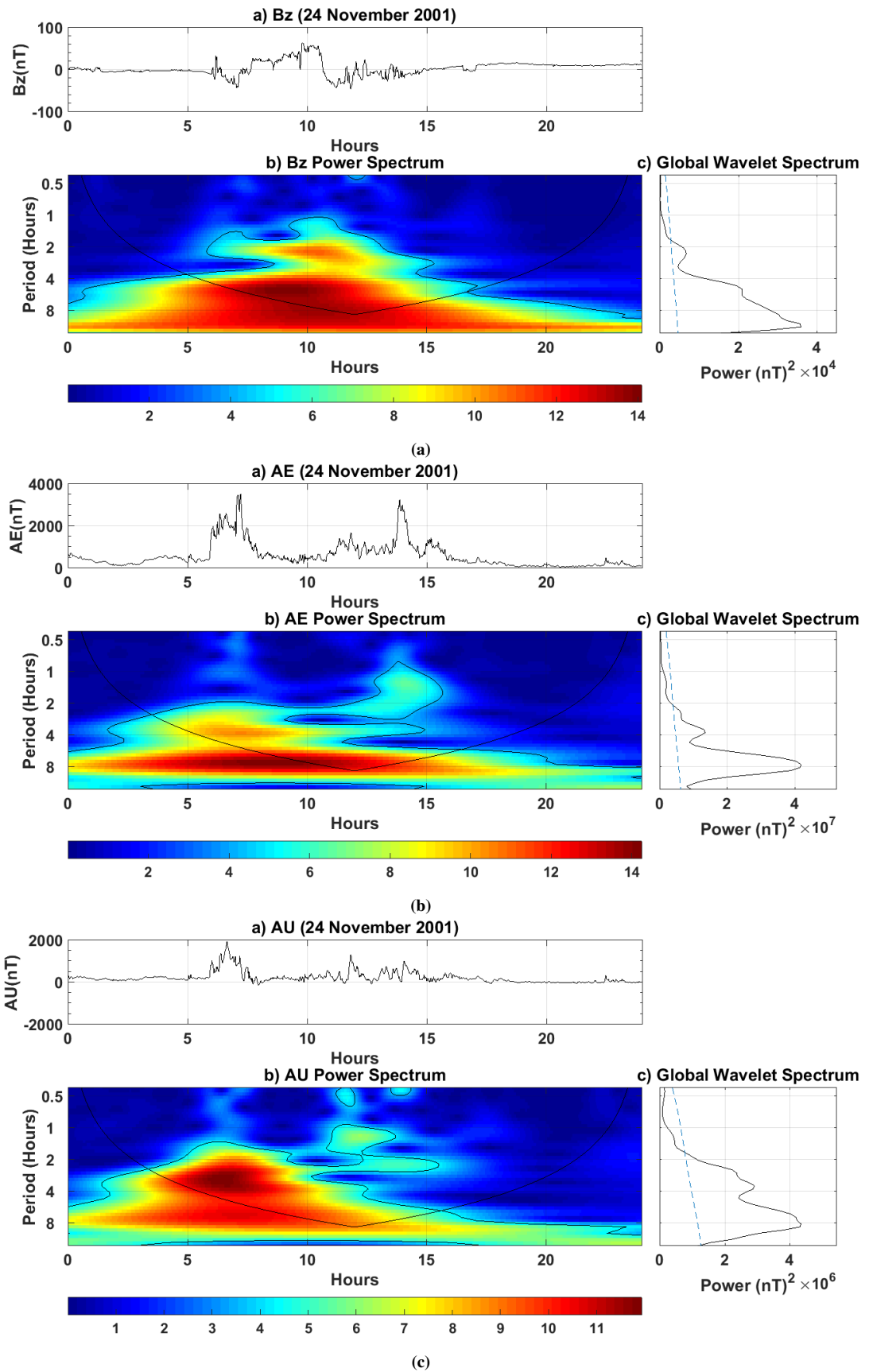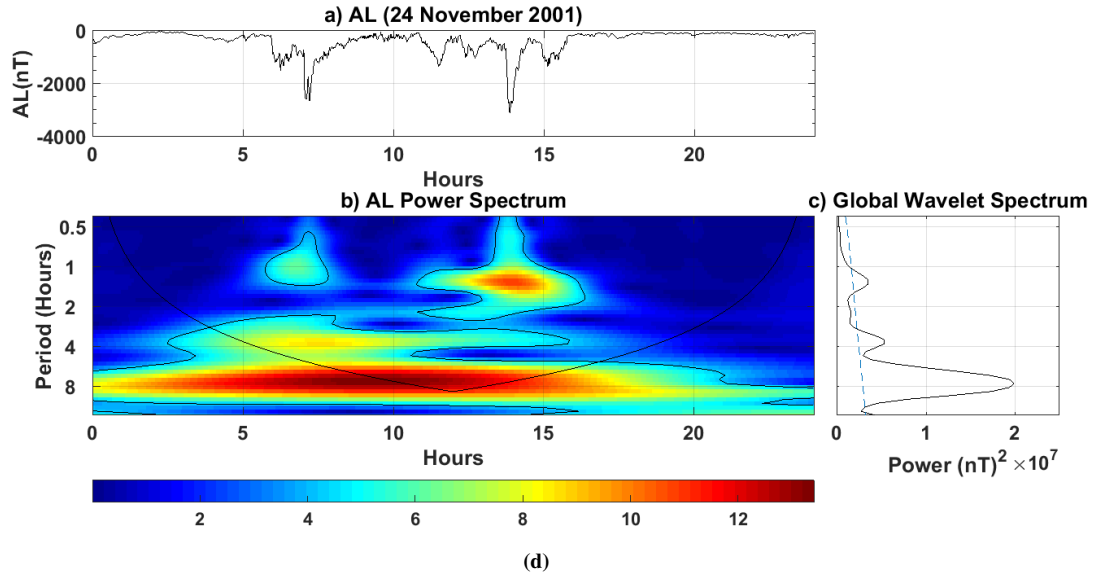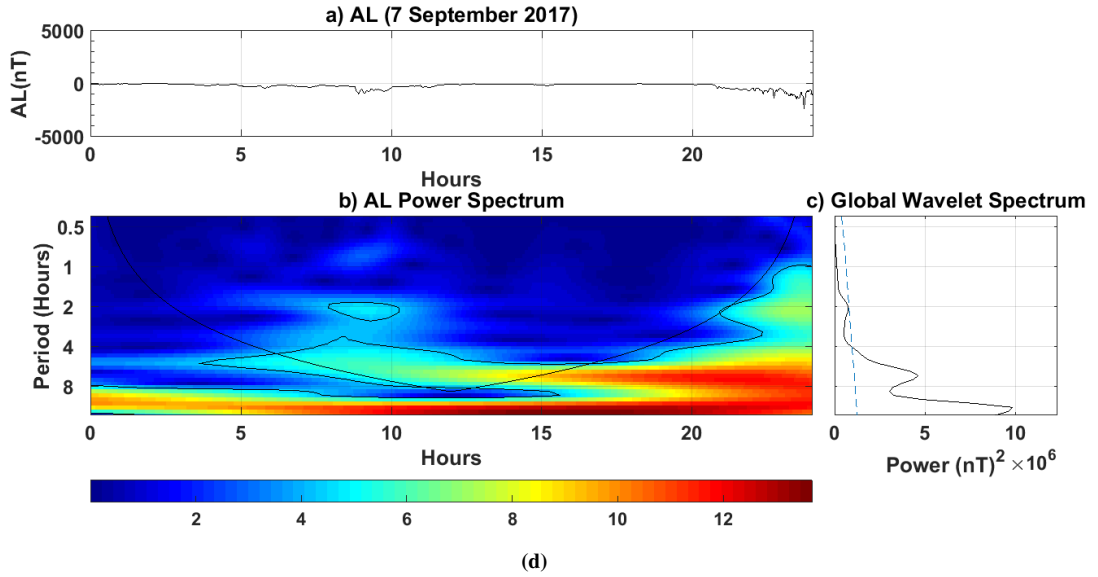**Figure 52:** (Contd.) In each sub-panel, the sub-sub-panel a) Time series b) Cross-wavelet spectrum periodogram and c) The GWS for B_z, AE, AU, and AL for SSS of 8 September 2017.

lag. Referring the Figures 53e, 53f and 53g, the correlation coefficient of 0.90, 0.97, and 0.99 with zero time lags was noticed between IMF B_z and AE for the SSS of August 24, 2005, September 7, 2017, and September 8, 2017, respectively. It can be regarded as the AE index's quick reaction to changes in the IMF B_z index. Pandit et al. (2018) observed 0.50 correlation coefficient association between the AE index and the disruption of the IMF B_z during a strong geomagnetic storm. In 2018, Adhikari et al. discovered that the correlation coefficient between FAC-AE is 0.80 with a time lead of 50 minute during SSS on January 21, 2001, and that of the cross correlation coefficient between FAC-B_z in phase with -0.50 at time lag of 60 minute (Adhikari et al., 2018). Bargatze et al. (1985) investigated the connection between solar wind characteristics and the auroral electrojet lower AL index and discovered two pulse peak responses with a time lag of 20 minute for strong geomagnetic levels and 60 minute for moderate geomagnetic levels. The first peak was linked to solar wind coupling-driven magnetospheric activity, whereas the second was linked to the energy release previously deposited in the magnetotail-driven magnetospheric activity. Poudel et al. (2019) found that the magnetospheric response to solar wind invasion is quite swift during SSSs, with a correlation value of -0.74 at zero-time lag between the IMF B_z and energy dissipated at auroral region (U_r). This study shows due to intense geomagnetic and auroral activities during magnetic reconnection between the IMF and a north-south component of the Earth's magnetic field, the degree of correlation between the IMF B_z and AE discovered is high almost with no lag.
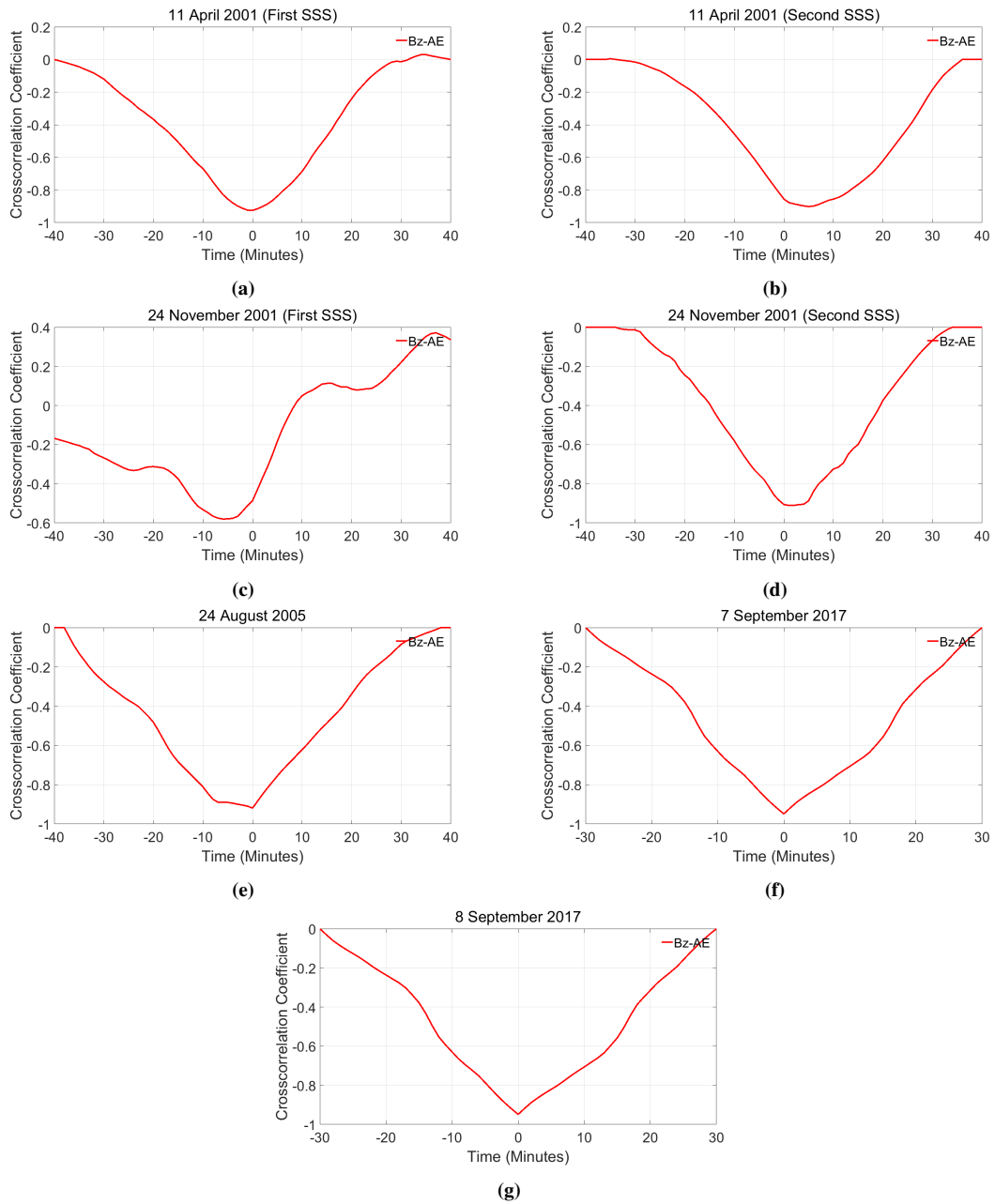
Figure 53: Cross correlation between IMF B_z and AE index during SSSs events on 11 April 2001, 24 November 2001, 24 August 2005, and 7 and 8 September 2017 (Pandit et al., 2020).

4.2.2 Signature of SSSs at High, Middle and Equatorial Latitude on H-Component of Geomagnetic Field

This sub-section describes the findings of geomagnetic field disruption reported at equatorial, middle, and high latitude observatories during the SSSs of September 7 and 8, 2017. The geophysical location, name and code of observatories used in this study shown in the table 2 in the previous section 3.4.2.1. Figure 30 shows a world map with magnetic observatories used in our study. The result obtained for the study of FAC, PCV, TE, JH, AP, and RC during the events of SSSs 7 and 8 September 2017 are discussed separately in this section.

4.2.2.1 General Background

The variation of geomagnetic field of the Earth is observed due to its rotation, its orbital motion and the orbital motion of moon around it. The diurnal variation is the most prominent of the regular variation. It is considered as the current flowing in E layer dayside of the ionosphere is the main cause of diurnal variation. A part from this, the current induced by electromagnetic induction on the Earth crust also contribute to this variation (Lanza et al., 2006). The regular diurnal variation changes with the time of the year, solar activity, atmospheric tides, movements of solar quiet foci, and geomagnetic latitude. Such variations can be observed on the day in which there is no disturbance in the magnetosphere due to its small intensities which are known as solar quiet days, S_q and variation in the field in the disturbed day is called disturbed day, S_d. The gravitation of the moon causes atmospheric tide is another cause of the regular variation (Jankowski & Sucksdorff, 1996). The third is yearly variation is because of the Earth moves around the Sun in its tilted orbit. Observation in Leivogur show geomagnetic field varies with the season of the year (Lanza et al., 2006). The diurnal variability of $S_q(H)$ shows that the east-west direction has a longer coherent length than the north-south direction. (Rastogi, 2007). This is produced by two huge vertices of electric currents in ionosphere during the day-side. The two vertices, which are located around 40° latitude near the Sun meridian, are caused by a dynamo current passing in the ionosphere due to atmospheric tidal movement over the geomagnetic field. Around 3° of the magnetic equator, a current concentration along the west-east direction known as the equatorial electrojet causes daily fluctuations of up to 200 nT. The geomagnetic storms and the magnetic substorms are two driver of the irregular variation. At mid latitude, magnetic stations are the other important factors for irregular variation identified as a convection bay, which occurs in the evening and night hours having duration of 1 hour to 2 hour. The main causes of these bays are ionospheric current flowing at 65° to 70° latitude, parallel with geomagnetic field lines. The annual, semi-annual and solar cycle variation is used to describe of seasonal variation of S_q. The S_q current exhibit seasonal variability in low

to mid latitudes (Mansilla, 2013). The annual variation at higher latitude observatories is owing to considerable ionospheric conductivity changes seen between the summer and winter seasons. The sun zenith angle is smallest in equinoxes and largest in both solstices in the mid-low latitudes, and it is one of the main sources of strong ionospheric conductivities at both equinoxes. Because of the existence of equatorial electrojects, the seasonal fluctuation in S_q at low-mid latitude is not readily seen (Rastogi, 1974). Hence the equatorial electrojet exhibit semiannual variation (Stening, 1995). During disturbed days i.e. on the days of geomagnetic storm, an additional disturbance (S_d) is imposed on the normal daily variation (S_q). The specific features and intensities on each magnetometer is related to its global position, ionospheric current, ground conductivity, types of magnetometer used, and local time. In this study, the CWT and cross correlation have been used to reveal the common features of these signatures.

4.2.2.2 Variability on H-Component

The H-component variation during SSSs is discussed in this section. When the magnetosphere is peaceful, the recorded H-component's behavior should be smoother than during disturbed periods, making it easier to spot differences caused by the start of SSSs events. Figure 54(a) shows delta H variations at equatorial stations API, GUA, KOU, and MBO, while Figure 54(b) shows delta H variations at mid-latitude stations ABG, BOU, DUR, and PHU, and Figure 54(c) shows delta H variations at high-latitude stations ABK, FCC, MGD, and UPS, respectively. When IMF B_z shifted southward on September 7 and 8, 2017, the two SSSs incidents happened at 23:45 UT (7th September) and 13:00 UT (8th September). The usual quietest day signatures of H-component of geomagnetic field fluctuations for each station are obtained by the average of all quiet days (5 days) of a particular month (Vichare et al., 2012). Stening et al. (2007); Vichare et al. (2012) pointed that the quietest day curves for all stations show different trends, which could be attributable to a range of factors like seasonal change, local time, and the distance of the station from the presence of S_q current system's focus, and among the others station. The SSSs interval or magnetically disturbed period can be noticed in the Figure 54 with respect to their respective quiet days values. For all observatories prior to the occurrence of SSSs, the quietest day, as well as the most disturbing day graphs, show similar fingerprints. The nature of fluctuations varies depending on the observatory. At high latitude, the observation arrives earlier than at equatorial and mid latitude. At ABG and PHU, the H-component was lower than at the equatorial station. The depression in the H-component observed at ABK station is the greatest of all the stations. The reconnection of IMF Bz with the earth magnetic field could be the proposed mechanism underlying these events(Gonzalez et al., 1994), during which many charge particles and plasma were injected into Earth's magnetosphere and ionosphere (Kamide et al., 1998) leads to widening and intensifying in the existing current system.
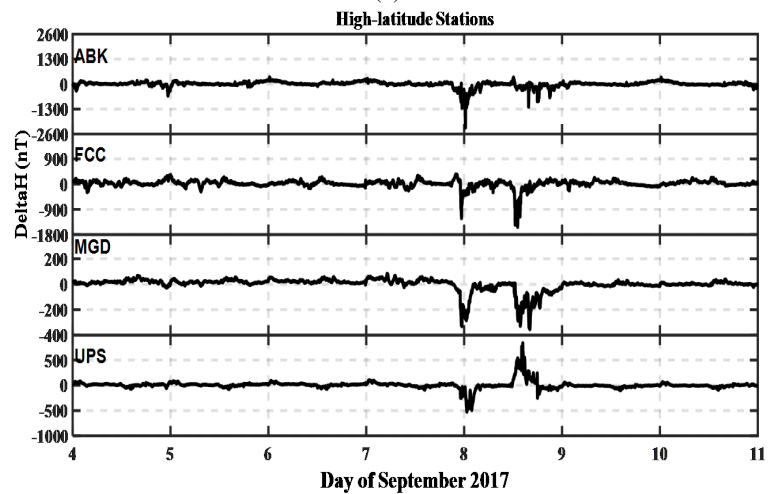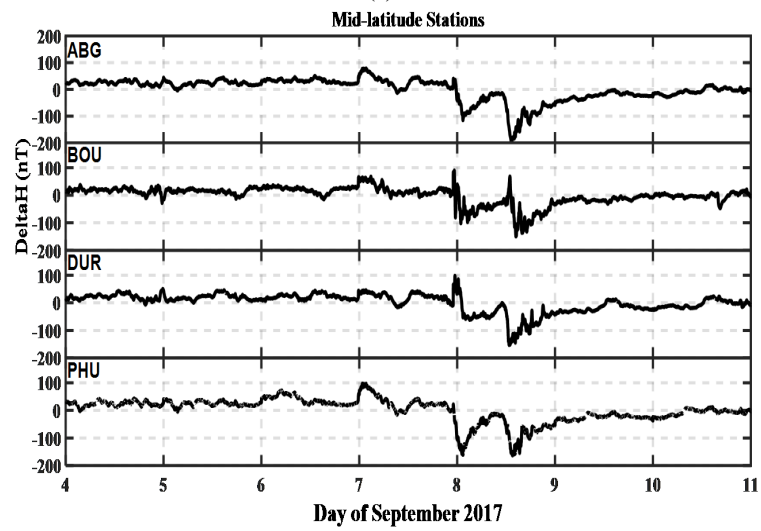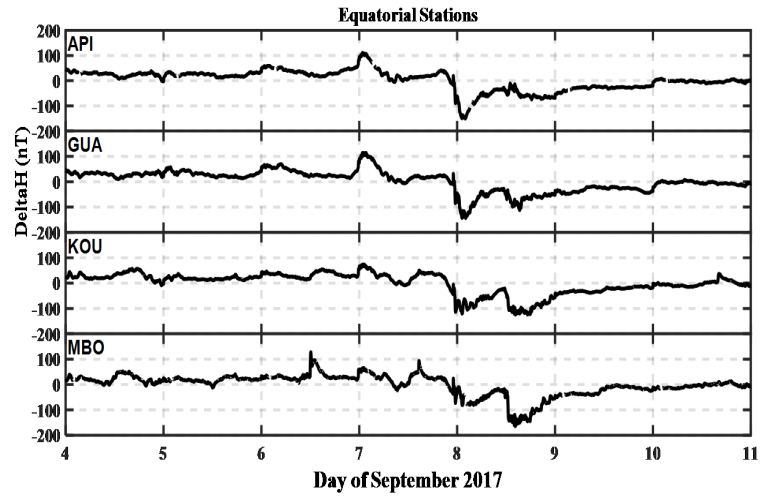
Figure 54: Variation of *H*-component of the Earth's magnetic field at equatorial (API, GUA KOU, and MBO) on top panel, middle latitude (ABG, BOU, DUR, and PHU) on middle panel, and high latitude (ABK, FCC, MGD, and UPS) on bottom panel during SSSs of 7 and 8 September 2017, respectively.

106

As a result, the ring's current dominance at the middle and low-latitudes, its impact can be seen in magnetic data collected in those locations. The increased ionospheric current resulted in faster electric field penetration at the equator than at mid-latitudes (Fejer et al., 2008). In 2012, Tsuji et al. suggested that the H-component at dip and low latitude is caused by a current that is different from the dominating current at medium latitude Tsuji et al. (2012). Within 3° latitude around the magnetic equator, Egedal (1947) observed the greatest variance in the H-component. Chapman (1951) investigates the effect of east-west electric equatorial electrojet current in the E area on daily H fluctuation. The simultaneous disturbance observed at each station with a certain feature is due to a variety of factors, including global position, magnetometer type, ionospheric conditions, ground conductivity, and local time (Rastogi, 2005).

Figures 55 (a) to (l) show the time series and results of Scalograms of delta H at equatorial (API, GUA, KOU, and MBO), medium (ABG, BOU, DUR, and PHU), and high latitude (ABK, FCC, MGD, and UPS) during the SSSs event on September 7 and 8, 2017. The scalogram represents the signal energy in wavelet space using a log2 function that accentuates minor fluctuations. In this analysis, the local regularity variations are indicated using the squared of amplitude of the coefficients of wavelet. The horizontal scale in the Figures depicts time in hours, while the vertical scale denotes periodicity in minute. The intensity of delta H in $(nT)^2$ depicted in the scalogram is represented by the color indicator chart on the right hand side. The delta H signal's characteristic is significantly changeable in time in the scalograms. At 24 UT and 37 UT, higher-intensity power regions can be seen, with various scales at different stations.

Moreover, in Figures 55(a) to (d) stronger wavelet power areas of intensities 2 $(nT)^2$ and 1 $(nT)^2$; 2.5 $(nT)^2$ and 1 $(nT)^2$; 2.5 $(nT)^2$ and 1.5 $(nT)^2$; 2.2 $(nT)^2$ and 2.2 $(nT)^2$ are seen more consistently in equatorial stations (API, GUA, KOU, and MBO), similarly, from scalogram 55(e) to (h) at mid latitude (ABG, BOU, DUR, and PHU) stronger wavelet power areas of intensities 1.5 $(nT)^2$ and 2.5 $(nT)^2$; 4 $(nT)^2$ and 6 $(nT)^2$; 2 $(nT)^2$ and 3.5 $(nT)^2$; 1.5 $(nT)^2$ and 2 $(nT)^2$ and stronger wavelet power regions with intensities 6 $(nT)^2$ and 4 $(nT)^2$; 5 $(nT)^2$ and 8 $(nT)^2$; 4 $(nT)^2$ and 6 $(nT)^2$; 5 $(nT)^2$ and 4.5 $(nT)^2$ are observed at SSSs at 24 UT and 37 UT with the same period from scalogram 55(i) to (l) at high latitude (ABK, FCC, MGD, and UPS). The increased particle intensities in the ring current system are thought to be caused by the southern IMF B_z caused by Alfvén waves (Guarnieri et al., 2006). According to Trivedi et al. (2005) the persistent and impulsive pulsations in the H-field at São Martinho da Serra São Martinho da Serra (SMS) are caused to particle precipitations in the Magnetic Anomaly region of South Atlantic. Da Costa et al. (2011) investigated the wavelet coefficient amplitudes of the H-component of the Earth's magnetic field in the SAMA-affected region and found that they were highly linked with energetic particle fluxes (protons and electrons). The ring

current energy density is dominated by ions with energies lying between 20 keV to 200 keV. The quantity of ring current increased by depositing charged particles, causing the *H* signal to be disrupted. Rastogi (2005) analyzed the energy injection at the time of the geomagnetic storm, which showed a large depression on the *H* component of the Earth's magnetic field at high and mid-latitude observatories. Their study suggest the ring current remained significant only when B_z was found negative.
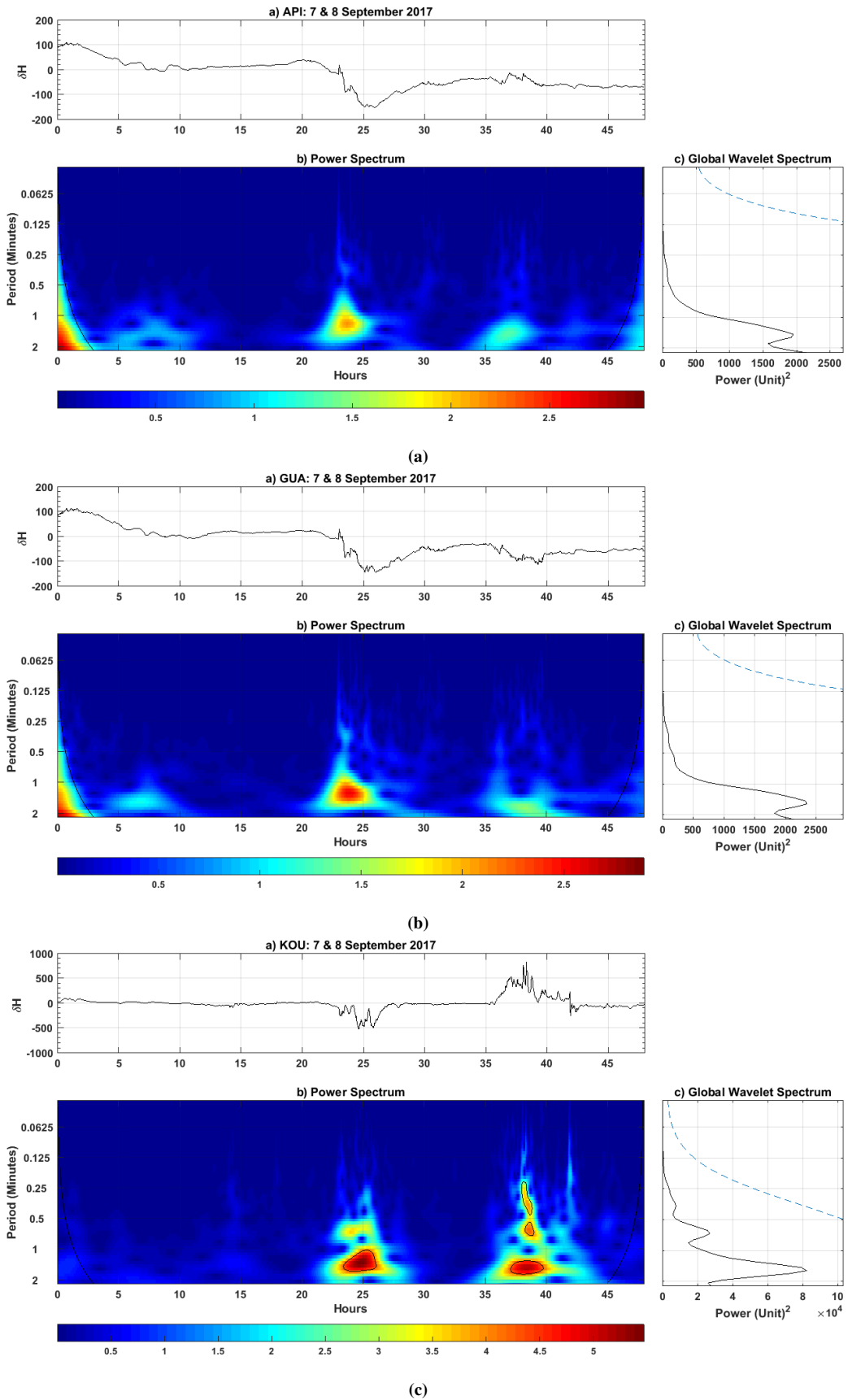
Figure 55: (a-l) Scalogram showing of variation of *H*-component of the Earth's magnetic field at equatorial station (API, GUA KOU, and MBO), mid-latitude (ABG, BOU, DUR, and PHU), and high latitude (ABK, FCC, MGD, and UPS) during SSS of 7 and 8 September 2017, respectively.

109

(d)

(e)

(f)

Figure 55: (Contd.) (a-l) Scalogram showing of variation of *H*-component of the Earth's magnetic field at equatorial station (API, GUA KOU, and MBO), mid-latitude (ABG, BOU, DUR, and PHU), and high latitude (ABK, FCC, MGD, and UPS) during SSS of 7 and 8 September 2017, respectively.

110

(g)

(h)

(i)

Figure 55: (Contd.) (a-l) Scalogram showing of variation of *H*-component of the Earth's magnetic field at equatorial station (API, GUA KOU, and MBO), mid-latitude (ABG, BOU, DUR, and PHU), and high latitude (ABK, FCC, MGD, and UPS) during SSS of 7 and 8 September 2017, respectively.

111

(j)

(k)

(l)

Figure 55: (Contd.) (a-l) Scalogram showing of variation of *H*-component of the Earth's magnetic field at equatorial station (API, GUA KOU, and MBO), mid-latitude (ABG, BOU, DUR, and PHU), and high latitude (ABK, FCC, MGD, and UPS) during SSS of 7 and 8 September 2017, respectively.

112

4.2.2.3   Polar Cap Voltage, Field Aligned Current and Solar Wind Energy

Figure 56 depicts time series of energy input as FAC in Am^{-2}, PCV in kV, RC in W, JH in W, AP in W, TE in W, and SYM-H in nT during the SSSs occurrences of September 7 and 8, 2017. And Figure 57 represents scalogram of energy input as FAC in Am^{-2}, PCV in kV, RC in W, JH in W, AP in W, TE in W, and SYM-H in nT during the SSSs occurrences of September 7 and 8, 2017. On September 7 and 8, the greatest values of FAC, PCV, RC, JH, AP, TE, and SYM-H were 10 Am^{-2}, 10×10^5 kV, 15×10^{12} W, 13×10^{11} W, 2×10^{11} W, 6×10^{14} W, -145 nT and 8 Am^{-2}, 6×10^5 kV, 12×10^{12} W, 14×10^{11} W, 2×10^{11} W, 7×10^{14} W, and -100 nT, respectively. The wavelet power zones of higher intensity were found between 24 UT and 37 UT with intensities of 2 Am^{-2} and 3 Am^{-2}; 5.5 kV and 3.5 kV; 3 W and 4 W; 1.5 W and 3 W; 2 W and 4 W; 2 W and 4 W; 7 W and 6 W for FAC, PCV, TE, AP, JH, and RC, respectively. Søraas et al. (2004) found that during magnetic storm occurrences, the SYM-H and AE indices are in close agreement with RC particle injections. Adhikari et al. (2020) investigated the energy injected in the form of JH, RC, and AP for the powerful geomagnetic storms of latest three solar cycles 22, 23, and 24. Their findings indicate that the most energy was deposited in the form of RC and the least during AP. In 1978, Akasofu projected that RC injection would account for 90 % of energy dissipation during a geomagnetic storm (Akasofu, 1964). In 1998, Knipp et al. and in 2009, Turner et al. found that during storm events, JH prevails over other types of magnetospheric energy sinks as a dissipation channel (Knipp et al., 1998; Turner et al., 2009). Poudel et al. (2019) came up with a similar finding. Later research by Tenfjord & Østgaard (2013) looked at several periods and events of varying lengths and found that JH was the most important energy source, compared to RC injection and AP.

4.2.2.4   Cross Correlation Analysis of H-Component

Figure 58(a) to (f) show the cross correlation of the *H*-component of the Earth magnetic field at equatorial latitude (API, GUA KOU, and MBO), middle latitude (ABG, BOU, DUR, and PHU), and high latitude (ABK, FCC, MGD, and UPS) with FAC, PCV, RC, JH, AP, TE, and SYMH during SSS of 7 and 8 September 2017, respectively. The lagging of time between two time series is represented by the horizontal axis, while the correlation coefficient is represented by the vertical axis. The panels of Figures 58(a), (b), and (c) show correlation of delta *H* with FAC, PCV, RC, JH, AP and TE, with high anticorrelation coefficients ranging from -0.70 to -1.0 for equatorial stations API, GUA KOU, and MBO, respectively, with zero-time lag for PCV and a 30 minute time lag for RC. At mid-latitude stations ABG, BOU, DUR, except PHU, a positive cross correlation coefficient of 0.40 to 1.0 is found between delta *H* and FAC, PCV, RC, JH, AP, and TE. But with a value of -0.70 to -0.90, PHU (mid-latitude) exhibits a negative correlation.
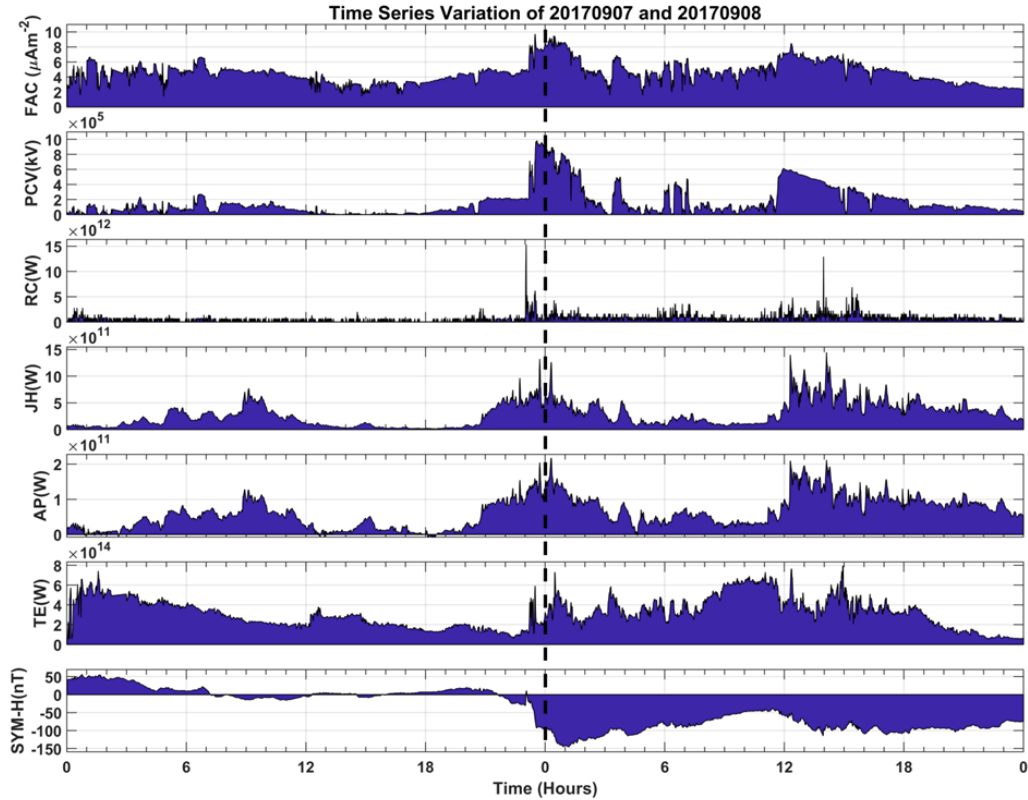
Figure 56: From top to bottom panels show variation of FAC, PCV, RC, JH, AP, and TE, and SYM-H during SSS of 7 and 8 September 2017, respectively.

Similarly, the cross-correlation coefficients of delta H with FAC, PCV, RC, JH, AP, and TE reported at high latitude sites were similar to those observed at equatorial stations lying between -0.70 to -1.0. All of the station in Figure 58(d), (e), and (f) have a negative correlation. For all parameters, the correlation coefficient of delta H with FAC, PCV, RC, JH, AP, and TE at the equatorial station was found between -0.70 to -1.0 with zero-time lag. At mid latitude, the coefficient of correlation found between -0.7 to -1.0 with a zero-time lag for PCV and a 250 minute time lag for ring current, whereas at high latitude, the coefficient of correlation was found between -0.40 to -0.80. In IMF B_z, the zero lag represents a quick reaction of the coupling effect at high latitude when the magnetosphere is perturbed (Marques de Souza et al., 2018). When the RC energy is dominant, (Adhikari et al., 2018) discovered the strongest connection between FAC-SYM-H pair with correlation 1 with zero-time delays.
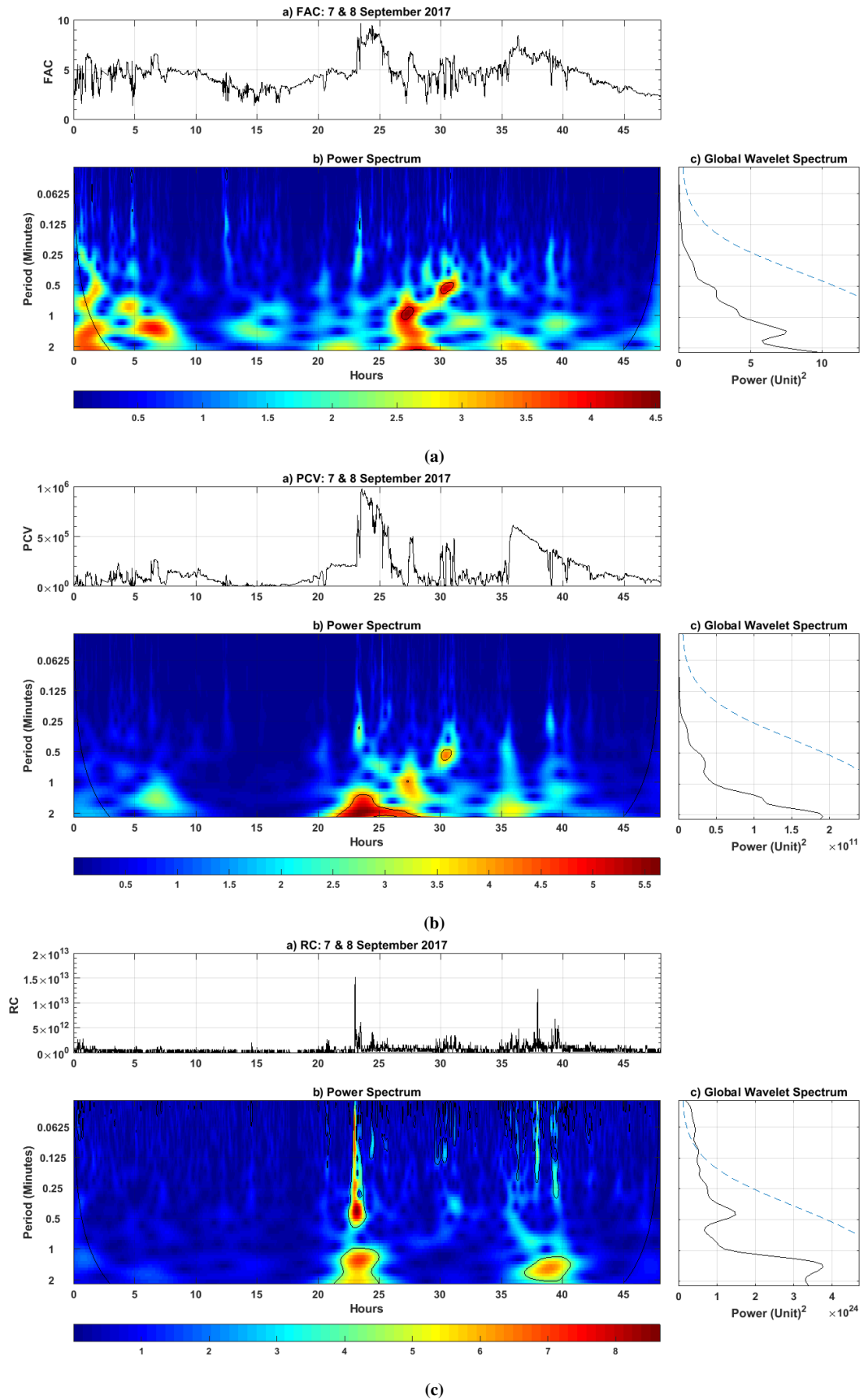
Figure 57: (a) to (f) Scalogram showing variation of FAC, PCV, RC, JH, AP, and TE during SSS of 7 and 8 September 2017, respectively.
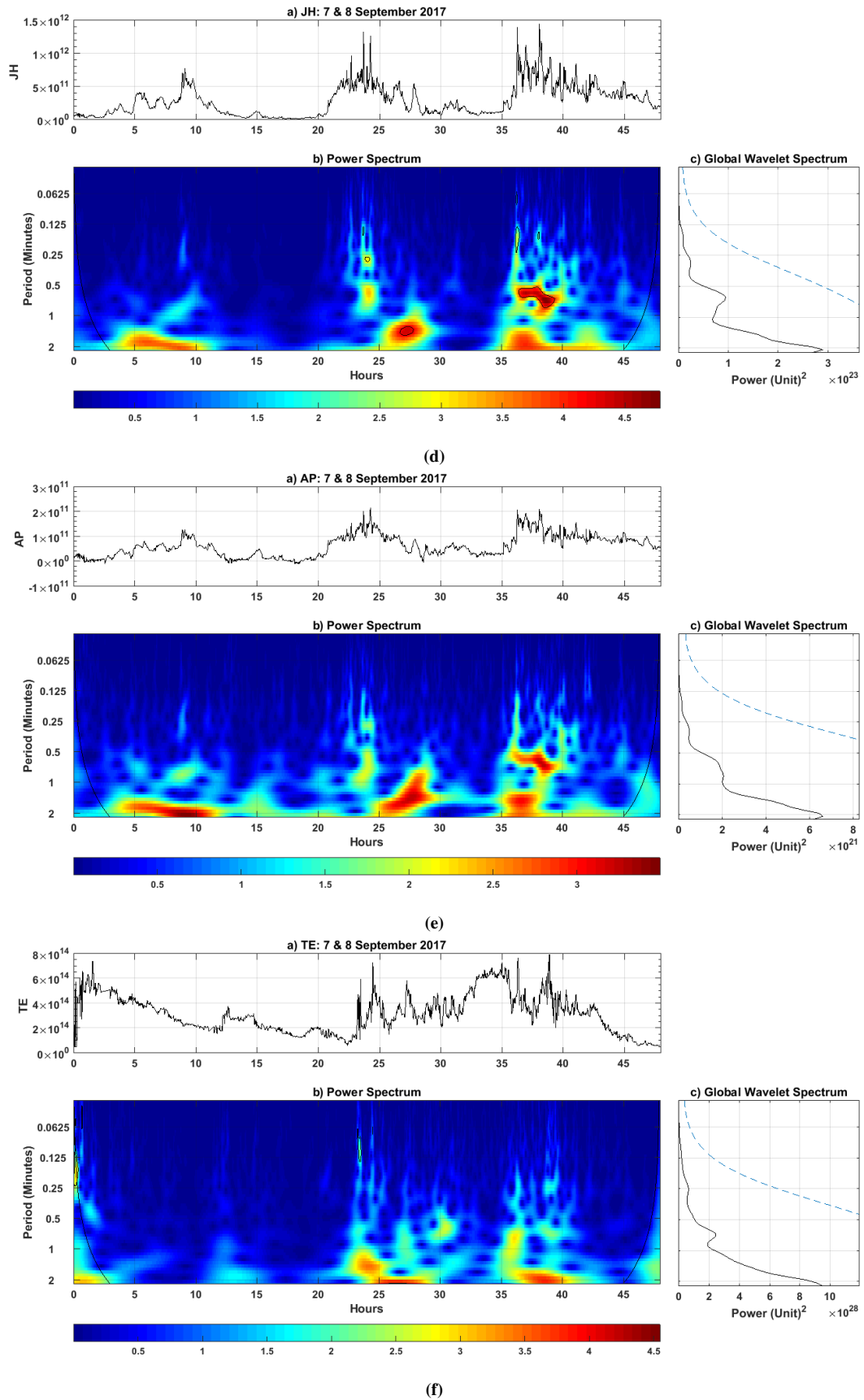
Figure 57: (Contd.) (a) to (f) Scalogram showing variation of FAC, PCV, RC, JH, AP, and TE during SSS of 7 and 8 September 2017, respectively.
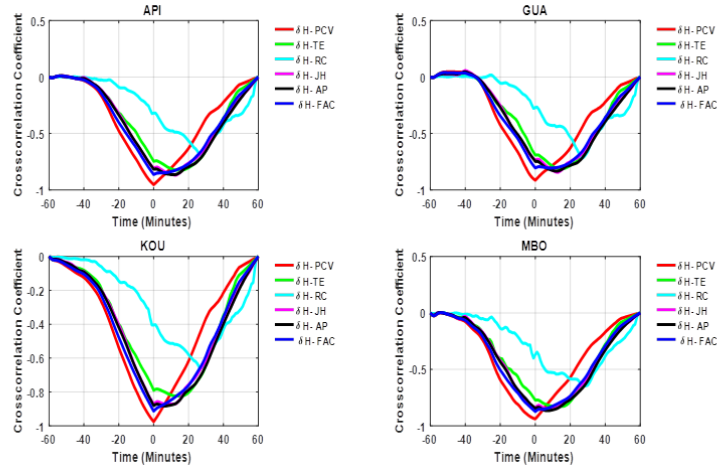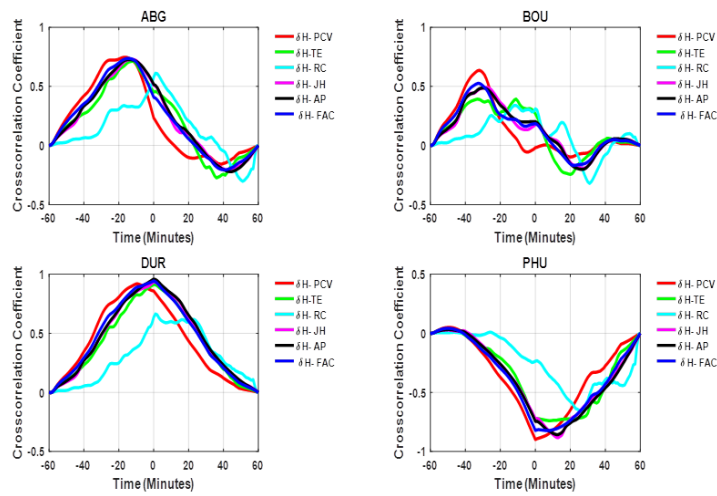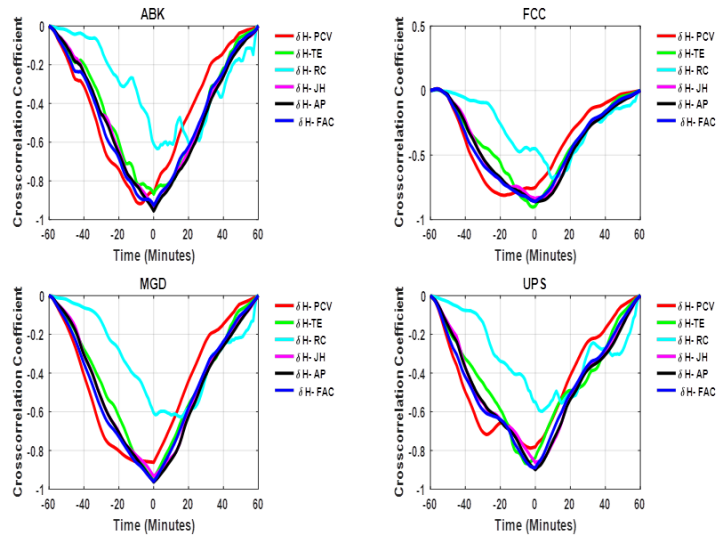
Figure 58: Cross correlation of delta H-component of the Earth's magnetic field at (a) equatorial (API, GUA KOU, and MBO), (b) mid-latitude (ABG, BOU, DUR, and PHU), and (c) high latitude (ABK, FCC, MGD, and UPS) stations with FAC, PCV, RC, JH, AP, and TE during SSSs of 7 and 8 September 2017, respectively.
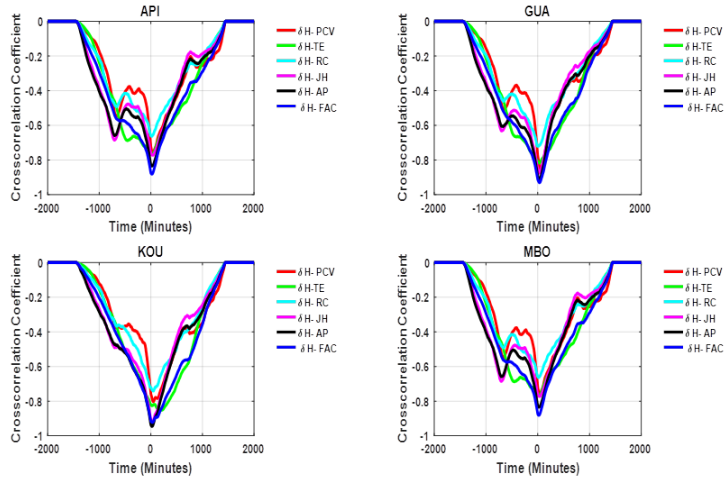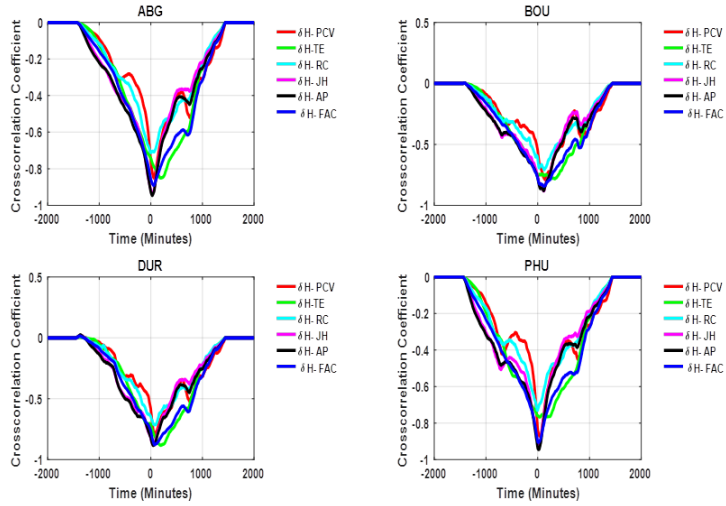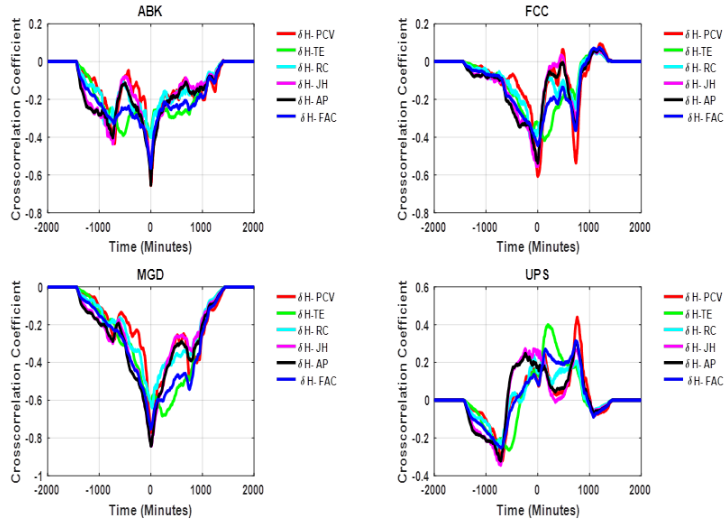
Figure 58: (Contd.) Cross correlation of *H*-component of the Earth's magnetic field at (a) equatorial (API, GUA KOU, and MBO), (b) mid-latitude (ABG, BOU, DUR, and PHU), and (c) high latitude (ABK, FCC, MGD, and UPS) stations with FAC, PCV, RC, JH, AP, and TE during SSS of 7 and 8 September 2017, respectively.

4.2.3 Effect of SSSs on Ionospheric Parameters

This section attempted to investigate effect of SSS on ionospheric parameters such as critical frequency (foF_2), virtual height ($h'F$) and height of maximum electron density (hmF_2) at middle latitude station Boulder, Colorado, USA (40.0° N, 105.0° W).

4.2.3.1 General Background

The influence of geomagnetic disruption on the ionospheric parameter has long been researched and is a major component of space weather occurrences. Open particle flux is transferred into the geomagnetic tail as a consequence of recombination at the magnetopause on the dayside of magnetosphere. When there is a considerable accumulation of open flux, the tail becomes unstable and undergoes major reconfiguration. The substorm, which begins around 6 R_E to 10 R_E, is the last stage of the cycle (Lui, 1991). It is preceded by a development phase that might last anywhere from 1 hour to 2 hour. The commencement of the expansion phase is marked by a significant brightening of the aurora and the formation of the substorm current wedge. The recovery phase, which begins after the maximum deviation of the magnetometers towards midnight in the auroral oval, is the third and last aspect of the substorm. Energetic particles entering Earth's upper atmosphere at high latitude during periods of strong geomagnetic perturbations, depositing a considerable quantity of energy in the ionosphere at high latitudes. Auroral electric currents by means of Joule heating to transmit energy to the neutral gas. On a global scale, thermospheric winds, pressure fields, and gravity waves created at F region heights have been forced to spread from auroral to middle and low latitudes, generating variation in the density, composition, and circulation of the ionosphere-thermosphere system, including TEC. (Nava et al., 2016; Jones, 1971). Since Breit and Tuve's first ionosphere study in 1926 (Breit & Tuve, 1926), numerous more ionosonde studies have been conducted to quantify the ionosphere's electron density, particularly the maximum of electronic density in the F_2 layer: NmF_2 (Rishbeth & Garriott, 1969). Since two decades, Global Navigation Satellite Systems (GNSS) receivers have provided access to the TEC of the ionosphere. NmF_2 and VTEC provide information on variations in ionospheric ionization.

4.2.3.2 Variability in Ionospheric Parameters

This section illustrates the variation in foF_2, $h'F$, and hmF_2 during SSSs events from the quiet day situation. The quiet day is selected among the month's quietest days. The reference quiet days for the selected SSSs events is listed in table 7. Figure 59(a) to (c) depict the range of foF_2, $h'F$, and hmF_2 values for the quiet days chosen along with the range of values for the event selected days. These Figures represent the ionospheric measurements to the SSSs of August 24, 2005, September 7, 2017, and September

8, 2017, and their respective quiet days on 20 August 2005 and 28 September 2017, respectively. In each graphic, the dotted line indicates fluctuation during quiet days, while the solid line represents ionospheric variability during SSS. Discontinuity in each plot indicates unavailability of data for that instant. Figure 59(a) shows that during SSS on August 24, 2005, there was a drop in foF_2 but an increase in $h'F$ and hmF_2 as compared to the quiet day. Figure 59(b) shows that the observed values of foF_2, $h'F$, and hmF_2 during SSS on September 7, 2017 were higher than on a quiet day. In Figure 59(c), the values of $h'F$ recorded during SSS on September 8, 2017 is lower than the quiet day value, but the values of foF_2 and hmF_2 are greater than the quiet day value. Tsurutani et al. (2015) hypothesized that during the southward rotation of the IMF B_z energy is deposited in the magnetosphere/magnetotail liberated as plasma parcel in the course of SSSs resulting in the greatest ionospheric current during their occurrences, potentially creating a power outage on Earth. Hajra et al. (2016) studied long-term data on SSSs from 1981 to 2012 and discovered that the possibility of occurrence of the SSSs in any solar cycle phases, with the maximum occurrence frequency of 3.8 year^{-1} was found of in due course of the descending phase. Their research indicated that the occurrence of SSS is unrelated to the strength of geomagnetic storm. The SSSs known to occur in the instant of the main phase of the storm create high current in ionospheric even at lower latitudes which can result in power outages on Earth. Tsurutani et al. (2015) pointed that during an extreme magnetic storm, a significant ionospheric current creates a large variation in $\partial B/\partial t$ in power transmission lines, which causes Geomagnetic Induced Current (GIC) and power outage. In a study of polar cap potential and polar cap index in the course of SSS, Adhikari, Baruwal, & Chapagain (2017) discovered that the PCV and merging electric field during SSSs are 20 times larger than the potential created during HILDCAA. Their research also found that during SSSs, a huge rise in FAC causes powerful aurora, which can interrupt and jam communication signals, and during these events, the large drop in potential can produce dramatic and quick changes in space weather. Despirak et al. (2018) examined 131 SSS events between 1998 and 2016, and found SSS under various interplanetary manifestations: 45.2 % of SSSs lying under CME i.e. sheet, 42.0 % under MC, 8.3 % under ejecta. No any SSS event was identified during HSS from coronal hole or CIR. Despirak et al. (2019) used the SuperMAG electric field data to study the two SSSs on September 7 and 8, 2017, and discovered existence of ionospheric current across the globe along with these SSSs. Poudel et al. (2019) investigated different amount of energy lay down into magnetosphere by different events. Approximately, 5.5199×10^{11} W, 5.3365×10^{11} W, 3.4618×10^{11} W, 1.0367×10^{12} W, and 5.8772×10^{10} W energy are delivered into magnetosphere during substorm, intense storm, HILDCAA, SSS and quiet day respectively. They discovered that the most energy was deposited during the SSS, which might result in a strong ionospheric storm to changes in ionospheric characteristics. Increases and decreases in foF_2 are caused
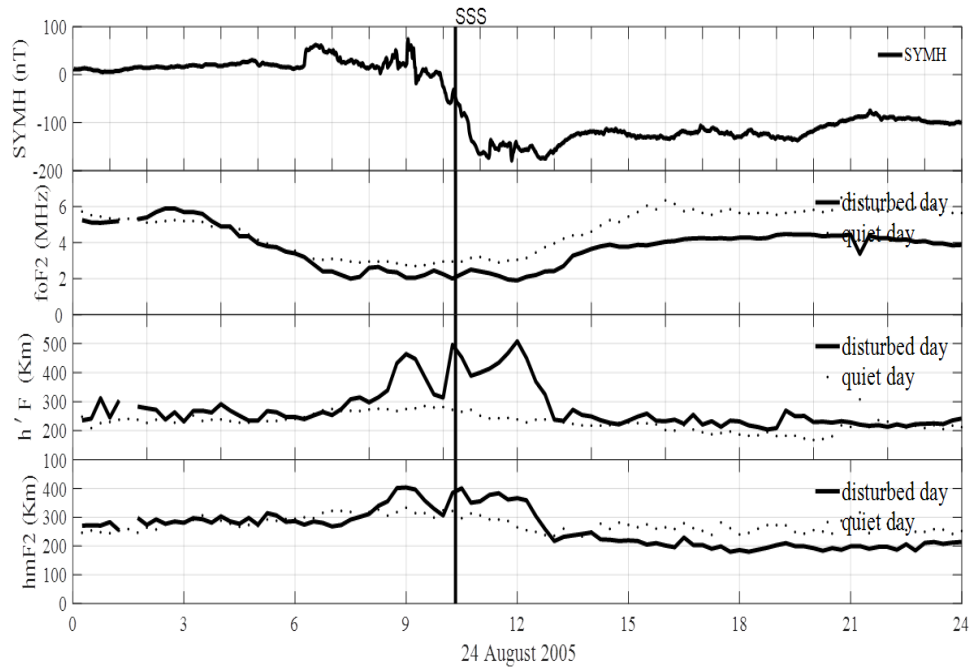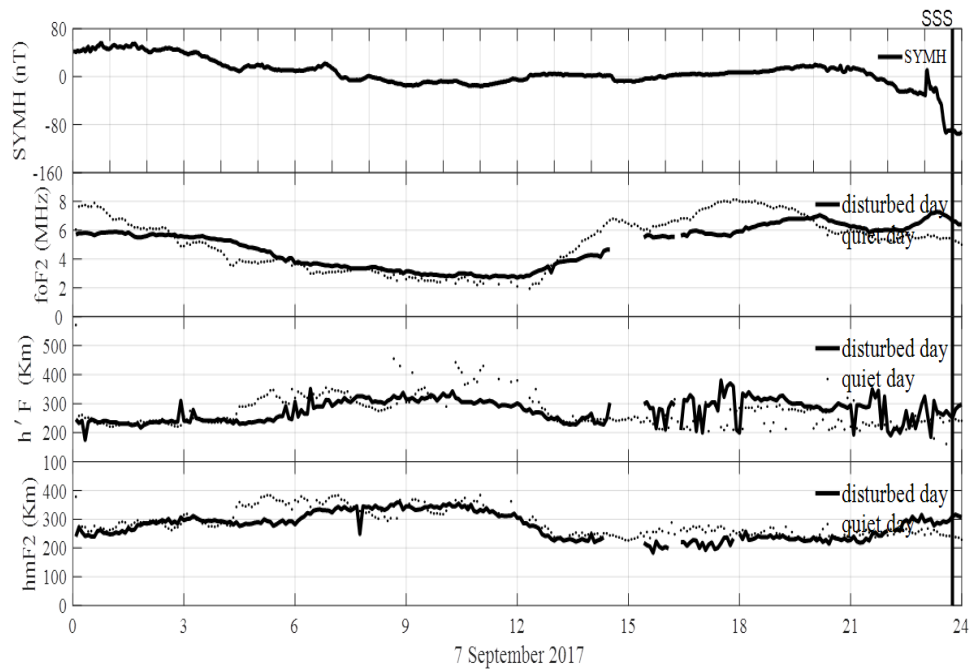
Figure 59: SYM-H variation in nT (first panel), critical frequency (foF_2) in MHz (second panel), virtual height ($h'F$) in km (third panel), and height of maximal electron density (hmF_2) in km (fourth panel). The dotted line depicts fluctuations on quiet days, whereas the solid line depicts variation on SSS days of 24 August 2005, 7 September 2017, and 8 September 2017, respectively (Pandit et al., 2020).

by the positive and negative ionospheric storm (Belehaki & Tsagouri, 2002) and their impact dependent on LT (Prolss, 1995; Rishbeth, 1998). During geomagnetic storms, changes in neutral composition (Prölss et al., 1988; Mikhailov et al., 1992) have an

121
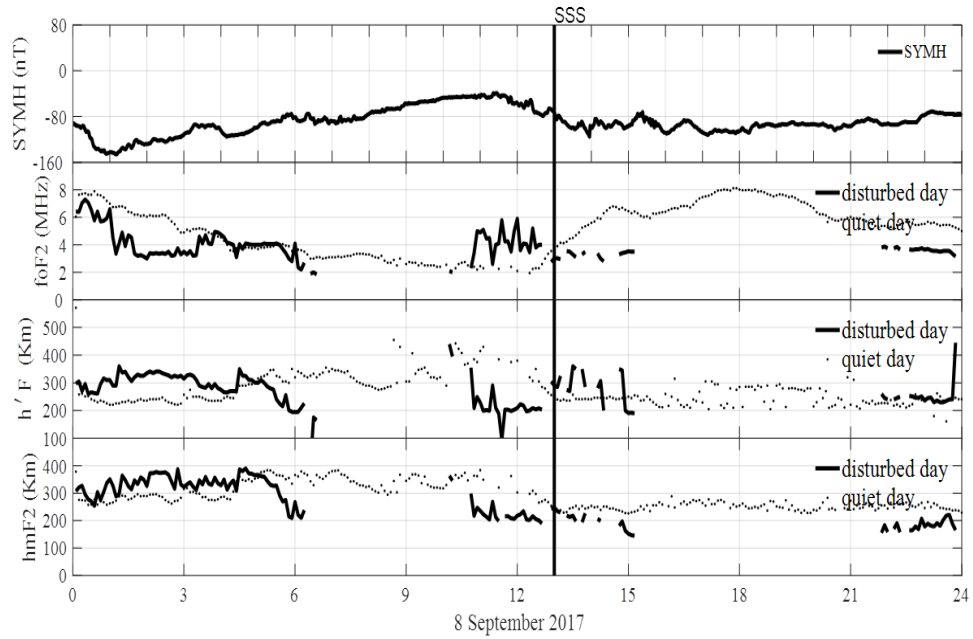
(c)

Figure 59: (Contd.) SYM-H variation in nT (first panel), critical frequency (foF_2) in MHz (second panel), virtual height ($h'F$) in km (third panel), and height of maximal electron density (hmF_2) in km (fourth panel). The dotted line depicts fluctuations on quiet days, whereas the solid line depicts variation on SSS days of 24 August 2005, 7 September 2017, and 8 September 2017, respectively (Pandit et al., 2020).

impact on negative ionospheric storms (L. R. Cander & Mihajlovic, 1998; L. Cander, 1993; Proelss, 1993). Prolss proposed in 1993 that meridional wind causes positive ionospheric storms, while changes of neutral composition generate negative ionospheric storms (Proelss, 1993). During a geomagnetic storm, the energy deposited at pole latitude causes a traveling ionospheric disturbance that superimposes with gravity waves and travels quickly towards the equator, generating a daytime positive ionospheric storm that lifts the F_2 layer to higher elevation during daytime. Energy released at polar latitude during geomagnetic storm can produce a compositional shift that extends equatorwards and disrupts the F_2 layer ionosphere at mid-latitude.

4.2.3.3 Analysis of Ionospheric Parameters Using CWT

Figures 60(a) to (c) depict scalograms for critical frequency (foF_2) in MHz, virtual height ($h'F$) in km, and height of maximum electron density (hmF_2) in km obtained on SSSs of August 24, 2005, respectively. In the Figures, the horizontal scale represents time in hours, whereas the vertical scale represents periodicity in minute. The graphic, whose color can be seen from the right hand side, depicts the units in the square for F_2 layer critical frequency (foF_2), virtual height ($h'F$), and maximum electron density height (hmF_2). During the SSS 10:20 UT on August 24, 2005, the power zones of the

122

maximum intensity were shown more constantly at time scales of roughly 16 minute to 32 minute in Figure 60(a). In this plot, the background intensity has changed from 0.5 $(nT)^2$ to 1.5 $(nT)^2$ for foF_2. Similarly, in Figures 60(b) & 60(c) the background intensity rose from 0.5 $(nT)^2$ to 2 $(nT)^2$ for $h'F$ and 0.5 $(nT)^2$ to 1.5 $(nT)^2$ for hmF_2. These plots shows the change in foF_2, $h'F$, and hmF_2 during the SSS as a result of deposition of energy in the magnetosphere-ionosphere as the consequences of the coupling between the northward component of geomagnetic field and the southward component of the IMF B_z. The energy and plasma carried through reconnection mechanism produces a rapid spike in ionospheric current, resulting in an ionospheric storm, as well as changes in communication signals and power blackouts on Earth's surface. Figures 61(a) to (c) and Figures 62(a) to (c), are identical to Figures 60(a) to (c), but they pertain to SSS occurrences on September 7th and 8th, 2017. Figures 61(a) to (c) show the power area with the highest intensity around 23:45 UT during SSS of 7 September 2017 with durations ranging from 27.9 minute to 64 minute. In scalogram of foF_2, $h'F$, and hmF_2, the background intensity increased from 0.5 $(nT)^2$ to 2 $(nT)^2$. Similarly, in Figure 62(a) to (c) for SSS on 8 September 2017, the highest-intensity power area is seen at 13:00 UT with periods ranging from 27.9 minute to 64 minute. In scalogram of foF_2, the background intensity changed from 1 $(nT)^2$ to 3 $(nT)^2$; in scalogram of $h'F$, background intensity changed from 1 $(nT)^2$ to 4 $(nT)^2$; and in hmF_2, background intensity increased from 0.5 $(nT)^2$ to 2 $(nT)^2$. During the southwards turning of IMF B_z, the active and passive periods found in foF_2, $h'F$, and hmF_2 are indicators of energy and plasma imparted in the course of the reconnection process between IMF B_z and geomagnetic field. In 2019, Srebrov observed the persistence of short-term period in a large quantity of huge datasets of magnetic indices, ionospheric parameters, and IMF B_z using CWT (Srebrov et al., 2019).
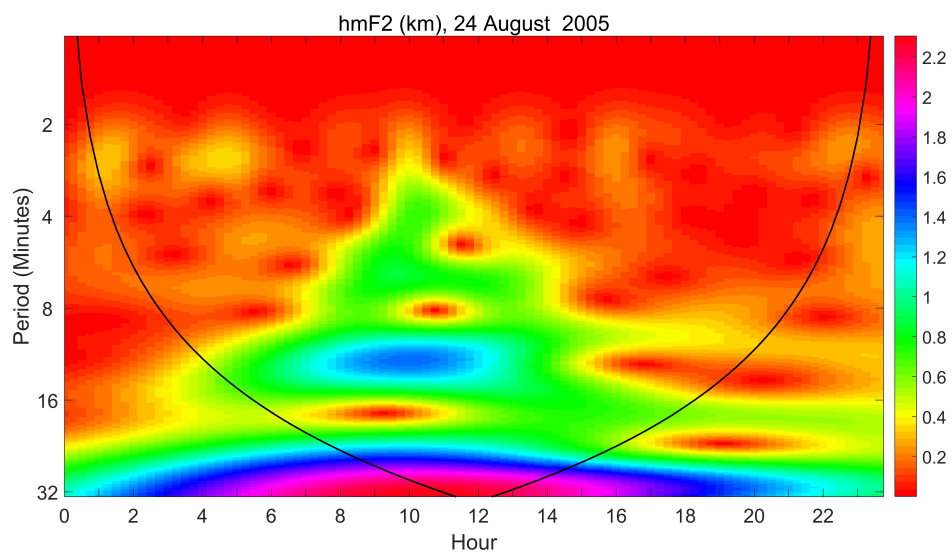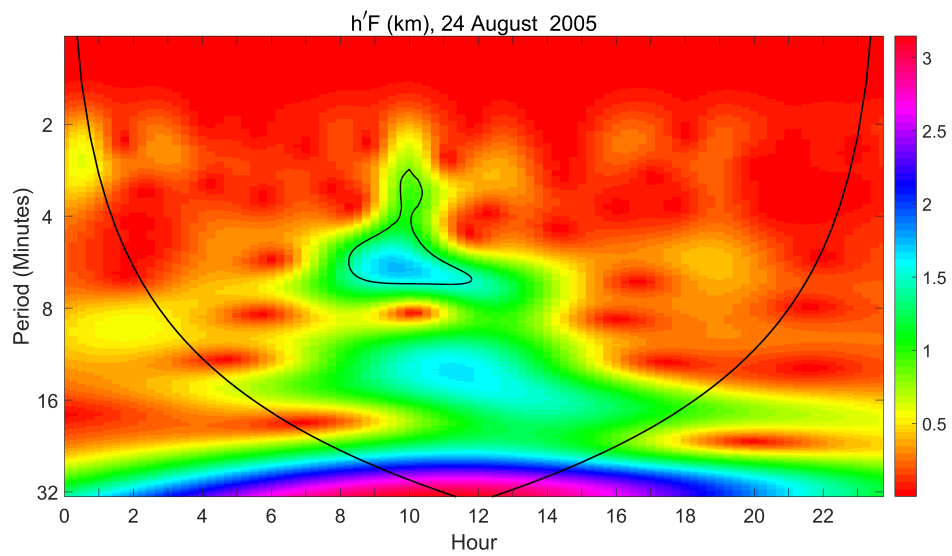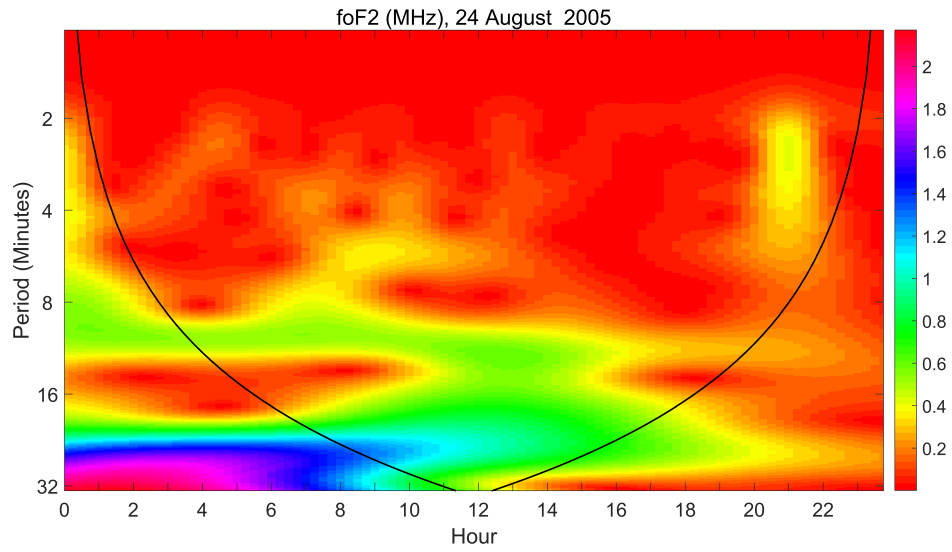
Figure 60: Scalogram of critical frequency (foF_2) in MHz (a), virtual height ($h'F$) in km (b), and height of peak electron density (hmF_2) in km (c) on the SSS day of 24 August 2005 (Pandit et al., 2020).

124
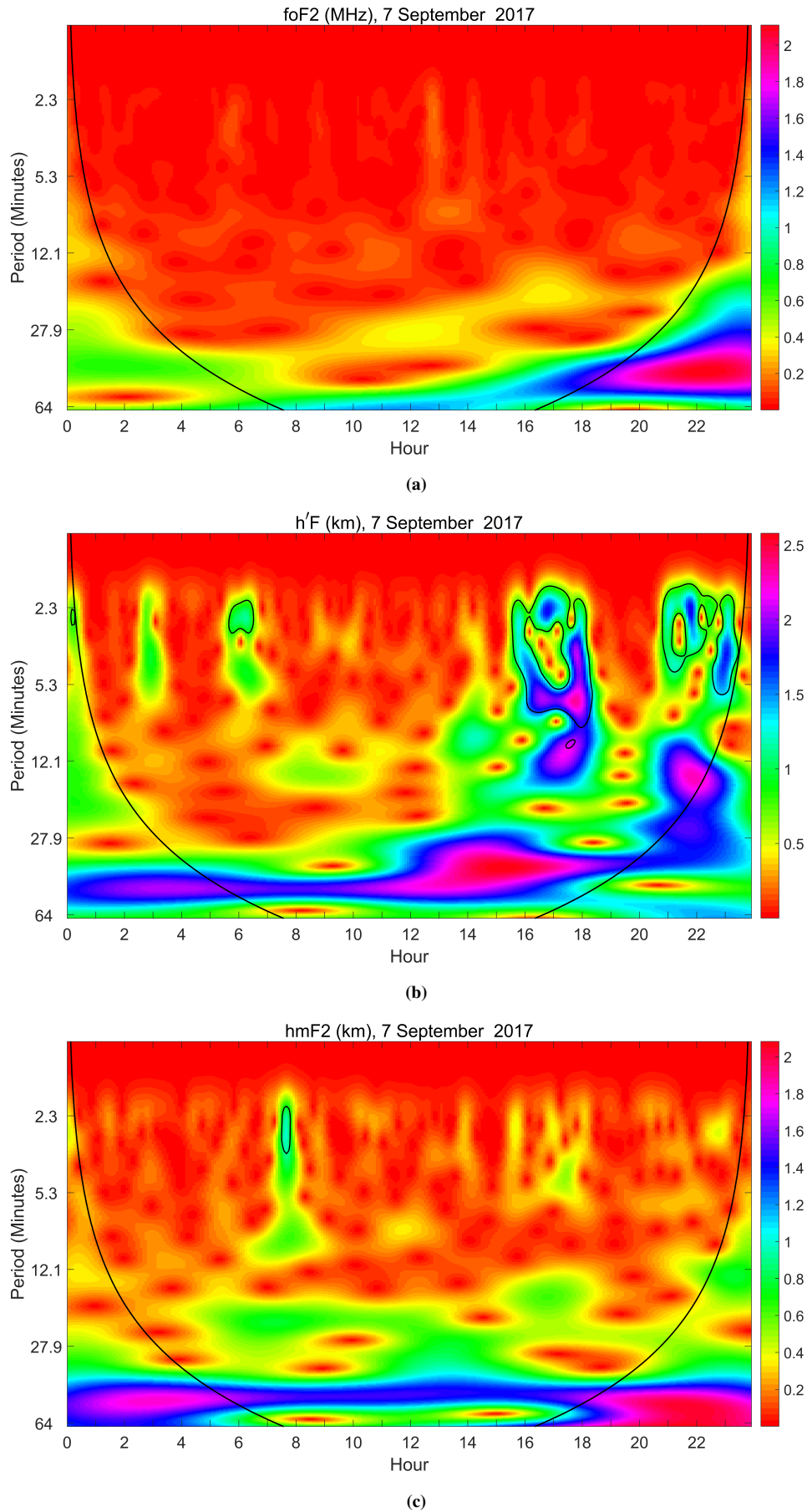
Figure 61: Scalogram of critical frequency (foF_2) in MHz (a), virtual height ($h'F$) in km (b), and height of peak electron density (hmF_2) in km (c) on the SSS day of 7 September 2017 (Pandit et al., 2020).
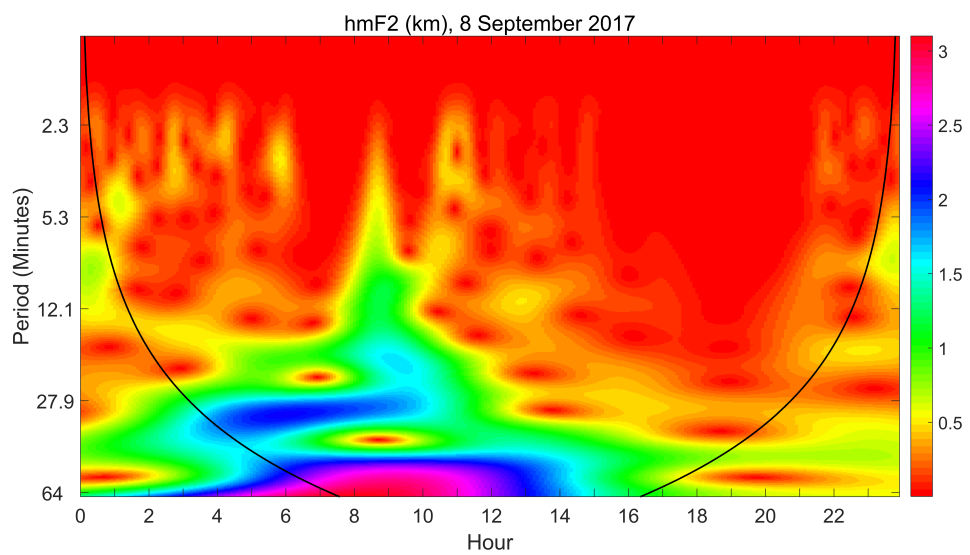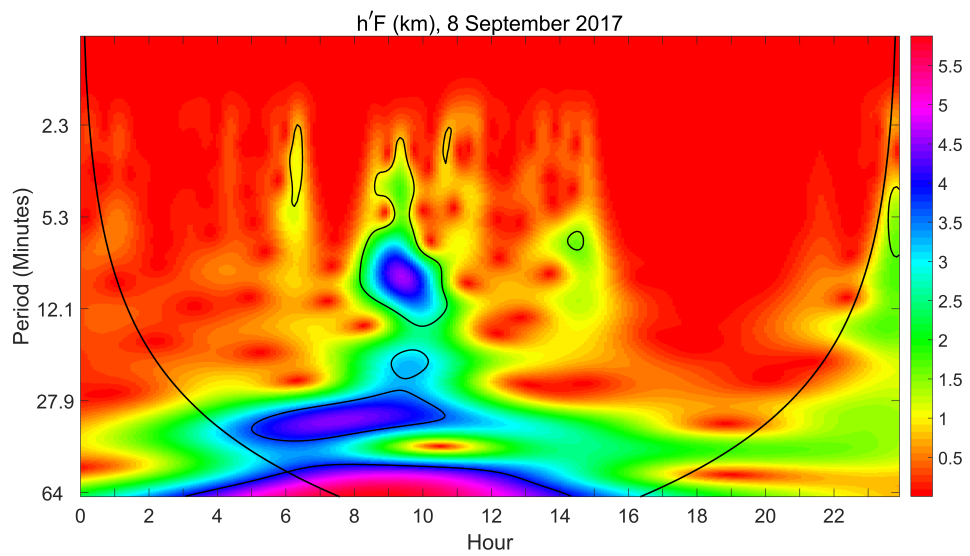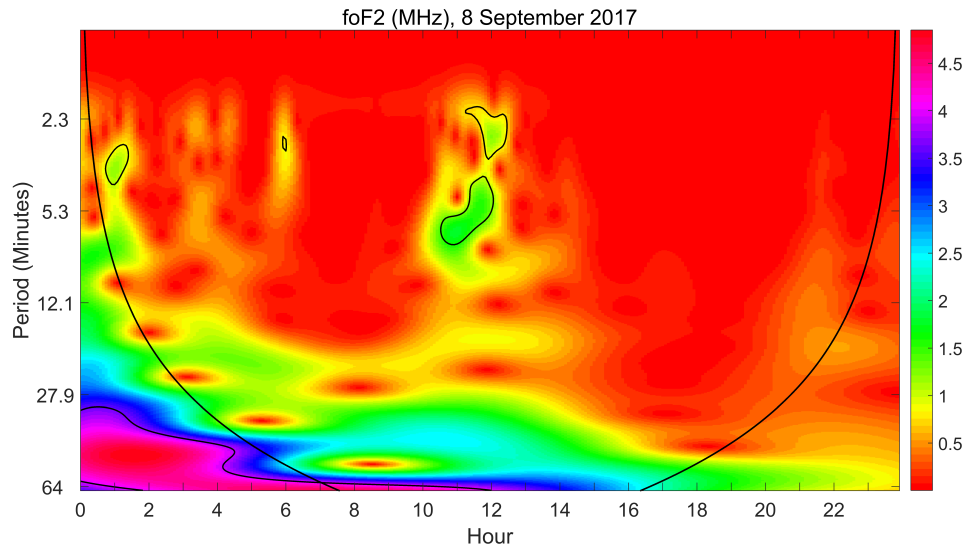
Figure 62: Scalogram of critical frequency (foF_2) in MHz (a), virtual height ($h'F$) in km (b), and height of peak electron density (hmF_2) in km (c) on the SSS day of 8 September 2017 (Pandit et al., 2020).

4.2.4   Signatures of Disturbed Ionosphere Due to Super Storms above Nepal

This section describes the geophysical contest of four super storms of solar cycle 24 and its impact on ground based GPS VTEC data obtained from three stations of Nepal. It also discusses a comparative study between GPS VTEC and VTEC obtained from CODG and IGSG GIM and satellite data for thermospheric O/N_2 ratio.

4.2.4.1   Global Geophysical Contest during Super Storms

Figures 63 to 66 depict 1-minute variations in the solar wind, interplanetary parameters, polar cap indices, and geomagnetic indices for the periods 14-24 March 2015, 18-28 June 2015, 24 May-3 June 2017, and 3-13 September 2017, respectively, including a few days before and after the geomagnetic storm on 17 March 2015, 22 June 2015, 27 May 2017, and 7 September 2017. Variations in solar wind velocity (V_x) in km s^{-1}, IMF B_z in nT, solar wind pressure (P_{sw}) in nPa, polar cap indices PCN and PCS indices in mV m^{-1}, auroral indices (AE AU AL AO) in nT, and SYM-H in nT are shown in the first, second, third, fourth, fifth, and sixth panels, respectively. Each Figure the vertical dotted line illustrates the storm's quick onset SSC and the horizontal lines with double arrow head represents main and recovery phase of the storm, respectively. Discontinuity in each plot appears due to unavailability of data for that instant.

The Super Storm of March 2015:- In Figure 63 a SSC is recorded around 04:45 UT, followed by an increase in average solar wind speed from 550 km s^{-1} to 600 km s^{-1} and solar wind pressure from 20 nPa to 30 nPa. The CME erupted from a magnetic filament on 15 March 2015 and reached the Earth on 17 March. The minor rise in solar wind speed on the 20th and 21st of March is due to a coronal hole, which transfers additional momentum and energy during the recovery phase, extending it for 7 days. During this storm with a minimum of -20 nT, the IMF B_z fluctuates rapidly southward and northward. The SYM-H was around -132 nT during the main phase around 20:30 UT, while the lowest value SYM-H observed during this storm was < -200 nT. During the storm's main phase, a reduction in the H component indicates the intensification of the westward ring current, while an increase in the H component predicts a sluggish return to normal on March 18. During this storm, the largest value of AE observed was 2000 nT, and fluctuating IMF B_z at higher V_x values are the characteristic of a high-speed streamer traveling around the Earth.

The Super Storm of June 2015:- Similarly, for the storm on June 22, 2015, the three SSC were observed at 13:43 UT on June 21, 5:45 UT on June 22, and 18:33 UT on June 22. The solar wind speed increased from 300 km s^{-1} to 350 km s^{-1}, 350 km s^{-1} to 400 km s^{-1}, and 420 km s^{-1} to 700 km s^{-1} during the first, second, and third shocks, respectively. The density of the solar wind shifted dramatically from 10 cm^{-3} to 50 cm^{-3}.
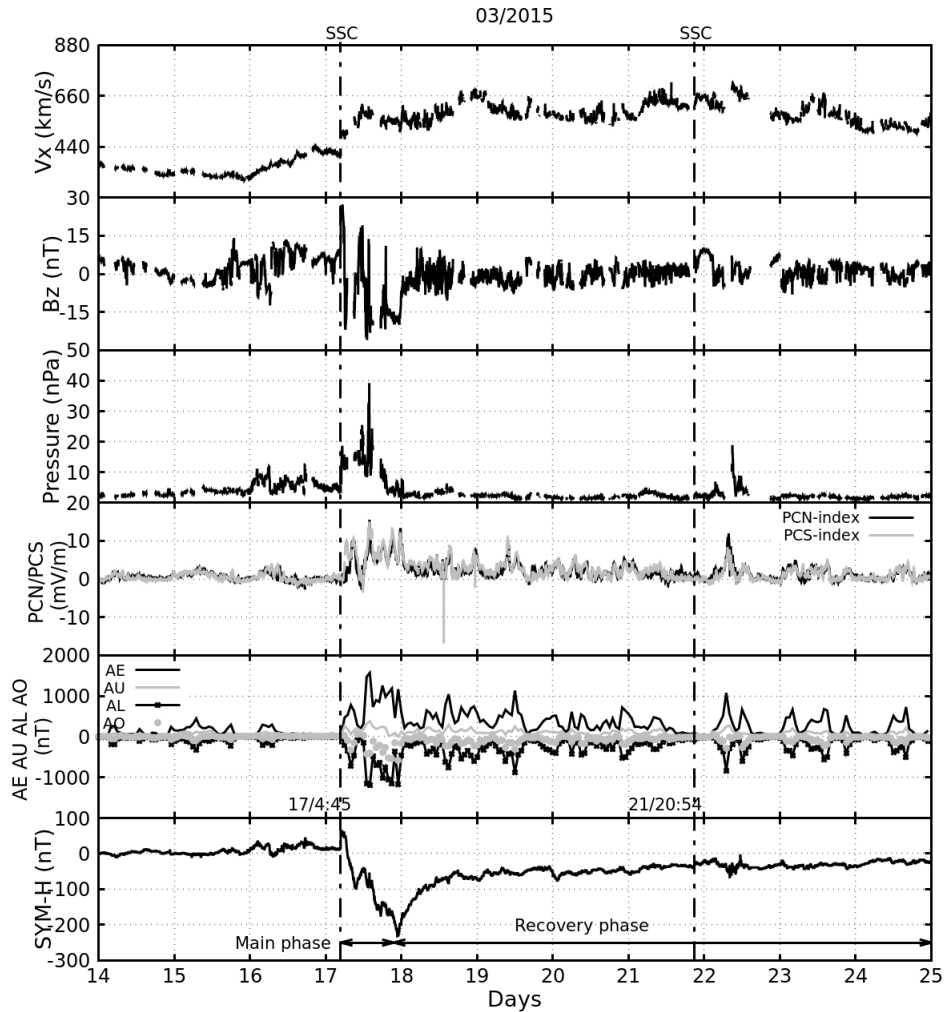
Figure 63: From top to bottom represents the alterations of solar wind speed (V_x) in km s^{-1}, IMF B_z in nT, pressure (P_{sw}) in nPa, polar cap indices (PCN/PCS) in mV m^{-1}, auroral indices (AE, AU, AL, AO) in nT, and SYM-H in nT during super storm of March 2015 (Pandit et al., 2022).

During the first, second, and third shocks, the highest positive SYM-H is 40 nT, 40 nT, and 90 nT, respectively. During the storm's primary and recovery phases, the key feature is fast large-amplitude fluctuation of IMF B_z. On June 22, it was likewise detected a minimum value -37.6 nT at 19:20 UT. In the course of the main phase, the AE value obtained was 2300 nT. As shown in Figure 64, the SYM-H hits -200 nT at 5:30 UT on June 23 when the B_z had a negative value for a longer period of time.

The Super Storm of May 2017:- On the 27th of May, 2017, at 15:34 UT, an SSC was observed during the storm. The storm starts quietly but quickly intensifies, with solar wind speeds ranging from 300 kms^{-1} to 400 km s^{-1} and pressures ranging from 1 nPa to 15 nPa. Figure 65 indicates the main phase began on May 27 and ended on May 30, with a minimum Dst excursion of -125 nT. The event continued till May 30, 2017. On May 28th, the greatest AE index was 2000 nT, with a minimum of IMF B_z -18 nT.

The Super Storm of September 2017:- During the storm on September 7, 2017, a first
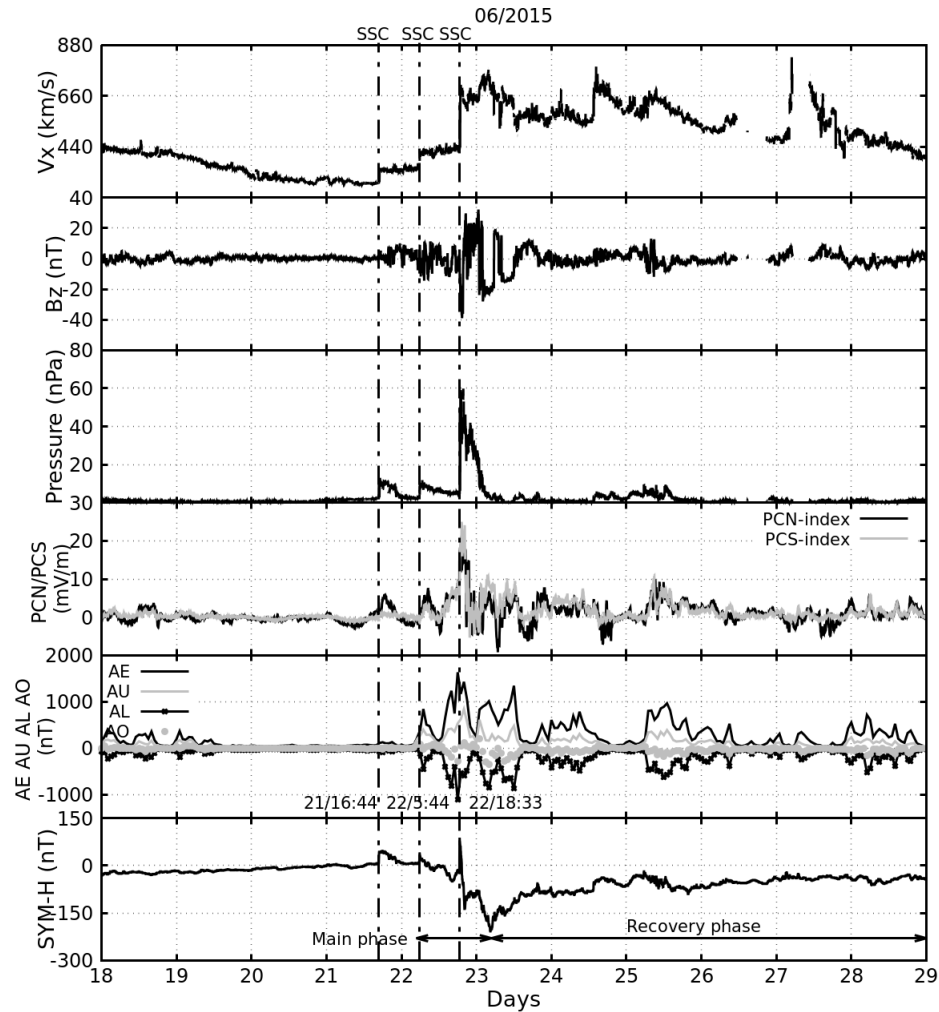
Figure 64: From top to bottom represents the alterations of solar wind speed (V_x) in km s^{-1}, IMF B_z in nT, pressure (P_{sw}) in nPa, polar cap indices (PCN/PCS) in mV m^{-1}, auroral indices (AE, AU, AL, AO) in nT, and SYM-H in nT during super storm of June 2015 (Pandit et al., 2022).

SSC was discovered on September 6th at 23:44 UT, and a second on September 7th at 23:00 UT. On September 8th, two substantial minimums of SYM-H were detected the one with -142 nT at 02:00 UT, and another with -122 nT at 15:00 UT. As in Figure 66, the SYM-H's minimum and AE's maximum bursts do not exactly correspond in time. The highest AE values recorded were 1300 nT and 1500 nT. The minimum SYM-H and AE maxima were 3 hour and 2 hour sooner, respectively; one probable explanation is that the geomagnetic disturbance shifted from higher to lower latitudes. Despite this, Polar Cap (PC) bursts have the same pattern as SYM-H minima. The solar wind velocity and pressure quickly changed from 450 km s^{-1} to 650 km s^{-1} and 600 to 850 km s^{-1}; 1 nPa to 14 nPa and 1 nPa to 10 nPa, respectively, between the first and second strokes. Table 8 summarizes the characteristics of the four storms events used in this study.
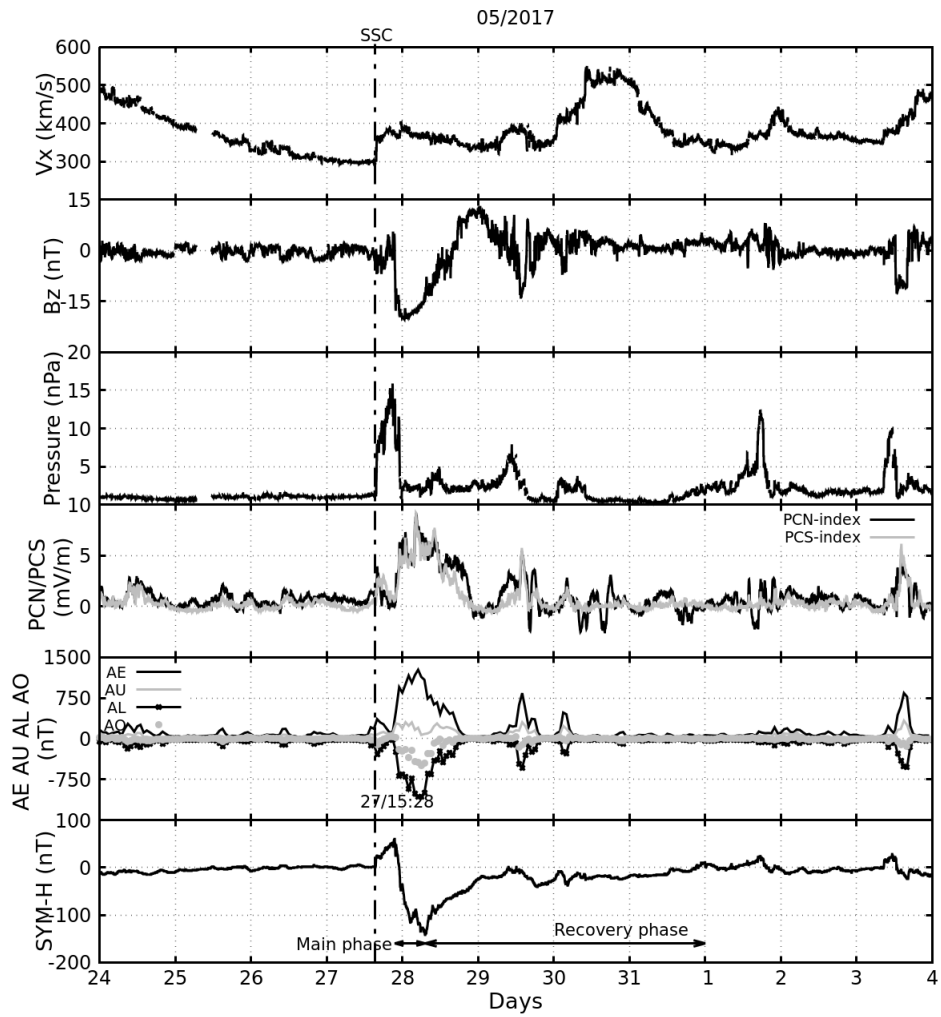
Figure 65: From top to bottom represents the alterations of solar wind speed (V_x) in km s^{-1}, IMF B_z in nT, pressure (P_{sw} in nPa), polar cap indices (PCN/PCS) in mV m^{-1}, auroral indices (AE, AU, AL, AO) in nT, and SYM-H in nT during super storm of May 2017 (Pandit et al., 2022).
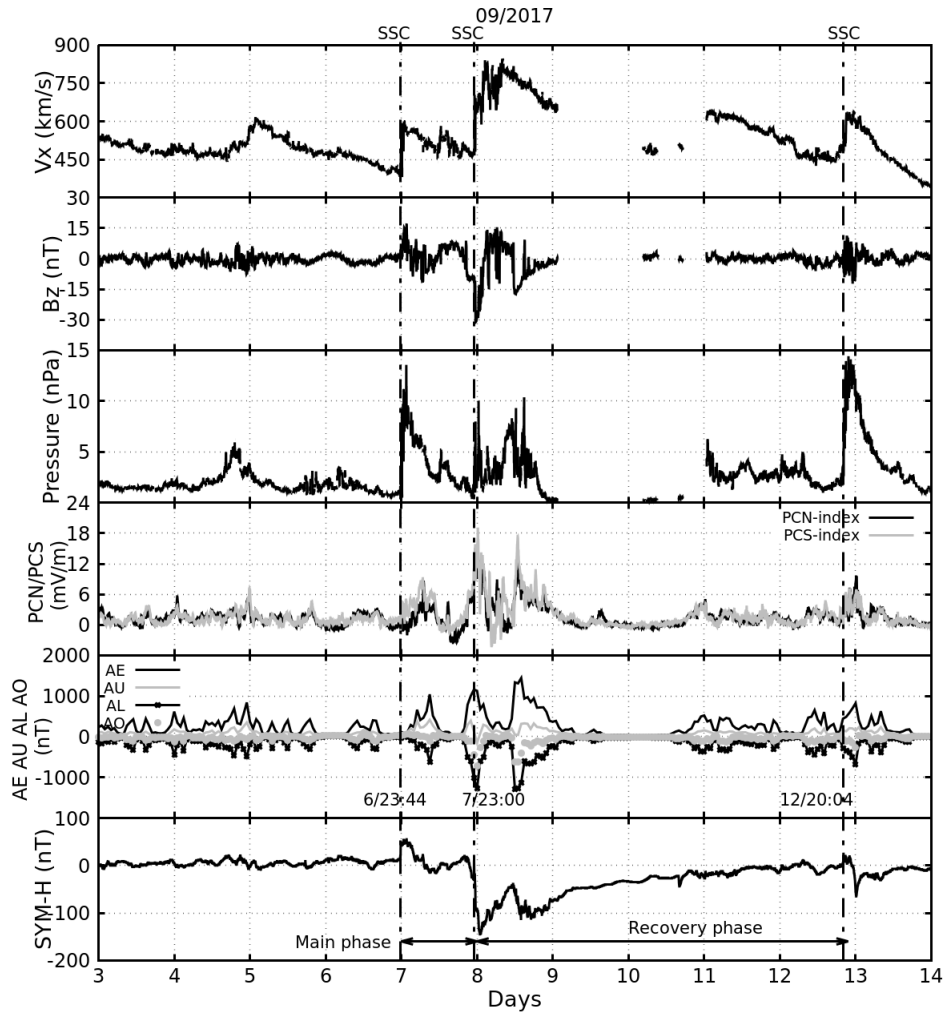
Figure 66: From top to bottom represents the alterations of solar wind speed (V_x) in km s^{-1}, IMF B_z in nT, pressure (P_{sw}) in nPa, polar cap indices (PCN/PCS) in mV m^{-1}, auroral indices (AE, AU, AL, AO) in nT, and SYM-H in nT during super storm of September 2017 (Pandit et al., 2022).

Table 8: Summarizes the characteristics of the four super intense storms events used in this study (Pandit et al., 2022).

Date	SSC	Season	Event started Local time in Nepal	Case	Dst	SYM-H	Kp	AE
March 2015	March 17 04:45 UT & March 21 20:54 UT	Equinox	LT = 4.45 + 5.45 10 hr 30 min	CME + HSSW	-225 nT	-250 nT	8	2000 nT 12:00 UT on 17 March 2017
June 2015	June 21 16:43 UT, June 22 05:45 UT & June 22 18:33 UT	Summer Solstice	Last SSC LT = 18.33 + 5.45 0 hr 30 min	CME + HSSW	-207 nT	-275 nT	8	2800 nT 18:00 UT on 22 June 2015
May 2017	May 27 15:28 UT	Summer Solstice	LT = 15.46 + 5.45 21 hr 13 min	CME	-125 nT	-150 nT	7	2100 nT 6:00 UT on 28 May 2017
September 2017	September 6 23:44 UT, September 7 23:00 UT & September 12 20:04 UT	Equinox	First SSS LT = 23.73 + 5.45 5 hr 29 min	CME	-142nT	-150 nT	8	2600 nT 14:00 UT on 8 September 2017

4.2.4.2   GPS VTEC during Quiet and Storm Period

Using GPS data from selected three stations of Nepal from 14 to 24 March 2015, 18 to 28 June 2018, 24 May to 3 June 2017, and 3 to 13 September 2017, Figure 67 (a), (b), (c), and (d) demonstrate the temporal change of VTEC during geomagnetic storms and geomagnetic quiet days. The VTEC of stations BRN2, JMSM, and NAST in Nepal is represented by the first, second, and third panels in each illustration. Each panel's dotted black curve indicates average daily variance (computed average of four day before storm started). The calm day variation for each storm is estimated using an average of data from the 13th to 16th of March 2015, the 18th to 21st of June 2015, the 23rd to 26th of May 2017, and the 3rd to 6th of September 2017. Each Figure's vertical line illustrates the storm's quick onset SSC. The distance between the chosen stations is only $3°$ latitudinal and $4°$ longitudinal; the electric field disturbances reach the daylight ionosphere at the same time, with identical intensity and duration. As a result, a large latitudinal and longitudinal variation in ionospheric response between these three sites is negligible. A dome-shaped VTEC was observed at each location. The trend of VTEC variation before a storm is virtually identical to that of regular variation, but when a geomagnetic storm begins, it becomes disrupted.

The following are the observations for each case:

The Storm of March 2015:- The three days leading up to the storm (from March 14-16) are marked by a similar dome-shaped diurnal oscillation, with a maximum value of 95 TECU to 100 TECU. The magnetic storm began on the 17th of March in the morning sector, and the diurnal maximum was recorded at 90 TECU (Figure 67a). The decline in the afternoon is erratic and occurs in cascades. The diurnal maximum on March 18 is extremely low (30 TECU), representing a -70 percent reduction. It's the same on all three stations. Since March 20, when the level of 105 TECU was detected, the recovery phase has been quick. The arrival of the March 22 magnetic disturbance has been pinpointed to the early hours of the night. It produces a positive storm with a single peak at 120 TECU with an increase of $+20\%$, followed by a little negative phase on March 23rd.

The Storm of June 2015:- This storm occurs during the summer, when daytime temperatures are lower than the March equinox of the same year. The diurnal maximum of the VTEC declined steadily from 70 TECU to 45 TECU in the four days leading up to the storm (Figure 67b). Over the last two days of the quiet period (from June 20-21), the overall content has already fallen below our baseline. The initial shock wave was felt in the early hours of the 22nd of June. The diurnal variation of June 22, which remains below this standard, is unaffected. The following days show no major variations save for a continuous reduction in the diurnal maximum until it reaches a minimum on June 26

(for example, from 49 TECU to 31 TECU for JMSM). At the three stations, we can see a double peak on June 23 and low values on June 23 and 24 during night with -5 TECU or a decrease of -50 %.

The Storm of May 2017:- It's a summer storm once again, but this time it's in the declining portion of the solar cycle, thus the VTEC values are lower than in 2015, around 30 TECU in the day time and 10 TECU at night (Figure 67c). The magnetic storm begins in the late morning of May 27th. On the 28th and 29th of May, the VTEC was slightly higher than our baseline, ranging from 3 TECU to 5 TECU (+10%). It drops only late in the recovery phase, on the 30th and 31st of May, to a maximum of 20 TECU with an increase of -30%.

The Storm of September 2017:- The phase is repeated in 2017, however this time around at the fall equinox, resulting in higher VTEC values than in the summer. The VTEC values ranges from 10 TECU at night to 40 TECU during the day (Figure 67d). The storm begins late in the evening of September 7 (05:29 LT). Depending on the station, VTEC rises quickly to a daily high of 14 LT at 50 TECU to 60 TECU (+45 percent). We're in the midst of a good storm. The VTEC is -8 TECU (-30 percent) lower on four days later (10th September), followed by a new beneficial effect on 11th September. With such a long wait, it's difficult to connect the magnetic storm to the second storm, which doesn't start until September 12 at 20:04 UT.

4.2.4.3 Thermospheric O/N$_2$ Ratio from Satellite Data

Figure 68 (a), (b), (c), and (d) depict the global change of the thermospheric O/N$_2$ ratio, as measured by GUVI/TIMED, during four geomagnetic storms: March 16–21, 2015, June 20–25, 2018, May 26–29, 2017, and September 6–10, 2017. On the basis of observed satellite data, the following behavior at the location of the Nepalese GPS station JMSM has noted:

- For the March 2015 storm, on March 18, a large reduction in the O/N$_2$ ratio was observed.

- For the June 2015 storm, the O/N$_2$ ratio began to decline on June 22 and peaked on June 23.

- In the case of the May 2017 storm, there was no discernible change in the O/N$_2$ ratio.

- On the 8th and 9th of September, during the September 2017 storm, a large increase in the O/N$_2$ ratio was noticed.

The thermospheric composition ratio of O/N$_2$ restored to its typical profile after all of the geomagnetic storms. The GUVI satellite O/N$_2$ has the same behavior as the VTEC
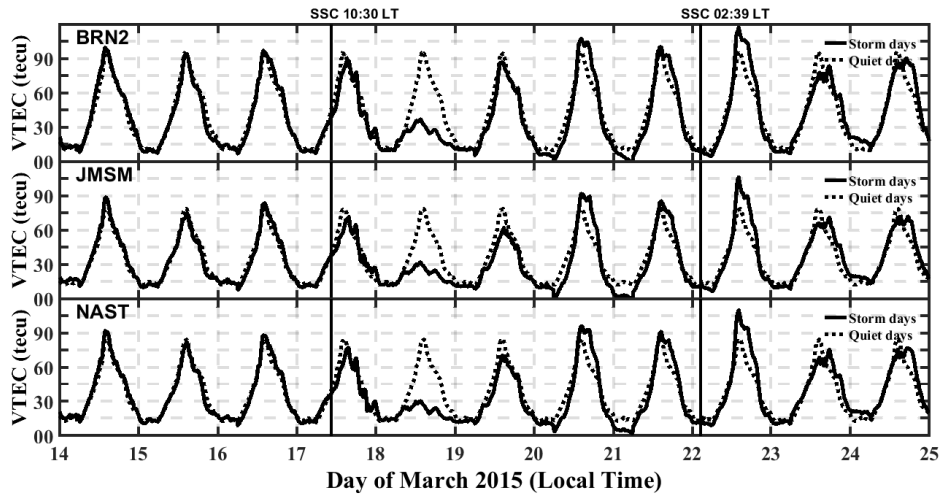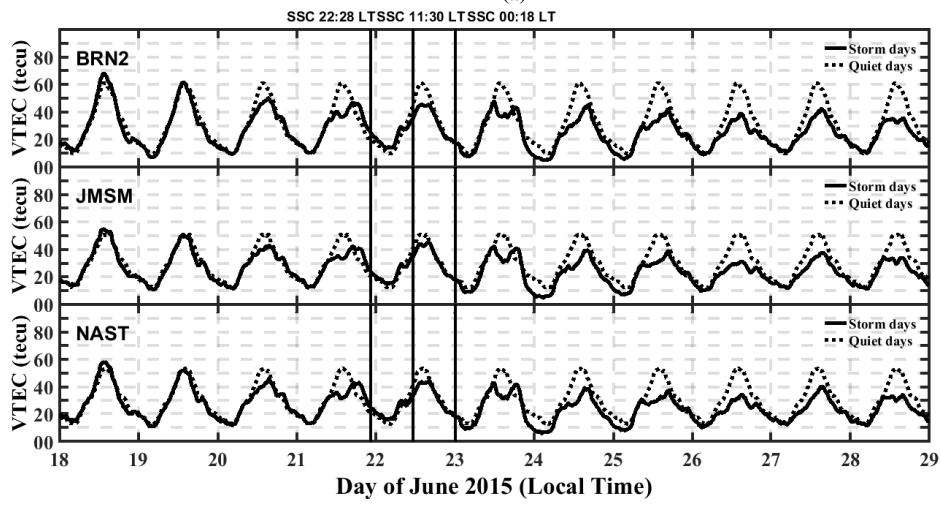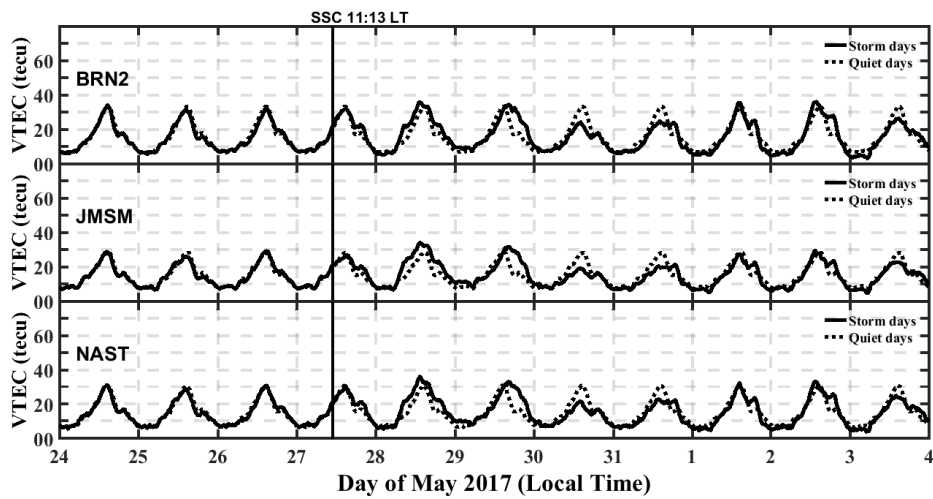
Figure 67: VTEC variation during geomagnetic storm of 14–24 March 2015, 18-28 June 2015, 24 May-3 June 2017, and 3-13 September 2017. The dotted curve on each panel represents the quiet day variation and solid curves for the geomagnetic stormy days (Pandit et al., 2022).
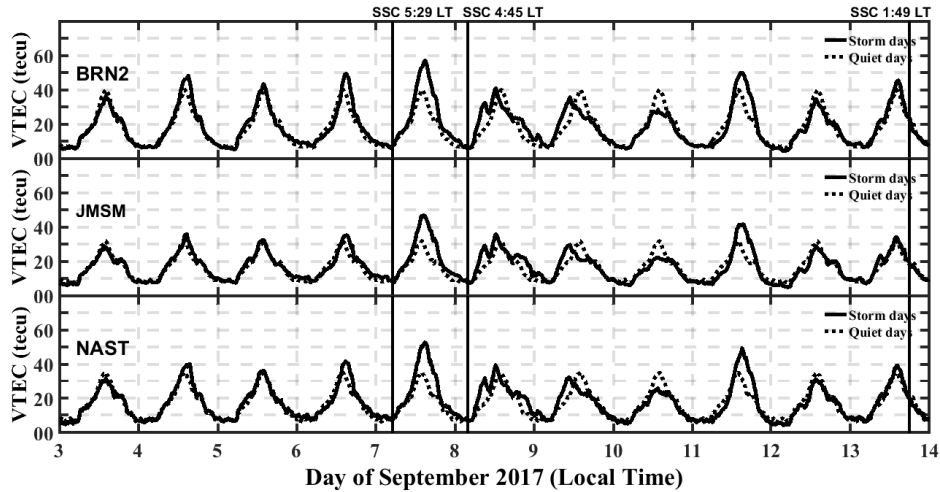
Figure 67: (Contd.) VTEC variation during geomagnetic storm of the period 14–24 March 2015, 18-28 June 2015, 24 May-3 June 2017, and 3-13 September 2017. The dotted curve on each panel represents the quiet day variation and solid curves for the geomagnetic stormy days (Pandit et al., 2022).

recorded from ground-based GPS sites for all storms. We see negative storms in March and June of 2015, as well as a positive storm in September of 2017. The change in VTEC during the storm of May 2017 is positive but extremely faint, and the change in O/N_2 on satellite data is not particularly evident.

4.2.4.4 Comparison between GPS, CODG and IGSG VTEC

The three variations of the VTEC (1) resulting from our RINEX processing in the form of a continuous line in black, (2) calculated by the GIM/CODG model by a square (1 point every hour), and (3) estimated by the IGSG model by an asterisk (1 point every 2 hours) have been represented in Figures 69 (a, b, c, d) for the four selected storms. From top to bottom, BRN2, JMSM, and NAST are represented by three panels in each Figure. A vertical red line has been used to notify us of the hourly position of the shock waves. We have kept the largest daily difference to measure the difference between our modeling and the two GIM maps. These disparities in data for the three stations are shown in Tables 9 and 10 for the storm of March 2015 and September 2017, respectively. The values for two storms i.e. in June 2015 and May 2017 are modest and negligible, they are not reported in this thesis. The following are the comparisons for each storm:

March 2015:- The three days preceding the storm of March 14-16 are marked by higher day values of roughly 10 TECU to 15 TECU, i.e. +15%, than the two GIM models. The two models accurately restore the time and level of the following days, which make up the storm period and the return phase. We find the initial observation with day values of the two models trimmed compared to our model in a same order of magnitude of 10 TECU to 15 TECU during the recovery phase and the positive phase of March 22.

136

Table 9: Difference in RINEX VTEC for three Nepalese GPS stations with CODG and IGSG during geomagnetic storm of 14-24 March 2015 (Pandit et al., 2022).

Days	JMSM RINEX -CODG	JMSM RINEX -IGSG	NAST RINEX -CODG	NAST RINEX -IGSG	BRN2 RINEX -CODG	BRN2 RINEX -IGSG
14	9	10	10	10	6	9
15	11	7	11	13	13	13
16	16	16	13	16	10	11
17	2	2	4	5	-4	-4
18	0	1	-3	-2	-3	-3
19	-1	0	-1	-5	-3	-4
20	10	21	12	19	7	19
21	3	8	3	8	12	13
22	16	17	19	19	10	14
23	-3	-2	7	8	1	1
24	1	1	-10	-7	-3	-4

Table 10: Difference in RINEX VTEC for three Nepalese GPS stations with CODG and IGSG during geomagnetic storm of 3-13 September 2017 (Pandit et al., 2022).

Days	JMSM RINEX -CODG	JMSM RINEX -IGSG	NAST RINEX -CODG	NAST RINEX -IGSG	BRN2 RINEX -CODG	BRN2 RINEX -IGSG
3	-3	-3	3	3	-2	-2
4	5	5	5	12	0	9
5	-3	-3	0	1	-5	-5
6	-5	-2	5	7	0	2
7	3	3	8	6	2	12
8	0	-3	0	0	1	-10
9	-1	0	0	-8	0	-7
10	-4	-9	-2	-13	0	-5
11	0	-2	0	0	4	14
12	-2	-4	3	10	-2	0
13	0	0	5	3	0	-2

Figure 68: Illustration of thermospheric O/N_2 ratio acquired from the GUVI/TIMED in the course of geomagnetic storms of the period 16-21 March 2015, 20-25 June 2015, 26-29 May 2017, and 6-10 September 2017. The black dot on each panel, represents the location of JMSM station (Pandit et al., 2022).

The primary phase of the negative ionospheric storm in Nepal occurred in March 2015, while the recovery phase occurred on March 18-19. The diurnal variation of TEC shows

138
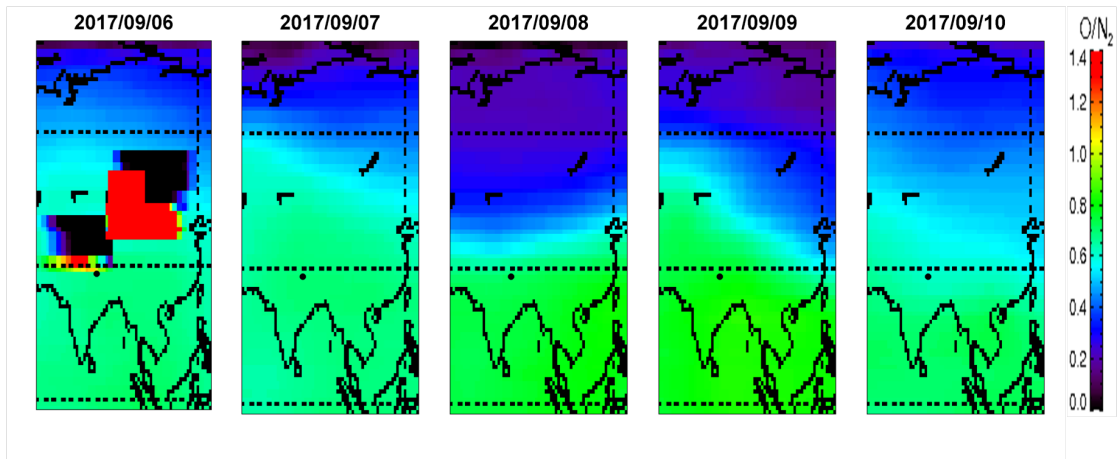
(d)

Figure 68: (Contd.) Illustration of thermospheric O/N$_2$ ratio acquired from the GUVI/TIMED in the course of geomagnetic storms of the period 16–21 March 2015, 20-25 June 2015, 26-29 May 2017, and 6-10 September 2017. The black dot on each panel, represents the location of JMSM station (Pandit et al., 2022).

wavelike oscillation during the primary and recovery phases. This could be caused by PPEF, traveling ionospheric disturbance, or a variety of other factors. The decrease in TEC during the recovery phase was linked to a shift in neutral gas composition, which lowers the O/N$_2$ ratio (De Jesus et al., 2013). According to Astafyeva et al. (2015), the second IMF B_z lasted longer during the current storm and has a more complex influence. Using GUVI-TIMED satellite observations, they analyzed the O/N$_2$ ratio changes in the course of this geomagnetic storm and confirmed a substantial O/N$_2$ composition change. Ramsingh et al. (2015) evaluated the ionospheric response in the Indian and Indonesian sectors following the storm on March 17, 2015 the St. Patrick's Day. They proposed that the F region perturbations during the main phase were caused by PPEF.

June 2015:- The VTEC's diurnal variation shows high levels at the start of the period and a reasonably regular decline over the next 10 days, with either a single maximum peak or a double peak. Despite this daily variability, the two GIM models show a very significant association with our representation: Differences of fewer than 2 TECU exist. TEC changes at Nepalese stations did neither rise nor decrease before or during the storm's main phase or recovery phase in June 2015. During the evening, there is an increase in PRE at each station. During the pre-storm and post-storm of the mid-diurnal TEC, wavelike properties with a noon bite pattern were observed. Singh & Sripathi (2017) used a GPS TEC map to analyze the temporal and latitudinal variation of TEC during the storm of June 22-24, 2015. They discovered that on June 22nd, EIA was suppressed and partly moved to the Northern Hemisphere up to 0° to 35° geographic latitude at 11:00 LT to 17:00 LT. Due to the westward electric field, EIA was suppressed in the absence of crest development and a negative storm effect Counter Electrojet (CEJ). They also discovered that powerful westward DDEFs suppressed EIA and a negative

139

ionospheric storm on June 24 in the Northern Hemisphere. Şentürk (2020) observed hemispheric asymmetry in ionospheric response in both TEC maps and GNSS TEC data from the first phase to the major phase of the storm in June 2015. Negative ionospheric storm phases were observed in northern latitudes (summer hemisphere), while strong positive ionospheric storm phases were observed in southern latitudes (winter hemisphere). Because the June 2015 storm coincided with the June solstice, dominant summer-to-winter circulation (Millward et al., 1996) and seasonal impacts (Kil & Paxton, 2006) may have dominated hemisphere asymmetry of VTEC responses. The negative phase recorded on June 23 is consistent with their study's TEC maps.

May 2017:- The outcome is quite similar to that of the previous instance. During the high values of the VTEC of 29th May, however, the two GIM models give greater levels of 5 TECU. At night, the situation is reversed (-4 TECU on 30 to 31 May night). When compared to the other two stations, the daily differences are larger for the BRN2 station, which is closest to the dip equator (JMSM and NAST). In May 2017, an increase in VTEC was noticed in Nepal during the storm's main phase on 28th May, which gradually decreased during the storm's post-recovery phase on 30th May. L. Liu et al. (2020) investigated this storm and discovered a 120 % increase in VTEC in the instant of the main phase of the storm on May 28 due to the southward turning of IMF B_z and eastward penetration of the electric field. A negative storm was found on the 30th of May over the Asian sector, approximately two days after the main phase, due to thermospheric composition changes, i.e. a reduction in the O/N_2 ratio. In the diurnal plot, an increase in TEC owing to PRE can be seen in the evening.

September 2017:- The GIM modeling is correct when the diurnal maxima is between 30 TECU and 40 TECU. Above 50 TECU, the difference becomes negative, peaking at -10 TECU BRN2 and NAST on 7th September. The IGSG model, which has a lower latitude, shows the most significant differences on BRN2. On all three curves, the lowest VTEC values were seen on 10th September. The night values do not fluctuate much throughout the course of ten days. In the time of the main and healing phases of the September 2017 storm in Nepal, daytime VTEC enhancement occurred at all stations on September 8 and 9. The wave-like changes in VTEC on September 8 could be attributable to high-latitude Travelling Atmospheric Disturbancess (TADs) caused by increased Joule heating in the course of the magnetic storm (Fuller-Rowell et al., 1994). On the 11th of September, there was a considerable midday VTEC boost when compared to the 10th September. During the initial phase of the storm, while IMF Bz was southerly, the neutral wind was not much disrupted, (Lei et al., 2018) observed an increase in VTEC over similar latitudes, which they attributed to an increase in eastward electric fields due to PPEF (Balan et al., 2013). Weak VTEC depletions on September 9 to 10 could be linked to shift neutral composition in storm time that spanned high to

low latitudes. The GUVI [O/N$_2$] data for the magnetic storms of March 17 and June 22, 2015 was analyzed by Nava et al. (2016); Kashcheyev et al. (2018). The results of a global investigation illustrate the importance of a station's LT at the commencement of a storm. The VTEC lowers significantly in Asia during the storm of March 17, 2015, which begins at 4:45 UT, as we saw in our data in Nepal, while it grows in America. In the case of the storm on June 22, 2015, which starts at 18:33 UT, the Asian sector sees an increase in VTEC while the American sector sees a fall in VTEC.

In summary, the observations of the two global ionospheric models CODG and IGSG:

- give lower VTEC values (−10 to −20 %) than at stations in Nepal when the level is above 50 TECU, which is mostly observed during magnetically quiet periods;

- give slightly lower values (−1 TECU to −3 TECU) at night;

- correctly restore the level during the main phases of storms, even if these are very negative;

- show a lower result at BRN2 when compared to CODG, the IGSG model meant to synthesis all of the GIM maps performs poorly.

The daily variations of VTEC obtained from the CODG and IGSG models for summer (June 2015 and May 2017) and equinoctial storms (March 2015 and September 2017) revealed that VTEC values are lower in summer than at the equinoxes (March 2015 and September 2017). The VTEC is judged to be stronger in 2015 because 2015 is at the start of the declining phase of sunspot cycle 24, and 2017 is nearing the end of the falling phase of the minimum of sunspots number.

Hernández-Pajares et al. (2009) discovered a large discrepancy in VTEC calculation over the ocean where just a few GPS receivers are present, and one hour resolution may be the reason why the storm time effect cannot be analyzed in detail. Legrand & Simon (1989) evaluated more than a century and a half of magnetic data and discovered that there were 67 percent of magnetic quiet days, meaning that CODG and ISGS do not represent the data of Nepal during the equinoxes more than two-thirds of the time. During periods of high magnetic activity, on the other hand, the storm homogenizes the ionosphere, removing geographic heterogeneity.

The gap between observed and model data could be due to a local effect that CODG and IGSG don't replicate (Matuura, 1974; Christian et al., 2013). The findings of Panda et al. (2013, 2015) are consistent with this conclusion. The computed VTEC in October 2012 and the GIM match well at locations near the magnetic equator, however there are significant variations (up to 20 TECU or 40%) at the Delhi station, which is located towards the northern ridge of the equatorial anomaly. Several physical phenomena found at low latitudes, particularly vertical plasma drifts, show rapid longitudinal fluctuations
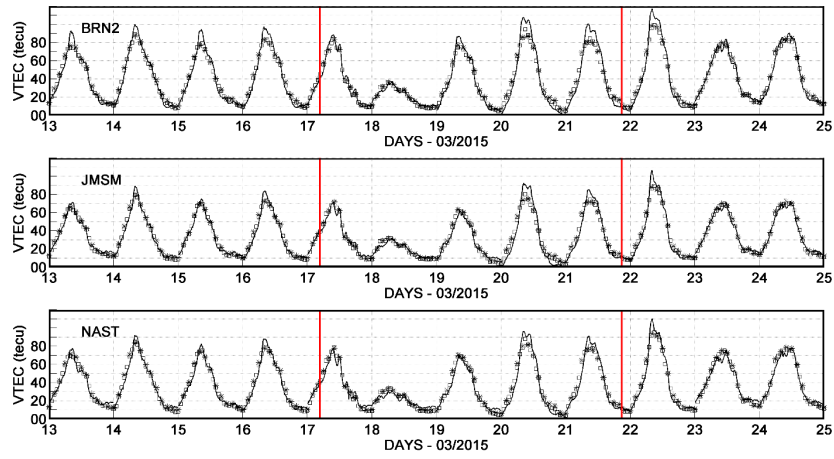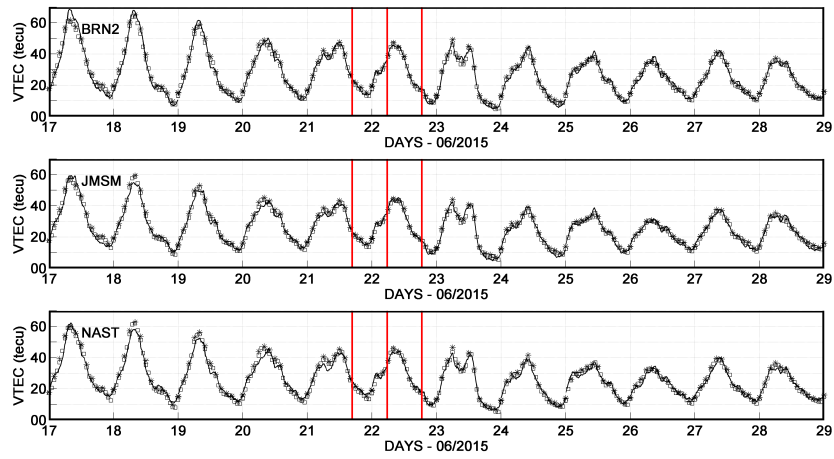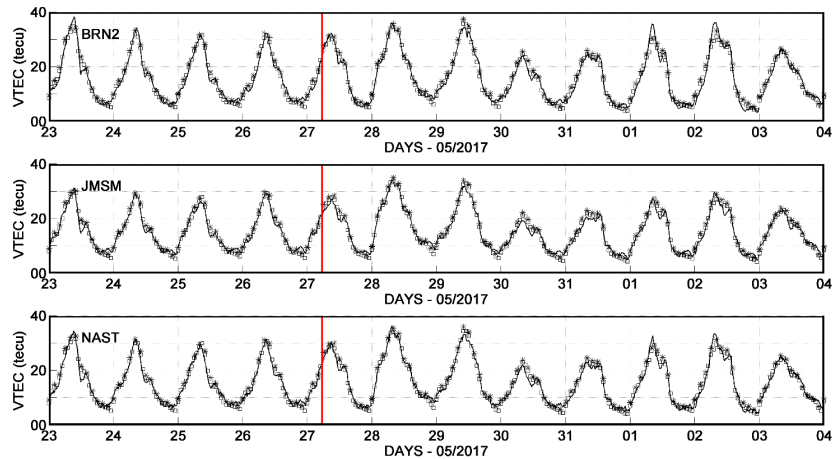
Figure 69: Variations of GPS VTEC, CODG, and IGSG for JMSM, NAST, and BRN2 stations during geomagnetic storm of 14-24 March 2015, 18-28 June 2015, 24 May-3 June 2017, and 3-13 September 2017. On each panel the solid black curve represents GPS VTEC, black square with white background curve for CODG, and black asterisks curve for IGSG (Pandit et al., 2022).
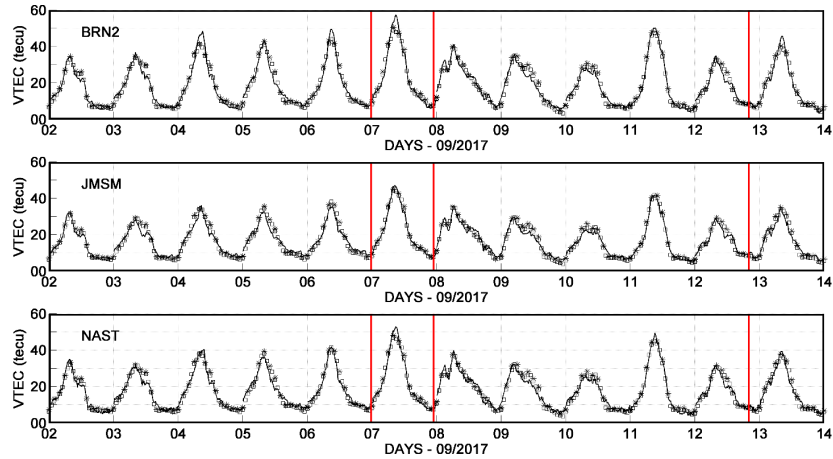
(d)

Figure 69: (Contd.) Variations of GPS VTEC, CODG, and IGSG for JMSM, NAST, and BRN2 stations during geomagnetic storm of 14-24 March 2015, 18-28 June 2015, 24 May-3 June 2017, and 3-13 September 2017. On each panel the solid black curve represents GPS VTEC, black square with white background curve for CODG, and black asterisks curve for IGSG (Pandit et al., 2022).

that are not replicated by GIM models (Fejer et al., 1981, 1991). Many GNSS stations already exist at low latitudes, particularly on islands. However, in order to comprehend the variability of the ionosphere in this geographic location, the densification is not uniform. The scientific community must take action to expand the network and, as a result, enhance TEC modeling. During magnetic quiet days, the disparity between VTEC RINEX and VTEC models is higher, according to this study. This means that there is a lot of geographic variation during magnetic calm times. CODG uses a small number of geodetic stations in Nepal's immediate neighborhood. This circumstance could account for the TEC disparities between local measurements and global-scale simulations.

CHAPTER 5

5. CONCLUSION AND RECOMMENDATIONS

5.1 Conclusion

This chapter includes the summary of our research findings of this thesis work and recommendations for the future research fields of interest.

Ionospheric Variability over Nepal:- The characteristics of regular and disturbed ionospheric variability over Nepal (located at mid-latitude) has been studied using GPS TEC data from Nepal. The regular ionospheric variability is studied using long term data from year 2008 to 2018 of the solar cycle 24 and the geomagnetically disturbed time ionospheric variability has been analyzed taking the cases of four super intense geomagnetic storms events of the same solar cycle. For regular variability of VTEC, data from four GPS stations: KKN4 (27.80° N, 85.27° E), GRHI (27.95° N, 82.49° E), JMSM (28.80° N, 83.74° E), and DLPA (28.98° N, 82.81° E) are used. On the other hand, to study variability of VTEC during super intense geomagnetic storm, data of stations BRN2 (26.51° N, 87.27° E), NAST (27.65° N, 85.32° E), and JMSM (28.80° N, 83.74° E) are utilized. The regular variation is studied on the basis of diurnal, monthly, seasonal, yearly and over entire solar cycle. Correlation of VTEC with SSN and solar flux radiation has been analyzed to identify the dependency of VTEC on SSN and solar flux. Furthermore, features of ionosphere during disturbed condition of ionosphere is compared with global ionospheric models: CODG and IGSG. Our study shows, the diurnal variation of VTEC depends on solar cycle phases. A flat diurnal peak is observed during minimum and descending year of solar cycle, but a Gaussian with varying peak amplitude is noticed during ascending and maximum phases of the solar cycle. The maximum TEC lies around 11:00 LT to 14:00 LT and minimum is noticed in the pre-dawn periods. Day to day variability is identified in each station and the maximum VTEC is found at KKN4 and minimum at DLPA station. The wavy nature of diurnal profile is identified in years 2008, 2009, and 2010, whereas the parabolic nature is detected in years from 2011 to 2017. During minimum years of solar cycle ionosphere is characterized by lower value of TEC and during maximum year of solar cycle, it has higher VTEC, which resemble with variation in the SSN and solar flux of respective year. VTEC rises linearly in the summer month, whereas steep rise is identified in the month of winter. Two dimensional plots of VTEC reveals that in year 2009 equinoctial asymmetry is absent and in year 2011 the spring VTEC is less intense than autumn, but in 2014 and 2015 spring VTEC is intense than autumn. Equinoctial asymmetry of

VTEC is identified due to difference in solar flux between equinoxes. In the years 2011, 2012 and 2013, the autumn-maximum is greater than the spring-maximum. The winter VTEC in 2011 (except at DLPA) and 2014 is identified greater than the summer peak in all the stations. The SSN and solar flux has minimum value in year 2009 and maximum in 2014, respectively.

The characteristics of disturbed ionosphere due to substorms and super intense geomagnetic storm has been studied by analyzing impact of SSSs on horizontal components of geomagnetic field at equatorial, mid-latitude and high latitudes magnetic stations and F_2 layer ionospheric parameters at mid-latitude.

Characteristics of Solar Wind Plasma Parameters and Magnetic Indices during SSSs:- SSSs are the intense substorms described by SML or AL index < -2500 nT. The global context of solar wind plasma parameters and IMF during SSSs is analyzed using five SSSs events on 11 April 2001, 24 November 2001, 24 August 2005, 7 September 2017, and 8 September 2017. The coupling between the solar wind-magnetosphere during SSSs are studied using auroral electrojet indices AE, AU, AL and IMF B_z. The CWT and GWS also have been used to analyze the time response of auroral electrojet indices to IMF B_z of solar wind. The scalogram of CWT spectrum shows the main periodicities are present during the SSSs events. The power area of higher intensity is seen in time scale approximately, for IMF B_z between 2 $(nT)^2$ to 1 $(nT)^2$ and 5 $(nT)^2$ to 4 $(nT)^2$; AE between 16 $(nT)^2$ to 4 $(nT)^2$ and 4 $(nT)^2$ to 2 $(nT)^2$; AU between 16 $(nT)^2$ to 8 $(nT)^2$ and 4 $(nT)^2$ to 2 $(nT)^2$; and AL between 8 $(nT)^2$ to 4 $(nT)^2$ and 4 $(nT)^2$ to 2 $(nT)^2$ for SSSs during two SSSs events of 11 April 2001 at 16:00 UT and 20:00 UT, respectively. The strong power for the IMF B_z between 16 $(nT)^2$ to 4 $(nT)^2$ and 4 $(nT)^2$ to 2 $(nT)^2$; AE between 10 $(nT)^2$ to 6 $(nT)^2$ and 4 $(nT)^2$ to 2 $(nT)^2$; AU between 8 $(nT)^2$ to 4 $(nT)^2$ and 4 $(nT)^2$ to $(nT)^2$2; and AL between 10 $(nT)^2$ to 6 $(nT)^2$ and 2 $(nT)^2$ to 1 $(nT)^2$ during the time at 7:00 UT and 13:00 UT of SSSs event November 24, 2001, respectively. The strong power area for IMF B_z lies between 4 $(nT)^2$ to 2 $(nT)^2$; AE between 8 $(nT)^2$ to 2 $(nT)^2$ and 4 $(nT)^2$ to 2 $(nT)^2$; AU between 8 $(nT)^2$ to 2 $(nT)^2$; and AL between 8 $(nT)^2$ to 2 $(nT)^2$ during the time at 10:20 UT of SSS event August 24, 2005. The strong power for the IMF B_z, AE, AU, and AL found lying between 8 $(nT)^2$ to 4 $(nT)^2$ during the time of SSS event 7 September 2017 at 23:45 UT and strong power for IMF B_z lies between 8 $(nT)^2$ to 4 $(nT)^2$; AE between 8 $(nT)^2$ to 4 $(nT)^2$; AU between 8 $(nT)^2$ to 2 $(nT)^2$ and AL between 8 $(nT)^2$ to 4 $(nT)^2$ during the time at 13:00 UT of SSS event September 8, 2017. The GWS indicates the most energetic periods are present during the SSSs events. The time lag between the IMF B_z and AE index has studied using cross-correlation. A correlation coefficient of ~-0.95 and 0.90 noticed during the first and second occurance of SSSs with zero-time lag on April 11, 2001. Similarly, the correlation between IMF B_z and AE was noticed 0.60 for first SSS and

0.90 during second SSS of November 24, 2001 with approximately, zero time lag. The correlation coefficients of 0.90, 0.97, and 0.99 with zero time lags were noticed between IMF B_z and AE for the SSS of 24 August 2005, 7 September 2017, and 8 September 2017, respectively. The higher value of cross-correlation coefficient during each event shows the good correlation between AE and IMF B_z. This study reinforces concept of the coupling between solar wind-magnetosphere by means of inter connection between IMF B_z and geomagnetic field during SSSs.

Signature of SSSs at High, Middle and Equatorial Latitudes on H-Component of Geomagnetic Field:-Under the effect of variation of SML index during September 7 and 8, 2017, we attempted to contribute an understanding of the variability of the horizontal component of the Earth's magnetic field and energy deposited inside magnetosphere-ionosphere coupling as FAC, PCV, RC, JH, AP, and TE. Data were taken from geomagnetic observatories at high latitude (ABK, FCC, MGD, and UPS), mid-latitude (ABG, BOU, DUR, and PHU), and equatorial stations (API, GUA, KOU, and MBO). The fluctuation in H-component is noticed high during SSSs than on the quie days. Using CWT, the study showed transient characteristics in signals related to particle and energy flows during magnetic reconnection. We also discovered a discrepancy in the mid-latitudinal response in the northern hemisphere, which is expected considering the ionospheric and local temporal effects connected to the magnetosphere at the time of SSSs. For FAC, PCV, TE, AP, JH, and RC, the higher intensity wavelet power areas were detected somewhere around 24 UT and 37 UT with intensities of 2 and 3; 5.5 and 3.5; 3 and 4; 1.5 and 3; 2 and 4; 2 and 4; 7 and 6 for FAC, PCV, TE, AP, JH, and RC, respectively. This inconsistency in normal tend of H-component may be induced by external agents of space weathers, magnetic storms and partially due to magnetospheric disturbances.

Effect of SSSs on Ionospheric Parameters:- The energy deposited in ionosphere during SSSs produces impact on its parameters. The response of SSSs on 24 August 2005, 7 September 2017, and 8 September 2017 on F_2 layer parameters foF_2, $h'F$ and hmF_2 are analyzed. The ionosonde data is taken from Boulder, Colorado, USA (40° N, 105° W). The positive ionospheric storm is noticed during SSSs events of 24 August 2005 and 8 September 2017, which has confirmed by decrease in foF$_2$ and negative ionospheric storm during SSS on 7 September 2017 is confirmed by increase in foF$_2$. The CWT analysis show during SSS of 24 August 2005 coupling in magnetosphere lies during ~ 16 minute to 32 minute and during SSSs of 7 and 8 September 2017, it is identified in the course of 27.9 minute to 64 minute. Our study gives a concept for occurrence of SSS, but its actual physical mechanism in scientific community has not been identified.

Signatures of Disturbed Ionosphere Due to Super Storms above Nepal and Thermospheric O/N$_2$:- In this work, we have attempted to investigate the impact of four super

intense geomagnetic storms (March 2015, June 2015, May 2017 and September 2017) of solar cycle 24 on ionosphere over Nepal. The TEC observed during these periods showed positive and negative ionospheric storms after sudden commencement. Negative ionospheric storm is identified during storm of March 2015 and June 2015, whereas positive ionospheric storm is noticed during storm of May 2017, and September 2017. The VTEC obtained from GPS observations file is compared with global ionospheric models: CODG and IGSG. The study shows, the difference between RINEX VTEC and the model data from CODG and IGSG on Nepalese stations is significant beyond 5 TECU in absolute values. The signatures of predominance morning and afternoon peeks and night time peaks along with the noon bite out profile only identified in RINEX VTEC data but not in the two models CODG and IGSG. Thus, our study recommend for implantation of data of Nepalese GPS station in the global modeling to improve the evolution of VTEC so that the current difference becomes insignificant.

5.2 Recommendations for Future Work

There is plenty of research left on the analyses of numerous difficulties presented in various chapters of this thesis to include other related events. The outcomes and accomplishments of this study contribute to future topics of research project and development directions, which can be summarized as follows:

The landform waves originate in Nepal from the tallest Himalayan mountains, which travel through the stratosphere and lower thermosphere, depositing their energy to those regions and giving rise to secondary gravity waves that can impact on VTEC. For this research, we concentrate only on the ordinary behavior of VTEC, which doesn't allow us to investigate these waves in our climatology research. In the future, another study should be conducted to examine the impact of the wave generated from Himalayas regions on VTEC and also the impact of low atmosphere on VTEC by examining each day separately and employing phase processing technique of GPS signals. Moreover, we have left the study of effect on VTEC due to moderate and weak storms for the future work.

The ionospheric data from globally scattered ionosonde sites can be used to provide a worldwide picture of the impact of SSSs ionospheric parameters. The general perspective of impact of SSSs on horizontal component of geomagnetic field can be obtained by studying from numerous magnetic data across the globe. Inter-hemispheric comparative study on ionospheric parameters and horizontal component of geomagnetic storm could also be future research interest. Furthermore, multi-instrument observations such as ground and satellite based measurements will be the important study to investigate the dynamics of the ionosphere in this region.

CHAPTER 6

6. SUMMARY

6.1   Summary

In this thesis work, we examined how space weather affects solar wind plasma characteristics and how it affects ionospheric variation at mid-latitude. The study's major purpose is to better understand how solar forcing causes short- and long-term variations in solar wind plasma and ionospheric characteristics. The ionosphere is known to change dramatically in its density, temperature, and composition during the course of the solar cycle due to variations in solar activity. Electromagnetic radiation and solar energetic particles originated from solar energetic events are the primary drivers of solar wind plasma and ionospheric changes, as well as the resulting effects to investigate ways that can be utilized to speculate and ease effects due to space weather events on technological devices in space, which are useful to the human kind based technology on the Earth and space-observations. The chapter 1 is stated with motivation of the research by setting specific questions for investigation. It also introduces how ionospheric phenomena and its variability affect our life by producing threat to the critical infrastructure. A brief description of general feature, caprices and vagaries of most prevalent phenomena e.g. EEJ, EIA, PRE, PPEF, and DDEF are discussed. Chapter 2 provides information on relevancy of this thesis work and coherency to the existing knowledge and method used. Chapter 3 provides the overview of geophysical location area of interest, data sets, and methodologies used to analyze the data, and a brief account of devices from which the data chosen for investigation. The main outcomes of the thesis work is discussed in chapter 4. Chapter 5 deals with the conclusion of the entire thesis work and recommendation of future work. The following are decent findings of this thesis study based on data analysis and modeling approaches:

- The shape of diurnal profile of VTEC variation is clearly dependent on the phases of solar cycle: a flat peak in diurnal is noticed during the solar minimum and descending phases of the solar cycle and during the ascending and maximum phases the diurnal plot has Gaussian pattern with different peak amplitudes. The research illustrates that diurnal TEC peaks around 11:00 LT and 14:00 LT, with the lowest levels in the early morning hours. The mean diurnal profile has a wave-like profile in the years 2008, 2009, and 2010, whereas in 2011, 2012, 2013, 2014, 2015, 2016, and 2017, it has a parabolic appearance. Lower value of VTEC signify the week ionospheric activities during minimum phase and greater value

of VTEC signify the higher activities during the maximum phase which are was well synchronized with SSN and solar flux index.

- The solar wind-magnetosphere coupling during two SSSs events has been analyzed using CWT and GWS methods. Both spectrum identified, the most energetic periods are present during the SSSs. The cross-correlation analysis between the IMF B_z and AE index shows the average correlation coefficient ~ -0.88 between the AE and IMF B_z and approximately, with zero lag. Our study supports the previous existing facts that magnetic reconnection between southward IMF B_z and geomagnetic field at the magnetosphere takes place due to the solar wind-magnetosphere coupling during SSSs. The scatting of H-component variation noticed is more during SSS than that on the normal quiet day condition. The pattern of variations was inconsistent and irregular. The decrease of H component has coherency with the large increase of AE index and decrease of AL index of auroral current. The CWT found transient features in signal related to the essential processes of particle and energy transfers during magnetic reconnection. The study of ionospheric parameter had provided the belief of physical components responsible for SSSs event which is still unclear in the scientific community. The scientific community is still working on an understanding of the physical process responsible for the SSSs occurrence.

- The discrepancy in GPS VTEC has acquired during super intense geomagnetic storm on the Nepalese GPS stations is significant beyond 5 TECU in absolute values than two global models CODG and IGSG. The another issue that has noticed in the two models' representations, the signatures in the VTEC noon bite out a profile with a predominance of morning and afternoon peak and nighttime peak were not clearly seen. Because the existing disparities are large, so our study recommend for incorporating certain Nepalese GPS stations into global modeling which could improve the evolution of the VTEC.

Our study has provided some sort of pre-information on forthcoming ionospheric plasma behaviour over Nepal. The understanding of physical process could help in possible refinement in speculating and forecasting quiet and storm time redistribution of ionospheric plasma and creation of irregularities.

REFERENCES

Aarons, J., & Rodger, A. S. (1991). The effects of electric field and ring current energy increases on F layer irregularities at auroral and subauroral latitudes. *Radio Science*, *26*(4), 1115–1129.

Abdu, M. (2001). Outstanding problems in the equatorial ionosphere–thermosphere electrodynamics relevant to spread F. *Journal of Atmospheric and Solar-Terrestrial Physics*, *63*(9), 869–884.

Adhikari, B., Baruwal, P., & Chapagain, N. P. (2017). Analysis of supersubstorm events with reference to polar cap potential and polar cap index. *Earth and Space Science*, *4*(1), 2–15.

Adhikari, B., Dahal, S., & Chapagain, N. P. (2017). Study of field-aligned current (FAC), interplanetary electric field component (Ey), interplanetary magnetic field component (Bz), and northward (x) and eastward (y) components of geomagnetic field during supersubstorm. *Earth and Space Science*, *4*(5), 257–274.

Adhikari, B., Dahal, S., Sapkota, N., Baruwal, P., Bhattarai, B., Khanal, K., & Chapagain, N. P. (2018). Field-Aligned Current and Polar Cap Potential and Geomagnetic Disturbances: A Review of Cross-Correlation Analysis. *Earth and Space Science*, *5*(9), 440–455.

Adhikari, B., Mishra, R. K., Pandit, D., Bhattarai, B., & Chapagain, N. P. (2017). Ionospheric Effect of Non-Storm Hildcaa (High Intensity Long Duration Continuous Auroral Activity). *Journal of Institute of Science and Technology*, *22*(1), 34–40.

Adhikari, B., Poudel, P., & Mishra, R. K. (2020). An Association of solar wind Energy Dynamics with polar Cap Potential and Field Aligned Current during Major Intense Geomagnetic Storms of Solar Cycles 22, 23 and 24. *Earth and Space Science Open Archive ESSOAr*.

Akasofu, S.-I. (1964). The development of the auroral substorm. *Planetary and Space Science*, *12*(4), 273–282.

Akasofu, S.-I. (1981). Energy coupling between the solar wind and the magnetosphere. *Space Science Reviews*, *28*(2), 121–190.

Akasofu, S.-I., & Chapman, S. (1961). The ring current, geomagnetic disturbance, and the Van Allen radiation belts. *Journal of Geophysical Research*, *66*(5), 1321–1350.

Akasofu, S. I., & Chapman, S. (1972). Solar-terrestrial physics. *Quarterly Journal of the Royal Meteorological Society*, *99*(422), 793–793.

Alfvén, H. (1942). Existence of electromagnetic-hydrodynamic waves. *Nature*, *150*(3805), 405–406.

Alken, P., & Maus, S. (2007). Spatio-temporal characterization of the equatorial electrojet from CHAMP, Ørsted, and SAC-C satellite magnetic measurements. *Journal of Geophysical Research: Space Physics*, *112*(A9), A09305–A09305.

Anderson, D., Anghel, A., Yumoto, K., Ishitsuka, M., & Kudeki, E. (2002). Estimating daytime vertical $\vec{E} \times \vec{B}$ drift velocities in the equatorial F-region using ground-based magnetometer observations. *Geophysical Research Letters*, *29*(12), 37–1.

Anderson, D., & Roble, R. (1974). The effect of vertical $\vec{E} \times \vec{B}$ ionospheric drifts on F region neutral winds in the low-latitude thermosphere. *Journal of Geophysical Research*, *79*(34), 5231–5236.

Ansari, K., Park, K.-D., & Panda, S. K. (2019). Empirical Orthogonal Function analysis and modeling of ionospheric TEC over South Korean region. *Acta Astronautica*, *161*, 313–324.

Appleton, E. V. (1946). Two anomalies in the ionosphere. *Nature*, *157*(3995), 691–691.

Appleton, E. V., & Ingram, L. (1935). Magnetic storms and upper-atmospheric ionisation. *Nature*, *136*(3440), 548–549.

Araki, T. (1977). Global structure of geomagnetic sudden commencements. *Planetary and Space Science*, *25*(4), 373–384.

Arikan, F., Erol, C., & Arikan, O. (2004). Regularized estimation of vertical total electron content from GPS data for a desired time period. *Radio Science*, *39*(6), 1–10.

Astafyeva, E., Zakharenkova, I., & Förster, M. (2015). Ionospheric response to the 2015 St. Patrick's Day storm: A global multi-instrumental overview. *Journal of Geophysical Research: Space Physics*, *120*(10), 9023–9037.

Azzouzi, I., Migoya-Orue, Y., Mazaudier, C. A., Fleury, R., Radicella, S. M., & Touzani, A. (2015). Signatures of solar event at middle and low latitudes in the Europe-African sector, during geomagnetic storms, October 2013. *Advances in Space Research*, *56*(9), 2040–2055.

Bagiya, M. S., Joshi, H. P., Iyer, K. N., Aggarwal, M., Ravindran, S., & Pathan, B. M. (2009). Tec variations during low solar activity period (2005–2007) near the

equatorial ionospheric anomaly crest region in india. *Annales Geophysicae*, *27*(3), 1047–1057.

Baker, D., Pulkkinen, T., Hesse, M., & McPherron, R. (1997). A quantitative assessment of energy storage and release in the Earth's magnetotail. *Journal of Geophysical Research: Space Physics*, *102*(A4), 7159–7168.

Balan, N., & Bailey, G. (1995). Equatorial plasma fountain and its effects: Possibility of an additional layer. *Journal of Geophysical Research: Space Physics*, *100*(A11), 21421–21432.

Balan, N., Batista, I., Abdu, M., MacDougall, J., & Bailey, G. (1998). Physical mechanism and statistics of occurrence of an additional layer in the equatorial ionosphere. *Journal of Geophysical Research: Space Physics*, *103*(A12), 29169–29181.

Balan, N., Otsuka, Y., Nishioka, M., Liu, J., & Bailey, G. (2013). Physical mechanisms of the ionospheric storms at equatorial and higher latitudes during the recovery phase of geomagnetic storms. *Journal of Geophysical Research: Space Physics*, *118*(5), 2660–2669.

Balogh, A., Gosling, J., Jokipii, J., Kallenbach, R., & Kunow, H. (1999). *Corotating interaction regions* (Vol. 7). Berlin/Heidelberg, Germany, Springer Science & Business Media.

Bame, S., Asbridge, J., Feldman, W., & Gosling, J. (1976). Solar cycle evolution of high-speed solar wind streams. *The Astrophysical Journal*, *207*, 977–980.

Banks, P. M., Schunk, R. W., & Raitt, W. J. (1976). The topside ionosphere: A region of dynamic transition. *Annual Review of Earth and Planetary Sciences*, *4*(1), 381–440.

Bargatze, L. F., Baker, D., McPherron, R., & Hones Jr, E. W. (1985). Magnetospheric impulse response for many levels of geomagnetic activity. *Journal of Geophysical Research: Space Physics*, *90*(A7), 6387–6394.

Basu, S., Groves, K., Basu, S., & Sultan, P. (2002). Specification and forecasting of scintillations in communication/navigation links: current status and future plans. *Journal of Atmospheric and Solar-Terrestrial Physics*, *64*(16), 1745–1754.

Belehaki, A., & Tsagouri, I. (2002). Investigation of the relative bottomside/topside contribution to the total electron content estimates. *Annals of Geophysics*, *45*(1), 73–86.

Benz, A. (2008). Flare Observations. *Living Reviews in Solar Physics*, *5*(1), 1–64.

Biermann, L. F. (2013). Solar Corpuscular Radiation and the Interplanetary Gas. In *A source book in astronomy and astrophysics, 1900–1975*. Massachusetts, USA, Harvard University Press.

Birkeland, K. (1913). *The Norwegian aurora polaris expedition 1902-1903*. H. Aschelhoug & Company.

Blagoveshchensky, D., Pirog, O., Polekh, N., & Chistyakova, L. (2003). Mid-latitude effects of the May 15, 1997 magnetic storm. *Journal of Atmospheric and Solar-Terrestrial physics*, *65*(2), 203–210.

Blanc, M., & Richmond, A. D. (1980). The ionospheric disturbance dynamo. *Journal of Geophysical Research: Space Physics*, *85*(A4), 1669–1686.

Bothmer, V., & Daglis, I. A. (2007). *Space weather: physics and effects*. Berlin/Heidelberg, Germany, Springer Science & Business Media.

Breit, G., & Tuve, M. A. (1926). A test of the existence of the conducting layer. *Physical Review*, *28*(3), 554.

Bremer, J. (2005). Investigations of long-term trends in the ionosphere with world-wide ionosonde observations. *Advances in Radio Science*, *2*(G. 2), 253–258.

Broussard, R., Sheeley, N., Tousey, R., & Underwood, J. (1978). A survey of coronal holes and their solar wind associations throughout sunspot cycle 20. *Solar Physics*, *56*(1), 161–183.

Budden, K. G. (1985). *The Propagation of Radio Waves*. Cambridge, England, Cambridge University Press.

Buonsanto, M. J. (1999). Ionospheric storms—A review. *Space Science Reviews*, *88*(3), 563–601.

Burkard, O. (1951). Die halbjährige Periode der F 2-Schicht-Ionisation. *Archiv für Meteorologie, Geophysik und Bioklimatologie, Serie A*, *4*(1), 391–402.

Burlaga, L., Sittler, E., Mariani, F., & Schwenn, a. R. (1981). Magnetic loop behind an interplanetary shock: Voyager, Helios, and IMP 8 observations. *Journal of Geophysical Research: Space Physics*, *86*(A8), 6673–6684.

Cander, L. (1993). On the global and regional behaviour of the mid-latitude ionosphere. *Journal of Atmospheric and Terrestrial Physics*, *55*(11), 1543-1551.

Cander, L. R., & Mihajlovic, S. (1998). Forecasting ionospheric structure during the great geomagnetic storms. *Journal of Geophysical Research: Space Physics*, *103*(A1), 391–398.

Cerveny, R. S. (2006). *Freaks of the storm: from flying cows to stealing thunder, the world's strangest true weather stories*. New York, USA, Basic Books.

Chapagain, N. P. (2011). *Dynamics of equatorial spread F using ground-based optical and radar measurements*. Utah State University, Logan, Utah, USA.

Chapagain, N. P., Fejer, B. G., & Chau, J. L. (2009). Climatology of postsunset equatorial spread F over Jicamarca. *Journal of Geophysical Research: Space Physics*, *114*(A7), A07307–A07307.

Chapagain, N. P., Makela, J. J., Meriwether, J. W., Fisher, D. J., Buriti, R. A., & Medeiros, A. F. (2012). Comparison of nighttime zonal neutral winds and equatorial plasma bubble drift velocities over brazil. *Journal of Geophysical Research: Space Physics*, *117*(A6).

Chapagain, N. P., Taylor, M. J., Makela, J. J., & Duly, T. M. (2012). Equatorial plasma bubble zonal velocity using 630.0 nm airglow observations and plasma drift modeling over Ascension Island. *Journal of Geophysical Research: Space Physics*, *117*(A6), A06316–A06316.

Chapman, S. (1951). The equatorial electrojet as detected from the abnormal electric current distribution above Huancayo, Peru, and elsewhere. *Archiv Fuer Meteorologie, Geophysik und Bioklimatologie, Serie A*, *4*(1), 368–390.

Chapman, S., & Bartels, J. (1940). *Geomagnetism*. Oxford University Press, Oxford, England.

Chapman, S., & Ferraro, V. C. (1930). A new theory of magnetic storms. *Nature*, *126*(3169), 129–130.

Chen, P., Liu, H., Ma, Y., & Zheng, N. (2020). Accuracy and consistency of different global ionospheric maps released by IGS ionosphere associate analysis centers. *Advances in Space Research*, *65*(1), 163–174.

Christian, Z., Ouattara, F., Emmanuel, N., Rolland, F., & Francois, Z. (2013). CODG TEC variation during solar maximum and minimum over Niamey. *European Scientific Journal*, *9*(27), 74–80.

Chun, F. K., & Russell, C. T. (1997). Field-aligned currents in the inner magnetosphere: Control by geomagnetic activity. *Journal of Geophysical Research: Space Physics*, *102*(A2), 2261–2270.

Cid, C., Palacios, J., Saiz, E., Cerrato, Y., Aguado, J., & Guerrero, A. (2013). Modeling the recovery phase of extreme geomagnetic storms. *Journal of Geophysical Research: Space Physics*, *118*(7), 4352-4359.

Ciraolo, L., & Spalla, P. (1997). Comparison of ionospheric total electron content from the Navy Navigation Satellite System and the GPS. *Radio Science*, *32*(3), 1071–1080.

Cliver, E. (2006). The 1859 space weather event: Then and now. *Advances in Space Research*, *38*(2), 119–129.

Coker, C., Hunsucker, R. D., & Lott, G. (1995). Detection of auroral activity using GPS satellites. *Geophysical Research Letters*, *22*(23), 3259–3262.

Coley, W., McClure, J., & Hanson, W. (1990). Equatorial fountain effect and dynamo drift signatures from AE-E observations. *Journal of Geophysical Research: Space Physics*, *95*(A12), 21285–21290.

Cowling, T. (1948). Electrical conductivity of the ionospheric D region. *Nature*, *162*(4108), 142–143.

Cox, L., & Evans, J. (1970). Seasonal variation of the O/N2 ratio in the F 1 region. *Journal of Geophysical Research*, *75*(31), 6271–6286.

Da Costa, A. M., Domingues, M. O., Mendes, O., & Brum, C. G. M. (2011). Interplanetary medium condition effects in the South Atlantic Magnetic Anomaly: A case study. *Journal of Atmospheric and Solar-Terrestrial Physics*, *73*(11), 1478–1491.

Daglis, I. A., Thorne, R. M., Baumjohann, W., & Orsini, S. (1999). The terrestrial ring current: Origin, formation, and decay. *Reviews of Geophysics*, *37*(4), 407–438.

Dani, T., & Sulistiani, S. (2019). Prediction of maximum amplitude of solar cycle 25 using machine learning. In *Journal of physics: Conference series* (Vol. 1231, p. 012022).

Danilov, A., & Lastovicka, J. (2001). Effects of geomagnetic storms on the ionosphere and atmosphere. *International Journal of Geomagnetism and Aeronomy*, *2*(3), 209–224.

Dashora, N., & Suresh, S. (2015). Characteristics of low-latitude TEC during solar cycles 23 and 24 using global ionospheric maps (GIMs) over Indian sector. *Journal of Geophysical Research: Space Physics*, *120*(6), 5176–5193.

Daubechies, I. (1992). *Ten lectures on wavelets*. Pennsylvania,USA, Society for Industrial and Applied Mathematics (SIAM).

Davis, T. N., & Sugiura, M. (1966). Auroral electrojet activity index AE and its universal time variations. *Journal of Geophysical Research*, *71*(3), 785–801.

De Abreu, A., Fagundes, P., Bolzan, M., de Jesus, R., Pillat, V., Abalde, J., & Lima, W. (2014). The role of the traveling planetary wave ionospheric disturbances on the equatorial F region post-sunset height rise during the last extreme low solar activity and comparison with high solar activity. *Journal of Atmospheric and Solar-Terrestrial Physics*, *113*, 47–57.

De Abreu, A., Fagundes, P., Bolzan, M., Gende, M., Brunini, C., De Jesus, R., . . . Lima, W. (2014). Traveling planetary wave ionospheric disturbances and their role in the generation of equatorial spread-F and GPS phase fluctuations during the last extreme low solar activity and comparison with high solar activity. *Journal of Atmospheric and Solar-Terrestrial Physics*, *117*, 7–19.

De Abreu, A., Fagundes, P., Gende, M., Bolaji, O., De Jesus, R., & Brunini, C. (2014). Investigation of ionospheric response to two moderate geomagnetic storms using GPS–TEC measurements in the South American and African sectors during the ascending phase of solar cycle 24. *Advances in Space Research*, *53*(9), 1313–1328.

De Jesus, R., Sahai, Y., Fagundes, P., De Abreu, A., Brunini, C., Gende, M., . . . Pillat, V. (2013). Response of equatorial, low-and mid-latitude F-region in the American sector during the intense geomagnetic storm on 24–25 October 2011. *Advances in Space Research*, *52*(1), 147–157.

De La Torre, A., Alexander, P., Llamedo, P., Hierro, R., Nava, B., Radicella, S., . . . Wickert, J. (2014). Wave activity at ionospheric heights above the Andes Mountains detected from FORMOSAT-3/COSMIC GPS radio occultation data. *Journal of Geophysical Research: Space Physics*, *119*(3), 2046–2051.

De Lucas, A., Gonzalez, W. D., Echer, E., Guarnieri, F., Dal Lago, A., Da Silva, M., . . . Schuch, N. (2007). Energy balance during intense and super-intense magnetic storms using an Akasofu ε parameter corrected by the solar wind dynamic pressure. *Journal of Atmospheric and Solar-Terrestrial Physics*, *69*(15), 1851–1863.

Despirak, I., Kleimenova, N., Gromova, L., Gromov, S., & Malysheva, L. (2019). Supersubstorms during strong magnetic storm on 7 September 2017. In *E3s web of conferences* (Vol. 127, p. 01010).

Despirak, I., Lubchich, A., & Kleimenova, N. (2018). Large-scale structure of solar wind and appearance of supersubstorms. *Physics of Auroral Phenomena*, *41*(1), 11–13.

Despirak, I., Lyubchich, A., Kleimenova, N., Gromova, L., Gromov, S., & Malysheva, L. (2021). Longitude Geomagnetic Effects of the Supersubstorms during the

Magnetic Storm of March 9, 2012. *Bulletin of the Russian Academy of Sciences: Physics*, *85*(3), 246–251.

Dimmock, A., Nykyri, K., Karimabadi, H., Osmane, A., & Pulkkinen, T. (2015). A statistical study into the spatial distribution and dawn-dusk asymmetry of dayside magnetosheath ion temperatures as a function of upstream solar wind conditions. *Journal of Geophysical Research: Space Physics*, *120*(4), 2767–2782.

Domingues, M. O., Mendes Jr, O., & da Costa, A. M. (2005). On wavelet techniques in atmospheric sciences. *Advances in Space Research*, *35*(5), 831–842.

D'silva, S., & Choudhuri, A. (1993). A theoretical model for tilts of bipolar magnetic regions. *Astronomy and Astrophysics*, *272*, 621–633.

Dungey, J. W. (1961). Interplanetary magnetic field and the auroral zones. *Physical Review Letters*, *6*(2), 47–48.

Eccles, J., St. Maurice, J., & Schunk, R. (2015). Mechanisms underlying the prereversal enhancement of the vertical plasma drift in the low-latitude ionosphere. *Journal of Geophysical Research: Space Physics*, *120*(6), 4950–4970.

Echer, E., Gonzalez, W. D., Tsurutani, B. T., & Gonzalez, A. C. (2008). Interplanetary conditions causing intense geomagnetic storms (Dst≤– 100 nT) during solar cycle 23 (1996–2006). *Journal of Geophysical Research: Space Physics*, *113*(A5), A05221–A05221.

Egedal, J. (1947). The magnetic diurnal variation of the horizontal force near the magnetic equator. *Terrestrial Magnetism and Atmospheric Electricity*, *52*(4), 449–451.

Farley, D., Bonelli, E., Fejer, B. G., & Larsen, M. (1986). The prereversal enhancement of the zonal electric field in the equatorial ionosphere. *Journal of Geophysical Research: Space Physics*, *91*(A12), 13723–13728.

Fejer, B. G., Blanc, M., & Richmond, A. D. (2017). Post-storm middle and low-latitude ionospheric electric fields effects. *Space Science Reviews*, *206*(1), 407–429.

Fejer, B. G., De Paula, E., Gonzalez, S., & Woodman, R. (1991). Average vertical and zonal F region plasma drifts over Jicamarca. *Journal of Geophysical Research: Space Physics*, *96*(A8), 13901–13906.

Fejer, B. G., Farley, D., Gonzales, C., Woodman, R., & Calderon, C. (1981). F region east-west drifts at Jicamarca. *Journal of Geophysical Research: Space Physics*, *86*(A1), 215–218.

Fejer, B. G., Gonzales, C., Farley, D., Kelley, M. C., & Woodman, R. (1979). Equatorial electric fields during magnetically disturbed conditions 1. The effect of the interplanetary magnetic field. *Journal of Geophysical Research: Space Physics*, *84*(A10), 5797–5802.

Fejer, B. G., Jensen, J. W., & Su, S.-Y. (2008). Quiet time equatorial F region vertical plasma drift model derived from ROCSAT-1 observations. *Journal of Geophysical Research: Space Physics*, *113*(A5), A05304–A05304.

Fejer, B. G., Larsen, M., & Farley, D. (1983). Equatorial disturbance dynamo electric fields. *Geophysical Research Letters*, *10*(7), 537–540.

Fejer, B. G., & Scherliess, L. (1995). Time dependent response of equatorial ionospheric electric fields to magnetospheric disturbances. *Geophysical Research Letters*, *22*(7), 851–854.

Fejer, B. G., & Scherliess, L. (1997). Empirical models of storm time equatorial zonal electric fields. *Journal of Geophysical Research: Space Physics*, *102*(A11), 24047–24056.

Fejer, B. G., Tracy, B. D., & Pfaff, R. F. (2013). Equatorial zonal plasma drifts measured by the C/NOFS satellite during the 2008–2011 solar minimum. *Journal of Geophysical Research: Space Physics*, *118*(6), 3891–3897.

Feldman, U., Landi, E., & Schwadron, N. (2005). On the sources of fast and slow solar wind. *Journal of Geophysical Research: Space Physics*, *110*(A7), A07109–A07109.

Forsyth, R., & Gosling, J. (2001). Corotating and transient structures in the heliosphere. In M. R. . S. E. Balogh A. (Ed.), *The Heliosphere Near Solar Minimum: The Ulysses Perspective*. New York, NY: Springer.

Friedman, H. (1986). *Sun and Earth*. California, USA, Scientific American Library.

Fuller-Rowell, T., Codrescu, M., Moffett, R., & Quegan, S. (1994). Response of the thermosphere and ionosphere to geomagnetic storms. *Journal of Geophysical Research: Space Physics*, *99*(A3), 3893–3914.

Garrett, H., Dessler, A., & Hill, T. W. (1974). Influence of solar wind variability on geomagnetic activity. *Journal of Geophysical Research*, *79*(31), 4603–4610.

Ghimire, B. D., Chapagain, N. P., Basnet, V., Bhatta, K., & Khadka, B. (2020). Variation of Total Electron Content (TEC) in the Quite and Disturbed days and their correlation with Geomagnetic Parameters of Lamjung Station in the year of 2015. *Bibechana*, *17*, 123–132.

Gjerloev, J. (2012). The SuperMAG data processing technique. *Journal of Geophysical Research: Space Physics*, *117*(A9), A09213–A09213.

Goncharenko, L., Foster, J., Coster, A., Huang, C., Aponte, N., & Paxton, L. (2007). Observations of a positive storm phase on September 10, 2005. *Journal of Atmospheric and Solar-Terrestrial Physics*, *69*(10), 1253–1272.

Gonzalez, W. D., Echer, E., Clua-Gonzalez, A., & Tsurutani, B. T. (2007). Interplanetary origin of intense geomagnetic storms (Dst<- 100 nT) during solar cycle 23. *Geophysical Research Letters*, *34*(6), L06101.

Gonzalez, W. D., Joselyn, J.-A., Kamide, Y., Kroehl, H. W., Rostoker, G., Tsurutani, B. T., & Vasyliunas, V. (1994). What is a geomagnetic storm? *Journal of Geophysical Research: Space Physics*, *99*(A4), 5771–5792.

Gonzalez, W. D., Tsurutani, B. T., & De Gonzalez, A. L. C. (1999). Interplanetary origin of geomagnetic storms. *Space Science Reviews*, *88*(3), 529–562.

Gosling, J. (1997). Coronal mass ejections: An overview. *American Geophysical Union Geophysical Monograph Series*, *99*, 9–16.

Grodji, F., Doumbia, V., Boka, K., Amory-Mazaudier, C., Cohen, Y., & Fleury, R. (2017). Estimating some parameters of the equatorial ionosphere electrodynamics from ionosonde data in West Africa. *Advances in Space Research*, *59*(1), 311–325.

Grossmann, A., Morlet, J., & Paul, T. (1985). Transforms associated to square integrable group representations. I. General results. *Journal of Mathematical Physics*, *26*(10), 2473–2479.

Guarnieri, F. L., Tsurutani, B. T., Gonzalez, W. D., Echer, E., Gonzalez, A. L., Grande, M., & Soraas, F. (2006). ICME and CIR storms with particular emphasis on HILDCAA events. In *Ilws workshop* (pp. 19–20).

Gupta, J. K., & Singh, L. (2000). Long term ionospheric electron content variations over delhi. *Annales Geophysicae*, *18*(12), 1635–1644.

Haase, J. S., Dautermann, T., Taylor, M. J., Chapagain, N., Calais, E., & Pautet, D. (2011). Propagation of plasma bubbles observed in Brazil from GPS and airglow data. *Advances in Space Research*, *47*(10), 1758–1776.

Hada, T., & Kennel, C. (1985). Nonlinear evolution of slow waves in the solar wind. *Journal of Geophysical Research: Space Physics*, *90*(A1), 531–535.

Hajra, R., Echer, E., Tsurutani, B. T., & Gonzalez, W. D. (2013). Solar cycle dependence of High-Intensity Long-Duration Continuous AE Activity (HILDCAA)

events, relativistic electron predictors? *Journal of Geophysical Research: Space Physics*, *118*(9), 5626–5638.

Hajra, R., Tsurutani, B. T., Echer, E., Gonzalez, W. D., & Gjerloev, J. W. (2016). Supersubstorms (SML≤ − 2500 nT): Magnetic storm and solar cycle dependences. *Journal of Geophysical Research: Space Physics*, *121*(8), 7805–7816.

Hanson, W., & Moffett, R. (1966). Ionization transport effects in the equatorial F region. *Journal of Geophysical Research*, *71*, 5559–5572.

Hargreaves, J. K. (1992). *The solar-terrestrial environment: an introduction to geospace-the science of the terrestrial upper atmosphere, ionosphere, and magnetosphere*. Cambridge, England, Cambridge university press.

Hasegawa, M. (1960). On the position of the focus of the geomagnetic Sq current system. *Journal of Geophysical Research*, *65*(5), 1437–1447.

Heelis, R., Sojka, J. J., David, M., & Schunk, R. (2009). Storm time density enhancements in the middle-latitude dayside ionosphere. *Journal of Geophysical Research: Space Physics*, *114*(A3), A03315.

Henderson, M., Reeves, G., Belian, R., & Murphree, J. (1996). Observations of magnetospheric substorms occurring with no apparent solar wind/IMF trigger. *Journal of Geophysical Research: Space Physics*, *101*(A5), 10773–10791.

Hernández-Pajares, M., Juan, J., Sanz, J., Orus, R., Garcia-Rigo, A., Feltens, J., . . . Krankowski, A. (2009). The IGS VTEC maps: a reliable source of ionospheric information since 1998. *Journal of Geodesy*, *83*(3-4), 263–275.

Hofmann-Wellenhof, B., Lichtenegger, H., & Collins, J. (1992). *Global Positioning System (GPS). Theory and practice*. Midtown Manhattan, New York, Springer.

Howe, R. (2009). Solar interior rotation and its variation. *Living Reviews in Solar Physics*, *6*(1), 1–75.

Hubbard, B. B. (1996). *The world according to wavelets the story of a mathematical technique in the making*. Natick, Massachusetts A K Peters, CRC Press.

Hui, D., Chakrabarty, D., Sekar, R., Reeves, G. D., Yoshikawa, A., & Shiokawa, K. (2017). Contribution of storm time substorms to the prompt electric field disturbances in the equatorial ionosphere. *Journal of Geophysical Research: Space Physics*, *122*(5), 5568–5578.

Hunsucker, R. D. (1991). Radio techniques for probing the terrestrial ionosphere. *Physics and Chemistry in Space*, *22*, 293.

Hunsucker, R. D., & Hargreaves, J. K. (2007). *The high-latitude ionosphere and its effects on radio propagation.* Cambridge, England, Cambridge University Press.

Iijima, T., & Potemra, T. (1982). The relationship between interplanetary quantities and Birkeland current densities. *Geophysical Research Letters*, *9*(4), 442–445.

Iijima, T., & Potemra, T. A. (1976). Field-aligned currents in the dayside cusp observed by Triad. *Journal of Geophysical Research*, *81*(34), 5971–5979.

Iyemori, T. (1990). Storm-time magnetospheric currents inferred from mid-latitude geomagnetic field variations. *Journal of Geomagnetism and Geoelectricity*, *42*(11), 1249–1265.

Jain, A. (1987). Reversal of E x B drift and post-sunset enhancement of the ionospheric total electron content at equatorial latitudes. *Indian Journal of Radio and Space Physics*, *16*, 267-272.

Jankowski, J., & Sucksdorff, C. (1996). IAGA Guide for magnetic measurements and observatory practice [Computer software manual]. Warsaw, Poland: International Association of Geomagnetism and Aeronomy.

Jing, J., Yurchyshyn, V. B., Yang, G., Xu, Y., & Wang, H. (2004). On the relation between filament eruptions, flares, and coronal mass ejections. *The Astrophysical Journal*, *614*(2), 1054–1062.

Johnson, J. R., & Wing, S. (2014). External versus internal triggering of substorms: An information-theoretical approach. *Geophysical Research Letters*, *41*(16), 5748–5754.

Jones, K. (1971). Storm time variation of F2-layer electron concentration. *Journal of Atmospheric and Terrestrial Physics*, *33*(3), 379–389.

Judge, P. G., & Thompson, M. J. (2011). Solar and stellar activity: diagnostics and indices. *Proceedings of the International Astronomical Union*, *7*(S286), 15–26.

Kamide, Y., & Brekke, A. (1975). Auroral electrojet current density deduced from the Chatanika radar and from the Alaska meridian chain of magnetic observatories. *Journal of Geophysical Research*, *80*(4), 587–594.

Kamide, Y., & Chian, A. C.-L. (2007). *Handbook of the solar-terrestrial environment.* Springer Science & Business Media, Berlin/Heidelberg, Germany.

Kamide, Y., & Kokubun, S. (1996). Two-component auroral electrojet: Importance for substorm studies. *Journal of Geophysical Research: Space Physics*, *101*(A6), 13027–13046.

Kamide, Y., Richmond, A. D., & Matsushita, S. (1981). Estimation of ionospheric electric fields, ionospheric currents, and field-aligned currents from ground magnetic records. *Journal of Geophysical Research: Space Physics*, *86*(A2), 801–813.

Kamide, Y., Yokoyama, N., Gonzalez, W. D., Tsurutani, B. T., Daglis, I., Brekke, A., & Masuda, S. (1998). Two-step development of geomagnetic storms. *Journal of Geophysical Research: Space Physics*, *103*(A4), 6917–6921.

Kan, J., & Lee, L. (1979). Energy coupling function and solar wind-magnetosphere dynamo. *Geophysical Research Letters*, *6*(7), 577–580.

Kane, R. P. (2002). Some implications using the group sunspot number reconstruction. *Solar Physics*, *205*(2), 383–401.

Kashcheyev, A., Migoya-Orué, Y., Amory-Mazaudier, C., Fleury, R., Nava, B., Alazo-Cuartas, K., & Radicella, S. (2018). Multivariable comprehensive analysis of two great geomagnetic storms of 2015. *Journal of Geophysical Research: Space Physics*, *123*(6), 5000–5018.

Katz, R. W. (1988). Use of cross correlations in the search for teleconnections. *Journal of Climatology*, *8*(3), 241–253.

Kelley, M. C. (1989). *The Earth's ionosphere: Plasma physics and electrodynamics*. Academic Press, Massachusetts, United States.

Kelley, M. C. (2009). *The Earth's ionosphere: plasma physics and electrodynamics*. Cambridge, Massachusetts Academic Press.

Kelley, M. C., Fejer, B. G., & Gonzales, C. (1979). An explanation for anomalous equatorial ionospheric electric fields associated with a northward turning of the interplanetary magnetic field. *Geophysical Research Letters*, *6*(4), 301–304.

Kelley, M. C., Makela, J. J., Chau, J. L., & Nicolls, M. J. (2003). Penetration of the solar wind electric field into the magnetosphere/ionosphere system. *Geophysical Research Letters*, *30*(4).

Kepko, L., McPherron, R., Amm, O., Apatenkov, S., Baumjohann, W., Birn, J., . . . Sergeev, V. (2015). Substorm current wedge revisited. *Space Science Reviews*, *190*(1), 1–46.

Khadka, S. M. (2018). *Multi-Diagnostic Investigations of the Equatorial and Low-Latitude Ionospheric Electrodynamics and Their Impacts on Space-Based Technologies* (Unpublished doctoral dissertation). Boston College, Massachusetts, USA.

Khan, A., & Jin, S. (2018). Gravity wave activities in Tibet observed by COSMIC GPS radio occultation. *Geodesy and Geodynamics*, *9*(6), 504–511.

Kil, H., & Paxton, L. J. (2006). Ionospheric disturbances during the magnetic storm of 15 July 2000: Role of the fountain effect and plasma bubbles for the formation of large equatorial plasma density depletions. *Journal of Geophysical Research: Space Physics*, *111*(A12), A12311–A12311.

Kivelson, M. G., Kivelson, M. G., & Russell, C. T. (1995). *Introduction to space physics*. Cambridge, England, Cambridge university press.

Klobuchar, J. A. (1991). Ionospheric effect on GPS. *GPS World*, *2*(4), 48–51.

Klobuchar, J. A. (1996). Ionospheric effects on GPS. In S.-J. Parkinson B.W (Ed.), *Global positioning system: theory and application.* Washington, DC: American Institute of Aeronautics and Astronautics.

Knipp, D., Emery, B., Engebretson, M., Li, X., McAllister, A., Mukai, T., . . . others (1998). An overview of the early November 1993 geomagnetic storm. *Journal of Geophysical Research: Space Physics*, *103*(A11), 26197–26220.

Koskinen, H. E. (2011). *Physics of space storms: From the solar surface to the Earth.* Berlin/Heidelberg, Germany, Springer Science & Business Media.

Koskinen, H. E., & Tanskanen, E. I. (2002). Magnetospheric energy budget and the epsilon parameter. *Journal of Geophysical Research: Space Physics*, *107*(A11), 1415–1425.

Krankowsky, D., Kasprzak, W., & Nier, A. O. (1968). Mass spectrometric studies of the composition of the lower thermosphere during summer 1967. *Journal of Geophysical Research*, *73*(23), 7291–7306.

Krieger, A., Timothy, A., & Roelof, E. (1973). A coronal hole and its identification as the source of a high velocity solar wind stream. *Solar Physics*, *29*(2), 505–525.

Lakhina, G., Alex, S., Mukherjee, S., & Vichare, G. (2006). On magnetic storms and substorms. In N. Gopalswamy & A. Bhattacharyya (Eds.), *Proceedings of the ilws workshop.* Goa, India.

Lakshmi, D. R., Veenadhari, B., Dabas, R. S., & Reddy, B. M. (1997). Sudden post-midnight decrease in equatorial f-region electron densities associated with severe magnetic storms. *Annales Geophysicae*, *15*(3), 306–313.

Lal, C. (1996). Seasonal trend of geomagnetic activity derived from solar-terrestrial geometry confirms an axial-equinoctial theory and reveals deficiency in planetary indices. *Journal of Atmospheric and Terrestrial Physics*, *58*(13), 1497–1506.

Langley, R. B. (2000). GPS, the Ionosphere, and the Solar Maximum. *GPS world*, *11*(7), 44–49.

Lanza, R., Meloni, A., et al. (2006). *The Earth's magnetism*. Midtown Manhattan, New York City, Springer.

Legrand, J. P., & Simon, P. A. (1989). Solar cycle and geomagnetic activity: a review for geophysicists. Part 1. The contributions to geomagnetic activity of shock waves and of the solar wind. *Annales Geophysicae*, *7*, 565-593.

Lei, J., Huang, F., Chen, X., Zhong, J., Ren, D., Wang, W., . . . et al. (2018). Was magnetic storm the only driver of the long-duration enhancements of daytime total electron content in the Asian-Australian sector between 7 and 12 September 2017? *Journal of Geophysical Research: Space Physics*, *123*(4), 3217–3232.

Leutbecher, M., & Volkert, H. (2000). The propagation of mountain waves into the stratosphere: Quantitative evaluation of three-dimensional simulations. *Journal of the Atmospheric Sciences*, *57*(18), 3090–3108.

Lewis, R. V., Freeman, M. P., Rodger, A. S., Reeves, G. D., & Milling, D. K. (1997). The electric field response to the growth phase and expansion phase onset of a small isolated substorm. *Annales Geophysicae*, *15*(3), 289–299.

Li, Y., Luhmann, J., Lynch, B., & Kilpua, E. (2011). Cyclic reversal of magnetic cloud poloidal field. *Solar Physics*, *270*(1), 331–346.

Liu, G., & Shen, H. (2017). A severe negative response of the ionosphere to the intense geomagnetic storm on March 17, 2015 observed at mid-and low-latitude stations in the China zone. *Advances in Space Research*, *59*(9), 2301–2312.

Liu, L., Wan, W., Chen, Y., & Le, H. (2011). Solar activity effects of the ionosphere: A brief review. *Chinese Science Bulletin*, *56*(12), 1202–1211.

Liu, L., Wan, W., Ning, B., & Zhang, M.-L. (2009). Climatology of the mean total electron content derived from GPS global ionospheric maps. *Journal of Geophysical Research: Space Physics*, *114*(A6), A06308–A06308.

Liu, L., Zou, S., Yao, Y., & Aa, E. (2020). Multi-scale ionosphere responses to the May 2017 magnetic storm over the Asian sector. *GPS Solutions*, *24*(1), 1–15.

Lui, A. (1991). A synthesis of magnetospheric substorm models. *Journal of Geophysical Research: Space Physics*, *96*(A2), 1849–1856.

Macana, R., Moirangthem, T., & Baik, O. (2018). Shielding effectiveness of electromagnetic energy from 50-ohm radio frequency heating system for disinfestation

of stored grains. In *2018 asabe annual international meeting* (p. 1). American Society of Agricultural and Biological Engineers.

Maeda, K., Hedin, A., & Mayr, H. (1986). Hemispheric asymmetries of the thermospheric semiannual oscillation. *Journal of Geophysical Research: Space Physics*, *91*(A4), 4461–4470.

Mahesh, P., Roshni, A., Shweta, M., & Purohit, P. (2019). Latitudinal variation of ionospheric TEC at Northern Hemispheric region. *Russian Journal of Earth Sciences*, *19*(1), ES1003–ES1003.

Manju, G., Devasia, C. V., & Sridharan, R. (2007). On the seasonal variations of the threshold height for the occurrence of equatorial spread f during solar minimum and maximum years. *Annales Geophysicae*, *25*(4), 855–861.

Mannucci, A., Tsurutani, B., Iijima, B., Komjathy, A., Saito, A., Gonzalez, W., . . . Skoug, R. (2005). Dayside global ionospheric response to the major interplanetary events of october 29–30, 2003 "halloween storms". *Geophysical Research Letters*, *32*(12).

Mannucci, A., Tsurutani, B. T., Abdu, M., Gonzalez, W. D., Komjathy, A., Echer, E., . . . Anderson, D. (2008). Superposed epoch analysis of the dayside ionospheric response to four intense geomagnetic storms. *Journal of Geophysical Research: Space Physics*, *113*(A3), A00A02–A00A02.

Manoj, C., Maus, S., Lühr, H., & Alken, P. (2008). Penetration characteristics of the interplanetary electric field to the daytime equatorial ionosphere. *Journal of Geophysical Research: Space Physics*, *113*(A12), A12310–A12310.

Mansilla, G. A. (2013). Solar Cycle and Seasonal Distribution of Geomagnetic Storms with Sudden Commencement. *Earth Science Research*, *3*(1), 50–55.

Mari, G., & Popescu, M. (2004). Solar flare cycles. *Romanian Reports in Physics*, *56*(2), 141–169.

Marques de Souza, A., Echer, E., Jose Alves Bolzan, M., & Hajra, R. (2018). Cross-correlation and cross-wavelet analyses of the solar wind IMF B_z and auroral electrojet index AE coupling during HILDCAAs. *Annales Geophysicae*, *36*(1), 205-211.

Martyn, D. F. (1955). The physics of the ionosphere. *The Physical Society, London*, *254*, 260–264.

Matuura, N. (1974). Electric fields deduced from the thermospheric model. *Journal of Geophysical Research*, *79*(31), 4679–4689.

Maunder, E. W. (1904). The solar origin of the disturbances of terrestrial magnetism. *Astronomische Nachrichten*, *167*(11), 177–182.

Mavromichalaki, H., & Vassilaki, A. (1998). Fast plasma streams recorded near the Earth during 1985–1996. *Solar physics*, *183*(1), 181–200.

Mazaudier, C., & Venkateswaran, S. V. (1990). Delayed ionospheric effects of the geomagnetic storms of March 22, 1979 studied by the sixth co-ordinated data analysis workshop (CDAW-6). *Annales Geophysicae*, *8*, 511-518.

McPherron, R. L. (1991). Physical processes producing magnetospheric substorms and magnetic storms. *Geomagnetism*, *4*, 593–739.

McPherron, R. L., Russell, C. T., & Aubry, M. P. (1973). Satellite studies of magnetospheric substorms on August 15, 1968: 9. Phenomenological model for substorms. *Journal of Geophysical Research*, *78*(16), 3131–3149.

Mendes, O. J. (1992). *A origem interplanetaria eo desenvolvimento da fase principal das tempestades geomagneticas moderadas (1978–1979)* (Unpublished doctoral dissertation). PhD thesis, INPE-5445-TDI/491, São José dos Campos, São Paulo, Brazil.

Mendes Jr, O., Domingues, M. O., Da Costa, A. M., & De Gonzalez, A. L. C. (2005). Wavelet analysis applied to magnetograms: Singularity detections related to geomagnetic storms. *Journal of Atmospheric and Solar-Terrestrial Physics*, *67*(17-18), 1827–1836.

Menvielle, M., & Marchaudon, A. (2007). Geomagnetic indices in solar-terrestrial physics and space weather. In *Space weather*. Midtown Manhattan, New York City, Springer.

Miesch, M. S., & Teweldebirhan, K. (2016). A three-dimensional Babcock–Leighton solar dynamo model: initial results with axisymmetric flows. *Advances in Space Research*, *58*(8), 1571–1588.

Mikhailov, A., Terekhin, Y. L., Skoblin, M., & Mikhailov, V. (1992). On the physical mechanism of the ionospheric storms in the F2-layer. *Advances in Space Research*, *12*(10), 269–272.

Millward, G., Rishbeth, H., Fuller-Rowell, T., Aylward, A., Quegan, S., & Moffett, R. (1996). Ionospheric F 2 layer seasonal and semiannual variations. *Journal of Geophysical Research: Space Physics*, *101*(A3), 5149–5156.

Mochalov, V., & Mochalova, A. (2019, October). Extraction of ionosphere parameters in ionograms using deep learning. In *E3s web of conferences* (Vol. 127, p. 01004).

Mohanakumar, K. (2008). *Stratosphere troposphere interactions: an introduction.* Berlin/Heidelberg, Germany, Springer Science & Business Media.

Morioka, A., Miyoshi, Y., Seki, T., Tsuchiya, F., Misawa, H., Oya, H., . . . et al. (2003). AKR disappearance during magnetic storms. *Journal of Geophysical Research: Space Physics*, *108*(A6), 1226–1234.

Mullan, D. J. (2000). Solar Physics: from the deep interior to the hot corona. In *From the Sun to the great attractor.* Midtown Manhattan, New York City, Springer.

Narayanan, V. L., Gurubaran, S., Shiny, M. B., Emperumal, K., & Patil, P. (2017). Some new insights of the characteristics of equatorial plasma bubbles obtained from Indian region. *Journal of Atmospheric and Solar-Terrestrial Physics*, *156*, 80–86.

Narayanan, V. L., Sau, S., Gurubaran, S., Shiokawa, K., Balan, N., Emperumal, K., & Sripathi, S. (2014). A statistical study of satellite traces and evolution of equatorial spread F. *Earth, Planets and Space*, *66*(1), 1–13.

Nava, B., Rodríguez-Zuluaga, J., Alazo-Cuartas, K., Kashcheyev, A., Migoya-Orué, Y., Radicella, S., . . . Fleury, R. (2016). Middle-and low-latitude ionosphere response to 2015 St. Patrick's Day geomagnetic storm. *Journal of Geophysical Research: Space Physics*, *121*(4), 3421–3438.

Nishida, A. (1968). Coherence of geomagnetic dp 2 fluctuations with interplanetary magnetic variations. *Journal of Geophysical Research*, *73*(17), 5549–5559.

Nishida, A., & Akasofu, S.-I. (1979). Geomagnetic Diagnosis of the Magnetosphere (Physics and Chemistry in Space, Volume 9). *Physics Today*, *32*(7), 57.

Obayashi, T., & Nishida, A. (1968). Large-scale electric field in the magnetosphere. *Space Science Reviews*, *8*(1), 3–31.

Olsen, N., Hulot, G., & Sabaka, T. J. (2010). *Handbook of geomathematics: Sources of the Geomagnetic Field and the Modern Data That Enable Their Investigation.* Berlin Heidelberg: Springer.

Ondoh, T., & Marubashi, K. (2001). *Science of space environment.* Amsterdam, Netherlands, IOS Press.

Østgaard, N., Vondrak, R., Gjerloev, J., & Germany, G. (2002). A relation between the energy deposition by electron precipitation and geomagnetic indices during substorms. *Journal of Geophysical Research: Space Physics*, *107*(A9), 1246–1252.

Ouattara, F., Amory-Mazaudier, C., Fleury, R., Lassudrie Duchesne, P., Vila, P., & Petit-didier, M. (2009). West African equatorial ionospheric parameters climatology based on Ouagadougou ionosonde station data from June 1966 to February 1998. *Annales Geophysicae*, *27*(6), 2503-2514.

Ouattara, F., & Amory-Mazaudier, C. (2012). Statistical study of the equatorial F2 layer critical frequency at Ouagadougou during solar cycles 20, 21 and 22, using Legrand and Simon's classification of geomagnetic activity. *Journal of Space Weather and Space Climate*, *2*, A19–A19.

Panda, S. K., Gedam, S. S., & Jin, S. (2015). Ionospheric TEC variations at low latitude Indian region. *Satellite Positioning-Methods, Models and Applications. In Tech-Publisher, Rijeka, Croatia*, 149–174.

Panda, S. K., Gedam, S. S., & Rajaram, G. (2013). Ionospheric characteristics of low latitude anomaly zone over indian region by ground based gps, radio occultation and spim model predictions. In *2013 ieee international geoscience and remote sensing symposium - igarss* (p. 1839-1842).

Pandit, D., Amory-Mazaudier, C., Fleury, R., Chapagain, N., & Adhikari, B. (2022). VTEC observations of intense geomagnetic storms above nepal: comparison with satellite data, CODE and IGSG models. *Indian Journal of Physics*, 1–18.

Pandit, D., Chapagain, N. P., & Adhikari, B. (2020). Study of Ionospheric Variability during Super Substorms. *Journal of Nepal Physical Society*, *6*(2), 74–84.

Pandit, D., Chapagain, N. P., Adhikari, B., & Mishra, R. K. (2018). Solar Activities and Its Impact on Space Weather. *Proceedings of the International Astronomical Union*, *13*(S340), 149–150.

Pandit, D., Chapagain, N. P., Adhikari, B., Nemirovskaya, I. A., Gordeev, V. V., Kovalenko, D., . . . et al. (2021). Analysis of the solar wind IMF B z and auroral electrojet index during supersubstorms. *Russian Journal of Earth Sciences*, *21*(5), ES5006– ES5006.

Pandit, D., Ghimire, B., Amory-Mazaudier, C., Fleury, R., Prasad Chapagain, N., & Adhikari, B. (2021). Climatology of ionosphere over Nepal based on GPS total electron content data from 2008 to 2018. *Annales Geophysicae*, *39*(4), 743-758.

Papitashvili, V., Rich, F., Heinemann, M., & Hairston, M. (1999). Parameterization of the Defense Meteorological Satellite Program ionospheric electrostatic potentials by the interplanetary magnetic field strength and direction. *Journal of Geophysical Research: Space Physics*, *104*(A1), 177–184.

Parker, E. N. (1958). Dynamics of the interplanetary gas and magnetic fields. *The Astrophysical Journal*, *128*, 664-675.

Pham Thi Thu, H., Amory-Mazaudier, C., & Le Huy, M. (2011). Time variations of the ionosphere at the northern tropical crest of ionization at Phu Thuy, Vietnam. *Annales Geophysicae*, *29*(1), 197–207.

Phillips, K. J. (1995). *Guide to the Sun*. Cambridge, England, Cambridge University Press.

Pincheira, X., Abdu, M., Batista, I., & Richards, P. (2002). An investigation of ionospheric responses, and disturbance thermospheric winds, during magnetic storms over South American sector. *Journal of Geophysical Research: Space Physics*, *107*(A11), 1379–1395.

Pizzo, V. J. (1985). Interplanetary shocks on the large scale - A retrospective on the last decade's theoretical efforts. *Washington DC American Geophysical Union Geophysical Monograph Series*, *35*, 51-68.

Portillo, A., Herraiz, M., Radicella, S., & Ciraolo, L. (2008). Equatorial plasma bubbles studied using African slant total electron content observations. *Journal of Atmospheric and Solar-Terrestrial Physics*, *70*(6), 907–917.

Poudel, P., Silwal, A., Ghimire, B., Gautam, S., Karki, M., Chapagain, N., . . . Amory-Mazaudier, C. (2022). A study of vtec above nepal exploring different calibration techniques, including a comparison with the nequick-2 model. *Astrophysics and Space Science*, *367*(4), 1–16.

Poudel, P., Simkhada, S., Adhikari, B., Sharma, D., & Nakarmi, J. J. (2019). Variation of solar wind parameters along with the understanding of energy dynamics within the magnetospheric system during geomagnetic disturbances. *Earth and Space Science*, *6*(2), 276–293.

Proelss, G. W. (1993). On explaining the local time variation of ionospheric storm effects. *Annales Geophysicae*, *11*(1), 1-9.

Prölss, G., Roemer, M., & Slowey, J. (1988). Dissipation of solar wind energy in the Earth's upper atmosphere: The geomagnetic activity effect. *Advances in Space Research*, *8*(5-6), 215–261.

Prolss, G. W. (1995). *Ionospheric F-region storms. handbook of atmospheric electro-dynamics, edited by: Volland, H*. CRC Press.

Pulkkinen, T. I., Partamies, N., Huttunen, K., Reeves, G., & Koskinen, H. E. (2007). Differences in geomagnetic storms driven by magnetic clouds and ICME sheath regions. *Geophysical Research Letters*, *34*(2), L02105–L02105.

Rama Rao, P. V. S., Gopi Krishna, S., Niranjan, K., & Prasad, D. S. V. V. D. (2006). Temporal and spatial variations in TEC using simultaneous measurements from the Indian GPS network of receivers during the low solar activity period of 2004-2005. *Annales Geophysicae*, *24*(12), 3279-3292.

Ramsingh, Sripathi, S., Sreekumar, S., Banola, S., Emperumal, K., Tiwari, P., & Kumar, B. S. (2015). Low-latitude ionosphere response to super geomagnetic storm of 17/18 March 2015: Results from a chain of ground-based observations over Indian sector. *Journal of Geophysical Research: Space Physics*, *120*(12), 10–864.

Rao, S. S., Chakraborty, M., Kumar, S., & Singh, A. (2019). Low-latitude ionospheric response from GPS, IRI and TIE-GCM TEC to Solar Cycle 24. *Astrophysics and Space Science*, *364*(12), 1–14.

Rao, S. S., Sharma, S., & Pandey, R. (2019). Study of solar flux dependency of the winter anomaly in GPS TEC. *GPS Solutions*, *23*(1), 1–10.

Rastogi, R. (1974). Westward equatorial electrojet during daytime hours. *Journal of Geophysical Research*, *79*(10), 1503–1512.

Rastogi, R. (2005). Magnetic storm effects in H and D components of the geomagnetic field at low and middle latitudes. *Journal of Atmospheric and Solar-Terrestrial Physics*, *67*(7), 665–675.

Rastogi, R. (2007). Day-to-day variability of the equatorial electrojet current in the South American sector. *Earth, Planets and Space*, *59*(5), 459–461.

Regmi, R. P., Kitada, T., Dudhia, J., & Maharjan, S. (2017). Large-scale gravity current over the middle hills of the Nepal Himalaya: Implications for aircraft accidents. *Journal of Applied Meteorology and Climatology*, *56*(2), 371–390.

Richmond, A. D. (1995). Ionospheric electrodynamics. In H. Volland (Ed.), *Handbook of atmospheric electrodynamics.* New York, NY: CRC Press.

Richmond, A. D., Matsushita, S., & Tarpley, J. (1976). On the production mechanism of electric currents and fields in the ionosphere. *Journal of Geophysical Research*, *81*(4), 547–555.

Rishbeth, H. (1971). Polarization fields produced by winds in the equatorial F-region. *Planetary and Space Science*, *19*(3), 357–369.

Rishbeth, H. (1998). How the thermospheric circulation affects the ionospheric F2-layer. *Journal of Atmospheric and Solar-Terrestrial Physics*, *60*(14), 1385–1402.

Rishbeth, H., & Garriott, O. K. (1969). *Introduction to ionospheric physics*. New York, United States, Academic Press.

Rishbeth, H., Müller-Wodarg, I. C. F., Zou, L., Fuller-Rowell, T. J., Millward, G. H., Moffett, R. J., . . . Aylward, A. D. (2000). Annual and semiannual variations in the ionospheric F2-layer: II. Physical discussion. *Annales Geophysicae*, *18*(8), 945-956.

Rishbeth, H., & Setty, C. (1961). The F-layer at sunrise. *Journal of Atmospheric and Terrestrial Physics*, *20*(4), 263–276.

Roberts, P. H. (2007). Alfvén's theorem and the frozen flux approximation. In E. Gubbins Davidand Herrero-Bervera (Ed.), *Encyclopedia of Geomagnetism and Paleomagnetism.* Midtown Manhattan, New York City, Springer.

Robinson, R., & Zanetti, L. (2021). Auroral energy flux and Joule heating derived from global maps of field-aligned currents. *Geophysical Research Letters*, *48*(7), e2020GL091527.

Rostoker, G. (1972). Geomagnetic indices. *Reviews of Geophysics*, *10*(4), 935–950.

Rothwell, P. (1963). Diffusion of ions between F layers at magnetic conjugate points. In A. Stricland (Ed.), *Proceedings of international conference held at london july 1962.* Institude of Physics and the Physical Society, London.

Rungraengwajiake, S., Supnithi, P., Tsugawa, T., Maruyama, T., & Nagatsuma, T. (2013). The variation of equatorial spread-F occurrences observed by ionosondes at Thailand longitude sector. *Advances in Space Research*, *52*(10), 1809–1819.

Ruohoniemi, J., & Greenwald, R. (1995). Observations of IMF and seasonal effects in high-latitude convection. *Geophysical Research Letters*, *22*(9), 1121–1124.

Russell, C. T. (1971). Geophysical coordinate transformations. *Cosmic Electrodynamics*, *2*(2), 184–196.

Russell, C. T., & McPherron, R. (1973). Semiannual variation of geomagnetic activity. *Journal of Geophysical Research*, *78*(1), 92–108.

Sandholt, P. E., Carlson, H. C., & Egeland, A. (2006). *Dayside and polar cap aurora* (Vol. 270). Berlin/Heidelberg, Germany, Springer Science and Business Media.

Sarris, T. E., Li, X., Tsaggas, N., & Paschalidis, N. (2002). Modeling energetic particle injections in dynamic pulse fields with varying propagation speeds. *Journal of Geophysical Research: Space Physics*, *107*(A3), SMP1–SMP10.

Sastri, J. H. (1998). On the development of abnormally large postsunset upward drift of equatorial F region under quiet geomagnetic conditions. *Journal of Geophysical Research: Space Physics*, *103*(A3), 3983–3991.

Sazykin, S. (2000). *Theoretical studies of penetration of magnetospheric electric fields to the ionosphere*. Utah State University, Logan, Utah, USA.

Schaer, S. (1999). *Mapping and predicting the earths ionosphere using the Global Positioning System. 1999. 205p* (Unpublished doctoral dissertation). Ph. D. dissertation. University of Bern, Bern, Switzerland.

Scherliess, L., & Fejer, B. G. (1997). Storm time dependence of equatorial disturbance dynamo zonal electric fields. *Journal of Geophysical Research: Space Physics*, *102*(A11), 24037–24046.

Schunk, R., & Nagy, A. (1925). *Physics, Plasma Physics, and Chemístry.* Cambridge, England, Cambridge University Press.

Schunk, R., & Sojka, J. J. (1996). Ionosphere-thermosphere space weather issues. *Journal of Atmospheric and Terrestrial Physics*, *58*(14), 1527–1574.

Schwenn, R. (2006). Space weather: the solar perspective. *Living Review Solar Physics*, *3*(2), 5–53.

Şentürk, E. (2020). Investigation of global ionospheric response of the severe geomagnetic storm on June 22-23, 2015 by GNSS-based TEC observations. *Astrophysics and Space Science*, *365*(7), 1–15.

Sharma, K., Dabas, R., & Ravindran, S. (2012). Study of total electron content variations over equatorial and low latitude ionosphere during extreme solar minimum. *Astrophysics and Space Science*, *341*(2), 277–286.

Shibata, K., & Magara, T. (2011). Solar flares: magnetohydrodynamic processes. *Living Reviews in Solar Physics*, *8*(1), 1–99.

Shim, J. S. (2009). *Analysis of total electron content (TEC) variations in the low-and middle-latitude ionosphere*. Utah State University, Logan, Utah, USA.

Shimeis, A., Amory-Mazaudier, C., Fleury, R., Mahrous, A., & Hassan, A. (2014). Transient variations of vertical total electron content over some African stations from 2002 to 2012. *Advances in Space Research*, *54*(11), 2159–2171.

Singh, R., & Sripathi, S. (2017). Ionospheric response to 22–23 June 2015 storm as investigated using ground-based ionosondes and GPS receivers over India. *Journal of Geophysical Research: Space Physics*, *122*(11), 11–645.

Smith, J. M., Rodrigues, F. S., & de Paula, E. R. (2015). Radar and satellite investigations of equatorial evening vertical drifts and spread f. *Annales Geophysicae*, *33*(11), 1403–1412.

Søraas, F., Aarsnes, K., Oksavik, K., Sandanger, M., Evans, D., & Greer, M. (2004). Evidence for particle injection as the cause of Dst reduction during HILDCAA events. *Journal of Atmospheric and Solar-Terrestrial Physics*, *66*(2), 177–186.

Spilker Jr, J. J., Axelrad, P., Parkinson, B. W., & Enge, P. (1996). *Global positioning system: theory and applications, volume I*. American Institute of Aeronautics and Astronautics.

Srebrov, B., Kounchev, O., & Simeonov, G. (2019). Wavelet Analysis of Big Data in the Global Investigation of Magnetic Field Variations in Solar-Terrestrial Physics. *arXiv preprint arXiv:1905.12923*.

Sridharan, R., Bagiya, M. S., Sunda, S., Choudhary, R., Pant, T. K., & Jose, L. (2014). First results on forecasting the spatial occurrence pattern of L-band scintillation and its temporal evolution. *Journal of Atmospheric and Solar-Terrestrial Physics*, *119*, 53–62.

Stening, R., Reztsova, T., et al. (2007). Variation of Sq focus latitudes in the Australian/Pacific region during a quiet sun year. *Journal of Atmospheric and Solar-Terrestrial Physics*, *69*(6), 734–740.

Stening, R. J. (1995). Variations in the strength of the Sq current system. *Annales Geophysicae*, *13*(6), 627-632.

Stolle, C., Manoj, C., Lühr, H., Maus, S., & Alken, P. (2008). Estimating the daytime equatorial ionization anomaly strength from electric field proxies. *Journal of Geophysical Research: Space Physics*, *113*(A9), A09310–A09310.

Sugiura, K. T. B. A., M., & Menvielle, M. (1991). *Equatorial dst index 1957–1986*. Saint-Maur-Des-Fosses: International Service of Geomagnetic Indices Publications Office.

Tariku, Y. (2015). TEC prediction performance of the IRI-2012 model over Ethiopia during the rising phase of solar cycle 24 (2009–2011). *Earth Planets*, *67*, 1–10.

Tenfjord, P., & Østgaard, N. (2013). Energy transfer and flow in the solar wind-magnetosphere-ionosphere system: A new coupling function. *Journal of Geophysical Research: Space Physics*, *118*(9), 5659–5672.

Titheridge, J. (1972). Determination of ionospheric electron content from the Faraday rotation of geostationary satellite signals. *Planetary and Space Science*, *20*(3), 353–369.

Torrence, C., & Compo, G. P. (1998). A practical guide to wavelet analysis. *Bulletin of the American Meteorological Society*, *79*(1), 61–78.

Triskova, L. (1989). The vernal-autumnal asymmetry in the seasonal variation of geomagnetic activity. *Journal of Atmospheric and Terrestrial physics*, *51*(2), 111–118.

Trivedi, N., Pathan, B., Schuch, N. J., Barreto, M., & Dutra, L. (2005). Geomagnetic phenomena in the South Atlantic anomaly region in Brazil. *Advances in Space Research*, *36*(10), 2021–2024.

Tsuji, Y., Shinbori, A., Kikuchi, T., & Nagatsuma, T. (2012). Magnetic latitude and local time distributions of ionospheric currents during a geomagnetic storm. *Journal of Geophysical Research: Space Physics*, *117*(A7), A07318–A07318.

Tsurutani, B. T., & Gonzalez, W. D. (1987). The cause of high-intensity long-duration continuous AE activity (HILDCAAs): Interplanetary Alfvén wave trains. *Planetary and Space Science*, *35*(4), 405–412.

Tsurutani, B. T., Gonzalez, W. D., Gonzalez, A. L., Guarnieri, F. L., Gopalswamy, N., Grande, M., ... et al. (2006). Corotating solar wind streams and recurrent geomagnetic activity: A review. *Journal of Geophysical Research: Space Physics*, *111*(A7), A07S01–A07S01.

Tsurutani, B. T., Gonzalez, W. D., Tang, F., Akasofu, S. I., & Smith, E. J. (1988). Origin of interplanetary southward magnetic fields responsible for major magnetic storms near solar maximum (1978–1979). *Journal of Geophysical Research: Space Physics*, *93*(A8), 8519–8531.

Tsurutani, B. T., Hajra, R., Echer, E., & Gjerloev, J. W. (2015). Extremely intense (sml ≤−2500 nT) substorms: isolated events that are externally triggered? *Annales Geophysicae*, *33*(5), 519–524.

Tsurutani, B. T., Lakhina, G. S., & Hajra, R. (2020). The physics of space weather/solar-terrestrial physics (STP): what we know now and what the current and future challenges are. *Nonlinear Processes in Geophysics*, *27*(1), 75–119.

Tsurutani, B. T., Mannucci, A., Iijima, B., Abdu, M. A., Sobral, J. H. A., Gonzalez, W., ... others (2004). Global dayside ionospheric uplift and enhancement associated with interplanetary electric fields. *Journal of Geophysical Research: Space Physics*, *109*(A08302).

Tsurutani, B. T., & Meng, C.-I. (1972). Interplanetary magnetic-field variations and substorm activity. *Journal of Geophysical Research*, *77*(16), 2964–2970.

Tsurutani, B. T., Verkhoglyadova, O. P., Mannucci, A. J., Saito, A., Araki, T., Yumoto, K., . . . others (2008). Prompt penetration electric fields PPEFS and their ionospheric effects during the great magnetic storm of 30–31 october 2003. *Journal of Geophysical Research: Space Physics*, *113*(A05311).

Tsurutani, B. T., & Zhou, X.-Y. (2003). Interplanetary shock triggering of substorms: Wind and Polar. *Advances in Space Research*, *31*(4), 1063–1067.

Tsurutani, B. T., Zhou, X.-Y., Arballo, J., Gonzalez, W. D., Lakhina, G., Vasyliunas, V., . . . et al.. (2001). Auroral zone dayside precipitation during magnetic storm initial phases. *Journal of Atmospheric and Solar-Terrestrial Physics*, *63*(5), 513–522.

Turner, N. E., Cramer, W. D., Earles, S. K., & Emery, B. A. (2009). Geoefficiency and energy partitioning in CIR-driven and CME-driven storms. *Journal of Atmospheric and Solar-Terrestrial Physics*, *71*(10-11), 1023–1031.

Tyagi, T. R., & Das Gupta, A. (1990). Beacon satellite studies and modelling of total electron contents of the ionosphere. *Indian Journal of Radio and Space Physics*, *19*, 424-438.

Verbanac, G., Vršnak, B., Živković, S., Hojsak, T., Veronig, A., & Temmer, M. (2011). Solar wind high-speed streams and related geomagnetic activity in the declining phase of solar cycle 23. *Astronomy & Astrophysics*, *533*, A49–A49.

Vichare, G., Rawat, R., Hanchinal, A., Sinha, A. K., Dhar, A., & Pathan, B. (2012). Seasonal evolution of S q current system at sub-auroral latitude. *Earth, Planets and Space*, *64*(11), 1023–1031.

Wang, H. (2005). Properties of remote flare ribbons associated with coronal mass ejections. *The Astrophysical Journal*, *618*(2), 1012–1019.

Webb, D., Lepping, R., Burlaga, L., DeForest, C., Larson, D., Martin, S., . . . Rust, D. (2000). The origin and development of the May 1997 magnetic cloud. *Journal of Geophysical Research: Space Physics*, *105*(A12), 27251–27259.

Weimer, D. R., Reinleitner, L. A., Kan, J. R., Zhu, L., & Akasofu, S.-I. (1990). Saturation of the auroral electrojet current and the polar cap potential. *Journal of Geophysical Research: Space Physics*, *95*(A11), 18981–18987.

Wright, J. (1963). The F-region seasonal anomaly. *Journal of Geophysical Research*, *68*(14), 4379–4381.

Xystouris, G., Sigala, E., & Mavromichalaki, H. (2014). A complete catalogue of high-speed solar wind streams during solar cycle 23. *Solar Physics*, *289*(3), 995–1012.

Ya'acob, N., Abdullah, M., & Ismail, M. (2008). Determination of GPS total electron content using single layer model (SLM) ionospheric mapping function. *International Journal of Computer Science and Network Security*, *8*(9), 154–160.

Yizengaw, E. (2004). *Imaging the ionosphere* (Unpublished doctoral dissertation). La Trobe University, Melbourne, Australia.

Yonezawa, T. (1959). On the seasonal and non-seasonal annual variations and the semi-annual variation in the noon and midnight electron densities of the F_2 layer in middle latitudes. *Journal of the Radio Research Laboratory*, *6*, 293–309.

Yue, X., Schreiner, W. S., Hunt, D. C., Rocken, C., & Kuo, Y.-H. (2011). Quantitative evaluation of the low Earth orbit satellite based slant total electron content determination. *Space Weather*, *9*(9), S09001–S09001.

Zhang, S.-R., Holt, J. M., Van Eyken, A. P., McCready, M., Amory-Mazaudier, C., Fukao, S., & Sulzer, M. (2005). Ionospheric local model and climatology from long-term databases of multiple incoherent scatter radars. *Geophysical Research Letters*, *32*(20), L20102–L20102.

Zhao, H., Li, X., Baker, D., Fennell, J., Blake, J., Larsen, B. A., . . . et al.. (2015). The evolution of ring current ion energy density and energy content during geomagnetic storms based on Van Allen Probes measurements. *Journal of Geophysical Research: Space Physics*, *120*(9), 7493–7511.

APPENDIX

A. Papers Published in International Journals

Adhikari, B., Pandit, D., Baruwal, P., Thapa, O., Adhikari, N., Kaphle, B., ... others (2021). Correlation of Alfvén Mach number with field aligned current, polar cap potential and dawn dusk electric field during Quiet and extreme solar wind conditions. *Indian Journal of Radio & Space Physics (IJRSP)*, *49*(3), 128–138.

Mishra, R. K., Adhikari, B., Pandit, D., & Chapagain, N. P. (2018). Characteristic of Solar Wind Parameters and Geomagnetic Indices during Solar Flares. *Proceedings of the International Astronomical Union*, *13*(S340), 257–258.

Pandit, D., Chapagain, N. P., Adhikari, B., & Mishra, R. K. (2018). Solar Activities and Its Impact on Space Weather. *Proceedings of the International Astronomical Union*, *13*(S340), 149–150.

Pandit, D., Chapagain, N. P., Adhikari, B., Nemirovskaya, I. A., Gordeev, V. V., Kovalenko, D., ... et al. (2021). Analysis of the solar wind IMF B z and auroral electrojet index during supersubstorms. *Russian Journal of Earth Sciences*, *21*(5), ES5006– ES5006.

Pandit, D., Ghimire, B., Amory-Mazaudier, C., Fleury, R., Prasad Chapagain, N., & Adhikari, B. (2021). Climatology of ionosphere over Nepal based on GPS total electron content data from 2008 to 2018. *Annales Geophysicae*, *39*(4), 743-758.

Poudel, P., Silwal, A., Ghimire, B., Gautam, S., Karki, M., Chapagain, N., ... Amory-Mazaudier, C. (2022). A study of vtec above nepal exploring different calibration techniques, including a comparison with the nequick-2 model. *Astrophysics and Space Science*, *367*(4), 1–16.

Pandit, D., Amory-Mazaudier, C., Fleury, R., Chapagain, N., & Adhikari, B. (2022). VTEC observations of intense geomagnetic storms above nepal: comparison with satellite data, CODE and IGSG models. *Indian Journal of Physics*, 1–18.

B. Papers Published in National Journals

Adhikari, B., Mishra, R. K., Pandit, D., Bhattarai, B., & Chapagain, N. P. (2017). Ionospheric Effect of Non-Storm HILDCAA (High Intensity Long Duration Continuous Auroral Activity). *Journal of Institute of Science and Technology*, *22*(1), 34–40.

Dhakal, S., Adhikari, B., Pudasainee, K., Chapagain, N. P., Pandit, D., Dahal, S., . . . Chhatkuli, D. N. (2019). Correlation of solar wind velocity with different parameters during geomagnetic disturbances. *Bibechana*, *16*, 165–176.

Pandit, D., Chapagain, N. P., & Adhikari, B. (2020). Study of Ionospheric Variability during Super Substorms. *Journal of Nepal Physical Society*, *6*(2), 74–84.

Rana, B., Chapagain, N., Adhikari, B., Pandit, D., Pudasainee, K., Chapagain, S., & Chhatkuli, D. (2019). Study of total electron content and electron density profile from satellite observations during geomagnetic storms. *Journal of Nepal Physical Society*, *5*(1), 59–66.

C. Participation in Conferences, Seminars, Workshops and Lecture Series

- "Nepal Young Science Summit" organized by Brainycube Research Organization, Nepal, July 29-30, 2017.
  Poster presentation: "The Solar-Terrestrial Interaction and Its Impact on Space Weather"

- "International Conference on Physics of Space and Materials (ICPSM 2017)" organized by Department of Physics, St. Xavier's College, Maitighar, Kathmandu, Nepal, September 2-3, 2017.
  Oral presentation: "Variation on Electron Density and Electron, Ion and Neutral Temperature during Geomagnetic Storm"

- "Scientific secession of NPS 34th Annual Convention" organized by Nepal Physical Society, Nepal, December 22-23, 2017.
  Oral presentation: "A study of Solar Wind velocity under Different Geomagnetic Storm"

- "International Conference on Nano-Materials and Computational Physics" organized by Central Department of Physics, Kirtipur, Kathmandu, Nepal, December 27-28, 2017.
  Poster presentation: "Response of Partial, Annular and Total Solar Eclipse on Solar Wind Parameters and Geomagnetic Indices"

- "IAU Symposium 340: Long -Term datasets for the understanding of solar and Stellar Magnetic Cycles" organized by International Astronomical Union (IAU),Jaipur, India, February 19- 24, 2018.
  Poster presentation: "Solar Activities and Its Impact on Space Weather"

- "23rd International Conference of International Academy of Physical Sciences (CONIAPS XXIII)" organized by National Academy of Science and Technology, Kathmandu, Nepal, November 16-18, 2018.
  Oral presentation: "Variation in Solar Wind Velocity under Super Intense Geomagnetic Storms"

- "National Young Scientists Conference (NYSS2019)" organized by Ministry of Industry, Tourism, Forests and Environment state no. 3 Hetauda, Makwanpur, Nepal, April 23-24, 2019.
  Oral presentation: "Study on TEC during Super Substorms during GPS Data"

- "Conference on Physical Sciences and Astronomy" organized by Association of Nepali Physicists in America (ANPA), USA, July 19-21 , 2019.
  Oral presentation: "Variation in Total Electron Content (TEC) and Horizontal

Component of Earth's Magnetic Field during Super Substorms"

- "National Symposium on Research, Development and Innovation in Physics (NSDIRP-2019)" organized by Department of Physics, St. Xavier's College, Maitighar, Kathmandu, Nepal, September 3-4, 2019.
  Oral presentation: "Response in Total Electron Content during Solar Eclipse Observed from Nepal"

- "The 8th Asian Conference on Colloid & Interface Science" organized by Pulchowk Campus, Institute of Engineering, Lalitpur, Kathmandu, Nepal, September 24-27, 2019.
  Oral presentation: "Effect of Super Intense Geomagnetic Storm on Ionospheric Parameters"

- "Three Days Online School on Space and Atmospheric Physics" organized by Department of Physics, St. Xavier's College, Kathmandu, Nepal, August 5-7, 2020.
  Oral presentation: "Fundamental Concept on Space Science and Data Analysis"

- "ANPA Conference" organized by Association of Nepali Physicists in America (ANPA), USA, July 17-19, 2020.
  Oral presentation: "Analysis on the North-South Component of Geomagnetic Field with the Interplanetary Magnetic Field during Intense Geomagnetic Storms of 22 June 2015 and 25 August 2018"

- "International Conference on Frontiers of Physics -2022 (ICFP-2022)" organized by Nepal Physical Society, Nepal, January 22-25, 2022.
  Oral presentation: "Study of Total Electron Content (TEC) during year of Solar Cycles 23 and 24 at Jomsom, Nepal"

- "Workshop on Space Weather Effects on GNSS Operations at Low Latitudes" organized by The Abdus Salam International Centre for Theoretical Physics (ICTP), Italy, April 23 - May 4, 2018.

- "Workshop on Space Weather and Upper Atmosphere Physics (WSWUAP-2019)" jointly organized by Amrit Campus, Kathmandu, Nepal and ICTP, Italy, September 23-27, 2019.

- "Research Training workshop" organized by Kathmandu BernHardt College, Bafal, Kathmandu, Nepal, November 29, 2019.

- "African Workshop on GNSS and Space Weather" organized by The Abdus Salam International Centre for Theoretical Physics (ICTP), Italy, October 05-06, 2020.

- "School on Space and Atmospheric Physics" organized by Department of Physics,

St. Xavier's College, Kathmandu, Nepal, August 5-7, 2020.

- "Short course on Space and Atmospheric Science" organized by Centre for Space Science and Technology Education in Asia and the Pacific (CSSTEAP) (Affiliated to the United Nations) conducted by Physical Research Laboratory, Ahmedabad, India, December 7-14, 2020.

- "Three Days Workshop on Data Analysis: Python and Origin" organized by Department of Physics, St. Xavier's College, Kathmandu, Nepal, January 24-26, 2021.

- "NPS School of Computing" organized by Nepal Physical Society, Kathmandu, Nepal, July 4, 2020 - January 31, 2021.

- "Short course on Use of Space Technology for Weather and Climate Studies" organized by Centre for Space Science and Technology Education in Asia and the Pacific (CSSTEAP) (Affiliated to the United Nations) and conducted at Space Applications Centre, ISRO, Ahmedabad, India, May 17-31,2021.

- "Eastern Africa GNSS and Space Weather Capacity Building Workshop" organized by The Abdus Salam International Centre for Theoretical Physics (ICTP), Italy, June 21-25, 2021.

- "Short course on Coastal Zone Management in Response to Natural Hazards and Climate Variability" organized by Centre for Space Science and Technology Education in Asia and the Pacific (CSSTEAP) (Affiliated to the United Nations) and conducted by Indian Institute of Remote Sensing, Indian Space Research Organization, Dehradun, India, July 26 - August 06, 2021.

- "Short course on Coastal Zone Management in Response to Natural Hazards and Climate Variability" organized by Centre for Space Science and Technology Education in Asia and the Pacific (CSSTEAP) (Affiliated to the United Nations) and conducted by Indian Institute of Remote Sensing, Indian Space Research Organization, Dehradun, India, July 26 - August 06, 2021.

- "Short course on Introduction to Satellite Navigation" organized by Centre for Space Science and Technology Education in Asia and the Pacific (CSSTEAP) (Affiliated to the United Nations) and conducted at Space Applications Centre, ISRO, Ahmedabad, India, September 13 - 24, 2021.

- "Lecture Series on Research Methodology" organized by Central Department of Physics, Tribhuvan University, Kirtipur, Kathmandu, Nepal, November 6 – December 22, 2017.

Analysis of the solar wind IMF B_z and auroral electrojet index during supersubstorms

Drabindra Pandit[1,2], Narayan P. Chapagain[3], and Binod Adhikari[2,4]

This work examines the coupling between solar wind interplanetary magnetic field (IMF B_z) and auroral electrojet (AE) index during supersubstorms (SSSs) of 11 April 2001 and 24 November 2001. The SSSs are particularly intense substorms with the value of $SML < -2500$ nT; $AL < -2500$ nT. For the detail analysis, the data set of 1 min time resolution of IMF B_z and AE index in the geocentric solar magnetospheric (GSM) coordinate system are used. The spectral characteristics of SSSs events are studied using continuous wavelet transforms (CWT) and global wavelet spectrum (GWS). The cross-correlation analysis also has been applied to study the correlation and time lag between IMF B_z and AE index. The spectrum identified the main periodicities of the IMF B_z and AE index during these events. The short-lived periodicity of high-frequency signals are identified between 70 to 256 minutes and 80 to 256 minutes during 11 April 2001 and 24 November 2001, respectively. The global wavelet spectrum (GWS) identifies the most energetic periods are present during the SSSs. Cross-correlation analysis shows that the AE index correlates (correlation coefficient ~ -0.6) with IMF B_z at time lag of approximately zero. These results support the previously existing facts that the magnetic reconnection between southward directed IMF B_z and the northward pointed Earth's magnetic field at the dayside magnetopause is the primary mechanism for transferring solar wind energy into magnetosphere and ionosphere during the SSSs events.
KEYWORDS: Geomagnetic index; interplanetary magnetic field; supersubstorms; magnetosphere; magnetic reconnection.

1. Introduction

Magnetospheric substorm is one of the prevailing and elementary phenomena, occurs due to energy deposition into the Earth's magnetosphere

and ionosphere [*Akasofu,* 1964]. The Substorm accompanied by a short-lived surge in earthward convection in the magnetotail followed by a global change in the magnetic morphology of the tail, representing a transfer of stored magnetic energy due to imbalance in the day-side and night-side reconnection rates [*McPherron et al.,* 1973]. During magnetic reconnection between southward directed IMF and the northward pointed Earth's magnetic field at the dayside magnetopause, energy is transferred into magnetosphere/magnetotail [*Tsurutani and Meng,* 1972; *Echer et al.,* 2008]. The substorms were believed as the integral part of the magnetic storms [*Gonzalez et al.,* 1994] but later it was found to occur independent of the storm

[1]Central Department of Physics, IOST, Tribhuvan University, Kirtipur, Kathmandu, Nepal

[2]Department of Physics, St. Xavier's College, Maitighar, Kathmandu, Nepal

[3]Department of Physics, Amrit Campus, Tribhuvan University, Kathmandu, Nepal

[4]Department of Physics, Patan Multiple Campus, Tribhuvan University, Lalitpur, Nepal

[*Tsurutani and Meng,* 1972] and also outside the main phase of the magnetic storm [*Hajra et al.,* 2013]. Supersubstorms (SSSs) are very intense substorms with large values of the SML or AL indices < -2500 nT [*Tsurutani et al.,* 2015]. The SML index is the generalization of the AL index, calculated by all stations of the SuperMAG network located not only at auroral latitude ($\sim 60°$ to $70°$ geomagnetic latitudes) but also located at other higher and lower latitudes [*Gjerloev,* 2012; *Rostoker,* 1972].

The SSSs as an isolated event was invented by *Tsurutani et al.* [2015]. They pointed out that the SSSs are triggered by a small region of very high-density solar wind pressure pulse impinged upon the magnetosphere with a duration ranging from 17 to 50 minutes. The SSSs events are recorded by the long-term southward direction of IMF B_z. *Hajra et al.* [2016] found that SSSs occurred during all phases of the solar cycle, but the highest occurrence rate of 3.8 year^{-1} identified in descending phase, while the smallest frequency appeared during the minimum phase of the solar cycle. Their study also showed about 77% of SSSs related to a small region of very high-pressure pulses impinge upon the magnetosphere. It was shown by *Despirak et al.* [2018] that 42% of SSSs events were observed during the magnetic cloud (MC), 45.2% in the sheath, and 8.3% in the ejecta. *Despirak et al.* [2019] studied two supersubstorms that occurred during the strong magnetic storm on 7–8 September 2017 and found that ionospheric currents developed during SSSs were recorded on the global scale around the Earth. *Despirak et al.* [2021] in their recent paper entitled "Longitude geomagnetic effect of the SSSs during magnetic storm of March 9, 2012" mentioned that the effect of SSSs developed on a global scale in longitude, from before midnight, through the night and morning, and also into the day sector. *Henderson et al.* [1996] showed that periodic activity like sawtooth events found directly correlated with corresponding solar wind dynamic pressure enhancements. *Sergeev* [1996] suggested the energy flow from the solar wind into the magnetosphere becomes too large to dissipate without the periodic occurrence of substorms. Using CWT analysis, *de Souza et al.* [2018] analyzed the behavior of HILDCAAs event occurring between 1995 to 2011 and noted that the main periods of AE index lying between 4 and 12 h, which is 50%

of the total identified periods. The paper by Srebrov et al. (Srebrov et al., 2019, Wavelet Analysis of Big Data in the Global Investigation of Magnetic Field Variations in Solar-Terrestrial Physics. arXiv preprint arXiv:1905.12923) reported that modes (wave packages) with different periods, the order of 20 to a few hundred minutes with a significant amplitude detected in the CWT analysis of a large amount of heterogeneous data of geomagnetic field, ionospheric parameters, and IMF. *Maggiolo et al.* [2017] analyzed the delay in time response of geomagnetic activity to the solar wind and obtained a good correlation between IMF B_z and AE with a correlation coefficient of -0.5. *Echer et al.* [2017] pointed out that the response of the IMF B_z during the September/October 2003 storm and noted that the main periodicities for the cross-correlation during 1.8 to 3.1 hours.

This paper aims to study the couplings between the IMF B_z and auroral electrojet index during two supersubstorms events. The events, data sets, and adopted methodologies are described in section 2. A brief description of the results and discussion are presented in section 3. Conclusions of the entire work are discussed in section 4.

2. Methodology

In this work, two supersubstorms events during 11 April 2001 and 24 November 2001 were selected using a threshold of SuperMAG $AL/SML <$ -2500 nT as suggested by *Tsurutani et al.* [2015]. The data set for interplanetary parameters of 1 min time resolution were downloaded from the OMNI website https://omniweb.gsfc.nasa.gov/form/omni_min.html). The wavelet transforms, particularly continuous wavelet transforms (CWT) at different scales and the cross-correlation techniques (CCT) are used to find the relation between IMF B_z and AE index. The CWT is used to divide continuous time-series data into wavelets which use a very redundant and finely detailed description of a signal in terms of time and frequency. If a and b represent the dilation and translation parameters that vary continuously, then the continuous wavelet transform becomes

$$W(a,b) = \int f(t)\varphi^*\left(\frac{t-b}{a}\right)dt$$

where φ^* represents complex conjugate of φ and the function $W(a,b)$ represents the wavelets coefficients. For $a > 0$, variation of scale parameter
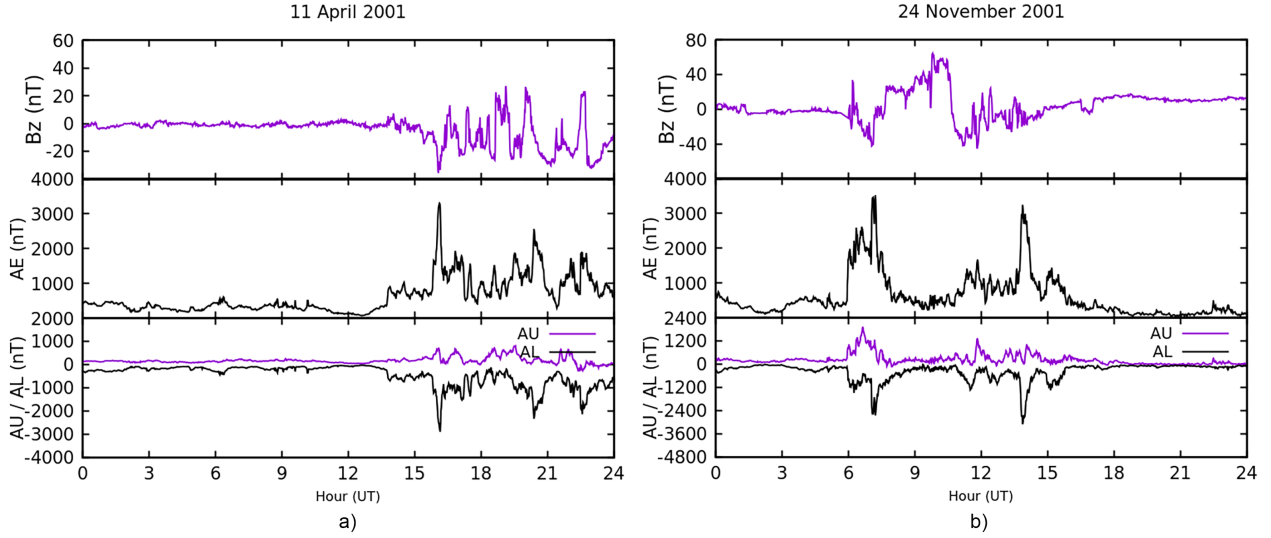
Figure 1. (a) and (b) from top to bottom represent: southward component of interplanetary magnetic field (B_z in nT), auroral electrojet index (AE in nT), auroral electrojet upper (AU in nT) and auroral electrojet lower (AL in nT) during two SSSs events occurred on 11 April 2001 and 24 November 2001, respectively.

gives dilation effect and for $a < 0$, it gives contraction effect of the mother wavelet function. It becomes convenient to identify the low and high frequency and longer and shorter duration present in the signal. For signal processing, a scalogram is used to visualize the wavelet transform which represents the square of the amplitude of the coefficient. It illustrates the distribution of signal energy in time, t, and scale a [*Adhikari et al.,* 2017a; *Lee and Yamamoto,* 1994]. The global wavelet spectrum (GWS) is also used to identify the most energetic periods present on the cross-wavelet analysis and it is obtained by

$$\text{GWS} = \int TW(a,b)|^2 db$$

The cross-correlation measures the similarity between variables in time series and also explores unseen information [*Adhikari and Chapagain,* 2015; *Liou et al.,* 2001]. The value of cross correlation lies near the vicinity of ± 1 implies the highest correlation and its value near zero showed moderate or low correlation [*Katz,* 1988]. The zero value of correlation infers no correlation between these two-time series variables. In this paper, cross-correlation is applied to obtain correlation coefficients and time lag between the IMF B_z and AE index.

3. Results and Discussion

In this section, we analyzed the solar wind IMF B_z and AE indices, and their coupling relationships using CWT, GWS, and cross-correlation analysis.

3.1. Solar Wind Interplanetary Magnetic Field (IMF B_z) and Auroral Electrojet Indices (AE, AU, AL)

Figure 1a and Figure 1b show an overview plot of the solar wind interplanetary magnetic field IMF B_z, auroral electrojet (AE), auroral electrojet upper (AU), and auroral electrojet lower (AL) indices associated with two SSSs events identified by the SML (AL) index < -2500 nT on 11 April 2001 and 24 November 2001, respectively. Two SSSs have occurred on each event day. On 11 April 2001, the day started as a quiet geomagnetic event with less fluctuation in IMF B_z represented at the top panel of the plot. There was southward turning of IMF $B_z \sim -39$ nT before the onset of the first SSS $\sim$15:20 UT. After the first SSS, a strong oscillation occurs in IMF B_z between 28 nT to -25 nT and it becomes several times negative around peak value -25 nT, caused by the Alfven waves [*Guo et al.,* 2016]. This is a common feature of a solar wind

stream associated with a coronal hole. A strong energy coupling and modulation of the magnetosphere by an intermittent but strong southward component of IMF B_z are favorable for the development of aurora [*Echer et al.,* 2017]. The second panel shows the variation of the auroral electrojet index which acquired peak values 3500 nT and 2500 nT during the first and second SSS events, respectively. A higher AE index indicates enormous energy, which is indulged into the Earth's magnetosphere by transfer of energy and momentum from the solar wind. Consequently, high Joule heating is produced near high latitude. During Joule heating, particle flux precipitated collides with neutral gas and loses its kinetic energy near the auroral region [*Suji and Prince,* 2018]. The third panel of Figure 1a reproduces the AU and AL indices associated with SSSs. The first SSS event took place approximately from 15:53 UT to 16:33 UT for 40 minutes and the second SSS started after 4 hrs and 23 min gap approximately from 20:16 UT to 20:51 for 35 min as indicated by a sharp decrease in AL index. During the first SSS, the peak value of the AL index is -2903 nT around $\sim 16:09$ UT and during the second SSS, the peak value of the AL index is -2339 nT around $\sim 20:23$ UT. Similarly, the values of the AU index are 500 nT and 200 nT during the first and second SSSs, respectively. In general, the AL index takes highly negative value but with the mixing of magnetospheric ring current in ionosphere sometimes it may create small positive variation [*Adhikari and Chapagain,* 2015]. The maximum perturbation generated in the AU index gives strength of eastward electrojet and in the AL index; it gives the individual strength of westward electrojet [*Weimer et al.,* 1990].

Figure 1b is rather similar to the first but it shows the event of SSS of 24 November 2001. On the first panel of Figure 1b, the IMF B_z has a southward component of ~ -28 nT and -21 nT prior to both SSS events. The southward component of IMF B_z is means of identifying solar energy transfer to magnetosphere through magnetic reconnection at the dayside magnetosphere [*Echer et al.,* 2008; *Hajra et al.,* 2016]. The AE index on the second panel ranging from 0 to 4000 nT, depicts two different SSS events that have occurred during the interval of 8 hr with the similar type of the highest peaks 3500 nT and 3200 nT. The two SSSs of 24 November 2001 occurred $\sim 07:00$ UT

and $\sim$13:45 UT for the duration of 50 min and 30 min, respectively. The peak values of the AL index found during two SSSs are -2500 nT and -3400 nT. Strong burst is not noticed in the AU index as the AE and AL indices. The value of the AU index was found to be ~ 1200 nT and 600 nT during two SSSs events, respectively. The first SSS event was caused by southward IMF B_z in the sheath and the second event by southward IMF B_z in the magnetic cloud [*Tsurutani et al.,* 2015]. The two SSS events appear to be caused by interplanetary sheath [*Hajra et al.,* 2016] which is characterized by multiple IMF B_z changes.

Moreover, SSS is an isolated event; it can exit inside the superstorms, triggered by solar wind high-pressure pulse. This was noted by *Tsurutani et al.* [2015]. Seventy-four SSSs occurred within the year 1981 to 2012 were identified by *Hajra et al.* [2016]. Their study reported that SSSs can occur in all phases of the solar cycle with the highest occurrence frequency recorded in descending phase. They also show SSSs follow an annual variation. Their study again pointed out that 77% of SSSs were associated with a small region of very high increase in pressure pulses impinging upon the magnetosphere. [*Adhikari and Chapagain,* 2015] found that during SSSs the polar cap potential and merging electric field was a hundred times higher than it developed during high intensity long duration auroral activities (HILDCAAs). Variation of field-aligned current (FAC) along with solar wind parameters for three SSSs was studied by *Adhikari et al.* [2017b] and concluded that FAC is the prime cause for east-west perturbation of magnetic field at high latitude for SSS events to occur, during that instant the value of AE was found greater than 3000 nT. The study of ionospheric current by *Despirak et al.* [2019] during two SSS of 7–8 September 2017 found that the SSS has a global effect to the ionospheric current. The impact related to SSS was studied by *Tsurutani et al.* [2020] and pointed out that SSS events may occur within magnetic storms that can cause GIC due to strong dB/dt effect in ground stations but by earlier researcher have been attributed to "magnetic storms" as the real cause of it. The increase in solar wind IMF B_z and auroral electrojet indices reveal the transfer of energy and momentum from the solar wind to the magnetosphere to produce the power outages on the Earth [*Tsurutani et al.,* 2015].
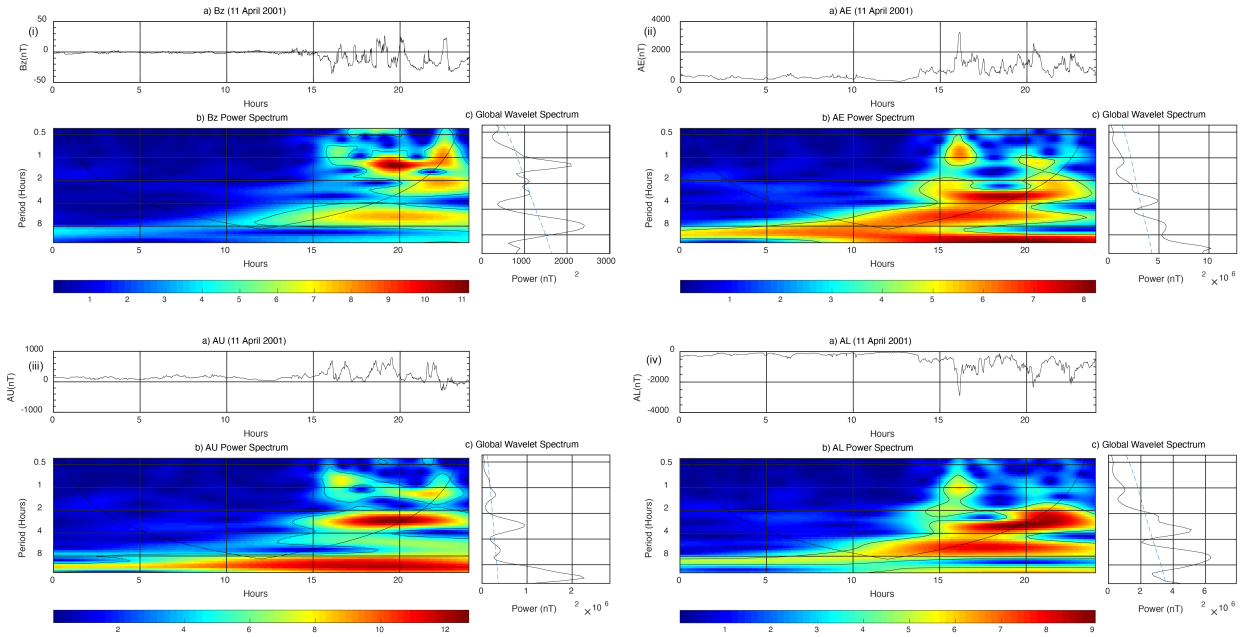
Figure 2. In (i) panel a) Time series of IMFBz b) Cross-wavelet spectrum periodogram during SSS of 11 April 2001 and c) The global wavelet spectrum shows the period of correlation. The (ii), (iii) and (iv) panel represent the same for AE, AU and AL, respectively.

3.2. Continuous Wavelet Signature

In Figure 2, the panel (i)–(iv) show a) the time series variations b) the power spectrum and c) the GWS of southward component of interplanetary magnetic field (IMF B_z), auroral electrojet index (AE), auroral electrojet upper (AU) and auroral electrojet lower (AL) during SSS on 11 April 2001, respectively. In the power spectrum plot, the square modulus of the wavelet coefficient provides the energy distribution in the time scale. A small perturbation in signal energy is visualized using a log2 function in wavelet space represented in the scalogram. It helps to understand the behavior of energy at a certain scale [*Domingues et al.*, 2005]. The abrupt change in the parameters such as magnetic field is characterized by a scalogram. These perturbations appear on scalograms through scattering frequencies even short and medium periods have their high amplitudes. The most important advantage of using scalogram analysis is to observe the distribution of amplitudes in larger scales. The horizontal axis in this figure represents time in an hour and the vertical axis represents the periodicity in minutes. The square of the actual amplitude

of the wavelet coefficients represented in plots is indicated by the color bar on the right-hand side of the plot and has units in $(nT)^2$. They represent the square estimation of the actual value of the parameters. In the scalogram, the region of stronger wavelet power is shown in black (horizontal color indicator chart) and the region of low wavelet power is visualized in blue. The maximum and minimum wavelet power on the scalogram corresponds to high and low peak intensity. In each plot, it reveals highly variable signals in time without continuous periodicity. In Figure 2, the background intensity 1 $(nT)^2$ has found increased to 11 $(nT)^2$ for IMF B_z, 1 to 8 $(nT)^2$ for AE, 2 to 12 $(nT)^2$ for AU and 1 to 9 $(nT)^2$ for AL. The power area of higher intensity is seen time scale between approximately 2 to 1 and 5 to 4; AE between 16 to 4 and 4 to 2; AU between 16 to 8 and 4 to 2 and AL between 8 to 4 and 4 to 2 for time $\sim$ 16:00 UT and $\sim$ 20:00 UT, respectively for SSSs event of 11 April 2001, respectively. The results from the scalogram pointed out that some characteristics of solar wind and interplanetary parameters are confirmed the abrupt change in the magnetic field. The high intensity with max-
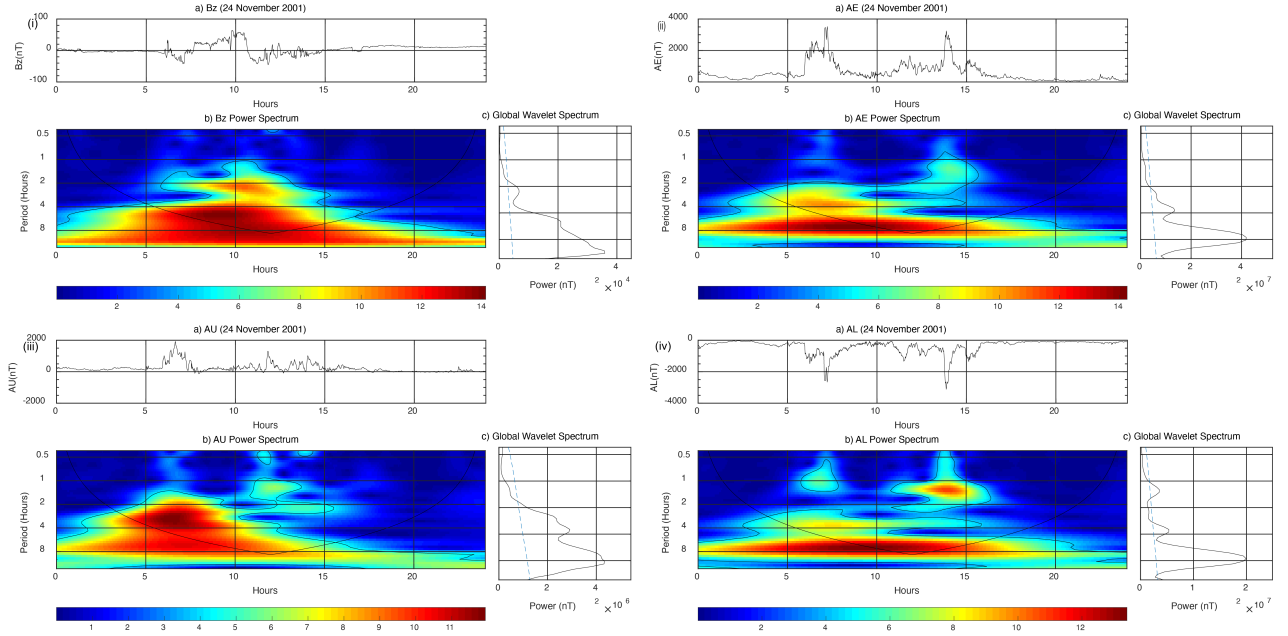
Figure 3. In (i) panel a) Time series of IMF B_z b) Cross-wavelet spectrum periodogram during SSS of 24 November 2001 and c) the global wavelet spectrum shows the period of correlation. The (ii), (iii) and (iv) panel represent the same for AE, AU and AL, respectively.

imum periodicity observed in all panels indicates the effect presented by the SSS events. The short duration trend has a significant effect on the indices AE, AL, AU, and IMF B_z during SSSs. It means that during the short pulse, thermal energy and energetic particles are injected into the magnetosphere/magnetotail which may cause a power blackout on the Earth.

Figure 3 is similar to Figure 2 but refers to the supersubstorm of 24 November 2001 in which two SSSs noticed the first SSS at ~07:00 UT and the second at 13:45 UT. The small perturbation in signal energy is visualized using a log2 function in wavelet space represented in the scalogram. The scalograms for each parameter on 24 November 2001 follow the same numerical method as the previous event and its interpretation is the same as in the previous event. In Figure 3, the background intensity 2 $(nT)^2$ has been found increased to 14 $(nT)^2$ for the IMF B_z, AE, AL, and 1 to 12 $(nT)^2$ for AU indices, respectively. In Figure 3, the areas corresponding to strong power found for the IMF B_z between 16 to 4 and 4 to 2; AE between 10 to 6 and 4 to 2; AU between 8 to 4 and 4 to 2 and between 10 to 6 and 2 to 1 for

time ~07:00 UT and ~13:00 UT of SSSs event of 24 November 2001, respectively. In each figure, some of the strong power areas lie outside the cone of influence. The IMF B_z, AE, AU, and AL indices have more or less the same spectral behaviors. Hence, there exists a one-to-one correspondence between the IMF B_z and the AE, AU, and AL indices. This wavelet analysis clearly supports the existing coupling between solar-wind-magnetosphere during SSS events. From this analysis, it can be understood that some characteristics effects are seen on auroral electrojet indices during the SSSs. These indices were highly disturbed at the time of SSSs, and the highest values of relative amplitudes are seen on scalogram. These relative amplitudes allow for the identification of quiescent and non-quiescent periods in the magnetic signals. Thus, using this tool, the intrinsic processes of energy transfer are being surveyed. This fact confirms the known concept that the penetration of charged particles and energy injection are more frequent during reconnection mechanism between the IMF B_z and geomagnetic field at magnetosphere during SSSs [*Mendes et al.,* 2004; *Morioka et al.,* 2003].

3.3. Global Wavelet Spectrum

The subplots (c) of Figure 2 and Figure 3 show the GWS of the IMF B_z, AE, AU, and AL indices during SSS on 11 April 2001 and 24 November 2001, respectively. It analyzes the distribution of the correlated major periods between the two variables. In Figure 2, the two periods of higher correlation be noticed at ∼16:00 UT and ∼20:00 UT with energy value 1500 and 2200 (nT)^2 for IMF B_z; 10×10^6 and 5×10^6 (nT)^2 for AE; 2.4×10^6 and 1×10^6 (nT)^2 for AU and 6×10^6 and 5×10^6 (nT)^2 for AL, which correspond with the duration of the two SSS occurred on 11 April 2001. In Figure 3, the two periods of higher correlation identified at ∼ 07:00 UT and ∼ 13:00 UT with energy value 3×10^4 and 2×10^4 (nT)^2 for IMF B_z; 4.2×10^7 and 1.5×10^7 (nT)^2 for AE; 4.2×10^6 and 3×10^6 (nT)^2 for AU; 2×10^7 and 0.5×10^7 (nT)^2 for AL during two SSS events of 24 November 2001. The paper by *Adhikari et al.* [2018] reported that the ICME related storm during 20–21 November 2003 correlation identified during the period of 64 to 16 with energy value 2.5×10^{10} V^2, HSS related storm of 17 July 2004 correlation identified during the period of 64 min with energy value 9×10^{10} V^2, ICME related substorm of 24 October 2002 correlation identified during period of 24 min with energy value 7.2×10^9 V^2. During study of SSS on 21 January 2005 *Adhikari et al.* [2018] found the correlation coefficient during the period of 30 min with energy value 9×10^{11} V^2 in Polar cap voltage (PCV). The IMF B_z, AE, AU, and AL indices have almost the same spectral characteristics and hence there is a one-to-one correspondence between the IMF B_z and AE, AU, and AL indices on both SSSs. These results support the existing correlation between the IMF B_z and AE, AU, and AL indices. Three periods of higher correlation were identified by *de Souza et al.* [2018] during the study of HILDCA with maximum energy 1.2×10^6 (nT)^2 due to efficient solar wind coupling between IMF B_z associates with Alfvan wave fluctuation and geomagnetic field which was identified as the main cause of geomagnetic activity related to HILDCA [*Tsurutani and Gonzalez*, 1987]. During SSS the short pulsation coupling mechanism between IMF B_z and geomagnetic field may cause large energy released for the destruction of space and terrestrial assets [*Tsurutani et al.*, 2015].

3.4. Cross Correlation Analysis

Figure 4a and Figure 4b represent the cross-correlation between the IMF B_z and AE index during two SSSs occurred at 15:53 UT and 20:16 UT on 11 April 2001 and Figure 4c and Figure 4d represent during two SSSs occurred at 07:00 UT and 13:45 UT on 24 November 2001. The cross-correlation determines the degree of correlation and time lag between two time series. In the plot, the horizontal axis represents time lags between two-time series and the vertical axis represents the correlation coefficient. The time scale in minutes indicates which index leads or lags before and after they get correlated. From Figure 4a–Figure 4d, it seems that IMF B_z and AE index correlated with a correlation coefficient ∼ −0.6 approximately with zero-time lag. It can be interpreted as the prompt response on the AE index to the changes that occur on the IMF B_z. The prompt response in the AE index due to the perturbation of the IMF B_z during intense geomagnetic storm reported by *Pandit et al.* [2018] and they found the correlation between them with a coefficient 0.5. In *Adhikari et al.* [2018] observed correlation coefficient between FAC-AE is 0.8 with time lead of 50 min during SSS on 21 January 2001 and they also showed cross correlation between FAC-B_z in phase with correlation coefficient −0.5 at time lag of 60 min. The correlation between solar wind parameters and auroral electrojet lower (AL) index was studied by *Bargatze et al.* [1985] and found that two pulse peak responses in a time lag of 20 min for strong geomagnetic level and 60 min for moderate geomagnetic level. The first peak was associated with magnetospheric activity driven by solar wind coupling and the second was related to magnetospheric activity driven by the release of energy previously stored in the magnetotail. A study of SSSs of 20 November 2003 by *Poudel et al.* [2019] pointed out that the magnetospheric response to the solar wind invasion is pretty quick during the SSSs events and also showed a correlation coefficient between the IMF B_z and energy dissipated at auroral region (Ur) of −0.744 at zero-time lag. In this study, the correlation between the IMF B_z and AE was identified as high almost with no lag due to strong geomagnetic and auroral activities during magnetic reconnection between the interplanetary magnetic field and a north-south component of the geomagnetic field.
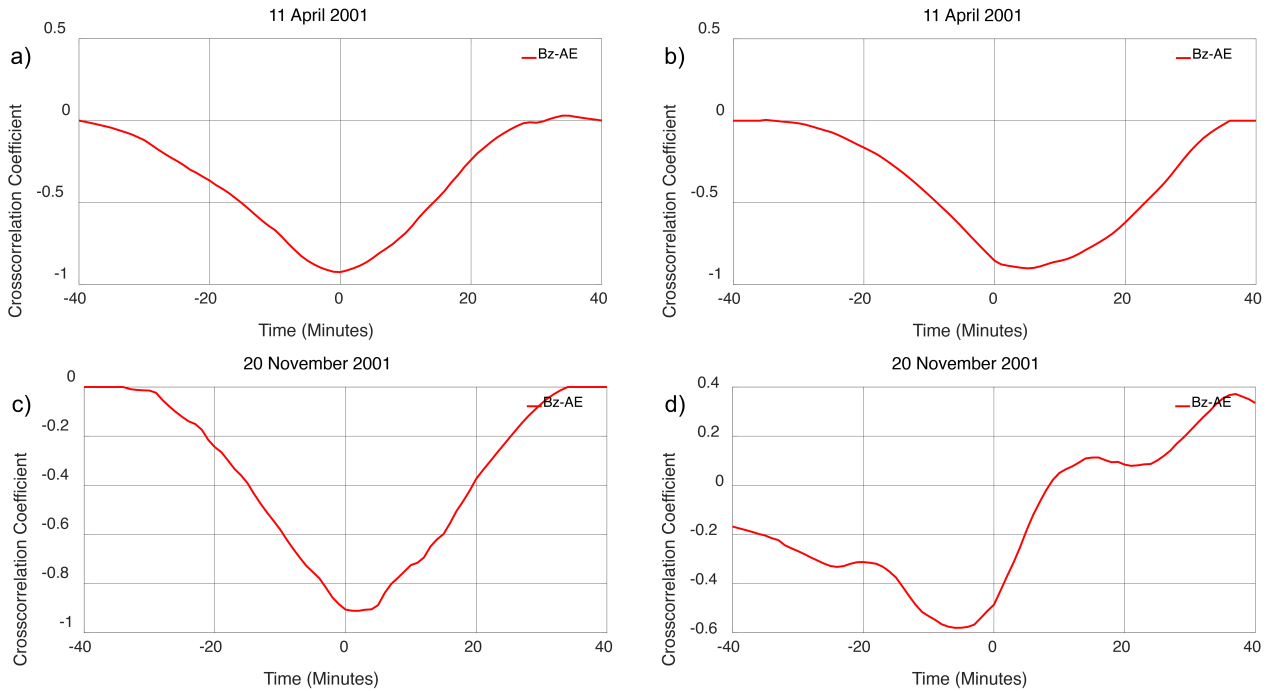
Figure 4. (a) and (b) Cross correlation between IMF B_z and AE index during two SSSs events occurred at 15:53 UT and 20:16 UT on 11 April 2001 and (c) and (d) represent the same during two SSSs events occurred at 07:00 UT and 13:45 UT on 24 November 2001.

4. Conclusion

In this work, we studied the solar wind-magnetosphere coupling during two supersubstorms (SSSs) events on 11 April 2001 and 24 November 2001. The time response of auroral electrojet index to solar wind interplanetary magnetic field (IMF B_z) during coupling has been analyzed using continuous wavelet transforms (CWT) and global wavelet spectrum (GWS) methods. The spectrum identified the main periodicities of the IMF B_z and AE index during these events. The short-lived periodicity of high-frequency signals are identified between 70 to 256 minutes and 80 to 256 minutes during 11 April 2001 and 24 November 2001, respectively. The global wavelet spectrum (GWS) identifies the most energetic periods are present during the SSSs. We also applied cross-correlation analysis to study the correlation and time lag between the IMF B_z and AE index. Through the correlation analysis technique, the correlation coefficient ~ -0.6 was obtained between the AE and IMF B_z approximately with zero lag. This study supports the previous existing facts that the solar wind-magnetosphere coupling during SSSs is mainly due to magnetic reconnection between southward IMF B_z and geomagnetic field at the magnetosphere.

References

Adhikari, B., N. P. Chapagain (2015), Polar cap potential and merging electric field during high intensity long duration continuous auroral activity, *J. Nepal Phys. Soc.*, *3*, No. 1, 6–17, **Crossref**

Adhikari, B., P. Baruwal, N. P. Chapagain (2017a), Analysis of super substorm events with reference to polar cap potential and polar cap index, *Earth and Space Science*, *4*, 2–15, **Crossref**

Adhikari, B., S. Dahal, N. P. Chapagain (2017b), Study of field aligned current (FAC), interplanetary electric field component (E_y), interplanetary magnetic field component (B_z), and northward (x) and eastward (y) components of geomagnetic field during super substorm, *Earth and Space Science*, *4*, 257–274, **Crossref**

Adhikari, B., S. Dahal, et al(2018), Field-aligned current and polar cap potential and geomagnetic disturbances: A review of cross-correlation analysis, *Earth and Space Science*, *5*, 440–455, **Crossref**

Akasofu, S. I. (1964), The development of the auroral substorm, *Planet. Space Sci.*, *12*, 273–282, **Crossref**

Bargatze, L. F., D. N. Baker, et al. (1985), Magnetospheric impulse response for many levels of geomagnetic activity, *J. Geophys. Res.*, *90*, 6387–6394, **Crossref**

de Souza, A., M. E. Echer, et al. (2018), Cross-correlation and cross-wavelet analyses of the solar wind IMF B_z and auroral electrojet index AE coupling during HILDCAAs, *Ann. Geophys.*, *36*, 205–211, **Crossref**

Despirak, I. V., A. A. Lyubchich, N. G. Kleimenova (2018), Large scale structure of solar wind and appearance of supersubstorm, Physics of auroral phenomena, *Proc. XLI Annual seminar* p. 11–13, PGI, Apatity.

Despirak, I., N. Kleimenova, et al. (2019), Super substorms during strong magnetic storm on 7 September 2017, *E3S Web of Conferences*, *127*, 01010, **Crossref**

Despirak, I. V., A. A. Lyubchich, et al. (2021), Longitude Geomagnetic Effects of the Supersubstorms during the Magnetic Storm of March 9, 2012, *Bulletin of the Russian Academy of Sciences: Physics*, *85*, No. 3, 246–251, **Crossref**

Domingues, M. O., O. Mendes, A. M. da Costa (2005), Wavelet techniques in atmospheric sciences, *Advances in Space Research*, *35*, No. 5, 831–842, **Crossref**

Echer, E., W. D. Gonzalez, et al. (2008), Interplanetary conditions causing intense geomagnetic storms ($Dst \leq 100$ nT) during solar cycle 23 (1996–2006), *J. Geophys. Res.*, *113*, A05221, **Crossref**

Echer, E., A. Korth, et al. (2017), Global geomagnetic responses to the IMF B_z fluctuations during the September/October 2003 high-speed stream intervals, *Ann. Geophys.*, *35*, 853–868, **Crossref**

Gjerloev, J. W. (2012), The SuperMAG data processing technique, *J. Geophys. Res.*, *117*, A09213, **Crossref**

Gonzalez, W. D., J. A. Joselyn, et al. (1994), What is a geomagnetic storm qm?, *Journal of Geophysical Research*, *99*, 5771–5792, **Crossref**

Guo, J., F. Wei, et al. (2016), Alfvén waves as a solar-interplanetary driver of the thermospheric disturbances, *Sci. Rep.*, *6*, 18,895, **Crossref**

Hajra, R., B. T. Tsurutani, et al. (2016), Supersubstorms ($SML < 2500$ nT): Magnetic storm and solar cycle dependences, *J. Geophys. Res. Space Physics*, *121*, 7805–7816, **Crossref**

Hajra, R., B. T. Tsurutani, et al. (2013), Solar cycle dependence of high intensity long-duration continuous AE activity (HILDCAA) events, relativistic electron predictors?, *J. Geophys. Res. Space Physics*, *118*, 5626–5638, **Crossref**

Henderson, M. G., J. S. Murphree, J. M. Weygand (1996), Observationsof auroral substorms occurring together with preexisting "quiet time" auroral patterns, *J. Geophys. Res.*, *101*, 24,621–24,640, **Crossref**

Katz, R. W. (1988), Use of cross correlations in the search for teleconnections, *J. Climatology*, *8*, 241–253, **Crossref**

Lee, D. T. L., A. Yamamoto (1994), Wavelet analysis: theory and applications, *Hewlett-Packard Journal*, *45*, No. 6, 44.

Liou, K., P. T. Newell, C. L. Meng (2001), Seasonal effect on auroral particle acceleration and precipitation, *Journal of Geophysical Research*, *106*, 551, **Crossref**

Maggiolo, R., M. Hamrin, et al. (2017), The delayed timeresponse of geomagnetic activity to thesolar wind, *Journal of Geophysical Research: Space Physics*, *122*, 11,109–11,127, **Crossref**

McPherron, R. L., C. T. Russell, M. P. Aubry (1973), Satellite studies of magnetospheric substorms on August 15, 1968. Phenomenological model for substorms, *J. Geophys. Res.*, *78*, 3131–3149, **Crossref**

Mendes, O. J., M. O. Domingues, et al. (2004), Wavelet analysis applied to magnetograms: singularity detections related to geomagnetic storms, *VI Latin-American Conference on Space Geophysics* 1, p. 177, InstitutoNatcional de PesquisasEspaciais, Sao Jose dos Campos.

Morioka, A., Y. Miyoshi, et al. (2003), AKR disappearance during magnetic storms, *Journal of Geophysical Research*, *108*, No. A6, 1226–1235, **Crossref**

Pandit, D., N. P. Chapagain, et al. (2018), Activities and Its Impact on SpaceWeather, Long-Term Datasets for the Understandingof Solar and Stellar Magnetic Cycles Proceedings IAU Symposium No. 340, 2018 International Astronomical Union 2018, *Journal of Geophysical Research*, **Crossref**

Poudel, P., S. Simkhada, et al. (2019), Variation of solar wind parameters along with the understanding of energydynamics within the magnetospheric system during geomagnetic disturbances, *Earth and Space Science*, *6*, 276–293, **Crossref**

Rostoker, G. (1972), Geomagnetic indices, *Rev. Geophys.*, *10*, 935–950, **Crossref**

Sergeev, V. A. (1996), Energetic particles as tracers of magnetospheric configuration, *Adv. Space Res.*, *18*, 161–170, **Crossref**

Suji, K. J., P. R. Prince (2018), Global and local Joule heating during substorms in St. Patrick's Day 2015 geomagnetic storm, *Earth Planets Space*, *70*, 167, **Crossref**

Tsurutani, B. T.,   W. D. Gonzalez (1987), The cause of high-intensity long duration continuous *AE* activity (HILDCAAS): interplanetary alfven wave trains, *Planetary and Space Science*, *35*,   400–412, **Crossref**

Tsurutani, B. T.,   C. I. Meng (1972),   Interplanetary magnetic-field variations and substorm activity, *J. Geophys. Res.*, *77*,   2964–2970, **Crossref**

Tsurutani, B. T., R. Hajra, et al.   (2015),   Extremely intense ($SML \leq 2500$ nT) substorms: Isolated events that are externally triggered?, *Ann. Geophys. Commun.*, *33*,   519–524, **Crossref**

Tsurutani, B. T.,   G. S. Lakhin,   R. Hajra (2020), The physics of space weather/solar-terrestrial physics (STP): what we know now and what the current and future challenges are, *Nonlin. Processes Geophys.*, *27*,   75–119, **Crossref**

Weimer, D. R.,   L. A. Reinleitner, et al.   (1990), Saturation of the auroral electrojet current and the polar cap potential, *Journal of Geophysical Research*, *95*,   18,981–18,987, **Crossref**

Corresponding author:

Drabindra Pandit, Central Department of Physics, IOST, Tribhuvan University, Kirtipur, Kathmandu, Nepal. (drabindrapandit087@gmail.com)

Annales
Geophysicae

Climatology of ionosphere over Nepal based on GPS total electron content data from 2008 to 2018

Drabindra Pandit[1,6]**, Basudev Ghimire**[1,6]**, Christine Amory-Mazaudier**[2,3]**, Rolland Fleury**[4]**,**
Narayan Prasad Chapagain[5]**, and Binod Adhikari**[6]

[1]Central Department of Physics, IOST, Tribhuvan University, Kathmandu, Nepal
[2]Sorbonne Université, Ecole polytechnique, Institut Polytechnique de Paris, Université Paris Saclay, Observatoire de Paris,
CNRS, Laboratoire de Physique des Plasmas (LPP), 75005 Paris, France
[3]T/ICT4D, Abdus Salam ICTP, Trieste, Italy
[4]Lab-STICC, UMR 6285, Institut Mines-Télécom Atlantique, Brest, France
[5]Department of Physics, Amrit Campus, Tribhuvan University, Thamel, Kathmandu, Nepal
[6]Department of Physics, St. Xavier's College, Maitighar, Kathmandu, Nepal

Correspondence: Drabindra Pandit (drabindrapandit087@gmail.com)

Abstract. In this study, we analyse the climatology of ionosphere over Nepal based on GPS-derived vertical total electron content (VTEC) observed from four stations as defined in Table 1: KKN4 (27.80° N, 85.27° E), GRHI (27.95° N, 82.49° E), JMSM (28.80° N, 83.74° E) and DLPA (28.98° N, 82.81° E) during the years 2008 to 2018. The study illustrates the diurnal, monthly, annual, seasonal and solar cycle variations in VTEC during all times of solar cycle 24. The results clearly reveal the presence of equinoctial asymmetry in TEC, which is more pronounced in maximum phases of solar cycle in the year 2014 at KKN4 station, followed by descending, ascending and minimum phases. Diurnal variations in VTEC showed the short-lived day minimum which occurs between 05:00 to 06:00 LT (local time) at all the stations considered, with diurnal peaks between 12:00 and 15:00 LT. The maximum value of TEC is observed more often during the spring equinox than the autumn equinox, with a few asymmetries. Seasonal variation in TEC is observed to be a manifestation of variations in solar flux, particularly regarding the level of solar flux in consecutive solstices.

1 Introduction

Total electron content (TEC) is a crucial parameter of ionosphere comprising high concentrations of electrons and ions formed under the ionization of extreme ultraviolet (EUV) radiation and solar X-rays. The lower atmospheric disturbance also contributes to ionospheric variability (Anderson and Fuller-Rowell, 1999; Prikryal et al., 2010). Numerous periodic and aperiodic variabilities identified in the ionosphere make the impact on the applications involving the radio link between satellites and the ground, which plays vital role in the communication, navigation and surveillance, with important consequences for the reliability and accuracy of the service (Guo et al., 2015). The global positioning system (GPS) is widely used in recent appliances which encounter the largest errors in the path due to disturbed ionospheric free electrons, emphasizing the need to study GPS–TEC variability. The application of GPS technology gives scientists insight into the shape and behaviour of the ionosphere. A list of factors affecting TEC includes ionospheric electron density, ion–electron temperature, composition, dynamic variations with altitude, latitude, longitude, local time, seasons, solar and magnetic activity. Because the equatorial ionosphere is highly vulnerable, it poses major threats to communication signals. The ionosphere at the mid latitude is less variable; hence, most of the observations and measurements are taken from this region, whereas the high latitude ionosphere is sen-

sitive to outer space as it is connected by geomagnetic field lines (Akala et al., 2013; Parwani et al., 2019). The study of VTEC at the low–mid ionosphere showed solar activity dependence (Shimeis et al., 2014). TEC has been studied by a large number of researchers; Rama Rao et al. (1980) studied the diurnal variation in TEC at Waltair, India, and found a short-lived predawn minimum, a steep early morning rise followed by broad mid-afternoon maximum and a steep post-sunset fall. The relation between TEC and the sunspot number (SSN), $F_{10.7}$ and EUV was studied by Dabas et al. (1993), who pointed out that TEC has a nonlinear relation with SSN and a linear relation with $F_{10.7}$ and EUV. Ouattara and Amory-Mazaudier (2012) showed the impact of solar activity on diurnal variability during different phases of the solar cycle. An analogous study was carried out around the globe using various methods of TEC, such as diurnal, monthly, seasonal and solar cycle and solar activity dependency, e.g. in South Asia (Chauhan et al., 2011; Walker et al., 1994), in South America (Sahai et al., 2007; Natali and Meza, 2011; Akala et al., 2013; de Abreu et al., 2014), over North America (Huo et al., 2009; Perevalova et al., 2010), in Africa (Shimeis et al., 2014; D'ujanga et al., 2012; Ouattara and Fleury, 2011; Zoundi et al., 2012), over Brazil (Venkatesh et al., 2014a, 2014b, 2015), over Japan (Zakharenkova et al., 2012; Mansoori et al., 2016) and over China (Guo et al., 2015; Zhao et al., 2007; Liu et al., 2013).

TEC studied at the Jet Propulsion Laboratory for the years 1998–2008 found stronger annual TEC variation in the Southern Hemisphere, and the variation in phase and amplitude is more in the conjugate hemisphere (Liu et al., 2009). Galav et al. (2010) found semiannual periodicity in daytime TEC, the spring equinox shows the highest TEC, and winter solstices are the lowest in India. The winter anomaly, semiannual anomaly and annual anomaly are described by Liu and Chen (2009) and Rishbeth and Garriott (1998). Global-scale TEC research found that the effect on TEC was stronger during the day than at night and also at low latitudes than at high latitudes. The effect on TEC is seen more on the either side of the magnetic equator than at the magnetic equator (Liu et al., 2009). Dashora and Suresh (2015) analysed the characteristics of low latitude TEC data of solar cycles 23 and 24 over Indian sector using global ionospheric data. A double hump structure in the solar flux and in TEC was identified at the low latitude station of Varanasi, India, in the ionospheric response using the GPS TEC, IRI (International Reference Ionosphere) and TIE-GCM (Thermosphere–Ionosphere–Electrodynamics General Circulation Model) TEC of solar cycle 24 by Rao et al. (2019a). Parwani et al. (2019) studied the latitudinal variation in ionospheric TEC in the northern hemispheric region and found that the diurnal TEC has a higher value in low latitudes than in mid and high latitudes and in the seasonal variation maximum in spring and autumn than in summer and winter.

Many studies on TEC have been conducted in Asia; however, no result for the climatology of TEC over Nepal, for a long time series, about one solar cycle has been reported up to now. In this paper, we present, for the first time, characteristics of ionosphere in Nepal, such as the diurnal, annual, seasonal and solar cycle dependence of TEC on the local ionospheric conditions, using GPS TEC data obtained from the four GPS stations of KKN4, GRHI, JMSM and DLPA (see Table 1). Our study includes GPS TEC data from 2008 to 2018 of solar cycle 24, including all four phases of this sunspot cycle, the minimum phase of the years 2008–2009, the ascending phase of the years 2010–2011, the maximum phase from 2012 to 2014 and the descending phase of years 2015–2018. The second section of this paper includes the data set and methodology, and the third includes the results and discussion. The concluding remarks are discussed in the last section.

2 Data set

Total electron content (TEC) is the total number of electrons integrated along the path from the receiver to each GPS satellite which orbits the Earth at an altitude of 20 200 km. It measures in TEC units (TECU), where 1 TECU = 10^{16} electron per square metre. The TEC is obtained as follows (Hofmann-Wellenhof et al., 1992):

$$\text{TEC} = \int_R^S N_e(h)\,dh, \tag{1}$$

where N_e is electron density, R is the receiver altitude, and S is the satellite altitude. The dual frequency GPS receiver in the two L-bands of frequency $f_1 = 1575.42$ MHz and $f_2 = 1227.60$ MHz provide the carrier phase and pseudo-range measurements. The TEC is calculated from the L1 and L2 pseudo-range and carrier phase (Hofmann-Wellenhof et al., 1992). Using the pseudo-range and phase data, TEC is calculated as follows:

$$\text{TEC} = \frac{1}{40.3}\left(\frac{f_1^2 f_2^2}{f_2^2 - f_1^2}\right)(P_1 - P_2), \tag{2}$$

where P_1 and P_2 are the pseudo-ranges for frequencies f_1 and f_2, respectively.

The TEC obtained by this method is called slanted TEC (STEC), which is a measure of the total electron content of the ionosphere along the ray path from the satellite to receiver and has to be converted to vertical TEC (VTEC) using the equation (Titheridge, 1972).

$$\text{VTEC} = (\text{STEC} - B_s - B_u)\left(\sqrt{1 - \left(\frac{(R_e \times \cos\varepsilon)^2}{(R_e + h)^2}\right)}\right), \tag{3}$$

where B_s and B_u are the biases of instruments of satellites and receivers, respectively, ε is the elevation angle of the satellite, and $R_e = 6371$ km is the mean radius of the Earth.

For this study, data were carried out with GPS data taken from four GPS stations (DLPA, JMSM, KKN4 and GRHI) from Nepal. The details of the stations, including their geographical and geomagnetic coordinates, are shown in Table 1 and universal time is used for all time references. The GPS data of the four stations were downloaded from http://www.unavco.org, last access: 15 March 2020, which is freely available to all users. These data are available in RINEX (Receiver Independent Exchange) format v2.1, which is a standard ASCII (American Standard Code for Information Interchange) format. The temporal resolution of this data is 15 min. The raw data are then processed using software developed by Rolland Fleury (Lab-STICC, UMR 6285, Institut Mines-Télécom Atlantique, site de Brest, France, 19 July 2018; available at http://www.girgea.org, last access: 19 July 2018), which runs on a Windows operating system to obtain the required TEC.

The data for the solar indices sunspot number (SSN) and solar flux index (F10.7) to study long term solar activity are taken from Royal Observatory of Belgium, Brussels (http://sidc.oma.be/silso/home, last access: 6 April 2020), and OMNIWeb (http://omniweb.gsfc.nasa.gov/, last access: 6 April 2020). SSN is one of the most the consistent solar indices and effectively describes solar activities, and the are valuable for forecasting space weather phenomena. The solar flux index provides the information about the total emission produced by the Sun at the wavelength of F10.7 cm to the Earth.

In this study, we use GPS-derived TEC from RINEX files, using this method to obtain TEC calibrated at 15 min for all measures. Between 30 s VTEC sequences, the elevation may vary. This leads to variation in the VTEC, depending on the constellation and not just the variation in the content over that period. We have chosen to do the regression over a period 15 min, with the VTEC obtained displayed in the middle of this period. This makes it possible to have four points over 1 h and, therefore, to have an evolution of the VTEC 4 times more precise than that of global ionosphere maps (GIMs), which are currently in time steps of 1 or 2 h, depending on the organization. So, it provides a better possibility to see and characterize finer local structures in RINEX-derived TEC than in GIMs.

This study analyses variations in VTEC during different phases of solar cycle 24, along with the annual, seasonal and diurnal variations. For this, the local seasons are classified as winter (November–February), spring (March and April), summer (May–August) and autumn (September and October). The classifications of the selected years, as per solar cycle phases, are presented in Table 2.

3 Results and discussion

In this section, we present the diurnal, monthly, seasonal, solar cycle and geomagnetic variation in GPS TEC over Nepal

during the solar cycle-24. Figure 1 represents the position of chosen GPS stations in Nepal for this study and Fig. 2 represents the variation in the sunspot number and solar flux during the period 2008–2018.

3.1 Diurnal variation

Figure 3a exemplifies the diurnal variation in VTEC in LT observed during 2 February 2009, 2012, 2014, 2016 and 2017 during the minimum, inclining, maximum and declining phases of solar cycle 24 at the KKN4 station in Nepal. The plot shows that, before sunrise $\sim 05{:}00$ LT, VTEC becomes minimum and reaches a maximum around 11:00–14:00 LT and later decreases in the evening and at night. The diurnal peak is noticed between 11:00 and 14:00 LT, though the peak values change every month. The VTEC plots reveal a growth from dawn to a highest value of about 5 to 98 TECU after the daylight hours, and it decreases to the lowest value prior to dusk, with a time difference of ± 1 to 2 h. A flat curve with minor peaks is identified during the minimum and descending phases, whereas the dome shape is noticed during the maximum phase and multiple peaks and troughs at varying positions are observed during ascending phases. Overall, the VTEC shows a normal trend of diurnal behaviour, with the lowest values at dawn and dusk and the highest value during the midday. The maximum vertical total electron content values in the diurnal curve were noticed during the maximum phases of the solar cycle in 2014 and 2012 during the ascending phases, whereas the minimum values were observed in 2016, 2017 and 2009 during the descending phases. The diurnal variation in VTEC was studied by plotting similar curves for all the days from years 2008 to 2018 for all four chosen stations. In general, the diurnal VTEC behaviour exhibits a solar cycle dependency. The diurnal variability in VTEC for all the days is not presented due to constraint of space. In our study, the mean diurnal curves for the KKN4 station for years 2008, 2009 and 2010 exhibit a wave-like profile, whereas the mean diurnal curves of years 2011–2017 show a parabolic nature, which is shown in Fig. 3b. The similar diurnal profile was noticed for all stations considered. The diurnal graphs (Fig. 3) show a better synchronization of VTEC with SSN and solar flux (Fig. 2).

The observed diurnal VTEC pattern reflects the signature of different solar events. The noon bite-out profile with asymmetric peaks, parabolic profile and wave profile with morning, evening and night peaks and a few complex structures are noted in the diurnal profile. The quiet day activity at the minimum phase, the fluctuating activity during the increasing phase, shock activity during the maximum phase and recurrent activity during the declining phase was noticed in the study of ionospheric parameters at the Ouagadougou ionosonde station data in West Africa by Ouattara et al. (2009).

The upward $\boldsymbol{E} \times \boldsymbol{B}$ drift velocity plays an important role in producing the nighttime post-sunset enhancement. The aver-

Table 1. The selected GPS stations and their coordinates, the data of which are used in the study.

SN	ID	Locations	Geog. Lat.	Geog. Long.	Geom. Lat.	Geom. Long.	Dip. Lat.	Local time (LT)
1	KKN4	Kakani, Nepal	27.80° N	85.27° E	18.62° N	159.41° E	43.86	UT + 05:45 h
2	GRHI	Ghorahi, Nepal	27.95° N	82.49° E	18.94° N	156.82° E	44.25	UT + 05:45 h
3	JMSM	Jomsom, Nepal	28.80° N	83.74° E	19.71° N	158.06° E	45.31	UT + 05:45 h
4	DLPA	Dolpa, Nepal	28.98° N	82.81° E	19.94° N	157.21° E	46.03	UT + 05:45 h

Table 2. Classification of selected years according to the solar cycle phases.

Interval	Years	Solar cycle phases
I	2008–2009	The minimum phase of solar cycle 24
II	2010–2011	The increasing phase of solar cycle 24
II	2012–2014	The maximum phase of solar cycle 24
IV	2015–2018	The decreasing phase of solar cycle 24

age plasma flux required for the enhancement in equatorial latitude found $(2.2 \pm 0.9) \times 10^{12}\,\mathrm{m^{-2}\,s^{-1}}$ by Jain (1987) in India. Tariku (2015) studied the pattern of GPS-TEC over the African sector during 2008 to 2009 and 2012 to 2013 and found small enhancements in the VTEC in the night-time $\sim$ between 21:00 and 23:00 LT, especially for equinoctial months, and then drops again mostly after 23:00 LT. The enhancement was mostly found in equinoctial months during high solar activities, and during the low solar activities phase in the solstice, the pre-reversal enhancement was much smaller. A diurnal plot (Fig. 3) of the ionosphere over Nepal shows a similar result of pre-reversal enhancement during the high solar activities of 2012 and 2014 but not during the low solar activities of 2009 and 2017.

Mountains generate relief waves which propagate to the stratosphere and lower thermosphere (Leutbecher and Volkert, 2000). Studies on these waves have been made in Nepal in the lower atmosphere (Regmi and Maharjan, 2015; Regmi et al., 2017). Other studies have shown the impact of relief waves on the ionosphere in the Andes (Torre et al., 2014) and Tibet (Khan and Jin, 2018). In Fig. 3a, we see oscillations which cannot be interpreted directly as the signature of the waves. In fact, for the processing of GPS data, we use pseudo-range signals which can be affected by reflections on surrounding reliefs and by waves.

3.2 Monthly variation in TEC

Figure 4 shows the monthly variability in VTEC for the maximum phase of solar cycle year 2014 at KKN4 station. The plot is obtained using the average of the daily data. The plot shows the maximum in equinoctial months (March and April) and the minimum in solstices (January and June). The rise or fall of TEC in each curve follows the diurnal pattern, which is the prominent peak in the midday with different peak amplitude. The lowest VTEC peak is observed during January and the highest in March. Late afternoon peak are

seen in March, June and September, whereas the peak centred at $\sim$ 02:00 LT for rest of the months. A significant plat peak is noticed in December, whereas the steep rise in VTEC is noticed in March, April and October. The monthly variation in VTEC was studied by plotting similar curves for all the months from years 2008 to 2018 for all four chosen stations. The plot shows clear wave activity in the mean diurnal curve for years 2008, 2009 and 2010, and from the years 2011 to 2017 the stiff rise in VTEC was noticed (plots are not included in this paper). In general, the sunrise times in summer and winter are 05:15 and 06:45 LT, which differ by 1.5 h. During summer 2014, the maximum and minimum TEC observed is 21 and 12 TECU, whereas in winter the maximum and minimum TEC noticed is 25 and 15 TECU, respectively (Fig. 4). It also seems that during sunrise time in summer the VTEC is linear, but during the winter it is steep.

3.3 Seasonal variation in TEC

Figure 5 shows a 2D diurnal plot of VTEC at JMSM station for all four phases (I minimum – 2009; II ascending – 2011; III maximum – 2014; IV descending – 2015) of solar cycle 24, which explains how the diurnal VTEC varies hourly during the four phases. In the ionosphere over Nepal, the features of equinoctial asymmetry is distinctly noticed in 2D plots of years 2009, 2011, 2014 and 2015 in Fig. 5a–d, respectively. From Fig. 5a–d, it can be observed that equinoctial asymmetry is not noticed in 2009, in 2011 autumn is more intense than spring, and in 2014 and 2015 spring VTEC is greater than autumn. In the year 2009, equinoctial asymmetry is not noticed during low solar activities. But in the year 2011, the autumn is more intense than spring, which is a feature of the equatorial ionization anomaly (EIA) crest latitude, and in the year 2014, the difference between equinoctial asymmetry is less (spring > autumn), which is again characteristic of the EIA trough station. And in 2015, the asymme-
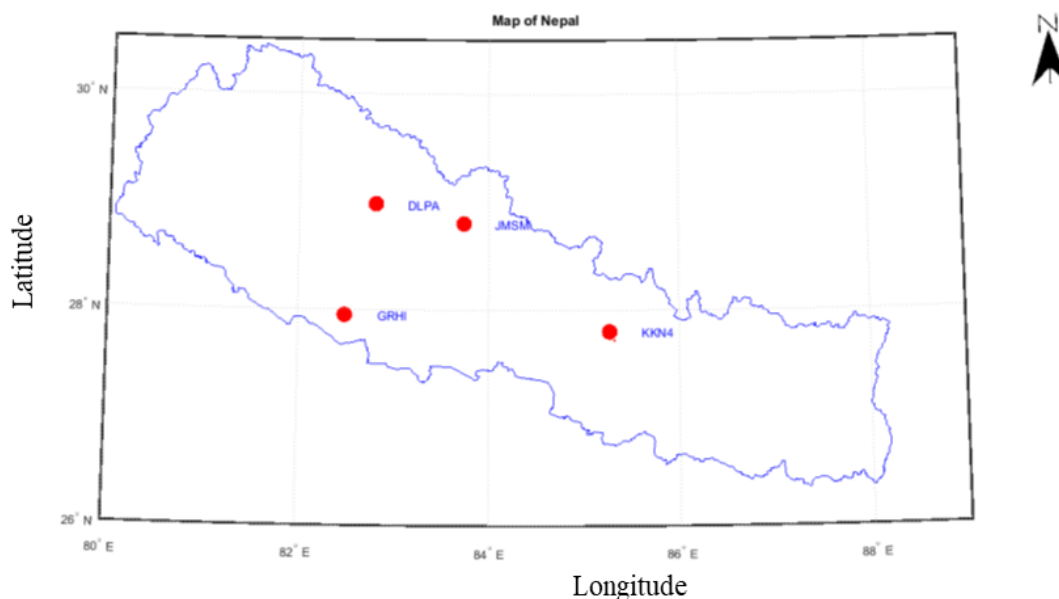
Figure 1. A map of Nepal showing locations of GPS stations used in our study.
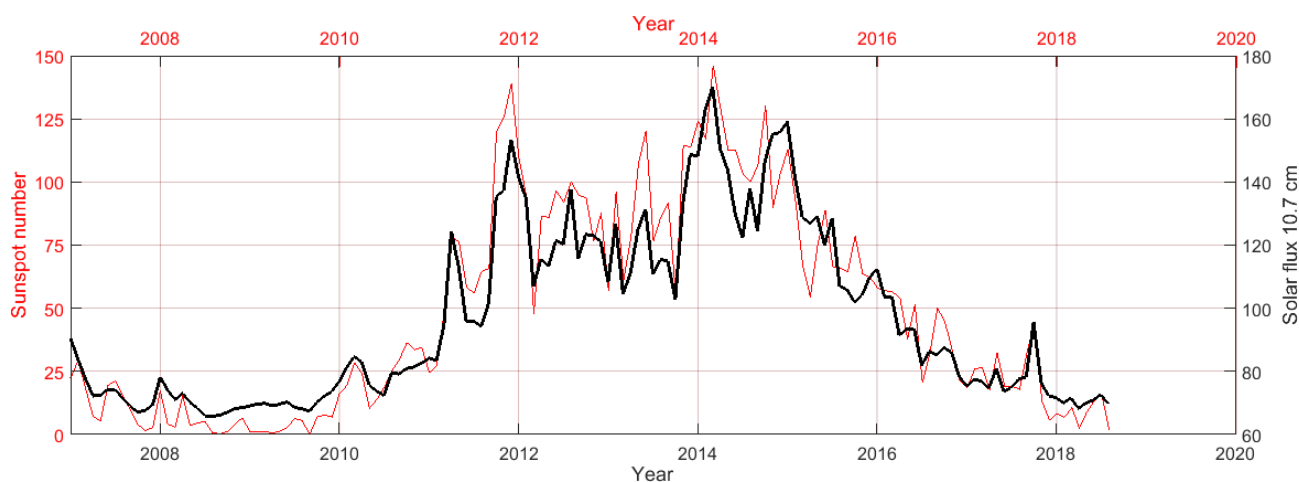

Figure 2. Display the variations in the sunspot numbers and solar flux for the year 2008 to 2018.

try very high (spring > autumn), which is the general feature of TEC at all latitudes.

In Fig. 6a–e, each panel separately represents the VTEC variation during the autumn, spring, summer and winter seasons for the years 2008, 2009, 2011, 2014 and 2015 at KKN4, GRHI, JMSM and DLPA, respectively. The plots show that the maximum value of VTEC is ∼ 95 TECU in spring 2014, which is the maximum year of the sunspot cycle, and the minimum value is 10 TECU in 2009 winter, which is the minimum year of the sunspot cycle. In the increasing and decreasing phases of solar cycle, the VTEC gradually increases and decreases, depending on the amount of UV that arrives at the Earth. In general, the plots show that VTEC is maximum during spring followed by autumn, summer and winter, except for a few cases. Similarly, pre-

vious studies of GPS TEC for the year 2014 over Nepal also reported the highest value of VTEC in March and lowest in December, with distinct the seasonal variations and having higher values in spring and lower in the winter season (Ghimire et al., 2020b). During the sunspot minimum years of 2008–2010, there are no semiannual variations in the VTEC, and it also seems that the summer VTEC is as strong as the autumn VTEC. For the years 2011 to 2016 the semiannual variations are noticed. During the year 2017, we observed the same pattern as for the years 2008–2010, where the summer VTEC is as strong as the autumn VTEC. At the station KKN4, the VTEC in autumn is very weak in year 2015, and it is smaller than the VTEC in summer. In year 2011, the VTEC is larger in winter than in summer at KKN4, whereas at GRHI and JMSM the winter VTEC is smaller
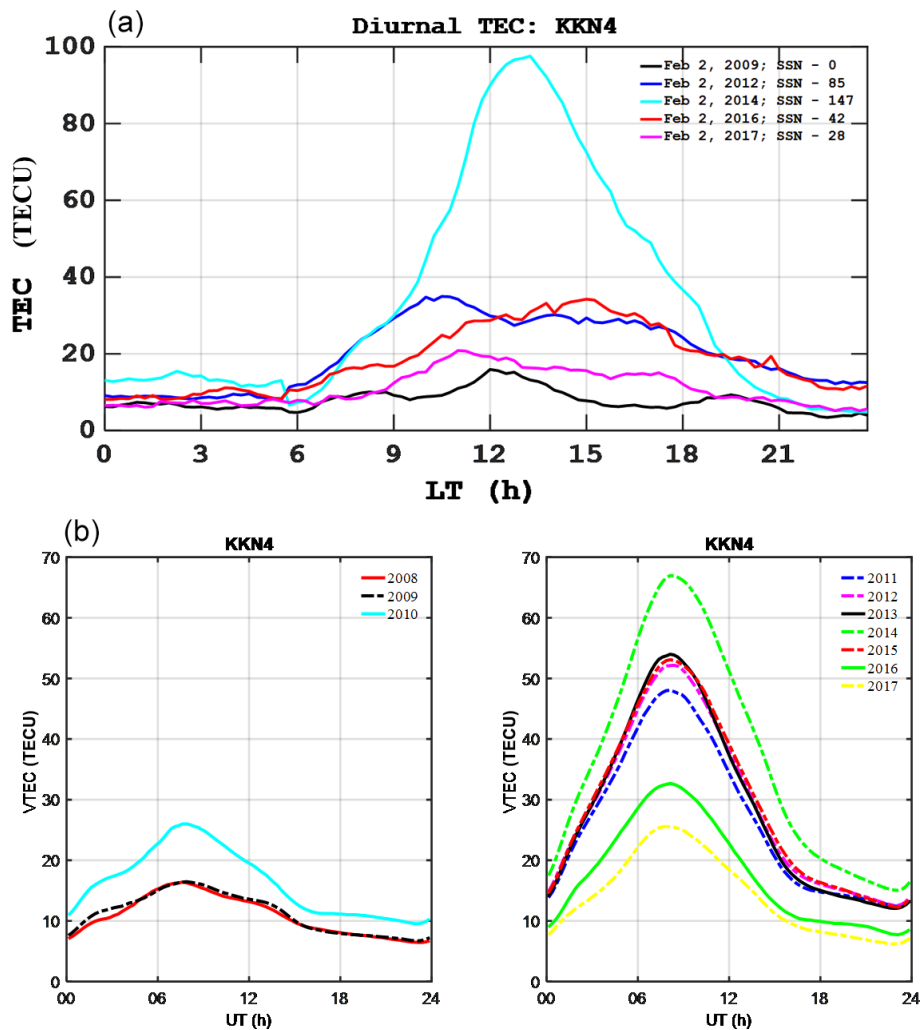
Figure 3. (a) Diurnal variation in vertical TEC at KKN4 GPS station. The black, blue, light green, red and pink colour lines represent the diurnal variation for the years 2009, 2012, 2014, 2016 and 2017. **(b)** Yearly mean diurnal variation in vertical TEC; the left represents the wave-like nature and the right represents the parabolic nature.

than the summer one in years 2011 and 2014. At DLPA, the winter VTEC is not larger than the summer VTEC. In year 2008, the spring VTEC identified more than the autumn value for GRHI, JMSM and DLPA but less than the autumn value is observed at KKN4. In year 2009, only at JMSM, spring noticed greater values than autumn. The autumn VTEC is greater than spring for all stations in 2011, except at JMSM where it is equal to spring. Large asymmetry is noticed between spring and autumn in year 2014. In year 2015, the summer peak is higher than the autumn. In the present study the VTEC is larger in winter than the VTEC in summer that is noticed in 2011 and 2014. At KKN4 station, a VTEC that is larger in winter than the VTEC in summer is noticed in the year 2014, and the same applies at GRHI in 2014 and 2016 and at JMSM 2014 and 2016. The VTEC that is larger in winter than in summer is not noticed at DLPA (Fig. 6c and d).

The solar flux dependency of the winter anomaly in GPS TEC has been studied by Rao et al. (2019b). The result showed that, when the level of solar flux in winter month is greater than the corresponding summer month, the winter anomaly is observed irrespective of whether the phases of solar cycle are is high or low. Their study also pointed out that the winter anomaly in GPS-derived TEC may not be a feature of any geophysical significance. The winter or seasonal anomaly is introduced due to temperature changes (Appleton, 1935), interhemispheric transport of ionization (Rothwell, 1963), significant changes in the Sun–Earth distance (Yonezawa, 1959; Buonsanto, 1986), seasonal variation in O/N_2 concentration (Rishbeth and Setty, 1961; Wright, 1963; Rishbeth et al., 2000; Zhang et al., 2005) and the upward movement of energy flux (Maeda et al., 1986). The winter anomaly is related to solar activity. Tyagi and Das Gupta (1990) and Bagiya et al. (2009) have reported an ab-
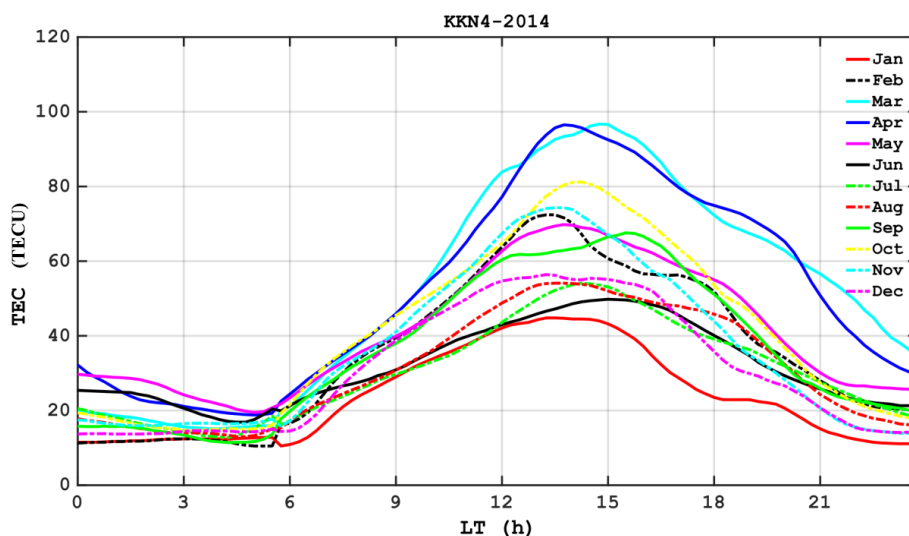
Figure 4. Monthly variation in vertical TEC in LT for each month of 2014 at KKN4 station.

sence of the winter anomaly in low solar activities at low latitudes. The change in composition of the constituents being identified as the cause of the winter anomaly was coined by Rishbeth and Setty (1961). The least VTEC in the June solstice (in the Northern Hemisphere) during the low and high solar activity phase may be due to the asymmetric heating, which results in the transport of neutral constituents from the summer to the winter hemisphere, reducing the rate of recombination. The reduction in the recombination rate in winter causes the greater rise of VTEC in winter than in summer. Gupta and Singh (2000) studied TEC over Delhi and concluded that the winter anomaly in TEC appears only during higher solar activity. This winter anomaly is due to the closer distance of the Earth to the Sun and the direction of the wind from the summer season to the winter (Shimeis et al. 2014). Krankowsky et al. (1968) and Cox and Evans (1970) separately pointed out that the ratio of O/N_2 becomes twice its value in winter than in summer as a result of higher electron loss rate in summer than in winter. Torr and Torr (1973) observed the winter anomaly in the critical frequency of ionospheric F2 layer (foF_2) under different solar activity at the mid latitude of the Northern Hemisphere, and a similar result was observed in the Southern Hemisphere during high solar activity. Furthermore, they noticed that lower solar activity results equal a lower winter anomaly. In general, the June solstice anomaly is higher than the December solstice, but in an earlier study done at Agra GPS station, they noticed some abnormalities in the solstice behaviour, demonstrating higher VTEC in the summer anomaly than the autumn and winter anomalies, with higher VTEC than in summer (Bagiya et al., 2011).

In Fig. 7, the top left panel represents the variation in VTEC during spring, bottom left during autumn, top right during summer and bottom right during winter from 2008

to 2017 at KKN4. In spring, the difference in VTEC between high and low solar activity is 65 TECU, in autumn it is 53 TECU, in summer it is 45 TECU, and in winter it is 40 TECU, respectively. In Fig. 8, the top panel represents VTEC variability during the minimum and increasing phases, whereas the bottom panel represents the maximum and decreasing phases of solar cycle 24 using the GPS station at GRHI. The plot shows that equinoctial asymmetry is not observable during the minimum solar of cycle 2008 and 2009, but it is clearly distinguishable during other phases of solar cycle.

The important parameter for the semiannual variation in ionospheric ionization is the variation in the atomic/molecular ratio, i.e. the concentration of the O/N_2 ratio. At the solstice, there is circulation of the meridional wind of about $25 \, m \, s^{-1}$ in the middle and low latitudes from summer to winter hemisphere (Rishbeth et al., 2000). These winds carry nitrogen-rich air produced in the summer hemisphere into lower latitudes by upwelling in higher latitudes, thus reducing O/N_2 ratio. At the equinox, there is no prevailing meridional circulation. The ratio O/N_2 depends specially on the horizontal circulation, and its seasonal changes accompany the change in global thermospheric circulation between the pattern from summer to winter around the solstices to a symmetrical pattern at equinoxes. The six possible reasons for seasonal and semiannual variations in the F_2 layer, discussed by Rishbeth (1998), are as follows: (a) the compositional changes due to large-scale dynamical effects in the thermosphere, (b) variations in the geomagnetic activities, (c) energy of the solar wind, (d) the inputs from lower atmospheric phenomena such as waves and tides, (e) change in atmospheric turbulence and (f) anisotropy of solar and EUV emissions in the solar latitude (Burkard, 1951).
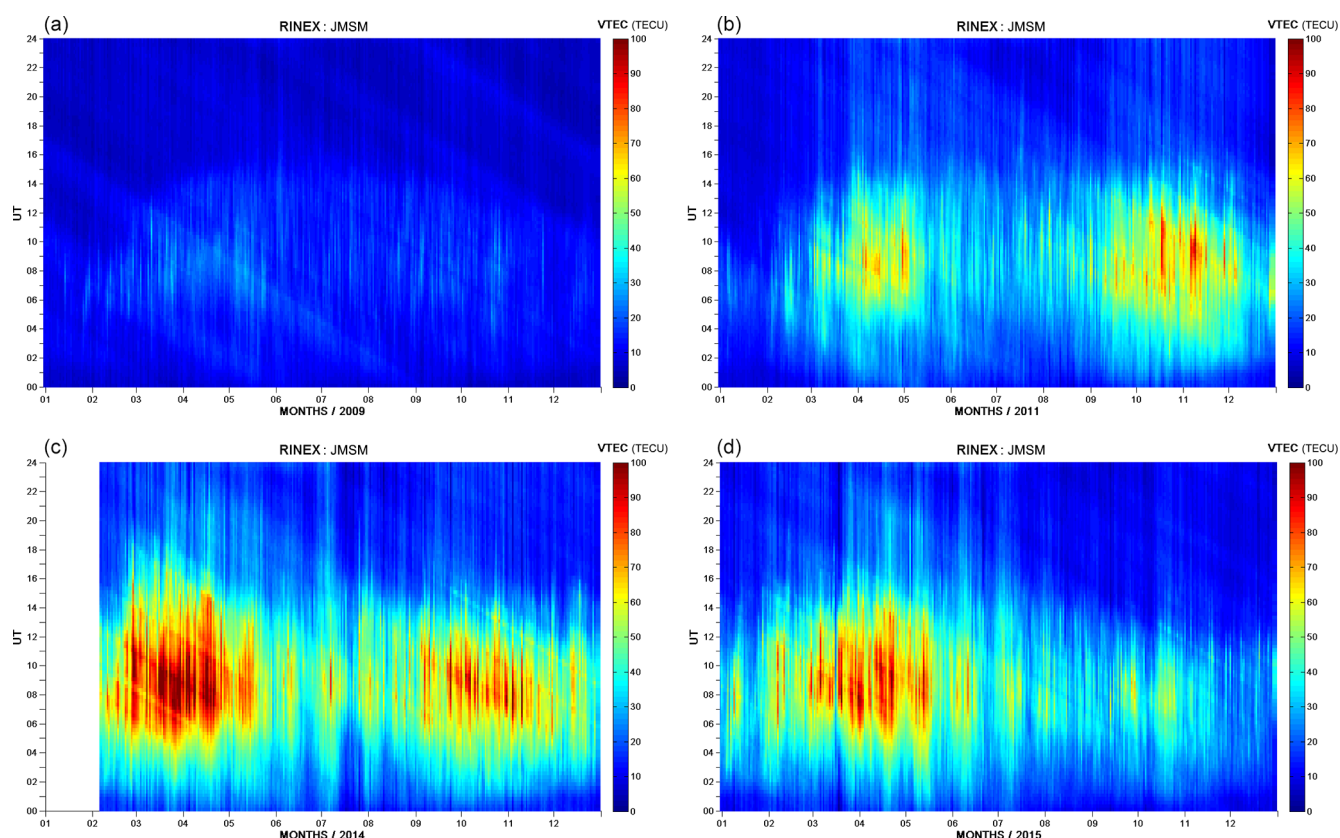
Figure 5. (a–d) A two-dimensional (2D) variation in vertical TEC according to UT at the JMSM station for one of the years of the minimum (2009), ascending (2011), maximum (2014) and descending (2015) phases of solar cycle 24.

In 2019, Ansari et al. (2019) found the minimum value of TEC in January, which becomes a maximum in April, decreases in June–July and is followed by an increase in magnitude of the second maximum in September–October and later a decrease until December at CHLM, JMSM and GRHI in year 2017. Referring to Fig. 8, our result for semiannual variation shows that the minimum value of VTEC is found in January, which becomes the maximum in March–April, decreases in June–July, is followed by an increase in magnitude of the second maximum in October–November and later decreases until December at GRHI in years 2009 to 2018.

The asymmetry between the two equinoxes is due to geophysical parameters as magnetic indices related to geomagnetic activity (Triskova, 1989) and the interplanetary magnetic field (IMF Bz) the interplanetary component of magnetic field (Russell and McPherron, 1973). The equinoctial asymmetry observed in VTEC is explained by (i) the axial hypothesis (ii) the Russell–McPherron (RM) effect and (iii) the equinoctial hypothesis (Lal, 1996; Shimeis et al., 2014).

Ouattara and Amory-Mazaudier (2012) made a statistical model of the F_2 layer, at equatorial latitudes, based on data obtained during three sunspot cycles. This model shows the influence of the different types of geomagnetic activity defined by Legrand and Simon (1989) and the asymmetry of

equinoxes due to the magnetic activity. The asymmetry between the two equinoctial peaks is also due to the asymmetry of the thermospheric parameters that influence the ionosphere as neutral wind and changes in composition (Balan et al., 1998)

3.4 Solar cycle variation in TEC

Figure 9 shows the annual mean values of VTEC, solar flux index and sunspot number during the solar cycle from years 2008 to 2018. The black, blue, green and red lines represent the VTEC variation at stations KKN4, GRHI, JMSM and DLPA, whereas pink and light green lines represents variation in SSN and solar flux index, respectively. The plot shows that VTEC gradually begins to increase in 2009 and reaches a maximum in 2014. Then it begins to decrease until 2018, which agrees with the sunspot number and solar flux variation in the same plot. The figure shows that the maximum value of the peak of ionization in 2014 is about 37 TECU in the maximum phase of the solar cycle, and the minimum value in 2008 is about 11 TECU in the minimum phase of solar cycle. The observed VTEC variation corresponds to the amount of UV reaching the Earth.
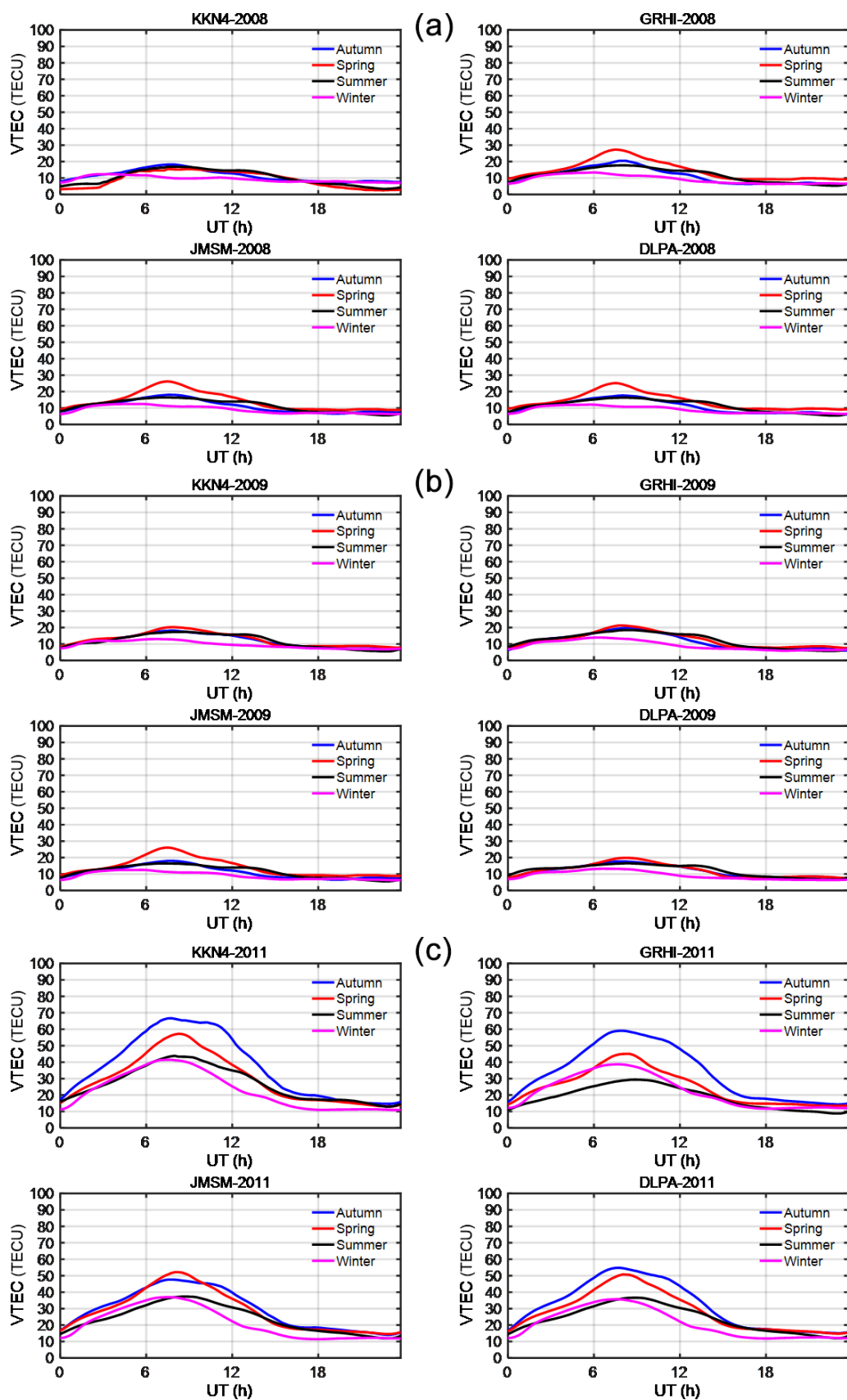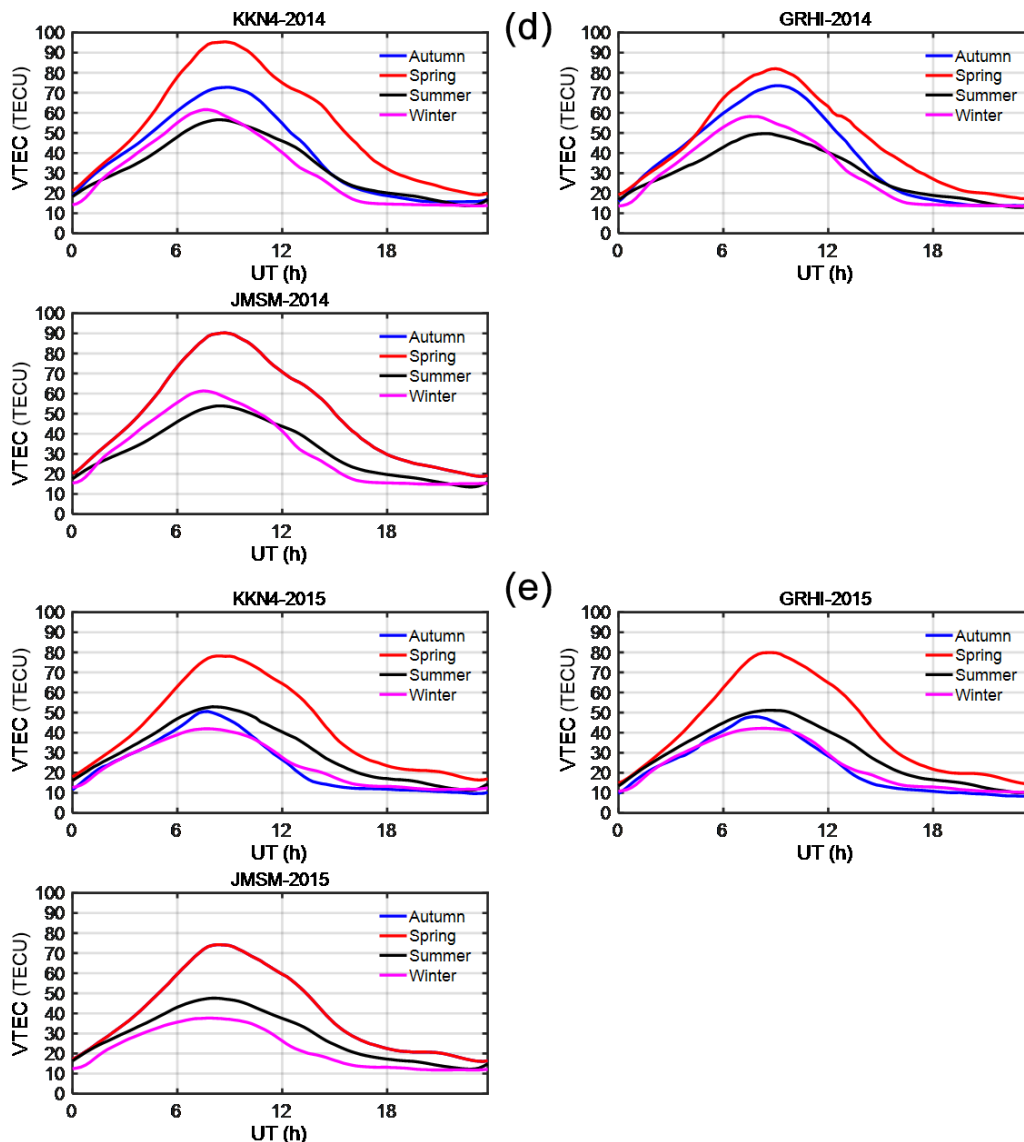
Figure 6.

Figure 6. Seasonal variability in VTEC during years 2008 **(a)**, 2009 **(b)**, 2011 **(c)**, 2014 **(d)** and 2015 **(e)** for KKN4, GRHI, JMSM and DLPA stations.

Similarly, the solar flux increases are from 2011 onward; the measured VTEC also exhibits the highest magnitude for the year 2014. The maximum VTEC value shows a decreasing trend from years 2015 to 2018 at all the stations used for this study. It is observed from the graph that the average annual VTEC shows better synchronization with SSN and solar flux index.

The patterns of the solar cycles play a major role in the solar variability, i.e. solar radiation and sunspot number consequently influence the ionosphere. Solar cycle 24 is the smallest solar cycle since the start of the spatial era (1957), in which a peak is noticed in 2014 and a few major solar flares erupted from the Sun in February and October 2014 (Kane, 2002), so the maximum VTEC is noticed in February and October as shown in Fig. 8. Again, from Fig. 8, a higher value

for sunspot and solar flux was reported in February 2011, corresponding to an X-class solar flare at which a higher value of VTEC was noted in station considered. Sharma et al. (2012) studied how the VTEC variation in Delhi lies near the equatorial crest region during low solar activities in years 2007 to 2009 and found that TEC has a short-lived day minimum between 05:00–06:00 LT and gradual increase, and it reaches its peak value between 12:00 and 14:00 LT. The day minimum was found to be flat during most of the nighttime hours (22:00 to 06:00 LT). Their results show a magnitude of daily maximum TEC decreases from 2007 to 2009 due to decreases in the solar flux. They also found TEC seasonal behaviour depends on the solar cycle, and the largest daily TEC is observed during the equinoctial month at Delhi. In 2020, Ghimire et al. (2020a), studied the diurnal variation in TEC at
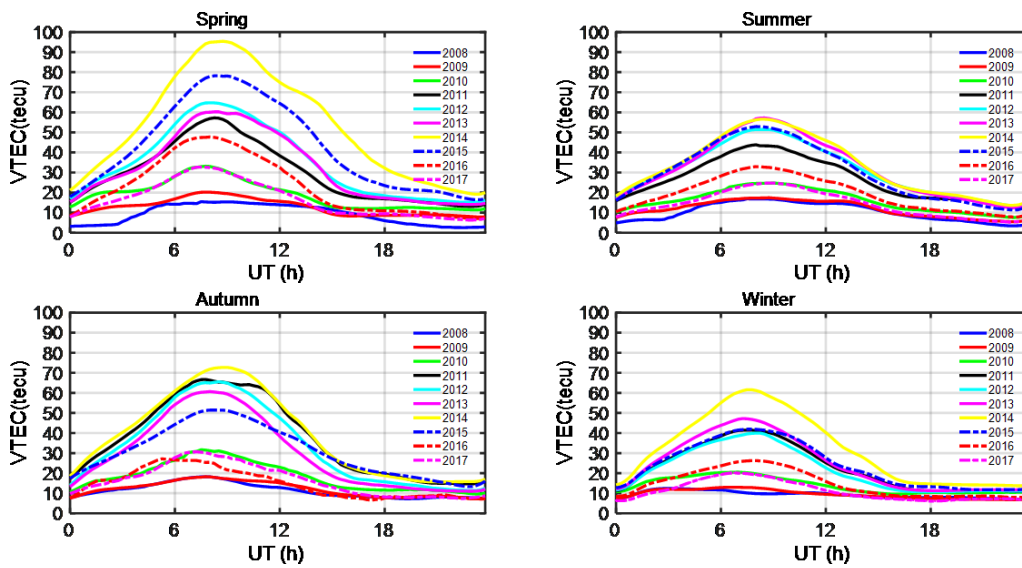
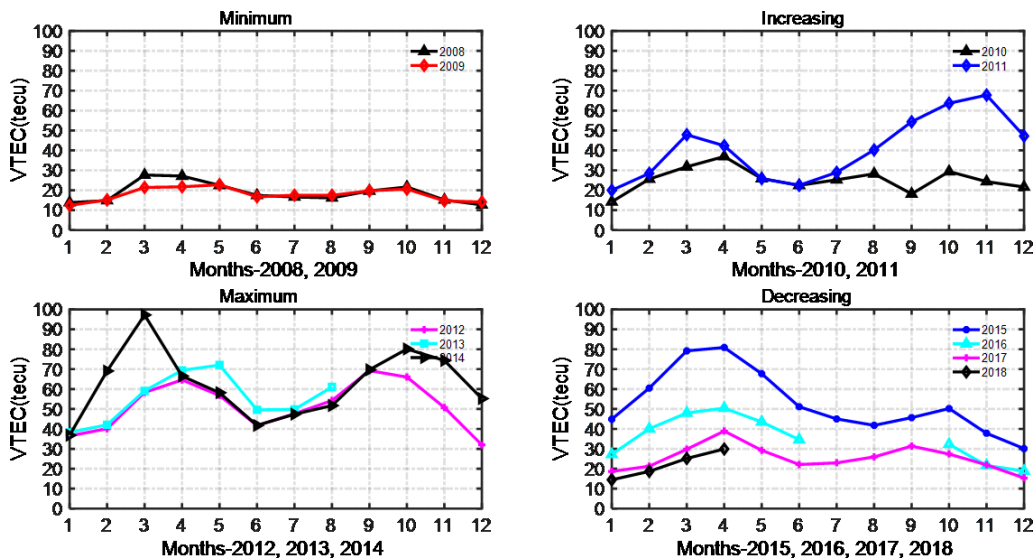**Figure 7.** Mean yearly seasonal variations in VTEC for 2008 to 2017 at KKN4.

Figure 8. VTEC variability in GRHI station during minimum, increasing, maximum and decreasing phases of solar cycle 24.

JMJG (Lamjung, Nepal) station for the year 2015 and found the minimum in the pre-dawn, a steady increase in the early morning followed by afternoon maximum and then a gradual decrease after sunset; a similar pattern is also observed our study.

In the African sector, Tariku (2015) observed, from 2008 to 2009 and 2012 to 2013, high values of VTEC during the low and high solar activity phases. According to their findings, the diurnal VTEC values attained a maximum in the time interval of 13:00 to 16:00 LT, and the least values are mostly at around 06:00 LT. A similar result is noticed in all considered Nepalese GPS stations during the low solar active phases of solar cycle 24 in Nepal. The maximum diur-

nal variability in the VTEC in 2014 is caused by a solar active period confirmed by maximum sunspot number (SSN) and solar flux index (shown in Fig. 2). The VTEC is greater in 2012 due to the second maximum in SSN and solar flux, and the minimum VTEC in 2009 and 2017 is supported by the minimum SSN and solar flux, which is confirmed by the synchronization of VTEC with SSN and solar flux (Fig. 9). In the ionosphere over Nepal, the diurnal VTEC maximum occurs approximately between 12:00 to 14:00 LT. Similar to Delhi station in Nepal, the day minimum was found to be flat during most of the nighttime hours (22:00 to 06:00 LT). In general, the value of diurnal peak in VTEC is maximum during the spring equinoxes, except in 2011 in which the autumn
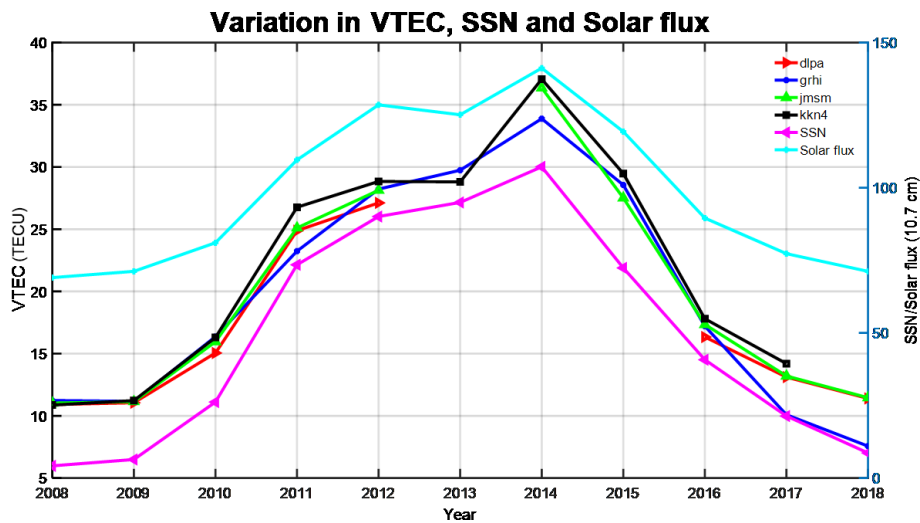
Figure 9. Annual mean VTEC variability in the KKN4, GRHI, JMSM and DLPA stations for the SSN and solar flux during year 2008–2018.

VTEC is maximum. As the solar flux decreases from 2008 to 2009, the daily maximum VTEC values show a decreasing trend.

4   Conclusions

This paper investigates the diurnal, monthly, seasonal and solar cycle variations in VTEC at four mid–low latitude stations, namely KKN4 (27.80° N, 85.27° E), GRHI (27.95° N, 82.49° E), JMSM (28.80° N, 83.74° E) and DLPA (28.98° N, 82.81° E) in Nepal.

The following conclusions are found:

– The shape of the mean diurnal variation in VTEC depends on the solar cycle phases, i.e. a flat diurnal peak is observed during minimum and descending phases of the solar cycle, whereas a Gaussian with different peak amplitude is noticed during the ascending and maximum phases of the solar cycle.

– The study may reveal that diurnal TEC maximizes at around 11:00 to 14:00 LT, with a minimum in the pre-dawn periods.

– Day-to-day variation in VTEC is significant in all the station. The maximum is noticed at KKN4 and the minimum at DLPA.

– The mean diurnal profile in the years 2008, 2009 and 2010 exhibit a wave-like nature, whereas a parabolic nature is observed in the years 2011, 2012, 2013, 2014, 2015, 2016 and 2017.

– The week ionospheric activities are characterized by lower TEC values during the minimum phase, and strong activities are characterized by a higher value

of VTEC during the maximum phase, i.e. VTEC has shown proper synchronization with SSN and solar flux.

– The monthly plot shows that, during the sunrise time in summer, the VTEC is linear, whereas it is steep during the winter.

– Equinoctial asymmetry is not noticed in 2009; in 2011, the autumn is more intense than the spring, and in 2014 and 2015, the spring VTEC is greater than the autumn.

– Equinoctial asymmetry peaks are noticed in spring (March and April) and autumn (September and October), with higher values being observed during spring.

– The equinoctial asymmetry is noticed in all the available stations due to difference in the F10.7 cm for the two equinoxes.

– The spring maximum is smaller than autumn maximum, mainly during years 2011–2013 and also during year 2008 for one station; these years are years of the minimum or increasing phase of the sunspot cycle.

– The VTEC in winter is greater than the VTEC in summer and is observed in all the available stations at the maximum of the sunspot cycle in 2014 and in one other station during the year 2011.

– During the year 2009 of the sunspot minimum, the VTEC in winter is greater than the VTEC in summer and is not observed for all the stations. There is no equinoctial asymmetry, i.e. it is very weak (compare to the year of the maximum), except at JMSM.

– It seems that, in Nepal for some years, there is no semi-annual variation, as we observe sometimes that the summer VTEC is larger than VTEC in the autumn.

The highest Himalayan mountains on Earth in Nepal are the source of landform waves that travel through the stratosphere and the lower thermosphere, where they deposit their energy and give birth to secondary gravity waves that can affect VTEC. In our climatology study, we analyse average behaviours that do not allow the study of these waves. Another study analysing each day individually and using the phase processing of GPS signals should be done in the future to analyse the impact of the Himalayas on VTEC and the impact of the low atmosphere on VTEC.

on space weather effects on Global Navigation Satellite System (GNSS) operations at low latitudes.

References

Akala, A. O., Rabiu, A. B., Somoye, E. O., Oyeyemi, E. O., and Adeloye, A. B.: The Response of African equatorial GPS TEC to intense geomagnetic storms during the ascending phase of solar cycle 24, J. Atmos. Sol. Terr.-Phy., 98, 50–62, https://doi.org/10.1016/j.jastp.2013.02.006, 2013.

Ansari, K., Park, K. D., and Panda, S. K.: Empirical and orthogonal function analysis and modeling of ionospheric TEC over South Korean region, Acta Astronaut., 161, 313–324, https://doi.org/10.1016/j.actaastro.2019.05.044, 2019.

Anderson, D. and Fuller-Rowell, T.: The ionosphere, Space environment topics SE-14, Report, Space Environment Center, Boulder, 1999.

Appleton, E. V. and Ingram, L. J.: Magnetic Storms and Upper-Atmospheric Ionisation, Nature, 136, 548–549, https://doi.org/10.1038/136548b0, 1935.

Bagiya, M. S., Joshi, H. P., Iyer, K. N., Aggarwal, M., Ravindran, S., and Pathan, B. M.: TEC variations during low solar activity period (2005–2007) near the Equatorial Ionospheric Anomaly Crest region in India, Ann. Geophys., 27, 1047–1057, https://doi.org/10.5194/angeo-27-1047-2009, 2009.

Bagiya, M. S., Iyer, K. N., Joshi, H. P., Tsugawa, T., Ravindra, S., Sridharan, R., and Pathan, B. M.: Low-latitude ionospheric-thermospheric response to storm time electro dynamical coupling between high and low latitudes, J. Geophys. Res., 116, A01303, https://doi.org/10.1029/2010JA015845, 2011.

Balan, N., Batista, I. S., Abdu, M. A., Macdougall, J., and Bailey, G. J.: Physical mechanism and statistics of occurrence of an additional layer in the equatorial ionosphere, J. Geophys. Res., 103, 169–181, https://doi.org/10.1029/98JA02823, 1998.

Buonsanto, M. J.: Possible effects of the changing Earth-Sun distance on the upper atmosphere, S. Pacific J. Nat. Sci, 8, 58–65, available at: https://uspaquatic.library.usp.ac.fj/gsdl/collect/spjnas/index/assoc/HASHd462.dir/doc.pdf (last access: 23 June 2021), 1986.

Burkard, O.: Die halbjährige Periode der F_2-Schicht-Ionisation, Arch. Meteor. Geophy. A, 4, 391–402, https://doi.org/10.1007/BF02246815, 1951.

Chauhan, V., Singh, O. P., and Singh, B.: Diurnal and seasonal variation of GPS-TEC during a low solar activity period as observed at a low latitude station Agra, Indian J. Radio Space, 40, 26–36, available at: http://nopr.niscair.res.in/handle/123456789/11195 (last access: 23 June 2021), 2011.

Cox, L. P. and Evans, J. V.: Seasonal variation of the O/N_2 ratio in the F_1 region, J. Geophy. Res., 75, 6271, https://doi.org/10.1029/JA075i031p06271, 1970.

D'ujanga, F. M., Mubiru, J., Twinamasiko, B. F., Basalirwa, C., and Ssenyonga, T. J.: Total Electron Content Variations in Equatorial Anomaly Region, Adv. Space Res., 50, 441–449, https://doi.org/10.1016/j.asr.2012.05.005, 2012.

Dabas, R. S., Lakshmi, D. R., and Reddy, B. M.: Solar activity dependence of ionospheric electron content and slab thickness using different solar indices, Pure Appl. Geophys., 140, 721–728, https://doi.org/10.1007/BF00876585, 1993.

Dashora, N. and Suresh, S. : Characteristics of low-latitude TEC during solar cycles 23 and 24 using global ionospheric maps (GIMs) over Indian sector, J. Geophys. Res.-Space, 120, 5176–5193, https://doi.org/10.1002/2014JA020559, 2015.

de Abreu, A. J., Fagundes, P. R., Gende, M., Bolaji, O. S., de Jesus, R., and Brunini, C. : Investigation of ionospheric response to two moderate geomagnetic storms using GPS-TEC measurements in the South American and African sectors during the ascending phase of solar cycle 24, Adv. Space Res., 53, 1313–1328, https://doi.org/10.1016/j.asr.2014.02.011, 2014.

Galav, P., Dashora, N., Sharma, S., and Pandey, R.: Characterization of low latitude GPS-TEC during very low solar activity phase, J. Atmos. Sol. Terr.-Phy., 72, 1309–1317, https://doi.org/10.1016/j.jastp.2010.09.017, 2010.

Ghimire, B. D., Chapagain, N. P., Basnet, V., Bhatt, K., and Khadka, B.: Variation of Total Electron Content (TEC) in the quiet and disturbed days and their correlation with geomagnetic parameters of Lamjung Station in the year of 2015, Bibechana, 17, 123–132, available at: https://www.nepjol.info/index.php/BIBECHANA/article/view/26249/22107 (last access: 17 March 2021), 2020a.

Ghimire, B. D., Chapagain, N. P., Basnet, V., Bhatta, K., and Khadka, B.: Variation of GPS- TEC Measurements of the Year 2014: A Comparative Study with IRI – 2016 Model, Journal of Nepal Physical Society, 6, 90–96, https://doi.org/10.3126/jnphyssoc.v6i1.30555, 2020b.

Guo, J., Li, W., Liu, X., Kong, Q., Zhao, C., and Guo, B.: Temporal-spatial variation of global GPS-derived total electron content, 1999–2013, PloS ONE, 10, e0133378, https://doi.org/10.1371/journal.pone.0133378, 2015.

Gupta, J. K. and Singh, L.: Long term ionospheric electron content variations over Delhi, Ann. Geophys., 18, 1635–1644, https://doi.org/10.1007/s00585-001-1635-8, 2000.

Hofmann-Wellenhof, B., Lichtenegger, H., and Collins, J.: GPS: Theory and Practice, Springer Verlag, Wien, ISBN 978-3-211-82364-6 and 978-3-7091-3298-5 (eBook), 1992.

Huo, X. L., Yuan, Y. B., Ou, J. K., Zhang, K. F., and Bailey, G. J.: Monitoring the Global-Scale Winter Anomaly of Total Electron Contents Using GPS Data, Earth Planets Space, 61, 1019–1024, https://doi.org/10.1186/BF03352952, 2009.

Jain, A. R.: Reversal of $E \times B$ drift & post sunset enhancement of the ionospheric total electron content at equatorial latitudes, Indian J. Radio Space, 16, 267–272, available at: http://nopr.niscair.res.in/handle/123456789/36497 (last access: 26 June 2021), 1987.

Kane, R. P.: Some implications using the group sunspot number reconstruction, Sol. Phys., 205, 383–401, https://doi.org/10.1023/A:1014296529097, 2002.

Khan, A. and Jin, S.: Gravity wave activities in Tibet observed by Cosmic GPS radio occultation, Geodesy and Geodynamics., 9, 504–511, https://doi.org/10.1016/j.geog.2018.09.009, 2018.

Kramkowsky, D., Kasprazak, W. T., and Nier, A. O.: Mass spectrometric studies of the composition of the lower thermosphere during summer 1967, J. Geophys. Res., 73, 7291–7306, https://doi.org/10.1029/JA073i023p07291, 1968.

Lal, C.: Seasonal trend of geomagnetic activity derived from solar-terrestrial geometry confirms an axial-equinoctial theory and reveals deficiency in planetary indices, J. Atmos. Terr. Phys., 58, 1497–1506, https://doi.org/10.1016/0021-9169(95)00182-4, 1996.

Legrand, J. P. and Simon, P. A.: Solar cycle and geomagnetic activity: A review for geophysicists. Part I. The contributions to geomagnetic activity of shock waves and of the solar wind, Ann. Geophys., 7, 565–578, available at: http://www.ipgp.jussieu.fr/~legoff/Download-PDF/Soleil-Climat/IndicesAA/annales-geophysicaeI-89-7-565-578.pdf (last access: 23 June 2021), 1989.

Martin, L. and Volkert, H.: The Propagation of Mountain Waves into the Stratosphere: Quantitative Evaluation of Three-Dimensional Simulations, J. Atmos. Sci., 57, 3090–3108, https://doi.org/10.1175/1520-0469(2000)057<3090:TPOMWI>2.0.CO;2, 2000.

Liu, L. B., Wan, W. X., Ning, B. Q., and Zhang, M. L.: Climatology of the mean total electron content derived from GPS global ionospheric maps, J. Geophys. Res., 114, A06308, https://doi.org/10.1029/2009JA014244, 2009.

Liu, G., Huang, W., Gong, J., and Shem, H.: Seasonal variability of GPS-VTEC and model during low solar activity period 2006–2007 near the equatorial ionization anomaly crest location in Chinese zone, Adv. Space Res., 51, 366–376, https://doi.org/10.1016/j.asr.2012.09.002, 2013.

Liu, L. B. and Chen, Y. D. : Statistical analysis of solar activity variations of total electron content derived at Jet Propulsion Laboratory from GPS observations, J. Geophys. Res., 114, A10311, https://doi.org/10.1029/2009JA014533, 2009.

Maeda, K., Hedin, A. E., and Mayr, H. G.: Hemispheric asymmetries of the thermospheric semiannual oscillation, J. Geophys. Res.-Space, 91, 4461–4470, https://doi.org/10.1029/JA091iA04p04461, 1986.

Mansoori, A. A., Parvaiz, A. K., Rafi, A., Roshni, A., Aslam, A. M., Shivangi, B., Bhupendra, M., Purohit, P. K., and Gwal, A. K.: Evaluation of long term solar activity effects on GPS derived TEC, J. Phys. Conf. Ser., 759, 012069, https://doi.org/10.1088/1742-6596/759/1/012069, 2016.

Natali, M. P. and Meza, A.: Annual and semiannual variations of vertical total electron content during high solar activity based on GPS observations, Ann. Geophys., 29, 865–873, https://doi.org/10.5194/angeo-29-865-2011, 2011.

Parwani, M., Atulkar, R., Mukherjee, S., and Purohit, P. K.: Latitudinal variation of ionospheric TEC at northern hemispheric region, Russian Journal of Earth Sciences, 19, ES1003, https://doi.org/10.2205/2018ES000644, 2019.

Perevalova, N. P., Polyakova, A. S., and Zalizovski, A. V.: Diurnal Variation of the Total Electron Content under Quiet Helio-Geomagnetic Conditions, J. Atmos. Sol. Terr.-Phy., 72, 997–1007, https://doi.org/10.1016/j.jastp.2010.05.014, 2010.

Prikryl, P., Jayachandran, P. T., Mushini, S. C., Pokhotelov, D., MacDougall, J. W., Donovan, E., Spanswick, E., and St.-Maurice, J.-P.: GPS TEC, scintillation and cycle slips observed at high latitudes during solar minimum, Ann. Geophys., 28, 1307–1316, https://doi.org/10.5194/angeo-28-1307-2010, 2010.

Ouattara, F. and Amory-Mazaudier, C.: Statistical study of the equatorial F2 layer at Ouagadougou during solar cycles 20, 21, 22 using Legrand and Simon's classification

of geomagnetic activity, J. Space Weather Spac., 2, A19, https://doi.org/10.1051/swsc/2012019, 2012.

Ouattara, F. and Fleury, R.: Variability of CODG TEC and IRI 2001 Total Electron Content (TEC) during IHY Campaign Period (21 March to 16 April 2008) at Niamey under Different Geomagnetic Activity Conditions, Sci. Res. Essays, 6, 3609–3622, https://doi.org/10.5897/SRE10.1050, 2011.

Ouattara, F., Amory-Mazaudier, C., Fleury, R., Lassudrie Duchesne, P., Vila, P., and Petitdidier, M.: West African equatorial ionospheric parameters climatology based on Ouagadougou ionosonde station data from June 1966 to February 1998, Ann. Geophys., 27, 2503–2514, https://doi.org/10.5194/angeo-27-2503-2009, 2009.

Rama Rao, P. V. S., Nru, D., and Srirama Rao, M.: Study of some low latitude ionospheric phenomena observed in TEC measurements at Waltair, India, in: Proceedings COSPAR/URSI Symp. Warsaw, Poland, edited by: Wernik, A. W., 51, 19–23 May 1980.

Rao, S. S., Chakraborty, M., Kumar, S., and Singh, A. K.: Low-latitude ionospheric response from GPS, IRI and TIE-GCM TEC to Solar Cycle 24, Astrophys. Space Sci., 364, 216, https://doi.org/10.1007/s10509-019-3701-2, 2019a.

Rao, S. S., Sharma, S., and Pandey, R.: Study of solar flux dependency of the winter anomaly in GPS TEC, GPS Solut., 23, 4, https://doi.org/10.1007/s10291-018-0795-x, 2019b.

Regmi, R. P. and Maharjan, S.: Trapped mountain wave excitations over the Kathmandu valley, Nepal, Asia-Pac. J. Atmos. Sci., 51, 303–309, https://doi.org/10.1007/s13143-015-0078-1, 2015.

Regmi, R. P., Kitada, T., Dudha, J., and Maharjan, S.: Large-scale gravity over the middle hills of the Nepal Himalayas: implication for aircraft accidents, J. Appl. Meteorol. Clim., 56, 371–389, https://doi.org/10.1175/JAMC-D-16-0073.1, 2017.

Rishbeth, H.: How the thermospheric circulation affects the ionospheric F2-layer, J. Atmos. Sol.-Terr. Phy., 60, 1385–1402, https://doi.org/10.1016/S1364-6826(98)00062-5, 1998.

Rishbeth, H. and Setty, C. S. G. K.: The F-layer at sunrise, J. Atmos. Terr. Phys., 20, 263–276, https://doi.org/10.1016/0021-9169(61)90205-7, 1961.

Rishbeth, H., Müller-Wodarg, I. C. F., Zou, L., Fuller-Rowell, T. J., Millward, G. H., Moffett, R. J., Idenden, D. W., and Aylward, A. D.: Annual and semiannual variations in the ionospheric F2-layer: II. Physical discussion, Ann. Geophys., 18, 945–956, https://doi.org/10.1007/s00585-000-0945-6, 2000.

Rothwell, P.: Diffusion of ions between F layers at magnetic conjugate points, in Proceedings International Conference on the Ionosphere, Institute of Physics and Physical Society, London, 217–221, 1963.

Russell, C. T. and McPherron, R. L.: Semiannual variation of geomagnetic activity, J. Geophys. Res., 78, 92–108, https://doi.org/10.1029/JA078i001p00092, 1973.

Sahai, Y., Becker-Guedes, F., and Fagundes, P. R.: Response of Nighttime Equatorial and Low Latitude F-Region to the Geomagnetic Storm of August 18, 2003, in the Brazilian Sector, Adv. Space Res., 39, 1325–1334, https://doi.org/10.1016/j.asr.2007.02.064, 2007.

Sharma, K., Dabas, R. S., and Ravindran, S.: Study of total electron content over equatorial and low latitude ionosphere during extreme solar minimum, Astrophys. Space Sci., 341, 277–286, https://doi.org/10.1007/s10509-012-1133-3, 2012.

Shimeis, A., Amory-Mazaudier, C., Fleury, R., Mahrous, A. M., and Hassan, A. F.: Transient variations of vertical total electron content over some African stations from 2002 to 2012, Adv. Space Res., 54, 2159–2171, https://doi.org/10.1016/j.asr.2014.07.038, 2014.

Tariku, Y. A.: Patterns of GPS-TEC variation over low-latitude regions (African sector) during the deep solar minimum (2008 to 2009) and solar maximum (2012 to 2013) phases, Earth Planets Space, 67, 35, https://doi.org/10.1186/s40623-015-0206-2, 2015.

Titheridge, J. F.: The total electron content of the southern mid-latitude ionosphere, 1965–1971, J. Atmos. Terr. Phys., 35, 981–1001, https://doi.org/10.1016/0021-9169(73)90077-9, 1972.

Torr, M. R. and Torr, D. G.: The seasonal behavior of the F2-layer of the ionosphere, J. Atmos. Terr. Phys., 35, 22–37, https://doi.org/10.1016/0021-9169(73)90140-2, 1973.

Torre, A., Alexander, P., Llamedo, P., Hierro, R., Nava, B., Radicella, S., Schmidt, T., and Wickert, J.: Wave activity at ionospheric heights above the Andes Mountains detected from FORMOSAT3/COSMIC GPS radio occultation data, J. Geophys. Res.-Space, 119, 2046–2051, 2014.

Triskova, L.: The vernal-autumn asymmetry in the seasonal variation of geomagnetic activity, J. Atmos. Terr. Phys., 51, 111–118, https://doi.org/10.1016/0021-9169(89)90110-4,1989.

Tyagi, T. R. and Das Gupta, A.: Beacon satellite studies and modeling of total electron content of ionosphere, Indian J. Radio Space, 424–438, available at: http://nopr.niscair.res.in/handle/123456789/36307 (last access: 23 June 2021), 1990.

Venkatesh, K., Fagundes, P. R., de Jesus, R., de Abreu, A. J., and Sumod, S. G.: Assessment of IRI-2012 Profile Parameters by Comparison with the Ones Inferred Using NeQuick2, Ionosonde and FORMOSAT-1 Data during the High Solar Activity over Brazilian Equatorial and Low Latitude Sector, J. Atmos. Sol. Terr.-Phy., 121, 10–23, https://doi.org/10.1016/j.jastp.2014.09.014, 2014a.

Venkatesh, K., Fagundes, P. R., Seemala, G. K., de Jesus, R., and Pillat, V. G.: On the Performance of the IRI-2012 and NeQuick2 Models during the Increasing Phase of the Unusual 24th Solar Cycle in the Brazilian Equatorial and Low-Latitude Sectors, J. Geophys. Res., 119, 5087–5105, https://doi.org/10.1002/2014JA019960, 2014b.

Venkatesh, K., Fagundes, P. R., Prasad, D. S. V. V. D., Denardini, C. M., de Abreu, A. J., de Jesus, R., and Gende, M.: Day-to-Day Variability of Equatorial Electrojet and Its Role on the Day-to-Day Characteristics of the Equatorial Ionization Anomaly over the Indian and Brazilian Sectors, J. Geophys. Res., 120, 9117–9131, https://doi.org/10.1002/2015JA021307, 2015.

Walker, G. O., Ma, J. H. K., and Golton, E.: The equatorial ionospheric anomaly in electron content from solar minimum to solar maximum for South East Asia, Ann. Geophys., 12, 195–209, https://doi.org/10.1007/s00585-994-0195-0, 1994.

Wright, J. W.: The F-region seasonal anomaly, J. Geophys. Res., 68, 4379–4381, https://doi.org/10.1029/JZ068i014p04379, 1963.

Yonezawa, T.: On the seasonal and non-seasonal annual variations and the semiannual variation in the noon and midnight densities of the F2 layer in middle latitudes II, J. Radio Res. Lab., 6, 651–668, available at: https://ci.nii.ac.jp/naid/10003355670/ (last access: 23 June 2021), 1959.

Zakharenkova, I. E., Cherniak, I. V., Krankowski, A., and Shagimuratov, I. I.: Analysis of Electron Content Variations over Japan

during Solar Minimum: Observations and Modeling, Adv. Space Res., 52, 1827–1836, https://doi.org/10.1016/j.asr.2014.07.027, 2012.

Zhang, S. R., Holt, J. M., Anthony, P., Eyken, V., McCready, M., Amory-Mazaudier, C., Fucao, S., and Sulzer, M.: Ionospheric local model and climatology from long-term databases of multiple incoherent scatter radars, Geophys. Res. Lett., 32, L20102, https://doi.org/10.1029/2005GL023603, 2005.

Zhao, B., Wan, W., Liu, L., Mao, T., Ren, Z., Wang, M., and Christensen, A. B.: Features of annual and semiannual variations derived from the global ionospheric maps of total electron content, Ann. Geophys., 25, 2513–2527, https://doi.org/10.5194/angeo-25-2513-2007, 2007.

Zoundi, C., Ouattara, F., Fleury, R., Amory-Mazaudier, A., and Lassudrie-Duchesne, P.: Seasonal TEC Variability in West Africa Equatorial Anomaly Region, European Journal of Scientific Research, 77, 309–319, available at: https://hal.sorbonne-universite.fr/hal-00968583 (last access: 23 June 2021), 2012.

Correlation of Alfvén Mach number with field aligned current, polar cap potential and dawn dusk electric field during Quiet and extreme solar wind conditions

Binod Adhikari[a,c]*, Drabindra Pandit[a,c], Prashrit Baruwal[c], Opendra Thapa[a], Niraj Adhikari[a], Bidur Kaphle[a], Pratik Bhattarai[a], Narayan P. Chapagain[d] & Sarala Adhikari[e]

[a]Department of Physics, St. Xavier's College, Tribhuvan University, Kathmandu 44600, Nepal

[b]Department of Physics, Patan Multiple College, Tribhuvan University, Lalitpur 44700, Nepal

[c]Central Department of Physics, Tribhuvan University, Kathmandu 44600, Nepal

[d]Department of Physics, Amrit Campus, Tribhuvan University, Kathmandu 44600, Nepal

[e]Department of Environmental Science, Tri-Chandra College, Tribhuvan University, Kathmandu 44600, Nepal

This paper has been performed to study the Alfvenic Mach number (M_A) in relation to Field Aligned Currents (FACs), Polar Cap Potential (PCV), Dawn Dusk Electric Field (Ey) during different geomagnetic conditions. The relations of M_A with FACs, PCV and interplanetary electric field (IEF)-E_Y not solely dependent on any solar wind parameter but also associate with prior, main, and post conditions of geomagnetic storms. This study has shown that Prior to the arrival of interplanetary shock (IS), M_{MS} and M_A show good relationship with FAC, PCV, EFY, and solar wind parameters, as the space weather seems unperturbed. The positive correlations among the various parameters have obtained due to the merging of two different interplanetary coronal mass ejections (ICMEs) driven solar storms and consequential intense southward interplanetary magnetic field. The negative relationships among the selected parameters may have been due to the slow recovery of the IMF-Bz component. This study indicate that the preceding solar winds could be associatedon the variance of M_A of a geomagnetic event, in turn might have its effects on FACs, PCV, Ey and in other solar wind parameters.

1 Introduction

The solar wind is a magnetized plasma of charged particles, viz alpha particles, protons, electrons, etc. that flows outward from the Sun[1]. When the solar wind magnetic field interacts with Earth's magnetic field, the excitation of the movement of electric current increases on increasing energies, in the magnetospheric-ionospheric (MI) system, result in geomagnetic storms, sub-storms, and aurora[2-3]. One aspect of the interaction of the solar wind and embedded interplanetary magnetic field (IMF) with the terrestrial magnetosphere is the generation of currents, geomagnetically-aligned electric currents, at high latitudes in the ionosphere and magnetosphere called Field Aligned Currents (FACs)[4].

High altitude region (R1) and low altitude (R2) of FACs electronically couple the magnetospheric and ionospheric plasma and release the stress applied on the outer magnetospheric plasma to the

ionosphere and upper atmosphere[5-7]. During the dayside magnetopause reconnection, R1 and R2 become more significant and this mechanism is the major driven internal process related to magnetic storm/sub-storm. Large FACs are associated with polar regions that spans variation in polar cap potential due to reconnection process, when magnetic field lines intervene with IMF, on the dayside magnetosphere and in the magnetotail. For PCV in detail, references are herein[8-13]. PCV is crucial for delineation of the coupled magnetosphere-ionosphere system[12,14].

The Ey component of interplanetary electric field (IEF), $Ey = (Vsw)_x \times IMF(Bz)$ maps down to the ionosphere as a convection Ey field. Under southward IMF Bz conditions, when the geomagnetic field merges with the IMF, a dawn-to-dusk convection Ey field is formed due to the R1-FACs closing in the high-altitude ionospheric dynamo region that can modify the orbits of charged particles by shifting them towards the dawn sector[15-16].

---

*Corresponding author (E-mail: binod.adhi@gmail.com)

Alfven Mach number (M_A) characterizes the strength of the magnetic field. It is given as $\frac{Vsw}{V_A}$; where Vsw is solar wind velocity and V_A is Alfven speed, the speed with which hydrodynamic waves can propagate[17]. Sub-Alfvenic $M_A S$ (<1), the magnetic field lines shape the plasma whereas super-Alfvenic (>1) conditions, it is the opposite. Sub-Alfvenic M_A corresponds to a strong magnetic field while a super-Alfvenic M_A corresponds to a weak magnetic field[18]. Furthermore, when the solar wind M_A is high then thermal plasma forces dominate but when it is low, magnetic forces dominate. The coupling efficiency, ratio of output to input into M-I system, increases as a function of M_A[19]. Iijima and Potemra[20] and Kasranetal[21] have deduced a linear relation between large-scale FACs and Vsw. Similarly, PCV has also been found to be related to Vsw. Furthermore, Wilder et al[22] found an anti-correlation of the dawn FAC strength with both the M_A and the SYM-H index. Adhikari et al[23] estimated the FAC and PCV values, their observed relationship, good positive correlation, validates the occurring of physical mechanism as FAC leads PCV. However, there has been less or no effort to find the relation of M_A to FAC, PCV, and Ey.

The drastic variation in an interaction of solar wind, due to low or high Mach number, with magnetosphere rendered a behavior of CME; however, geo-effective CMEs tend to have low (in average) Mach number. With the fall in Alfven M_A, the magnetic force as a flow rises; shows anti-correlation[24-25]. Furthermore, Borosky and Denton[26] found similar result for magnetic cloud associated with CMEs. The magnetosonic and Alfvén Mach numbers relation is: $M_{MS} = V_{SW}/\left(V_S^2 + V_A^2\right)^{1/2}$ and $MA = V_{SW}/V_A$ respectively (where V_s, V_A, and V_{sw} are sonic, Alfvén speeds, and Solar wind speed). During magnetic clouds, M_A and M_{MS} are even closer to each other (usually in the low Mach number regimes); these are characterized by unusually low temperatures[27]. Lower bound of ($M_{MS} \geq 6.9$) for solar cycle (SC) 24 is larger in comparison with SC 22 and SC 23.

Fairfield et al[28] observed distant bow shock locations unraveling a much thicker magnetosheath during low Mach number regime. Upstream M_A shows Good agreement with bow shock[29]. Wang, J. et al[30] found sunward movement of subsolar bow shock with increase in IMF Bz field strength and decrease in M_{MS} solar wind. Magnetic clouds are featured with

low M_A. Also, the higher the M_A value, slower is the sunward flow; no sunward flow is expected for $M_A > 3.26$. Furthermore, decrease in M_A value (low Mach number) hint of an expansion of bow shock surface; however, high Ma >25 shocks are very rare in near earth environment. Some of such unusual cases were observed in this paper.

As we know, M_A is calculated from Band Vsw. Despite this, we have carried out our analysis to examine the variation of patterns during the quiet and extreme solar wind conditions. Since these parameters determine the change in the value of FAC, PCV, and IEF-Ey, there must be a direct relation between the M_A and the parameters of FAC, PCV, and IEF-Ey. In this study, our aim is to investigate the relation of M_A with FACs, PCV, and IEF-Ey under different solar wind conditions. Furthermore, our study includes the effect of preceding solar wind on the M_A of the geomagnetic condition, which if studied further would help to explain the unusual behavior observed in various parameters during the geomagnetic storms.

2 Dataset and Methodology

Our database consists of 1-minute resolution IMF-B and its southward component (Bz) (nT) and the various solar wind parameters such as Vsw (km/s), proton density (Nsw; i^+/cm^3), temperature (Tsw; K), and flow pressure (Psw, nPa) and Alfvén Mach Number (M_A) provided by the Omni Data Explorer. Three different types of events: a quiet, ICME driven, and a co-rotating interaction region (CIR) driven events fall under this database for years from 2001-2005. We adopted Iijima and Potemra[20] and Moon[31] method to estimate the values of FAC, PCV, and dawn-dusk IEF-Eyrespectively as:

$$FAC = 0.328\sqrt{\sqrt{n_p}V_{sw}B_T Sin\frac{\theta}{2}} + 1.4 \qquad \dots (1)$$

and

$$PCV = V_{sw} B_T Sin^2\left(\frac{\theta}{2}\right) \times 7R_e \qquad \dots (2)$$

In these equations, n_p is the solar wind density (n/cc), V_{sw} is the solar wind speed (km/s), B_T is transverse IMF (nT); $B_T = \sqrt{B_y^2 + B_z^2}$ and θ represents the angle between the Earth's magnetic field and the total IMF vector $\theta = \cos^{-1}(\frac{B_Z}{B})$.

In Eq (2) l_o is the effective length of the X line in a schematic which is empirically determined as $l_o=7R_E$, where R_E is the radius of Earth $(6.48\times 10^6 m)$.

In addition, we studied the cross correlation between the Alfvenic M_A and different solar wind parameters like IMF-B, IEF-Ey and Vsw, and other parameters such as FACs, PCV, and SYMH during the events. This methodology offered a clear insight into the relation between these parameters during the periods investigated.

3 Results and Discussion

In this section, we discuss the Alfvenic Mach number in relation to field aligned currents, polar cap potential, dawn dusk electric field during the quieted day and geomagnetic storms.

Event-1: 23 December 2005 (The quietest day)

Quiet days (Q days) are the geomagnetically least disturbed days with Kp (not included in plots) values less than 3 and insignificant fluctuation in geomagnetic indices like AE and SYM-H). Figure 1 depicts the unperturbed state of the MI system; no prior, main, and post event are separately observed for 23rd December 2005. Fifth panel from top, shows the minimum value of 25 (10e4 K) for temperature while SYM-H index and IMF Bz varied within ±5nT. The solar wind parameter values, from panel 3-6, show gradually decreasing trend towards night side. The overall variation in data sets show the geomagnetically quiet event.

In Fig. 2, the variation in AE index value reached the maximum of ~75 nT, while negligible variation was observed on Alfvenic M_A, FACs, PCV, and dawn-to-dusk IEF Ey. The value of M_A reached the maximum of ~28 (>25) at ~3 UT and remained consistent for 6 UT- 18 UT[32]; however, the average magnetic field (B) in Fig. 1 dropped down to minimum value of 2 nT and SYM-H value to 1 nT. The value of FAC also ranged from 1.5 to 3 amp. The values of PCV and IEF Ey ranged between 1 to ~3 kV and between ~-1.5 to ~1 mV/m respectively. The fluctuation in M_A, FAC, PCV values on dayside was slightly higher than that with night side due to the consequences of solar wind parameters. The low value of FAC was due to the less interaction of IMF with the geomagnetic field that resulted in a decrease in plasma movement through the magnetosphere and a decrease in the electric currents[33-34].
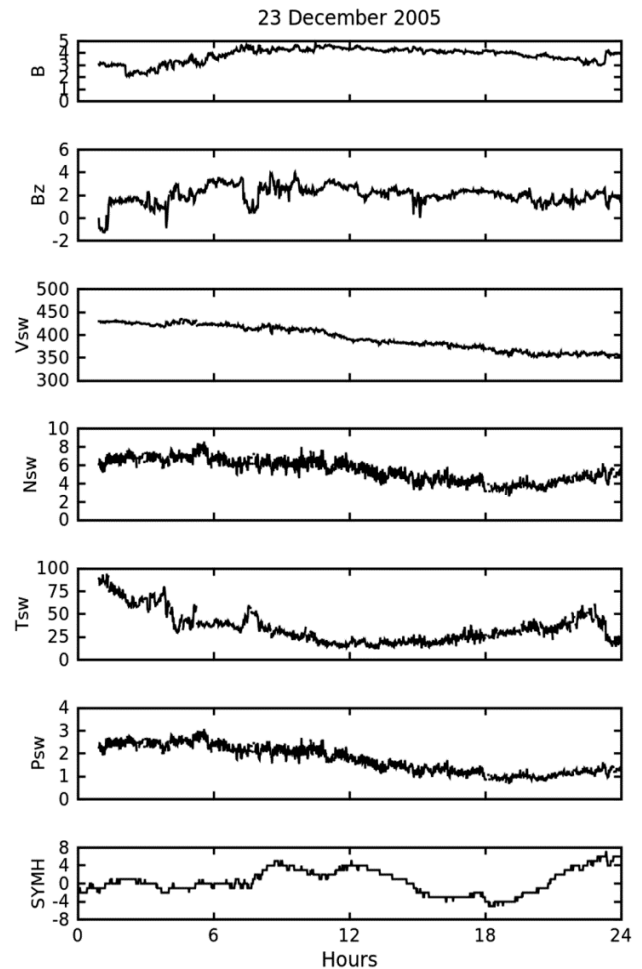

Fig. 1 — Represents the variation in IMF components and solar wind parameters observed on 23 December 2005. From top to bottom: (a) IMF magnitude (B; nT), (b) southward component of IMF (Bz; nT), (c) velocity of solar wind (Vsw; km/s), (d) density of solar wind (Nsw; i+/cm3), (e) temperature of solar wind (10e4Tsw; K), (f) flow pressure of solar wind (Psw; nPa), and (g) SYMH index (nT).

Event-2: 31 March 2001 (ICME driven)

Figure 3 depicts the fluctuation in the IMF components and solar wind parameters during the ICME driven storm that occurred on 31 March 2001. The impingement of solar wind with bow shock of Earth can be identified with the sudden increase in negative SYM-H value. Sudden abrupt increase in solar wind parameters shows the flow and deflection of charge particles with the compression magnetosphere. The prior storm phase started at ~ 0100 UT and lasted till 0300 UT, followed by the abnormal short lived four swings showing negative IMF Bz excursion can be responsible for intense superstorms. During main storm phase, Vsw and IMF
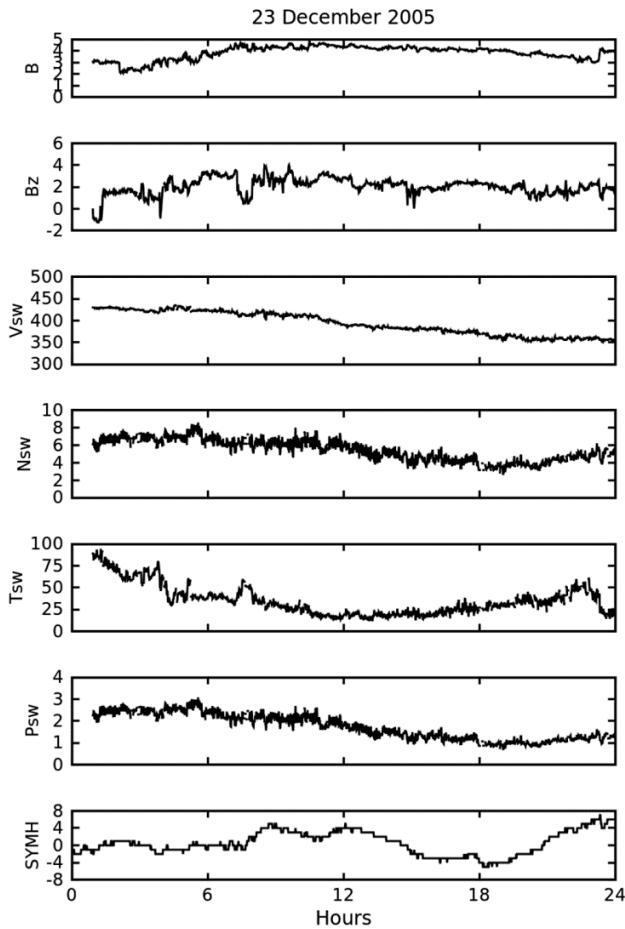
ADHIKARI *et al.*: CORRELATION OF ALFVÉN MACH NUMBER WITH FIELD ALIGNED CURRENT, POLAR CAP POTTENTIAL AND DAWN DUSK ELECTRIC FIELD

131

Fig. 2 — The different parameters are shown for 23 December 2005. From top to bottom: (a) Alfven Mach number (M_A), (b) magnetosonicmach number (Mms), (c) field aligned current (FAC; amp), (d) polar cap potential (PCV; kV), (e) dawn dusk electric field (EFY; mV/m), (f) AE index (nT), and (g) SYMH index (nT).
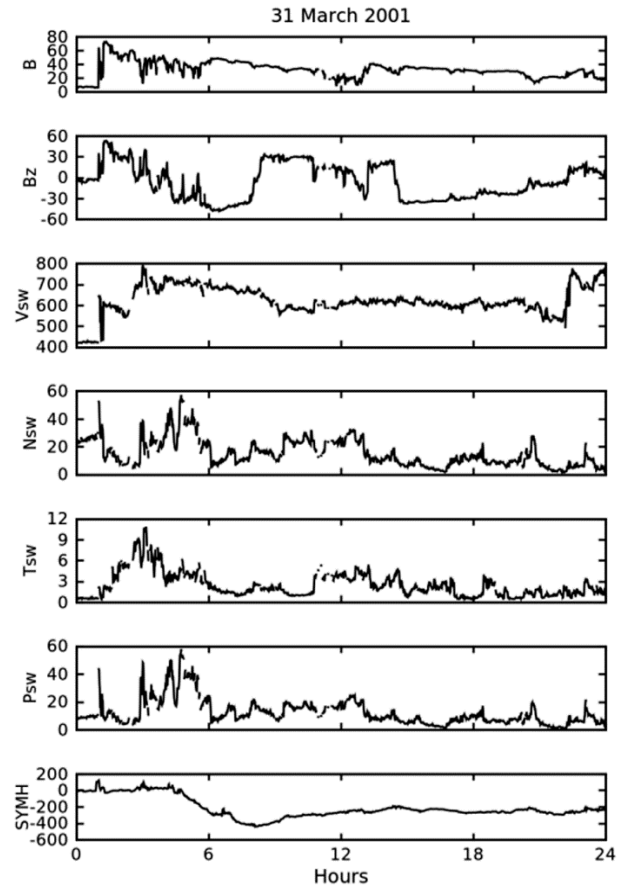
Fig. 3 — Represents the variation in IMF components and solar wind parameters observed on 31 March 2001. From top to bottom: (a) IMF magnitude (B; nT), (b) southward component of IMF (Bz; nT), (c) velocity of solar wind (Vsw; km/s), (d) density of solar wind (Nsw; i+/cm3), (e) temperature of solar wind (10e5, Tsw; K), (f) flow pressure of solar wind (Psw; nPa), and (g) SYMH index (nT). At Ma maximum, the solar wind velocity, temperature, density

B follow a similar pattern. The negative maximum IMF Bz value (~ -40 nT) slowed down the recovery phase; however, the SYM-H index attains its maximum value of -440 nT at ~ 0800 UT. The gradual recovery phase occurs during the post storm event.

Figure 4 shows the variation in estimated parameters, AE, and SYMH index (identical to Fig. 3 in the bottom panel). The second row from the bottom shows the AE index, which ranges from 100 nT to 2400 nT. The fluctuation of AE is irregular with a maximum value at about ~1700 UT indicates the precipitation of charged particles glowing the ionosphere. The third, fourth, and fifth panels from top show the line plots of FACs, PCV and dawn-to-dusk IEF Ey. These show a similar pattern of

variations because they hinge on the strength of solar wind-magnetosphere interactions[33]. This shows that the FACs, PCV and IEF Ey are linearly correlated to each other. For intense superstorms, the average value of IEF Ey is ~23.5 mV/m[35]. The value of M_A ranges from 1 to 20 show satisfactory data whereas the value of Mms ranges from 1 to 8 such that M_A and Mms have shown direct relation to each other.

The fluctuations in FAC and PCV are associated with the swift of southward IMF Bz component responsible for a change in the electric field of cross-magnetosphere[36]. Positive in SYMH value depicts the compression phase of geomagnetic storm with the flow of eastward magnetopause current[37].
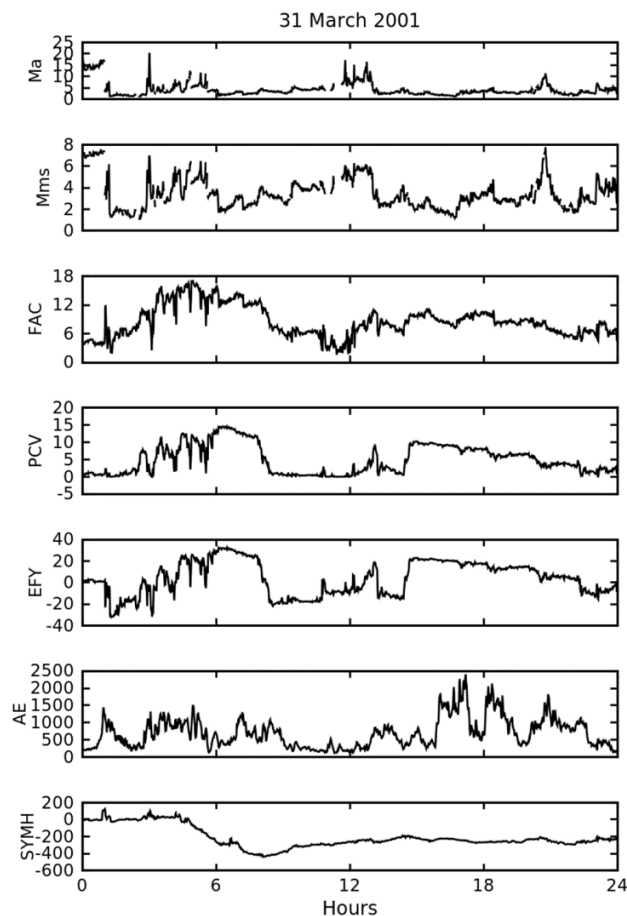
Fig. 4 — The different parameters are shown for 31 March 2001. From top to bottom: (a) Alfven Mach number (M_A), (b) magnetosonicmach number (Mms), (c) field aligned current (FAC; amp), (d) polar cap potential (PCV; kV), (e) dawn dusk electric field (EFY; mV/m), (f) AE index (nT), and (g) SYMH index (nT).
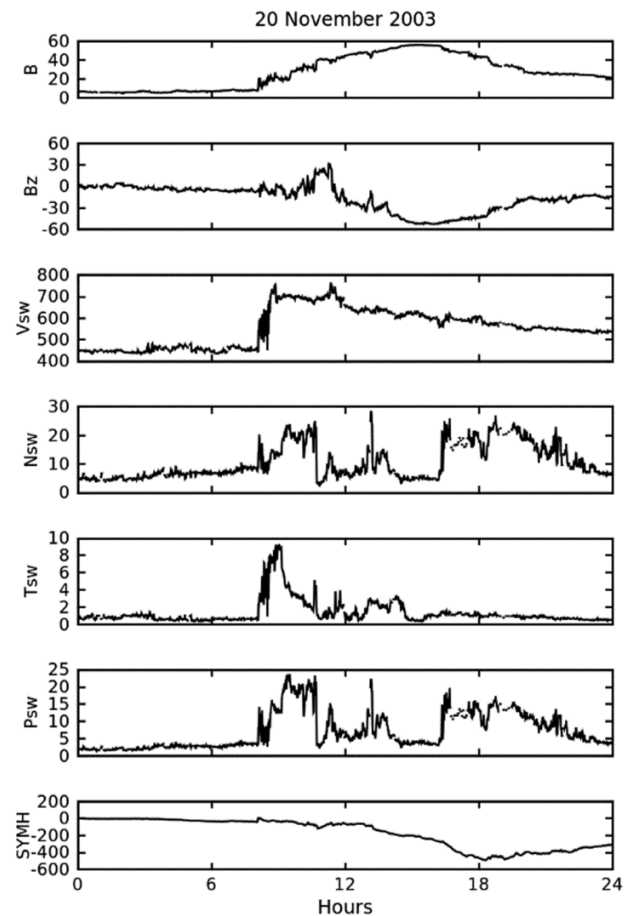
Fig. 5 — Represents the variation in IMF components and solar wind parameters observed on 20 November 2003. From top to bottom: (a) IMF magnitude (B; nT), (b) southward component of IMF (Bz; nT), (c) velocity of solar wind (Vsw; km/s), (d) density of solar wind (Nsw; i+/cm^3), (e) temperature of solar wind (10e5 Tsw; K), (f) flow pressure of solar wind (Psw; nPa), and (g) SYMH index (nT).

Event-3: 20 November 2003 (ICME event)

In Figs 5 and 6, we can observe the variation in the various parameters associated with the ICME event occurred at 20 November 2003. The rises and falls in the various parameters help us deduce the underlying condition of M_A, FAC, PCV, and dawn-to-dusk IEF Ey derived from the Interplanetary and solar wind parameters. At around 09:00 UT, sudden increase in solar wind parameters in Fig. 5 marked the commencement of the storm. Rapid fluctuations of parameters in both the Figs 5 and 6, during 09:15 UT till 11:15 UT, for 2 hours of interval between first northward IMF-Bz excursion and the slight recovery phase before the second negative IMF Bz excursion was observed; however, the average magnetic field B shows gradual increasing trend reaching the maximum value of ~60 nT at 15:30 UT with the

decreasing SYM-H (symmetric-H) value till 18:00 UT. The multiple peak values of AE during the storm, indicates the ongoing auroras. During the storm, FAC ranged from 3 to 15 amp while Vsw ranged from 400 km/s to 750 km/s. The variation pattern of FAC is similar to that of Vsw. The findings of Iijima and Potemra[20] and, regarding the existence of a linear relation between FAC and Vsw, support our finding. In addition, anti-relationship between IMF Bz and IEF Ey was observed: negative IMF Bz excursion (max. ~50 nT) deflects towards southward, meanwhile, an IEF Ey (max. ~35 mV/m) increases eastward. This leads to an increase in magnitude of ionospheric Cross PCV which establishes a linear correlation between PCV and Vsw[38-40]. During this event, the value of PCV varied between 0 and 15 kV.
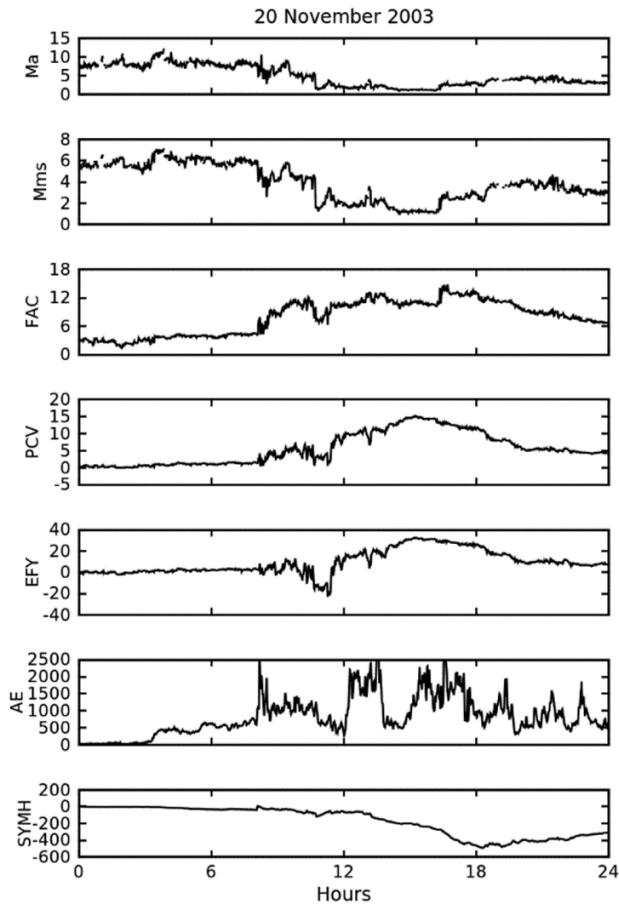
Fig. 6 — The different parameters are shown for 20 November 2003. From top to bottom: (a) Alfven Mach Number (M_A), (b) magnetosonicmach number (Mms), (c) field aligned current (FAC; amp), (d) polar cap potential (PCV; kV), (e) dawn dusk electric field (EFY; mV/m), (f) AE index (nT), and (g) SYMH index (nT).

According to Chapman and Cairns[17], when the value of solar wind velocity increases during the beginning of storm, the M_A also increases and shows the same fluctuation as Vsw throughout the disturbance period. Regarding this storm, as the solar wind increased, the value of M_A decreased that is completely the opposite of the observation of Chapman and Cairns[17]. This observed variability helps us conclude that an inverse relationship can also exist between Vsw and M_A during a strong super solar storm. Furthermore, as there is only a gradual or incomplete recovery noticed in the IMF-Bz after the storm, we believe this delay in the recovery may be the reason for the establishment of a negative relation between Vsw and M_A. In this storm and during its the main phase, there was a rapid and remarkable decrease in the IMF Bz component while it tried to

recover slowly after the storm main phase but did not recover completely by the end of this event. As the Alfven M_A denotes the magnetic field strength, we conclude that this slow recovery of IMF-Bz was a responsible factor for the inverse relation of Vsw and Alfven M_A observed.

As PCV, FAC, and IEF Ey are all directly proportional to Vsw, and IEF-Ey is inversely proportional to Vsw, we can conclude the existence of an inverse relation among PCV, FAC, and IEF Ey with M_A during this ICME driven solar superstorm.

Event-4: 15 May 2005 (CIR event)

Figures 7 and 8 depict the variation in interplanetary and solar wind parameters due to the CIR storm structure occurred at 15 May 2005. The storm commenced with the positive increment of SYM-H value, indicating the flow of current along the magnetopause due the rapid compression of bow shock. During the prior phase of ICME events (Figs. 3-6), there was an abrupt increment in solar wind parameters. However, in the case of CIR event in prior phase, there existed a gradual increment in solar wind parameters with the commencement of storm. In prior phase, the data show missing values but the SYM-H attends ~ 3 hours (03:00 UT to 06:00 UT) of positive increment value before the main phase of CIR event. This indicates that the large amount of energy was ejected in the magnetopause unlike during the ICME event. In addition, strong auroral effect with the AE minimum value of ~ 500 nT was observed. An abrupt increase in M_A value with minimum of 10 and maximum value of ~ 48 was observed, which is very rare in our solar space environment. The M_A values are vital for the characterization of collision less shocks. During the main phase of storm, the lowest value of SYM-H approximately -305nT at ~ 08:20 UT was observed and thus classified as a major geomagnetic storm based on criteria suggested by Gonzalez et al[3]. Vsw maintained the mean value of ~800 km/s throughout event. Meanwhile, Psw fluctuated between ~2 nPa and ~58 nPa from 03:00 UT to 09:00 UT. The variation of FAC and PCV in CIR event is like earlier ICME events; however, during the post event, i.e., recovery phase the fluctuation in parameters showed negligible response. As such, we have a positive relation between Vsw and the variables of FACs, PCV and IEF Ey but these variables have a negative relation with M_A. Thus, we conclude the existence of
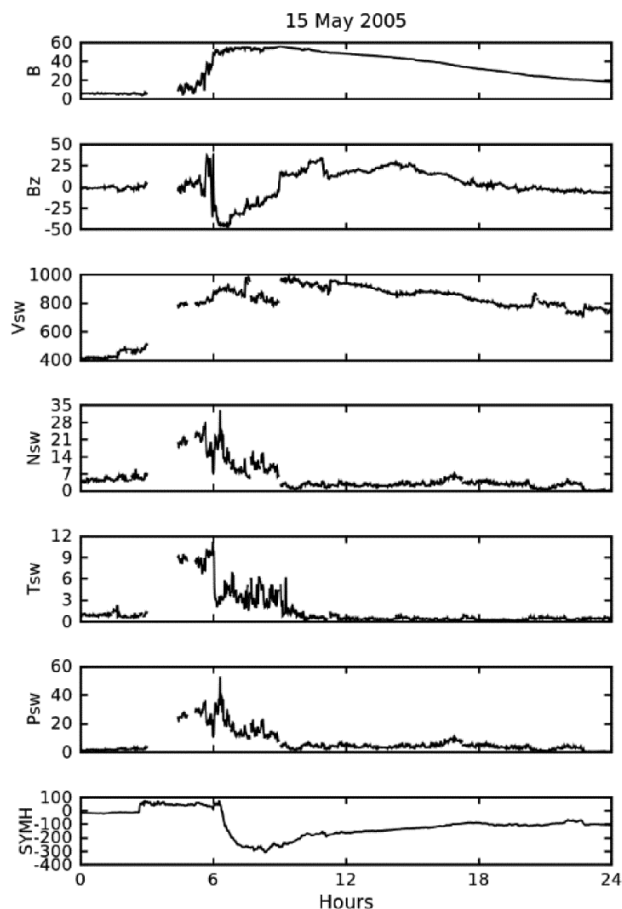
Fig. 7 — Represents the variation in IMF components and solar wind parameters observed on 15 May 2005. From top to bottom: (a) IMF magnitude (B; nT), (b) southward component of IMF (Bz; nT), (c) velocity of solar wind (Vsw; km/s), (d) density of solar wind (Nsw; i+/cm^3), (e) temperature of solar wind (10e5, Tsw; K), (f) flow pressure of solar wind (Psw; nPa), and (g) SYMH index (nT).

a negative relation between M_A and these variables (i.e., FACs, PCV and IEF Ey) during this storm.

Cross correlations

In Figs 9-12, the graphs of cross-correlation coefficient versus time in minutes are plotted. Cross correlation is the standard, multi-time scale, statistical tool that estimate time delay between two different time scale parameters as a function of time lag to draw new information[41-43]. Pearson's correlation coefficient (r) is the best and most used correlation coefficient up to now. The correlation coefficient ranges between -1 and 1. In this paper, we have employed the cross-correlation technique used by Tsurutani et al[44], Panditet al[45] and Adhikari et al[23] to analyze and compare the correlation between Alfven
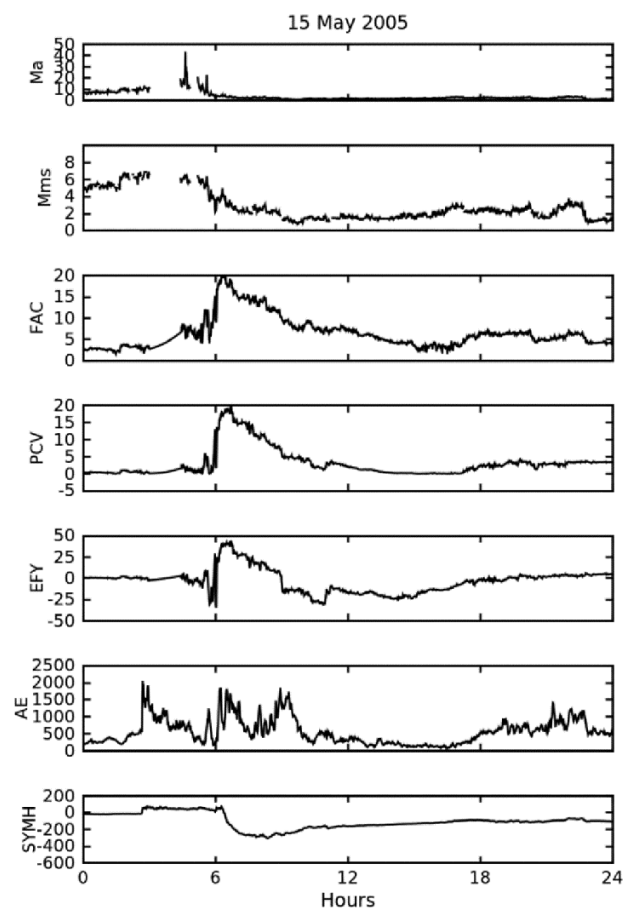
Fig. 8 — The different parameters are shown for 15 May 2005. From top to bottom: (a) Alfven Mach number (M$_A$), (b) magnetosonicmach number (Mms), (c) field aligned current (FAC), (d) polar cap potential (PCV), (e) dawn dusk electric field (EFY), (f) AE index (nT), and (g) SYMH index (nT).

M_A and the parameters of FACs, PCV, and dawn-to-dusk IEF Ey. The timescale is used to determine the lead or lag between parameters at the time of correlation. Here, the sequential order, in which variables are used, determines the time scale. As all our major parameters (i.e, Alfven M_A, FACs, PCV, dawn-to-dusk IEF Ey), which are denoted by IMF-Ey in the cross-correlation graphs, are related to solar wind, we expected some relation between them. In addition, we could see some relations among them through the help of cross correlation. Even though M_A is calculated from Band Vsw, we have carried our analysis to examine the variation of patterns during the quiet and extreme solar wind conditions.

In ICME driven event of 31 March 2001, Fig. 9 depicts the positive correlation between M_A and FAC with a coefficient of 0.8 with zero lag, whereas Korth et al[46] found no detectable dependence of FAC on

ADHIKARI *et al.*: CORRELATION OF ALFVÉN MACH NUMBER WITH FIELD ALIGNED CURRENT, POLAR CAP POTTENTIAL AND DAWN DUSK ELECTRIC FIELD
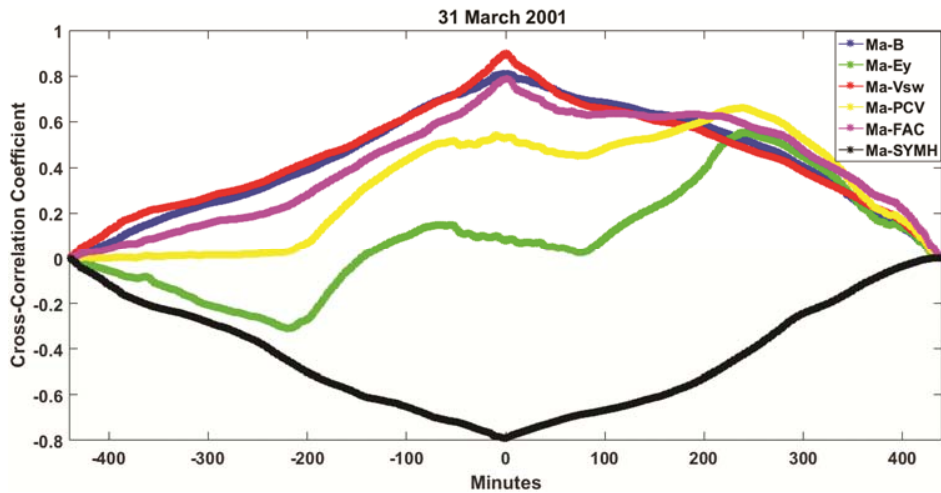
135

Fig. 9 — The line plots illustrate the cross-correlations of Alfven Mach number (M_A) with B (blue), Ey (green), Vsw (red), PCV (yellow), FAC (pink), and SYMH (black) during 31 March 2001.
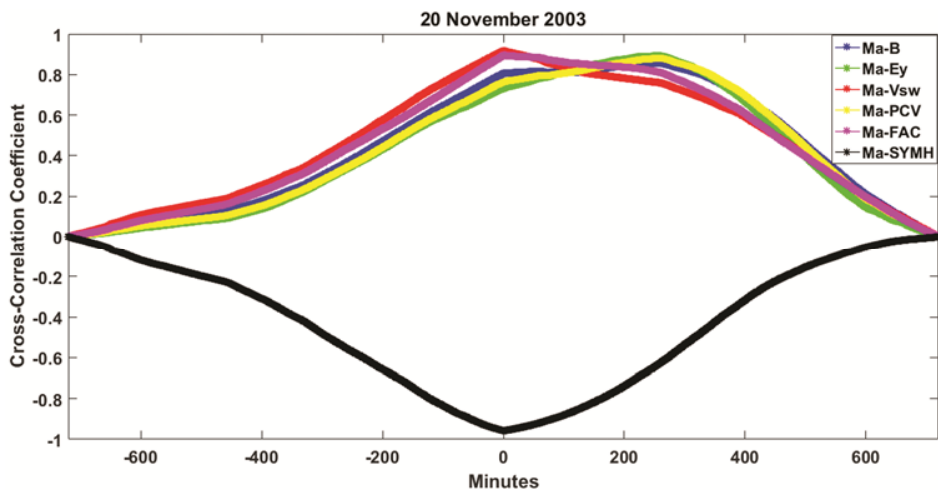

Fig. 10 — The line plots illustrate the cross-correlations of Alfven Mach number (M_A) with B (blue), Ey (green), Vsw (red), PCV (yellow), FAC (pink), and SYMH (black) during 20 November 2003.

Alfven M_A when normalizing the FAC to the median solar-wind electric field and dynamic pressure. Good anti-correlation of M_A and SYM-H was observed. But showed poor correlation of M_A with the IEF-Ey and had moderate relationship with PCV might be due to the unpreceded major storm. So, the solar energetic particles content in the interplanetary field was less and was not affected in a considerable amount by the solar wind following this ICME event. However, another ICME related event we observed was 20 November 2003, during which we found that M_A was in positive correlation with FAC and with no time lag. In addition, we also observed that M_A was in positive correlation with PCV and the Ey and with a time lag of ~ +200 min. This result was somewhat different

from the earlier ICME event of 31 March 2001 because the 20 November 2003 storm was led by another ICME event as well, thus, SEPs were greatly affected by the solar winds. Moreover, SYM-H was also in a negative correlation with M_A during this 20 November 2003 storm. We also studied one CIR event occurring on 15 May 2005 and we found expected results during this event as well. In our cross correlations, we observed positive correlation between M_A and FAC and PCV, whereas Ey was not in relation with M_A. All these relations occurred with a 0-time lag. In addition, like other geomagnetic events, SYM-H was in negative correlation with M_A with a ~ -50 min time lag. One distinct observation we made during the studying of these events was that
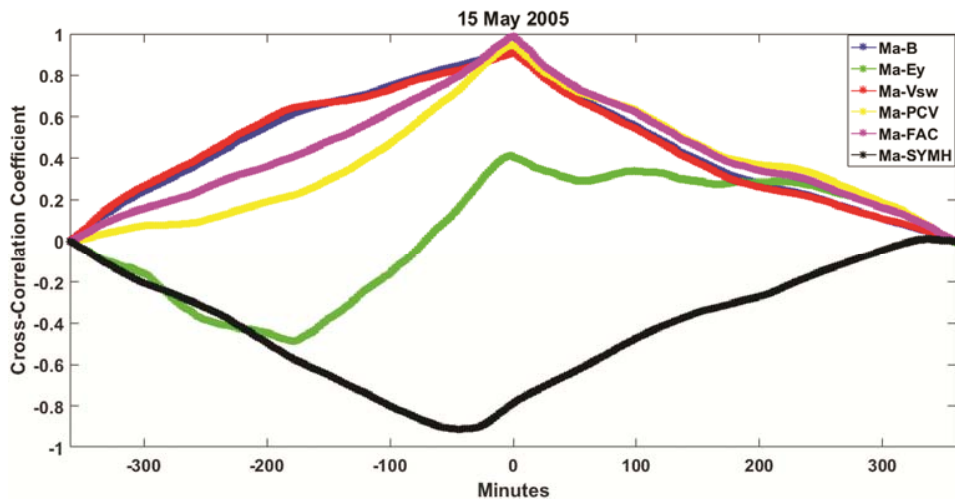
Fig. 11 — The line plots illustrate the cross-correlations of Alfven Mach number (M_A) with B (blue), Ey (green), Vsw (red), PCV (yellow), FAC (pink), and SYMH (black) during 15th May 2005.
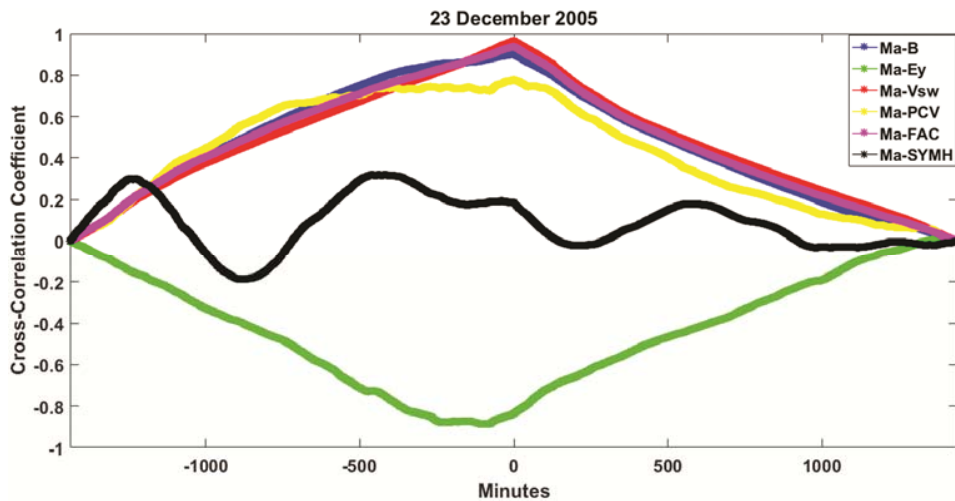

Fig. 12 — The line plots illustrate the cross-correlations of Alfven Mach number (M_A) with B (blue), Ey (green), Vsw (red), PCV (yellow), FAC (pink), and SYMH (black) during 23 December 2005.

M_A, FAC, PCV, and Ey started showing some relation after the beginning of the initial phase. Before the initial phase, they showed no correlation. This also supports the fact that M_A, FAC, PCV and Ey are somehow governed by the solar wind condition.

However, we came across some unexpected results during the quiet day of 23 December 2005. In the cross-correlation figure of this event, we found out that M_A was in correlation with FAC and PCV and in no correlation with SYM-H. These were found, as expected, but we observed also that the IEF Ey was in a negative correlation with M_A with a ~ -100 minutes time lag. This was not a scientifically meaningful result. The result we obtained regarding Ey was due

to the presence and movements of SEPs leading to the solar-wind magnetosphere coupling, which was due to the viscous penetration and ionic penetration[47].

Correlation between M_A and other parameters such as PCV and IEF Ey is dependent on the nature of the storm which can be seen through the different results we obtained during two ICME events (on 31 March 2001 when M_A was in no correlation with PCV and Ey, and on 20 November 2003 when positive correlations between M_A and PCV and Ey were found). Here, the former event was not preceded by any other solar event, whereas the later was preceded by strong solar storms. In addition, for the quiet period of 23 December 2005, we found a negative

ADHIKARI *et al.*: CORRELATION OF ALFVÉN MACH NUMBER WITH FIELD ALIGNED CURRENT,
POLAR CAP POTTENTIAL AND DAWN DUSK ELECTRIC FIELD

137

correlation between M_A and Ey due to the viscous penetration. From these, we can conclude that the conditions governing the variations of M_A, FACs, PCV, and IEF Ey during the storm periods investigated were somehow similar during the disturbed period and were closely related to the prevailing solar wind conditions. However, the viscous penetration during the quiet day led to some scientifically not meaningful results regarding the condition of Ey during the quiet period. All these correlations are further supported by our observational results and discussions documented in our previous study.

4 Conclusions

To unveil the subtlety in geomagnetic storms due to different solar events, we have analyzed the fluctuations of Alfven Mach number associated with magnetic fields of different solar events. Geomagnetic storms are associated with solar wind conditions and reflect the features of CME, ICME, CIR, HSS etc. Often, the magnetic fields are crucial for identifying the behavior of geomagnetic storms. Furthermore, in this study, we have analyzed the solar wind variables such as M_A, large-scale FACs, PCV, and dawn dusk IEF E_Y during different solar wind activities. The relations of Mach number with FACs, PCV and IEF E_Y are not solely dependent on any solar wind parameter but are affected by various conditions prior, during, and post the storm events regarding their prevailing solar maxima or minima conditions, ICMEs or CIR driven storms etc. Furthermore, conclusions of this paper are as follows:

(i) Prior to the arrival of interplanetary shock (IS), M_{MS} and M_A show good relationship with FAC, PCV, EFY, and solar wind parameters; as the space weather seems unperturbed.

(ii) On average, the value of M_{MS} (~6) during Quiet event is like the average value (~6) of M_{MS} prior to the arrival of interplanetary shock of CIR and ICME events.

(iii) After the arrival of IS: abrupt increase in M_A shows the flow of eastward magnetopause current. However, a rapid decrease in M_A value is observed with the increase in negative interval of SYMH, the compression of Earth's magnetosphere results in geomagnetic disturbance.

(iv) During the main phase of geomagnetic storm on all events, cross-correlation analysis substantiates the result obtained with good correlation

coefficient of M_A with FAC, PCV and other parameters of solar wind, agrees with results of previous research. We found that there is zero-time delay of M_A with both Vsw and FAC on all events. However, correlation of M_A with Ey showed erratic.

(v) On CIR event (15 May 2005): during the main phase of geomagnetic storm followed by recovery phase, the M_A value reaches lower (on average) to 1. Interestingly, however, there is sharp increase in M_A (~ 45) value during the arrival of IS which is even greater than the value of M_A during the Quiet event. Such shocks are very rare in near space weather environment and are momentary might be due to predominance of the solar maxima condition.

The positive correlations among the various parameters were due to the merging of two different ICMEs driven solar storms and consequential intense southward interplanetary magnetic field. The negative relationships among the selected parameters may have been due to the slow recovery of the IMF Bz component. Since, M_A is influenced by the variations in any components of the IMF, so, the delay in IMF Bz recovery can be a scientifically meaningful reason of negative correlation among these parameters. The negative correlations observed between the Mach number and the IEF Ey could be due to the viscous and ionic penetrations too. We also conclude that the preceding solar wind could have vast effect on the variance of M_A of a geomagnetic event, in turn might have its effect on FACs, PCV, Ey, and also in other solar wind parameter.

References

1   Russell C T & Vaisberg O, *Venus*, (1983) 873.
2   Chapman S & Bartels J, *Geomagnetism Volume II: Analysis of the Data, and Physical Theories,* Oxford University Press, (1940).
3   Gonzalez W D, Joselyn J A, Kamide Y, Kroehl H W, Rostoker G, Tsurutani B T & Vasyliunas V M, *J Geophys Res: Space Phys*, 99(A4) (1994) 5771.

4   Cloutier P A & Anderson H R, *Space Sci Rev*, 17(2-4) (1975) 563.

5   Iijima T & Potemra T A, *J Geophys Res*, 81(34) (1976b) 5971.

6   Chun F K & Russell C T, *J Geophys Res: Space Phys*, 102(A2) (1997) 2261.

7   Chapagain N, *Journal of Institute of Science and Technology (JIST)*, 20 (2) (2015) 84.

8   Papitashvili, V O, Rich F J, Heinemann M A & Hairston M R, *J Geophys Res: Space Phys*, 104(A1) (1999) 177.

9   Siscoe G L, Crooker N U & Siebert K D, *J Geophys Res: Space Phys,* 107(A10) (2002) SMP-21.

10   Hairston, M R, Hill T W & Heelis R A, *Geophys Res Lett*, 30(6) (2003).

11   Pedatella N M, Forbes J M & Richmond A D, *J Geophys Res: Space Phys*, 116 (2011).

12   Adhikari B, Baruwal P & Chapagain N P, *Earth Space Sci*, 4(1) (2017a) 2.

13   Mishra R K, Adhikari B, Pandit D & Chapagain N P, *Characteristic of Solar Wind Parameters and Geomagnetic Indices during Solar Flares*, Long-Term Datasets for the Understanding of Solar and Stellar Magnetic Cycles Proceedings IAU Symposium No. 340, (2018).

14   Boyle C B, Reiff P H & Hairston M R, *J Geophys Res: Space Phys,* 102(A1) (1997) 111.

15   Antonova E E & Ganushkina N Y, *Eur. Space Agency Spec Publ SP*, 389 (1996) 43.

16   Barbosa D D & Kivelson M G, *Geophys Res Lett*, 10(3) (1983) 210.

17   Chapman J F & Cairns I H, *J Geophys Res: Space Phys*, *108* (A5) (2003).

18   Eriksson S & Rastätter L, *Geophys Res Lett*, 40 (2013) 1257.

19   Lavraud B, Larroque E, Budnik E, Génot V, Borovsky J E, Dunlop M W & Ruffenach A, *Space Phys*, 118(3) (2013) 1089.

20   Iijima T & Potemra T A, *Geophys Res Lett*, 9(4) (1982) 442.

21   Kasran F A M, Jusoh M H, Adhikari B & Ab Rahim S A E, *J Phy: Conference Series*, 1152, (2019) 012027.

22   Wilder F D, Eriksson S, Korth H, Baker J B H, Hairston M R, Heinselman C & Anderson B J, *Geophys Res Lett*, 40 (2013) 2489.

23   Adhikari B, Dahal S, Sapkota N, Baruwal P, Bhattarai B, Khanal K & Chapagain N P, *Earth Space Sci*, 5(9) (2018) 440.

24   Spreiter J R, Summers A L & Alksne A Y, *Planet Space Sci*, 14(3) (1966a) 223.

25   Biernat H K, Erkaev, N V, Farrugia C J, Vogl D F & Schaffenberger W, *Nonlinear Process Geophys*, 7 (2000) 201.

26   Borovsky J E & Denton M H, *J Geophys Res*, 111 (2006a) A07S08.

27   Gosling J T, Geophys. Monogr. Ser., 58 (1990) 343.

28   Fairfield D H, Iver H C, Desch M D, Szabo A, Lazarus A J & Aellig M R, *J Geophys Res*, 106 (2001) 361.

29   Merka J, Szabo A, Slavin J A & Peredo M, *J Geophys Res* 110 (A4) (2005) 4202.

30   Wang J, Guo Z, Ge Y S, Du A, Huang C & Qin P, *J Space Weather and Space Clim,* 8 (2018) A41.

31   Moon G H, *J Astron Space Sci*, 29(3) (2012) 259.

32   Sundberg T, Burgess D, Scholer M, Masters A & Sulaiman A H, *The Astrophysical Journal,* 836(1) (2017).

33   Jankovicova D, Dolinsky P, Valach F &Voros Z, *J Atmos Sol Terr Phys*, 64 (2002) 651.

34   Echer E, Gonzalez W D, Vieira, L E A Dal Lago A, Guarnieri F L, Prestes A, Gonzalez A L C & Schuch N J, *Braz. J Phys*, 33(1) (2003) 115.

35   Weimer D R, *J Geophys Res: Space Phys*, 106(A7) (2001) 12889.

36   Adhikari B, Dahal S & Chapagain N P, *Earth Space Sci*, 4(5) (2017b) 257.

37   Kakad B, Kakad A, Ramesh D S & Lakhina G S, *J Space Weather and Space Clim*, 9 (2019).

38   Shepherd S G, *J. Atmos Sol Terr. Phys*, 69(3) (2007) 234.

39   Adhikari B & Chapagain N P, *Journal of Nepal Physical Society (JNPS)*, 3(1) (2015) 6.

40   Subedi A, Adhikari B & Mishra R K, *Himalayan Physics*, (2017) 80.

41   Katz R W, *J Climatol*, 8(3) (1988) 241.

42   Vichare G, Rawat R, Hanchinal A, Sinha A K, Dhar A & Pathan B M, *Earth planets space*, *64*(11) (2012) 1023.

43   Usoro A E, *J Statistical and Econometric Methods*, 4(1) (2015) 63.

44   Tsurutani B T, Gould T, Goldstein B E, Gonzalez W D & Sugiura M, *J Geophys Res: Space Phys*, 95(A3) (1990) 2241.

45   Pandit D, Chapagain N P, Adhikari B and Mishra R K, *Activities, and Its Impact on Space Weather,* Long-Term Datasets for the Understanding of Solar and Stellar Magnetic Cycles Proceedings IAU Symposium No. 340, (2018), doi:10.1017/S1743921318001308.

46   Korth H, Anderson B J & Waters C L, *Ann Geophys,* 28(2) (2010).

47   Baumjohann W, *Solar wind-magnetosphere coupling*, (1986) 3.

Solar Activities and Its Impact on Space Weather

Drabindra Pandit[1,2,3]**, Narayan P. Chapagain**[2]**, Binod Adhikari**[1,3] **and Roshan K. Mishra**[1]

[1]Dept. of Physics, St. Xavier's College, Tribhuvan University
Maitighar, Kathmandu, Nepal

[2]Dept. of Physics, Patan Multiple Campus, Tribhuvan University
Patandhoka, Lalitpur, Nepal

[3]Central Dept. of Physics, Tribhuvan University
Maitighar, Kathmandu, Nepal
email: `drabindrapandit087@gmail.com`, `npchapagain@gmail.com`, `binod.adhi@gmail.com`,
`roshanmishra.phy@gmail.com`

Abstract. The Sun is an active star and its magnetic field fluctuates from a fraction of a second to a long period of time. The solar wind, CME, solar prominence, solar flares, solar particle and solar filament are the direct result of solar magnetic activity effects on the interplanetary space, Earth's magnetosphere and ionosphere. The intensity of irruption of these phenomena from the Sun's surface depends upon its phases. The extreme events affect technology both in space and on the ground.The data obtained from series of observations can help to predict solar activities and safekeeping to the space technology. In this study the cross correlations between IMF Bz, solar wind velocity(Vsw) and interplanetary electric field(Ey) with AE and SYM-H are studied. The results reveal that strong geomagnetic disturbances have high impact on the components of space weather than weak disturbances have.

Keywords. Interplanetary space, Earth's magnetosphere, Geomagnetic disturbances etc.

1. Introduction

The Sun has nearly 11 year of solar cycle which has maximum, minimum, ascending and descending phases. It is more active during maximum phases of solar cycle where it has maximum sunspots number and during minimum phases it is less active and has minimum number of sunspots. During active phases of the Sun tremendous amount of plasma and magnetic field are released into interplanetary space (Parker 1958), which interacts with the Earth's magnetosphere and a part of plasma particles and their kinetic energy enters into magnetosphere resulting into geomagnetic storm (Gonzalez *et al.*, 1987),substorm, auroral and Australian borealis in the northern and southern sky respectively that ultimately affect the technology borne in space or on the ground (Eastwood *et al.*, 2017). The parameters used to study their strength are solar wind parameters and geomagnetic indices (Adhikari *et al.*, 2017).

2. Result and Discussion

During intense magnetic storm the southward component of interplanetary magnetic field (IMF Bz) is strong and there occurs magnetic reconnection between this field and geomagnetic field, which produces open field lines, allowing mass, energy and momentum pervade into the Earths magnetosphere. Such events affect more on intense storm day than during quiet day.
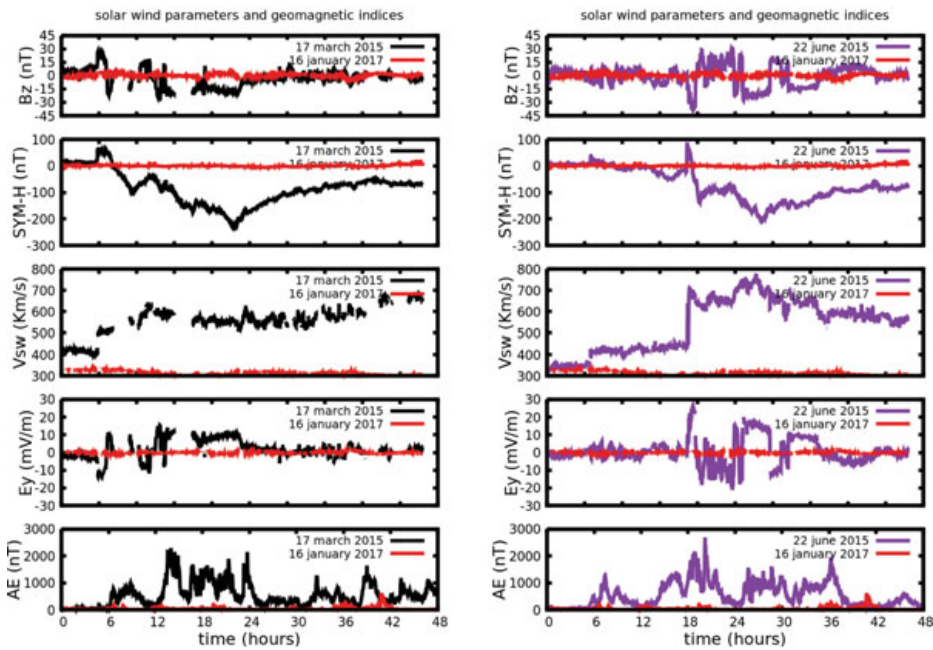
Figure 1. The panel from top to bottom show the variation of interplanetary magnetic field (Bz in nT), SYM-H (nT), solar wind speed (Vsw in Km/s), interplanetary electric field (Ey in mV/m), Aurora index (AE in nT) on 17 March 2015 intense storm and 16 January 2017 quiet day (left) and 22 June 2015 intense storm and 16 January 2017 quiet day (right) respectively.
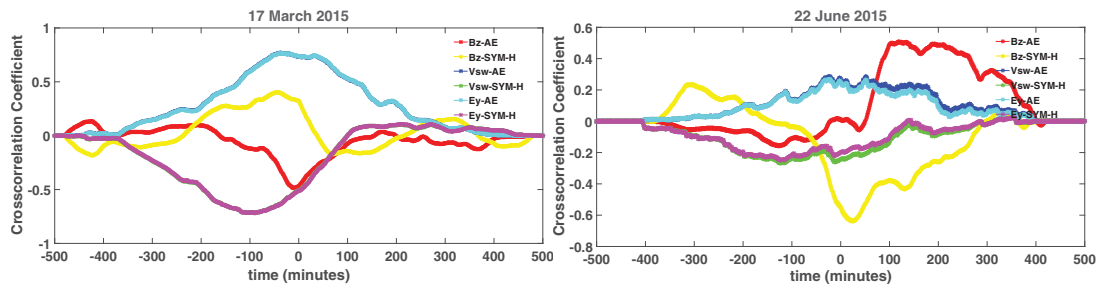

Figure 2. Showing variation in cross-correlation coefficients versus time(min) for Bz(nT)-AE(nT), Bz(nT)-SYM-H(nT), Vsw(Km/s)-AE(nT), Vsw(Km/s)-SYM-H(nT), Ey(mV/m)-AE(nT), Ey(mV/m)-SYM-H(nT) on 17 March 2015 (left) and 22 June 2015 (right) respectively.

3. CONCLUSION

During geomagnetic storms, the interaction occurs between the Sun's and the Earth's magnetic field. Energy and charged particles are injected into the Earth's magnetosphere, which decrease the Earths magnetic field and affect the ground and space-based technologies. It is also found that cross correlations between Vsw-AE and Ey-AE are positive and between Ey-SYM-H is negative whereas the cross correlations between Bz-AE, Bz-SYM-H and Vsw-SYM-H vary with time, taking positive and negative values.

References

Parker, E. N. 1958, *Astrophysical Journal*, 128, 664

Gonzalez, W. D. & Tsurutani, B. T. 2018, *Planet Space Sci.*, 1987, 35,1101

Eastwood, J. P., Biffis, E., Hapgood, M. A., Green, L., Bisi, M. M., Bentley, R. D.,Wicks, R., Mckinnell, L. A., & Gibbs, M. and Burnett, C. 2017, *Risk Analysis*, 2

Adhikari, B., Mishra, R. K., Pandit, D., & Bhatterai, B., Chapagain N. P. 2017, *JIST*, 22 (1), 45

Characteristic of Solar Wind Parameters and Geomagnetic Indices during Solar Flares

Roshan K. Mishra[1], Binod Adhikari[2], Drabindra Pandit[3] and Narayan P. Chapagain[4]

[1]Dept. of Physics, St. Xavier's College, Tribhuvan University
Maitighar, Kathmandu, Nepal
email: `roshanmishra.phy@gmail.com`

[2]Dept. of Physics, St. Xavier's College, Tribhuvan University
Maitighar, Kathmandu, Nepal
email: `binod.adhi@gmail.com`

[3]Dept. of Physics, St. Xavier's College, Tribhuvan University
Maitighar, Kathmandu, Nepal
email: `drabindrapandit087@gmail.com`

[4]Dept. of Physics, Patan Multiple Campus, Tribhuvan University,
Patan Dhoka, Lalitpur, Nepal
email: `npchapagain@gmail.com`

Abstract. Active sun is characterized by compelling short-lived flash of solar eruption like solar flare, coronal mass ejections (CMEs), high-speed solar winds and solar energetic particles along with colossal release of energy and mass. This paper proposes a new method to evaluate solar wind parameters and geomagnetic indices based on wavelet analysis during the solar flares. The crucial role of IMF-Bz (interplanetary magnetic field) is examined for the two solar flares events. The key result obtained from our study is substantial dependence of solar flare intensity on IMF-Bz together with solar wind velocity. We also observed the duration of solar flares and their effect on ionospheric and ground based parameters.

Keywords. Solar Flares, Continuous Wavelet Analysis, Space Weather, Periodicity

---

1. Introduction

Solar wind possesses tremendous amount of kinetic and electrical energy, some part of it directly enters the earths magnetosphere causing a turmoil to the geomagnetic activities and eventually resulting to geomagnetic storms, sub-storms and aurora (Chapman & Bartels 1962 ; Gonzalez *et al.* 1994). Geomagnetic indices characterizes the variability of the earths magnetic field in all its complexity in a single number.

2. WAVELET ANALYSIS

Continuous Wavelet Transform (CWT) is used to provide the reliable description of the signal in term of time and frequency domain, which expresses a continuous signal into wavelets. The CWT coefficient is defined as

$$W(a,b) = \int f(t)\phi^*((t-b)/a)dt$$

where $\phi^\star$ represents the complex conjugate of ϕ and the parameters a and b are scaling and shifting factors respectively and W (a, b) gives the values of the coefficients (Adhikari *et al.* 2017; Adhikari *et al.* 2018).
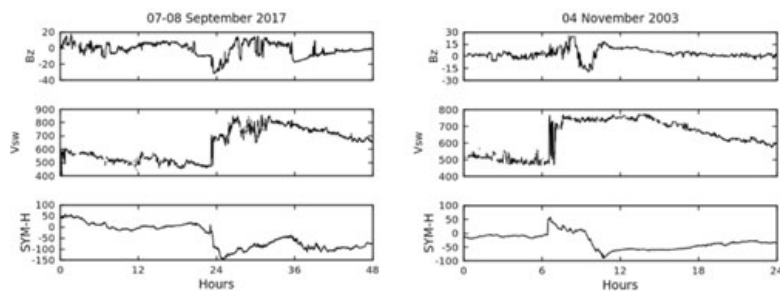
Figure 1. Plot of the hourly variation of Bz, Vsw, and SYM-H component on 07-08 September 2017 (left) and 04 November 2003 (right)
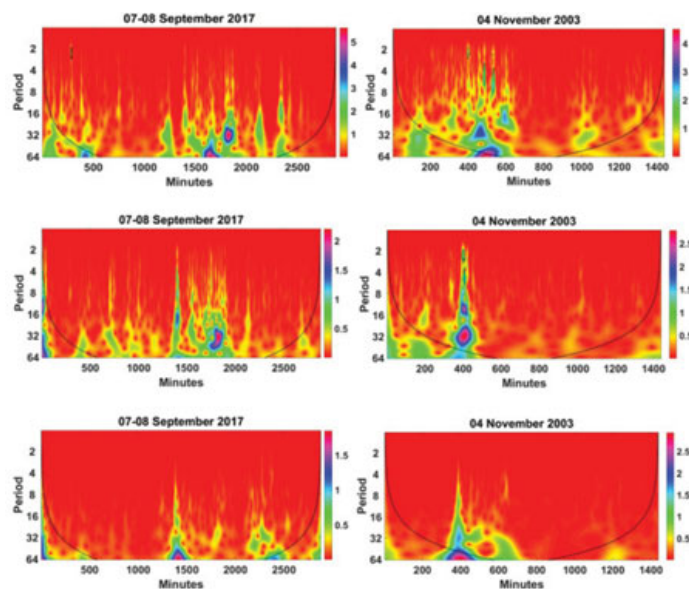

Figure 2. Scalograms for IMF-Bz (top), Vsw (middle) and SYM-H (Bottom)

3. Result and Discussion

Our analysis verifies that the power intensities of IMF-Bz, Vsw and SYM-H show a high spectral variability. Results present that both higher and small periodicities are observed on each parameter. The periodicities around 64 to 2 minutes are seen at the time of flare.

4. CONCLUSION

The CWT analysis on IMF-Bz, Vsw and SYM-H shows higher and small periodicities during the peak phase of solar flare. The periodicities variation of 64 to 2 minutes have been observed on each parameter, however the periodicity of 64 -32 portrait larger power regions.

References

Adhikari B., Mishra R. K., Pandit D., Bhattarai B. & Chapagain N. P. 2017, *JIST*, 22 (1), 45

Adhikari B., Sapkota N., Bhattarai B., Mishra R. K., Bohora S., Chapagain N. P. & Regmi B. 2018, *Russ. J. Ea.*, 18, 1

Chapman, S. & Bartels, J. 1962, *Geomagnetism, Clarendon Press, Oxford*, 1

Gonzalez, W. D., Josely, J. A., Kamide, Y., Korehi, H. W., Rostoker, G., Tsuruntani, B. T., & Vasylianas V. M. 1994, *Journal of Geophysical Research: Space Physics*, 99, 5771

ORIGINAL ARTICLE

A study of vTEC above Nepal exploring different calibration techniques, including a comparison with the NeQuick-2 model

P. Poudel[1] · A. Silwal[1] · B.D. Ghimire[2,3] (ID) · S.P. Gautam[3] · M. Karki[4] · N.P. Chapagain[4] · B. Adhikari[2] · D. Pandit[2,3] · C. Amory-Mazaudier[5,6]

Abstract

In this paper, we investigate the performance of the NeQuick 2 (NeQ-2) model with respect to Ciraolo's and Gopi's derived ionospheric vertical Total Electron Content (vTEC) during the years 2014 and 2015. GPS observables derived from dual-frequency receivers over western Nepal (Simikot, Bhimchula, and Nepalganj) are processed to obtain the experimental vTEC utilizing Gopi's and Ciraolo's calibration procedures. The monthly and seasonal behavior of vTEC obtained from each calibration technique is compared with the vTEC obtained from the NeQ-2 model during a quiet period. It is observed that the vTEC value obtained from all studied approaches started to increase from 00:00 Universal Time (UT = Local Time(LT) +5:45), reached a maximum around 08:00 UT (13:45 LT), followed by a decrease, attaining a minimum value around 23:00 UT (4:45 LT). Moreover, a comparative study showed that vTEC computed using the Ciraolo calibration technique overestimates GPS vTEC, calculated in all hours and months by Gopi's approach. In the Spring and Summer, vTEC derived using Ciraolo's TEC calibration overestimates NeQ-2 and underestimates it in the Autumn and Winter. It is found that NeQ-2 model vTEC is favorably associated with GPS vTEC obtained using the Gopi procedure in Spring and correlates with the Ciraolo technique in Autumn. Two GPS vTEC estimations demonstrate superior consistency in the Summer and Winter seasons over the region of Nepal. It is found that the mean absolute difference between NeQ-2 prediction and GPS vTEC procured through the Gopi approach is less on the storm event day. By contrast, it is discovered less by the Ciraolo technique when the storm is recovering (except for a few cases).

Keywords Calibration technique · NeQuick model · vTEC · Absolute deviation · Geomagnetic storm

1 Introduction

The ionosphere, an upper atmospheric region comprising free ions and electrons, perturbs the electromagnetic signals passing through it (Appleton 1932; Hagfors and Schlegel 2001; Goodman 2005). The main parameter of the iono-sphere responsible for the disruption of trans-ionospheric wave propagation is Total Electron Content (TEC). It is defined as the integrated electron density between the ground receiver and Global Navigation Satellite System (GNSS) satellites along a one-meter squared ray path through the ionosphere. (Otsuka et al. 2002; Bagiya et al. 2009; Silwal et al. 2021a). TEC is a prime source of error for ground-based receivers to space satellite communication and navigation system (Dabas 2000; Jin et al. 2007); thus, significant efforts have been made over the last few decades to understand the spatial and temporal variation of ionospheric TEC (e.g., Fejer 1997; Bhuyan et al. 2003; Olwendo and Cesaroni 2016; Ogwala et al. 2019; Silwal et al. 2021b) and to develop TEC models (e.g., Bilitza 1990; Radicella and Zhang 1995; Jakowski et al. 2011b; Okoh et al. 2016).

TEC can be estimated using carrier-phase and code observables derived from dual-frequency GNSS receivers (Hernández-Pajares et al. 2011). TEC measured through

✉ B.D. Ghimire
basudev@sxc.edu.np

[1] Patan Multiple Campus, Tribhuvan University, Lalitpur, Nepal

[2] St. Xavier's College, Maitighar, Kathmandu, Nepal

[3] Central Department of Physics, Tribhuvan University, Kirtipur, Nepal

[4] Amrit Campus, Tribhuvan University, Kathmandu, Nepal

[5] LPP, Polytechnique, Sorbonne Universites, Paris, France

[6] T/ICT4D, The Abdus Salam International Center for Theoretical Physics, Trieste, Italy

Dual-frequency GNSS receivers around the Earth is the most accepted approach for interpreting the ionosphere because they provide data with better accuracy in both time and space (Kumar and Singh 2011; Fagundes et al. 2016). However, TEC derived from carrier-phase measurement is equivocal due to inherent uncertainty in the carrier cycle, whereas code measurement estimates are typically noisy (Abe et al. 2017). GNSS-TEC data accuracies are limited by instrumental thermal noise, tropospheric effects, higher-order ionospheric effect, and multipath (Hoque and Jakowski 2012). Thus, GNSS observables should be processed carefully to estimate TEC. A wide range of techniques (Ciraolo et al. 2007; Arikan et al. 2004; Montenbruck et al. 2014) has been developed to realize the accuracy in GNSS-TEC data and every one of them makes distinct presumptions and approximations to simplify the methodology. Carrano and Groves (2006) believe that differential code measurement should be leveled into the differential carrier phase measurement to eliminate the content noise of the code measurements and the undefined ambiguity of the carrier phase. However, some researchers (Ciraolo et al. 2007) trust that TEC approximation using carrier phase would be enough to avoid the noise content of the code measurement. Whatever the estimation procedure, the dual-frequency GNSS receivers can compute TEC utilizing the differential delay information they get from different-frequency radio signals.

Despite this, GNSS single frequency systems users rely on ionospheric models to mitigate ionospheric and other navigation errors. Empirical models such as International Reference Ionosphere (IRI) and NeQ-2, based on numerical integration of underlying datasets of different ionospheric parameters, calculate the electron density at a particular height and the ionospheric TEC (Rawer et al. 1978; Bilitza et al. 2017; Bilitza 2018; Nava et al. 2008). The NeQ-2 is the evolution of the DGR profiler proposed by Di Giovanni and Radicella (1990). The NeQ-2 profile formulation consists of semi-Epstein layers with a modeled thickness parameter (Radicella and Leitinger 2001) and three anchor points: the E-layer peak, the F1-layer peak, and the F2-layer peak. These anchor points can be quantified using the ionosonde parameters *fo*E, *fo*F1, *fo*F2, and M(3000)F2 (Coïsson et al. 2006). The NeQ-2 model, which is intended for use in trans-ionospheric propagation applications, has been upgraded on a continuous basis, including NeQuick 1 and NeQuick 2 (Nava et al. 2008). It is implemented by making considerable improvements to the bottom-side (Leitinger et al. 2005) and topside (Coïsson et al. 2006) description and optimization of computer programs. This model can estimate TEC up to the height of 20,200 km.

For users of ionospheric models, model prediction accuracy is always a primary concern. Comparing ionospheric model estimations to real-time experimental data is a prevalent approach used by ionospheric researchers to assess

model accuracy and validate them for useful applications (Migoya-Orué et al. 2008; Rabiu et al. 2014; Tariku 2015; Cherniak and Zakharenkova 2016; Okoh et al. 2018; Sharma et al. 2018). Researchers (Ezquer et al. 2018; Okoh et al. 2018; Tariku 2020) compared different ionospheric TEC models (IRI, IRI-plas, and NeQ-2) using GNSS measurements and concluded that NeQ-2 performs better than other models regardless of time or location. Ahoua et al. (2018) compared observed TEC derived from a nearby GNSS dual-frequency receiver to the NeQ-2 model performance for quiet and storm days over South Africa during the ascending phase of the solar cycle (2009–2011). They reported that the NeQuick model has close reliability for magnetic quiet and disturbed days, while solar activity affects its accuracy (better in moderate than in high solar activity). Yu et al. (2012) evaluated the monthly average of the NeQ-2 model over China during the quietest period and discovered that the NeQ-2 predicts GPS TEC accurately (except for a few cases). As indicated previously, there is also considerable variation in the approaches used to estimate the TEC by GNSS observables, and each of them claims to have an accurate approach. Some researchers conducted a comparative study on TEC values derived from various calibration techniques, while others integrated the model with various GPS vTEC estimations (Abe et al. 2017; Pignalberi et al. 2020; Tornatore et al. 2021). Abe et al. (2017) compared the performance of the calibration approach developed by Ciraolo et al. (2007) (hereafter Ciraolo) and the one developed by Seemala and Valladares (2011) (hereafter Gopi) by using vTEC generated by the European Geostationary Navigation Overly System Processing Set (EGNOS PS) algorithm as a reference during geomagnetic quiet and disturbance periods. They found that Gopi's approach is more reliable in the low-latitude region, while Ciraolo's approach is more reliable in the mid-latitude region.

As mentioned earlier, several early pieces of research study the performance of modeled vTEC with respect to GPS vTEC in different solar time and geophysical regions. We have perceived that they have used any TEC calibration techniques to estimate TEC from GPS/GNSS observables and carried out a comparative study to observe model prediction performance to experimental observations. A review of past studies led us to wonder whether model-estimated vTEC performs similarly to vTEC obtained using various GPS TEC estimating approaches. To address this query, we employed the International Telecommunication Union (ITU) vTEC model (NeQ-2) in conjunction with two widely used GPS TEC estimating techniques, Gopi's and Ciraolo's. As far as we are aware, no concurrent comparison of the performance of modeled vTEC and GPS vTEC derived using different techniques based on monthly and seasonal variation has been conducted. Also, this is the first study that reports the performance of the NeQ-2 model over the region

Table 1 Details of GPS-stations used in the present study

S. No	Station's Name	Station's Location	Geographic Latitude	Geographic Longitude	Geomagnetic Latitude	Geomagnetic Longitude
1	SMKT	Simikot, Nepal	29.9694° N	81.8065° E	21.29° N	156.34° E
2	BMCL	Bhimchula, Nepal	28.6558° N	81.7144° E	19.99° N	156.15° E
3	NPGJ	Nepalganj, Nepal	28.1172° N	81.5953° E	19.46° N	156.00° E

of Nepal (26°22′N to 30°27′N and 80°4′E to 88°12′E). We believe that this type of study is important not only for determining the model's reliability and validity but also for determining the most appropriate technique for the model's TEC assimilation technique. The paper is organized as follows: Sect. 2 is for data and methods, and Sect. 3 is dedicated to results and discussion. The conclusion of all results is summarized in Sect. 4.

2 Data set and methodology

This study used GPS-derived vTEC from Simikot (hereinafter referred to as SMKT), Bhimchula (hereafter referred to as BMCL), and Nepalganj (hereafter referred to as NPGJ) for the years 2014–2015. Table 1 shows the location of stations in geographic and geomagnetic coordinates as shown in Fig. 1. The geomagnetic coordinates introduced in the table are geomagnetic dipole coordinates based on the current inclination of the magnetic field.

The GPS observables produced by dual-frequency receivers along the studied stations are extracted in the Standard Receiver Independent Exchange (RINEX) format v2.1, a standard ASCII format. UNAVCO makes these data publicly available on its website, https://www.unavco.org/. It is necessary to process the GPS-TEC RINEX files to retrieve the ionospheric observables. The complete explanation of acquiring ionospheric observables using GPS is discussed in Mannucci et al. (1999). For dual-frequency measurement, the path range of signal transmitted from a satellite to the receiver is expressed by carrier phase and Pseudo-range measurement (code measurement) (Ya'acob et al. 2010; Nie et al. 2018). These measurements are conventionally used to estimate slant TEC (sTEC). The equations to determine sTEC using code and phase measurement are:

$$\text{sTEC}_P = \frac{1}{40.3}\left[\frac{1}{L_1^2} - \frac{1}{L_2^2}\right]^{-1}(P_1 - P_2) - (B_s + B_r + e_p)$$

$$(1)$$

$$\text{sTEC}_c = \frac{1}{40.3}\left[\frac{1}{L_1^2} - \frac{1}{L_2^2}\right]^{-1}(\lambda_1 C_1 - \lambda_2 C_2)$$
$$- (\lambda_1 N_1 + \lambda_2 N_2 + e_c) \qquad (2)$$

In the Eqs. (1) and (2), λ_1 and λ_2 are the wavelengths corresponding to frequency L_1 (1575.42 MHz) and L_2 (1227.60 MHz), respectively. The sTEC_p is the sTEC estimation using code-delay measurement; sTEC_c is the sTEC estimation using carrier phase measurement; P_1 and P_2 are the code-delay measurement on L_1 and L_2 frequency, respectively; B_s indicates the satellite differential code biases; B_r is the receiver differential code biases; C_1 and C_2 are the carrier phase measurement on L_1 and L_2 frequency, respectively; N_1 and N_2 are the ambiguity integer measure on the carrier phase on L_1 and L_2 frequency, respectively; e_p and e_c are the noise and multipath errors concerned with code and carrier phase measurements, respectively (Abe et al. 2017).

As sTEC depends on the elevation of the ray path, equivalent vTEC is calculated using the approach proposed by Klobuchar (1986). In this technique, the vTEC is estimated by taking projection from sTEC adopting the thin shell model at the height of around 350 km to 450 km as ionospheric pierce point (IPP).

$$\text{vTEC} = \text{sTEC} \times \cos\left(\sin^{-1}\left[R_E \cos\Theta/(R_E + h)\right]\right) \qquad (3)$$

Where R_E is Earth's radius; Θ is the elevation angle at the ground station; and h is the height of precise point (350 km in this study). The elevation of the cut-off angle is selected as 20°.

Ciraolo's GNSS-TEC calibration is based on carrier-phase measurements from GPS-only or GPS-plus-GLONASS satellite systems without considering code inter-frequency biases (Ciraolo et al. 2007; Abe et al. 2017). On the other hand, Gopi's TEC calibration method takes into account code inter-frequency biases and GPS-only carrier phase measurements. We have used the Ciraolo GNSS-TEC (GNSS_2018 version) and Gopi GPS-TEC (GPS Gopi v2.9.4) software. Both TEC estimation software provide vTEC data. We collected data of 15 seconds intervals using GNSS_2018 and 30 seconds using GPS Gopi v2.9.4 TEC calibration software. Later, this observation is converted to an hour resolution by taking the arithmetic mean, resulting in 24 data sets for a given day.

The corresponding modeled vTEC was computed on an hourly basis for a specific day using NeQuick 2. From these hourly data, the mean vTEC for a given month is estimated

Fig. 1 Map representing the studied station's location. The horizontal axis represents geographical longitude, and the vertical axis represents geographical latitude
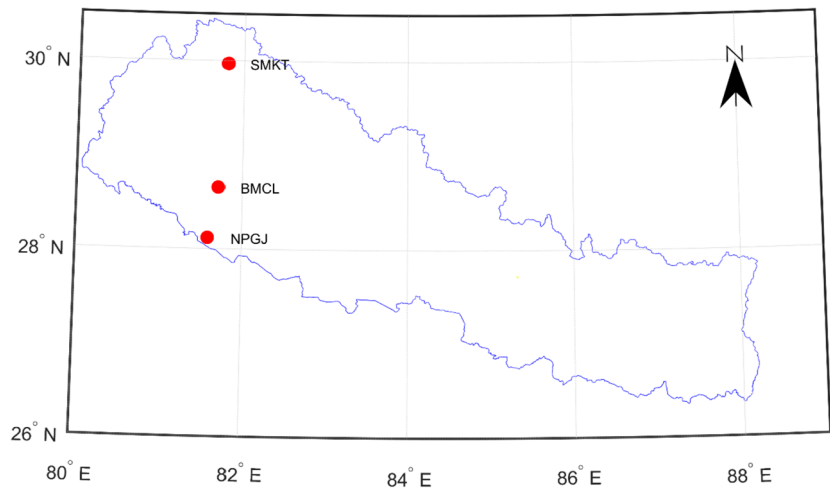
at a 1-hour resolution. The model package includes FOR-TRAN 77 subroutines and a driver program. The driver application allows calculating TEC for any ground to satellite ray path. The basic input in the model are coordinates and solar flux and eventually provided vTEC at a specific point in space and time as output. The daily solar flux (F10.7) data made available by the National Oceanic and Atmospheric Administration (NOAA) at ftp://ftp.swpc.noaa.gov/pub/indices/old indices/ is utilized as input solar flux for the particular day.

We examined the monthly and seasonal variation in vTEC during quiet days in 2014 and 2015. The years 2014 and 2015 fall within sunspot cycle 24, a relatively weak sunspot cycle. The year 2014 occurs during the sunspot cycle's maximum phase, while 2015 occurs during the sunspot cycle's declining phase (refer to Fig. 5). Each month's top five magnetically quiet days were chosen using data from the World Data Center for Geomagnetism in Kyoto (http://wdc.kugi.kyoto-u.ac.jp/wdc/Sec3.html). The obtained hourly vTEC measurements of a month's quiet days were processed using simple arithmetic mean to obtain 24 data points for each month of the year under study. Additionally, we chose three geomagnetically disturbed events of varying intensity to validate the NeQ-2 model's performance during ionospheric disruptions. The Dst, Kp, and Ap indexes were used to define the strength and phases of geomagnetic events.

Additionally, seasonal variations were investigated by calculating the arithmetic mean of three months' data for each season: Spring (March, April, and May), Summer (June, July, and August), Autumn (September, October, and November), and Winter (December, January, and February). To compare the different estimations of vTEC and NeQ-2, we present the deviation in vTEC, defined as the difference between the vTEC of the NeQ-2 model (NeQ-2) and the mean vTEC obtained by the Ciraolo (vTEC(C)) and Gopi

(vTEC(G)) approach, at each instant of time. Hence,

Deviation in vTEC, d(NeQ-2, Ciraolo)

$$= \text{NeQ-2} - \text{vTEC (C))} \tag{4}$$

$$\text{Deviation in vTEC, d(NeQ-2, Gopi)} = \text{NeQ-2} - \text{vTEC (G)} \tag{5}$$

This technique has been applied to several previous research works of Sharma et al. (2010), Amabayo et al. (2014), Silwal et al. (2021a).

3 Results and discussion

In this section, the performance of the modeled vTEC ((NeQ-2)) has been evaluated with respect to measured vTEC (using Ciraolo's and Gopi's TEC calibration techniques) observed by the stations: SMKT, BMCL, and NPGJ over the region of Nepal. We primarily discuss the quiet time variation of NeQ-2 prediction regarding Gopi's and Ciraolo's TEC calculations and the discrepancy between them through monthly and seasonal analysis. Additionally, we compare one TEC estimation approach to another in a geomagnetically disturbed condition.

3.1 Quiet time monthly variation

Figure 2(a) and 2(b) portray the diurnal variation of the monthly mean vTEC derived utilizing Ciraolo's calibration, Gopi's calibration procedures, and NeQ-2 model from the stations SMKT, BMCL, and NPGJ of the quiet days of the selected period. It is observed from the figures that vTEC estimated employing all mentioned procedures and model starts increasing from its lowest value around at 00:00 UT (05:45 LT), attain the daily maximum peak value at around
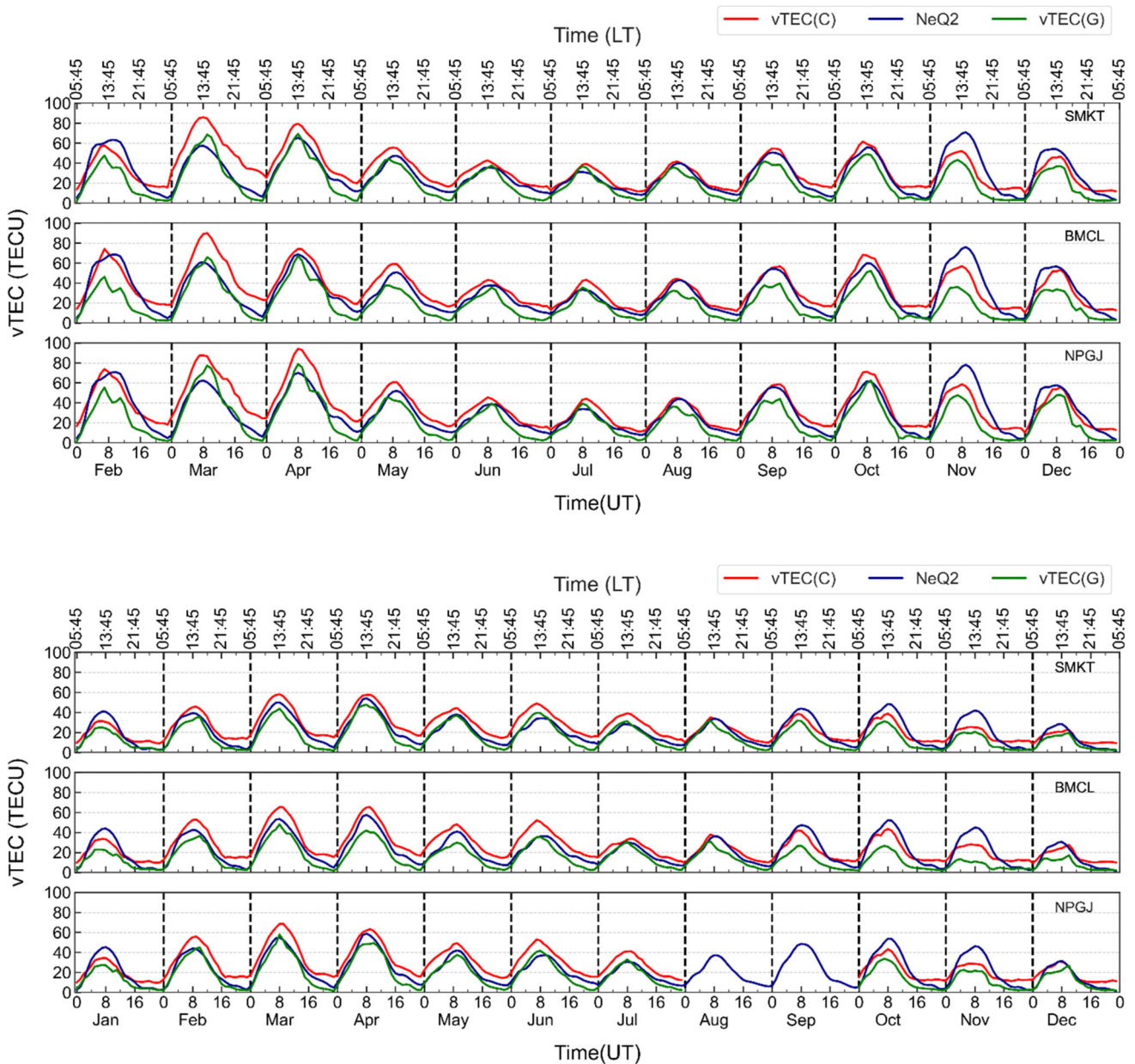
🖄 Springer

Fig. 2 Diurnal variation of the monthly averaged GPS vTEC derived from Gopi's calibration technique (green curve), Ciraolo's calibration technique (red curve), and NeQ-2 modeled vTEC (blue curve) during the years a) 2014 and b) 2015

08:00 UT (13:45 LT). Hereafter the TEC gradually decreases, achieving a minimum at around 23:00 UT (4:45 LT). This increment in vTEC after sunrise is a very expected phenomenon because the elevation of solar radiation intensity increases the ionization process in the upper atmosphere causing a high concentration of electrons near the F layer of the ionosphere (Okoh et al. 2018; Sharma et al. 2020). As the sun sets, the reduction of solar radiation amplitude lowers the production of the electron, causing a gradual decrement in TEC. The similar diurnal variation pattern of GPS-derived vTEC (both vTEC(C) and vTEC(G)) and NeQ-2 model in-

dicates that NeQ-2 provides a good representation of diurnal TEC variation.

The deviation in mean hourly vTEC from the model and measured using different calibration methods are displayed in Figs. 3(a) and 3(b). They demonstrate that the difference in vTEC(C), vTEC(G) and NeQ-2 with respect to one another varies with stations, months, and hours of the day. From March to October 2014 and from February to August 2015, NeQ-2 underestimated vTEC(C) in all hours over all the studied regions. However, NeQ-2 overestimate vTEC(C) during the time interval 03:00–16:00 UT in the remaining months. The maximum difference in vTEC estimation be-

 Springer
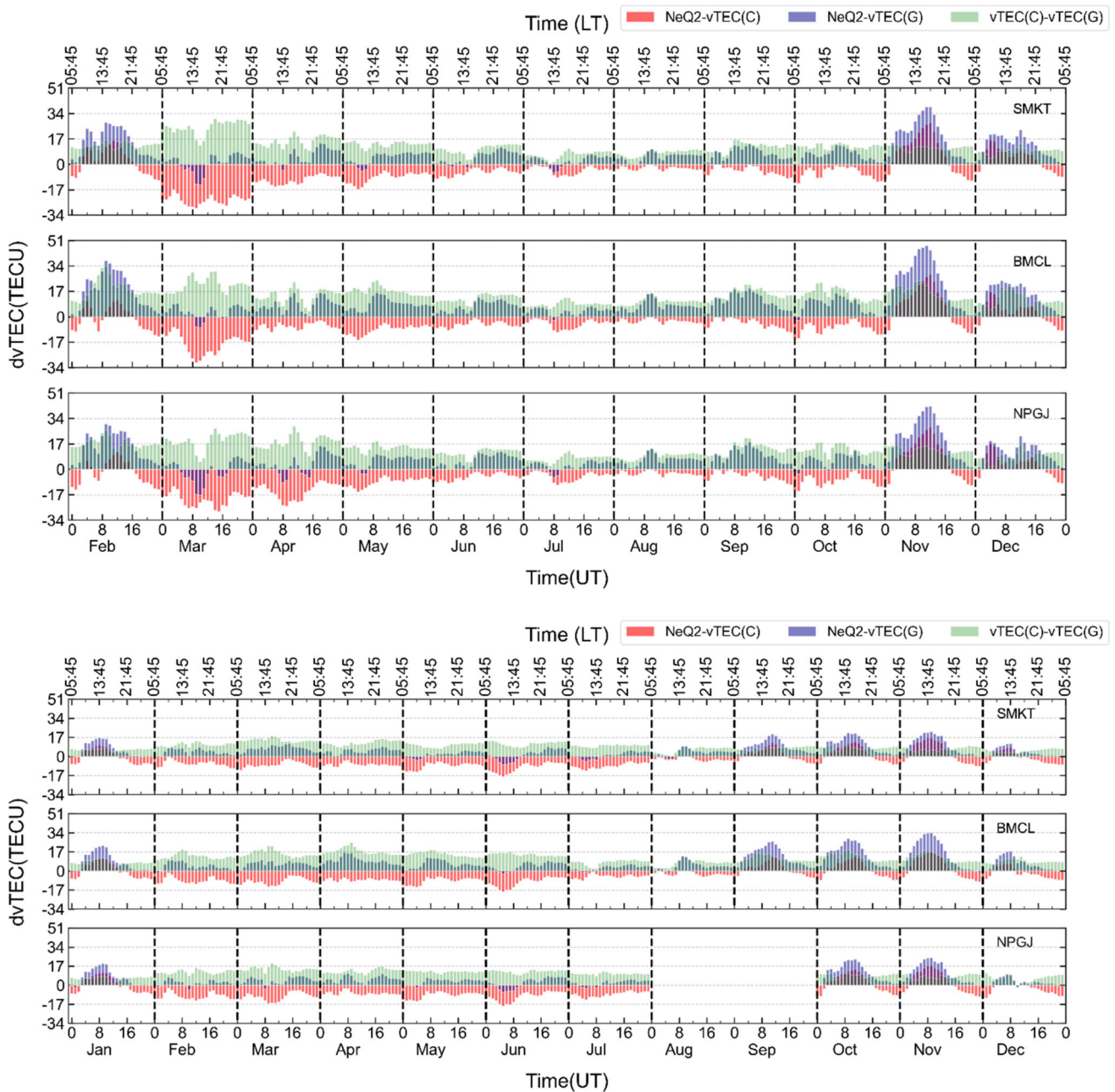
Fig. 3 Deviation of monthly averaged diurnal vTEC estimated using Ciraolo's and Gopi's calibration approach from NeQ-2 model vTEC (red and blue bars respectively), vTEC estimated using Gopi's calibration approach from Ciraolo calibration approach (green bars) over the studied stations for years a) 2014 and b) 2015

tween them is observed between 07:00–10:00 UT in March (2014) (< -30 TECU) and 05:00–8:00 UT in July (2015) (~ -17 TECU). The low deviation value between vTEC(C) and NeQ-2 is discerned in August in both years. NeQ-2 overestimated vTEC(G) except in March and a few daily hours of April, May, and July 2014 (except BMCL). In 2015, the same overestimation was observed except for time intervals 04:00–10:00 UT in June and July, 00:00–8:00 UT in August, and May's morning hours. The highest devia-

tion between NeQ-2 and vTEC(G) is observed in the daytime hour of November with 38.49 TECU, 47.66 TECU and 41.88 TECU (10:00 UT in 2014), and 22.19 TECU, 34.07 TECU, and 24.57 TECU (09:00 UT in 2015) over SMKT, BMCL, and NPGJ stations, respectively. The negligible difference between NeQ-2 and vTEC(G) can be observed after 17:00 UT in October, November, December, and January and before 8:00 UT in June and August. The comparative study of two GPS TEC calibrations shows that vTEC(C)
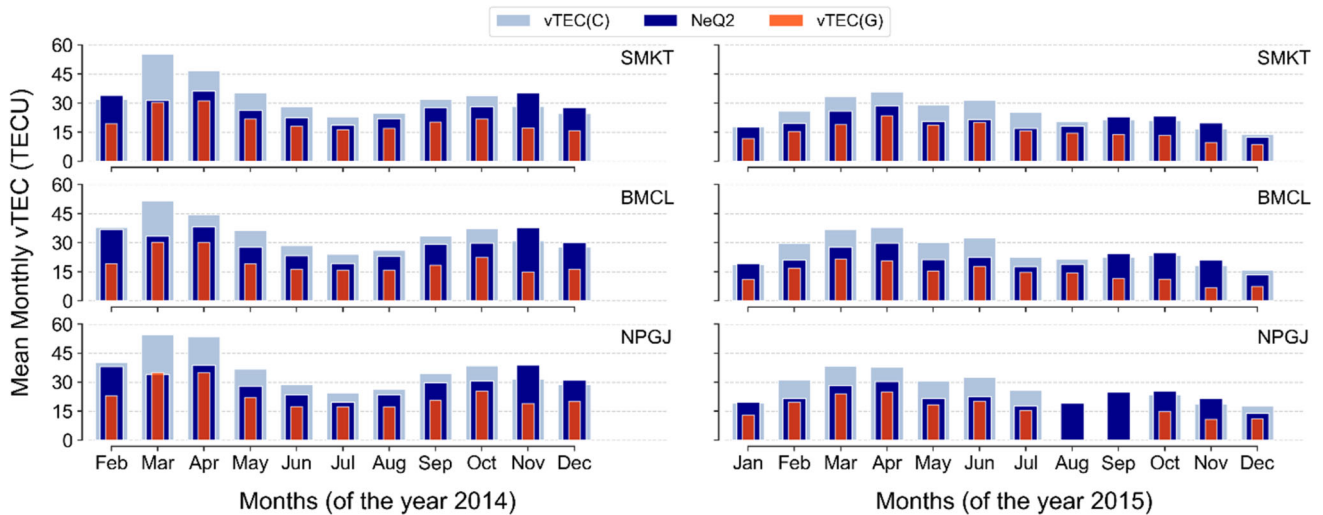
Fig. 4 Mean monthly vTEC of year obtained using Ciraolo's calibration approach, Gopi's calibration technique, and NeQ-2 model in 2014 and 2015

Fig. 5 Variation of solar flux F10.7 count and Sunspots number (27-day running average) from 2009 to 2019 (solar cycle 24). The plot in the upper corner represents the magnified view of the flux 10.7 and sunspots of the years 2014 and 2015
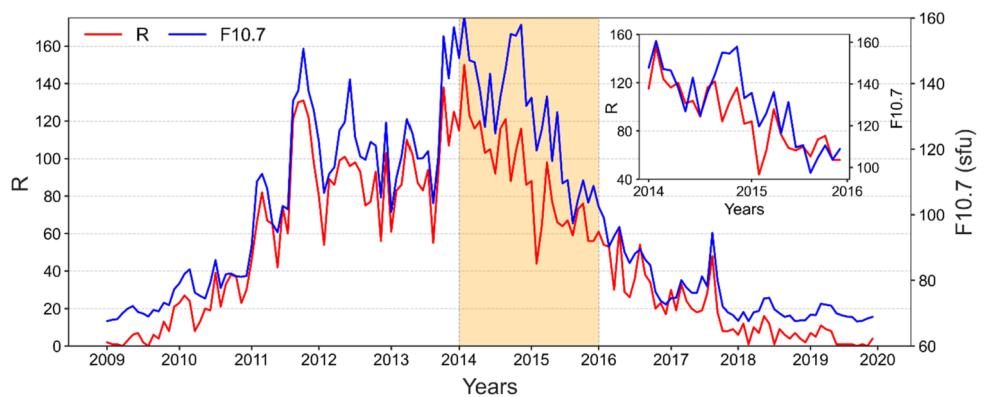
overestimate vTEC(G) in all hours and months. It has been found that the largest deviation of vTEC(G) from vTEC(C) occurs during the daytime hour of March (>30 TECU in 2014 and 17 TECU in 2015), while the least deviation has been recorded in August. The overestimation of GPS vTEC derived from the Ciraolo calibration over Gopi calibration technique during the quiet days of October 2013 was shown by Abe et al. (2017) at the grid point of the mid-latitude region.

In addition, the monthly mean vTEC (C) and vTEC(G) was highest in March as refered in Fig. 4. However, NeQ-2 showed a maximum mean monthly vTEC in April and November, with an almost similar vTEC count in 2014. On the other hand, we observed significantly low vTEC in November than in April 2015. This can be due to the impact of solar flux count, which was passed as an input parameter in the NeQ-2 model. NeQ-2 predicts the mean electron density from analytical profiles, depending on solar-activity-related input values: sunspot number or solar flux (Nava et al. 2008). High solar radio flux F10.7 in October and November 2014 and significantly low flux count in 2015

can be summarized from Fig. 5. The lowest mean vTEC is recorded in July 2014 and December 2015 by all vTEC estimation methods over all the studied stations.

As a common test framework, our monthly results show that NeQ-2 overestimates or underestimates the GPS-vTEC derived from both approaches at different times and months. Such report is presented in different studies (e.g., Venkatesh et al. 2014; Chekole et al. 2019: Gopi's calibration technique, Olwendo et al. 2016: Ciraolo's calibration technique). The comparatively low magnitude of monthly mean vTEC is distinguished in 2015 than in 2014 over all stations. This can be described as the influence of solar activity on vTEC during the solar cycle. GPS vTEC almost follows the F10.7 index, whose value increases with ascending of the solar cycle and decreases with the fall of the Solar Cycle (Rao et al. 2019). The year 2014 was in solar maximum, whereas 2015 was in the descending phase, as shown in Fig. 5. The influence of solar activity on GPS-TEC over the study area is also supported by the report of Guo et al. (2015). The overall analysis shows the semiannual variation in vTEC estimated by either approach.

Table 2 The seasonal mean of absolute deviation of NeQ-2 modeled vTEC from GPS vTEC derived using Ciraolo's calibration technique and Gopi's calibration technique, and vTEC deviation between two GPS TEC estimations their standard deviation over SMKT, BMCL, and NPGJ during the quiet days in 2014 and 2015

Stations	Absolute mean ± SD for the year 2014				Absolute mean ± SD for the year 2015			
	Spring	Summer	Autumn	Winter	Spring	Summer	Autumn	Winter
SMKT								
d(NeQ-2, Ciraolo)	14.48 ± 2.01	4.13 ± 1.07	5.26 ± 3.22	4.39 ± 2.62	7.73 ± 1.77	6.91 ± 2.07	6.54 ± 3.62	4.43 ± 2.24
d(NeQ-2, Gopi)	4.22 ± 2.98	4.06 ± 2.58	10.59 ± 6.42	7.39 ± 4.96	4.62 ± 1.91	3.46 ± 1.65	9.68 ± 6.55	4.08 ± 3.51
d(Ciraolo, Gopi)	18.10 ± 1.96	8.18 ± 2.05	11.70 ± 1.14	8.51 ± 1.09	12.35 ± 0.84	9.03 ± 1.35	7.38 ± 0.91	6.04 ± 1.14
BMCL								
d(NeQ-2, Ciraolo)	11.10 ± 2.12	4.32 ± 0.95	4.89 ± 3.53	3.96 ± 3.10	8.77 ± 1.60	5.89 ± 1.68	6.57 ± 3.53	4.52 ± 2.47
d(NeQ-2, Gopi)	6.53 ± 1.95	6.10 ± 1.77	13.77 ± 8.61	8.69 ± 6.17	7.07 ± 2.64	4.13 ± 2.16	13.51 ± 9.96	6.55 ± 6.22
d(Ciraolo, Gopi)	17.63 ± 2.12	10.42 ± 1.50	15.38 ± 3.09	10.65 ± 2.61	15.85 ± 2.59	9.77 ± 1.17	11.52 ± 2.96	8.96 ± 2.06
NPGJ								
d(NeQ-2, Ciraolo)	14.57 ± 3.00	4.27 ± 1.03	4.6 ± 3.56	3.94 ± 3.27	8.75 ± 1.54	9.33 ± 2.87	7.7 ± 4.45	4.54 ± 2.78
d(NeQ-2, Gopi)	4.10 ± 3.01	4.99 ± 2.19	11.38 ± 6.89	6.70 ± 3.96	4.37 ± 1.86	3.31 ± 1.54	11.19 ± 7.83	3.77 ± 3.15
d(Ciraolo, Gopi)	17.41 ± 1.79	9.26 ± 1.66	13.08 ± 1.89	8.92 ± 1.37	13.12 ± 0.66	11.29 ± 0.64	8.40 ± 1.22	5.88 ± 2.16

3.2 Quiet time seasonal variation

This section presents the seasonal trend of NeQ-2, vTEC (C) and vTEC(G) and the discrepancy between them. For this, we have included January and February 2016 to make a full two years' seasonal study (as data of winter months of 2014 were not available).

The right panel in Figs. 6(a) and 6(b) shows that the deviation of vTEC(C) from NeQ-2 is maximum in the spring season. In this season, the deviation is observed between −15.26 TECU and −7.63 TECU in 2014 and between −5.82 TECU and −11.85 TECU in 2015 over the studied stations. The lowest deviation was observed in the time interval of 04:00 UT–17:00 UT during Winter, where the deviation value is below 5 TECU. In the Autumn and Winter seasons of the years under study, NeQ-2 overestimates vTEC(G) in the time interval of 02:00 UT–16:00 UT but underestimates in other hours of the day. The NeQ-2 exceeds vTEC(G) for all seasons except a few hours in the Spring 2014 and Summer 2015 with nominal value. The highest deviation between them was witnessed at 11:00 UT during Autumn with 21.24, 26.90, and 22.86 TECU in 2014 and 19.67, 27.14, 22.26 TECU in 2015 over SMKT, BMCL, and NPGJ, respectively. In Spring and Summer, deviation plots (Fig. 6) manifest a low discrepancy between vTEC (G) and NeQ-2. The vTEC(C) overestimates vTEC(G) in all hours and seasons of the studied period. However, the overestimation value is highest during the Spring season and lowest between the time interval 04:00–13:00 UT of the Winter.

Figure 7 depicts the mean monthly vTEC of 2014 (left) and 2015 (right) obtained using the Ciraolo calibration approach, Gopi calibration technique, and NeQ-2 model. The mean seasonal vTEC displayed in Fig. 7 shows the high vTEC count by all studied approaches in Spring, followed by Autumn in 2014, and the lowest in Summer. This result supports the report of Tariku (2015). The seasonal variation of vTEC is ascribed to the structure of the magnetic field and the effect of the solar zenith angle (Rama Rao et al. 2006; Wu et al. 2008). However, Zou et al. (2000) have given credit to change in oxygen and molecular nitrogen concentration in the ionospheric layer as the leading cause of seasonal variations of vTEC. In 2015, Ciraolo's and Gopi's calibration estimated the highest mean seasonal vTEC in Spring, followed by Summer, Autumn, and Winter. However, NeQ-2 predicted mean seasonal VTEC follows the order: Spring, Autumn, Summer, and Winter. Also, NeQ-2 dominates the GPS estimations for any of the calibration approaches in Autumn, and it overestimates Gopi's calibrated VTEC in all other seasons.

The result from the mean absolute deviation between studied approaches (Table 2) shows that the highest mean absolute difference between NeQ-2 and vTEC(C) in the Spring season with a mean absolute deviation of 14.48, 11.10, and 14.57 TECU along with a standard deviation of 2.01, 2.12 and 3.00 (in 2014) and 7.73, 8.77, and 8.75 TECU with a standard deviation of 1.77, 1.60, and 1.54 (in 2015) over SMKT, BMCL, and NPGJ, respectively. On the other hand, in another equinox season, i.e., Autumn, a high mean absolute deviation between NeQ-2 and vTEC(G) is observed (see Table 2). In this season, the high standard deviation between NeQ-2 and vTEC(G) reveals a high discrepancy in deviation value between these approaches. These results manifest the low performance of NeQ-2 with vTEC(C) in the Spring season and with vTEC(G) in the Autumn season. However, NeQ-2 shows good performance with vTEC(C) in Summer 2014 but with vTEC(G) in 2015. Similarly, the low
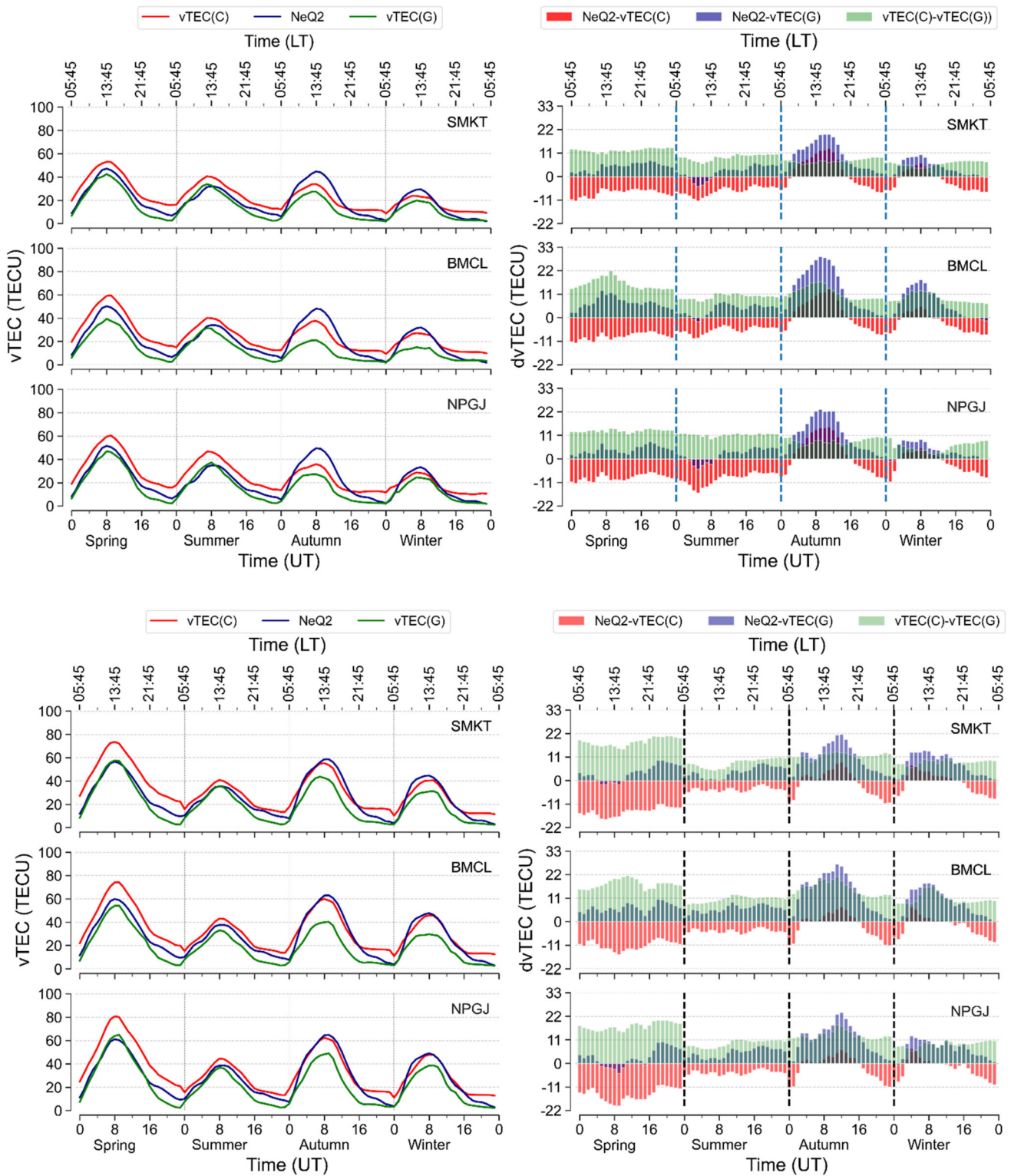
Fig. 6 Left panel represents the variation of the seasonal averaged diurnal GPS vTEC derived from Gopi's calibration technique (green curve), Ciraolo calibration technique (red curve), and NeQ-2 modeled vTEC (blue curve), and the right panel represents the deviation of seasonal vTEC estimated using Ciraolo's and Gopi's calibration approach from NeQ-2 modeled vTEC (red and blue bars respectively), vTEC estimated using Gopi's calibration approach from Ciraolo's calibration approach (green bars) over the studied stations for the years a) 2014 and b) 2015
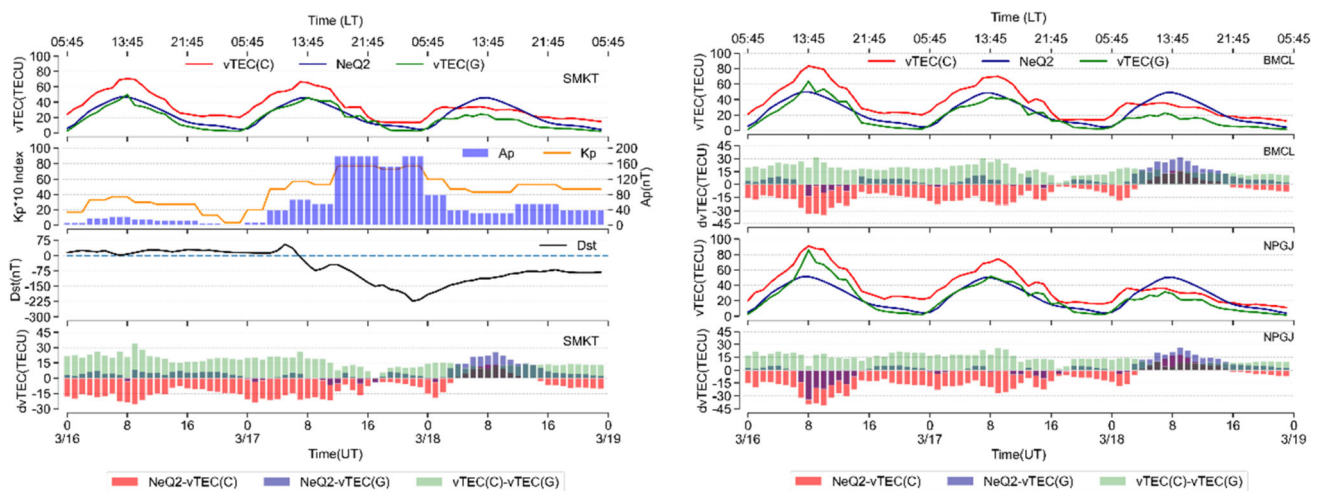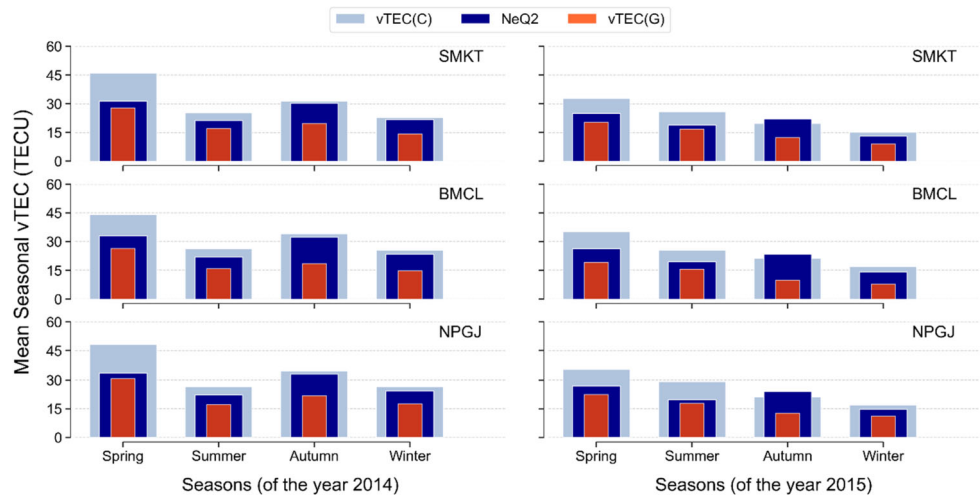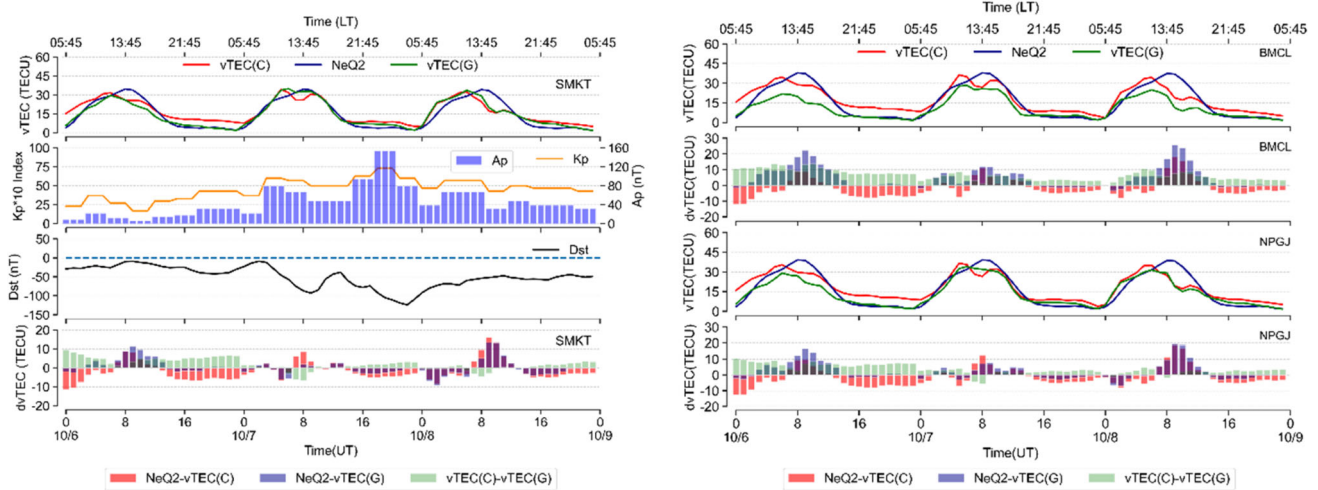
Fig. 8 Variation of diurnal vTEC estimated using Ciraolo's and Gopi's calibration approach, and NeQ-2 modeled vTEC along with the deviation between them during 16–18 March 2015. The second and third panels of the left side representing the Kp and Ap, and Dst indexes manifest an intense geomagnetic storm on 17 March

mean absolute deviation and standard deviation of vTEC(C) with respect to NeQ-2 in Winter of 2014 describe the good performance of NeQ-2 with vTEC(C) in solar maxima. Still, in the Winter of 2015, the standard deviation is higher between NeQ-2 and vTEC(G). In 2014, the mean absolute deviation between vTEC, procured from the two calibration approaches, is high in Spring and then in Autumn, whereas in 2015, it is high in Spring and then in Summer. The lowest mean absolute deviation between them is observed in Winter (see Table 2).

3.3 Disturbed diurnal variation

To study the effect of different geomagnetic storms on vTEC obtained from mentioned calibration techniques and model, we have considered the mean hourly vTEC value on the storm day, a day before, and a day after the storm. The

Dst, Kp, and Ap indexes were used to define the strength of the storm, which are plotted against Universal Time (UT) as shown in the second and third panels of Figs. 8, 9, and 10.

As seen in Fig. 8, the severe storm starts to develop after 7:00 UT on 17 March 2015 with a declination in the Dst index and lasts for around 22:00 UT with a peak Dst index of −223 nT. The peak Kp and Ap values were recorded as 7.7 and 179 nT during this period, respectively. During the storm's main phase, an interplanetary electric field penetrates the ionospheric area for several hours, loading interplanetary particles into the ionosphere (Kumar and Singh 2010; Adhikari et al. 2019). This produces a strong decrease in the Dst index during the storm's main phase. The disturbance of the ionospheric region in the main phase could be attributed to the rapid fluctuation of GPS vTEC (Mishra et al. 2020). During storm time, the rapid fluctuation in vTEC(C) and vTEC(G) can be discerned. How-

Fig. 9 Variation of diurnal vTEC estimated using Ciraolo's and Gopi's calibration approach, and NeQ-2 modeled vTEC along with the deviation between them from 6 October 2015 to 8 October 2015. The second and third panels of the left side representing the Kp and Ap, and Dst indexes manifest a strong geomagnetic storm on 7 October

ever, NeQ-2 responds normally with no significant change in the curve's structure. The gradual decrement in deviation of NeQ-2 from vTEC(C) and between two experimental vTEC is observed with the increment in the storm's intensity. These differences in magnitude are less than the quiet day of March 2015 (refer Fig. 2 (b)). The recovery phase started and remained throughout the day from the first hour in a universal time on 18 March. On this day, vTEC(G) and vTEC(C) are comparatively lower than the previous day, and no peak was formed during afternoon hours as observed in quiet days of March 2015 (Fig. 3(b)). Similar findings were also described by Fagundes et al. (2016) over low latitude regions. Nevertheless, NeQ-2 responds normally and overestimates both calibrations, contrasting the result observed on the quiet day of March 2015. The low mean absolute difference and standard deviation value between NeQ-2 and vTEC (G) than vTEC(C) on 17 March 2015 (see Table 3) reveals the good performance of NeQ-2 with Gopi's calibration than Ciraolo's calibration during the main event day of the storm. However, in the recovery phase, the performance of NeQ-2 is higher with vTEC(C) than vTEC(G). In comparison to the quiet day of March 2015, the magnitude of mean absolute difference and standard deviation between two calibrations is high in event day (17 March 2015) and low in recovery day (18 March 2015), indicating consistency in the vTEC estimation by two calibration procedures is high in the recovery phase of the severe storm than the main phase.

Figure 9 illustrates the gradual decrease in Dst, exhibiting a two-step response with minima of −93 nT around 9 UT and −124 nT at 22:00 UT on 7 October 2015 with Kp ∗ 10 index above 7 and Ap value of 154 nT. It is observed that on 7 October (storm day), all three approaches have shown similar results, except for a few mid-day hours. Also,

there is an insignificant deviation between vTEC procured from three approaches (except for a few hours of noontime). This result is different from that observed in the quiet day, when we observed substantial deviation between vTEC(C), vTEC(G), and NeQ-2 (Fig. 2 (b)). The storm effect on both studied GPS vTEC estimations is observed with oscillation in vTEC value. But as in the previous storm, NeQ-2 does not show a noticeable response to the storm. The low mean absolute difference and standard deviation of NeQ-2 with respect to vTEC(G) than vTEC(C) on 7 October reveal that the performance of NeQ-2 is higher with Gopi's calibration than Ciraolo's (except for BMCL, where vTEC(C) shows consistency with NeQ-2) in strong event day (Table 3). On 8 October, when the storm goes through the recovery phase, however, the absolute mean deviation of vTEC(G) vs NeQ-2 is low compared to vTEC(C), but the high standard deviation reveals a high discrepancy in the deviation of vTEC(G) from NeQ-2 within the low value. The low absolute mean deviation between two GPS estimations in disturbed days than that of quiet days with low standard deviation reveals a consistency in the estimations of two calibrations in geomagnetic event conditions than in the quiet days.

Figure 10 manifests the variation of vTEC(C) and vTEC(G) and NeQ-2 along with the storm indices during 11–13 September 2015. On 12 September, at around 2:00 UT, Dst decreased to −30 nT, revealing a minor storm, but at 16:00 UT, the Dst value increased suddenly from −9 nT to 19 nT and then abruptly decreased to −90 nT at 23:00 UT. At this moment, Kp and Ap increased to 6 and around 95 nT, rispectively. As in the previous storms, we observed a very low discrepancy between vTEC(C), vTEC(G), and NeQ-2 compared to the quiet day of the same month. During the recovery phase, which started after 23:00 UT on 12
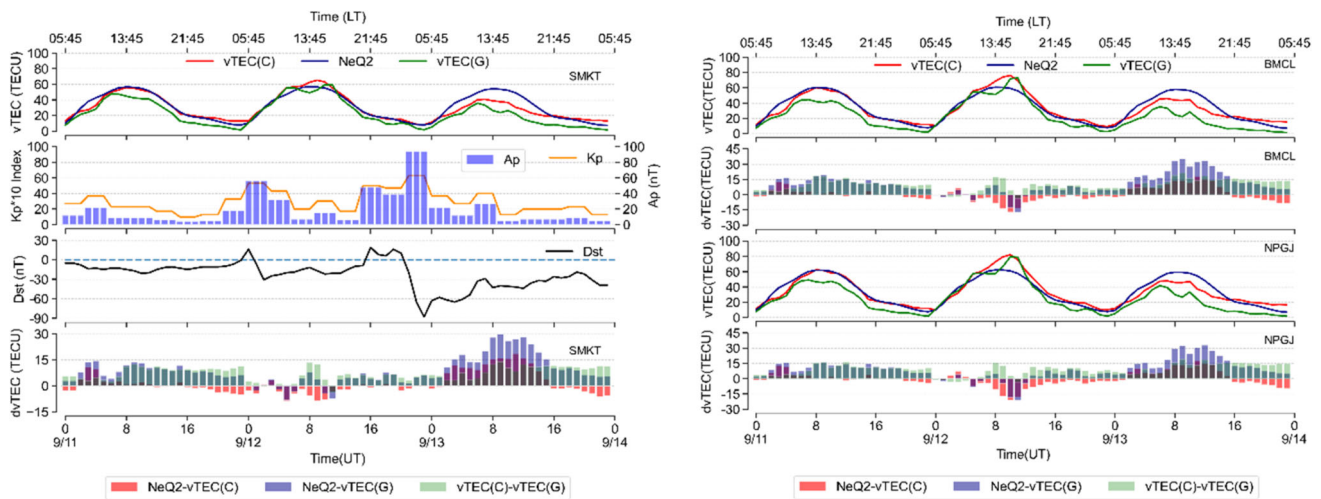
Fig. 10 Variation of diurnal vTEC estimated using Ciraolo's and Gopi's calibration approach, and NeQ-2 modeled vTEC along with the deviation between them from 11 September 2014 to 13 September ber 2014. The second and third panels of the left side representing the Kp and Ap, and Dst indexes manifest a moderate geomagnetic storm on 12 September

Table 3 The mean absolute deviation of NeQ-2 modeled vTEC from GPS vTEC derived using Ciraolo's calibration technique and Gopi calibration technique, and vTEC deviation between two GPS TEC estimations their standard deviation over SMKT, BMCL, and NPGJ during the event day and the day next to the event

	Severe event		Quiet day	Strong event		Quiet day	Moderate event		Quiet day
	17 March	18 March	March 2015	7 October	8 October	Oct 2015	12 Sept	13 Sept	Sep 2014
SMKT									
d(NeQ-2, Ciraolo)	14.12 ± 7.02	8.32 ± 4.90	7.46 ± 2.63	3.44 ± 1.96	5.03 ± 3.67	6.32 ± 3.58	2.81 ± 2.63	8.17 ± 5.73	4.43 ± 2.79
d(NeQ-2, Gopi)	3.2 ± 2.09	11.0 ± 7.81	7.16 ± 2.49	1.95 ± 1.55	3.93 ± 3.69	9.99 ± 6.90	4.37 ± 2.30	15.03 ± 8.45	7.35 ± 3.70
d(Ciraolo, Gopi)	14.63 ± 6.27	12.92 ± 1.56	14.62 ± 1.57	1.88 ± 1.68	1.54 ± 1.20	7.78 ± 1.29	4.68 ± 3.35	9.13 ± 3.20	11.71 ± 2.98
BMCL									
d(NeQ-2, Ciraolo)	14.28 ± 7.16	8.33 ± 5.13	9.31 ± 3.07	3.82 ± 2.42	5.33 ± 4.23	6.25 ± 3.34	4.74 ± 4.47	7.86 ± 4.74	4.54 ± 3.09
d(NeQ-2, Gopi)	3.89 ± 3.20	13.82 ± 9.88	6.07 ± 2.50	4.15 ± 3.85	5.92 ± 7.54	13.53 ± 9.50	5.29 ± 4.04	17.53 ± 9.92	10.75 ± 5.28
d(Ciraolo, Gopi)	17.16 ± 7.42	14.03 ± 2.45	15.38 ± 3.13	4.45 ± 1.83	5.42 ± 2.49	12.26 ± 3.20	6.57 ± 4.63	13.19 ± 4.00	15.19 ± 3.47
NPGJ									
d(NeQ-2, Ciraolo)	15.81 ± 6.15	8.44 ± 5.46	10.06 ± 3.61	4.08 ± 2.70	5.66 ± 4.41	7.25 ± 3.89	6.26 ± 5.61	7.73 ± 4.42	4.58 ± 2.98
d(NeQ-2, Gopi)	3.35 ± 2.33	10.92 ± 7.42	4.67 ± 2.57	2.80 ± 1.93	4.36 ± 5.47	10.73 ± 7.82	5.47 ± 5.11	15.76 ± 9.38	9.01 ± 4.83
d(Ciraolo, Gopi)	15.4 ± 5.42	9.47 ± 2.49	14.47 ± 2.04	2.52 ± 1.12	2.22 ± 1.11	8.83 ± 1.50	6.60 ± 4.24	12.14 ± 4.54	13.55 ± 3.71

September and remained for the whole day on 13 September, GPS vTEC estimated by both calibrations underestimate NeQ-2. The NeQ-2 did not show a noticeable change in this event as well. The small value of absolute mean difference and small standard deviation between NeQ-2 and vTEC(C) than vTEC(G) on 12 September 2015 manifests

more consistency of NeQ-2 with Ciraolo's than Gopi's calibration during moderate storm day. A similar result was obtained on 13 September 2015, which goes through the recovery phase. The consistency in the vTEC estimation by two GPS TEC calibrations is seen in disturbed days than in quiet days. Also, NeQ-2 shows good performance with both

calibrations in the main event day but low performance in recovery day in comparison to quiet day (see Table 3).

An analysis of NeQuick modeled and GPS vTEC obtained using various calibration methods reveals that the NeQuick model does not capture the impacts of magnetic storms in any case, whereas vTEC (C) and vTEC (G) still react to geomagnetic phenomena by changing vTEC. Twinomugisha et al. (2017) also reported a similar result over the east African equatorial region. Ahoua et al. (2018) also concluded that the NeQuick model has comparable reliability in quiet and disturbed days; somewhat, its accuracy is affected by solar activity (better in moderate than in high solar activity). Probably, Figs. 8–10 show that both GPS-TEC estimation approach responds similarly in a storm event. Our result indicates that GPS VTEC estimated by any of the studied approaches experience a decrement in their peak value during the recovery phase compared to event day.

4 Conclusions

In the process of investigating the performance of the TEC model with respect to TEC derived using different GPS-TEC calibration techniques, we have made a comparative study of the NeQ-2 model with two GPS-TEC estimations (Ciraolo's GNSS TEC and Gopi's GPS TEC) using three specific ground-based GPS stations located at the western part of Nepal. The ground-based GPS stations considered in this study lies almost in the same longitude (81.70 $\pm$ 0.10° E) and near latitude (29.0 $\pm$ 1.0° N) region. We examined the monthly and seasonal quiet time variation vTEC obtained from all three approaches along with the diurnal variation in three geomagnetic events of varying intensity. Based on the results obtained from the study, the following conclusions have been made:

1) The GPS vTEC derived using Ciraolo's calibration approach overestimates vTEC from Gopi's calibration for all months and hours over the studied stations. In comparison, it overestimates NeQ-2 prediction throughout the Spring and Summer months while underestimating it during the Winter and Autumn day hours. Except for a few hours in the spring months of 2014 (March and April), NeQ-2 overestimates the Gopi calibrated GPS vTEC.

2) In Spring and Autumn, a greater difference between NeQ-2 predicted vTEC and vTEC estimated using the Ciraolo calibration process is observed, but a lower deviation is observed in Summer and Winter. However, there is a significant overestimation of NeQ-2 over the Gopi-derived vTEC during the Autumn and Winter months. This demonstrates how NeQ-2 responds differently to various GPS estimation techniques. Furthermore, the difference between the vTEC determined by employing two

GPS TEC estimations is highest in the Spring months and lowest in the Winter months.

3) The fact that both GPS-TEC calibration procedures and the NeQ-2 model estimate high TEC values for respective months in 2014 (solar maximum) and low values for respective months in 2015 (solar medium) demonstrates that both GPS and modeled vTEC are affected by solar activity and follow solar parameters such as solar flux F10.7 and sunspot numbers that describe the solar activity.

4) The result from the study of mean absolute deviation and standard deviation clearly depicts that NeQ-2 modeled vTEC shows higher performance with vTEC estimated using Gopi's approach in Spring season and with Ciraolo's approached vTEC in Autumn season. In addition, the consistency in the vTEC calculation by two GPS TEC estimation procedures is higher in Summer and Winter than in other seasons.

5) The lower mean absolute deviation between vTEC estimated by two GPS TEC calibration procedures and the observed lower value of standard deviation in strong and moderate events compared to the quiet days of the respective event months reflects the high performance of two GPS vTEC estimates compared to each other in a geomagnetically disturbed period than that of a quiet one. However, additional research is necessary to adequately address this finding, which we have placed as future work.

6) NeQ-2 is a climatological model designed to predict the quiet time TEC variation. Our study shows that NeQ-2 model does not capture any of the geomagnetic events. However, we have made a study to figure out the deviation of NeQ-2 prediction in comparison to GPS vTEC estimations under storm effect using two calibration approaches. It is observed that the mean absolute deviation between the Ciraolo approach GPS vTEC and NeQ-2 estimation is less in the day when the storm goes through the recovery phase. In contrast, the deviation between NeQ-2 and GPS vTEC approximated by Gopi's procedure is less on the main event day (except a few cases).

We discovered a disparity in the vTEC values acquired using different processing algorithms, despite using the same GPS observable. These discrepancies could be explained by each calibration procedure's bias-leveling computation (Abe et al. 2017). However, the study did not address which method of GNSS-VTEC estimate is the most reliable and appropriate for the analyzed location. In the future, the performance of vTEC estimation utilizing the studied GPS VTEC calibration procedure will be compared to that of alternative calibration techniques and models in order to determine the most effective estimation technique. Furthermore, this study is focused exclusively on the years 2014 and 2015.

⁂ Springer

This work will be expanded in the future to examine the performance of GPS-VTEC and NeQ-2 over a prolonged time period, including solar minimum.

Data Availability All the datasets used for this work can be received upon request to the corresponding author.

Declarations

Conflict of Interest The authors declare that they have no conflict of interest.

Ethical approval Not applicable.

References

Abe, O.E., Villamide, X.O., Paparini, C., Radicella, S.M., Nava, B., Rodríguez-Bouza, M.: Performance evaluation of GNSS-TEC estimation techniques at the grid point in middle and low latitudes during different geomagnetic conditions. J. Geod. **91**(4), 409–417 (2017). https://doi.org/10.1007/s00190-016-0972-z

Adhikari, B., Sapkota, N., Dahal, S., Bhattarai, B., Khanal, K., Chapagain, N.P.: Spectral characteristic of geomagnetically induced current during geomagnetic storms by wavelet techniques. J. Atmos. Sol.-Terr. Phys. **192**, 104777 (2019). https://doi.org/10.1016/j.jastp.2018.01.020

Ahoua, S.M., Habarulema, J.B., Obrou, O.K., Cilliers, P.J., Zaka, Z.K.: Evaluation of the NeQ-2 model performance under different geomagnetic conditions over South Africa during the ascending phase of the solar cycle (2009–2012). Ann. Geophys. **36**(5), 1161–1170 (2018). https://doi.org/10.5194/angeo-36-1161-2018

Amabayo, E.B., Anguma, S.K., Jurua, E.: Tracking the ionospheric response to the solar eclipse of 3 November, 2013. Int. J. Atmos. Sci. **2014**, 127859 (2014). https://doi.org/10.1155/2014/127859

Appleton, E.V.: Wireless studies of the ionosphere. IEE Proc. Wirel. Sect. Inst. **7**(21), 257–265 (1932). https://doi.org/10.1049/pws.1932.0027

Arikan, F.E.Z.A., Erol, C.B., Arikan, O.: Regularized estimation of vertical total electron content from GPS data for a desired time period. Radio Sci. **39**(6), RS6012 (2004). https://doi.org/10.1029/2004RS003061

Bagiya, M.S., Joshi, H.P., Iyer, K.N., Aggarwal, M., Ravindran, S., Pathan, B.M.: TEC variations during low solar activity period (2005-2007) near the Equatorial Ionospheric Anomaly Crest region in India. Ann. Geophys. **27**(3), 1047–1057 (2009). https://doi.org/10.5194/angeo-27-1047-2009

Bhuyan, P.K., Chamua, M., Bhuyan, K., Subrahmanyam, P., Garg, S.C.: Diurnal, seasonal and latitudinal variation of electron density in the topside F-region of the Indian zone ionosphere at solar minimum and comparison with the IRI. J. Atmos. Sol.-Terr. Phys. **65**(3), 359–368 (2003). https://doi.org/10.1016/S1364-6826(02)00294-8

Bilitza, D.: International Reference Ionosphere 1990. National Space Science Data Center, NSSDC 90-22, Greenbelt, Maryland (1990)

Bilitza, D.: IRI the International Standard for the Ionosphere. Adv. Radio Sci. **16**, 1–11 (2018). https://doi.org/10.5194/ars-16-1-2018

Bilitza, D., Altadill, D., Truhlik, V., Shubin, V., Galkin, I., Reinisch, B., Huang, X.: International Reference Ionosphere 2016: from ionospheric climate to real-time weather predictions. Space Weather **15**(2), 418–429 (2017). https://doi.org/10.1002/2016SW001593

Carrano, C.S., Groves, K.M.: The GPS segment of the AFRL-SCINDA global network and the challenges of real-time TEC estimation in the equatorial ionosphere. In: Proceedings of the 2006 National Technical Meeting of The Institute of Navigation, pp. 1036–1047 (2006)

Chekole, D.A., Giday, N.M., Nigussie, M.: Performance of NeQuick 2, IRI-Plas 2017 and GIM models over Ethiopia during varying solar activity periods. J. Atmos. Sol.-Terr. Phys. **195**, 105117 (2019). https://doi.org/10.1016/j.jastp.2019.105117

Cherniak, I., Zakharenkova, I.: NeQuick and IRI-Plas model performance on topside electron content representation: spaceborne GPS measurements. Radio Sci. **51**(6), 752–766 (2016). https://doi.org/10.1002/2015RS005905

Ciraolo, L., Azpilicueta, F., Brunini, C., Meza, A., Radicella, S.M.: Calibration errors on experimental slant total electron content (TEC) determined with GPS. J. Geod. **81**(2), 111–120 (2007). https://doi.org/10.1007/s00190-006-0093-1

Coïsson, P., Radicella, S.M., Leitinger, R., Nava, B.: Topside electron density in IRI and NeQ-2: features and limitations. Adv. Space Res. **37**(5), 937–942 (2006). https://doi.org/10.1016/j.asr.2005.09.015

Dabas, R.S.: Ionosphere and its influence on radio communications. Resonance **5**(7), 28–43 (2000). https://doi.org/10.1007/BF02867245

Di Giovanni, G., Radicella, S.M.: An analytical model of the electron density profile in the ionosphere. Adv. Space Res. **10**(11), 27–30 (1990)

Ezquer, R.G., Scidá, L.A., Orué, Y.M., Nava, B., Cabrera, M.A., Brunini, C.: NeQuick 2 and IRI Plas VTEC predictions for low latitude and South American sector. Adv. Space Res. **61**(7), 1803–1818 (2018). https://doi.org/10.1016/0273-1177(90)90301-F

Fagundes, P.R., Cardoso, F.A., Fejer, B.G., Venkatesh, K., Ribeiro, B.A.G., Pillat, V.G.: Positive and negative GPS-TEC ionospheric storm effects during the extreme space weather event of March 2015 over the Brazilian sector. J. Geophys. Res. Space Phys. **121**(6), 5613–5625 (2016). https://doi.org/10.1002/2015JA022214

Fejer, B.G.: The electrodynamics of the low-latitude ionosphere: recent results and future challenges. J. Atmos. Sol.-Terr. Phys. **59**(13), 1465–1482 (1997)

Goodman, J.M.: Operational communication systems and relationships to the ionosphere and space weather. Adv. Space Res. **36**(12), 2241–2252 (2005). https://doi.org/10.1016/j.asr.2003.05.063

Guo, J., Li, W., Liu, X., Kong, Q., Zhao, C., Guo, B.: Temporal-spatial variation of global GPS-derived total electron content, 1999–2013. PLoS ONE **10**(7), e0133378 (2015). https://doi.org/10.1371/journal.pone.0133378

Hagfors, T., Schlegel, K.: Earth's ionosphere. In: The Century of Space Science, 1559–1584. Springer, Dordrecht (2001). https://doi.org/10.1007/978-94-010-0320-9_64

Hernández-Pajares, M., Juan, J.M., Sanz, J., Aragón-Àngel, À., García-Rigo, A., Salazar, D., Escudero, M.: The ionosphere: effects, GPS modeling and the benefits for space geodetic techniques. J. Geod. **85**(12), 887–907 (2011). https://doi.org/10.1007/s00190-011-0508-5

Hoque, M.M., Jakowski, N.: Ionospheric propagation effects on GNSS signals and new correction approaches. Global navigation satellite systems signal. Theory Appl. **381**, 405 (2012). https://doi.org/10.5772/30090

Jakowski, N., Mayer, C., Hoque, M.M., Wilken, V.: Total electron content models and their use in ionosphere monitoring. Radio Sci. **46**(6), RS0D18 (2011b). https://doi.org/10.1029/2010RS004620

Jin, S.G., Cho, J., Park, J.: Ionospheric slab thickness and its seasonal variations observed by GPS. J. Atmos. Sol.-Terr. Phys. **69**(15), 1864–1870 (2007). https://doi.org/10.1016/j.jastp.2007.07.008

Klobuchar, J.: Design and characteristics of the GPS ionospheric time-delay algorithm for single frequency users. In: Proceedings of PLANS'86 – Position Location and Navigation Symposium, Las Vegas, Nevada, 4–7 November 1986 pp. 280–286 (1986). 4–7

Kumar, S., Singh, A.K.: February. The effect of geomagnetic storm on GPS derived total electron content (TEC) at Varanasi, India. J. Phys. Conf. Ser. **208**(1), 012062 (2010). https://doi.org/10.1088/1742-6596/208/1/012062. 2010

Kumar, S., Singh, A.K.: GPS derived ionospheric TEC response to geomagnetic storm on 24 August 2005 at Indian low latitude stations. Adv. Space Res. **47**(4), 710–717 (2011). https://doi.org/10.1016/j.asr.2010.10.015

Leitinger, R., Zhang, M.-L., Radicella, S.M.: An improved bottomside for the ionospheric electron density model NeQ-2. Ann. Geophys. **48**(3), 525–534 (2005)

Mannucci, A.J., Iijima, B., Sparks, L., Pi, X.Q., Wilson, B., Lindqwister, U.: Assessment of global TEC mapping using a threedimensional electron density model. J. Atmos. Sol.-Terr. Phys. **61**, 1227–1236 (1999). https://doi.org/10.1016/S1364-6826(99)00053-X

Migoya-Orué, Y.M., Radicella, S.M., Coïsson, P., Ezquer, R.G., Nava, B.: Comparing TOPEX TEC measurements with IRI predictions. Adv. Space Res. **42**(4), 757–762 (2008). https://doi.org/10.1016/j.asr.2007.09.041

Mishra, R.K., Adhikari, B., Chapagain, N.P., Baral, R., Das, P.K., Klausner, V., Sharma, M.: Variation on solar wind parameters and total electron content over middle-to low-latitude regions during intense geomagnetic storms. Radio Sci. **55**(11), e2020RS007129 (2020). https://doi.org/10.1029/2020RS007129

Montenbruck, O., Hauschild, A., Steigenberger, P.: Differential code bias estimation using multi-GNSS observations and global ionosphere maps. In: Proceedings of the 2014 International Technical Meeting of the Institute of Navigation, pp. 802–812 (2014)

Nava, B., Coisson, P., Radicella, S.M.: A new version of the NeQuick ionosphere electron density model. J. Atmos. Sol.-Terr. Phys. **70**(15), 1856–1862 (2008). https://doi.org/10.1016/j.jastp.2008.01.015

Nie, W., Xu, T., Rovira-Garcia, A., Zornoza, J.M.J., Subirana, J.S., Gonzalez-Casado, G., et al.: Revisit the calibration errors on experimental slant total electron content (TEC) determined with GPS. GPS Solut. **22**(3), 1–11 (2018). https://doi.org/10.1007/s10291-018-0753-7

Ogwala, A., Somoye, E.O., Ogunmudimu, O., Adeniji-Adele, R.A., Onori, E.O., Oyedokun, O.: Diurnal, seasonal and solar cycle variation of total electron content and comparison with the IRI-2016 model at Birnin Kebbi. Ann. Geophys. Discuss. **1**(30) (2019). https://doi.org/10.5194/angeo-2018-134

Okoh, D., Owolabi, O., Ekechukwu, C., Folarin, O., Arhiwo, G., Agbo, J., Bolaji, S., Rabiu, B.: A regional GNSS-VTEC model over Nigeria using neural networks: a novel approach. Geod. Geodyn. **7**(1), 19–31 (2016). https://doi.org/10.1016/j.geog.2016.03.003

Okoh, D., Onwuneme, S., Seemala, G., Jin, S., Rabiu, B., Nava, B., Uwamahoro, J.: Assessment of the NeQ-2-2 and IRI-Plas 2017 models using global and long-term GNSS measurements. J. Atmos. Sol.-Terr. Phys. **170**, 1–10 (2018). https://doi.org/10.1016/j.jastp.2018.02.006

Olwendo, O.J., Cesaroni, C.: Validation of NeQuick 2 model over the Kenyan region through data ingestion and the model application in ionospheric studies. J. Atmos. Sol.-Terr. Phys. **145**, 143–153 (2016). https://doi.org/10.1016/j.jastp.2016.04.011

Olwendo, O.J., Yamazaki, Y., Cilliers, P.J., Baki, P., Doherty, P.: A study on the variability of ionospheric total electron content over the East African low-latitude region and storm time ionospheric variations. Radio Sci. **51**(9), 1503–1518 (2016). https://doi.org/10.1002/2015RS005785

Otsuka, Y., Ogawa, T., Saito, A., Tsugawa, T., Fukao, S., Miyazaki, S.: A new technique for mapping of total electron content using GPS network in Japan. Earth Planets Space **54**(1), 63–70 (2002). https://doi.org/10.1186/BF03352422

Pignalberi, A., Pietrella, M., Pezzopane, M., Habarulema, J.B.: Investigating different vTEC calibration methods for data assimilation in ionospheric empirical models. Adv. Space Res. **68**(5), 2138–2151 (2020). https://doi.org/10.1016/j.asr.2020.10.040

Rabiu, A.B., Adewale, A.O., Abdulrahim, R.B., Oyeyemi, E.O.: TEC derived from some GPS stations in Nigeria and comparison with the IRI and NeQ-2 models. Adv. Space Res. **53**(9), 1290–1303 (2014). https://doi.org/10.1016/j.asr.2014.02.009

Radicella, S.M., Leitinger, R.: The evolution of the DGR approach to model electron density profiles. Adv. Space Res. **27**(1), 35–40 (2001). https://doi.org/10.1016/S0273-1177(00)00138-1

Radicella, S.M., Zhang, M.-L.: The improved DGR analytical model of electron density height peofile and total electron content in the ionosphere. Ann. Geophys. **38**, 35–41 (1995). https://doi.org/10.4401/ag-4130

Rama Rao, P.V.S., Gopi Krishna, S., Niranjan, K., Prasad, D.S.V.V.D.: Temporal and spatial variations in TEC using simultaneous measurements from the Indian GPS network of receivers during the low solar activity period of 2004–2005. Ann. Geophys. **24**(12), 3279–3292 (2006). https://doi.org/10.5194/angeo-24-3279-2006

Rao, S.S., Chakraborty, M., Kumar, S., Singh, A.K.: Low-latitude ionospheric response from GPS, IRI and TIE-GCM TEC to solar cycle 24. Astrophys. Space Sci. **364**(12), 1–14 (2019). https://doi.org/10.1007/s10509-019-3701-2

Rawer, K., Bilitza, D., Ramakrishnan, S.: Goals and status of the International Reference Ionosphere. Rev. Geophys. **16**(2), 177–181 (1978). https://doi.org/10.1029/RG016i002p00177

Seemala, G.K., Valladares, C.E.: Statistics of total electron content depletions observed over the South American continent for the year 2008. Radio Sci. **46**(5), RS5019 (2011). https://doi.org/10.1029/2011RS004722

Sharma, S., Dashora, N., Galav, P., Pandey, R.: Total solar eclipse of July 22, 2009: its impact on the total electron content and ionospheric electron density in the Indian zone. J. Atmos. Sol.-Terr. Phys. **72**(18), 1387–1392 (2010). https://doi.org/10.1016/j.jastp.2010.10.006

Sharma, S.K., Ansari, K., Panda, S.K.: Analysis of ionospheric TEC variation over Manama, Bahrain, and comparison with IRI-2012 and IRI-2016 models. Arab. J. Sci. Eng. **43**(7), 3823–3830 (2018). https://doi.org/10.1007/s13369-018-3128-z

🖉 Springer

Sharma, S.K., Singh, A.K., Panda, S.K., Ansari, K.: GPS derived ionospheric TEC variability with different solar indices over Saudi Arab region. Acta Astronaut. **174**, 320–333 (2020). https://doi.org/10.1016/j.actaastro.2020.05.024

Silwal, A., Gautam, S.P., Poudel, P., Karki, M., Adhikari, B., Chapagain, N.P., Mishra, R.K., Ghimire, B.D., Migoya-Orue, Y.: Global positioning system observations of ionospheric total electron content variations during the 15th January 2010 and 21st June 2020 solar eclipse. Radio Sci. **56**(5), 1–20 (2021a). https://doi.org/10.1029/2020RS007215

Silwal, A., Gautam, S.P., Chapagain, N.P., Karki, M., Poudel, P., Ghimire, B.D., Mishra, R.K., Adhikari, B.: Ionospheric response over Nepal during the 26 December 2019 solar eclipse. J. Nepal Phys. Soc. **7**(1), 25–30 (2021b). https://doi.org/10.3126/jnphyssoc.v7i1.36970

Tariku, Y.A.: TEC prediction performance of the IRI-2012 model over Ethiopia during the rising phase of solar cycle 24 (2009–2011). Earth Planets Space **67**(1), 1–10 (2015). https://doi.org/10.1186/s40623-015-0312-1

Tariku, Y.A.: Pattern of the variation of the TEC extracted from the GPS, IRI 2016, IRI-Plas 2017 and NeQuick 2 over polar region, Antarctica. Life Sci. Space Res. **25**, 18–27 (2020). https://doi.org/10.1016/j.lssr.2020.02.004

Tornatore, V., Cesaroni, C., Pezzopane, M., Alizadeh, M.M., Schuh, H.: Performance evaluation of VTEC GIMs for regional applications during different solar activity periods, using RING TEC values. Remote Sens. **13**(8), 1470 (2021). https://doi.org/10.3390/rs13081470

Twinomugisha, F., Ssebiyonga, N., D'ujanga, F.M.: TEC derived from some GPS stations in East African equatorial region and comparison with the TEC from NeQuick2 model. Adv. Space Res. **60**(9), 1905–1920 (2017). https://doi.org/10.1016/j.asr.2017.07.018

Venkatesh, K., Fagundes, P.R., Seemala, G.K., de Jesus, R., de Abreu, A.J., Pillat, V.G.: On the performance of the IRI-2012 and NeQuick2 models during the increasing phase of the unusual 24th solar cycle in the Brazilian equatorial and low-latitude sectors. J. Geophys. Res. Space Phys. **119**(6), 5087–5105 (2014). https://doi.org/10.1002/2014JA019960

Wu, C.C., Liou, K., Shan, S.J., Tseng, C.L.: Variation of ionospheric total electron content in Taiwan region of the equatorial anomaly from 1994 to 2003. Adv. Space Res. **41**(4), 611–616 (2008). https://doi.org/10.1016/j.asr.2007.06.013

Ya'acob, N., Abdullah, M., Ismail, M.: GPS total electron content (TEC) prediction at ionosphere layer over the equatorial region. In: Trends in Telecommunications Technologies (2010). https://doi.org/10.5772/8474

Yu, X., She, C., Liu, D., Zhen, W.: A preliminary study of the NeQuick model over China using GPS TEC and ionosonde data. In: IS-APE2012, pp. 627–630 (2012). https://doi.org/10.1109/ISAPE.2012.6408849

Zou, L., Rishbeth, H., Müller-Wodarg, I.C.F., Aylward, A.D., Millward, G.H., Fuller-Rowell, T.J., Moffett, R.J.: Annual and semi-annual variations in the ionospheric F2-layer. I. Modelling. Ann. Geophys. **18**(8), 927–944 (2000). https://doi.org/10.1007/s00585-000-0927-8

IJP Check for updates

ORIGINAL PAPER

VTEC observations of intense geomagnetic storms above Nepal: comparison with satellite data, CODE and IGSG models

D Pandit[1,6]* , C Amory-Mazaudier[2,3], R Fleury[4], N P Chapagain[5] and B Adhikari[6]

[1]Central Department of Physics, IOST, Tribhuvan University, Kathmandu, Nepal

[2]LPP, Polytechnique, Sorbonne Universités UPMC Paris 06, Paris, France

[3]T/ICT4D, Abdus Salam ICTP, Trieste, Italy

[4]Lab-STICC, UMR 6285, Institut Mines-Telecom Atlantique, Site de Brest, France

[5]Amrit Campus, Tribhuvan University, Thamel, Kathmandu, Nepal

[6]Department of Physics, St. Xavier's College, Maitighar, Kathmandu, Nepal

Abstract: In this article, we analyze vertical total electron content (VTEC) over Nepal for 4 periods: March 14–25, 2015, June 18–29, 2015, May 24–June 4, 2017, and September 3–14, 2017. In each period, there are quiet geomagnetic days and intense geomagnetic stormy days. The VTEC observed during these periods has observed both positive and negative ionospheric storms. We compared VTEC Receiver-Independent Exchange Format (RINEX) observations with the Global Ionospheric Map (GIM), Centre for Orbit Determination in Europe (CODE), and IGS working group (IGSG). We found in RINEX observation of the VTEC a noon bite out profile with predominance of morning and afternoon peaks and a nighttime peak, but this was not noticeable clearly with CODE and IGSG models. The comparison between RINEX TEC, CODE, and IGSG models shows that the GIM model does not estimate RINEX VTEC over Nepal. The disagreement between VTEC CODE/IGSG and VTEC RINEX is important during geomagnetically quiet periods, while there is good agreement between VTEC CODE/IGSG and VTEC RINEX during strong geomagnetic storms. We also find a greater disagreement between the models and the data at the equinoxes when the VTEC is larger. It is, therefore, necessary to introduce data from Nepal stations into the models CODE and IGSG in order to improve them.

1. Introduction

Gonzalez et al. [1] in their article title, 'What is a geomagnetic storm?', defined the two essential parameters, which are the Bz component of the interplanetary magnetic field (IMF) and the magnetic storm index Dst [2], which is the signature of the ring current circulating in the magnetosphere. Gonzales et al. [1] classified the magnetic storms in three classes: weak (-30 nT $<$ Dst < -50 nT), moderate (-50 nT $<$ Dst < -100 nT), and strong (Dst < -100nT). When the IMF-Bz is southward, in the opposite direction of the Earth's magnetic field, there is the reconnection between the IMF and the Earth's magnetic field [3] and an important amount of energy is transferred from the interplanetary medium to the magnetosphere. The auroral zone is directly impacted. Electric fields and electric currents are increased and create Joule heating at the origin of the thermal expansion of the atmosphere, leading to changes in temperatures, motions, and composition. There are also precipitations of the particle in the ionosphere as well as field aligned currents connecting the magnetosphere and ionosphere [4].

Three main physical processes are known to act at planetary scale via electrodynamics coupling between the auroral zone and the middle and low latitudes:

*Corresponding author, E-mail: drabindrapandit087@gmail.com

(1) There is the thermal expansion of the atmosphere with mass transport between the pole and the equator. This process, linked to Joule heating in the auroral zone, not only modifies temperatures, pressures, and motions but also chemistry and causes changes in the composition of the atmosphere, as theorized by Fuller-Rowell et al. [5, 6].

(2) There is the extension of the electric field of magnetospheric convection from the auroral zone to low latitudes, as theorized first by Vasyliunas [7].

(3) There is also the process of the disturbed ionospheric dynamo linked to the Joule heating, which creates a disturbance of the thermospheric winds, in turn generating disturbed electric fields and currents at medium and low latitudes, as theorized first by Blanc and Richmond [8]. These pioneering theoretical works made it possible to understand the influence of each physical process. Currently, numerical simulations with physical planetary models integrated many physical processes (Thermosphere-Ionosphere-Electrodynamics Global Circulation Model [TIEGCM] https://www.hao.ucar.edu/modeling/tgcm/, Coupled Thermosphere/Ionosphere Plasmasphere [CTIP] https://ccmc.gsfc.nasa.gov/modele/ctip.php).

This makes it possible to study the evolution of geophysical parameters during geomagnetic storm. For several decades, Global Navigation Satellite System (GNSS) and, in particular, Global Positioning System (GPS) allowed the measurement of the number of electrons (Total Electron Content, TEC) that the satellite signal encounters during its path between the satellite and receivers on the Earth. TEC is mainly due to the electrons of the ionosphere, and therefore, the analysis of TEC allows us to study the variations of ionospheric ionization during geomagnetic storms. TEC allows observing positive ionospheric storms (an increase in TEC) or negative ionospheric storms (a decrease in TEC).

In Nepal, there is a network of more than ten GPS stations (https://www.unavco.org), some of which have been operating for more than one solar cycle. Network of GPS stations in Nepal was installed by UNAVCO to study the seismicity of the region (out of the scope of this paper). Since several years, the Nepalese network of GPS has been used for the study of the ionosphere and space weather.

Huang et al. [9] used GPS data of Nepal to measure ground deformation caused by the 2015 Nepal earthquake. Adhikari et al. [10] studied the seismogenic energy deposited during the Nepal earthquake (April 25, 2015) using GPS network data from Nepal. Ansari et al. [11] studied TEC during the low solar activity year of 2017 over Nepal and found that the singular spectral analysis (SSA) method could be a more successful tool for forecasting the TEC over Nepal than the Global Ionospheric Maps (GIMs) and International Reference Ionosphere extended to Plasmasphere (IRI-Plas) 2017. A model using an empirical orthogonal function was developed by Jamjareegulgarn et al. [12] to forecast TEC over Nepal. The climatology of TEC over Nepal was studied by Pandit et al. [13] using a solar cycle GPS data.

Our article is in the framework of space weather. We first analyze the Physics of the phenomena disturbing the ionosphere, and in particular, the TEC, which allows correct satellite positioning. Then we compare our TEC observations to the TEC maps for different conditions of geomagnetic activity in order to understand the effect of geomagnetic activity. We think that it is important to analyze the Physics to see in which cases the maps are worthy. These maps are produced to assist users, and we believe our study may help to improve them. Precisely, in this paper, we studied the impact of four intense geomagnetic storms (March 2015, June 2015, May 2017, and September 2017) of solar cycle 24 on VTEC data from Nepalese stations, and for the first time, we compared our observations to the Centre for Orbit Determination in Europe (CODE) and the IGS working group (IGSG) mapping models. Section 2 is devoted to the data set and data processing. Section 3 presents an analysis of storms. In Sect. 4, we compare the VTEC observations to the VTEC given by the mapping models, and then we conclude the results in Sect. 5.

2. Data sets, data processing, and models

2.1. Data sets

Different sources of data sets are used to characterize the intense storm of solar cycle 24.

The data sets from the ACE (Advanced Composition Explorer, www.srl.caltech.edu/ACE/) satellites are used to provide information on the key parameters of the solar wind, such as the southward component of the interplanetary magnetic field (IMF-Bz) and the solar wind velocity.

The magnetic indices SYM-H measure the intensity of the storm time ring current and the AE index provides a quantitative measure of magnetic activity and energy deposited in the auroral zone. The data sets for these indices were obtained from the website http://www.omniweb.gsfc. The data set for the Polar Cap magnetic index (PC index), which measures of the merging electric field at the polar region, was downloaded from http://www.isgi.unistra.fr/.

The behavior of the ionospheric response during the four storms, March 14–25, 2015, June 18–29, 2015, May 24–June 4, 2017, and September 3–14, 2017, over Nepal is

studied by using VTEC computed by the Fleury's software (MATLAB programming on www.girgea.org). The RINEX data file for GPS TEC is extracted from http://www.unavco.org. Figure 1 presents a map of Nepal with the locations of the GPS network and the stations used for this study, and Table 1 gives their geographic and geomagnetic coordinates.

We used the thermospheric O/N_2 ratio obtained from the website http://guvitimed.jhuapl.edu/ to compare the effect of storms on the ground-based GPS TEC and satellite data on the O/N_2 ratio.

2.2. Data processing—VTEC (Fleury's method)

The computation of VTEC is based on the standard procedure used for processing GPS pseudo-range measurements [14, 15]. For the conversion of Slant TEC (STEC) to vertical TEC (VTEC), we use the single-layer mapping function (MF) at 420 km [15, 16]. The STEC is conventionally calculated by the combination of the two dual-frequency pseudo-range measurements available on the daily RINEX 30 s files. Satellite differential code bias (DCB) is corrected using values provided by the CODE organization at the University of Bern. The receiver bias is calculated using the GIM/CODE model on the Pierce points with an elevation angle ε greater than 30°. This limit eliminates distant points where the horizontal gradient could become significant and data affected by multipath. The STEC estimate is based on the ionospheric MF, where

a is the Earth's radius (6371.2 km) and h_m, a reference altitude, has been taken at 420 km.

$$MF = \sqrt{1 - \left(\frac{a * \cos(\varepsilon)}{a + h_m}\right)^2}$$

The adjustment of the two STECs thus calculated (one from the RINEX data and the second from the GIM model) makes it possible to obtain the unknown daily DCB of the receiver. The VTEC above the receiver is obtained by a least-square regression weighted by the inverse of the square of the distance to the Pierce point over a time interval of 15 min.

2.3. MODELS CODE and IGSG

2.3.1. CODE

Since the creation of the International GPS Service (IGS) scientific community in 1998, several organizations (CODE, European Space Agency [ESA], Jet Propulsion Laboratory [JPL], Universitat Politècnica de Catalunya [UPC]) have created an ionosphere working group (IONO-WG) to produce global and daily VTEC maps using the ground station network. A standard writing format, IONEX (for IONosphere Map Exchange), has been adopted, providing the VTEC on a regular grid in 2.5° latitude and 5° longitude. Only the temporal rate has changed over time: every 2 h and then 1 h with daily continuity (and 15 min for rapid Universitat Politècnica de Catalunya Rapid GIM [UQRG]). One of the major difficulties lies in the
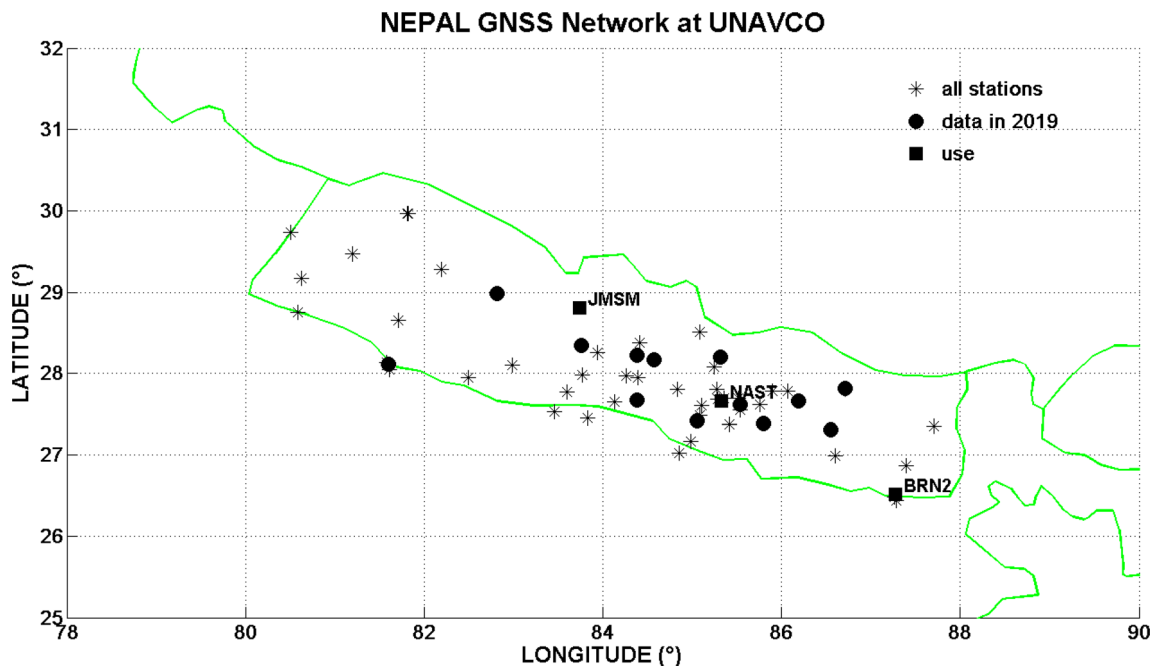

Fig. 1 A map of Nepal showing locations of GPS network and the stations used in our study

Table 1 Geographic and geomagnetic coordinates of GPS stations

Locations of GPS stations	ID	Geog. Lat.	Geog. Long.	Geom. Lat.	Geom. Long.	Dip Lat.	Local time (LT)
Biratnagar, Nepal	BRN2	26.51° N	87.27° E	17.22° N	161.19° E	41.56	UT + 5:45 h
Kathmandu, Nepal	NAST	27.65° N	85.32° E	17.47° N	169.37° E	43.61	UT + 5:45 h
Jomsom, Nepal	JMSM	28.80° N	83.74° E	19.70° N	150.05° E	45.31	UT + 5:45 h

determination of Differential Code Biases (DCB) on satellites, but especially on ground stations that involve different manufacturers and environmental changes. According to the organizations, different methods of developing STEC in VTEC have been used: Spherical Harmonics (CODE, ESA, Wuhan University [WHU], Chinese Academy of Sciences [CAS]), three-shell model (JPL), and tomographic methods with splines (UPC). The performance of these models was evaluated on the basis of ancillary measures of altimeters and radio occultation [17, 18]. GIM maps gain in quality with the increase in the number of ground stations (more than 500 currently) and the integration of new navigation systems (Glonass, Galileo, and Beidou). The difference between the estimations given by the GIM maps and the observations is of the order of 2 TECU during the sunspot minimum and can reach 10 TECU in the years of the sunspot maximum [19, 20]. The GIM maps provided by CODE (http://www.aiub.unibe.ch/download/CODE) is to compare with GPS TEC derived from the RINEX observational file obtained from GPS stations in Nepal.

2.3.2. IGSG

In fact, there are many Ionosphere Associate Analysis Centers (IAACs) that produce GIMs from the IGS network stations. In each case, the mathematical methods are different, so the results are not the same. The 'ionosphere group' of the IGS (IONO-WG) under the current responsibility of A. Krankowski [17] was aware of the problem and proposed an algorithm to combine all these particular solutions into one solution labeled IGS (IGSG). The GIM maps provided by IGSG (https://cddis.nasa.gov/archive/gnss/products/ionex/) to compare GPS TEC are derived from the RINEX observational files obtained from GPS stations in Nepal.

3. Results and discussion

3.1. Global geophysical context

Figure 2(a), (b), (c), and (d) shows 1-min resolution of variations in the solar wind interplanetary plasma parameters, polar cap indices, and geomagnetic indices for the periods of March 14–24, 2015, June 18–28, 2015, May 24–June 3, 2017, and September 3–13, 2017, including a few days before and after the geomagnetic storm that occurred on March 17, 2015, June 22, 2015, May 27, 2017, and September 7, 2017, respectively. The first, second, third, fourth, fifth, and sixth panels in each plot show variations in solar wind velocity (Vx in km/s), interplanetary magnetic field (in nT), solar wind pressure (in nPa), polar cap north and south indices (PCN/PCS in mV/m), auroral indices (AE AU AL AO in nT), and SYM-H (in nT), respectively. The vertical dotted line in each figure represents the Sudden Storm Commencement (SSC). The horizontal lines with double arrow heads in each plot represent the main phase and the recovery phase during the geomagnetic storms.

The coronal mass election (CME) erupted from the magnetic filament on March 15, 2015, and reached on the Earth on March 17. The SSC is characterized by an abrupt enhancement in the positive value of SYM-H before the start of the main phase of the geomagnetic storm, as indicated in Fig. 2a by dotted vertical lines, and is observed at 04:45 UT followed by an increase in average solar wind speed from 420 to 500 km/s and solar wind pressure from 20 to 30 nPa. On March 20 and 21, the slight increase in solar wind speed is noticed due to coronal hole, which transfer additional momentum and energy at the time of the recovery phase, making it prolonged for 7 days. Coronal holes are the region of open field lines in the solar corona that act as efficient conduits for flushing heated plasma from the corona, energizing the solar wind, and prolonging the recovery phase of the storm for many days. The rapid southward and northward fluctuation in IMF Bz occurs during the storm with a minimum of − 20 nT. During the main phase at 20:30 UT, the SYM-H was noticed at about -132 nT and the minimum value of SYM-H noticed during this storm was < -200 nT. During the main phase of the storm, the decrease in H component is the signature of the intensification of westward ring current and increase in H component indicates slow recovery to normal phase on 18 March. The maximum value of AE noticed during this storm is 2000 nT and oscillating IMF-Bz at higher values of Vx is the signature of a high-speed streamer flowing around the Earth.
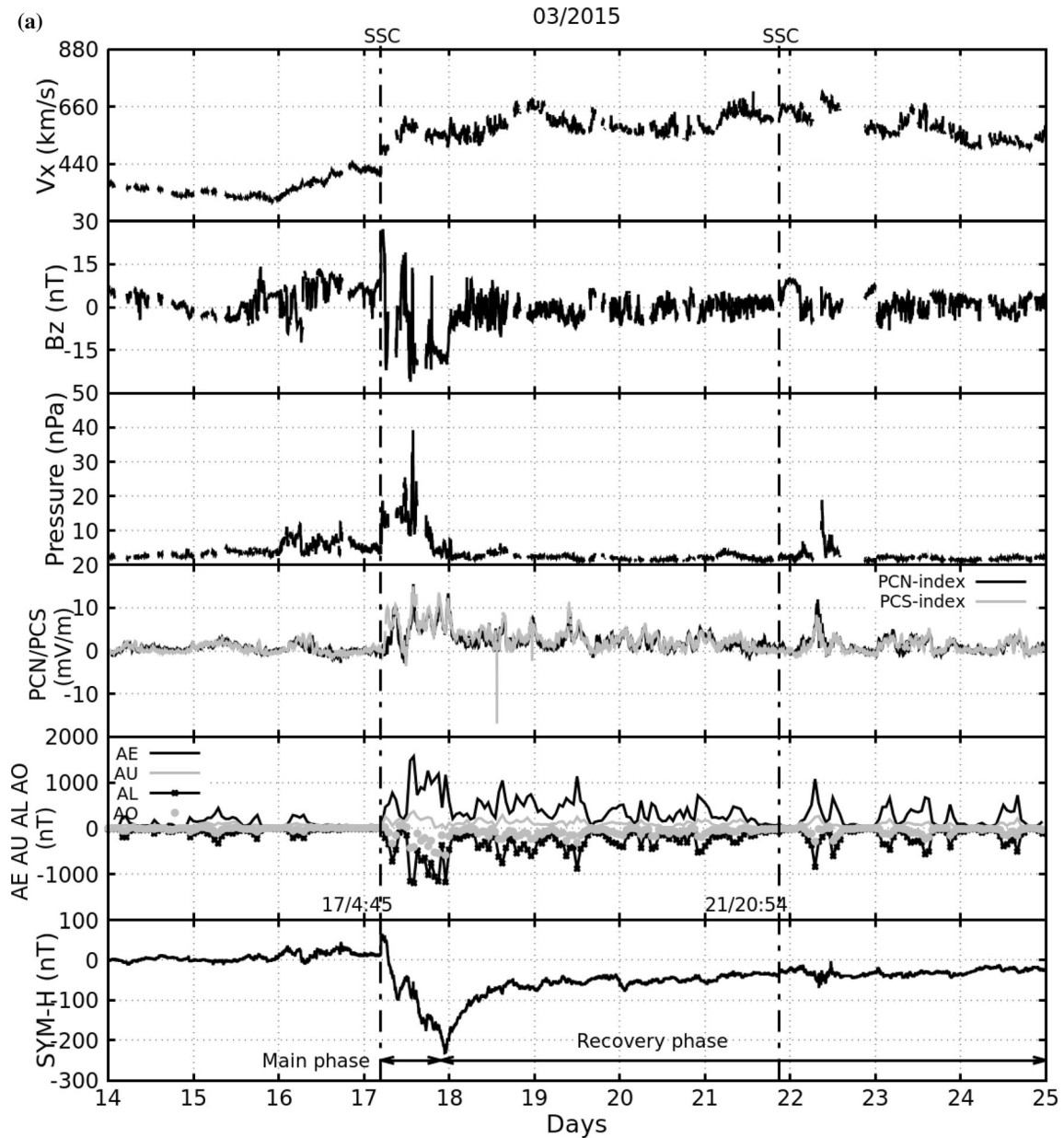
Fig. 2 (**a–d**) Variations of solar wind speed (Vx in km/s), interplanetary magnetic field IMF (Bz in nT), pressure (nPa), polar cap north (dark black curves) and south indices (faint black curves) in mV/m, auroral indices: AE (dark black curves), AU (faint black curves), AL (dark black curves with asterisk), AO (faint black doted curves) in nT, and SYM-H (nT) characterizing the geomagnetic storm during March 14–24, 2015, June 18–28, 2015, May 24–June3, 2017, and September 3–13, 2017, respectively. Vertical line in last panel represents sudden storm commencement and horizontal lines with double arrow heads represent the main and recovery phases

Likewise, for the storm of June 22, 2015, the three SSC were observed at 13:43 UT on June 21, 5:45 UT, and 18:33 UT on June 22, respectively. During the first, second, and third shocks, the solar wind speed increased from 300 to 350 km/s, 350 to 400 km/s, and 420 to 700 km/s, respectively. The maximum positive SYM-H during the first, second, and third shocks is 40 nT, ∼ 40 nT, and ∼ 90 nT, respectively. The main feature of this storm is the rapid, large-amplitude fluctuation of IMF Bz during its main and recovery phases. It was also observed with a minimum

value of − 37.6 nT at 19:20 UT on June 22. The AE value acquired during the main phase was 2300 nT. When the Bz has a negative value for a longer duration, the SYM-H reaches − 200 nT at ∼ 5:30 UT on 23 June.

During the storm of May 27, 2017, an SSC was observed at 15:34 UT on May 27. The storm begins quietly, with sudden changes in solar wind speed ranging from 300 to 400 km/s and pressure ranging from 1 to 15 nPa. The main phase began on May 27; recovery on May 28, with a minimum Dst excursion to − 125 nT, and the event
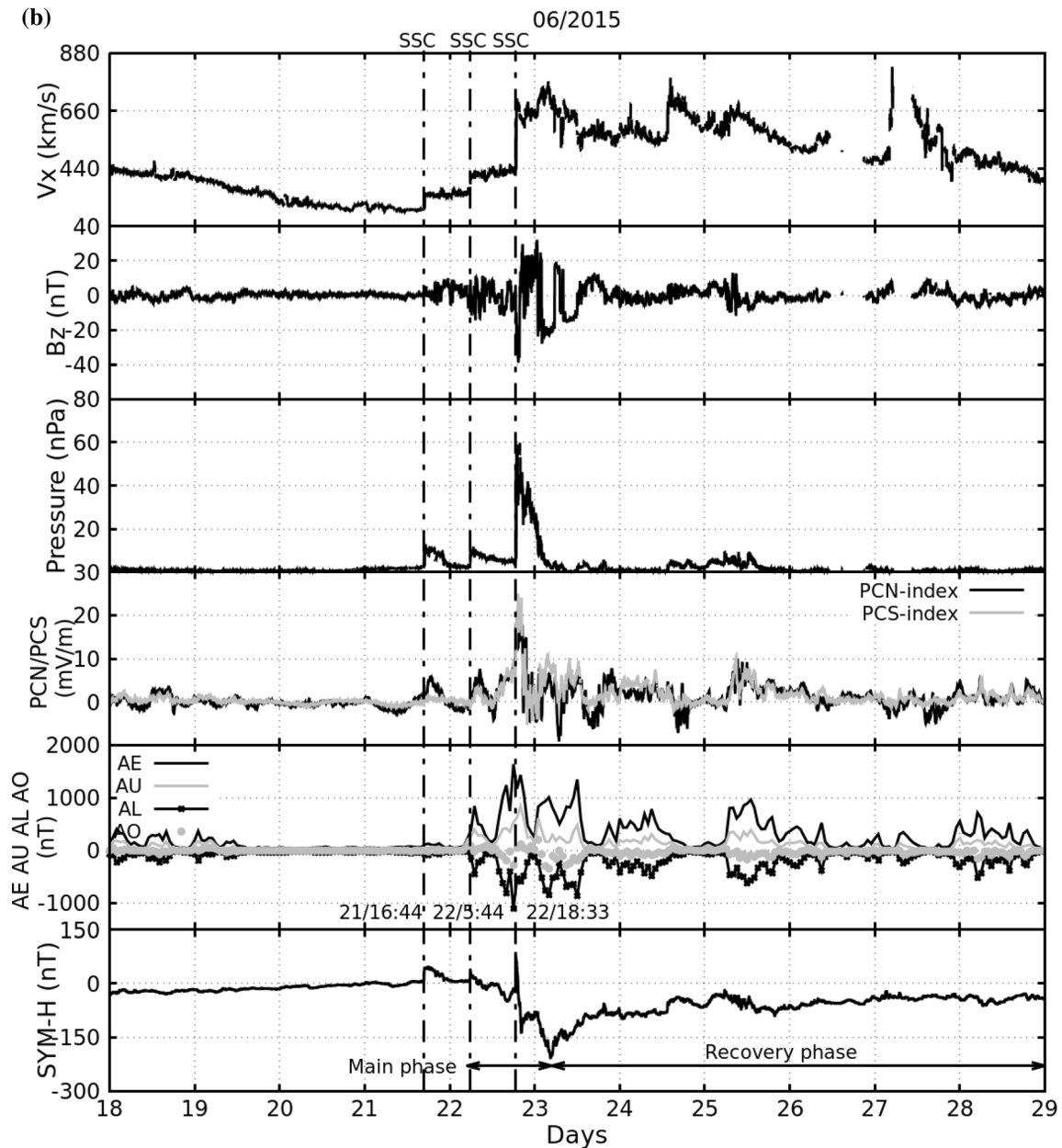
Fig. 2 continued

lasted until May 30, 2017. The maximum AE index was noticed ∼ 2000 nT with a minimum of IMF Bz ∼ − 18 nT on 28May.

During the storm of September 7, 2017, the first SSC was noticed on the 6th at 23:44 UT and the second, on the 7th at 23:00 UT. The first two significant minimums of SYM-H were observed on September 8 (− 142 nT) at 02:00 UT and the second on September 8 (− 122 nT) at 15:00 UT. The minimum value of SYM-H and the maximum bursts of AE do not coincide precisely in time. The maximum AE observed was 1300 nT and 1500 nT. The

time lag between the minimum SYM-H and AE maxima was 3 h and 2 h earlier, respectively. The possible cause is that the geomagnetic disturbance shifted from higher latitudes to lower latitudes. Nevertheless, the PC bursts follow the same trend as the SYM-H minima. During the first and second strokes, the quick changes in the solar wind velocity and pressure were from 450 to 650 km/s and 600–850 km/s; 1 to 14 nPa and 1 to 10 nPa, respectively.

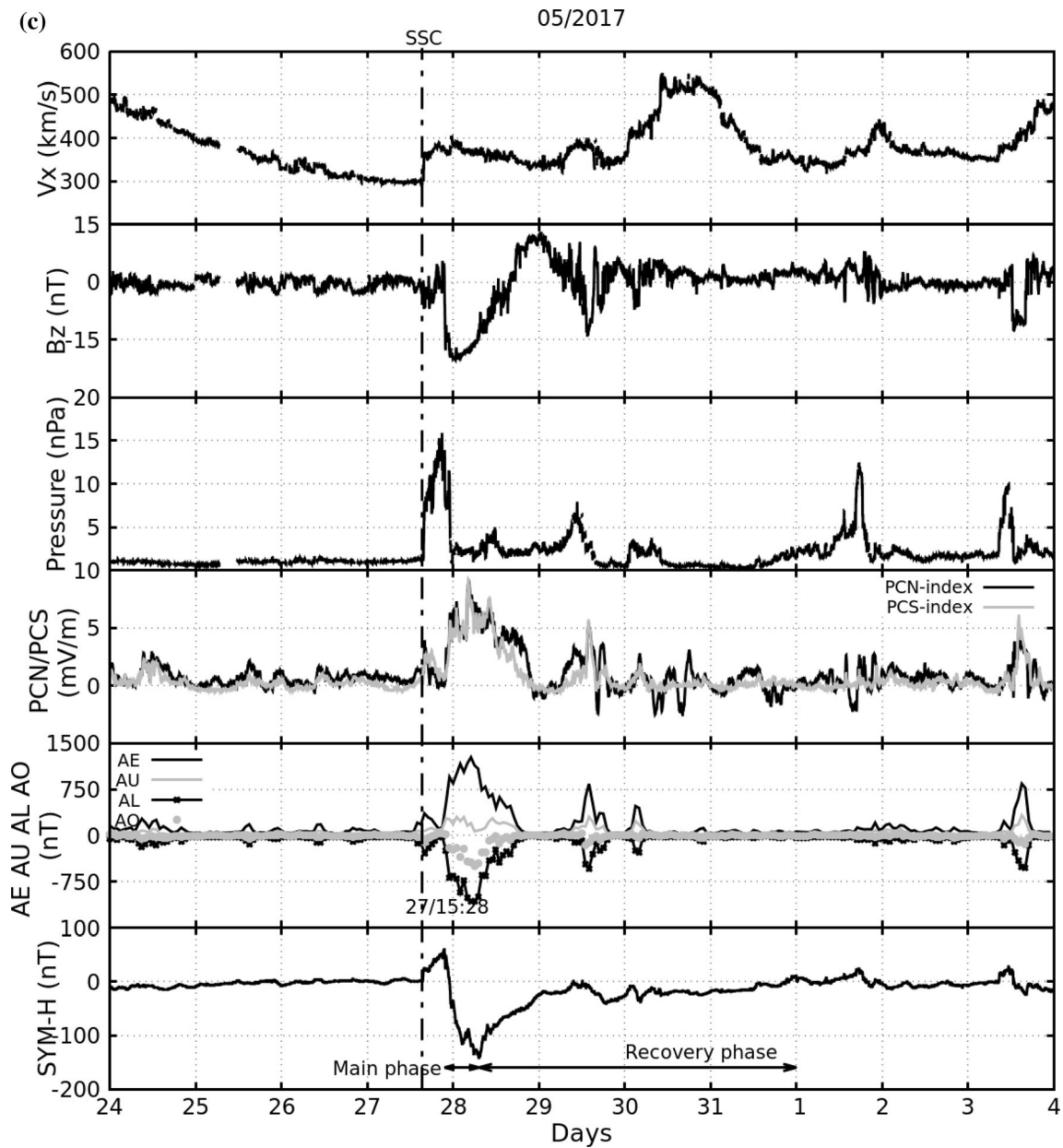Table 2 summarizes the characteristics of the four storms studied.

Fig. 2 continued

3.2. GPS VTEC

Figure 3(a), (b), (c), and (d) shows the temporal variation of VTEC during geomagnetic storms and geomagnetic quiet days, using GPS data from Nepal during March 14 to March 24, 2015, June 18 to June 28, 2018, May 24 to June 3, 2017, and September 3 to September 13, 2017, respectively. The first, second, and third panels in each figure represent the VTEC of stations BRN2, JMSM, and NAST in Nepal. The dotted black curve on each panel represents the average daily variation (a computed average of four days before the storm started). The quiet day variation is calculated from an average of data from March 13 to March 16, 2015, June 18 to June 21, 2015, May 23 to May 26, 2017, and September 3 to September 6, 2017 for the respective storms. The dark black curve indicates the variation in VTEC during storm time. The vertical line in each figure represents the SSC. The latitudinal (3°) and longitudinal (4°) distances between the selected stations are not very large; the electric field disturbances reach the daytime ionosphere at the same time, with similar intensity and duration. Hence, a marked latitudinal and longitudinal
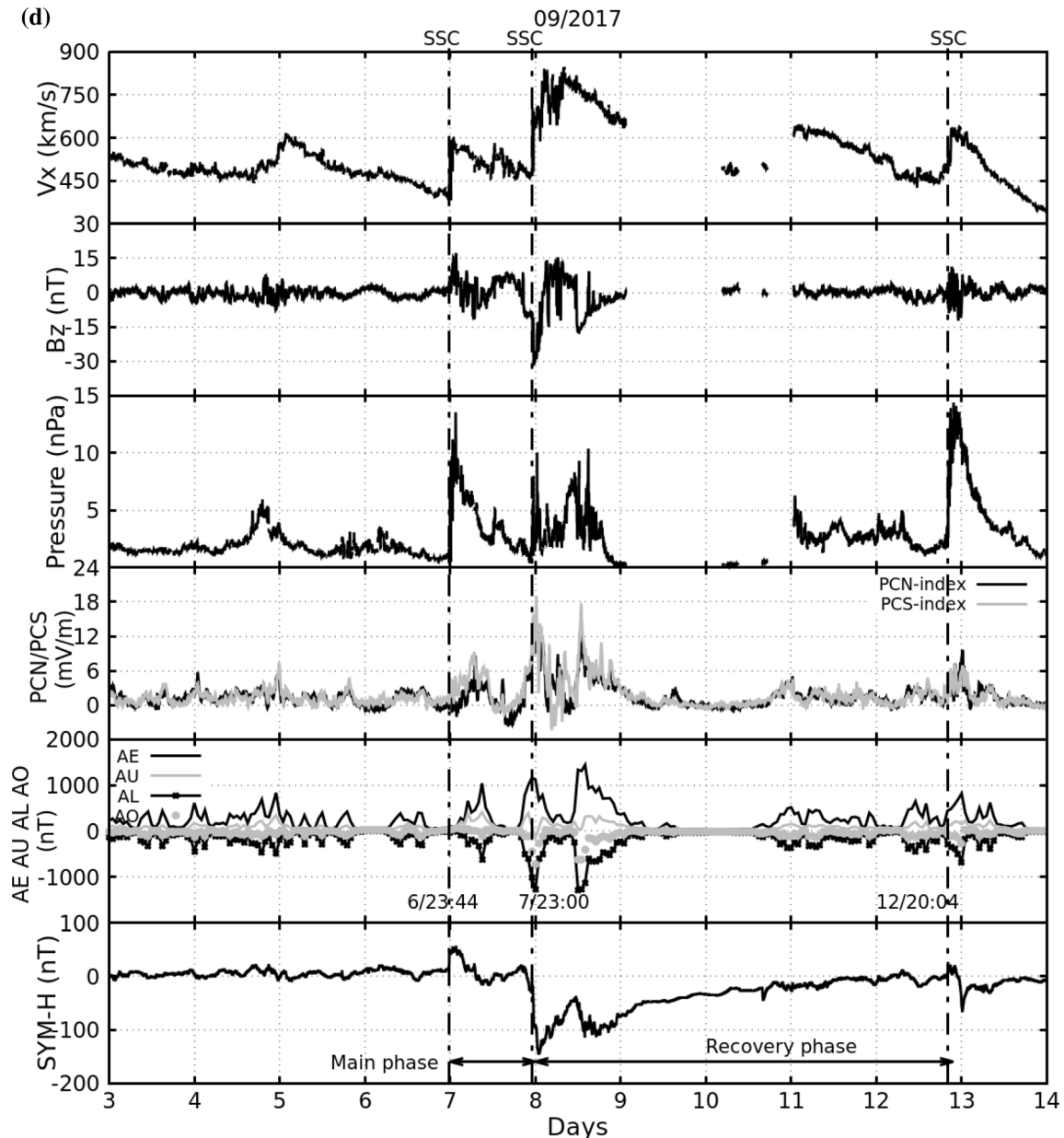
Fig. 2 continued

difference in the ionospheric response from these three stations is insignificant. In every station, a dome-shaped VTEC was observed. The trend of VTEC variation before the storm is almost similar to that of regular variation, but it gets disturbed when a geomagnetic storm starts.

The observations for each case of geomagnetic storms are as follows:

- *March 2015* The three days before the storm (14–16/03) are characterized by a similar dome-shaped diurnal variation with a maximum value of between 95 and 100

TECU. The onset of the magnetic storm was localized on 17/03 in the morning sector, and the diurnal maximum was observed at 90 TECU (Fig. 3a). The afternoon decay is irregular and occurs in cascades. The day of March 18 has a very low diurnal maximum (30 TECU), a decrease of − 70%. It is identical to all three stations. The recovery phase is rapid since the level of 105 TECU is present from March 20. The arrival of the magnetic disturbance on March 22 is localized at the beginning of the night. It results in a positive storm
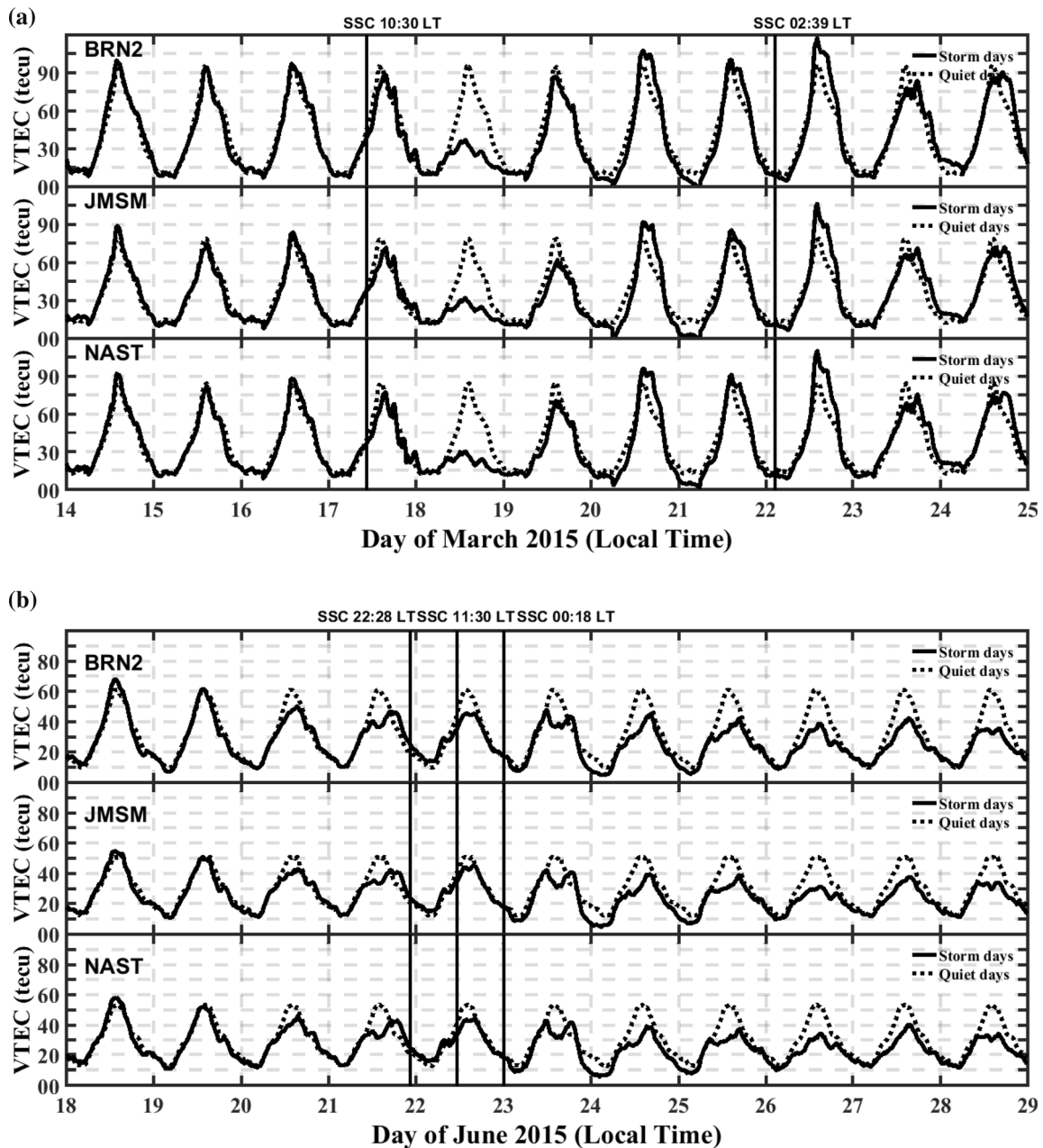
Fig. 3 (**a–d**) Variation of VTEC during geomagnetic storm of the period March 14–24, 2015, June 18–28, 2015, May 24–June 3, 2017, and September 3–13, 2018 (doted curves) and quiet days (solid curves), respectively

with a single peak at 120 TECU (+ 20%), followed by a slight negative phase on 23/03.

- *June 2015* This storm is located in the summer, with lower daytime values than the March equinox of the same year. Over the 4 days preceding the storm, the diurnal maximum of the VTEC decreased regularly from 70 to 45 TECU (Fig. 3b). The TEC is already below our reference over the last 2 days (20–21/06) of the quiet period. The first shock wave was localized at the beginning of the night of 22/06. It does not modify

the diurnal variation of 22/06, which remains below this reference. The following days do not show any significant variations, except that one can observe a regular decrease of the diurnal maximum until a minimum on 26/06 (for example, from 49 to 31 TECU for JMSM). We can note a double peak on June 23 at all three stations, as well as low values on June 23 and 24 (5 TECU or − 50%).

- *May 2017* It is again a summer storm but located in the descending phase of the solar cycle, so the VTEC
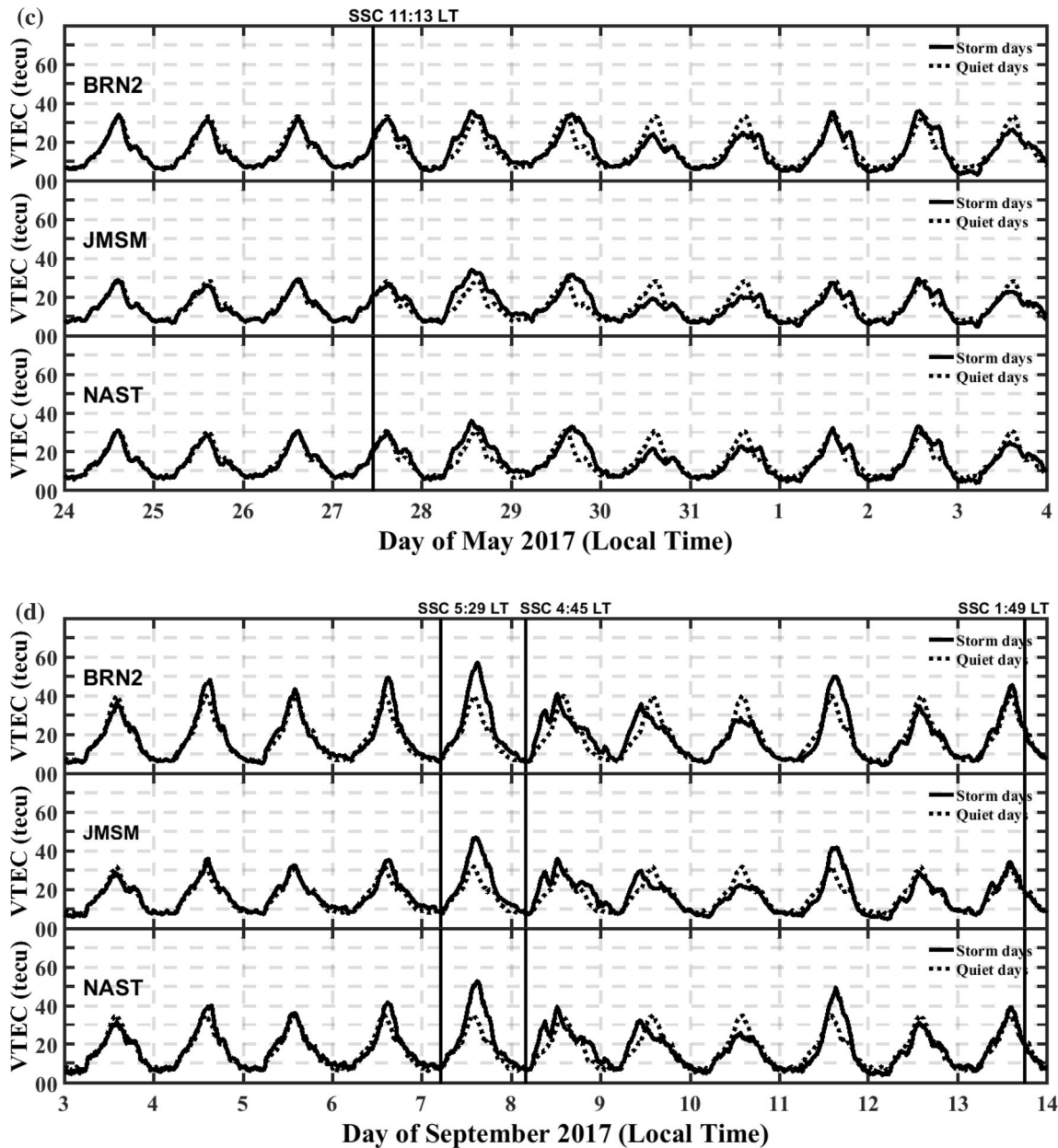
Fig. 3 continued

values are lower than in 2015, around 30 TECU by day and 10 TECU at night (Fig. 3c). The start of the magnetic storm is in the late morning of 27/05. The VTEC is slightly higher than our reference on 28 and 29/05, from 3 to 5 TECU, or + 10%. It becomes lower only late, in the recovery phase on 30 and 31/05, with a maximum of 20 TECU (− 30%).

- *September 2017* The period is again in 2017, but at the autumn equinox, so with higher VTEC values than in summer. The reference is between 10 TECU at night and a maximum of 40 TECU during the day (Fig. 3d). The start of the storm was late at night (05:29 LT) on

07/09. VTEC increases rapidly toward the daytime maximum of 14 LT at 50–60 TECU (+ 45%) depending on the station so this is a positive storm. Four days after (10/09), the VTEC is lower by − 8 TECU (30%), followed by a new positive effect on 11/09. With this long delay, it is difficult to make a link between the magnetic storm and the second storm, which began on September 12 at 20:04 TU.

3.3. Satellite data

Figure 4 (a), (b), (c), and (d) shows the global variation of the thermospheric O/N_2 ratio, obtained from the Global Ultraviolet Imager Thermosphere-Ionosphere, Mesosphere Energetics and Dynamics (GUVI-TIMED) during the four geomagnetic storms: March 16 to March 21, 2015, June 20 to June 25, 2018, May 26 to May 29, 2017, and September 6 to September 10, 2017.

At the location of the Nepalese GPS station JMSM, we observe the following behavior in the satellite data:

- For the storm of March 2015, on March 18, a significant decrease in the ratio of O/N_2 is noticed.
- For the storm of June 2015, the O/N_2 ratio started decreasing on June 22nd and became intense on June 23rd.
- For the storm of May 2017, no clear signature of change is noticed in the O/N_2 ratio.
- For the storm of September 2017, a significant enhancement in the ratio of O/N_2 is observed on September 8 and 9.

After all the geomagnetic storms, the thermospheric composition ratio of O/N_2 returned to its normal profile. For all the storms, the Global Ultraviolet Imager (GUVI) satellite O/N_2 ratio exhibits the same behavior as the VTEC measured from the ground-based GPS stations. We observed negative storms for March 2015 and June 2015, and a positive storm for September 2017. For the storm of May 2017, the change in VTEC is positive and very weak, and on satellite data, the change in O/N_2 is not very clear.

3.4. Comparison between GPS derived VTEC and CODE and IGSG models

For the four selected storms, we have represented in Fig. 5(a, b, c, d) the three variations of the VTEC (1) resulting from our RINEX processing in the form of a continuous line in black, (2) calculated by the GIM/CODE model by a square (1 point every hour), and (3) estimated by the IGSG model by an asterisk (1 point every 2 h). In each figure, we have three panels, correspondingly, from top to bottom, for BRN2, JMSM, and NAST. We have again recalled the hourly position of the shock waves with a vertical red line. To quantify the difference between our modeling and the two GIM maps, we have retained the maximum daily difference. Table 3 presents these differences for the March 2015 storm (Table 3a) and that of September 2017 (Table 3b) and for the three stations. The values are small and insignificant for the two other storms of June 2015 and May 2017, so they are not reported. The comparisons for each storm are as follows:

- *March 2015* The three days preceding the storm (14–16/03) are characterized by higher day values than those of the two GIM models of around 10–15 TECU, i.e., + 15%. All the following days, constituting the storm period and the return phase, are well restored in time and level by the two models. During the 22/03 recovery and positive phases, we find the initial observations with day values of the two models clipped compared to our model in an identical order of magnitude of 10–15 TECU. During March 2015, the negative ionospheric storm in Nepal took place in the main phase, and it continued during the recovery phase on March 18–19. During the main and recovery phases, the diurnal variation of TEC shows wave-like oscillations. This may be due to Prompt Penetration of Electric Field (PPEF), traveling ionospheric disturbances, or by other sources. The suppression in TEC during the recovery phase was attributed to the change in the composition of the neutral gas, which decreased the O/N_2 ratio [21]. Astafyeva et al. [22] pointed out that the second IMF Bz lasted longer during the present storm and caused a more complex effect. They investigated the O/N_2 ratio changes during this geomagnetic storm using GUVI-TIMED satellite measurements and confirmed strong O/N_2 composition changes. Ramsingh et al. [23] investigated the ionospheric response due to the St. Patrick's Day's storm on March 17, 2015, in the Indian and Indonesian sectors. They suggested that the F region disturbances during the main phase were produced by PPEF.

- *June 2015* The diurnal variation of the VTEC presents high levels at the beginning of the period and a fairly regular decrease during the 10 days with either a single maximum peak or a double peak. The main conclusion is that, despite this daily variability, the two GIM models show a very strong correlation with our representation: the differences are less than 2 TECU.

During June 2015, no increase or decrease in TEC variations was observed at the Nepalese stations before or after the main phase and recovery phase of the storm. Pre-reversal enhancement (PRE) is noticed at each station during the evening time. Wave-like characteristics with a noon bite pattern were noticed during the pre-storm and post-storm of the mid-diurnal TEC. To investigate the temporal and latitudinal variation of TEC using a GPS TEC map during the storm of June 22–24, 2015, Singh and Sripathi [24] found that on June 22, Equatorial Ionization Anomaly (EIA) was suppressed and partially shifted to the Northern Hemisphere up to 0°–35° geographic latitude at 11:00–17:00 LT. The suppression of EIA, the absence of crest formation, and the negative storm effects were due to the westward electric field (reversed electrojet). They also
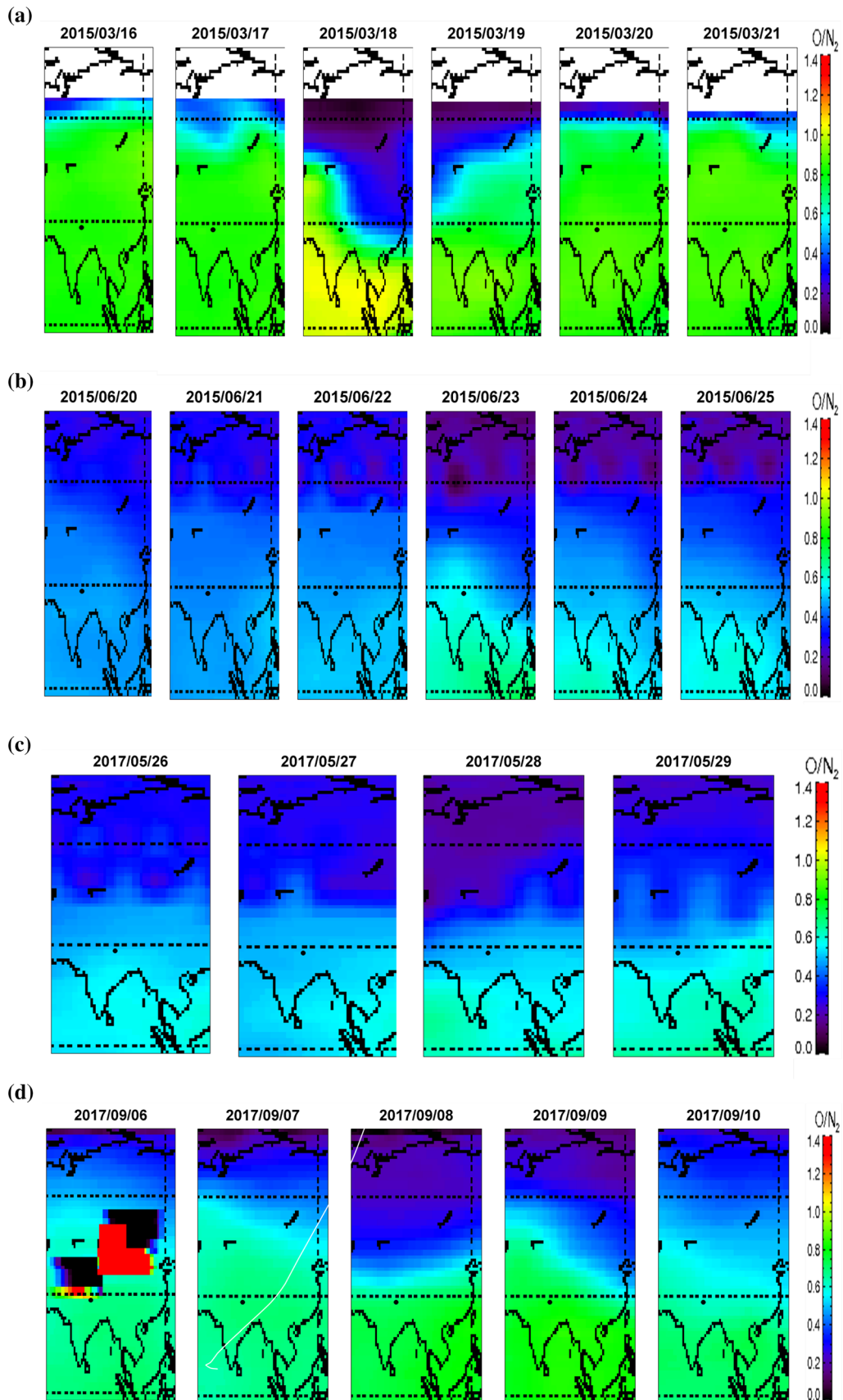
(a)

(b)

(c)

(d)

found the suppression of EIA and negative ionospheric storms on June 24 in the Northern hemisphere due to strong westward Disturbance Dynamo Electric Fields (DDEFs). Hemispheric asymmetry in ionospheric response was noticed in the period from the initial phase to the main phase of the storm of June 2015 in both TEC maps and GNSS TEC data by Senturk [25]. Negative phases of the ionospheric storm were seen in the northern latitudes (summer hemisphere), whereas strong positive phases of the ionospheric storm were seen in the southern latitudes (winter hemisphere). The storm of June 2015 occurred on the June solstice, so dominant summer-to-winter circulation [6] and seasonal effects [26] could dominate the hemispheric asymmetry of TEC responses. The negative phase were observed during the 23 June is consistent with TEC maps of their study.

- *May 2017* The conclusion is very close to the previous case. However, the two GIM models give higher levels of 5 TECU during the high values of the VTEC of

29/05. The result is reversed at night (-4 TECU on the night of 30–31/05). The daily differences are greatest for the BRN2 station, which is closest to the dip equator compared to the two other stations (JMSM and NAST). During May 2017, an increase in VTEC in Nepal was noticed during the main phase of the storm on May 28, which gradually decreased during the post-recovery phase on May 30. This storm was studied by Lui et al. [27] and found to have increased VTEC by 120% during the main phase of the storm on May 28 due to the southward turning of IMF Bz and eastward penetration of the electric field. On May 30, over the Asian sector, nearly 2 days after the main phase, a negative storm was identified due to thermospheric composition changes, i.e., a decrease in the O/N$_2$ ratio. An increase in TEC due to PRE is observed during the evening time in the diurnal plot.

- *September 2017* When the diurnal maximum is between 30 and 40 TECU, the GIM modeling is correct. The difference becomes negative above 50 TECU, i.e., it peaks down to -10 TECU (BRN2 and NAST on 07/09). The strongest differences are observed with the IGSG model, on BRN2, which is of lower latitude. The lowest VTEC values were observed on 10/09 on the three curves. Over the 10 days, there is little difference in the night values. In

Table 2 Characteristics of Geomagnetic storms of March 2015, June 2015, May 2017, and September 2017 of solar cycle 24

| Date	SSC	Season	Event started local time in Nepal	Case	Dst	SYM-H	Kp	AE
March 2015	March 17 04:45 UT and March 21 20:54 UT	Equinox	LT = 4.45 + 5.45 = 10 h 30 min	CME + HSSW	− 225 nT	− 250 nT	8	2000 nT ∼ 12:00 UT on March 17, 2015
June 2015	June 21 16:43 UT June 22 05:45 UT and June 22 18:33 UT	Summer Solstice	Last SSC LT = 18.33 + 5.45 = 0 h 18 min	CME + HSSW	− 207 nT	− 275 nT	8	2800 nT ∼ 18:00 UT on June 22, 2015
May 2017	May 27 15:28 UT	Summer Solstice	LT = 15.46 + 5.45 = 21 h 13 min	CME	− 125 nT	− 150 nT	7	2100 nT ∼ 06:00 UT on May 28, 2017
September 2017	September 6 23:44 UT September 7 23:00 UT September 12 20:04 UT and September 14 23:48 UT	Equinox	First SSC LT = 23.73 + 5.45 = 5 h 33 min	CME	− 142nT	− 150 nT	8	2600 nT ∼ 14:00 UT on September 8, 2017
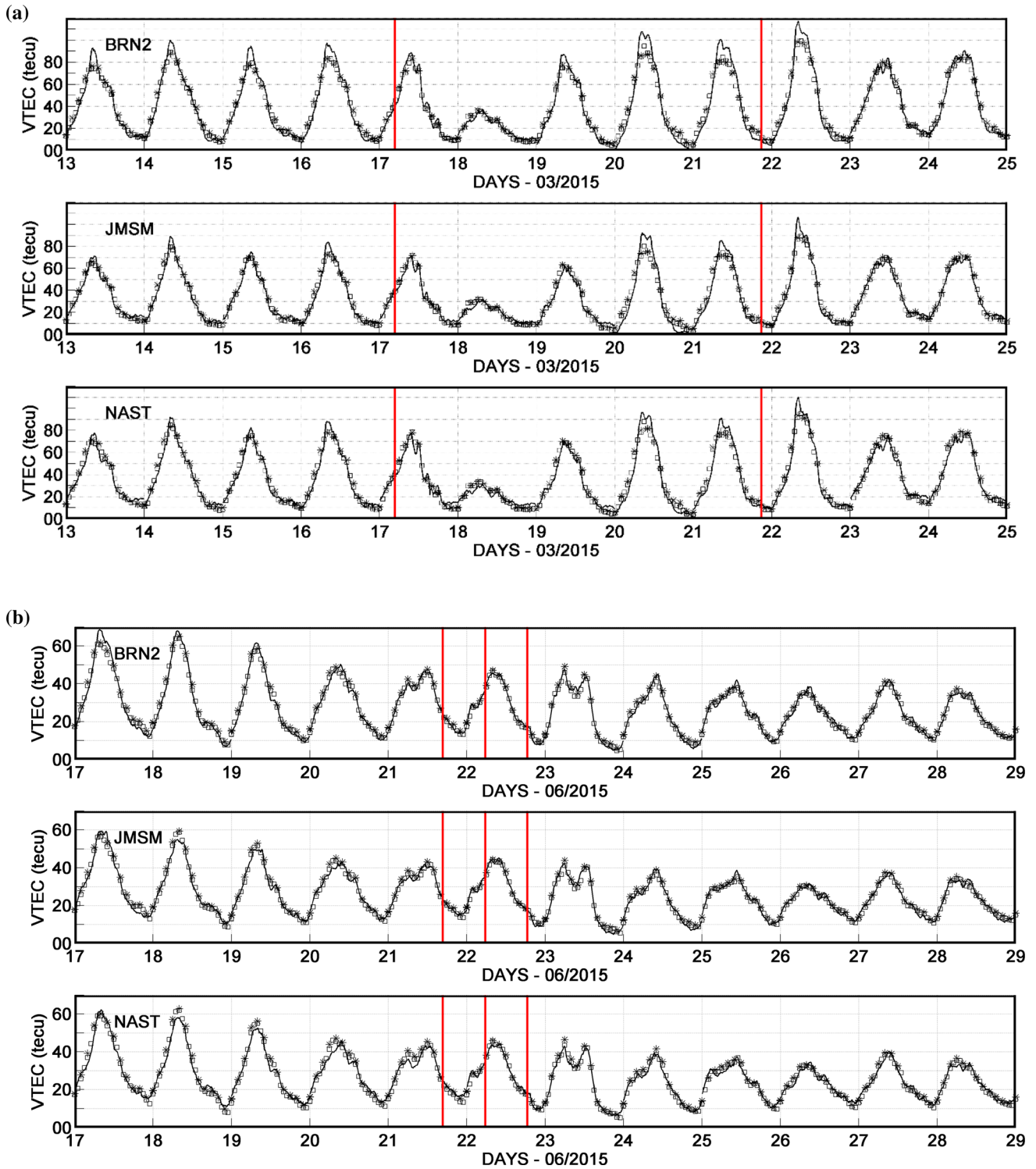
Fig. 5 (**a–d**) Variations of VTEC observed from GPSTEC, CODE, and IGSG for JMSM, NAST and BRN2 for three Nepalese stations during geomagnetic storm of the period March 14–24, 2015, June 18–28, 2015, May 24–June 3, 2017, and September 3–13, 2018, respectively. The solid black line on each panel represents GPSVTEC variation, whereas the black square with white background curve represents CODE and the variation in IGSG is represented by black asterisks curve
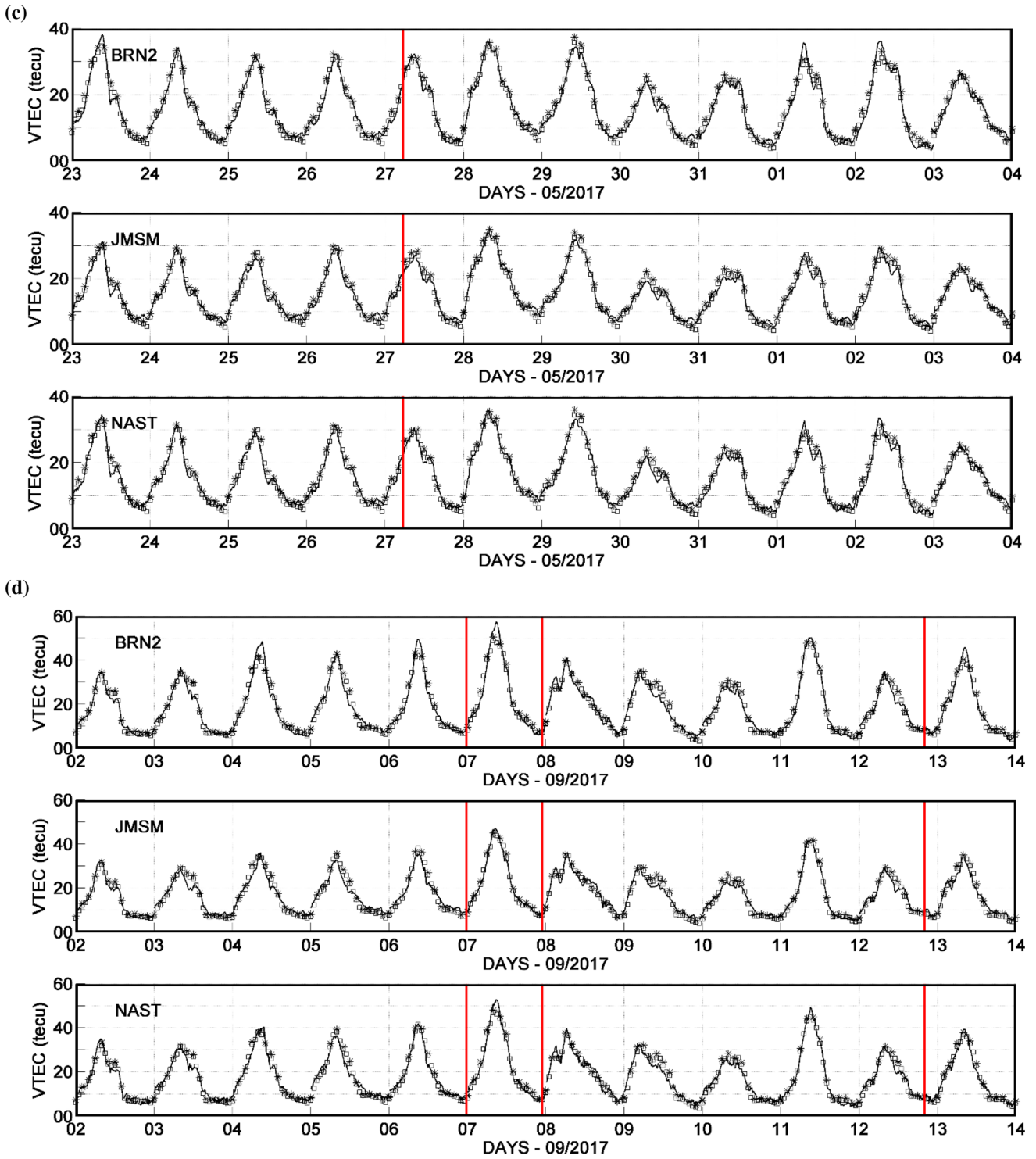
(c)

(d)

Fig. 5 continued

Table 3 Difference in RINEX VTEC for three Nepalese GPS stations JMSM, NAST, and BRN2 (a) with CODE and IGSG during geomagnetic storm of March 14–24, 2015, (b) with CODE and IGSG during geomagnetic storm of September 3–13, 2017

Days	JMSM		NAST		BRN2	
	RINEX-CODE	RINEX-IGSG	RINEX-CODE	RINEX-IGSG	RINEX-CODE	RINEX-IGSG
(a)						
14	9	10	10	10	6	9
15	11	7	11	13	13	13
16	16	16	13	16	10	11
17	2	2	4	5	− 4	− 4
18	0	1	− 3	− 2	− 3	− 3
19	− 1	0	− 1	− 5	− 3	− 4
20	10	21	12	19	7	19
21	3	8	3	8	12	13
22	16	17	19	19	10	14
23	− 3	− 2	7	8	1	1
24	1	1	− 10	− 7	− 3	− 4
(b)						
3	− 3	− 3	3	3	− 2	− 2
4	5	5	5	12	0	9
5	− 3	− 3	0	1	− 5	− 5
6	− 5	− 2	5	7	0	2
7	3	3	8	6	2	12
8	0	− 3	0	0	1	− 10
9	− 1	0	0	− 8	0	− 7
10	− 4	− 9	− 2	− 13	0	− 5
11	0	− 2	0	0	4	14
12	− 2	− 4	3	10	− 2	0
13	0	0	5	3	0	− 2

Nepal, during the main and recovery phases of the storm of September 2017, the daytime VTEC enhancement occurs at all the stations on September 8 and 9. The wave-like variations in VTEC on September 8 might be attributed to the traveling atmospheric disturbances (TADs) generated from high latitudes due to enhanced Joule heating during the storm time [5]. On September 11, there was a significant increase in daytime VTEC compared to September 10. Lei et al. [28] observed an increase in VTEC over similar latitudes for this storm, which they attributed to an increase in eastward electric fields caused by PPEF [29] when IMF Bz was southward and the neutral wind was not greatly disturbed during the initial phase of storm. Weak VTEC depletions on September 9 and 10 could be associated with the storm time neutral composition changes that extended from high latitudes to low latitudes.

Nava et al. [30] and Kashcheyev et al. [31] studied the GUVI [O/ N$_2$] data for the magnetic storms of March 17 and June 22, 2015. The study carried out on a global scale shows the importance of the local time of a station at the onset of the storm. The VTEC decreases significantly in Asia during the storm of March 17, 2015, which begins at 4.45 UT, as we observed in our data in Nepal, while it increases in America. Regarding the storm of June 22, 2015, which begins at 18:33 UT, it is the Asian sector that observes the increase in VTEC and the American sector that observes the decrease in VTEC.

In brief, the observations from the two global ionospheric models, CODE and IGSG, are:

- give lower VTEC values (− 10 to − 20%) than at stations in Nepal if the level is above 50 TECU, which is mostly observed during magnetically quiet periods;
- give slightly lower values (− 1 to 3 TECU) at night;
- correctly restore the level during the main phases of storms, even if these are very negative;
- show a lower result at BRN2 compared to the other two stations.

The IGSG model designed to synthesize all of the GIM maps has a degraded performance compared to CODE.

The daily variations of VTEC retrieved from the CODE and IGSG models for summer (June 2015 and May 2017) and equinoctial storms (March 2015 and September 2017) found that VTEC values are lower in summer than in the equinoxes (March 2015 and September 2017). The VTEC are found to be stronger in 2015 than in 2017 because 2015 is at the beginning of the decreasing phase of the sunspot cycle 24, and the year 2017 is at the end of the decreasing phase closer to the minimum of sunspots.

Hernandez-Pajares et al. [17] found a significant error in VTEC estimation over the ocean where only a few GPS receivers are located and one-hour resolution might be the reason why it is not good enough to analyze the storm time effect in detail. Legrand and Simon [32] analyzed a series of more than one century and half years of magnetic data and found there were 67% of magnetic quiet days, and thus more than two-thirds of the time, CODE and IGSG do not represent the data of Nepal during the equinoxes. On the contrary, during the periods of magnetic activity, the storm homogenizes the ionosphere, and geographic variability no longer exists. The discrepancy in the results between observed data and model data may be due to the local effect that CODE and IGSG do not reproduce [33, 34] and to the to the longitudinal variability of the physical process. This conclusion is consistent with the results obtained by Panda et al. [35, 36]. The authors find good agreement between the calculated VTEC in October 2012 and the Global Ionospheric Model at locations near the magnetic equator, but strong differences (20 TECU or 40%) are observed at the Delhi station, which is located near the northern ridge of the equatorial anomaly. Several physical phenomena present at low latitudes, and in particular, vertical plasma drifts, have rapid longitudinal variations [37, 38], and are not reproduced by GIM models. There are already many GNSS stations at low latitudes and, in particular, on many islands. However, the densification is not homogeneous in order to understand the variability of the ionosphere in this geographic region. Action from the scientific community is necessary to increase the network and thus improve the modeling of TEC.

This study showed that the difference between VTEC RINEX and the VTEC models is greater during the magnetic quiet days. This means that during the periods of magnetic quiet, there is wide geographic variability. There are very few geodetic stations used by CODE in the geographic vicinity of Nepal. This situation may explain the differences observed on the TEC between local measurements and global-scale modeling.

4. Conclusion

In this paper, we have attempted to reveal the impact of the intense geomagnetic storm of solar cycle 24 on VTEC over Nepal and compared the VTEC RINEX observations profile with models CODE and IGSG. The VTEC observed during these periods showed positive and negative ionospheric storms after the sudden storm commencement. After analyzing the results of VTEC obtained from RINEX observations and model data from CODE and IGSG, we have found the difference in VTEC between the two global models and the results obtained from the Nepalese GPS stations are significant beyond 5 TECU in absolute values. The second point is that the signatures in the VTEC noon bite out profile with a predominance of morning and afternoon peaks, and the nighttime peak was not clearly noticeable in the two models' representations. The discrepancies in the result between observed data and model data could be due to the local effect and also to the longitudinal variability of the physical process that the models do not produce. Therefore, the implantation of some Nepalese GPS stations in the global modeling could improve the evolution of the VTEC because the current differences are significant.

References

[1] W D Gonzalez, J A Joselyn, Y Kamide, H W Kroehl and G Rostoker *J. Geophys. Res.* **99** 5771 (1994)

[2] M Sugiura *Hourly Values of Equatorial Dst for the IGY* (Greenbelt, Maryland, United States: NASA Goddard Space Flight Center) (1963)

[3] J W Dungey *Phys. Rev. Lett.* **6** 47 (1961)

[4] (eds.) C I Meng, M J Rycroft and L A Frank *Auroral Physics* (Cambridge, UK: Cambridge University Press) (1991)

[5] T J Fuller-Rowell, M V Codrescu, R J Moffett and S Quegan *J. Geophys. Res.* **99** 3893 (1994)

[6] T J Fuller-Rowell, M V Codrescu, H Rishbeth, R J Moffett and S Quegan *J. Geophys. Res. Space Phys.* **101** 2343 (1996)

[7] V M Vasyliunas *Particles and Fields in the Magnetosphere*, (ed.) B M McCormac (New-York: Springer) p 60 (1970)

[8] M Blanc and A D Richmond *J. Geophys. Res.* **85** 1669 (1980)

[9] Y Huang, S Yang, Y Qiao, M Lin, B Zhao, and K Tan *Geod. Geodyn.* **8** 285 (1017)

[10] B Adhikari, S Dahal, M Karki, R K Mishra, S Sasmal and V Klausner *Geoenviron. Disasters* **7** 1 (2020)

[11] K Ansari, S K Panda and P Jamjareegulgarn *Acta Astronaut.* **169** 216 (2020)

[12] P Jamjareegulgarn, K Ansari and A Ameer *Acta Astronaut.* **177** 497 (2020)

[13] D Pandit, B Ghimire, C Amory-Mazaudier and R Fleury *Ann. Geophys.* **39** 743 (2021)

[14] B Hofmann-Wellenhof, H Lichtenegger and J Collins *Global Positioning System: Theory and Practice* (Wien, Austria: Springer) (1992)

[15] S Schaer *Doctoral dissertation* (*Bern University*, Bern) (1999)

[16] I Azzouzi, Y Migoya-Orue, C Amory-Mazaudier, R Fleury, S M Radicella and A Touzani *Adv. Space Res.* **56** 2040 (2015)

[17] M Hernandez-Pajares, J M Juan, J Sanz, R Orus, A Garcia-Rigo, A Komjathy, S Schaer and A Kranskowski *J. Geod.* **83** 263 (2009)

[18] P Chen and H Liu *Space Res.* **65** 163 (2020)

[19] M Hernández-Pajares, D Roma-Dollase, A Krankowski, R Ghoddousi-Fard, Y Yuan, Z Li, H Zhang, C Shi, J Feltens, A Komjathy, P Vergados, S Schaer, A Garcia-Rigo and J M Gmez-Cama In: *IGS Workshop 2016, 8–12 Feb, Sydney, Australia* (2016)

[20] D Roma-Dollase *Doctoral Dissertation* (Universitat Politècnica de Catalunya, Spain) (2019)

[21] R de Jesus, Y Sahai, P R Fagundes, A J de Abreu, C Brunini, M Gende and J A Bittencourt *Space Res.* **52** 147 (2013)

[22] E Astafyeva, I Zakharenkova and M Förster *J. Geophys. Res. Space Phys.* **120** 9023 (2015)

[23] S S Ramsingh, S Sreekumar, S Banola, K Emperumal, P Tiwari and B S Kumar *J. Geophys. Res. Space Phys.* **120** 10864 (2015)

[24] R Singh and S Sripathi *J. Geophys. Res. Space Phys.* **122** 11 (2017)

[25] E Sentürk *Astrophys. Space Sci.* **365** 1 (2020)

[26] H Kil *J. Geophys. Res.* **111** A12311 (2006)

[27] L Liu, S Zou, Y Yao and E Aa *GPS Solut.* **24** 1 (2020)

[28] J Lei, F Huang, X Chen, J Zhong, D Ren, W Wang et al *J. Geophys. Res. Space Phys.* **123** 3217 (2018)

[29] N Balan, Y Otsuka, M Nishioka and J Y Liu *J. Geophys. Res. Space Phys.* **118** 2660 (2013)

[30] B Nava, J Rodríguez-Zuluaga, K Alazo-Cuartas, A Kashcheyev, Y Migoya-Orué, S M Radicella and C Amory-Mazaudier *J. Geophys. Res. Space Phys.* **121** 3421 (2016)

[31] A Kashcheyev, Y Migoya-Orué, C Amory-Mazaudier, R Fleury and B Nava *J. Geophys. Res. Space Phys.* **123** 5000 (2020)

[32] J P Legrand and P A Simon *Ann. Geophys.* **7** 565 (1989)

[33] N Matuura *J. Geophys. Res.* **79** 4679 (1974)

[34] C Zoundi, O Frederic, N Emmanuel, R Fleury and Z Francois *Eur. Sci. J.* **9** 74 (2013)

[35] S K Panda, S S Gedam and G Rajaram In *2013 IEEE International Geoscience and Remote Sensing Symposium-IGARSS* 1839 (2013)

[36] (eds.) S K Panda, S S Gedam and S Jin *Satellite Positioning—Methods, Models and Applications* (London, UK: IntechOpen) (2015)

[37] B G Fejer, D T Farley and C A Gonzales *J. Geophys. Res. Space Phys.* **86** 215 (1981)

[38] B G Fejer, E R De Paula, S A Gonzalez and R F Woodman *J. Geophys. Res. Space Phys.* **96** 13901 (1991)

Study of Ionospheric Variability during Super Substorms

D. Pandit, N. P. Chapagain and B. Adhikari
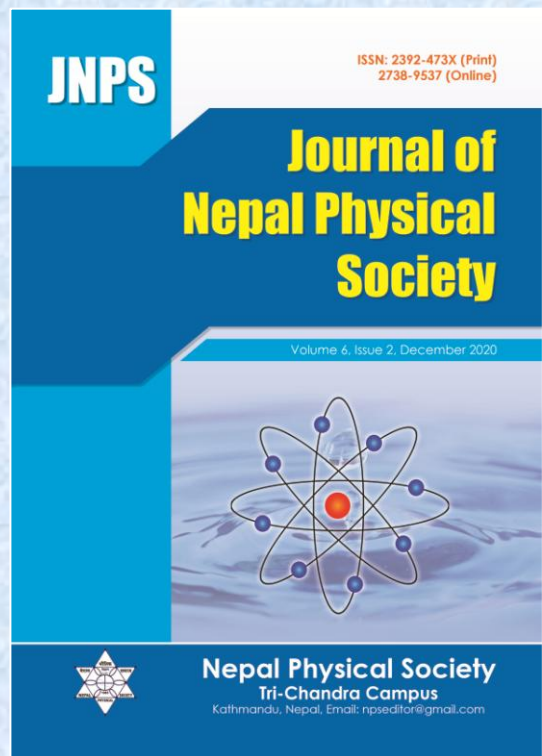
Study of Ionospheric Variability during Super Substorms

D. Pandit[1, 3], N. P. Chapagain[2] and B. Adhikari[3]

[1]Central Department of Physics, IOST, Tribhuvan University, Kirtipur, Kathmandu, Nepal
[2]Amrit Campus, Thamel, Kathmandu, Nepal
[3]St. Xavier's College, Maitighar, Kathmandu, Nepal
Corresponding Email: drabindra@sxc.edu.np

Abstract

This paper study variability of three ionospheric parameters foF2, h′F and hmF2 to investigate the middle latitude ionospheric effect at Boulder, Colorado, USA (40°N, 1105.0° W) during super substorms (SSSs) of 24 August 2005, and 7 September 2017 and 8 September 2017 respectively. Continuous wavelet transform (cwt) implemented to identify the low and high frequency and longer and shorter duration present in the signal. The result shows decrease in foF2 during SSSs of 24 August 2005 and 8 September 2017 and increase in foF2 during 7 September 2017. The highest fluctuation in h′F is noticed during SSS of 24 August 2005. The cwt shows that the coupling between solar wind and magnetosphere occurs between ~ 16 to 32 minutes for SSS of 24 August 2005 and between 27.9 to 64 minutes during super substorm of 7 and 8 September 2017 for all the ionospheric parameters respectively. This study leads to understand the impact of SSSs on communication signals due to energy injected in ionosphere during the coupling mechanism between magnetosphere-ionosphere.

Keywords: Magnetosphere, Ionosphere, continuous wavelet transform, Super sub-storm.

1. INTRODUCTION

Ionosphere is highly vulnerable region affected by a) solar ionizing radiation (solar rotation variation, solar cycle variation and formation and decay of active region); b) neutral atmosphere (acoustic and gravity wave, planetary waves, surface phenomena like earthquakes and volcanic eruption); c) electrodynamics (dynamo effects of low latitude phenomena, penetration of magnetospheric electric field, electric field from lightening and sprites); d) solar wind geomagnetic (magnetic storm, substorms, IMF/solar wind sector structure, energetic particle precipitation and Joule heating). The present study emphasizes on ionospheric variability during very intense substorm called Super Substorm (SML < - 2500 nT) [1], it is crucial for the researchers to understand the physical interaction processes in solar wind-Earth's magnetosphere-ionosphere system during this event. The huge injected energy accompanied with super substorm will result in thermospheric and ionospheric storms. The ionosphere during this super substorm will change in

complex ways resulting change in its critical frequency (foF2), maximum electron density height (hmF2) and virtual height (h′F). Many past researchers reported that the storm-time ionosphere changes in rather complicated ways. Due to its complexity its underlying physical processes are far from being fully understood. In 1997, Lakshmi [2] studied the response of the great storm of 13 March 1989 using ionosonde data over the equatorial and F-region in India. In 2002, Pincheira [3] studied the responses of magnetic storm on ionosphere and thermosphere over the South American sector using foF2, hmF2 and neutral winds extracted from measured hmF2, using interhemispheric plasma model. In Brazilian sector de Abreu et al, 2014a, b, c found that the occurrence of ESFs are closely related to daily variations of the h′F near equator. The relationship between spread-Fs and other ionospheric parameters, foF2 and h′F variations with the spreads-Fs have been studied by Rungraengwajiake [7], Smith [8], Liu and Shen [9]. The seasonal, solar and magnetic activity variabilities on h′F threshold have been investigated by Manju [10] and Narayanan [11,

12]. In 2020, Li studied the contribution of geomagnetic activity to ionospheric foF2 at different phases of solar cycle by spectral whitening method.

Many studies on storm, substorm has conducted for ionospheric parameters in different latitudes however no result for the SSSs on ionospheric parameters have been reported up to now. The list of researchers carried research on other area of SSSs are Tsurutani [1]; Hajra [13]; Adhikari [14-16]; Despirak [17, 18]; Tsurutani [19]. In this paper, we report for the first time the ionospheric responses during the 24 August 2005 and 7 and 8 September 2017 super substorm using ionosonde data measured at Boulder, Colorado, USA (40.0° N, 105.0° W). A brief description of data selection for these events is described in section 2. The results and discussion are presented in the section 3 and the conclusions of this work are summarized in section 4.

2. A BRIEF DESCRIPTION OF THE DATASET AND METHODOLOGY

2.1 Datasets

The three SSSs occurred on 24 August 2005, 7 September 2017 and 8 September 2017 were analyzed for the present study. Their corresponding interplanetary, solar wind and geomagnetic data is downloaded from http://nssdc.gsfc.nasa.gov/ omniweb database. To study the impact of SSSs on mid latitude the F-region parameters: critical frequency (foF2), virtual height (h′F) and height of peak electron density over Boulder, Colorado, USA (40.0° N, 105.0° W) is analyzed in relation to quiet-day values of these parameters closest to the respective storm times. The table 1 gives the list of the days including a reference quiet day for three SSSs. The ionosonde data for these parameters were downloaded from Global Ionospheric Radio

Observatory (GIRO) website https://ulcar.uml.edu/ DIDBase/.

2.2 Methodology

The continuous wavelet transform technique (cwt) is used to identify the singularity and transient structure present in the time series data. The signal energy in wavelet space is represented in scalogram using a log2 function. It allows the decomposition of data, functions or operators into different frequency or scale component [20] and each component present can be studied with its resolution which matches with its scale. The high and low frequency wavelet is very narrow and broad. Hence, it is a good technique to zoom in the short lived high frequency present as singularities and transient structures. The frequencies associated with wavelet transform detect the respective frequencies of the super substorms. The amplitudes of the wavelet coefficients are small [21] for smooth signals but for the singularities and transient structures it has larger amplitude. In the signal processing scalogram is used to visualize the square of the amplitude of the coefficient which illustrates as the distribution of signal energy in time t and scale a [14-16]. In this work, we identify quiescent and non-quiescent periods related to SSSs.

If a and b represent the dilation and translation parameters that vary continuously, then the continuous wavelet transform becomes

$$W(a, b) = \int f(t)\varphi * \left(\frac{t-b}{a}\right) dt \quad (1)$$

where $\varphi *$ represents complex conjugate of φ and the function W (a, b) represents the wavelets coefficients. For a > 0, variation of scale parameter gives dilation effect and for a < 0, it gives contraction effect of the mother wavelet function. Hence, it is convenient to identify the low and high frequency and longer and shorter duration present in the signal.

Table 1: Geographic and Geomagnetic Coordinates of ionosonde station.

Station	Geographic Latitude	Geographic Longitude	Geomagnetic Latitude	Geomagnetic longitude
Boulder	40.00° N	105.00° W	47.54° N	37.47° W

Table 2 : The list of study days including reference quiet days for each of the three storms.

Event	SSS day	Reference quiet day
1	24 August 2005	20 August 2005
2	7 September 2017	28 September 2017
3	8 September 2017	28 September 2017

3. RESULT AND DISCUSSION

In this section, we discuss and present the interplanetary, solar wind and geomagnetic data and the disturbance variations on the parameters foF2, h′Fand hmF2 during each SSS.

3.1 SSS of 24 August 2005

Figure 1 shows the time profile of solar wind parameters and geomagnetic indices of SSS 24 August 2005. The top three panels represent the variation of Vsw, T and Psw/Nsw (combined in panel three) while the bottom five panels show the variation in B/Bz, Ey, AE, SYM-H and AU/AL respectively. The sharp decrease in AL at 10:20 UT indicates the position of SSS. At the peaks the value of AL is -3954 nT. The value of SYM-H at the onset time of first SSS is +95 nT where its value goes to -170 nT during its peak value of AL. During the onset of the IMF Bz has turned towards southward direction. The value of Vsw, Tsw, Nsw, Ey and AE during the onset of event was ~ 600 Km/s, ~ 5X10^5 K, ~ 5 cm^{-3}, ~ 35 mV/m and ~ 3800nT respectively. It is seen from the plot that magnetosphere is much more sensitive to the solar wind dynamic pressure variations when the IMF is strongly southward than when it is weakly southward which trigger the release of the stored energy during southward field [1].
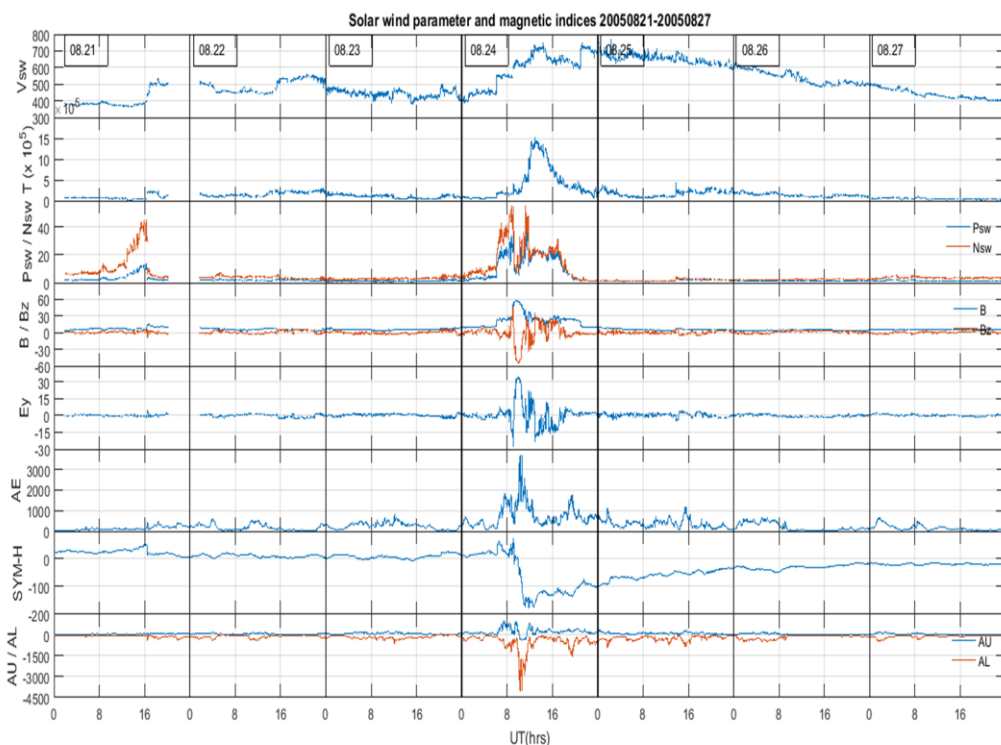

Fig. 1. From top to bottom shows the variations of solar wind speed (Vx in Km/s), temperature (T in K), pressure (Psw in nPa), plasma density (Nsw in cm^{-3}), total magnetic field (B, nT) interplanetary magnetic field IMF (Bz in nT), interplanetary electric field (Ey in mV/m), auroral index (AE in nT), SYM-H (in nT), aurora up (AU in nT) and aurora low (AL in nT) characterizing super substorm 21-27 August 2005 respectively.

3.2 SSS of 7 and 8 September 2017

In early September 2017, it was found a rapid development of group of sunspots and solar flare of class X9.3 and eruption of series of coronal mass ejection (CME) from the Sun. The solar flares M9.3 (4 September), X2.2 and X9.3 (6 September), M7.3 and X1.3 (7 September), M8.1 (8 September) and X8.2 (10 September) were identified respectively. First CME was detected in the morning of September 7 and a second CME was identified in afternoon of September 8. Figure 2 shows the time profile of solar wind parameters and geomagnetic indices on 7-8 September 2017. The top three panels represent the variation of solar wind velocity (Vsw in Km/s), temperature (T in K) and pressure (Psw in nPa)/ density (Nsw in m^{-3}) (combined in panel three) while the fifth panels show the variation in total magnetic field and interplanetary magnetic field B (in nT) /Bz (in nT), electric field (Ey in mV/m), AE , SYM-H and AU/AL in nT

respectively. The two sharp decrease in AL noticed on September 7 at ~23:45 UT and on 8 at ~13:00 UT with AL < -2500 nT indicate the position of two SSSs. The value of SYM-H at the onset time of first SSS is -145 nT during its peak value of AL and during second SSS the value of SYM-H noticed is -100nT. During the onset of September 7 SSS was intense because IMF Bz has turned intensively towards southward direction than on SSS of September 8. The value of Vsw, Tsw, Nsw, Ey and AE during the onset first and second event was ~ 575 Km/s, ~ 10^6 K,~ 6 cm^{-3}, ~ 25 mV/m and ~ 2500nT ; ~ 750Km/s, ~ 5X105 K, ~ 7 cm^{-3} ,~

10mV/m and ~ 2700nT respectively. The two events are isolated and large [1], duration of the first and the second event is ~15 minutes and ~25 minutes respectively. The interplanetary sheath is the causative of SSS events of September 7 and magnetic cloud of the September 8 [17]. Multiple magnetic fluctuations are the signature of sheath region. Similar to the figure 1, the figure 2 shows that magnetosphere is much more sensitive to the solar wind dynamic pressure variations when the IMF is strongly southward than when it is weakly southward which trigger the release of the stored energy during southward field [1].
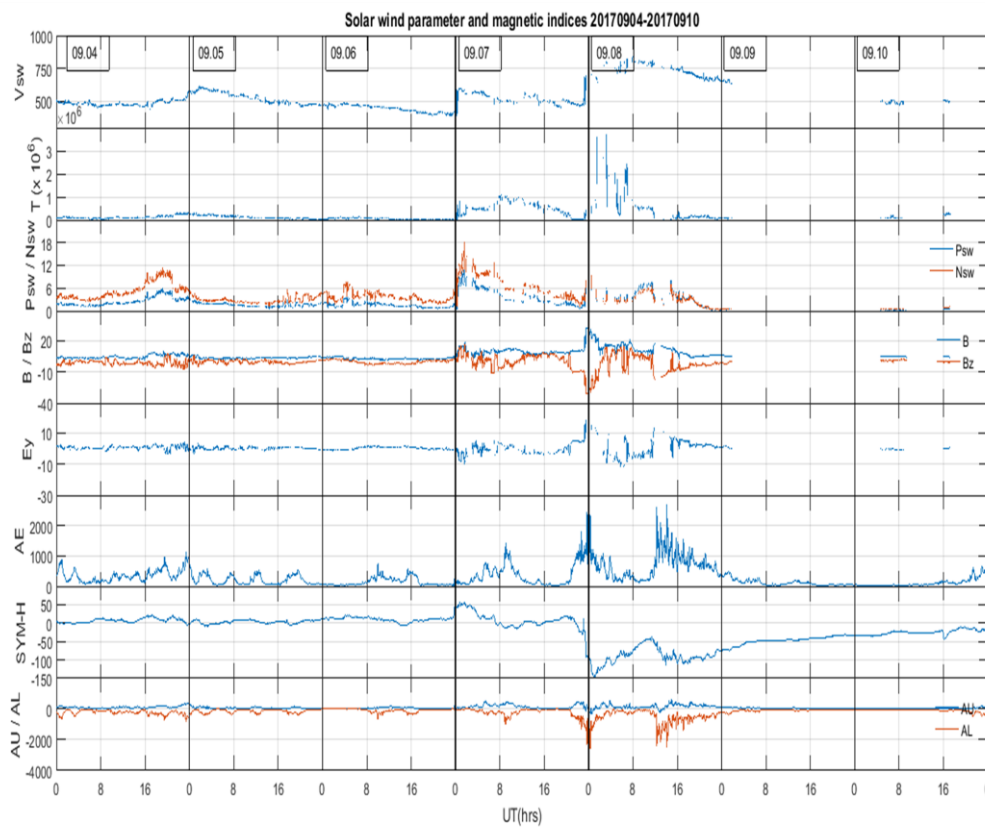

Fig. 2. From top to bottom shows the variations of solar wind speed (Vx in Km/s), temperature (T in K), pressure (Psw in nPa), plasma density (Nsw in cm^{-3}), total magnetic field (B, nT) interplanetary magnetic field IMF (Bz in nT), interplanetary electric field (Ey in mV/m), auroral index (AE in nT), SYM-H (in nT), aurora up (AU in nT) and aurora low (AL in nT) characterizing super substorm 4-10 September 2017 respectively.

3.3 Ionospheric responses

The ionospheric observations to the SSSs of 24 August 2005, 7 September 2017 and 8 September 2017 are shown in figure 3, 4 and 5 respectively. The dotted line in each figure represents the quiet day variation and the solid line represents ionospheric variability during SSSs. From the figure 3, it is observed the decrease in the foF2 but enhancement in h′ F and hmF2 during SSS of 24 August 2005 in compared with the quiet day. The

observed value of foF2, h′ F and hmF2 during SSS of 7 September 2017 is found higher than quiet day in figure 4. And in figure 5, the value of foF2 and hmF2 measured during SSS of 8 September 2017 higher than quiet day value but h′ F is observed lower than the quiet day. In 2015, Tsurutani [1] assumed that energy stored in magnetosphere/magnetotail during southward turning of IMF Bz released by plasma parcel during

SSSs result strongest ionospheric current during this events, potentially causing power outage on the Earth. Long term data 1981-2012 on SSSs was analyzed by Hajra [13] and found that SSSs can occurs in any phase of the solar cycle but it highest rate is 3.8 year^{-1} in the descending phase.
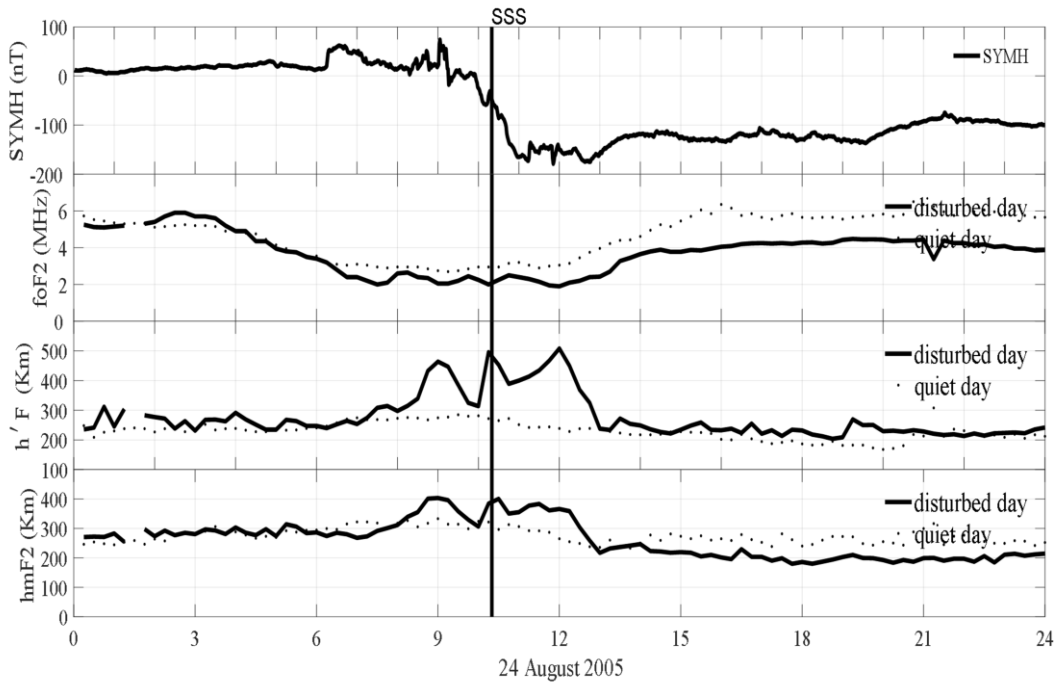

Fig. 3. Variation in SYMH (nT), critical frequency (foF2 in MHz), virtual height(h'F in Km) and height of peak electron density (hmF2 in Km). The dotted line represents the quiet day variation and the solid line represents the variations on the SSS day of 24 August 2005.
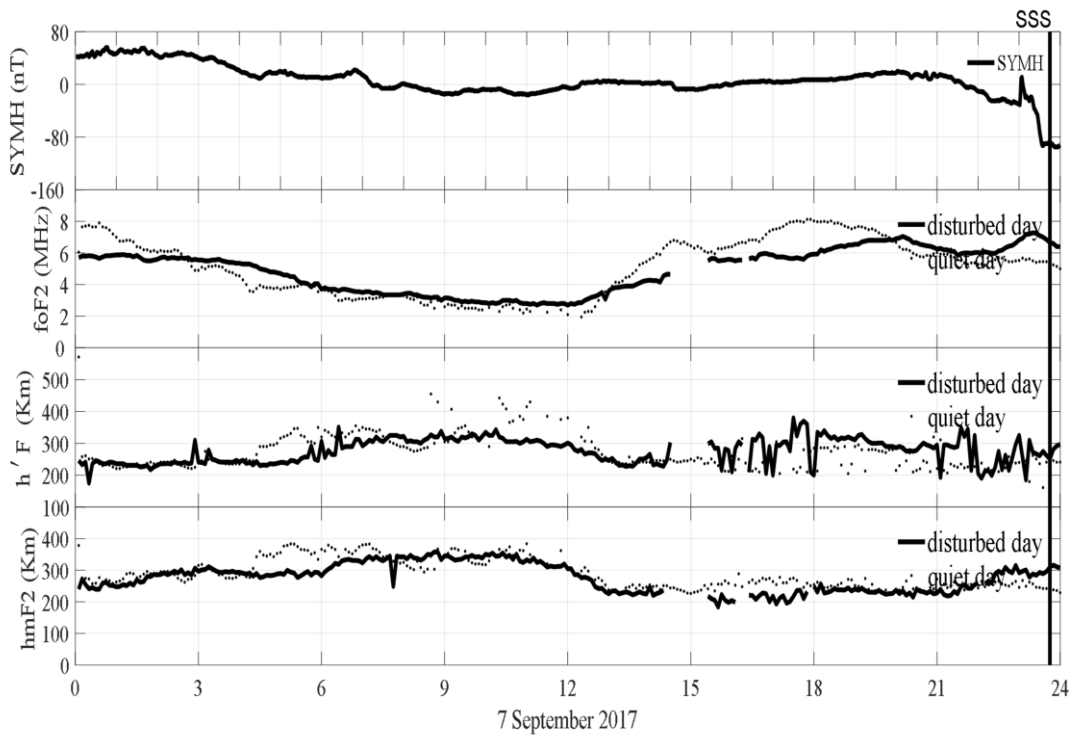

Fig. 4. Variation in SYMH (nT), critical frequency (foF2 in MHz), virtual height(h' F in Km) and height of peak electron density (hmF2 in Km). The dotted line represents the quiet day variation and the solid line represents the variations on the SSS day of 7 September 2017.

Fig. 5. Variation in SYMH (nT), critical frequency (foF2 in MHz), virtual height(h′ F in Km) and height of peak electron density (hmF2 in Km). The dotted line represents the quiet day variation and the solid line represents the variations on the SSS day of 8 September 2017.
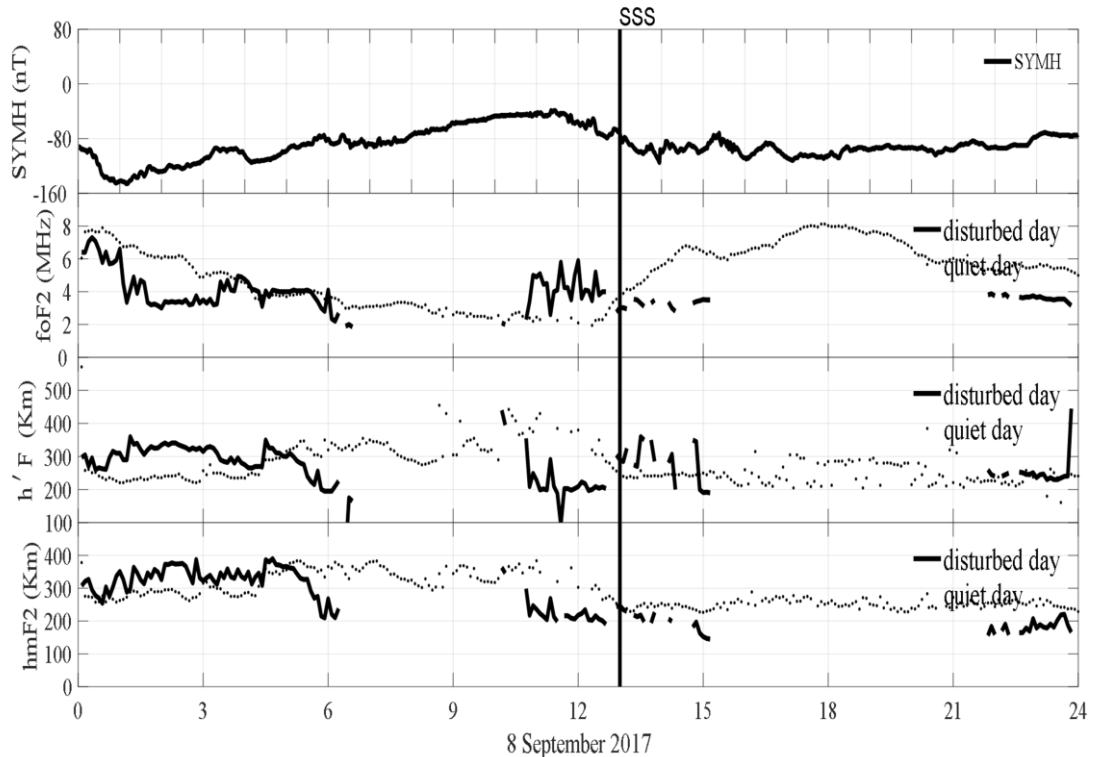
Their study shows the intensity of SSSs occurrence is independent to the intensity of magnetic storm and also found that the SSSs which occur during main phase of geomagnetic storm causes strong ionospheric current even at low latitude maycause of power outage on the Earth. A strong ionospheric current induces large fluctuation in $\frac{\partial B}{\partial t}$ in power transmission line induces GIC causes power outage during intense magnetic storm [1]. The study of polar cap potential and polar cap index during SSSs by Adhikari [15] found that polar cap potential and merging electric field are excitingly high and it is 20 time higher than the potential developed during HILDCAA. Their study further concluded that heavily increase in field aligned current during SSSs produces intense aurora which may disrupt and jammed the communication signals and large potential drop during these events may cause serious and rapid change in space weather condition. In total 131 SSSs event between 1998-2016 were studied by Despirak [18] and observed SSSs during interplanetary manifestation of coronal mass ejection ie sheeth (45.2%), magnetic cloud (42%) and ejecta (8.3%) none of the SSS event was identified during high speed streamer from coronal hole (CIR). The two SSSs

of 7 and 8 September 2017 was studied by Despirak [17] using SuperMAG electric field and found that the ionospheric current observed in global scale around the Earth during the event. In 2019, Poudel [22] studied the average energy deposited inside the magnetosphere during substorm (5.5199×10^{11} W), intense storm (5.3365×10^{11} W), HILDCAA (3.4618×10^{11} W), super substorm (1.0367×10^{12} W) and quiet day (5.8772×10^{10} W) found that the highest amount of energy deposited during super sub storm which may causes intense ionospheric storm to produced change in ionospheric parameters. The contribution of geomagnetic activity to ionospheric foF2 trends at different phases of the solar cycle was studied by Li [23] and found that the impact to the ionosphere is maximum during maximum geomagnetic activity, which usually happens in the declining phase of the solar cycle. The SSSs of 2005 and 2017 lay in the declining phase of the solar cycle 23 and 24.

The phenomena of positive and negative ionospheric strom causes increase and decrease in foF2 [24]. The positive and negative ionospheric storms effects are local time local time dependent [25, 26]. The change in neutral composition [27,

28] during geomagnetic storm influences negative ionospheric storm [29, 30, 31]. In 1993, Prolss [32] postulated that the positive ionospheric storm is caused by meridional wind negative ionospheric storm is caused by change in neutral composition. The energy deposited at polar latitude during geomagnetic storm produces a travelling ionospheric disturbance which superimpose with gravity waves and travel with high speed towards the equator causing day time positive ionospheric storm lifting daytime F2 layer to higher altitude. The energy deposited at polar latitude during solar wind may introduce compositional change which expands equator wards and produces F2 layer disturbance at middle latitude.

3.4 Continuous wavelet transform

Figure 6a, b and c represent scalogram for the critical frequency (foF2 in MHz), virtual height (h′ F in Km) and height of peak electron density (hmF2 in Km) during SSSs of 24 August 2005, 7 September 2017 and 8 September 2017. In the figures, the horizontal axis represents the time in hour and the vertical axis represents the periodicity in minutes. The amplitude represented in the plot whose color are demonstrated on the right side have units in their square for F2 layer critical frequency (foF2), virtual height (h′ F) peak density height (hmF2). The figure 6a show the power areas of the highest intensity more continuously at time scales approximately between 16-32 minutes during the SSS ~ 10:20 UT of 24 August 2005. In this region the background intensity is found to increased from 0.5 to 1.5 $(nT)^2$ foF2. Similarly, figures 6b and 6c the background intensity increased from 0.5 to 2 $(nT)^2$ in h′ F and 0.5 to 1.5 $(nT)^2$ in hmF2 respectively. This scalogram revels the change in foF2, h′ F and hmF2 during the SSS as result of energy deposited
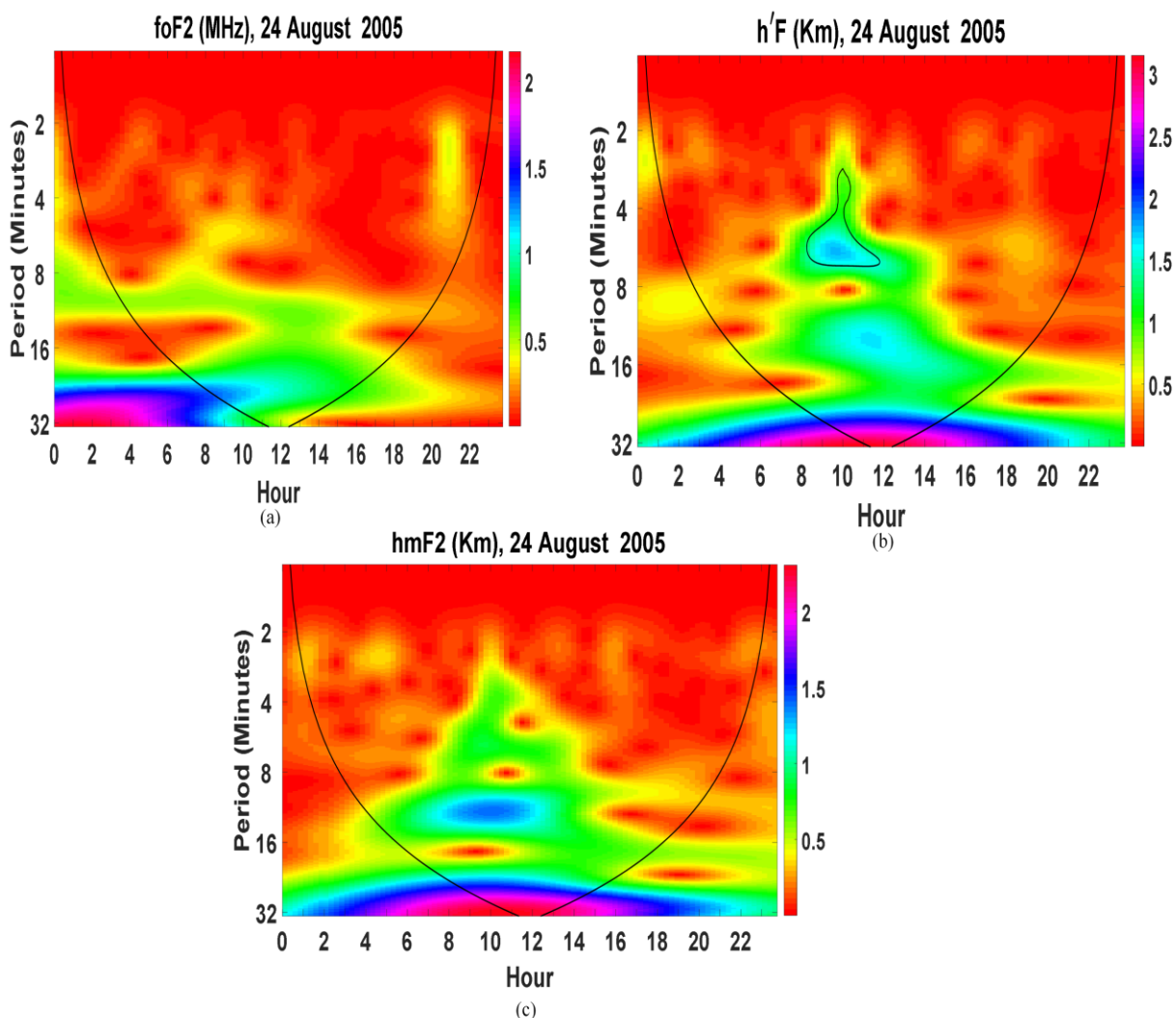

Fig. 6(a), (b) and (c) The scalogram of critical frequency (foF2 in MHz), virtual height(h′ F in Km) and height of peak electron density (hmF2 in Km) on the SSS day of 24 August 2005.

in magnetosphere-ionosphere by coupling mechanism between geomagnetic field and southward component of IMF Bz. The injected energy and charge particle causes sudden increase in inospheric current produces ionospheric storm along with variation in communication signal and power blackout in the Earth's surface. Figures 7a, b and c and the 8a, b and c are same as in figures 6a,b and c but it refers to the SSS events on 7 September 2017 and 8 September 2017. In figures 7a, b and c the power area of highest intensity is observed ~ 23:45 UT during SSS events with periods 27.9 to 64 minutes. The background intensity increased from 0.5 to 2 $(nT)^2$ for foF2, h′ F and hmF2 respectively. Similarly, the power

area of highest intensity is observed ~13:00 UT during SSS with periods 27.9 to 64 minutes. The background intensity for foF2 increased from 1 to 3 $(nT)^2$; for h′ F increased from 1 to 4 $(nT)^2$ and for hmF2 increases from 0.5 to 2 $(nT)^2$ respectively. This quiescent and non-quiescent periods identified in foF2, h′ F and hmF2 during southwards turning of IMF Bzis indicator of energy and particle injected during coupling mechanism between IMF Bz and geomagnetic field. In 2019, Bozhidar [32] analyzed large amount of heterogeneous data of geomagnetic indices, ionospheric parameters and IMF Bz using continuous wavelet transform and found the persistence of short-term period in it.
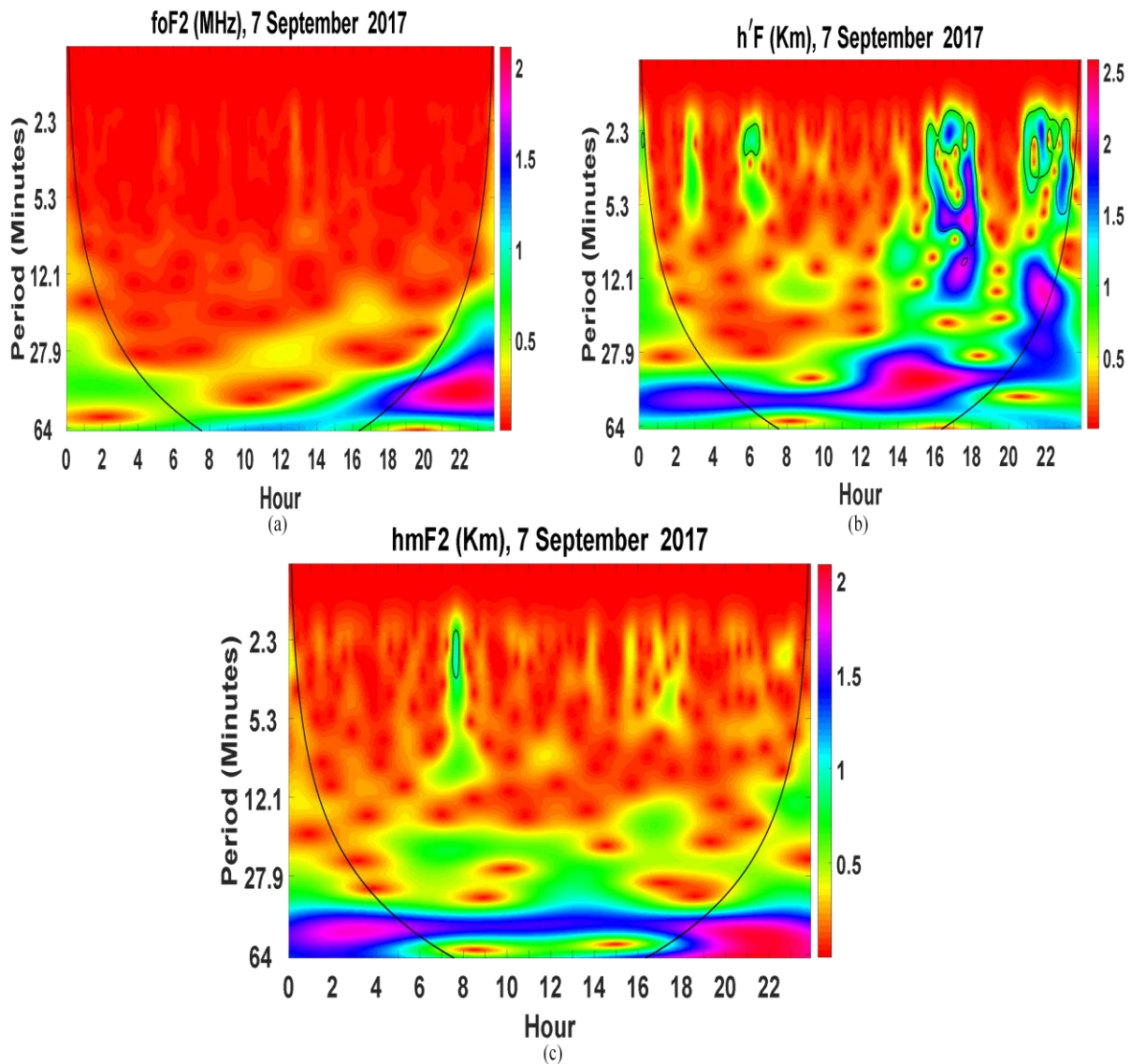

(a)

(b)

(c)

Fig. 7(a), (b) and (c) The scalogram of critical frequency (foF2 in MHz), virtual height (h′ F in Km) and height of peak electron density (hmF2 in Km) on the SSS day of 7 September 2017.
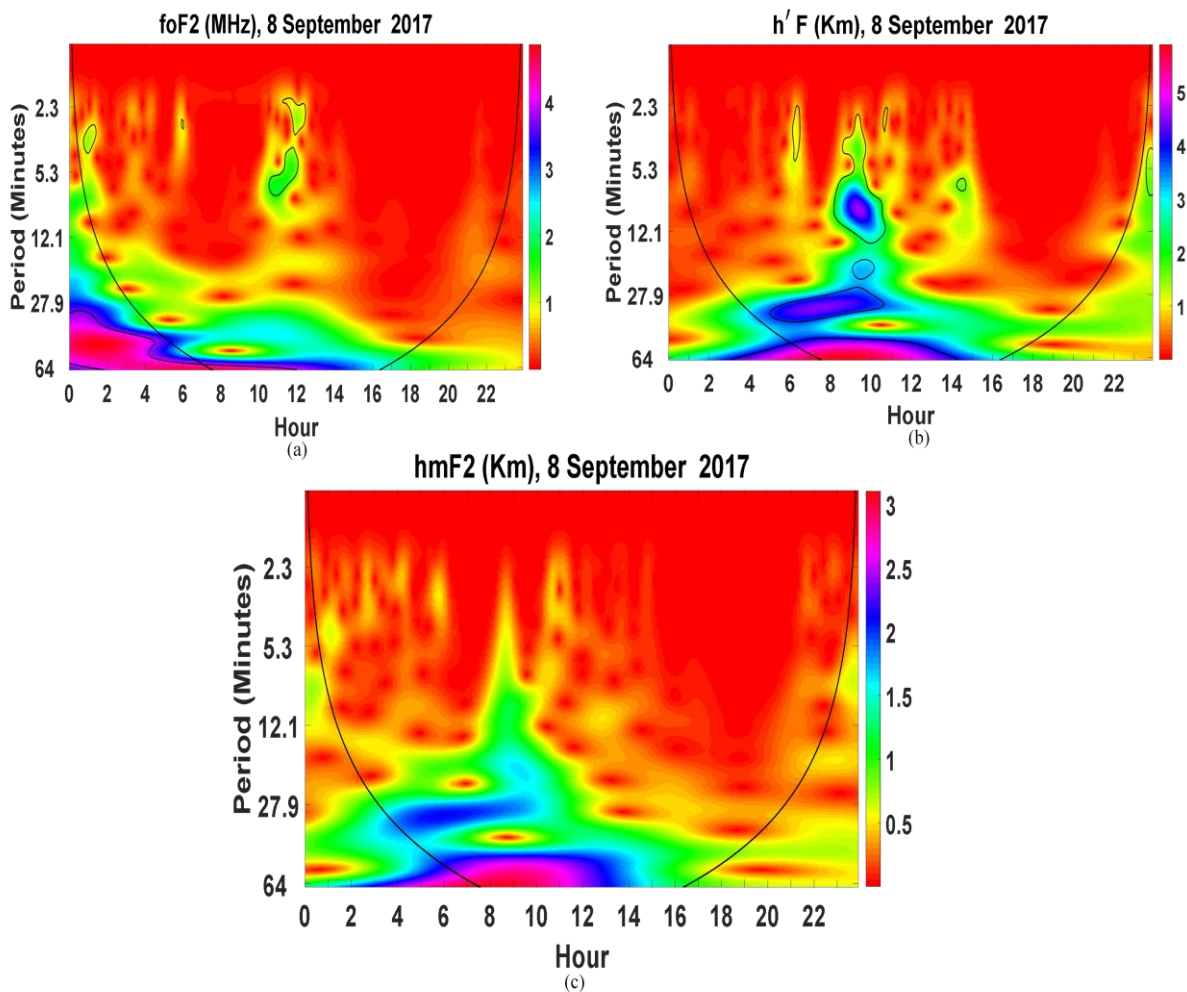
Fig. 8 (a), (b) and (c) The scalogram of critical frequency (foF2 in MHz), virtual height(h′ F in Km) and height of peak electron density (hmF2 in Km) on the SSS day of 8 September 2017.

4. CONCLUSION

The mid latitude ionospheric responses on F2 layer critical frequency (foF2), virtual height (h′ F) and peak height of electron density(hmF2) are analyzed using ionosonde data over Boulder, Colorado, USA (40°N, 1105.0° W) during super substorms of 24 August 2005, 7 September 2017 and 8 September 2017. The phenomena of decrease in foF2 during 24 August 2005 and 8 September 2017 SSSs caused by positive ionospheric storm and the increase in foF2 during SSS of 7 September 2017 caused by negative ionospheric storm was identified. The results of continuous wavelet transform (cwt) shows that the coupling between solar wind and magnetosphere occurs between ~16 to 32 minutes for SSS of 24 August 2005 and between 27.9 to 64 minutes during super substorm of 7 and 8 September 2017 for all the ionospheric parameters respectively. The highest fluctuation in h′F is noticed during SSS of 24 August 2005. This study provide concept of physical mechanism responsible for SSSs event which is still lacking and are in progress in scientific community. The global picture of SSSs can be obtained only after taking into account the ionospheric data from global stations.

ACKNOWLEDGEMENTS

REFERENCES

[1]   Tsurutani, B. T.; Hajra, R.; Echer, E.; & Gjerloev, J. W. Extremely intense (SML ≤ 2500 nT)

substorms: Isolated events that are externally triggered?, *AnGeo. Comm.*, **33**: 519–524 (2015).

[2] Lakshmi, D. R.; Veenabhari, B.; Dabas, R. S. & Reddy, B. M. Sudden post-midnigh decrease in equatorial F-region electron densities associated with severe magnetic storms. *Annales Geophysicae, European, Geosciences Union*, **5** (3): 306-313 (1997). hal-00316203.

[3] Pincheira, X. T.; Abdu, M. A.; Batista, I. S.; & Richards, P. G. An investigation of ionospheric responses, and disturbancethermospheric winds, during magnetic storms over South American sector, *J. Geophys. Res.,* **107** (A11): 1379 (2002).

[4] de Abreu, A. J.; Fagundes, P. R.; Bolzan, M. J. A.; de Jesus, R.; Pillat, V. G.; Abalde, J. R.; Lima, W. L. C. The role of the traveling planetary wave ionospheric disturbances on the equatorial F region post-sunset height rise during the last extreme low solar activity and comparison with high solar activity. *J. Atmos. Sol-Terr. Phys.,* **113**: 47–57 (2014c).

[5] de Abreu, A. J.; Fagundes, P. R.; Bolzan, M. J. A.; Gende, M.; Brunini, C.; de Jesus, R.; Pillat, V.G.; Abalde, J. R.; Lima, W. L. C. Traveling planetary wave ionospheric disturbances and their role in the generation of equatorial spread-F and GPS phase fluctuations during the last extreme low solar activity and comparison with high solar activity. *J. Atmo.s Sol-Terr. Phys.,* **117**: 7–19 (2014a).

[6] de Abreu, A. J.; Fagundes, P. R.; Gende, M.; Bolaji, O. S.; de Jesus, R.; Brunini, C. Investigation of ionospheric response to two moderate geomagnetic storms using GPS-TEC measurements in the South American and African sectors during the ascending phase of solar cycle 24. *Adv. Space Res.,* **53**: 1313–1328 (2014b).

[7] Rungraengwajiake, S.; Supnithi, P.; Tsugawa, T.; Maruyama, T.; Nagatsuma, T. The variation of equatorial spread-F occurrences observed by ionosondes at Thailand longitude sector. *Adv. Space Rec.*, **52**: 1809–1819 (2013).

[8] Smith, J. M.; Rodrigues, F. S.; de Palua, E. R. Radar and satellite investigations of equatorial evening vertical drifts and spread F. *Ann. Geophys.,* **33**: 1403–1412 (2015).

[9] Liu, G. Q. & Shen, H. A severe negative response of the ionosphere to the intense geomagnetic storm on March 17, 2015 observed at mid- and low-latitude stations in the China zone. *Adv. Space Res.* **59**: 2301–2312 (2017).

[10] Manju, G.; Devasia, C. V.; Sridharan, R. On the seasonal variations of the threshold height for the occurrence of equatorial spread F during solar minimum and maximum years. *Ann. Geophys.,* **25**: 855–861 (2007).

[11] Narayanan, V. L.; Gurubaran, S.; Berlin Shiny, M. B.; Emperumal, K. & Patil, P. T. Some new insights of the characteristics of equatorial plasma bubbles obtained from Indian region. *J. Atmos. Sol-Terr. Phys.,* **156**: 80–86 (2017).

[12] Narayanan, V. L.; Sau, S.; Gurubaran, S.; Shiokawa, K.; Balan, N.; Emperumal, K.; Sripathi, S. A statistical study of satellite traces and evolution of equatorial spread F, *Earth Planets Space,* **66**: 160 (2014).

[13] Hajra, R.; Tsurutani B. T.; Echer, E.; Gonzalez, W. D.; and Gjerloev, J. W. Supersubstorm (SML < _2500 nT) magnetic storm and solar cycledependences, *J. Geophys. Res. Space Physics*, **121**: 7805–7816 (2016).

[14] Adhikari, B.; Mishra, R. K.; Pandit, D.; Bhattarai, B.; and Chapagain, N. P. Ionospheric Effect of Non-Storm Hildcaa (High Intensity Long Duration Continuous Auroral Activity), *Journal of Institute of Science and Technology*, **22**: 2467-9240 (e) (2017c) ISSN: 2469-9062 (print).

[15] Adhikari, B. P.; Baruwal, P. and Chapagain, N. P. Analysis of supersubstorm events with reference to polar cap potential and polar capindex, *Earth Space Sci.*, **4**: 2–15 (2017a).

[16] Adhikari, B. S.; Dahal, S. and Chapagain, N. P. Study of field aligned current (FAC), interplanetary electric field component (Ey), interplanetary magnetic field component (Bz), and northward (x) and eastward (y) components of geomagnetic field during supersubstorm., *Earth and Space Science*, **4**: 257–274 (2017b). doi:10.1002/ 2017EA000258.

[17] Despirak, I.; Kleimenova, N.; Gromova, L.; Gromov, S.; and Malysheva, L. Supersubstorms during strong magnetic storm on 7 September 2017, *E3S Web of Conferences*, **127**: 01010 (2019). doi.org/10.1051/e3sconf/2019127010.

[18] Despirak, I. V.; Lubchich, A. A.; Kleimenova, N. G. Large-scale structure of solar wind and appearance of super substorms, *Physics of Auroral Phenomena, Proc. XLI Annual Seminar, Apatity,* 11-13 (2018). *Polar Geophysical Institute.*

[19] Tsurutani, B. T.; Lakhin, G. S.; and Hajra, R. The physics of space weather/solar-terrestrial physics (STP): what we know now and what the current and future challenges are. *Nonlin. Processes Geophys.*, **27**: 75–119 (2020).

[20] Daubechies, I. Ten lectures on wavelets [S.l.]: Society for Industrial and Applied Mathematics, PA, USA. (1992).

[21] Meyer, Y. Ondelettes Et Operateurs, Hermann, Paris (1990).

[22] Poudel, P.; Simkhada, S.; Adhikari, B.; Sharma, D.; & Nakarmi, J. J. Variation of solar wind parameters along with the understanding of

energy dynamics within the magnetospheric system during geomagnetic disturbances. *Earth and Space Science*, **6**: 276–293 (2019).

[23] Li, H.; Wang, J. S.; Chen, Z.; Xie, L.; Li, F. and Zheng, T. The contribution of geomagnetic activity to ionospheric foF2 trends at different phases of the solar cycle by SWM, *Atmosphere*, **11**: 616 (2020).

[24] Belehaki, A. and Tsagouri, I. Investigation of the relative bottomside/topside contribution to the total electron content estimates, *Annals of geophysics*, (2002). DOI: 10.4401/ag-3498.

[25] Prolss, G. W. Ionospheric F-region storms, in *Handbook of Atmospheric Electrodynamics*, 195-248 (1995). *II*, CRC Press.

[26] Rishbeth, H. How the thermospheric circulation affects the ionospheric F2-layer, *J. Atmos. Solar-Terr. Phys.* **60**: 1385-1402 (1998).

[27] Prolss, G. W.; Roemer, M. and. Slowey, J. W. Dissipation of solar wind energy in the earth's upper atmosphere: The geomagnetic activity effect, CIRA 1986, *Adv. Space Res.* **8** (5): 215-261 (1998).

[28] Mikhailov, A. V.; Yu, L.; Terekhin, M. G.; Skoblin, and Mikhailov, V. V. On the physical mechanism of the ionospheric storms in the F2-layer, *Adv. Space Res.,* **12** (10): 269-272 (1992).

[29] Cander, L. R. and Mihajlovic, S. J. Forecasting ionospheric structure during the great geomagnetic storms, *J. Geophys. Res.,* **103**: 391-398 (1998).

[30] Cander, L. R. On the global and regional behaviour of the mid-latitude ionosphere, *J. Atmos. Terr. Phys.* **55**: 1543-1551 (1993).

[31] Prolss, G. W. On explaining the local time variation of ionospheric storm effects, *Ann. Geophys.*, **11**: 1-9 (1993).

[32] Bozhidar, S.; Ognyan, K.; Georgi, S. Wavelet Analysis of Big Data in the Global Investigation of Magnetic Field Variations in Solar-Terrestrial Physics, arXiv:1905.12923v1 [physics.space-ph] (2019).

Lecture Series on

Research Methodology

6 November – 22 December 2017
Central Department of Physics
Tribhuvan University, Kirtipur, Nepal

Participation Certificate

Drabindra pandit

Central Department of physics T·U·

participated in **21 hours lecture series** on
Research Methodology delivered by **Prof. Dr. Subodh R. Shenoy,**
TIFR, India during 6 November to 22 December 2017.

Prof. Dr. Subodh R. Shenoy
Guest Speaker
Tata Institute of Fundamental Research, India

Prof. Dr. Binil Aryal
Head
CDP, TU, Kirtipur

IAU SYMPOSIUM 340
LONG TERM DATASETS FOR THE UNDERSTANDING OF
SOLAR AND STELLAR MAGNETIC CYCLES
19 - 24 FEBRUARY 2018
B. M. BIRLA AUDITORIUM, JAIPUR, INDIA

Certificate

This is to certify that **Drabindra Pandit** of **St. Xavier's College, Tribhuvan University, Kathmandu, Nepal** participated in the IAU Symposium 340 "Long Term Datasets for the Understanding of Solar and Stellar Magnetic Cycles" held at the B. M. Birla Auditorium, Jaipur, India during 19 – 24, February 2018. He/She presented a poster titled **Solar Activities and its Impact on Space Weather**.

Dipankar Banerjee
SOC and LOC Chair
IAU Symposium 340

The Abdus Salam
**International Centre
for Theoretical Physics**

IAEA

This is to certify that

Drabindra PANDIT

participated in and completed the

Workshop on
Space Weather Effects on GNSS Operations at Low Latitudes

Main Co-sponsors:
Institute for Scientific Research, Boston College, USA,
International Committee on GNSS, Institute of Navigation

23 April - 4 May 2018
ICTP, Trieste, Italy

Directors:
Patricia Doherty (Boston College),
Sandro M. Radicella (ICTP),
Bruno Nava (ICTP)
Local Organizer: Bruno Nava

Fernando Quevedo, Director

23RD INTERNATIONAL CONFERENCE OF INTERNATIONAL ACADEMY OF PHYSICAL SCIENCES

(CONIAPS XXIII)

On

Advances in Physical Sciences to Achieve Sustainable Development Goals

November 18, 2018

Organized by

NEPAL ACADEMY OF SCIENCE AND TECHNOLOGY, KATHMANDU, NEPAL

Certificate

This is to certify that Prof. /Dr./ Mr./Ms. ....Deabindea Pandit........ central......

Department of ...Physics..., T.U., nepal... has participated in the 23rd International Conference of International Academy of Physical Sciences on Advances in Physical Sciences to Achieve Sustainable Development Goals held at Nepal Academy of Science and Technology during November 16-18, 2018 and delivered Invited Lecture/Chaired a Session/ Presented a paper /Presented a paper in Young Scientist Award Category.

Title of the Invited Lecture/Paper ...variation in solar wind velocity under super intense gemagnetic storms........

Prof. P. N. Pandey	Dr. Buddhi Ratna Khadge	Ms. Ramila Raut
General Secretary	Convenor	Organizing Secretary
IAPS	CONIAPS XXIII	CONIAPS XXIII
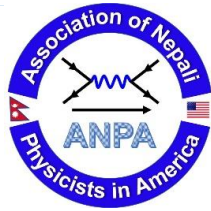
Certificate of Appreciation

THIS CERTIFICATE IS PRESENTED TO

MR. DRABINDRA PANDIT

Tribhuvan University, Nepal

FOR YOUR PRESENTATION DURING THE ANPA CONFERENCE 2020
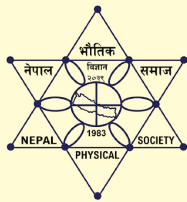
DR. CHET R. BHATT
CHAIR, ANPA CONFERENCE 2020

DR. SHREE K. BHATTARAI
PRESIDENT, ANPA

Nepal Physical Society

Ghantaghar, Kathmandu

Certificate of Participation

This certificate is awarded to

Mr. Drabindra Pandit **from**

Central Department of Physics, TU, Kirtipur for his successful participation in

NPS School of Computing - 2020

Conducted from July 4, 2020 to January 31, 2021.

....
Prof. Dr. Narayan Prasad Chapagain
President
Nepal Physical Society

....
Dr. Sunil Babu Shrestha
Chief Guest
Vice – Chancellor, NAST

....
Dr. Dibakar Sigdel
Instructor
Data Scientist, UCLA, USA

February 6, 2021

Nepal Physical Society

Ghantaghar, Kathmandu, Nepal

International Conference on Frontiers of Physics -2022
(ICFP-2022)

This Certificate of appreciation is awarded to

Drabindra Pandit

from IOST, Tribhuvan University, Nepal for his oral presentation on the

"Study of Total Electron Content (TEC) during year of Solar Cycles 23 and 24 at Jomsom, Nepal" in the

International Conference on Frontiers of Physics -2022

held on January 22-24, 2022 via virtual platform.

Prof. Dr. Narayan P. Chapagain

Conference Chair, ICFP-2022

President, Nepal Physical Society   February 1, 2022